



Delft University of Technology

## Coupling Harmonic Oscillators to Superconducting Quantum Interference Cavities

Corveira Rodrigues, I.C.

**DOI**

[10.4233/uuid:90c588b1-ebef-4ab8-b51f-b3221d8ad6cc](https://doi.org/10.4233/uuid:90c588b1-ebef-4ab8-b51f-b3221d8ad6cc)

**Publication date**

2021

**Document Version**

Final published version

**Citation (APA)**

Corveira Rodrigues, I. C. (2021). *Coupling Harmonic Oscillators to Superconducting Quantum Interference Cavities*. [Dissertation (TU Delft), Delft University of Technology]. <https://doi.org/10.4233/uuid:90c588b1-ebef-4ab8-b51f-b3221d8ad6cc>

**Important note**

To cite this publication, please use the final published version (if applicable).  
Please check the document version above.

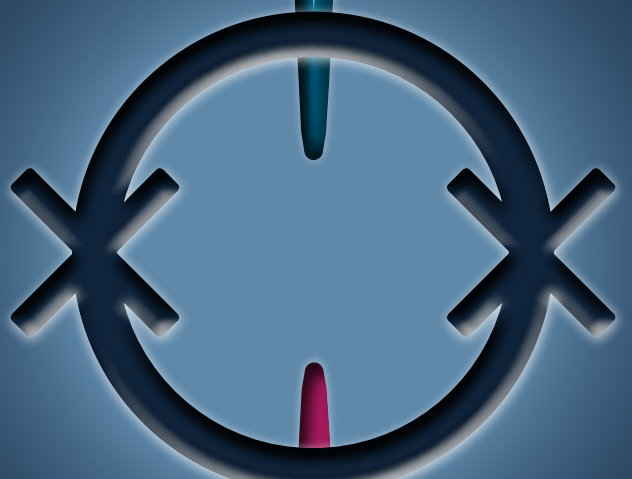
**Copyright**

Other than for strictly personal use, it is not permitted to download, forward or distribute the text or part of it, without the consent of the author(s) and/or copyright holder(s), unless the work is under an open content license such as Creative Commons.

**Takedown policy**

Please contact us and provide details if you believe this document breaches copyrights.  
We will remove access to the work immediately and investigate your claim.

# Coupling Harmonic Oscillators to Superconducting Quantum Interference Cavities



Inês C. Rodrigues



# **COUPLING HARMONIC OSCILLATORS TO SUPERCONDUCTING QUANTUM INTERFERENCE CAVITIES**

## **Dissertation**

for the purpose of obtaining the degree of doctor  
at Delft University of Technology  
by the authority of the Rector Magnificus Prof.dr.ir. T.H.J.J. van der Hagen,  
chair of the Board for Doctorates,  
to be defended publicly on  
Tuesday 25 May 2021 at 15:00 o'clock

by

**Inês Cristina CORVEIRA RODRIGUES**

Master of Science in Physics Engineering,  
University of Coimbra, Portugal,  
born in Coimbra, Portugal.

This dissertation has been approved by the promotores.

Composition of the doctoral committee:

Rector Magnificus,	chairperson
Prof. dr. G.A. Steele	Delft University of Technology, promotor
Prof. dr. S. Gröblacher	Delft University of Technology, promotor

Independent members:

Prof. dr. F Marquardt	Max Planck Institute, Germany
Prof. dr. G. Kirchmair	University of Innsbruck, Austria
Prof. dr. E. Verhagen	AMOLF, The Netherlands
Prof. dr. Y.M. Blanter	Delft University of Technology
Prof. dr. A.F. Otte	Delft University of Technology, reserve member



Delft  
University of  
Technology



*Printed by:* Gildeprint, Enschede

*Front & Back:* Illustration of a Radio-Frequency circuit (blue) and a mechanical resonator (violet) coupled to a Superconducting Quantum Interference Device.

Copyright © 2021 by I. C. Rodrigues

Casimir PhD Series 2021-08

ISBN 978-90-8593-474-5

An electronic version of this dissertation is available at  
<http://repository.tudelft.nl/>.

*To my family...*

*For their unconditional support and, for always believing in me.  
Even when I forget to believe in myself.*

*Para a minha família...*

*Pelo seu suporte incondicional e por sempre acreditarem em mim.  
Mesmo quando me esqueço de acreditar em mim própria.*



# CONTENTS

<b>Summary</b>	<b>xi</b>
<b>Samenvatting</b>	<b>xiii</b>
<b>1 Introduction</b>	<b>1</b>
1.1 Optomechanics: History and state of the art . . . . .	2
1.2 The motivation for flux-mediated optomechanics . . . . .	4
1.3 Beyond mechanical resonators as coupling elements . . . . .	6
1.4 Thesis outline . . . . .	7
<b>2 Theoretical background</b>	<b>9</b>
2.1 Harmonic oscillators . . . . .	10
2.1.1 Mechanical resonators . . . . .	10
2.1.2 LC resonators . . . . .	12
2.2 Superconducting QUantum Interference Device (SQUID) . . . . .	14
2.3 Hamiltonian of a SQUID cavity . . . . .	16
2.3.1 Impact of the Josephson non-linearity on energy levels . . . . .	19
2.4 SQUID cavity as a Duffing oscillator . . . . .	21
2.5 Radiation-Pressure coupling . . . . .	25
2.5.1 A general Hamiltonian . . . . .	25
2.5.2 Flux-mediated optomechanical coupling . . . . .	26
2.5.3 Photon-pressure coupling . . . . .	28
2.5.4 Optomechanical Kerr Hamiltonian . . . . .	30
2.5.5 Linearized Hamiltonian . . . . .	30
<b>3 Device design and fabrication</b>	<b>35</b>
3.1 Nano-bridge Josephson junctions . . . . .	36
3.2 2D and 3D SQUID Cavities . . . . .	38
3.2.1 Design considerations for SQUIDs with non-negligible loop inductance . . . . .	38
3.2.2 The kinetic inductance contribution . . . . .	41
3.2.3 Nanofabrication techniques . . . . .	42
3.3 Mechanical beams . . . . .	47
3.3.1 Maximizing $g_0$ in flux-mediated optomechanical systems . . . . .	47
3.3.2 Nanofabrication techniques . . . . .	51
3.4 RF microwave cavities . . . . .	52
3.4.1 Maximizing $g_0$ in photon-pressure systems . . . . .	52
3.4.2 Nanofabrication techniques . . . . .	57
3.5 The measurement challenge of SQUID cavities: Flux noise . . . . .	59

<b>4 Coupling microwave photons to a mechanical resonator using quantum interference</b>	<b>65</b>
4.1 Introduction . . . . .	66
4.2 Concept and device . . . . .	67
4.3 Interferometric characterization of the mechanical oscillator . . . . .	69
4.4 Tuning the optomechanical single-photon coupling rate . . . . .	71
4.5 Supplementary Information . . . . .	75
4.5.1 Device fabrication . . . . .	75
4.5.2 Measurement setup . . . . .	76
4.5.3 Cavity characterization . . . . .	79
4.5.4 Mechanical characterization . . . . .	88
4.5.5 Optomechanical device characterization . . . . .	92
<b>5 Four-wave-cooling to the single phonon level in Kerr optomechanics</b>	<b>99</b>
5.1 Introduction . . . . .	100
5.2 The device . . . . .	101
5.3 Driven Kerr-modes and dynamical Kerr backaction . . . . .	102
5.4 Multi-tone dynamical four-wave backaction . . . . .	106
5.5 Blue-detuned four-wave cooling close to the quantum ground-state . . . . .	108
5.6 Discussion . . . . .	111
5.7 Supplementary Information . . . . .	112
5.7.1 Device fabrication . . . . .	112
5.7.2 Measurement setup . . . . .	114
5.7.3 Power calibration . . . . .	117
5.7.4 The SQUID Cavity . . . . .	118
5.7.5 The optomechanical single-photon coupling rate . . . . .	124
5.7.6 The driven Kerr cavity . . . . .	125
5.7.7 Linearized Kerr optomechanics . . . . .	132
5.7.8 Equations of motion for linearized multi-tone Kerr optomechanics .	140
5.7.9 Three-tone dynamical Kerr backaction . . . . .	144
5.7.10 Four-wave OMIT . . . . .	147
5.7.11 Measurement and data analysis protocol for four-wave OMIT and four-wave dynamical backaction. . . . .	150
5.7.12 Data for OMIT and dynamical backaction on the red sideband of the signal resonance . . . . .	152
5.7.13 Multi-tone Kerr optomechanics with noise input . . . . .	152
5.7.14 Measurement and analysis protocols for thermal noise detection and four-wave cooling . . . . .	159
5.7.15 Thermal calibration of the residual mechanical phonon occupation . . . . .	166
5.7.16 Four-wave-cooling with a pump on the red sideband of the signal resonance . . . . .	167

---

<b>6 Photon-pressure strong-coupling between two superconducting circuits</b>	<b>169</b>
6.1 Introduction . . . . .	170
6.2 Concept and device . . . . .	172
6.3 Dynamical backaction between two circuits . . . . .	173
6.4 From photon-pressure induced transparency to the parametric strong-coupling regime . . . . .	175
6.5 Observation of photon-pressure-amplified thermal radio-frequency photons . . . . .	177
6.6 Discussion . . . . .	179
6.7 Supplementary Information . . . . .	180
6.7.1 Device fabrication . . . . .	180
6.7.2 Measurement setup . . . . .	182
6.7.3 The LF resonator . . . . .	186
6.7.4 The HF SQUID cavity . . . . .	187
6.7.5 Response functions and fitting routine . . . . .	193
6.7.6 Parametrically coupled LC oscillators . . . . .	194
6.7.7 Detection and amplification of thermal noise . . . . .	202
<b>7 Photon-pressure coupling with a hot radio-frequency circuit in the quantum regime</b>	<b>205</b>
7.1 Introduction . . . . .	206
7.2 Concept and device . . . . .	206
7.3 Characterization of the photon-pressure interaction . . . . .	209
7.4 Photon-pressure sideband cooling . . . . .	210
7.5 Normal-mode thermometry and ground-state cooling . . . . .	213
7.6 Discussion . . . . .	215
7.7 Supplementary Information . . . . .	215
7.7.1 Device fabrication . . . . .	215
7.7.2 Measurement setup . . . . .	218
7.7.3 The circuit model and flux dependence . . . . .	220
7.7.4 Response functions and fitting routine . . . . .	223
7.7.5 Zero-point fluctuations $\Phi_{\text{zpf}}$ and coupling rate $g_0$ . . . . .	225
7.7.6 Photon-pressure sideband cooling . . . . .	227
7.7.7 Temperature calibration . . . . .	230
7.7.8 Cooling the RF mode with increased thermal occupancy . . . . .	232
7.7.9 Theory of normal-mode thermometry . . . . .	233
7.7.10 System parameters for normal-mode thermometry . . . . .	234
<b>8 Conclusion</b>	<b>237</b>
<b>Acknowledgements</b>	<b>241</b>
<b>Curriculum Vitæ</b>	<b>247</b>
<b>List of Publications</b>	<b>249</b>
<b>References</b>	<b>251</b>



# SUMMARY

Optomechanical systems have become the leading platform for the manipulation and exploration of mechanical motion, both in the classical and quantum regimes. The research field where optical or microwave light is parametrically coupled to the displacement of a mechanical oscillator is rapidly evolving and has allowed for major breakthroughs in the last decades. Nevertheless, a large scope of the field still remains experimentally unexplored due to the difficulty in enhancing the optomechanical single-photon coupling strength and to freely target the natural frequency and quality factor of mechanical resonators.

This thesis focuses on two major branches which withstand these limitations. The first branch targets the experimental exploration of *flux-mediated optomechanical coupling* and the second, focuses on the implementation of an equivalent interaction between two superconducting circuits, which we refer to as *photon-pressure coupling*. Since both schemes can reach single-photon coupling strengths orders of magnitude larger than the current state of the art, the development of these two new platforms gives the field of optomechanics new resources for the investigation of unexplored regimes. Moreover, as the photon-pressure interaction allows for the quantum manipulation of superconducting RF circuits, whose quality factor and resonance frequency can be accurately targeted, the recently developed coupling scheme represents a first step towards radio-frequency quantum photonics.

**Chapter 1** will give a broad introduction to the field of optomechanics and present the goals and technological applications of realizing a *flux-mediated optomechanical coupling* and a *photon-pressure coupling*.

**Chapter 2** will provide the necessary tools for the theoretical understanding of the systems investigated in this thesis. It starts with a basic description of the main ingredients of our devices, i.e. the mechanical oscillator, the LC circuit and the Superconducting Quantum Interference Device (SQUID). After discussing the SQUID cavity Hamiltonian, the chapter will present a theoretical description of the radiation pressure interaction and explain the working principle of the platforms mentioned above.

**Chapter 3** focuses on the design and fabrication of the devices explored in this thesis. The section will describe the design considerations of nano-bridge SQUID cavities and will present the nanofabrication techniques utilized for the realization of SQUID cavities, of mechanical oscillators and of radio-frequency LC circuits. In addition, it will show how the explored platforms can be designed in a way which maximizes their respective

single-photon coupling strength  $g_0$  and presents an overview of the experimental challenges linked to flux-noise.

**Chapter 4** will be the first to show experimental results obtained in this thesis, where a *flux-mediated optomechanical system* was designed, fabricated and measured. Here, the reader can find a description of the working principle of a SQUID cavity coupled to a mechanical beam, a characterization of this optomechanical interaction and the experimental demonstration of the single-photon coupling strength  $g_0$  flux-tunability.

**Chapter 5** presents a blue-detuned sideband cooling technique in a *flux-mediated optomechanical system* by means of a strongly driven SQUID cavity. The section explores the behavior of the parametrically driven cavity, models the observed Kerr backaction effects and utilizes the regime of non-degenerate parametric amplification to implement a blue-detuned sideband-cooling scheme based on intracavity four-wave-mixing, achieving a final phonon occupancy of  $\sim 1.6$ .

**Chapter 6** demonstrates the implementation of a photon-pressure coupling between two superconducting circuits and shows the effects of *dynamical backaction* as well as *photon-pressure induced transparency* (PPIT). In addition, the chapter shows how the system can be brought into the *strong coupling regime* by flux-tuning the single-photon coupling strength  $g_0$  and demonstrates the detection of amplified RF thermal current fluctuations by means of a two-mode squeezing interaction.

Finally, **chapter 7** presents an optimized *photon-pressure system*, where the circuit geometry was modified to dramatically increase the single-photon coupling rate. It demonstrates how dynamical backaction can be utilized between the two circuits to remove thermal excitations of the RF mode and cool it to its *quantum ground-state*. Furthermore, in this experiment we present a *normal-mode thermometry* analysis, show that the system reaches the regime of *quantum coherent coupling*, where the multi-photon coupling rate  $g$  overcomes the cavity decay rate and the thermal decoherence rate of the RF mode, and achieve a single-photon quantum cooperativity of  $C_{q0} \sim 1$ .

**Chapter 8** will finalize the discussion presented in this thesis with a short overview of the performed investigations and of their possible impact on the future of microwave optomechanics and quantum technologies along with some personal insights on the future directions of these systems.

# SAMENVATTING

Optomechanische systemen zijn het leidende platform geworden voor de manipulatie en verkenning van mechanische beweging, zowel in de klassieke als in de kwantumregimes. Het onderzoeksgebied waar optisch of microgolflicht parametrisch wordt gekoppeld aan de verplaatsing van een mechanische oscillator, evolueert snel en heeft de afgelopen decennia grote doorbraken mogelijk gemaakt. Desalniettemin blijft een groot deel van het veld nog niet experimenteel bestudeerd vanwege de moeilijkheid om de optomechanische koppelingssterkte van een enkel foton te verbeteren en om de natuurlijke frequentie en kwaliteitsfactor van mechanische resonatoren goed te kunnen controleren.

Dit proefschrift concentreert zich op twee takken die deze beperkingen kunnen weerstaan. De eerste tak richt zich op de experimentele verkenning van flux-gemedieerde optomechanische koppeling, en de tweede richt zich op de implementatie van een gelijkwaardige interactie tussen twee supergeleidende circuits, die we foton-drukkoppeling noemen. Aangezien beide schema's enkel-foton koppelingssterktes kunnen bereiken die ordes groter zijn dan de huidige beste, geeft de ontwikkeling van deze twee nieuwe platforms het veld van de optomechanica middelen voor het onderzoek van nieuwe regimes. Bovendien vertegenwoordigt het recentelijk ontwikkelde koppelingsschema een eerste stap in de richting van radiofrequentie kwantumfotonica waarvan de kwaliteitsfactor en resonantiefrequentie nauwkeurig kunnen worden bepaald, aangezien de foton-druk interactie de kwantummanipulatie mogelijk maakt van supergeleidende RF-circuits.

**Hoofdstuk 1** zal een brede inleiding geven op het gebied van optomechanica en de doelen en toepassingen presenteren van het realiseren van een flux-gemedieerde optomechanische koppeling en een foton-druk koppeling.

**Hoofdstuk 2** zal de nodige hulpmiddelen bieden voor het theoretisch begrip van de systemen die in dit proefschrift worden onderzocht. Het begint met een basisbeschrijving van de belangrijkste ingrediënten van onze apparaten, namelijk de mechanische oscillator, het LC-circuit en het Superconducting Quantum Interference Device (SQUID). Na bespreking van de SQUID cavity Hamiltoniaan, zal dit hoofdstuk een theoretische beschrijving geven van de stralingsdrukinteractie en het werkingsprincipe van de bovengenoemde platforms toelichten.

**Hoofdstuk 3** richt zich op het ontwerp en de fabricage van de apparaten die in dit proefschrift worden onderzocht. Deze sectie beschrijft de ontwerppoverwegingen van

Nano-bridge SQUID-cavities en presenteert de nanofabricagetechnieken die worden gebruikt voor het maken van SQUID-cavities, van mechanische oscillatoren en van radiofrequentie LC-circuits. Bovendien zal het laten zien hoe de onderzochte platforms kunnen worden ontworpen op een manier die hun respectieve enkel-foton koppelingssterkte  $g_0$  maximaliseert en geeft het een overzicht van de experimentele uitdagingen in verband met fluxruis.

**Hoofdstuk 4** is de eerste hoofdstuk die experimentele resultaten laat zien die zijn verkregen in dit proefschrift, waarbij een flux-gemedieerd optomechanisch systeem werd ontworpen, gefabriceerd en gemeten. Hier kan de lezer een beschrijving vinden van het werkingsprincipe van een SQUID-cavity gekoppeld aan een mechanische balk, een karakterisering van deze optomechanische interactie en de experimentele demonstratie van de fluxafstembaarheid van de enkel-foton koppelingssterkte  $g_0$ .

**Hoofdstuk 5** presenteert een blauw-afgestemde zijbandkoelingstechniek in een flux-gemedieerd optomechanisch systeem door middel van een sterk aangedreven SQUID cavity. De sectie onderzoekt het gedrag van de parametrisch aangedreven holte, modelleert de waargenomen Kerr-terugwerkingseffecten en gebruikt het regime van niet-ontstaarde parametrische versterking om een blauw-afgestemde zijbandkoelingsschema te implementeren op basis van intracavitaire viergolfmenging, waardoor een fonon bezetting van  $\sim 1.6$  wordt bereikt.

**Hoofdstuk 6** demonstreert de implementatie van een foton-druk koppeling tussen twee supergeleidende circuits en toont de effecten van dynamische backaction en foton-druk geïnduceerde transparantie (PPIT). Daarnaast laat dit hoofdstuk zien hoe het systeem in het sterke koppelingsregime kan worden gebracht door flux-afstemming van de enkel-foton koppelingssterkte  $g_0$  en toont het de detectie van versterkte RF thermische stroomfluctuaties door middel van een twee-mode knijpinteractie.

Ten slotte presenteert **hoofdstuk 7** een geoptimaliseerd foton-druksysteem, waarbij de circuitgeometrie werd aangepast om de koppelingsnelheid van een enkel foton drastisch te verhogen. Het laat zien hoe dynamische backaction kan worden gebruikt tussen de twee circuits om thermische excitaties van de RF-modus te verwijderen en deze af te koelen tot zijn kwantumgrondtoestand. Bovendien presenteren we in dit experiment een normale modus thermometrieanalyse en laten we zien dat het systeem het regime van kwantumcoherente koppeling bereikt waarbij de koppelingsnelheid van meerdere fotonen  $g$  de vervalsnelheid van de holte en de thermische decoherentiesnelheid van de RF-modus overwint met een enkel-foton kwantumcoöperativiteit van  $C_{q0} \sim 1$ .

**Hoofdstuk 8** sluit de discussie af die in dit proefschrift wordt gepresenteerd met een kort overzicht van de uitgevoerde onderzoeken en hun mogelijke impact op de toekomst van microgolfoptomechanica en kwantumtechnologieën, samen met enkele persoonlijke inzichten over de toekomstige richtingen van deze systemen.

# 1

## INTRODUCTION

*Somewhere, something incredible is waiting to be known...*

Jules-Henri Poincare

*The chapter starts with a short historical summary of cavity optomechanics and the achievements accomplished by the field. It subsequently focuses on the technological opportunities associated with flux-mediated optomechanical systems and photon-pressure devices. At last, the chapter ends with the outline of this thesis.*

## 1

## 1.1. OPTOMECHANICS: HISTORY AND STATE OF THE ART

The exploration and utilization of the radiation-pressure force has walked a long developing path since the moment it was first proposed by Kepler in the 17th century [1], who noted that, when a comet is in transit, its dust tail points away from the sun.

Despite of this early realization, it was only more than two centuries later that these forces were explored in the context of cavity optomechanics. These advancements arose from the particular interest of Vladimir Braginsky in ultrasensitive interferometers for gravitational wave detection. Together with his interest, the emblematic picture of cavity optomechanics was born (see Fig. 1.1). From a simplified point of view, in these systems, the light field oscillating in an optical cavity is coupled to the motion of a mechanical oscillator and an experimental realization involving trapping light between a fixed and a movable mirror happened in 1983 [2].

By 1967, Braginsky and his colleagues could experimentally demonstrate the expected retardation effects of the radiation pressure force with the observation of damping and anti-damping of mechanical motion using a microwave cavity [3, 4]. These classical effects, which arise due to a finite cavity decay time, are known in literature as dynamical backaction are the key for radiation-pressure cooling/amplification techniques. Furthermore, some years later Braginsky also explored the fundamental limitations of the quantum fluctuations of the radiation-pressure force and their impact on the precision of displacement measurements [5, 6]. His and the theoretical work of Caves [7] on establishing the Standard Quantum Limit (SQL) became of extreme importance in gravitational wave detectors such as LIGO and VIRGO.

During the following decade, a lot of progressing work was done on the exploration of the optomechanical interaction. However, the typically achieved quality factors of the Fabry-Pérot cavities was restricting the prospect applications of optomechanics in the quantum regime. The development of nanofabrication techniques was therefore a fundamental tool to overcome these limitations, opening the door to another era of cavity optomechanics. It allowed, for example, for the engineering of optical microtoroid resonators, which, when containing mechanical modes were, earlier on, used to demonstrate radiation-pressure self-oscillations [8–10] and cavity cooling [11]. It also allowed for the development of micromirrors which were similarly used for the experimental demonstration of radiation-pressure cooling [12, 13]. After these initial promising demonstrations, the expansion towards new cavity optomechanical platforms had an exciting kick-off and systems such as membranes [14] and nanorods [15] coupled to Fabry-Pérot resonators, whispering gallery microdisks [16, 17] and microspheres [18–20], photonic crystals [21, 22], and evanescently coupled nanobeams [23] were realized.

A parallel competitor to such systems was the subfield of microwave optomechanics. The technological area where mechanical elements are embedded in superconducting resonant circuits, had gained independence and started to follow its own developing branch. Early demonstrations of this coupling approach were the insertion of a nanomechanical beam in a superconducting transmission line [24] or the incorporation of a flexible aluminum membrane into a lumped element superconducting resonator [25].

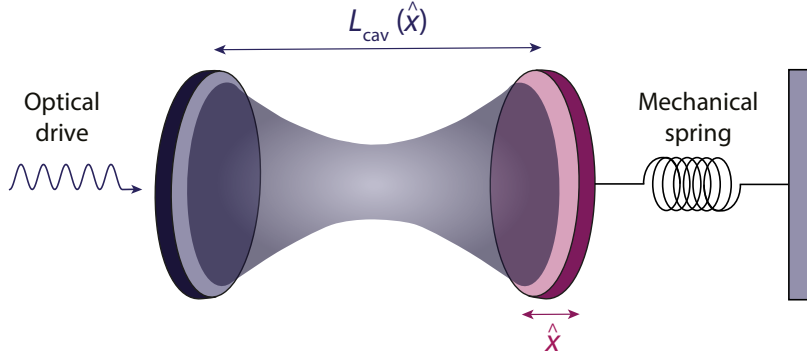


Figure 1.1: **Schematic representation of an optomechanical system.** Optical light is confined between two mirrors to form an oscillating light field with frequency  $\omega_0 = \pi c / L_{\text{cav}}$ , where  $c$  is the speed of light. As one of the mirrors acts a mechanical resonator, its displacement  $\hat{x}$  will modulate the cavity length  $L_{\text{cav}}(\hat{x})$  and therefore the resonance frequency of the electromagnetic mode.

Over the past 10 years, our increased understanding of these systems has allowed for major breakthroughs in the field. On one hand, a reduction of the bare mechanical decay rate due to a negative radiation-pressure damping allowed for microwave amplification [26], for the exploration of dynamical multistability [27, 28] and chaotic regimes [29, 30]. On the other hand, as the key for quantum control of mechanical displacements involves a significant reduction of their Brownian motion, the utilization of the positive backaction damping was the first step towards the performance of quantum operations.

The first demonstrations of radiation pressure ground state cooling go back to 2011 with both a microwave [31] and optical cavity [32] and later on brought systems into the regime of quantum coherent coupling [33, 34]. Furthermore, a comparable scheme was also used recently to cool a levitated nanosphere to its quantum ground state [35]. Once close to the quantum regime, i.e. once the mean phonon number is reduced to nearly a single excitation, experiments such as the generation of non-classical mechanical states of motion [36–38] were made possible. In addition, the radiation-pressure coupling has also allowed for the entanglement of mechanical oscillators [39, 40] and for the detection of mechanical displacement with an imprecision below the standard quantum limit [41–43]. Furthermore, measuring the randomness associated with back-action forces when detecting the position of a mechanical element [44], also known as photon shot noise was another benchmark of the field. Besides the advancements in the control of mechanical motion, the optomechanical interaction offers the possibility for the entanglement of either optical [45] or microwave [46] modes and for the squeezing of light fields [47–50].

Finally, as the radiation-pressure interaction allows mechanical degrees of freedom to be simultaneously coupled to both optical and microwave fields, many efforts have been made to use nano-mechanical resonators as a quantum link between superconducting microwave quantum processors and optical frequency quantum communication [51–54]. An extended discussion concerning the progress and central physical concepts of optomechanics can be found in Refs. [55–57].

## 1

## 1.2. THE MOTIVATION FOR FLUX-MEDIATED OPTOMECHANICS

The ability of optomechanics to measure and control the motion of mechanical resonators with masses varying from  $10^{-20}\text{g}$  to kilograms makes it an excellent platform to pursue quantum state preparation, control and characterization of macroscopic objects. A peculiar feature of this interaction is that the coupling between motion and the cavity fluctuations can be enhanced by coherently driving the system, which thereby increases the collective coupling strength  $g = \sqrt{n_c}g_0$ . Up to now, all the breakthroughs achieved by optomechanical systems relied on enhancing  $g$  by significantly increasing the cavity photon number  $n_c$ . This has allowed our community not only to reach the *strong coupling regime* [25, 58, 59] where  $g > \kappa$ , but also the *ultra-strong coupling regime* [60], where  $g \sim \Omega_0$ . However, in spite of these fruitful achievements this approach has several drawbacks, as for example, heating the mechanical mode far above the mode temperature in the optical domain [61] or non-equilibrium cavity noise in the microwave operation range [31, 62]. These sources of noise strongly restrict the achievable cooling limit and the possibility for mechanical quantum ground state preparation.

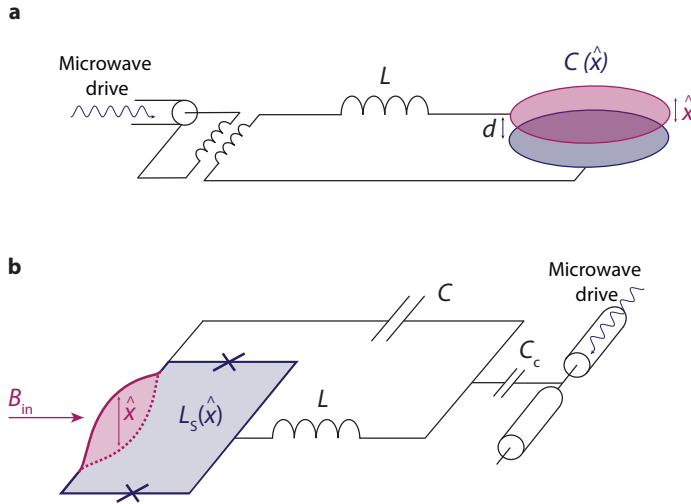


**Figure 1.2: Schematic representation of two distinct coupling schemes in microwave optomechanical systems.** **a** shows a schematic representation of a capacitive coupling scheme. Here, the top plate of a parallel plate capacitor is suspended to form a mechanical resonator. As the gap  $d$  between the two plates is varied due to the motion of the top plate, the circuit capacitance  $C(\hat{x})$  and therefore its resonance frequency  $\omega_0 = 1/\sqrt{LC(\hat{x})}$  will be modulated. In **b**, a schematic representation of a flux-mediated optomechanical coupling is shown. Here, the motion of a mechanical resonator will modify the total flux threading a Superconducting Quantum Interference Device (SQUID) in the presence of an in-plane magnetic field. As the SQUID is a flux-tunable non-linear element, its inductance is modulated by the oscillating mechanical beam  $L_S(\hat{x})$ . When incorporated in a microwave cavity, the resonance frequency of the LC circuit  $\omega_0 = 1/\sqrt{(L + L_S(\hat{x}))C}$  is parametrically modulated.

An approach to counter these limitations would be to boost the single-photon cou-

pling strength  $g_0$ , such that an increment of the cavity photon number would no longer be required. Ultimately, reaching the *single-photon strong coupling regime* [63], where  $g_0$  is larger than the cavity decay rate  $\kappa$  and the mechanical frequency  $\Omega_0$  would provide major advances in quantum state preparation of mechanical modes. The regime where a single cavity photon translates into a static mechanical displacement similar or greater than its zero point motion, would allow for the preparation of non-Gaussian mechanical states directly by coherently driving the system [63, 64]. Furthermore, this regime has been the inspiration for proposals such as the preparation of macroscopic mechanical cat states [65, 66] or the observation of photon blockade [67] as the condition  $\frac{2g_0^2}{\Omega_0} > \kappa$  is fulfilled.

Within the field of microwave optomechanics, most of the engineered devices so far focused on a capacitive coupling between mechanical motion and superconducting cavity modes (see Fig. 1.2a). In these systems, in order to maximize the single-photon coupling rate, the gap  $d$  between the capacitor plates has to be reduced as much as possible. Despite of great efforts in this direction, the most optimized devices have gaps of  $d \sim 50\text{ nm}$  and  $x_{\text{zpf}}/d \approx 10^{-7}$ . This technological barrier imposed by the difficult optimization of superconducting capacitive elements therefore limited the achieved single-photon coupling strengths to  $g_0 \approx 300\text{ Hz}$  [38], which is far from the single-photon strong coupling regime when considering that typical cavity linewidths and mechanical frequencies are on the order of hundreds of kHz and a few MHz, respectively.

Several proposals to further optimize the optomechanical single-photon coupling rate  $g_0$  in microwave systems were recently published [68–70] and they involved an alternative perspective regarding the circuit element which is modulated by mechanical motion. There the coupling relies on an inductance modulation instead of the typical capacitive approach. As seen in Fig. 1.2b, a possible way to engineer a flux mediated optomechanical system relies on a flux-tunable non-linear element, also known as Superconducting Quantum Interference Device (SQUID). When part of the SQUID loop is free to oscillate, forming a mechanical resonator, this motion will modulate the SQUID inductance and therefore the cavity resonance frequency. In chapters 4 and 5 of this thesis, an experimental demonstration of this new coupling concept will be presented. Proving itself to be an exciting route for the community, similar coupling schemes were reported shortly after the publication of the results presented in chapter 4. These include an optomechanical system where a cantilever containing a magnetic tip was utilized to modulate the resonance frequency of a SQUID cavity [71], or where a SQUID containing a mechanical beam was incorporated in a CoPlanar Waveguide (CPW) microwave resonator [72]. Furthermore a slightly different scheme, where a mechanical beam was coupled to a Transmon qubit was realized by Ref. [73].

In spite of the potential of using flux-mediated optomechanical systems to boost the single-photon coupling strength  $g_0$ , SQUID cavities have an intrinsic property which is typically considered a drawback: their Kerr non-linearity. In chapter 2, a discussion regarding the non-linearity of a SQUID cavity and its impact on the upper bound of drive photons the cavity can sustain before switching to a non-linear behavior will be presented. In contrast to a linear microwave cavity coupled to a mechanical element, the maximum drive-enhanced coupling strength in a flux-mediated optomechanical system

will be limited by the cavity non-linearity. As a large multi-photon coupling strength  $g$  is essential for several schemes such as quantum ground state cooling or quantum state transfer, engineering a system which boosts  $g_0$  without imposing a low threshold on  $n_c$  would add great value to the field of optomechanics. Therefore, one of the main efforts of this thesis was to design a flux-mediated optomechanical system with a large single-photon coupling strength  $g_0$  while still minimizing the cavity non-linearity. For information regarding the optimization of  $g_0$  in these systems, see section 3.3.1. Interestingly, even though the anharmonicity of the electromagnetic mode can be considered an undesired property by the field of optomechanics, when finely tuned it could also represent an additional resource to the radiation pressure interaction for the manipulation and control of mechanical motion. This innovative concept is explored in detail in chapter 5.

### 1.3. BEYOND MECHANICAL RESONATORS AS COUPLING ELEMENTS

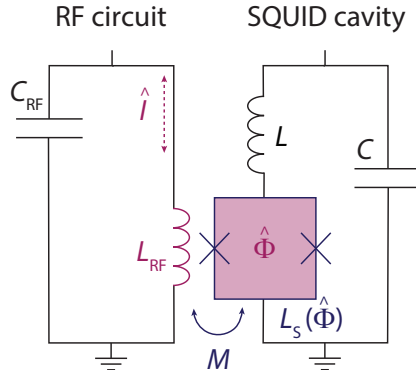


Figure 1.3: **Schematic representation of a photon-pressure system.** The oscillating current  $\hat{I}$  flowing in a radio-frequency LC circuit generates a magnetic field which couples to a Superconducting QUantum Interference Device (SQUID) via the mutual inductance  $M$ . As the SQUID is part of a second LC circuit, the oscillating magnetic flux  $\hat{\Phi}$  threading its loop will modulate the SQUID inductance  $L_S(\hat{\Phi})$  and subsequently generate a parametric modulation of the SQUID cavity resonance frequency  $\omega_0 = 1/\sqrt{(L + L_S(\hat{\Phi}))C}$ .

In spite of the radiation-pressure coupling being mostly explored in the context of a photon-phonon interaction between harmonic oscillators, it is in fact not exclusive of optomechanical systems. This interaction has been recently explored, for instance, in nanomechanical systems to dynamically control the coupling of the different modes of a mechanical resonator [74–77] and it has also been theoretically and experimentally explored in the context of superconducting circuits [78–81].

The advantages of the implementation of such coupling scheme between superconducting circuits are numerous. Since they profit from an extremely high design flexibility and precision in engineering resonance frequencies and quality factors, this platform could allow for the experimental investigation of new parameter regimes which are un-

conventional in standard optomechanical systems. Regimes such as reversed dissipation [82], reversed resonance frequency [83] or even the optomechanical single-photon strong coupling regime [63, 67] would be easily at reach.

Thrivingly, its potential applications are not constrained to the classical regime. As superconducting microwave resonators have demonstrated to be an excellent platform for quantum information and sensing technologies, photon-pressure systems operating in the quantum regime could enrich this rapidly developing field with quantum-limited parametric amplifiers [26, 82, 84–86], non-reciprocal devices [87–90] and photonic reservoir engineering [91, 92] as well as bosonic code quantum information processing using grid states [93]. In addition, photon-pressure coupled circuits could attain inspiration from the field of optomechanics to pursue RF-mediated generation of squeezed and entangled microwaves [46, 48], the generation of non-classical RF states [36], entanglement of distinct RF circuits [40] and the detection of current fluctuations below the standard quantum limit [43]. As shown in Fig. 1.3, this thesis presents a photon-pressure coupling platform where the resonance frequency of a SQUID cavity is coupled to the current flowing in a linear LC circuit (see section 2.5.3). This platform is utilized in chapter 6 to observe dynamical backaction between the two circuits, to parametrically amplify thermal RF current fluctuations and reach the *strong coupling regime* where  $g > (\kappa + \Gamma)/2$ , with  $\Gamma$  being the total decay rate of the RF mode. Furthermore, by developing an optimized design to considerably increase the single-photon coupling rate we cooled a hot RF circuit to the quantum ground-state while entering the strong coupling regime. The latter work is presented in chapter 7.

Equivalently to flux-mediated optomechanical systems, having a photon-pressure system which boosts the single-photon coupling strength  $g_0$  without restricting the maximum intracavity photon number  $n_c$  would be a major advantage and remarkably widen the range of applications of the system. Therefore, equivalent efforts were made along this thesis to optimize the single-photon coupling strength  $g_0$  while reducing the non-linearity of the SQUID cavities to be incorporated in photon-pressure systems. In addition to the discussion of the non-linearity of a SQUID cavity given in chapter 2, a short discussion regarding the design optimization for maximizing  $g_0$  in photon-pressure coupled system is given in section 3.4.1.

## 1.4. THESIS OUTLINE

This thesis is organized as follows. **Chapter 2** starts by providing the necessary theoretical tools for the understanding of the underlying physical principles of the systems experimentally explored in this thesis. **Chapter 3** brings focus to the design considerations required for the engineering these systems, as well as the different nanofabrication techniques explored for their realization. In **chapter 4** the reader can find a first experimental demonstration of a flux-mediated optomechanical system and in **chapter 5** the demonstration of blue-detuned sideband cooling by means of a parametrically driven SQUID cavity coupled to a nanobeam. Furthermore, in **chapters 6** and **7** show the realization of a photon-pressure coupling using two superconducting LC circuits. In short, **chapter 6** shows photon-pressure strong coupling between the two circuits and **chapter 7** demonstrates ground-state sideband cooling of a hot RF circuit.



# 2

## THEORETICAL BACKGROUND

*Imagination is more important than knowledge.*

Albert Einstein

*This chapter will provide the necessary theoretical tools for the understanding of the systems which are experimentally studied in the subsequent chapters. Along with mathematical descriptions, an intuitive idea of their physical interpretation will be provided as often as possible. The chapter starts with both a classical and a quantum description of mechanical and LC oscillators, followed by a short introduction to Superconducting QUantum Interference Devices (SQUIDs) and a quantization method of a circuit containing a non-linear Josephson element in series with a linear inductance. After presenting the Hamiltonian of a SQUID cavity and discussing its deviation from a harmonic oscillator, the system will be modeled as a classical Duffing oscillator. Finally, a theoretical description of an optomechanical system, followed by an explanation of the working principle of flux-mediated optomechanics and photon-pressure systems will be provided. The chapter ends with the linearization of an optomechanical Hamiltonian containing a Kerr non-linearity.*

## 2.1. HARMONIC OSCILLATORS

### 2.1.1. MECHANICAL RESONATORS

#### CLASSICAL DESCRIPTION

## 2

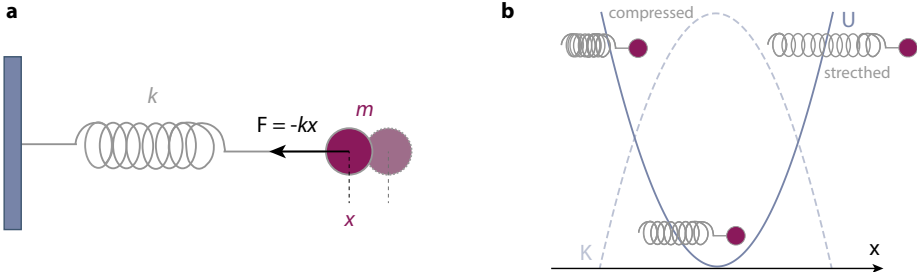


Figure 2.1: **Spring-mass system representation of a mechanical harmonic oscillator.** a The oscillator of mass  $m$ , which is represented by the violet element, is under a restoring force  $F = -kx$  arising from its attachment to a spring with stiffness coefficient  $k$ . The position  $x$  of the oscillator will oscillate around a equilibrium position as the spring is stretched or compressed from its relaxed position. The total energy is given by the kinetic ( $K$ ) and potential ( $U$ ) energy contributions which are plotted versus  $x$  in Fig. b.

The classical Hamiltonian of a mechanical oscillator is described in terms of the variables  $x$  and  $p$ , which respectively correspond to the position and momentum of an object of mass  $m$  under the restoring force  $F = -kx$ , where  $k$  is defined as the spring constant. The classical Hamiltonian, which describes the total energy of the system, is written as

$$H = \frac{p^2}{2m} + \frac{1}{2}m\Omega_m^2 x^2, \quad (2.1)$$

with  $\Omega_m = \sqrt{k/m}$  being the natural oscillation frequency. In the above expression, the first term corresponds to the potential energy and the second to the kinetic energy of the system. Based on the Hamilton equations

$$\dot{x} = \frac{\partial H}{\partial p} = \frac{p}{m} ; \quad \dot{p} = -\frac{\partial H}{\partial x} = -m\Omega_m^2 x \quad (2.2)$$

we can write the equation of motion of the mechanical resonator as

$$\ddot{x} + \Omega_m^2 x = 0. \quad (2.3)$$

Furthermore, in order to model the oscillator in the presence of dissipation to a thermal bath, we introduce a damping force in Eq. (2.3), proportional to the oscillator instantaneous velocity  $F = -\Gamma_m \dot{x}$ . The modified equation of motion

$$\ddot{x} + \Gamma_m \dot{x} + \Omega_m^2 x = 0 \quad (2.4)$$

describes a damped harmonic oscillator where  $\Gamma_m$  is the mechanical decay rate. Furthermore, when probing the system, an external driving force  $F_e = \frac{F_0}{m} e^{-i\Omega t}$  needs to be

taken into account. By re-writing the equation of motion in frequency space, we obtain the steady state solution

$$x_0 = \frac{1}{m[\Omega_m^2 - \Omega^2 - i\Omega\Gamma_m]} F_0 \quad (2.5)$$

from where we define the mechanical susceptibility as

$$\chi_m(\Omega) = \frac{1}{m[\Omega_m^2 - \Omega^2 - i\Omega\Gamma_m]}. \quad (2.6)$$

### QUANTUM DESCRIPTION

In order to quantize the motion of a mechanical oscillator, we switch to a quantum description of the system described above by following the method of canonical quantization first introduced by Dirac [94]. We start by replacing the canonical set of variables  $x, p$  by the quantum operators

$$\hat{x} = x \ ; \ \hat{p} = p \quad (2.7)$$

with the commutation relation  $[\hat{x}, \hat{p}] = i\hbar$ . The quantum Hamiltonian, with similar form to the one of Eq. (2.1), can now be written as a function of the newly introduced operators

$$\hat{H} = \frac{\hat{p}^2}{2m} + \frac{1}{2} m\Omega_m^2 \hat{x}^2. \quad (2.8)$$

Even though Eq. (2.8) provides a quantum description of a mechanical harmonic oscillator, it is of interest to write a general Hamiltonian which is independent of the chosen canonical variables. For this purpose, we introduce the annihilation and creation operators,  $\hat{b}$  and  $\hat{b}^\dagger$ , which are defined as function of  $\hat{x}$  and  $\hat{p}$  as

$$\hat{b} = \sqrt{\frac{m\Omega_m}{2\hbar}} \left( \hat{x} + \frac{i}{m\Omega_m} \hat{p} \right) \quad (2.9)$$

$$\hat{b}^\dagger = \sqrt{\frac{m\Omega_m}{2\hbar}} \left( \hat{x} - \frac{i}{m\Omega_m} \hat{p} \right) \quad (2.10)$$

with the commutation relation  $[\hat{b}, \hat{b}^\dagger] = 1$ . Note that, since the operators are not hermitian, they do not represent any physical variables. However, any operator with observable eigenvalues can abstractly be written as function of  $\hat{b}$  and  $\hat{b}^\dagger$ .

By re-writing  $\hat{x}$  and  $\hat{p}$  as function of  $\hat{b}$  and  $\hat{b}^\dagger$ , the Hamiltonian of a mechanical oscillator takes the general form

$$\hat{H} = \hbar\Omega_m \left( \hat{b}^\dagger \hat{b} + \frac{1}{2} \right). \quad (2.11)$$

By using the number operator  $\hat{n} = \hat{b}^\dagger \hat{b}$  and the time independent Schrödinger equation  $\hat{H}|\Psi\rangle = E|\Psi\rangle$  we can formulate the energy eigenvalues of this Hamiltonian based on the number of phonons  $n$  in the resonator  $E = \hbar\Omega_m(n + \frac{1}{2})$ . This expresses how the Hamiltonian eigenstates  $\Psi$ , also known as *Fock states* are arranged in discrete levels and equally split in energy. Additionally, this quantum picture describes a system which is

never at rest as it will always possess a finite energy, even when it is left in the absence of phonons (*vacuum state*) also known as zero-point energy, given by  $\hbar\Omega_m/2$ .

If the harmonic oscillator (as a bosonic system) is in thermal equilibrium with its bath, the particle distribution among the available set of discrete energy levels follows the Bose-Einstein statistics. The average phonon occupancy  $\bar{n}$  of the resonator is then given by

$$\bar{n} = \frac{1}{e^{\hbar\Omega_m/k_b T} - 1}, \quad (2.12)$$

where  $k_b$  is the Boltzmann constant and  $T$  is the bath temperature. The mechanical resonators studied in this thesis were typically thermalized with our dilution fridge temperature, which could be minimized to  $\approx 15\text{ mK}$ . With resonance frequencies usually ranging from 5 to 20 MHz, the occupancy of our beams would be close to hundreds of phonons, placing the resonator in a thermal state. Nevertheless, techniques such as optomechanical sideband cooling could, in principle, be utilized to reduce their thermal phonon occupation, ultimately placing the resonator in the quantum ground state  $\bar{n} < 1$ .

### 2.1.2. LC RESONATORS

An essential tool in the field of microwave optomechanics is the LC circuit. Since these circuits can currently be engineered via nanofabrication to have extremely low dissipation rates, they have become a key element in the design of more advanced and complex systems. Therefore, understanding the working principle of a LC harmonic oscillator is of evident importance.

#### CLASSICAL DESCRIPTION

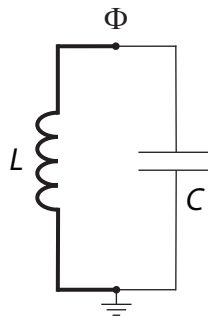


Figure 2.2: Circuit diagram of an LC oscillator where its elements are connected via two circuit nodes (Represented by •).

Fig. 2.2 shows a circuit diagram of an LC oscillator. In addition to the inductive and capacitive elements, identified as  $L$  and  $C$ , respectively, one can also find two circuit nodes. One of the nodes defined as ground node at the bottom of the circuit and an active node on the upper side. The nodes are the linking points between the branches that contain the circuit elements, creating the circuit network. Following the method of nodes, described in detail in Ref.[95], a unique path connecting the ground and active node, known as spanning tree, should be chosen.

When choosing the inductor as the linking element and therefore as the unique path, one can define the flux of the active node  $\Phi$  as the integral of the voltage  $V$  across its branch over time

$$\Phi = \int_{-\infty}^t V(t) dt. \quad (2.13)$$

Note that the lower integration value  $-\infty$  represents the case where the circuit was completely at rest and  $V(t = -\infty) = 0$ . Due to the simplicity of the circuit configuration, one can easily obtain the system Lagrangian as function of the previously defined node flux, as

$$L = \frac{C\dot{\Phi}^2}{2} - \frac{\Phi^2}{2L}. \quad (2.14)$$

Furthermore, by performing a Legendre transformation, that, for a system with a single degree of freedom, is given by

$$H = \dot{\Phi} \frac{\partial L}{\partial \dot{\Phi}} - L \quad (2.15)$$

and by introducing the charge variable as function of the branch voltage  $Q = C\dot{\Phi}$ , we obtain an expression for the total energy of the circuit

$$H = \frac{Q^2}{2C} + \frac{\Phi^2}{2L}. \quad (2.16)$$

An intuitive interpretation for the previous expression is by thinking of the total circuit energy as a combination of the electrical energy stored by the capacitor and magnetic energy stored by inductor.

### QUANTUM DESCRIPTION

The quantum version of the classical Hamiltonian of Eq. (2.16) is once again constructed by replacing the canonical variables  $Q$  and  $\Phi$  by the quantum operators  $\hat{Q}$  and  $\hat{\Phi}$ , with the canonical commutation relation  $[\hat{Q}, \hat{\Phi}] = i\hbar$  and it takes the form

$$\hat{H} = \frac{\hat{Q}^2}{2C} + \frac{\hat{\Phi}^2}{2L}. \quad (2.17)$$

If one compares the expression (2.17) to the Hamiltonian of the mechanical oscillator given by Eq. (2.8), one can quickly find the analogy between the operators position  $\hat{x}$  and flux  $\hat{\Phi}$  and the operators momentum  $\hat{p}$  and charge  $\hat{Q}$ . Here it becomes evident that the circuit behaves equivalently to a mass-spring system in a harmonic potential, but where the mass  $m$  is replaced by the capacitance  $C$  and the spring constant  $k$  by the inverse of the inductance  $1/L$ . Another way to represent the LC oscillator Hamiltonian can be obtained by the introduction of the natural resonance frequency  $\omega_0 = 1/\sqrt{LC}$  and takes the form

$$\hat{H} = \frac{\omega_0^2 C}{2} \left( \frac{\hat{Q}^2}{C^2 \omega_0^2} + \hat{\Phi}^2 \right). \quad (2.18)$$

Here, the energy operator  $\hat{H}$  of the one-dimensional harmonic LC circuit can be written as a function of the annihilation and creation operators with commutation relation

$[\hat{a}, \hat{a}^\dagger] = 1$  as

$$\hat{H} = \hbar\omega_0 \left( \hat{a}^\dagger \hat{a} + \frac{1}{2} \right) \quad (2.19)$$

with

$$\hat{a} = \sqrt{\frac{\omega_0 C}{2\hbar}} \left( \hat{\Phi} + i \frac{\hat{Q}}{\omega_0 C} \right) \text{ and } \hat{a}^\dagger = \sqrt{\frac{\omega_0 C}{2\hbar}} \left( \hat{\Phi} - i \frac{\hat{Q}}{\omega_0 C} \right). \quad (2.20)$$

or equivalently

$$\hat{\Phi} = \Phi_{\text{zpf}} \left( \hat{a} + \hat{a}^\dagger \right) \text{ and } \hat{Q} = \frac{Q_{\text{zpf}}}{i} \left( \hat{a} - \hat{a}^\dagger \right), \quad (2.21)$$

where  $\Phi_{\text{zpf}} = \sqrt{\frac{\hbar}{2\omega_0 C}}$  and  $Q_{\text{zpf}} = \sqrt{\frac{\hbar\omega_0 C}{2}}$ .

## 2.2. SUPERCONDUCTING QUANTUM INTERFERENCE (SQUID)

### THE JOSEPHSON JUNCTION

Before diving into the working principle of Superconducting QUantum Interference Devices (SQUIDs) [96], let us bring up the definition of a Josephson junction. A Josephson junction is a link between two superconductors, weak enough so that the overlap between the individual wavefunctions of each superconducting electrode can allow for tunneling of Cooper pairs.

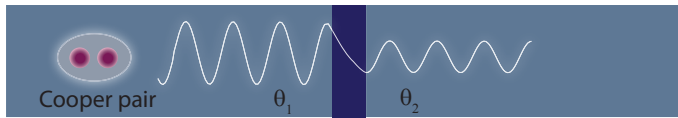


Figure 2.3: **Schematic representation of a Cooper pair tunneling through a non-superconducting barrier.** The Cooper pairs in each superconducting lead 1 and 2 (light blue areas) can be described by a common wavefunction  $\Psi_{1,2} = \sqrt{n_{1,2}} e^{i\theta_{1,2}}$  with phases  $\theta_1, \theta_2$  and number of particles  $n_1, n_2$ . As described by the first Josephson relation, the current flowing through the barrier depends on the phase difference between the superconducting electrodes.

The current flowing across a Josephson junction with a sinusoidal current-phase relation (CPR) is described by the first Josephson relation as

$$I(\varphi) = I_{c0} \sin(\varphi), \quad (2.22)$$

where  $I_{c0}$  is the maximum current that the junction can sustain before switching to the voltage state and  $\varphi = \theta_2 - \theta_1$  is the phase difference across the two superconducting leads (with phases  $\theta_2$  and  $\theta_1$ ). As a side note, a more extensive description about the type of junctions used in our devices is given in section 3.1.

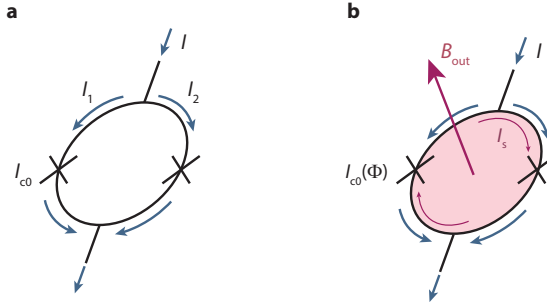


Figure 2.4: **Generation of a screening current by the SQUID when a magnetic field  $B_{\text{out}}$  is applied.** A schematic representation of a current biased SQUID in the absence (a) or presence (b) of a magnetic field applied out-of-plane with the device. In the absence of magnetic field, the transport current splits equally through both Josephson junctions (assuming two identical junctions of critical current  $I_{c0}$ ). In the presence of a magnetic field, the SQUID generates a screening current  $I_s$  in order to satisfy the fluxoid quantization principle, which leads to an effective reduction of the SQUID critical current  $2I_{c0}(\Phi)$ . The practical limitations arising from the generation of a screening current in SQUIDs with a large loop inductance is discussed in section 3.2.1.

## THE SQUID

A SQUID is defined as a superconducting loop containing two Josephson junctions in parallel. As shown in Fig. 2.4a, the current distribution in a SQUID operating in a zero voltage state, in the absence of a magnetic field is rather simple. Assuming it is formed by two Josephson junctions with a sinusoidal current phase relation and equal critical currents of  $I_{c0}$ , the total supercurrent passing through the SQUID is given by

$$I = I_1 + I_2 = I_{c0}(\sin\varphi_1 + \sin\varphi_2), \quad (2.23)$$

where  $I_1$  and  $I_2$  are the supercurrents flowing in each arm.

In addition, as the junctions are placed in a superconducting loop, in order to guarantee that the superconducting wavefunction is single-valued, the total phase change around the SQUID loop must always equal multiples of  $2\pi$ . Also known as fluxoid quantization, this boundary condition generates a correlation between the phase differences of the two Josephson junctions as

$$\varphi_2 - \varphi_1 = 2\pi \frac{\Phi}{\Phi_0} \quad (2.24)$$

where  $\Phi$  is the magnetic flux thread by the SQUID loop. The outcome of this principle becomes obvious when a magnetic field  $B_{\text{out}}$  is applied perpendicularly to the SQUID, creating a magnetic flux  $\Phi_{\text{out}}$ , as shown in Fig. 2.4b. In this case, the SQUID will generate a screening current  $I_s = \frac{I_{c0}}{2}(\sin\varphi_1 - \sin\varphi_2)$  which tries to compensate for the threading flux by adjusting the phase difference  $\varphi_2 - \varphi_1$  as required by Eq. (2.24). As it circulates around the loop, it will break the symmetry between the currents of the two arms as it increases the current of one arm while reducing it in the other but maintaining the relation of the total transport current given by Eq. (2.23). When dealing with a negligible loop

inductance, the total flux is given by  $\Phi = \Phi_{\text{out}}$  and the critical current  $I_c$  of the SQUID, which is given by the maximum value of the transport current can be written as

$$I_c(\Phi) = 2I_{c0} \left| \cos\left(\frac{\pi\Phi}{\Phi_0}\right) \right|. \quad (2.25)$$

Intuitively one can say that the fulfillment of the fluxoid quantization can be translated into an effective reduction of the SQUID critical current as the former will oscillate between a maximum value of  $2I_{c0}$  when  $\Phi/\Phi_0 = n\pi$  and 0 when  $\Phi/\Phi_0 = \frac{n\pi}{2}$ ,  $n \in \mathbb{Z}$ . Furthermore, the SQUID inductance can be written as

$$L_S(\Phi) = \frac{L_{j0}}{2 \left| \cos\left(\frac{\pi\Phi}{\Phi_0}\right) \right|}, \quad (2.26)$$

where  $L_{j0} = \frac{\Phi_0}{2\pi I_{c0}}$  is the Josephson inductance of a single junction.

In short, a Superconducting QUantum Interference Device is a flux-tunable element, whose variable inductance arises from the combination of the presence of non-linear Josephson junctions and the fulfillment of the fluxoid quantization condition in a superconducting loop. By incorporating a SQUID in a harmonic LC circuit, one can engineer a flux dependent resonant circuit with natural frequency  $\omega_0 = 1/\sqrt{L(\Phi)C}$  as its inductance now flux-tunable. Additionally, a description of the working principle of a SQUID with non-negligible loop inductance and its impact on the design of SQUID cavities is given in section 3.2.1.

### 2.3. HAMILTONIAN OF A SQUID CAVITY

As mentioned in chapter 1, the type of microwave cavities used in the systems presented in this thesis are not pure LC harmonic oscillators but they contain a Superconducting QUantum Interference Device (SQUID) placed in series with a linear inductor  $L$ . A SQUID, as described in section 2.2, is a superconducting loop containing two Josephson junctions in parallel, each of them having an inductance  $L_{j0}$ . When assuming a negligible loop inductance we can adopt a simplistic representation of the SQUID and replace it by a single Josephson junction of effective inductance  $L_j = L_S(\Phi)$ , as shown in Fig. 2.5.

As discussed in the beginning of section 2.2, a Josephson junction is physically described as a non-linear element, for which the current flowing across its terminals depends on the phase difference between the two superconducting leads. Its energy operator can be written as function of the gauge invariant phase difference as

$$\hat{H}_j = E_j [1 - \cos\hat{\varphi}], \quad (2.27)$$

where  $E_j = \Phi_0^2/4\pi^2 L_j$  is the Josephson energy,  $\Phi_0 = h/2e$  is the flux quantum. Here  $\hat{\varphi}$  is the gauge invariant phase difference, which is defined as a function of the flux  $\Phi$  of node 2 as  $\hat{\varphi} = \left( \frac{\Phi - \Phi_{\text{off}}}{\Phi_0} \right)$ . For simplicity, the flux offset  $\Phi_{\text{off}}$  will be set to a null value during the next steps. Furthermore, note that, the introduction of the phase difference operator can be intuitively understood as the degree of freedom of the junction is given by the

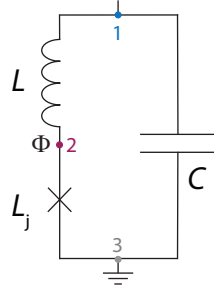


Figure 2.5: Simplified circuit diagram of a SQUID cavity with negligible loop inductance. In the presented system the SQUID inductance is  $L_j = L_S(\Phi)$ , as given by Eq. 2.26.

number of Cooper pairs flowing through the junction and not the total number of pairs in the circuit, as the latest is conserved.

In order to obtain the quantum Hamiltonian of the circuit, we continue with a *black box quantization method* [97], the same method used by the algorithm of the software QuCAT, described in detail in Ref.[98]. In this method, the junction is replaced by a parallel combination of a linear inductor of inductance  $L_j$ , a capacitance  $C_j$  and a non-linear element. The circuit is subsequently re-organized in order to evaluate the voltage  $V_j(\omega)$  generated when feeding an AC current  $I_j(\omega)$  across the junction terminals, as shown in Fig 2.6a.

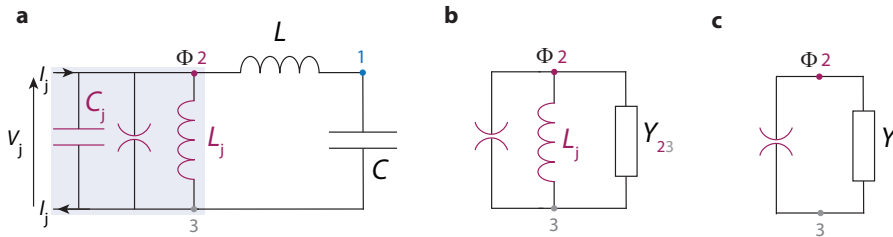


Figure 2.6: Modified circuit for the extraction of the admittance  $Y$ . a The Josephson junction is replaced by a linear inductor of  $L_j$ , linear capacitor  $C_j$  and a non-linear element. The voltage  $V_j(\omega)$  is measured across its terminals when applying a current  $I_j(\omega)$ . b Circuit simplification based on a star-mesh transformation to calculate the admittance  $Y_{23} = Y_L Y_C / (Y_L + Y_C)$  and remove node 1. c The linear part of the circuit is reduced to the total admittance  $Y = Y_{23} + Y_{Lj}$ .

The key of the approach is to pack all linear contributions of the circuit into a total admittance  $Y(\omega) = I_j(\omega) / V_j(\omega)$  and reduce the initial circuit to the one of Fig. 2.6c. For this, the circuit is initially simplified by removing the Josephson capacitance  $C_j$ , which is negligible for our circuits, and afterwards perform a star-mesh transformation to extract the admittance  $Y_{23}$  and remove node 1, as shown in Fig. 2.6b. The total admittance  $Y$  is

obtained as

$$Y = Y_{23} + Y_{1j} = \frac{1 - \omega^2 C(L + L_j)}{i\omega L_j(1 - \omega CL)}, \quad (2.28)$$

where the admittance of a circuit element is defined by the inverse of its characteristic impedance  $Y(\omega) = 1/Z(\omega)$ . The total admittance  $Y$  represented in Fig. 2.6c is, in fact, analogous to a parallel  $L_m C_m$  circuit which represents the mode of the circuit. The resonance frequency of the mode is extracted by evaluating the case for which  $Y(\omega) = 0$  and it has the form

$$\omega_m = \sqrt{\frac{1}{C(L + L_j)}}. \quad (2.29)$$

Furthermore, the mode capacitance  $C_m$  is given by

$$C_m = \frac{\text{Im}[Y'(\omega_m)]}{2} = C \left( \frac{L + L_j}{L_j} \right)^2 \quad (2.30)$$

and the mode inductance is obtained from the last two equations, as  $L_m = 1/(\omega_m^2 C_m)$ .

As one would intuitively think, the circuit Hamiltonian is given by a combination of the harmonic part of the circuit, which is described by the mode of admittance  $Y$  with resonance frequency  $\omega_m$  and a non-linear Josephson contribution expressed by the second term of the Hamiltonian

$$\hat{H} = \hbar\omega_m \left( \hat{a}^\dagger \hat{a} + \frac{1}{2} \right) + E_j \left[ 1 - \cos\hat{\phi} - \frac{\hat{\phi}^2}{2} \right]. \quad (2.31)$$

Let us emphasize that, since the quadratic contribution of the Josephson potential is already included in the extraction of the mode resonance frequency, this is subtracted from the Josephson contribution in expression (2.31).

When remembering the definition of the flux operator  $\hat{\Phi}$  based on the creation and annihilation operators given by Eq. (2.21) and by Taylor expanding the cosine function up the  $n^{\text{th}}$  order we can obtain the equivalent Hamiltonian

$$\hat{H} = \hbar\omega_m \left( \hat{a}^\dagger \hat{a} + \frac{1}{2} \right) - E_j \sum_2^n \frac{(-1)^n}{(2n)!} \left( \frac{\Phi_{\text{zpf}}(\hat{a} + \hat{a}^\dagger)}{\Phi_0} \right)^{2n}. \quad (2.32)$$

Furthermore, when only considering a second order Taylor expansion (which is valid for the small non-linear contributions existing in the devices under study in this thesis), we can take the resulting term depending on  $(\hat{a} + \hat{a}^\dagger)^4$  to be the only perturbation to the eigen-energies of the linear part of the Hamiltonian. Therefore, when computing  $\langle n | (\hat{a} + \hat{a}^\dagger)^4 | n \rangle$ , only the terms which conserve the number of excitations are kept and the previous expression is simplified to

$$\hat{H} = \hbar\omega_m \left( \hat{a}^\dagger \hat{a} + \frac{1}{2} \right) + \hbar \frac{\chi}{2} \left( (\hat{a}^\dagger \hat{a})^2 + \hat{a}^\dagger \hat{a} + \frac{1}{2} \right), \quad (2.33)$$

where  $\chi = -\frac{E_j}{\hbar} \left( \frac{\Phi_{zpf}}{\Phi_0} \right)^4$  is defined as the anharmonicity of the system arising from the non-linearity of the Josephson junction. Equivalently, the latest can also be written as a function of the original circuit parameters as

$$\chi = -\frac{e^2}{2\hbar C} \left( \frac{L_j}{L + L_j} \right)^3. \quad (2.34)$$

In the next section we will discuss the effect of this nonlinear contribution in the Hamiltonian to the energy levels of the oscillator.

### 2.3.1. IMPACT OF THE JOSEPHSON NON-LINEARITY ON ENERGY LEVELS

For a more intuitive understanding on the impact of the Josephson non-linearity on the circuit Hamiltonian let us consider the two examples described by Fig. 2.7.

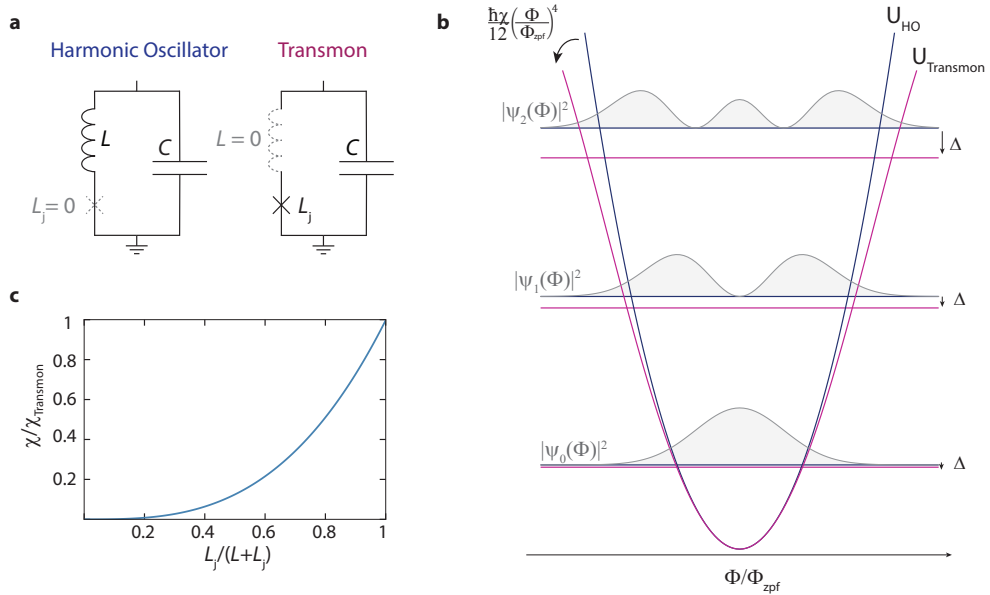


Figure 2.7: Comparison between the potential and the energy levels of a LC oscillator and a Transmon qubit. **a** Shows two circuit schematics, representing a harmonic oscillator and a Transmon qubit respectively on the left and right side. In **b**, the potential energy  $U$  of both circuits with respect to the normalized flux  $\varphi = \Phi/\Phi_{zpf}$ , together with the first three energy levels is shown. The deviation of the Transmon energy levels compared to the harmonic levels is given by  $\Delta = \chi \langle \varphi^4 \rangle / 12$  and therefore the shift is increased along the Fock state ladder. In addition, the probability distribution of the harmonic levels is also plotted on top of the respective lines. Figure **c** shows the anharmonicity as a function of inductance dilution, i.e., of the ratio between the Josephson inductance and the linear inductance. The anharmonicity is normalized to the Transmon case.

Fig. 2.7a shows two modifications to the circuit previously described. The first shows the case where the total inductance of the circuit is represented by the linear inductor

$L$  and there is a zero contribution of the Josephson junction. In this case, the circuit is well described as a pure LC oscillator. The second circuit represents the Transmon qubit (transmission-line shunted plasma oscillation qubit) [99, 100] which differs from the first case as the inductance of the circuit is completely expressed by  $L_j$ . Usually Transmon qubits work in a configuration where the Josephson junction is shunted with a large capacitance so that  $E_j/E_C \geq 50$ .

When plotting the potential energy of the harmonic circuit  $U = \frac{1}{2L_m}\Phi^2$  and of the Transmon circuit  $U = \frac{1}{2L_m}\Phi^2 + \frac{\hbar\chi}{12}\frac{\Phi^4}{\Phi_{zpf}^4}$  (see Fig. 2.7b), we see a clear modification arising from the anharmonicity  $\chi$ . The Transmon potential  $U_{\text{Transmon}}$  starts to gradually deviate from the harmonic potential  $U_{\text{HO}}$  for higher values of flux. This deviation from the harmonic behavior is, in fact, the key of the operation principle of the Transmon as a superconducting qubit. The energy levels of the Transmon eigenstates, represented by the horizontal violet lines in Fig. 2.7b are given by

$$\frac{E_n}{\hbar} = \omega_0 \left( n + \frac{1}{2} \right) + \chi \left( \frac{n^2}{2} + \frac{n}{2} + \frac{1}{4} \right). \quad (2.35)$$

Here the first term corresponds the energy levels of the LC harmonic oscillator, represented as dark blue lines in Fig. 2.7b. The second term represents the shift in the energy levels arising from the presence of a non-linear element of anharmonicity  $\chi$ , which increases for higher excitation numbers. In contrast with the HO, where all energy levels are equally spaced, the Transmon is analogous to an artificial atom, where the energy levels are non-equidistant and therefore, each transition can be addressed individually. Even though systems such as the Transmon qubit are of extreme relevance in quantum systems and quantum information, when working in optomechanical systems, the intrinsic non-linearity of the system is most of the times a parameter to minimize and keep under the limit  $|\chi| < \kappa$ . Only in this regime we can consider a weakly anharmonic potential as an approximation of a harmonic oscillator.

As explained in chapter 1, the essence of the *flux-mediated optomechanical coupling* and the *photon-pressure coupling* experimentally realized this thesis (see section 2.5.2 and 2.5.3) rely on the presence of a SQUID and therefore some non-linearity will be unavoidable. Nevertheless, as shown in Fig. 2.7c, by choosing a hybrid system, where the total inductance is a combination of linear inductance  $L$  and Josephson inductance  $L_j$  one can finely tune the amount of anharmonicity in the circuit by changing the participation ratio of the Josephson inductance.

## 2.4. SQUID CAVITY AS A DUFFING OSCILLATOR

When neglecting the presence of quantum fluctuations, we can model the dynamics of a SQUID cavity as a classical Duffing oscillator. Its classical Hamiltonian, which is analogous to the one of Eq. (2.32) when Taylor expanded to second order is given by

$$H = \frac{Q^2}{2C_m} + \frac{\Phi^2}{2L_m} + \frac{\hbar\chi}{12} \frac{\Phi^4}{\Phi_{\text{zpf}}^4}. \quad (2.36)$$

Furthermore, when applying the same method as for the mechanical oscillator by using the Hamilton equations on Eq. (2.36) and additionally adding a dissipation force  $F = -\kappa\dot{\Phi}$  to the system, one obtains the equation of motion for a damped Duffing oscillator

$$\ddot{\Phi} + \kappa\dot{\Phi} + \omega_0^2\Phi + \frac{\hbar\chi}{3C_m\Phi_{\text{zpf}}^4}\Phi^3 = 0, \quad (2.37)$$

where  $\kappa$  is the total decay rate of the cavity. Let us make use of the previously defined annihilation and creation operators  $\hat{a}, \hat{a}^\dagger$  in Eq. (2.20) to write a new set of classical analogue variables  $\alpha$  and  $\alpha^*$ , which are defined as

$$\alpha = \sqrt{\frac{\omega_0 C_m}{2\hbar}} \left( \Phi + i \frac{\dot{\Phi}}{\omega_1^*} \right) \quad (2.38)$$

$$\alpha^* = \sqrt{\frac{\omega_0 C_m}{2\hbar}} \left( \Phi - i \frac{\dot{\Phi}}{\omega_1} \right) \quad (2.39)$$

where  $\omega_1 = (\omega_0 - i\frac{\kappa}{2})$  is the modified resonance frequency due to the presence of a damping term under the realistic high  $Q$  approximation of  $Q \gg 1$ .

The equation of motion, now written as function of the new variable  $\alpha$  and under a Rotating Wave Approximation (RWA), takes the form

$$\dot{\alpha} + \left( i(\omega_0 + \beta|\alpha|^2) + \frac{\kappa}{2} \right) \alpha = 0, \quad (2.40)$$

with the newly defined anharmonic term  $\beta = \chi$  being responsible for Kerr shifting the resonance frequency of the cavity linearly with photon number as  $|\alpha| = \sqrt{n_c}$ .

When a drive field<sup>1</sup>  $S_d = S_0 e^{(-i\omega_d t + \phi)}$  is added to the system with  $S_0 = \sqrt{\kappa_e} S_{\text{in}}$  as follows from input-output theory [101] we can re-write the equation of motion in frequency space as

$$\alpha \left[ i(\beta|\alpha|^2 - \Delta) + \frac{\kappa}{2} \right] = \sqrt{\kappa_e} S_{\text{in}} e^{i\phi}, \quad (2.41)$$

with  $\Delta = \omega_d - \omega_0$  being the detuning of the drive from the resonance frequency. Furthermore, the real-valued term  $S_{\text{in}}$  describes the input field driving the SQUID cavity and it is normalized such that  $|S_{\text{in}}|^2$  is the input photon flux per second. When looking at

<sup>1</sup>The time dependent phase of the drive field  $S_d$  could also be written as  $+i\omega_d t$  by following an electrical engineering convention [102]. This would be fully equivalent as it would only determine the rotation direction of the field. Note that in some of the following chapters, the latter convention was used.

the analogy between a LC circuit and a *spring-mass system* and considering a capacitive (inductive) coupling of the resonator to a lossy environment by means of a feedline, the scaling factor  $\sqrt{\kappa_e}$  can be intuitively thought of an additional mass (spring) onto which the drive tone is applied on, regulating the net driving force amplitude.

When multiplying the previous expression by its complex conjugate and expressing  $|\alpha|^2$  as  $n_c$ , one obtains the third order polynomial

$$\beta^2 n_c^3 - 2\Delta\beta n_c^2 + \left(\Delta^2 + \frac{\kappa^2}{4}\right) n_c - \kappa_e S_{\text{in}}^2 = 0. \quad (2.42)$$

The real valued solutions of the previous expression, which can be found numerically, allow us to extract the intracavity photon number. In addition, the phase  $\phi$  of expression (2.41) can be written as

$$\phi = \text{atan2}\left(\frac{2(\Delta - \beta\alpha^2)}{\kappa}\right) \quad (2.43)$$

At this point the cavity response function can be written as

$$S_{11} = 1 - \sqrt{\kappa_e n_c} \frac{e^{-i\phi}}{S_{\text{in}}}. \quad (2.44)$$

Lets bring our attention to the schematic representation of both a linear and a Duffing response to external driving forces shown in Fig. 2.8a. When a drive tone is swept through the oscillator's resonance with a small enough power, Eq. (2.42) has a single real solution and the oscillator exhibits a linear response. However, when the power of the drive tone is increased and since  $\beta < 0$ , the resonance shape starts to bend towards lower frequency values, shown as Duffing response in Fig. 2.8a.

When the power reaches a certain threshold, Eq. (2.42) has three real solutions corresponding to points A, B and C with the middle one being an unstable solution and placing the resonator in a bistable regime, identified by the dashed line. The transition point from one to multi real-valued solutions is known as bifurcation point and can be identified as the critical point where A and C overlap in frequency. Following the work of Ref.[103] we see that, analytically, this occurs when the drive frequency is  $\omega_{\text{cr}} = \omega_0 - \frac{\sqrt{3}\kappa}{2}$ . In addition, the critical photon number necessary to bring the resonator into this bifurcation point can be obtained as

$$n_{\text{cr}} = \frac{\kappa}{\sqrt{3}\beta} \quad (2.45)$$

Fig. 2.8b shows how the critical photon number (normalized to the smallest plotted value) depends on the anharmonicity of the cavity when a drive tone is fixed at  $\omega_{\text{cr}}$ . When the Kerr nonlinearity is increased from 5 kHz to 100 kHz, the critical photon number is suppressed by a factor of 20, clearly indicating that one should try to minimize the non-linearity in order to preserve a linear response of the system to near resonant external drives.

When plotting the cavity response spectrum  $S_{11}$  in the linear and non-linear (Duffing) operation regimes, very distinct behaviors are observed. For the linear case, the cavity response is a typical absorption dip with a Lorentzian lineshape. However, in the Duffing regime, the response spectrum depends on the drive sweep direction, i.e. on the

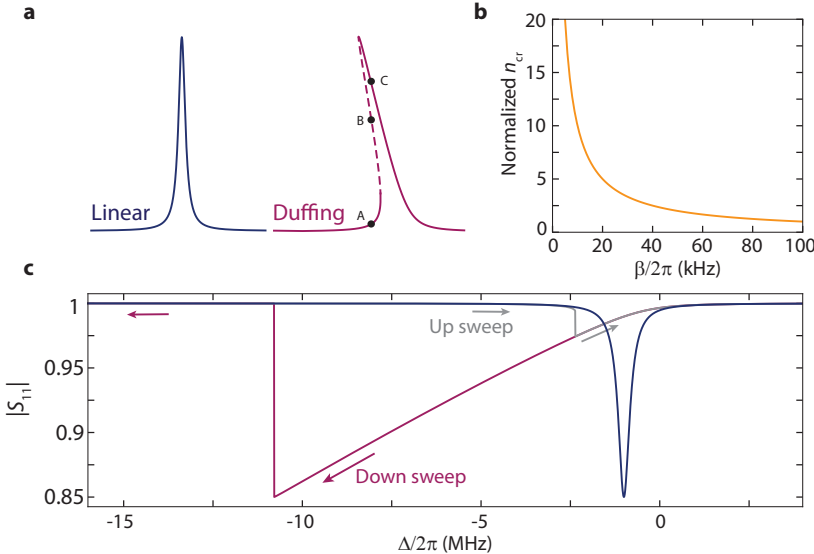


Figure 2.8: **Duffing oscillator response in the presence of a single drive tone.** **a** Schematic representation of the linear and Duffing response to an external drive tone. **b** Critical photon number  $n_{cr}$ , normalized to the smallest plotted value, depending on the circuit anharmonicity  $|\beta|$ . **c** Magnitude of the response spectrum  $|S_{11}|$  vs drive detuning from the bare resonance frequency  $\Delta = \omega_d - \omega_0$  in the linear regime, as blue curve, and in the Duffing regime as gray and violet curves, corresponding respectively to a frequency up-sweep and down-sweep.

initial conditions of the system. If one would perform a frequency up-sweep, the cavity would stay in a low-amplitude branch solution and the gray curve in Fig. 2.8c would be detected. However, when performing a frequency down-sweep, the selected branch would be the high-amplitude and the violet curve would be detected. For points where there is only a single solution, the response spectrum of the two directions coincides.

In typical optomechanical measurements, one would in fact have a strong detuned drive which brings the cavity into one of the branches and only use a weak probe tone to measure its linearized driven response. In this scenario, the input field is composed of a strong pump tone of frequency  $\omega_p$  and a weak probe tone with a time dependent field amplitude  $S_{pr}(t)$ . The total input field, in the rotating frame of the pump, is therefore given by  $S_{in} = S_p e^{-i(\omega_p t + \phi)} + S_{pr}(t) e^{-i\omega_p t}$ . In addition, the intracavity field is given as  $\alpha = \alpha_0 e^{-i\omega_p t} + \gamma_0(t) e^{-i\omega_p t}$ .

The equation of motion for the probe field can be obtained from the undriven equation of motion Eq. 2.40 by, once again, adding the presence of a driving term  $S_e = \sqrt{\kappa_e} S_{in}$ . Furthermore, after removing the pump steady-state solution, which is found for when  $\gamma_0, S_{pr} = 0$ , the expression takes the form

$$\dot{\gamma}_0 + \left[ -i(\Delta - \beta\alpha_0^2) + \frac{\kappa}{2} \right] \gamma_0 + \beta i \alpha_0^2 (\gamma_0 + \gamma_0^*) = \sqrt{\kappa_e} S_{pr} \quad (2.46)$$

In frequency space, the previous expression becomes

$$\left[ -i(\Delta - 2\beta\alpha_0^2 + \delta) + \frac{\kappa}{2} \right] \gamma_0(\delta) + \beta i \alpha_0^2 \gamma_0^*(-\delta) = \sqrt{\kappa_e} S_{\text{pr}}(\delta), \quad (2.47)$$

where  $\delta = \omega_{\text{pr}} - \omega_p$  is the detuning of the probe relative to the pump tone.

The term  $\beta i \alpha_0^2 \gamma_0^*(-\delta)$  in Eq. (2.47), which arises from the anharmonicity of the system, is in fact, a signature of a coupling between the signal field  $\gamma_0(\delta)$  and its mirrored conjugate  $\gamma_0^*(-\delta)$ , giving rise to an idler field  $\gamma_0(-\delta)$  of the cavity input field. In the lab frame, these two modes would appear at the same distance but on opposite sides of the pump. The total intracavity probe field can be expressed in terms of a Kerr susceptibility defined as

$$\chi_k = \frac{1}{\frac{\kappa}{2} - i(\Delta - 2\beta\alpha_0^2 + \delta)} \quad (2.48)$$

and of its conjugate  $\bar{\chi}_k = \chi_k^*(-\delta)$ . The expression takes then the form

$$\gamma_0(\delta) = \frac{\beta\alpha_0^2 \chi_k \bar{\chi}_k}{1 - \beta^2 \alpha_0^4 \chi_k \bar{\chi}_k} \sqrt{\kappa_e} S_{\text{pr}}^*(-\delta) + \frac{i \chi_k}{1 - \beta^2 \alpha_0^4 \chi_k \bar{\chi}_k} \sqrt{\kappa_e} S_{\text{pr}}(\delta). \quad (2.49)$$

From equation (2.49), we can see that an intracavity field  $\gamma_0(\delta)$  is generated at frequency  $\delta$  when a probe tone is sitting either at  $\delta$  or  $-\delta$ . However, for most of the experiments presented in this thesis, we only make use of a probe tone  $S_{\text{pr}}(\delta)$  and measure the cavity resonance at the same frequency  $\gamma_0(\delta)$ . In that case, the intracavity field can be reduced to the second term and the cavity susceptibility becomes

$$\chi_c = \frac{\chi_k}{1 - \beta^2 \alpha_0^4 \chi_k \bar{\chi}_k}. \quad (2.50)$$

Furthermore, the reflection parameter, i.e., the interference between the input and output fields, is written as

$$S_{11} = 1 - \frac{\kappa_e \chi_k}{1 - \beta^2 \alpha_0^4 \chi_k \bar{\chi}_k}. \quad (2.51)$$

Finally, the cavity resonance frequency can be found by extracting the real part of the resonant condition  $\chi_c^{-1} = 0$  and it is given, in the rotating frame of the pump frequency by

$$\delta_0 = \pm \sqrt{(\Delta - \beta\alpha_0^2)(\Delta - 3\beta\alpha_0^2)}. \quad (2.52)$$

Note that the two existing solutions correspond to the cavity and idler resonance frequencies. The resonance frequency in the lab frame finally becomes  $\omega_0 = \omega_p + \delta_0$ .

From Eq. (2.52) we see that since  $\delta_0$  depends on  $\beta\alpha_0^2$ , the resonance frequency will be power dependent. Fig. 2.9a shows how the anharmonicity impacts the resonance frequency shift with pump power in a two tone experiment with a far-detuned pump tone ( $\omega_p \gg \kappa$ ). Furthermore, in Fig. 2.9b, it is shown how the values of non-linearity translate into the ratio of linear and Josephson inductance. In optomechanical experiments, this frequency shift is something to be particularly careful about, as the detuning between the pump and the cavity resonance is a crucial parameter, that most of the times should preferably stay constant. For this reason, a shift higher than the cavity linewidth should be avoided.

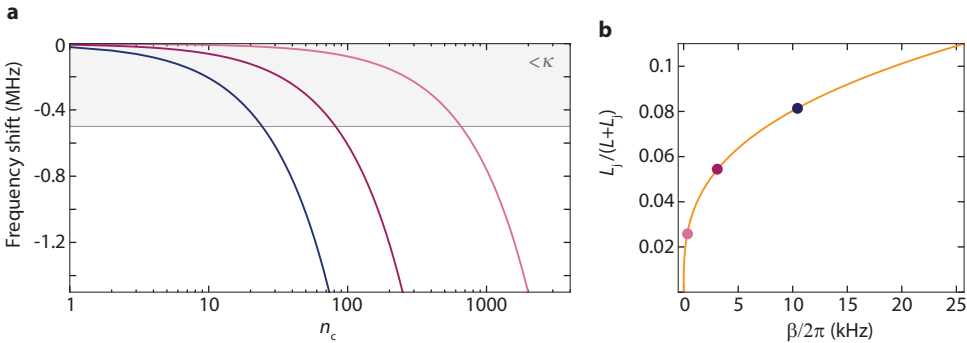


**Figure 2.9: Resonance frequency shift of a SQUID cavity in a two tone measurement scheme.** **a** Shows the resonance frequency shift vs intracavity photon number  $n_c$  due to the non-linearity  $|\beta|$ , when the cavity is driven by a far-detuned pump and measured by a weak probe tone. The three different curves correspond to distinct values of anharmonicity and the gray area represents the regime where the shift is smaller than the cavity linewidth, here set to  $\kappa = 2\pi \cdot 500\text{kHz}$ . **b** Shows how the anharmonicity translates into a ratio of Josephson and total inductance assuming a shunting capacitance of  $C = 1\text{pF}$ . The three dots represents the  $\beta$  of each of the curves represented in a.

The gray area in Fig. 2.9a represents the regime where the frequency shift is below a linewidth of  $2\pi \cdot 500\text{kHz}$ . However, as shown in Fig. 2.9a, the maximum number of photons that the cavity can sustain before shifting above this threshold strongly depends on the anharmonicity, and the higher the non-linearity is, the smaller is the critical photon number.

As a final message, it should be of clear evidence that, in order to perform optomechanical sideband driving schemes utilizing SQUID cavities, which is relevant as they grant the enhancement of the multi-photon coupling rate  $g$  (see Section 2.5.5), one would like to minimize the anharmonicity of the system. This can be done by finding an optimal balance between the Josephson and linear inductances of the circuit (more insights on how this requirement translates into the circuit design is given in chapter 3). Furthermore, when pursuing multi-tone driving schemes, as the one presented in chapter 5 one would need a slightly higher non-linearity. Nevertheless, this should also be carefully tuned as it will define the performance of the cooling scheme. For more details see chapter 5.

## 2.5. RADIATION-PRESSURE COUPLING

### 2.5.1. A GENERAL HAMILTONIAN

The energy operator  $\hat{H}$  of a system consisting of two uncoupled harmonic oscillators with frequencies  $\omega_0$  and  $\Omega_0$ , where their quantum ground-state energies are omitted, is written as

$$\hat{H} = \hbar\omega_0 \hat{a}^\dagger \hat{a} + \hbar\Omega_0 \hat{b}^\dagger \hat{b} \quad (2.53)$$

When implementing an optomechanical coupling, we are introducing, from a general point of view, a parametric modulation of the resonance frequency of one oscillator de-

pending on the quadrature amplitude of a second oscillatory mode ( $\hat{b} + \hat{b}^\dagger$ ). The most common implementation of this type of coupling is based on an optical cavity with frequency  $\omega_0$  which is formed by the light field trapped between a static mirror and freely moving mirror of mass  $m$ . As the latter oscillates with frequency  $\Omega_0$ , its displacement  $\hat{x} = x_{\text{zpf}}(\hat{b} + \hat{b}^\dagger)$  therefore modulates the cavity energy, as this one depends on the distance between the two mirrors. Here  $x_{\text{zpf}} = \sqrt{\frac{\hbar}{2m\Omega_0}}$  represents the mechanical zero-point fluctuation amplitude. The cavity resonance frequency, in the presence of such interaction is given by

$$\omega_0(x) = \omega_0 + x \frac{\partial \omega_0}{\partial x} + x^2 \frac{\partial^2 \omega_0}{\partial^2 x} + \dots \quad (2.54)$$

Let us now assume that all terms rather than the linear term can be neglected. The correction to the cavity energy then becomes

$$\hbar\omega_0(x)\hat{a}^\dagger\hat{a} = \hbar(\omega_0 - G\hat{x})\hat{a}^\dagger\hat{a}, \quad (2.55)$$

where  $G = \partial\omega_0/\partial x$  is defined as the pull parameter which describes the cavity responsivity to mechanical displacement. The new system Hamiltonian becomes a combination of the uncoupled Hamiltonian plus the interaction term as

$$\hat{H} = \hbar\omega_0(\hat{a}^\dagger\hat{a}) + \hbar\Omega_0(\hat{b}^\dagger\hat{b}) - \hbar g_0\hat{a}^\dagger\hat{a}(\hat{b} + \hat{b}^\dagger), \quad (2.56)$$

where  $g_0 = Gx_{\text{zpf}}$  is defined as the single-photon coupling strength, the rate at which a photon from the cavity converts into a phonon in the mechanical mode.

For simplicity, this initial description of the optomechanical Hamiltonian was done using the example of an optical cavity and an oscillating mirror. However, the systems explored in this thesis for the implementation of an optomechanical coupling consist either of a microwave cavity coupled to the displacement of a mechanical resonator (see chapter 4 and chapter 5) or of a microwave cavity coupled to the current flowing in a radio-frequency resonator (see chapter 6 and chapter 7). The definition of the single-photon coupling strength  $g_0$  will be discussed for the two cases in the following sections 2.5.2 and 2.5.3. Even though the definition of  $g_0$  depends on the system, the interaction Hamiltonian remains the same, allowing us to use the general form of Eq. (2.56).

### 2.5.2. FLUX-MEDIATED OPTOMECHANICAL COUPLING

As shortly mentioned in chapter 1, in a flux-mediated optomechanical system, a microwave cavity is combined with a mechanical resonator in a configuration where a fraction of the circuit inductance is modulated by the motion of a mechanical element. For the realization of this coupling scheme, one fully relies on a non-linear inductor to mediate the interaction between the mechanical and microwave modes. Our approach to experimentally engineer this system followed the theoretical proposal of Ref.[70], where a mechanical resonator is embedded in a Superconducting QUantum Interference Device (SQUID) as shown in Fig. 2.10a, i.e., part of the SQUID loop is free to oscillate, forming a mechanical resonator.

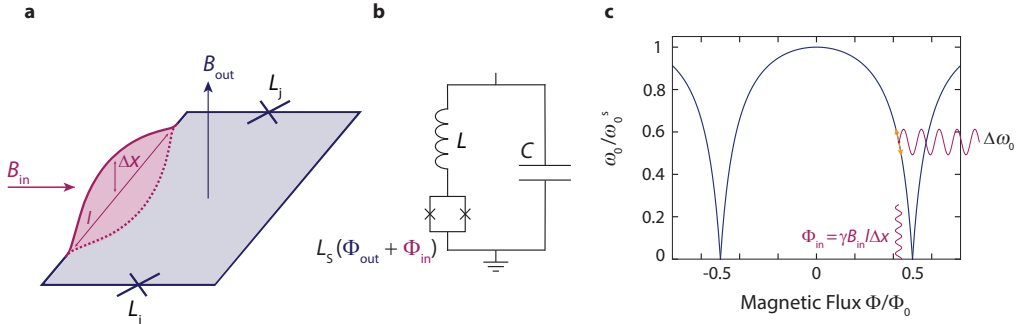


**Figure 2.10: Description of a flux-mediated optomechanical system.** **a** shows a schematic representation of a SQUID, part of whose loop is free to oscillate, forming a mechanical resonator of length  $l$ , which is displaced from its rest position by  $\Delta x$ . The system is in the presence of in-plane and out-of-plane magnetic fields  $B_{\text{in}}$  and  $B_{\text{out}}$ . **b** shows a circuit analogue of the system which combines the SQUID presented in panel **a** with a linear microwave cavity. As the cavity contains a non-linear inductor, its resonance frequency will be flux dependent. In **c**, the normalized resonance frequency depending on the total applied magnetic flux  $\Phi$  is shown. As the in-plane flux arises from the oscillating motion of the mechanical beam ( $\Phi_{\text{in}} = \gamma B_{\text{in}} l \Delta x$ ), when the SQUID cavity is biased to a non-integer value of  $\Phi_0$ , a parametric modulation of its resonance frequency arises from the optomechanical coupling to the mechanical oscillator.

The SQUID, as already mentioned in section 2.2, is a superconducting loop connected by two Josephson junctions in parallel<sup>2</sup>. In contrast to the non-linearity discussion of section 2.3, where the SQUID could be represented as a single Josephson junction, here its flux-tunable properties have to be taken into account, as they are the key of the described coupling scheme. In essence, the SQUID acts as a non-linear inductor whose inductance can be tuned by applying an external magnetic field. As follows from the discussion of section 2.2, in the ideal case of a negligible loop inductance, its inductance can be written as

$$L_S = \frac{L_{j0}}{2 \cos\left(\pi \frac{\Phi}{\Phi_0}\right)}, \quad (2.57)$$

where  $L_{j0}$  is the Josephson inductance of a single junction and  $\Phi$  is the total magnetic flux threading the SQUID. In the configuration of Fig. 2.10a, where both an in-plane and out-of-plane magnetic field are applied to the SQUID, the total flux will have contributions from both components

$$\Phi = \Phi_{\text{out}} + \Phi_{\text{in}} = B_{\text{out}} A_{\text{out}} + B_{\text{in}} A_{\text{in}}, \quad (2.58)$$

with  $A_{\text{out}}$  being the out-of-plane area enclosed by the SQUID loop, represented as dark blue, and  $A_{\text{in}}$  being the effective area formed by the out-of-plane mechanical motion, represented as violet.

When combining this SQUID configuration with a linear microwave cavity, the full system can be modeled by the circuit shown in Fig. 2.10b, where the SQUID inductance,

<sup>2</sup>This configuration is known as the DC-SQUID. The realization of a SQUID composed of a single Josephson junction is defined as the RF-SQUID. Through this thesis, the SQUID will always be referring to the DC-SQUID configuration.

depends on both in-plane and out-plane magnetic flux  $L_S = L_S(\Phi_{\text{out}} + \Phi_{\text{in}})$ . Therefore, when using the out-of-plane magnetic field to bias the SQUID, the cavity can be tuned into a point where the displacement dependent in-plane flux  $\Phi_{\text{in}} = \gamma B_{\text{in}} l \Delta x$  results in a modulation of the resonance frequency as shown in Fig. 2.10c, giving rise to an optomechanical interaction.

As the flux arising from the presence of the in-plane magnetic field entirely depends on the effective area originated from the displacement of the mechanical resonator, its zero-point motion can be translated into a fluctuating in-plane magnetic field. This is defined as the zero-point flux  $\Phi_{\text{zpf}}$  and is expressed as

$$\Phi_{\text{zpf}} = \gamma B_{\text{in}} l x_{\text{zpf}} \quad (2.59)$$

where  $\gamma$  accounts for the mode shape of the mechanical oscillations and is on the order of 1,  $l$  is the length of the beam and the zero-point motion is defined as  $x_{\text{zpf}} = \sqrt{\frac{\hbar}{2m\Omega_0}}$ . Furthermore, the single-photon coupling strength of a flux-mediated optomechanical system is given by

$$g_0 = \frac{\partial \omega_0}{\partial \Phi} \Phi_{\text{zpf}} = \frac{\partial \omega_0}{\partial \Phi} \gamma B_{\text{in}} l x_{\text{zpf}}. \quad (2.60)$$

An intuitive way of understanding the radiation-pressure force in flux-mediated optomechanics can be based on the SQUID flux quantization. When the SQUID is biased to non-integer values of  $\Phi_0$ , there is a generation of a screening current which flows across the loop, which subsequently induces an asymmetric splitting of the AC current applied to the SQUID. This asymmetric splitting will result in an oscillating loop current with frequency  $2\omega_0$  around a constant offset. To first order, the fast current oscillations can be neglected and therefore, in the presence of an in-plane magnetic field, the charge carriers responsible for the loop current offset will feel an effective Lorentz force which generates a displacement of the mechanical resonator. An experimental realization of this coupling scheme can be found in chapter 4 and chapter 5. Furthermore, for additional information on maximizing  $g_0$  in our flux-mediated optomechanical systems is given in section 3.3.1.

### 2.5.3. PHOTON-PRESSURE COUPLING

Photon-pressure interaction, a term used in analogy to an optomechanical system whose coupling arises from a radiation-pressure force, describes a system where the resonance frequency of a microwave cavity is parametrically modulated by the amplitude of the current flowing in a second circuit.

As for flux-mediated optomechanics, the implementation of a photon-pressure coupling relies on a SQUID to mediate the interaction between the two circuits. Based on the schematic diagram presented in Fig. 2.11a let us discuss the working principle of a photon-pressure system. Given a wire in which a current is flowing, as described by Bio-Savart law, a magnetic field will be generated and decay with the distance from the wire. If now a SQUID is placed in close proximity, a magnetic flux will arise as the current-generated magnetic field threads the area formed by the loop.

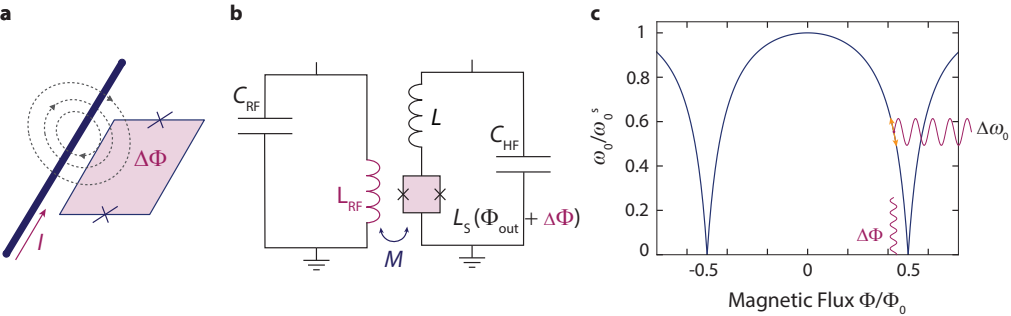


Figure 2.11: **Working principle of a photon-pressure system.** In a, a physical representation of the coupling scheme is shown. The wire, in which a current is flowing, generates a magnetic field that threads into the nearby SQUID loop, where  $\Delta\Phi$  is the flux arising from the current flowing in the wire. The photon-pressure system can be modeled by the circuit shown in b, where a radio-frequency (RF) cavity, formed by the wire of inductance  $L_{RF}$  and a capacitor  $C_{RF}$ , is coupled to a high frequency (HF) circuit via a mutual inductance  $M$ . The flux-tunable resonance frequency of the SQUID cavity, normalized to the sweet-spot ( $\Phi = 0$ ), is shown in c. The oscillating flux  $\Delta\Phi$ , arising from the RF current, results in a parametric modulation of the resonance frequency when the SQUID is biased into a non-integer value of  $\Phi_0$ .

In a photon-pressure system, the wire of inductance  $L_{RF}$  is placed in parallel with a capacitor  $C_{RF}$  to form a radio-frequency cavity of resonance frequency  $\Omega_0$  and a zero point current  $I_{zpf} = \sqrt{\frac{\hbar\Omega_0}{2L_{RF}}}$ . In addition, the SQUID of inductance  $L_S$ , is also part of a high frequency cavity with  $\omega_0$  operating at GHz frequencies. In this configuration, the zero point current  $I_{zpf}$  will give rise to a fluctuating zero point flux

$$\Phi_{zpf} = MI_{zpf}, \quad (2.61)$$

where  $M$  is the mutual inductance between the two circuits and depends on their geometric arrangement. The full system can be modeled by the circuit schematic of Fig. 2.11b, where the SQUID inductance  $L_S(\Phi_{out} + \Delta\Phi)$  depends on the flux modulations  $\Delta\Phi$  arising from the RF circuit and an externally applied out-of-plane flux  $\Phi_{out}$ .

Finally, by tuning the external magnetic flux  $\Phi_{out}$ , the SQUID can be flux-biased into a point where the AC current of the RF circuit induces linear parametric modulations of the resonance frequency of the HF cavity. The optomechanical coupling which arises from this modulation has a single-photon coupling strength given by

$$g_0 = \frac{\partial\omega_0}{\partial\Phi}\Phi_{zpf}. \quad (2.62)$$

Coming back to the analogy between photon-pressure and optomechanical systems, the equivalent to the radiation pressure force in this coupling scheme can be seen as electro-motive force acting on the RF inductor wire, which arises from the oscillating flux in the SQUID loop. As final remark, an experimental realization of a photon-pressure coupling scheme can be found in chapter 6 and chapter 7.

### 2.5.4. OPTOMECHANICAL KERR HAMILTONIAN

As discussed in section 2.3, the Hamiltonian of a SQUID cavity cannot always be approximated to the one of a harmonic oscillator. When incorporating a Josephson non-linearity in a LC circuit, the arising anharmonicity  $\chi$  and the induced deviation from the harmonic potential must be taken into account.

As both *flux-mediated optomechanical coupling* and *photon-pressure coupling* rely on the utilization of a microwave SQUID cavity, one should consider the following Hamiltonian

$$\hat{H} = \hbar\omega_0 \hat{a}^\dagger \hat{a} + \hbar\Omega_0 \hat{b}^\dagger \hat{b} + \hbar \frac{\chi}{2} (\hat{a}^\dagger \hat{a})^2 - \hbar g_0 \hat{a}^\dagger \hat{a} (\hat{b} + \hat{b}^\dagger), \quad (2.63)$$

where the third term  $\hbar \frac{\chi}{2} (\hat{a}^\dagger \hat{a})^2$  arises from the cavity Kerr non-linearity. Note that for the cases where the frequency shift due to the anharmonicity  $\chi$  is small, we can assume the optomechanical coupling to be of the form shown in Eq. (2.56), as the SQUID cavity can be approximated to be a harmonic LC oscillator.

### 2.5.5. LINEARIZED HAMILTONIAN

Let us now assume that the system in discussion consists of a driven microwave SQUID cavity coupled to a second oscillatory mode. For obtaining the linearized Hamiltonian, which is a valid approximation when the system is in the presence of a strong microwave drive tone, we follow the approach of Ref.[104]. Note that a simplified version of the linearization for the standard optomechanical Hamiltonian of Eq. (2.56) is given in Ref.[56].

The Heisenberg-Langevin equations that describe the equations of motion of the annihilation operators  $\hat{a}$  and  $\hat{b}$  of the un-driven system in the presence of dissipation and noise fluctuations are given by

$$\frac{d\hat{a}}{dt} = -i \left[ \hat{a}, \frac{\hat{H}}{\hbar} \right] - \frac{\kappa}{2} \hat{a} - \sqrt{\kappa_e} \hat{a}_{in}^e - \sqrt{\kappa_i} \hat{a}_{in}^i \quad (2.64)$$

$$\frac{d\hat{b}}{dt} = -i \left[ \hat{b}, \frac{\hat{H}}{\hbar} \right] - \frac{\Gamma}{2} \hat{b} - \sum_j \sqrt{\Gamma_j} \hat{b}_{in}^j. \quad (2.65)$$

Here  $\kappa$  and  $\Gamma$  are the total cavity and mechanical loss rates, respectively. The second term on the right hand side represents the leak of either photons ( $\kappa \hat{a}/2$ ) or phonons ( $\Gamma \hat{b}/2$ ) to a thermal bath. Furthermore, the terms  $\sqrt{\kappa_e} \hat{a}_{in}^e$  and  $\sqrt{\kappa_i} \hat{a}_{in}^i$  represent the driving of the SQUID cavity by the noise coming from the external or internal bath, respectively. Moreover, here we considered the possibility of the second oscillatory mode to be coupled to several baths. The environment noise coupling from each bath  $j$  is taken into account by the term  $\sum_j \sqrt{\Gamma_j} \hat{b}_{in}^j$ , where  $\Gamma_j$  is the decay rate of each channel.

Let us now take into consideration the presence of a microwave tone  $\alpha_d = \alpha_0 e^{-i\omega_d t}$ , which drives the cavity. An analogous way to include the drive term in the Hamiltonian<sup>3</sup>  $\hat{H}_{drive} = -i\hbar(\alpha_d^* \hat{a} - \alpha_d \hat{a}^\dagger)$  is to assume that the input field  $\hat{a}_{in}^e$  has an averaged value set by the drive  $\alpha_0$ .

<sup>3</sup>Note that, under our previous definition of  $\hat{a}$  and  $\hat{a}^\dagger$ , the presented form would represent a voltage source. Analogously, one could also represent the drive as a current source with  $\hat{H}_{drive} = \hbar(\alpha_d^* \hat{a} + \alpha_d \hat{a}^\dagger)$

Under the presence of this tone, it is convenient to switch to a frame rotating with the drive. For this, we make use of the unitary operator  $\hat{U} = e^{i\omega_d \hat{a}^\dagger \hat{a} t}$  and perform the Hamilton transformation  $\hat{H}' = \hat{U} \hat{H} \hat{U}^\dagger + i \frac{\partial \hat{U}}{\partial t} \hat{U}^\dagger$ . The modified Hamiltonian becomes

$$\hat{H}' = -\hbar \Delta \hat{a}^\dagger \hat{a} + \hbar \frac{\chi}{2} (\hat{a}^\dagger \hat{a})^2 + \hbar \Omega_0 \hat{b}^\dagger \hat{b} - \hbar g_0 \hat{a}^\dagger \hat{a} (\hat{b} + \hat{b}^\dagger), \quad (2.66)$$

with  $\Delta = \omega_d - \omega_0$  being the detuning between the drive and the cavity resonance. Furthermore the Heisenberg-Langevin equations are also modified and take the form

$$\frac{d\hat{a}}{dt} = -i \left[ \hat{a}, \frac{\hat{H}'}{\hbar} \right] - \frac{\kappa}{2} \hat{a} - \sqrt{\kappa_e} \alpha_0 - \sqrt{\kappa_e} \hat{a}_{in}^e - \sqrt{\kappa_i} \hat{a}_{in}^i \quad (2.67)$$

$$\frac{d\hat{b}}{dt} = -i \left[ \hat{b}, \frac{\hat{H}'}{\hbar} \right] - \frac{\Gamma}{2} \hat{b} - \sum_j \sqrt{\Gamma_j} \hat{b}_{in}^j \quad (2.68)$$

The explicit use of the term  $\sqrt{\kappa_e} \alpha_0$  in Eq. (2.67) comes from the fact that the previously defined external input field operator, in the presence of a drive tone, is composed of an average amplitude  $\alpha_0$  and noise fluctuations  $\hat{a}_{in}^e$ , as they both interact with the cavity via its loss channel to the external bath.

A clear consequence of the application of the drive is the displacement of the cavity field to a new average value. Furthermore, a response to this modification, is the emergence of a static radiation pressure force which will also induce a classical displacement of the mechanical resonator. Once the system reaches a new equilibrium, its dynamics can be described based on the fluctuations around these new static values. It is therefore convenient to express the operators  $\hat{a}$  and  $\hat{b}$  as

$$\hat{a} = \alpha + \delta \hat{a} \quad (2.69)$$

$$\hat{b} = \beta + \delta \hat{b} \quad (2.70)$$

where  $\alpha$  and  $\beta$  are the classical displacements induced by the drive tone and  $\delta \hat{a}$  and  $\delta \hat{b}$  are the fluctuation operators which encode the quantum effects of the system. By solving the Heisenberg-Langevin equations Eq. (2.67) and Eq. (2.68) (in the absence of the noise terms), when only accounting for the classical part of the newly defined operators, we find the following solution for the cavity field

$$\alpha = \frac{\sqrt{\kappa_e}}{\frac{\kappa}{2} + i(\chi|\alpha|^2 - \bar{\Delta})} \alpha_0, \quad (2.71)$$

where  $\alpha_0 = \alpha_0 e^{i\phi}$  and  $\phi = \text{atan2}\left(\frac{2(\bar{\Delta} - \chi|\alpha|^2)}{\kappa}\right)$ . In Eq. (2.71), the parameter  $\bar{\Delta} = \Delta + g_0(\beta + \beta^*)$  can be intuitively thought as a modification to the detuning between the drive and the cavity resonance introduced by the drive induced mechanical displacement, which shifts the cavity resonance frequency. In addition, the Kerr non-linearity also generates an additional frequency shift given by the term  $\chi|\alpha|^2$ . Under the assumption that the intracavity field is real-valued, the steady-state solution for the cavity field amplitude  $\alpha$

can be found by multiplying the previous relation (2.71) by its complex conjugate and numerically solving the third order polynomial

$$\chi^2 n_c^3 - 2\bar{\Delta}\chi n_c^2 + \left(\frac{\kappa^2}{4} + \bar{\Delta}^2\right) n_c - \kappa_e \alpha_0^2 = 0, \quad (2.72)$$

2

where  $|\alpha|^2 = n_c$ . Additionally the steady-state solution for the annihilation operator  $\hat{b}$  is given by

$$\beta = \frac{g_0 |\alpha|^2}{\Omega_0 + i \frac{\Gamma}{2}} \quad (2.73)$$

Here, it is helpful to calculate the corresponding mechanical displacement  $\bar{x} = x_{\text{zpf}}(\beta + \beta^*)$ . When assuming a high- $Q$  approximation we obtain

$$\bar{x} = x_{\text{zpf}} \frac{2g_0 |\alpha|^2}{\Omega_0}. \quad (2.74)$$

As seen in the previous expression, the total mechanical displacement, generated by a radiation pressure force  $F/\hbar = G|\alpha|^2$  is proportional to the cavity photon number as  $|\alpha|^2 = n_c$  and strongly depends on the ratio between the single-photon coupling strength and the mechanical frequency. Note that, for the case where  $g_0 > \Omega_0$ , a single intracavity photon will displace the mechanical oscillator by more than its zero point motion. Moreover, the mechanical displacement is also affected by the Kerr non-linearity through the steady state solution  $\alpha$ , which generates an effective reduction/enlargement of the total displacement  $\bar{x}$  for the case of a blue/red detuned drive tone.

By writing the Heisenberg Langevin equations as function of the operators  $\hat{a}$  (Eq. (2.69)) and  $\hat{b}$  (Eq. (2.70)), and removing the purely classical terms, the resulting equations of motion would be equivalent to the ones obtained with the starting Hamiltonian

$$\hat{H} = -\hbar \bar{\Delta} \delta \hat{a}^\dagger \delta \hat{a} + \frac{\chi}{2} |\alpha|^2 (\delta \hat{a} + \delta \hat{a}^\dagger)^2 + \hbar \Omega_0 \delta \hat{b}^\dagger \delta \hat{b} - \hbar g_0 (\alpha \delta \hat{a}^\dagger + \alpha \delta \hat{a} + \delta \hat{a}^\dagger \delta \hat{a}) (\delta \hat{b} + \delta \hat{b}^\dagger) \quad (2.75)$$

where  $\bar{\Delta} = \Delta + \frac{2g_0^2}{\Omega_0} |\alpha|^2 - \chi |\alpha|^2$  now also contains the contribution of the Kerr shift. Here, the term  $g_0 \delta \hat{a}^\dagger \delta \hat{a} (\delta \hat{b} + \delta \hat{b}^\dagger)$  acts as a non-linear shift of the cavity frequency due to the optomechanical interaction, however, as long as  $g_0 \ll \Omega_0, \kappa$  it is assumed to be negligible. For convenience, let us rename  $\delta \hat{b}$  as  $\hat{b}$  and  $\bar{\Delta}$  as  $\Delta$ . With this we get the linearized optomechanical Hamiltonian

$$\hat{H}_{\text{lin}} = -\hbar \Delta (\delta \hat{a}^\dagger \delta \hat{a}) + \frac{\chi}{2} n_c (\delta \hat{a} + \delta \hat{a}^\dagger)^2 + \hbar \Omega_0 (\hat{b}^\dagger \hat{b}) - \hbar g (\delta \hat{a}^\dagger + \delta \hat{a}) (\hat{b} + \hat{b}^\dagger), \quad (2.76)$$

where  $g = \sqrt{n_c} g_0$  is the enhanced multi-photon coupling strength and the last term on the right hand side is known as the interaction Hamiltonian  $\hat{H}_{\text{int}}$ . The quantum Heisenberg-Langevin equations of motion of the linearized system are given as

$$\frac{d}{dt} \delta \hat{a} = \delta \hat{a} \left( i \Delta - \frac{\kappa}{2} \right) + i g (\hat{b} + \hat{b}^\dagger) - i \chi n_c \delta \hat{a}^\dagger - \sqrt{\kappa_e} \hat{a}_{\text{in}}^e - \sqrt{\kappa_i} \hat{a}_{\text{in}}^i \quad (2.77)$$

$$\frac{d}{dt} \hat{b} = \left( -i \Omega_0 - \frac{\Gamma}{2} \right) \delta \hat{b} + i g (\delta \hat{a} + \delta \hat{a}^\dagger) - \sum_j \sqrt{\Gamma_j} \hat{b}_{\text{in}}^j \quad (2.78)$$

In the particular case where the detuning between the drive tone and the cavity resonance is  $\Delta = -\Omega_0$ , also known as the red sideband, a rotating wave approximation (RWA)<sup>4</sup> can be done by removing all the off-resonant terms. The following interaction Hamiltonian is obtained

$$\hat{H}_{\text{int}} = -\hbar g(\delta \hat{a}^\dagger \hat{b} + \delta \hat{a} \hat{b}^\dagger). \quad (2.79)$$

Eq. (2.79), also known as the *beam-splitter Hamiltonian*, describes the system dynamics where the creation of a photon annihilates a phonon and vice-versa. This type of interaction was experimentally used in this thesis, for example, for optomechanical cooling of a mechanical resonator (chapter 5) and of a radio-frequency circuit (chapter 7). Further applications such as quantum state transfer could also be applied when one fulfills  $g > \frac{\kappa+\Gamma}{2}$ , known as *strong coupling regime*. Additionally, if  $g > \kappa, n_{\text{th}}\Gamma$  the system is said to operate in the *regime of quantum coherent coupling*, where the rate at which excitations are exchanged between the two modes is faster than the mechanical thermal decoherence rate.

The omitted terms in the previous RWA are the only ones which stay present when applying a microwave drive on the blue sideband of the Kerr shifted cavity, i.e.  $\Delta = +\Omega_0$ . Also known as a *two-mode squeezing* interaction, the interaction Hamiltonian takes the form

$$\hat{H}_{\text{int}} = -\hbar g(\delta \hat{a} \hat{b} + \delta \hat{a}^\dagger \hat{b}^\dagger). \quad (2.80)$$

Contrary to the beam-splitter Hamiltonian, Eq. (2.80) describes the case where pairs of a single photon and a single phonon are either created or destroyed. These two-mode squeezed states are therefore correlated and one can describe them as quantum entangled pairs. This interaction is also similar to the one of a non-degenerate parametric amplifier, and therefore, ultimately lead to parametric amplification. This interaction is realized in chapter 6, for the detection of parametrically amplified thermal current fluctuations of a RF circuit.

---

<sup>4</sup>Note that the RWA performed for achieving the beam-splitter and two-mode squeezing Hamiltonian is not valid in the case of a system in the *ultra-strong coupling regime* where  $g \sim \Omega_0$  as the counter-rotating terms can no longer be ignored.



# 3

## DEVICE DESIGN AND FABRICATION

*Everything is theoretically impossible until it is done.*

Robert A. Heinlein

*The chapter starts by providing some insights regarding the physical working principle of nano-bridge Josephson junctions and it continues by taking a close look to the particular case of a SQUID with a non-negligible high screening parameter  $\beta_L$  and its impact on the resonance frequency flux modulations of a microwave SQUID cavity. Posterior to the discussion regarding the design considerations of SQUID cavities, follows a chronological narrative of the all the attempted approaches for the fabrication of 2D and 3D SQUID cavities and the reasoning behind their failure or success. The chapter continues with a short description of the fabrication techniques utilized for the releasing of mechanical beams and the engineering of RF microwave cavities and a short overview on the design requirements necessary for the optimization of their respective single-photon coupling strengths. Finally, an overview of the experimental challenges associated with flux noise will be presented.*

### 3.1. NANO-BRIDGE JOSEPHSON JUNCTIONS

As concluded from the discussion of section 2.4, when designing a SQUID cavity to be incorporated in an optomechanical or photon-pressure system, the non-linearity of the circuit should often be minimized. For this purpose, one can reduce the contribution of the Josephson junction by adding it in series with a linear inductor or by reducing its intrinsic inductance  $L_j$ . However, note that for high values of  $L_j$ , the necessary value of linear inductance required for maintaining a low anharmonicity while keeping the cavity resonance frequency in the typical 5 – 8 GHz range would make the circuit design extremely challenging. For example, a SQUID cavity made of junctions with  $L_j \sim 30\text{nH}$  would require a linear inductor of  $L \sim 3\mu\text{H}$  and a circuit impedance of  $Z \sim 140\text{M}\Omega$  to keep an anharmonicity of 100 kHz, which would be an extremely demanding technological task [107].

The inductance of a Josephson junction is related to its critical current, i.e. to the amount of current the junction can sustain before switching to a resistive state, as

$$I_c = \frac{\Phi_0}{2\pi L_j}, \quad (3.1)$$

where  $\Phi_0$  is the flux quantum. As for now, a key requirement when designing the SQUID cavities utilized in this thesis, is to engineer high critical current Josephson junctions. From the wide variety of available options when selecting a type of Josephson junction [108] (SIS, SNS, SFS, etc)<sup>1</sup>, the *nano-bridge Josephson junction*, also referred to as *weak link junction* in literature, is especially attractive as it is free of a lossy oxide, easy to fabricate and has intrinsically higher critical currents compared to the standard choice of SIS junctions. Moreover, as its cross section is considerably smaller, it has a much higher magnetic field resilience compared to other high critical current junctions [105, 106], which makes it a great option for flux-mediated optomechanical systems.

As shown in Fig. 3.1, a weak link junction can be designed as a 2D constriction where the banks are much wider than the path between them (also referred to as Dayem bridge), or a 3D constriction, where in addition, the path is much thinner than the electrodes. In essence, the non-linear behavior of a weak link junction arises from the geometric constriction between two superconducting banks (see Fig. 3.1). In contrast to tunnel junctions, where the non-superconducting area between the electrodes is characterized by a reduction in the Cooper pair density  $n_p$ , in a nano-bridge junction, the reduction of the total amount of Cooper pairs flowing between the two banks arises from a reduction of cross-sectional area in the link. In essence, in a tunnel junction, the current density  $J_p = 2en_p v_p$  stays constant as the decrement in Cooper pair density is balanced by an increment in Cooper pair velocity  $v_p$ . In the case of a nano-bridge junction, the enhancement of the cooper pair velocity  $v_p$  arising from the reduced cross sectional area results in an increment of the current density  $J_p$ . Nevertheless, this is balanced by the decrement in the total amount of carriers in the link, maintaining constant the total current flowing in the system.

---

<sup>1</sup>The acronyms stand for Superconductor/Insulator/Superconductor, Superconductor/Normal conductor/Superconductor and Superconductor/Ferromagnet/Superconductor, respectively.

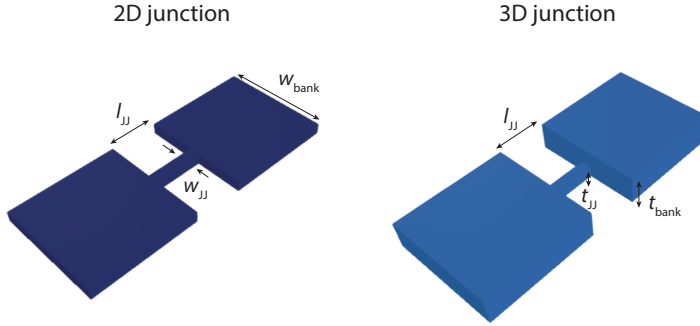


Figure 3.1: **Illustration of 2D and 3D weak link Josephson junctions.** A 2D junction, which is represented on the left, is formed by a narrow constriction of length  $l_{\text{JJ}}$  between two wide electrodes ( $w_{\text{JJ}} \ll w_{\text{bank}}$ ). Here the electrodes and the junction have the same thickness. The 3D junction, which is shown on the right side, is formed by narrow and thin constriction of length  $l_{\text{JJ}}$ , whose thickness is much smaller than the connecting banks ( $t_{\text{JJ}} \ll t_{\text{bank}}$ ).

Since the total phase difference across a nano-bridge Josephson, which is translated to the enhancement of Cooper pair velocity  $v_p$  in the junction, relies on the phase gradient between the banks and the link, the modeling of the current-phase relation (CPR) can be a complex problem. It strongly depends on the aspect ratio between the banks and the constriction and on material properties as the coherence length  $\xi^2$  and mean free path  $l^3$ . For instance, very short junctions, where the length  $l_{\text{JJ}}$  is much smaller than the coherence length  $l_{\text{JJ}} \ll \xi(T)$ , exhibit the characteristic sinusoidal CPR predicted by the first Josephson relation [109, 110]  $I(\varphi) = I_{\text{c}0}\sin(\varphi)$ . Note that, as the coherence length considerably increases with temperature, this regime is appreciably easier to achieve when the junctions are operated close to the critical temperature  $T \approx T_c$ . This effect is predicted by the *Aslamazov-Larkin* model [111, 112] and relies on a microscopic description of the Josephson effect.

In addition, when a junction falls into the dirty limit, where  $l_{\text{JJ}} \ll \sqrt{\xi l}$ , it is well described by the *Kulik-Omelyanchuk* model (KO-1) [113]. The current-phase relation is then given by

$$I(\varphi) = \frac{\pi\Delta}{eR_N} \cos \frac{\varphi}{2} \tan^{-1} \left( \sin \frac{\varphi}{2} \right), \quad (3.2)$$

where  $\Delta$  is the superconducting gap and  $R_N$  the junction normal state resistance.

A good approximation to this model can be obtained by considering the weak-link as a combination of a junction with a sinusoidal CPR in series with a linear inductor, as shown in Fig. 3.2. In this method, the current-phase-relation is not given in terms of the phase difference across the junction but in terms of total phase drop across the linear inductor  $\varphi_L$  and the junction  $\varphi_{Lj0}$  as

$$\varphi = \varphi_L + \varphi_{Lj} = \frac{2\pi L I}{\Phi_0} + \arcsin \left( \frac{I}{I_{\text{c}0}} \right) \quad (3.3)$$

<sup>2</sup>Characteristic Cooper pair size, i.e. characteristic correlation length in the superconducting wave-function.

<sup>3</sup>Average distance traveled by a particle between successive collisions

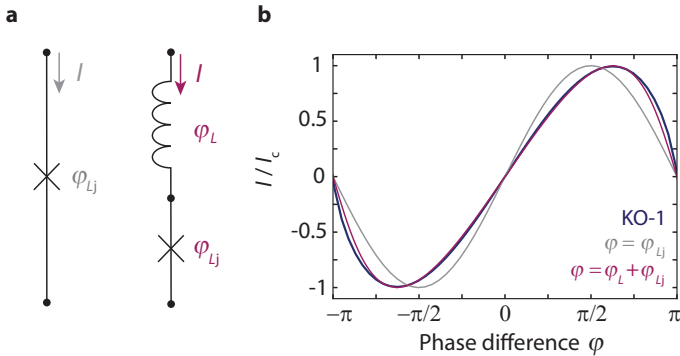


**Figure 3.2: Current phase relation of a single Josephson junction and of a junction in series with a linear inductor.** **a** presents the circuit diagram of a single Josephson junction with phase drop of  $\varphi_{Lj}$  on the left side and a second circuit diagram, on the right, containing the junction in series with a linear inductor. Here, the total phase drop is given by  $\varphi = \varphi_L + \varphi_{Lj}$ . In **b** the CPR of the single junction is represented as the gray curve, the CPR of the combination of the junction with a linear inductor of inductance  $L = 0.4L_j$  is shown as violet curve and the CPR predicted by the KO-1 model is represented as the dark blue curve.

As shown in Fig. 3.2**b**, there is a clear deviation of the KO-1 model from a sinusoidal CPR. However, by considering a phase drop of the form of Eq. (3.3), for an inductor  $L = 0.4L_{j0}$ , we obtain a very good approximation to the KO-1 model. At this point we can assume that this provides a good description of a weak-link junction, as the amount of linear inductance required to match the KO-1 model could be thought as the linear inductance of the connecting electrodes.

For simplicity, it is assumed along this thesis that the junctions utilized in the fabricated devices fall into the KO-1 regime and their behavior can be modeled by the linear inductance approximation. However, the extensive experimental study of the intrinsic properties of Aluminum weak link junctions by Refs. [114–116] reports some deviations from the KO-1 model, especially for 2D geometries.

## 3.2. 2D AND 3D SQUID CAVITIES

### 3.2.1. DESIGN CONSIDERATIONS FOR SQUIDS WITH NON-NEGLIGIBLE LOOP INDUCTANCE

As the essence of flux-mediated and photon-pressure systems relies on using an external oscillatory mode to modulate the magnetic flux coupled to the loop of a SQUID cavity, the coupling strength of these systems can be enhanced by increasing the area of the SQUID loop, subsequently increasing the SQUID loop inductance. As it will be discussed in this section, this plays a major role on the performance of our SQUID cavities.

In the discussion of section 2.2, the loop inductance contribution was neglected and the total flux seen by the SQUID was assumed to be of an exclusively external nature. However, for the case of a non-negligible loop inductance  $L_{loop}$ , the magnetic flux generated by the screening current  $\Phi_s = L_{loop}I_s$  also needs to be taken into account. The

total magnetic flux threading the loop is therefore given by

$$\Phi = \Phi_{\text{out}} + L_{\text{loop}} I_s. \quad (3.4)$$

The impact of the flux generated by the screening current to the total flux threading the SQUID will strongly depend on the magnitude of the loop inductance. This contribution can be discussed in terms of the screening parameter

$$\beta_L = \frac{2L_{\text{loop}}I_{c0}}{\Phi_0}. \quad (3.5)$$

As shown in section 2.2, for the cases where the loop inductance is negligible, i.e.  $\beta_L \ll 1$ , the total flux is only given by  $\Phi = \Phi_{\text{out}}$  and the critical current  $I_c$  of the SQUID, which is found by maximizing the transport current, takes the form

$$I_c = 2I_{c0} \left| \cos\left(\frac{\pi\Phi}{\Phi_0}\right) \right|. \quad (3.6)$$

3

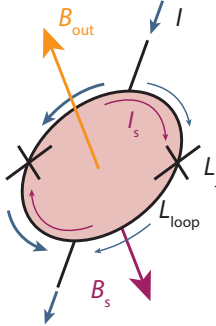


**Figure 3.3: Representation of a SQUID with non-negligible loop inductance in the presence of an external magnetic field  $B_{\text{out}}$ .** When a symmetric SQUID is in the presence of an external magnetic field  $B_{\text{out}}$ , it generates a screening current  $I_s$  which flows around its loop. As the SQUID has a non-negligible loop inductance  $L_{\text{loop}}$ , the screening current will generate an additional magnetic field, which at the inner part of the loop opposes the external field. This second contribution is represented by  $B_s$ . The total magnetic flux in the SQUID is given by  $\Phi = \Phi_{\text{out}} + \Phi_s$ .

However, for higher  $\beta_L$  values, i.e. when ratio of loop to Josephson inductance increases, the presence of a screening current will have a considerable impact on the net flux seen by the SQUID as  $\Phi_s$  tends to counter the applied magnetic field (see Fig. 3.3). Based on Eq. (2.23) and Eq. (3.4), the total flux  $\Phi$  and the transport current  $I$  flowing in the SQUID can be re-written as [96]

$$\Phi = \Phi_{\text{out}} - \frac{\Phi_0 \beta_L}{2} \sin\left(\pi \frac{\Phi}{\Phi_0}\right) \cos\left(\varphi_1 + \frac{\pi\Phi}{\Phi_0}\right) \quad (3.7)$$

$$I = 2I_{c0} \cos\left(\pi \frac{\Phi}{\Phi_0}\right) \sin\left(\varphi_1 + \frac{\pi\Phi}{\Phi_0}\right) \quad (3.8)$$

The SQUID critical current can be found numerically [117] by maximizing the transport current  $I$  with respect to the phase difference of a single junction  $\varphi_1$ , which is independently determined from Eq. (3.7). Since  $\beta_L$  only plays a role for non-zero values of  $\Phi$ , the critical current of an un-flux biased SQUID with high loop inductance will remain  $2I_{c0}$ . However, at half flux quantum it can be approximated as

$$I_c \left( \frac{\Phi_0}{2} \right) = 2I_{c0} \frac{\beta_L}{1 + \beta_L}. \quad (3.9)$$

### 3

The previous relation Eq. (3.9) provides an excellent description of the problem attached to SQUIDs with a large loop inductance, as it shows how the parameter  $\beta_L$  has a crucial impact on the maximum amplitude modulation of the SQUID critical current (see Fig. 3.4a). An helpful reference point is to consider the case where  $\beta_L = 1$ . In this case, the loop inductance is larger by approximately a factor of 3 ( $L_{\text{loop}}/L_{j0} = \pi$ ) and the critical current modulation is reduced by 50% compared to the ideal situation of a negligible loop inductance.

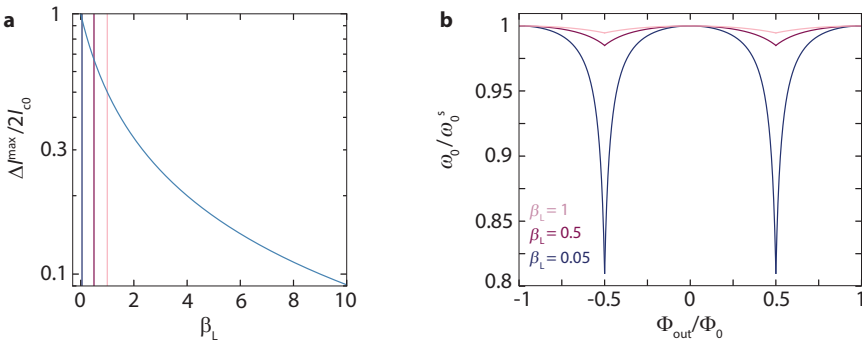


Figure 3.4: **Impact of  $\beta_L$  in critical current and resonance frequency modulations.** a shows how the maximum critical current modulation  $\Delta I^{\max} = 2I_{c0} - I_c(\Phi_0/2)$  is reduced compared to the ideal case of negligible loop inductance ( $\Delta I^{\max} = 2I_{c0}$ ), depending on the screening parameter  $\beta_L$ . The plotted values are normalized to  $2I_{c0}$ . The vertical lines, which correspond to a  $\beta_L$  of 0.05, 0.5 and 1, show a critical current modulation of 95%, 66% and 50% compared to the ideal case, respectively. When combining the SQUID with a linear LC circuit, the flux dependent critical current modulations will lead to a modulation of the resonance frequency, which also depend on the screening parameter  $\beta_L$ . In b, the resonance frequency normalized to the sweet spot frequency  $\omega_0/\omega_0^s$  is plotted versus external flux  $\Phi_{\text{out}}$  for three different values of  $\beta_L = 0.05, 0.5$  and 1.

Furthermore, as we deal with SQUID cavities, it is of interest to understand how this reduction in critical current modulations due to a high screening parameter  $\beta_L$  translates into a resonance frequency  $\omega_0$  modulation. In the typical circuit configuration of our devices where a bias current is not applied, Eq. (3.7) can be reduced to

$$\frac{\Phi}{\Phi_0} = \frac{\Phi_{\text{out}}}{\Phi_0} - \frac{\beta_L}{2} \sin \left( \pi \frac{\Phi}{\Phi_0} \right). \quad (3.10)$$

Additionally, based on the SQUID inductance

$$L_s(\Phi) = \frac{L_{s0}}{\cos\left(\pi\frac{\Phi}{\Phi_0}\right)}, \quad (3.11)$$

where  $L_{s0}$  is the SQUID inductance at zero field, the resonance frequency of a LC circuit containing SQUID in series with a linear inductor  $L$  takes the form

$$\omega_0(\Phi) = \frac{1}{\sqrt{C(L + L_s(\Phi))}}. \quad (3.12)$$

By equivalently expressing Eq. (3.12) in terms of the sweet-spot frequency  $\omega_0^s = \frac{1}{\sqrt{C(L + L_{s0})}}$ , the flux dependent resonance frequency (*flux-arch*) is given by

$$\omega_0(\Phi) = \frac{\omega_0^s}{\sqrt{\Lambda + \frac{1-\Lambda}{\cos\left(\pi\frac{\Phi}{\Phi_0}\right)}}}, \quad (3.13)$$

where  $\Lambda = L/(L + L_{s0})$ . Note that, in contrast to the case of a negligible loop inductance discussed in section 2.2,  $\Phi$  now represents the total flux in the SQUID given by the relation 3.10 and not the external flux  $\Phi_{\text{out}}$ .

In essence, the effects of a non-negligible screening parameter  $\beta_L$  will appear as a widening of the flux arch and result in a hysteretic flux-dependence. Although the flux-arch sweet spot will still occur for multiple values of  $\Phi_0$ , the total amount of external flux  $\Phi_{\text{out}}$  required for a full modulation, which in the ideal case was  $\Phi_0$ , will be increased. As consequence, for external flux values  $\Phi_{\text{out}}$  beyond  $\pm\frac{\Phi_0}{2}$ , the critical current will be multi-valued, generating what we later call *flux jumps*. Several examples of these jumps, where the SQUID cavity resonance frequency switches from a low point in the flux arch to another above it, can be seen in the experimental work reported in chapters 4, 5 and 6, and in the work of Refs.[120–122].

The flux dependent resonance of a SQUID cavity, normalized to the sweet-spot frequency, is plotted in Figure 3.4b for three different values of  $\beta_L$  (where the multi stable regime was omitted for clarity). As shown by the different plotted curves, an increment in screening parameter leads to a strong suppression in resonance frequency modulations.

In short, the biggest drawback of having a large loop inductance, and therefore a non-negligible screening parameter  $\beta_L$  is the suppression of resonance frequency modulations. As previously mentioned in sections 2.5.2 and 2.5.3, the optomechanical single-photon coupling strength strongly depends on the resonance frequency external flux responsivity  $\frac{\partial\omega_0}{\partial\Phi}$ , therefore minimizing  $\beta_L$  in our devices, becomes essential for achieving high coupling rates.

### 3.2.2. THE KINETIC INDUCTANCE CONTRIBUTION

Besides the self-inductance associated with the geometry of our circuit elements  $L_{\text{geo}}$ , which arises from the energy stored in the magnetic field, our devices typically have a

large kinetic inductance contribution due to the thin films utilized for their fabrication. As this inductance arises from the kinetic energy stored in the motion of the charge carriers, it can be calculated by equating the kinetic energy of the Cooper pairs to an equivalent inductive energy. The kinetic inductance of a superconducting wire with thickness  $t$ , length  $l$  and width  $w$  can then be written as [118]

$$L_k = \mu_0 \lambda_L^2 \frac{l}{wt}, \quad (3.14)$$

## 3

where  $\mu_0$  is the vacuum permeability and  $\lambda_L$  is the London penetration depth of the material. Note that the estimation of the kinetic inductance contribution used in the sections 3.3.1 and 3.4.1 was based on the reference value of  $L_k \approx 2.75 L_{\text{geo}}$  for an aluminum film of 20 nm. This was obtained by comparing the resonance frequency of an experimentally measured SQUID cavity with the simulations of the device using the software package SONNET.

As shown by Eq. (3.14), the kinetic inductance scales inversely with the thickness of the film. This is mostly reflected on the screening parameter  $\beta_L$  of SQUIDs composed of 2D nano-bridge Josephson junctions, which is considerably enhanced due to the kinetic inductance of the loop. Hence, switching to a 3D geometry where the thickness of the SQUID loop is increased, was essential for minimizing the screening parameter and optimizing the performance of nano-bridge SQUID cavities.

### 3.2.3. NANOFABRICATION TECHNIQUES

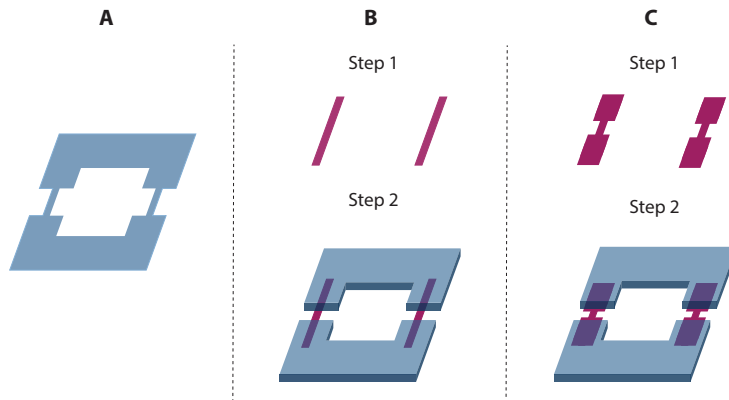
The process optimization for the fabrication of nano-bridge SQUIDs was not a straight forward process and before achieving a final working recipe, several approaches were followed. In this subsection, a description of each of the attempted fabrication methods in a chronological way and the reason behind their failure will be provided.

#### ATTEMPT 1: 3D SQUIDS via method B using evaporated aluminum films.

The very first pursued fabrication technique is shown in a schematic diagram in Fig. 3.5B and can be found in the summarizing Table 3.1 as attempt 1. The idea was to split the fabrication in two steps. The first, where 20 nm thick nano-bridge junctions would be patterned (see step 1 of Fig. 3.5B) in a *evaporation process*<sup>4</sup> followed by a *lift-off*<sup>5</sup> technique, and the second step where a 100 nm thick SQUID loop would be deposited on top of the junctions (step 2), also in an evaporation plus lift-off patterning procedure. A SEM image of one of these devices can be seen in Fig. 3.6c. Even though visually the SQUID fabrication appeared to be successful, once the devices were tested in a DC measurement scheme, extremely high resistances across the SQUIDs were measured and no supercurrent was found. The most probable reason for the failure of this attempt was the presence of a native aluminum oxide layer between the two patterned films, which could have been disrupting the electrical contact between the loop and the weak links.

<sup>4</sup>The evaporation processes in this thesis were done in a Temescal FC-2000 system. In this deposition method, a hot aluminum source evaporates into a vacuum chamber, subsequently traveling to the target object. The fact that the particles travel in vacuum makes it a highly directional process.

<sup>5</sup>The lift-off process used on evaporated films along this section was done via a warm N-Methyl-2-pyrrolidone (NMP) bath at  $\sim 60^\circ\text{C}$  with a steering magnet.



3

Figure 3.5: **Attempted methods for the nanofabrication of 2D and 3D SQUIDs.** A describes the fabrication process of 2D SQUIDS where the device patterning consists on a single step. In B it is shown the fabrication workflow for 3D SQUIDS, where the patterning of the nano-bridge junctions is done in step 1 and the patterning of the SQUID loop in step 2. Process C also shows a fabrication method for 3D SQUIDS with a modified step 1 in comparison with process B. Here the junctions are patterned simultaneously with large contact area pads which, later on, will be the galvanic connection point with the SQUID loop.

**ATTEMPT 2:** Fabrication of 3D SQUIDs using method B with evaporated aluminum films and including argon milling in between steps.

As a solution for the problem of attempt 1, we tried performing an *argon milling*<sup>6</sup> step in situ, prior to the second evaporation layer, in order to remove the aluminum oxide (see attempt 2 in Table 3.1). Surprisingly, the outcome of this new step resulted in the presence of black features around the latest patterned layer (see Fig. 3.6d and e). These features have been reported in literature [119, 123] as *black veil of death*, however a concrete explanation for their appearance or a quantitative study of their impact on the losses of the film, to our knowledge, has not been found. Furthermore, this was not the only problem attached to the new fabrication step. In addition, the high temperatures associated with the argon milling procedure were causing a deformation of the resist layer, which very often led to a galvanic contact between the two arms of the SQUID loop and, in addition, would cause the loop itself not to be released during lift-off (see Fig. 3.6a and b). Further efforts involving the re-design of the SQUID loop in order facilitate the lift-off, e.g. increasing the gap between the arms or modifying the shape of the arms from squared to rounded corners were done, however the devices showed similar results as the ones of attempt 1.

**ATTEMPT 3:** 2D SQUIDs using method A and evaporated aluminum films.

Due to the difficulty in combining the two layers, we switched to a 2D design, which is shown in Fig. 3.5A and is labeled in Table 3.1 as attempt 3. In this case, both the SQUID

<sup>6</sup>Here, argon ions are accelerated from a high energy ion gun into the surface of a substrate, in order to remove an overlying amorphous material layer.

3

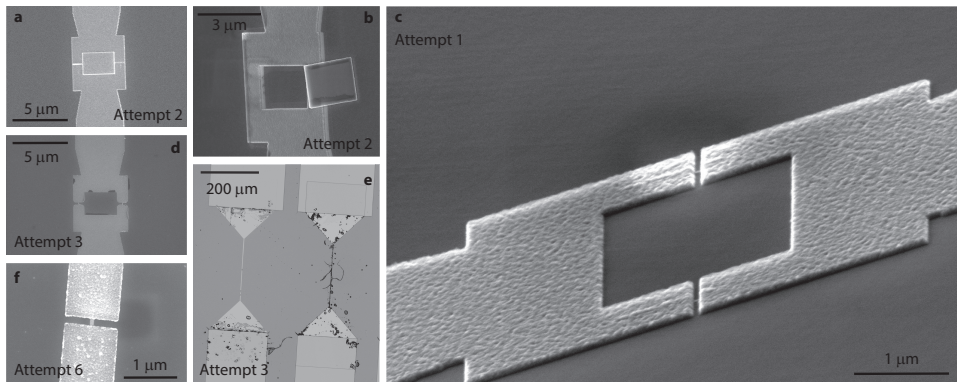


**Figure 3.6: Collected SEM and optical images of failed fabrication attempts.** **a** and **b** show examples where the SQUID loop and junction gap was not (fully) lifted-off. Panel **c** shows the case where the lift-off process was successful, however the device contained an aluminum oxide layer between the two patterns, which is not visible in the image. The presence of the so called *black veil of death* is visible in figs. **d** and **e**. In addition, an example of the weak adhesion of the thin aluminum on the substrate is shown in the optical image presented in **e**, where holes in the aluminum layer are visible at the edges of the patterned pads. Finally **f** shows an example of a failed 3D nano-bridge junction made with sputtered Aluminum films, where the contact area was etched away. The number of the attempted fabrication approach for which each sub-figure corresponds too is given in the label and a summary of the different utilized methods and corresponding success outcome can be found in Table 3.1

loop and the junctions were patterned simultaneously in a single evaporation plus lift-off step, where the whole film would have a thickness of  $\approx 20\text{ nm}$ . The most critical issue with this approach was the low adhesion between the aluminum film and the substrate, which resulted on the deposited layer "peeling off" during lift-off. The lift-off process, which was done via a warm N-Methyl-2-pyrrolidone (NMP) bath at  $\sim 60^\circ\text{C}$  with a steering magnet, was modified several times to different temperatures and steering strengths, but all the attempts ended up being unsuccessful trials. A common way to solve adhesion issues is by surface preparation [124]. To counter this problem we tried to perform an argon milling step on the substrate prior to the deposition of the single aluminum layer. This, on the other hand, brought back the *black veil of death* structures and seemed to not have solved the adhesion issue (see Fig. 3.6e). Therefore, the approach was no longer pursued.

**ATTEMPT 4:** 2D SQUIDs via method A using evaporated aluminum films on a thin layer of Titanium.

Attempt 4 consisted on following the fabrication procedure of attempt 3 but also including the evaporation of a thin layer of Titanium ( $\sim 2\text{ nm}$ ) *in situ*, prior to the aluminum deposition (attempt 4 in Table 3.1). This turned out to be a somewhat successful approach, as the adhesion problems were solved and the no further fabrication issues appeared. The devices were subsequently tested in DC and showed critical currents in the order of  $20 - 30\mu\text{A}$  as well as flux modulations. However, when the fabrication was repeated for SQUID cavities, extremely low Q factors were found ( $\sim 90$ ) and the method turned out to be not appropriate for the fabrication of high Q microwave SQUID cavities.

Attempt	Fabrication method	Outcome	Figure	Main issue	Research chapters
1	B with evaporated aluminum	✗	Fig. 3.6c	Presence of aluminum oxide between the two layers	N.A.
2	B with evaporated aluminum and an intermediate argon milling step	✗	Fig. 3.6a and b	Resist layer deformation causing a problematic lift-off	N.A.
3	A with evaporated aluminum	✗	Fig. 3.6d and e	Low surface adhesion	N.A.
4	A with evaporated aluminum and Ti adhesion layer	✗	N.A.	Cavities with low Q factors (~ 90)	N.A.
5	A with sputtered aluminum	✓	Fig. 3.7a and c	N.A.	4 and 6
6	B with sputtered aluminum and an intermediate argon milling step	✗	Fig. 3.6f	Junctions etched away by argon milling process	N.A.
7	C with sputtered aluminum and an intermediate argon milling step	✓	Fig. 3.7b and d	N.A.	5 and 7

3

Table 3.1: **Summary the different attempted fabrication methods and their success outcome.** The first column has a short description of the utilized method. The letters **A**, **B** and **C** correspond to different fabrication approaches. A schematic representation of these different methods is shown in Fig. 3.5. The third column presents the fabrication outcome of the utilized approach. The symbol ✓ represents a successful fabrication method and the symbol ✗ corresponds to a failed attempt. Column 4 describes the problem behind the fabrication recipe and the in the last column, the research chapter which explores a sample fabricated with the corresponding successful method is indicated. The methods are listed in chronological order. A detailed description of each of these methods, the reason for their failure and possible solutions for each problem are given in the text.

### ATTEMPT 5: 2D SQUIDS via method A and using sputtered aluminum films.

Since the fabrication of the nano-bridge SQUIDs using evaporated films was considerably challenging, we wondered about the possibility to switch to sputtered films, since in a *sputtering process*<sup>7</sup>, the deposition occurs as the atoms in a plasma medium slowly condense as a thin film on the substrate, therefore generating a good adhesion to the chip. Even though we worked with the peculiar combination of sputtering and lift-off, this turned out to be a successful approach (attempt 5 in Table 3.1) and the SQUID cavities made using this fabrication technique had *Q* factors on the order of ~ 10000. The primary reason why sputtered films are not usually combined with a lift-off technique is due to the fact that the deposition is less directional compared to an evaporation method. This causes the aluminum atoms to deposit not only on the surface but also on the resist sidewalls, therefore complicating the lift-off process as the resist is no

<sup>7</sup>The sputtering of aluminum films along this thesis was done via a DC sputtering deposition in a Alliance-concept AC450 machine.

longer exposed to the solvent. Our solution for this drawback was to place the sample on the bottom of the beaker in a strong ultrasonic bath for a few minutes. This would crack the thin aluminum layer covering the resist walls, making the lift-off process possible. Despite the appearance of *dog-ears*<sup>8</sup>, the remaining film would be undamaged by the technique. A detailed description of the whole fabrication recipe of 2D SQUIDs can be found in the supplementary material of chapters 4 and 6, as it was used to fabricate the SQUID cavities utilized in the experimental work reported in those chapters. In addition, a SEM image of a 2D SQUID can be seen in Fig. 3.7a and a zoom-in a 2D nano-bridge Josephson junction in Fig. 3.7c.

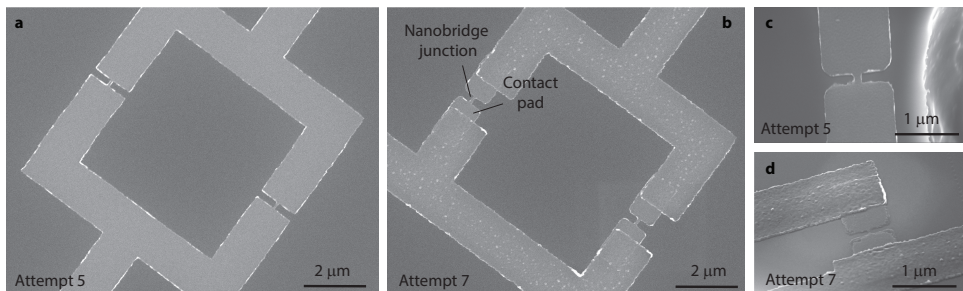


Figure 3.7: **SEM images of working 2D and 3D SQUIDs.** a shows a working 2D SQUID made by following the fabrication technique A with sputtered aluminum. A zoom-in of a nano-bridge Josephson junction is shown in c. A successfully working device fabricated with method C is shown in b. In addition, a zoom-in of a 3D Josephson junction fabricated with method C is presented in d. The number of the attempted fabrication approach is labeled in each of sub-figures and a summary of all the different utilized methods and corresponding success outcome is presented in Table 3.1.

### ATTEMPT 6: 3D SQUIDs using method B and sputtered aluminum films.

Despite of the success of the 2D fabrication procedure, the SQUID cavities made with this technique had an extremely high kinetic inductance contribution of approximately 70% of the total circuit inductance (see section 3.2.2). Furthermore, the kinetic inductance, which scales with the inverse of the material thickness, was also contributing to an elevated value of loop inductance. This resulted in SQUID cavities with considerably high screening parameters  $\beta_L$  (see section 3.2.1) with some devices reaching  $\beta_L \approx 6$ .

In order to make a second generation of devices with enhanced single-photon coupling strengths, the screening parameter  $\beta_L$  and therefore the loop inductance had to be reduced. Therefore, we opted for retrying the former 3D design (see Fig. 3.5B) but this time using sputtered films instead of evaporated (attempt 6 in Table 3.1). An image of a 3D Josephson junction fabricated using this approach can be seen in Fig. 3.6f. When the microwave SQUID cavities fabricated with this approach were tested, no resonances were found, indicating that the fabrication had not succeeded. With the existing knowledge that the film had a good adhesion to the substrate and that previous cavities

<sup>8</sup>Also known as *fences*, these are pieces of the coated sidewalls which are not completely removed during lift-off and stay attached to the edges of the patterned layer.

had shown high quality factors, the only remaining option was a problematic contact between the two layers.<sup>9</sup>

The true origin of the problem lied on the ion milling process performed to remove the aluminum oxide on top of the first layer. This turned out to be less directional than we originally assumed and the etching of the nano-bridge junctions was occurring not only from the top, but also from the sides, which caused the bridges to be completely etched away.

### ATTEMPT 7: 3D SQUIDs using method C and sputtered aluminum films.

3

A solution for the problem of attempt 6 was to pattern large area contact pads together with the nano-bridge junctions acting as the contact point between the constrictions and the SQUID loop. The fabrication approach was thus modified to the one of Fig. 3.5C and it is shown in Table 3.1 as attempt 7.

This also turned out to be a successful fabrication method, allowing us to fabricate devices with  $\beta_L \approx 0.7$ . Furthermore, a simple way to further improve this value would be by exposing the SQUID to an additional ion-milling step at the end of the fabrication. However, this had to be extremely short ( $\approx 10$  sec) to avoid etching away the junctions and should only be performed on the SQUID in order to not decrease the cavity Q factor. The idea behind this final step was not to decrease the loop inductance but to slightly decrease the critical current of the junctions by reducing their thickness and width. A SEM image of one of these devices is shown in Fig. 3.7b and a zoom-in of the junction in Fig. 3.7d. Furthermore, a detailed description of the fabrication steps can be found in the supplementary material of chapters 5 and 7, as the SQUID cavities utilized in those chapters were fabricated using this technique.

## 3.3. MECHANICAL BEAMS

### 3.3.1. MAXIMIZING $g_0$ IN FLUX-MEDIATED OPTOMECHANICAL SYSTEMS

The single-photon coupling strength of a flux-mediated optomechanical system where a mechanical beam is embedded in a SQUID loop (see section 2.5.2) is given by

$$g_0 = \frac{\partial\omega_0}{\partial\Phi} B_{\text{in}} l x_{\text{zpf}}. \quad (3.15)$$

Here  $\frac{\partial\omega_0}{\partial\Phi}$  is the cavity external flux responsivity,  $B_{\text{in}}$  is the applied in-plane magnetic field,  $l$  is length of the beam and  $x_{\text{zpf}}$  its zero-point fluctuations. The constant factor  $\gamma$  which accounts for the mode shape was omitted from Eq. (3.15) as its value is  $\approx 1$ . From Eq. (3.15), one would naively think that in order to boost the single-photon coupling strength  $g_0$ , all the terms should be individually increased. However, these parameters are not independent of each other and therefore, the design of mechanical beams should also take into account the impact of its geometry on other cavity parameters. The zero-

<sup>9</sup>Ironically enough, we were back on dealing with the same problem that we had encountered when we initially tried to fabricate 3D SQUIDs with evaporated films.

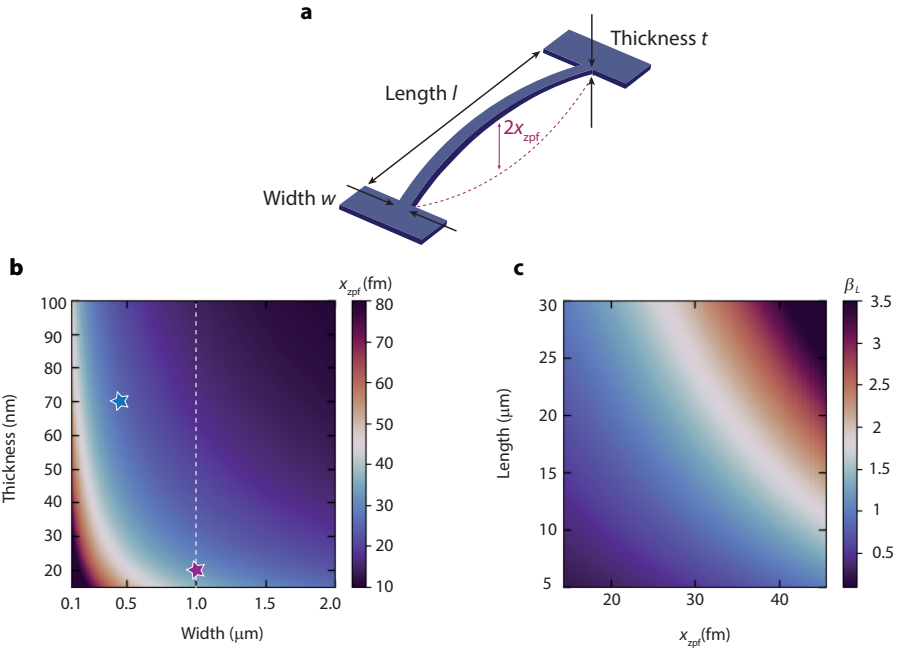


Figure 3.8: **Impact of engineering the beam dimensions on the screening parameter  $\beta_L$ .** a shows a schematic diagram of a mechanical beam of length  $l$ , width  $w$  and thickness  $t$ . The zero-point fluctuations of the beam are shown vs its width and thickness in b. The violet and blue stars correspond to the operating properties of the devices of chapters 4 and 5, respectively. In c, the effect of increasing the zero-point motion and the beam length on the screening parameter  $\beta_L$  is shown. For simplicity, here the width of both the beam and the loop wire was fixed to  $1\mu\text{m}$  (indicated by the white dashed line in a). In addition the junction critical current  $I_{c0}$  was kept constant and equal to  $10\mu\text{A}$ . When one increases the length  $l$ , or reduces the thickness of the beam, the loop inductance  $L_{\text{loop}}$  will increase, raising the screening parameter  $\beta_L$ . In c, the SQUID loop dimensions are given by  $3 \times l \mu\text{m}^2$ . The stars representing the devices of chapter 4 and 5, were not plotted in c since parameters such as width of the loop or junction critical current might differ. In addition, the loop inductance  $L_{\text{loop}}$ , which was calculated from the dimensions of the SQUID, was based on a geometric inductance per length of  $L_{\text{geo}} = 1\text{pH}/\mu\text{m}$  [118] and a kinetic inductance contribution which was adjusted accordingly to the thickness of the beam.

point motion  $x_{\text{zpf}}$  of a mechanical aluminum beam of length  $l$ , width  $w$  and thickness  $t$  as represented in Fig. 3.8a is given by [56]

$$x_{\text{zpf}} = \sqrt{\frac{\hbar}{2m\Omega_0}}, \quad (3.16)$$

where  $m = \rho \cdot t \cdot w \cdot l$  is the mass of the beam,  $\rho = 2700\text{kg/m}^3$  is the material density and  $\Omega_0$  is its resonance frequency. The resonance frequency of the out-of-plane mode, where the motion of the beam is perpendicular to the SQUID loop, can be obtained from the beam geometry. In the high-stress limit it is given by [125]

$$\Omega_0 = \pi \frac{a}{l}. \quad (3.17)$$

Here, the constant factor  $\alpha = \sqrt{\frac{\sigma}{\rho}}$  represents the phonon phase velocity in the beam and it has shown to be  $\approx 300$  m/s for many of our devices. This however, has a considerable dependence on the utilized sputtering process parameters as  $\sigma$  is the tensile stress of the film [24]. For simplicity, this value was considered constant during the following discussion. By using the last two expressions which relate the geometry of the beam and its mass and resonance frequency, the zero-point motion can be re-written independently of the beam length as

$$x_{\text{zpf}} = \sqrt{\frac{\hbar}{4\pi\rho\alpha tw}}. \quad (3.18)$$

Fig. 3.8b shows a color plot of the zero-point motion for different values of beam thickness and width. The beam fluctuations  $x_{\text{zpf}}$  can be maximized by decreasing the width and thickness of the beam, regardless of its length. However, by doing so and/or by increasing its length, the SQUID loop inductance and therefore the screening parameter  $\beta_L = \frac{2I_{\text{c}0}L_{\text{loop}}}{\Phi_0}$  are also enhanced. This is represented in Fig. 3.8c, for the case where the width of the beam and of the loop wire were set to  $1\mu\text{m}$ . While a thickness reduction translates into a higher kinetic inductance contribution (see section 3.2.2), an increment of the length of the resonator will rise the geometric and kinetic inductance of the loop. Note that a diminution in the width of the beam would have a similar effect to a reduction of its thickness.

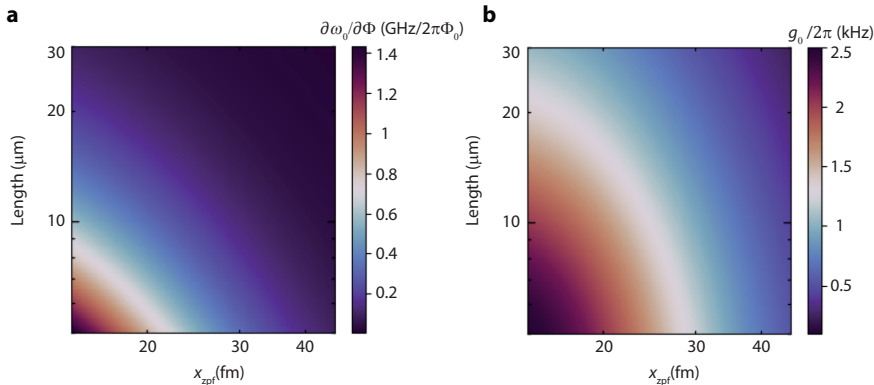


**Figure 3.9: Impact of engineering the dimensions of the beam on the flux responsivity and  $g_0$ .** In a, a color map of the cavity external flux responsivity  $\frac{\partial\omega_0}{\partial\Phi}$  at  $\Phi = 0.5\Phi_0$  vs the zero-point fluctuations  $x_{\text{zpf}}$  and the length of beam is shown. Here, the cavity sweet-spot frequency was considered to be  $7.25\text{GHz}$  and the total circuit inductance  $L = 730\text{pH}$ . In b the calculated single-photon coupling strength  $g_0$  of an optomechanical system exposed to an in-plane magnetic field  $B_{\text{in}} = 50\text{mT}$  is shown vs  $x_{\text{zpf}}$  and  $l$ . Here, the width of the SQUID loop remained constant and equal to  $3\mu\text{m}$ , the width of the loop wire was set to  $1\mu\text{m}$  and the junction critical current  $I_{\text{c}0}$  to  $10\mu\text{A}$ . Furthermore the x-axis of a and b were calculated based on a constant beam width equal to  $1\mu\text{m}$  and a variable thickness  $t$  as represented by the dashed white line in a.

As discussed in section 3.2.1, for higher values of the screening parameter  $\beta_L$ , the amount of external flux needed for a full modulation will go beyond  $0.5\Phi_0$  appearing as a widening of the SQUID cavity flux arch. This leads to an overlap of different flux archs,

which beyond the threshold value of  $\Phi_{\text{out}} = \pm 0.5\Phi_0$  leads to an unstable regime where the cavity resonance frequency is multi-valued. The corresponding threshold value for the resonance frequency increases with  $\beta_L$ , as the amplitude of the cavity frequency modulations are reduced. In fact, not only the operation frequency is modified, but also the flux-responsivity at that point is impacted.

In Fig. 3.9a, the flux responsivity of a  $3 \times l \mu\text{m}^2$  SQUID cavity of thickness  $t$  is estimated for the threshold flux operation point  $\Phi_{\text{out}} = 0.5\Phi_0$ <sup>10</sup>. This was found numerically by extracting the derivative of the resonance frequency versus external flux (Eq. 3.13). As shown in Fig. 3.9a, as the length  $l$  of the beam increases and/or the thickness  $t$  is reduced, thus enhancing the zero-point motion of the resonator, the external flux responsivity is considerably suppressed. Moreover, this effect translates into a strong limitation of the single-photon coupling strength  $g_0$ . Therefore, as seen in Fig. 3.9c, one cannot infinitely increase the zero-point fluctuations  $x_{\text{zpf}}$  or the beam length  $l$  to boost single-photon coupling strength, as it would appear from a first look to Eq. (3.15). Eventually the SQUID loop inductance and the screening parameter  $\beta_L$  will come into play and restrict  $g_0$  by reducing the cavity flux responsivity.

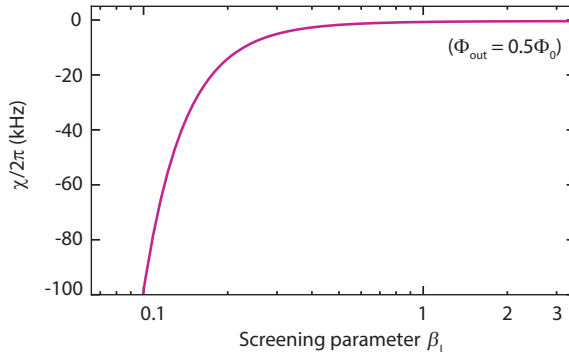


Figure 3.10: **SQUID cavity anharmonicity operating at  $\Phi_{\text{out}} = 0.5\Phi_0$  vs  $\beta_L$ .** A sweet-spot frequency of 7.25 GHz, a total circuit inductance of  $L = 730\text{pH}$  and a sweet spot Josephson inductance  $L_{j0} = 16.5\text{pH}$  were considered.

Furthermore, in the regime where  $g_0$  is highest, a different effect has to be considered. As the screening parameter  $\beta_L$  starts to decrease, the ratio between the cavity anharmonicity at an operation point  $\Phi_{\text{out}}$  and the sweet spot anharmonicity  $\chi(\Phi_{\text{out}})/\chi_{\text{sweet}}$  starts rising, therefore limiting the amount of drive photons the cavity can sustain before switching to a Duffing behavior (see section 2.4). Fig. 3.10 shows how the anharmonicity at  $\Phi_{\text{out}} = 0.5\Phi_0$  is modified by  $\beta_L$ .

In short, there is a trade-off between the cavity flux responsivity  $\frac{\partial\omega_0}{\partial\Phi}$  and maximum applicable drive powers. If one wants to engineer a device that tries to maximize the coupling strength  $g_0$  and explore optomechanical single-photon effects, the design of the system should focus on exclusively maximizing  $g_0$  and therefore minimizing the di-

<sup>10</sup>Note that the points within the unstable regime are still accessible experimentally. However, as the cavity is prone to *flux-jumping*, a proper magnetic shielding is vital for operating the device.

mensions of the beam. On the other hand, if one intends to explore optomechanical effects which rely on a highly enhanced multi-photon coupling strength  $g = \sqrt{n_c} g_0$ , designing a system with a slightly higher  $\beta_L$  would allow for an extended range where the intracavity photon numbers scale linearly with drive power. For this last approach, the key would be to minimize the kinetic inductance contribution to the SQUID loop.

### 3.3.2. NANOFABRICATION TECHNIQUES

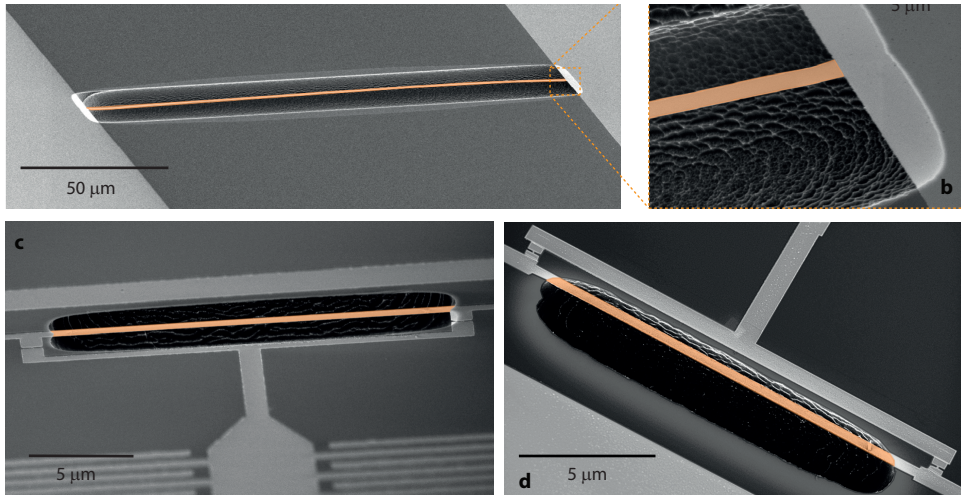


Figure 3.11: **Collection of SEM images showing different fabricated mechanical beams false colored in orange.** **a** shows a  $150\text{ }\mu\text{m}$  long mechanical beam fabricated during a release test and **b**, the corresponding zoom-in of the edge of the beam. The presented device was not measured. Figure **c** shows a 2D SQUID cavity where part of the loop was released to act as high  $Q$  mechanical beam. The presented device is the one of study in chapter 4. Finally **d** presents the 3D optomechanical SQUID cavity investigated in chapter 5. The thickness of the beam is  $\sim 80\text{ nm}$  in **d** and  $\sim 20\text{ nm}$  in the remaining figures. Here, bright parts are aluminum, dark parts are silicon and the suspended beams are false-colored with orange.

The fabrication of high- $Q$  mechanical beams to be embedded in a SQUID, as described in section 2.5.2, is based on suspending part of the loop by removing the underlying silicon substrate in an isotropic *reactive ion etching*<sup>11</sup> process [126]. As the etch is a combination of a chemical and physical etch, the directionality of the process can be tuned by randomizing the ions motion before they hit the sample surface, i.e., by increasing the gas pressure and decreasing RF power used to generate the plasma. In this way, the exposed silicon is etched in an isotropic way, making it possible to etch underneath the patterned beam. Moreover, the resonator is not damaged by the procedure as aluminum is not chemically selected by the plasma. A SEM image of a beam fabricated

<sup>11</sup>In a RIE process, a plasma is generated by applying a RF electromagnetic field, which ionizes the gas molecules. The ions are subsequently accelerated by a DC voltage that was generated by the deposition of free electrons on a isolated plate and eventually collide with the sample, chemically reacting with the exposed materials.

during a test release can be seen in Fig. 3.11**a** and **b**. Due to the optimal tensile stress of the sputtered films, the fabrication of these beams turned out to be very a simple and robust process, working for a wide range of beam dimensions and reaching quality factors on order of  $Q \sim 10^6$ . In order to engineer optomechanical devices, this release step was later on combined with the previously described fabrication of 2D and 3D SQUID cavities. Two of the resulting 2D and 3D devices are shown in Fig. 3.11**c** and Fig. 3.11**d** and they were the focus of the research presented in chapters 4 and 5, respectively.

## 3

### 3.4. RF MICROWAVE CAVITIES

#### 3.4.1. MAXIMIZING $g_0$ IN PHOTON-PRESSURE SYSTEMS

As discussed in section 2.5.3, in our photon-pressure systems, we explore an analogue of the radiation-pressure interaction by coupling the current flowing in a Radio-Frequency (RF) circuit to the resonance frequency of a high frequency SQUID cavity. The single-photon coupling strength of the system, as discussed in section 2.5.3 is given by

$$g_0 = \frac{\partial\omega_0}{\partial\Phi} \Phi_{\text{zpf}}, \quad (3.19)$$

where  $\frac{\partial\omega_0}{\partial\Phi}$  is the cavity external flux responsivity and  $\Phi_{\text{zpf}}$  is the zero-point flux.

#### COUPLING VIA MUTUAL INDUCTANCE

A schematic diagram of a possible coupling scheme between the RF resonator and the SQUID is shown in Fig. 3.12**a**. In this configuration the zero-point flux is given by  $\Phi_{\text{zpf}} = MI_{\text{zpf}}$ , where  $M$  is the mutual inductance between the RF inductor wire and the SQUID loop and  $I_{\text{zpf}}$  is the RF current fluctuations .

The vacuum current fluctuations  $I_{\text{zpf}}$  of the RF circuit, which is composed of a capacitor  $C_{\text{RF}}$  and inductor  $L_{\text{RF}}$ , can be written in terms of its resonance frequency  $\Omega_0 = \frac{1}{\sqrt{L_{\text{RF}}C_{\text{RF}}}}$  as

$$I_{\text{zpf}} = \sqrt{\frac{\hbar\Omega_0}{2L_{\text{RF}}}}. \quad (3.20)$$

As shown in Fig. 3.12**c**, the RF current fluctuations can be increased by decreasing the inductance of the circuit and fully optimized by also reducing its capacitance, which results in a higher resonance frequency (see Fig. 3.12**b**). From a design perspective, the inductance of the wire can be modified by changing its geometry. Moreover, a decrement in inductance can be achieved by reducing the length of the wire or by increasing its width and/or thickness, as kinetic inductance effects are reduced. In addition, since we work with parallel plate capacitors (PPCs), the capacitance of the circuit is given by

$$C_{\text{RF}} = \frac{\epsilon_0\epsilon_r A}{d_{\text{PPC}}}, \quad (3.21)$$

where  $\epsilon_0$  is the vacuum permittivity,  $\epsilon_r$  is the relative permittivity of the dielectric material, which for our devices is amorphous silicon ( $\epsilon_r \sim 11.9$ ),  $A$  is the area of the capacitor and  $d_{\text{PPC}}$  the distance between the plates.

In principle, the range of  $C_{RF}$  and  $L_{RF}$  presented in Fig. 3.12**b** and **c** could be extended towards higher and lower values. By doing so, one could design a circuit to operate in the GHz or kHz regime. In the latter case, in order to decrease the circuit resonant frequency and still maximize its current fluctuations, the capacitance would have to be the target term to increase. However, it is important to emphasize that, in this case, the method used in this thesis for the fabrication of the capacitive element would have to be adjusted. The fabrication limitation with our technique arises from shorts between the capacitor plates when the dielectric thickness is too small or the capacitor area is too large. More details regarding the fabrication of the circuit can be found in the next section.

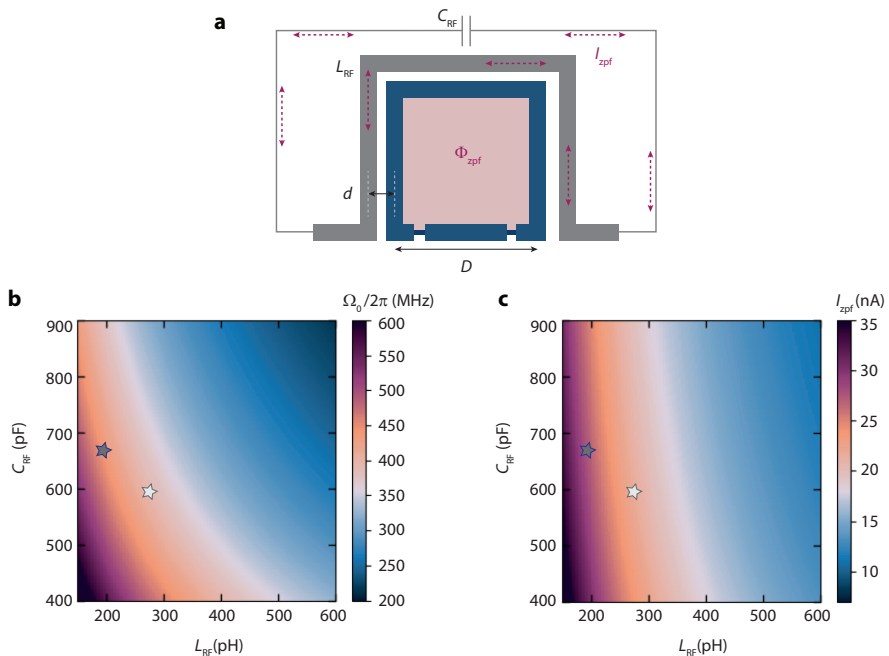


**Figure 3.12: Engineering the zero-point current fluctuations of a radio-frequency circuit.** a shows a schematic diagram of a RF circuit coupled to a SQUID, which in a photon-pressure system is part of a high frequency cavity. The RF circuit is composed of a capacitor  $C_{RF}$  and an inductor wire of inductance  $L_{RF}$ , placed at a distance  $d$  from a square SQUID with side length  $D$ . The resonance frequency and zero-point current of the RF circuit are plotted versus  $C_{RF}$  and  $L_{RF}$  in b and c. The white and gray stars correspond to the operating properties of chapter 6 and 7, respectively.

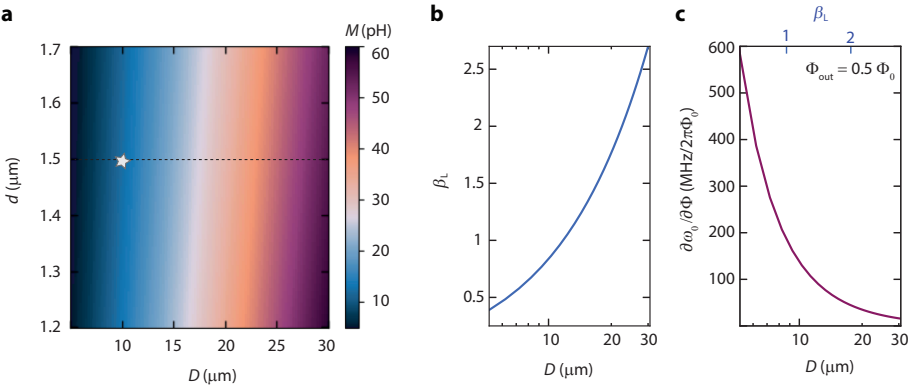
The coupling strength of the system not only depends on the current fluctuations of the RF circuit but on how much of the flux generated by these fluctuations is coupled to the SQUID. This is given by mutual inductance  $M$  between the RF inductor wire and the SQUID loop and is strongly dependent on the geometry of the coupling elements. In the case where the distance between their boundary lines is greater than zero, as shown in

Fig. 3.12a, the mutual inductance of the system can be approximated as [176]

$$M = 3 \frac{\mu_0}{2\pi} D \ln \left( \frac{d+D}{d} \right). \quad (3.22)$$

Here  $\mu_0$  is the vacuum permeability,  $D$  is the side length of a square SQUID<sup>12</sup> and  $d$  the distance between center lines of the RF inductor wire and the SQUID loop.

3



**Figure 3.13: Effect of changing the SQUID geometry on the mutual inductance and flux responsivity**  
In a, a color plot of the mutual inductance  $M$  vs the dimensions  $D$  and  $d$  is shown. The yellow star represents the operation point of the device of chapter 6 and the dashed line marks the chosen  $d$  value for the calculation of  $\Phi_{zpf}$  and  $g_0$ . The mutual inductance can be boosted by increasing the coupling perimeter. However, by doing so, the screening parameter  $\beta_L$  is also increased. b shows how  $\beta_L$  is altered by increasing the length  $D$ . The dimensions of the SQUID were translated into a loop inductance based on the geometric inductance per unit length  $L_{geo} = 1\text{pH}/\mu\text{m}$  and the kinetic inductance contribution was kept equal to  $L_k = 0.78L_{geo}$ . For the calculation of  $\beta_L$ , the Josephson junction critical current  $I_{c0}$  was assumed constant and equal to  $10\mu\text{A}$ . As shown in c, when the length  $D$  is increased, the SQUID cavity flux responsivity at  $\Phi_{out} = 0.5\Phi_0$  is strongly suppressed. Here, the sweet spot frequency was chosen to be  $\omega_{sweet} = 7.25\text{GHz}$  and the total HF circuit inductance  $L = 730\text{pH}$ .

Fig. 3.13a displays a color plot of the mutual inductance  $M$  between the two circuits for different values of  $D$  and  $d$ . Here and through the rest this subsection, we assume that both the RF wire and the SQUID loop have a constant width of  $1\mu\text{m}$ . As shown in Fig. 3.13a, the mutual inductance  $M$  can be mostly increased by extending the coupling perimeter, i.e. the path where the RF inductor wire is in close proximity to the SQUID loop, which is set by the side length  $D$  of the SQUID. However, when increasing the size of the SQUID loop, one is also enhancing the loop inductance and therefore the screening parameter  $\beta_L$ . In Fig. 3.13b, a plot of  $\beta_L$  vs the length  $D$  is shown. Furthermore, this increment in screening parameter can also be mapped into a reduced flux responsivity at the lowest frequency point before entering the unstable operating regime (see section 3.2.1) and it is shown in Fig. 3.13c. Note that, in order to describe the typical thin films used in our devices, a constant film thickness of  $t = 70\text{nm}$  was considered. This is equivalent to a kinetic contribution equal to 78% of the geometric inductance of the film

<sup>12</sup>As a side note, if one has experimental challenges concerning flux-noise, the SQUID geometry could be modified to a rectangular shape in order to maintain coupling perimeter, while reducing its area.

( $L_k = 0.78L_{\text{geo}}$ ). However, if one was to considerably reduce this thickness, the kinetic inductance would increase and shift  $\beta_L$  towards higher values, reducing the cavity flux responsivity even further. A good example of this is the device of chapter 6, where the kinetic inductance was  $L_k = 2.75L_{\text{geo}}$ , altering  $\beta_L$  from 0.36 (for the case of a negligible kinetic inductance) to 1.2.

Even though the zero-point flux can be maximized by individually tuning the zero-point current and the mutual inductance, as shown in Fig. 3.14a, the impact of the SQUID geometry on the flux responsivity changes the growing trend of  $g_0$  quite considerably. As shown Fig. 3.14b, the first thought that  $g_0$  (Eq. 3.19) could be boosted by maximizing the mutual inductance  $M$  is counteracted by the reduction of  $\frac{\partial \omega_0}{\partial \Phi}$  arising from the enlargement of the SQUID. In fact, the kinetic inductance contribution of the film is one of the primary reasons for the limitations in single-photon coupling strength, as it has a significant contribution to the loop inductance and  $\beta_L$ , even for SQUIDs with reduced loop size.

In short, in order to maximize  $g_0$ , high screening parameters  $\beta_L$  should be avoided. Besides reducing the SQUID dimensions, this can be achieved by reducing the critical current of the junctions and/or increasing the thickness of the film. Nevertheless, one should keep in mind the trade-off between  $\beta_L$  and anharmonicity  $\chi$  as discussed in the end of section 3.3.1 and its influence on the cavity non-linear behavior.

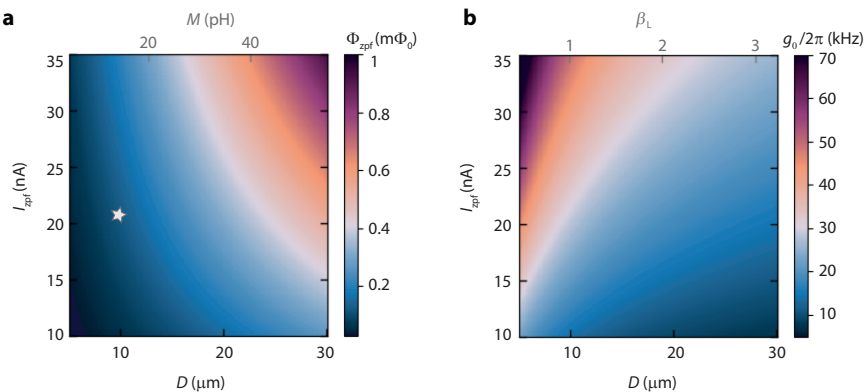


**Figure 3.14: Optimization of the zero-point flux  $\Phi_{\text{zpf}}$  and single-photon coupling strength  $g_0$ .** a shows how the zero-point flux changes depending on the length  $D$  and the RF current fluctuations  $I_{\text{zpf}}$ . A secondary  $x$ -axis containing the corresponding values of the mutual inductance  $M$  is plotted on top. The yellow star corresponds to the operating point of the device of chapter 6. In b a plot of the single-photon coupling strength  $g_0$  vs  $I_{\text{zpf}}$  and  $D$  is shown. Here, the operation point of the device of chapter 6 is not displayed as the both kinetic inductance contribution and junction critical current differed from those of the calculations. In both plots, the mutual inductance was calculated maintaining a constant distance between the wire and the SQUID loop of  $d = 1.5\mu\text{m}$ , which is indicated as dashed line in 3.13a.

## GALVANIC COUPLING

A another strategy to engineer a photon-pressure system is to galvanically connect the SQUID and the RF inductor wire, as shown in Fig. 3.15a. In this configuration, the current  $I$  oscillating in the radio-frequency circuit will split asymmetrically between the two arms of the SQUID. The current  $I_1$  will flow through the SQUID loop and  $I_2$  through the Josephson junctions. Here, the Josephson junctions are represented by a combination of a linear ( $L_{jL}$ ) and a non-linear ( $L_{j0}$ ) inductor. During the calculations presented in this subsection  $L_{jL}$  is considered to be  $0.4L_{j0}$ , as follows from the approximation to the current phase relation (CPR) of a nano-bridge junction presented in section 3.1.

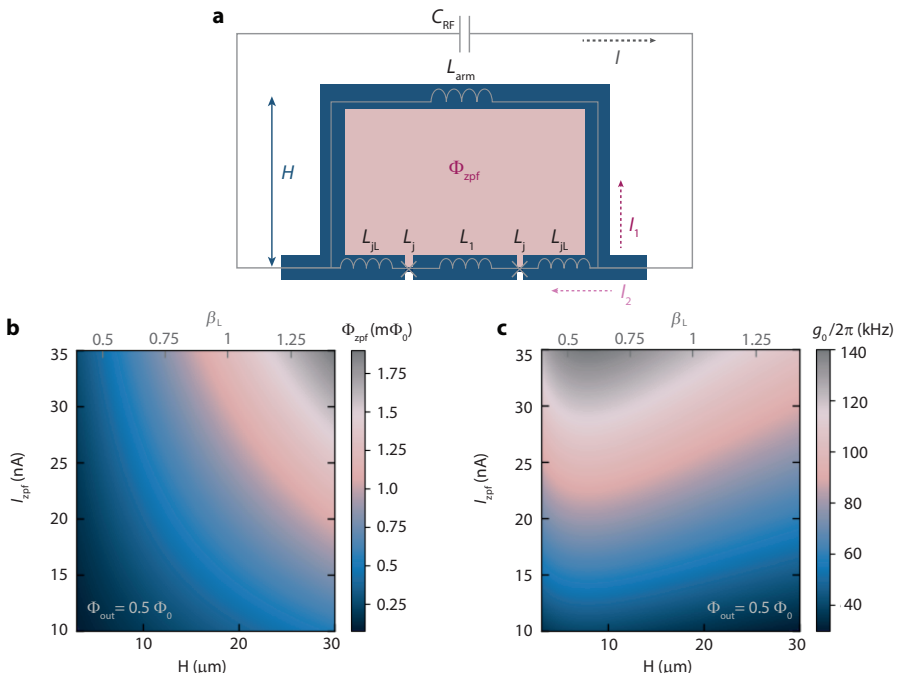


**Figure 3.15: Photon-pressure coupling via a galvanic connection scheme.** a shows a representation of a galvanic coupling scheme. More details regarding its working principle are given in the text. In b a color plot of the zero-point flux  $\Phi_{zpf}$  vs the height  $H$  of the SQUID loop and  $I_{zpf}$  is shown. The dimensions of the  $3 \times H \mu\text{m}^2$  loop were converted into a geometric inductance based on the reference value per unit length of  $L_{geo} = 1 \text{ pH}/\mu\text{m}$ . Furthermore the kinetic inductance contribution was set to  $L_k = 0.78 L_{geo}$  and the Josephson critical current at zero field to  $I_{c0} = 10 \mu\text{A}$ . Panel c shows how  $g_0$  depends on  $I_{zpf}$  and  $H$ . Here, the sweet spot frequency and total circuit inductance were kept at  $7.25 \text{ GHz}$  and  $L = 730 \text{ pH}$ , respectively. All values were estimated for the operation point  $\Phi_{out} = 0.5 \Phi_0$  and both plots display the corresponding values of  $\beta_L$  on a secondary  $x$ -axis. Furthermore the values of  $\partial\omega_0/\partial\Phi$  utilized for the calculation of  $g_0$  were obtained numerically by performing a derivative of Eq. (3.13).

According to the circuit layout of Fig. 3.15a, the total flux in the SQUID is given by a combination of the external flux  $\Phi_{out}$  and of the counteracting fluxes  $\Phi_1 = L_{arm}I_1$  and  $\Phi_2 = L_1 + 2L_{jL}$  generated in the upper and lower arm, respectively. The expression for the

total flux  $\Phi$  can be reduced to [127]

$$\Phi = \Phi_{\text{out}} - L_{\text{loop}}(1 - \alpha) \frac{I_{\text{zpf}}}{2} - L_{\text{loop}} I_c \sin\left(\pi \frac{\Phi}{\Phi_0}\right), \quad (3.23)$$

with  $L_{\text{loop}} = 2L_{\text{JL}} + L_1 + L_{\text{arm}}$  and where the parameter  $\alpha = \frac{2L_{\text{JL}} + L_1 - L_{\text{arm}}}{L_{\text{loop}}}$  describes the inductance asymmetry of the SQUID from the perspective of the RF currents.

The zero-point flux  $\Phi_{\text{zpf}}$ , which can be seen as an equivalent to a fluctuating external flux arising from the zero-point fluctuation current, is given by

$$\Phi_{\text{zpf}} = L_{\text{loop}}(1 - \alpha) \frac{I_{\text{zpf}}}{2} \quad (3.24)$$

$$= L_{\text{arm}} I_{\text{zpf}}. \quad (3.25)$$

The color plot displayed in Fig. 3.15b shows the zero-point flux  $\Phi_{\text{zpf}}$  of a galvanically connected photon-pressure system, where the SQUID is a  $3 \times H \mu\text{m}^2$  loop of variable height. By fixing the sweet-spot critical current of a single junction  $I_{c0}$  to  $10 \mu\text{A}$ , the screening parameter  $\beta_L = L_{\text{loop}}/\pi L_{j0}$  is estimated based on the loop dimensions and on the reference conversion factor per unit length of  $L_{\text{geo}} = 1\text{pH}/\mu\text{m}$  [118]. Here the thickness of the film used for the calculation of the kinetic inductance contribution was set  $t = 70 \text{ nm}$  in order to represent the typical thin films used in our devices and the width of the SQUID loop wire was set to  $1 \mu\text{m}$ . As seen in Fig. 3.15b, when one exclusively increases the height of the SQUID loop, both the screening parameter and the zero-point flux start to rise, as the arm inductance  $L_{\text{arm}}$  is enhanced. However, as the flux coupled into the loop is maximized by the galvanic connection, with this approach we attain higher values of  $\Phi_{\text{zpf}}$  while still maintaining a considerably low screening parameter. For instance, at  $I_{\text{zpf}} = 35 \text{nA}$ , while with the initial approach we achieved approximately  $\Phi_{\text{zpf}} = 0.7 \text{m}\Phi_0$  for  $\beta_L \sim 2.5$ , we now reach the same value for  $\beta_L \sim 0.8$ .

This improvement is strongly translated into a boost in the single-photon coupling rate  $g_0$  as shown in Fig. 3.15c, estimated for the threshold operation point  $\Phi_{\text{out}} = 0.5\Phi_0$ . With this new coupling scheme, which relies on maximizing the zero-point fluctuation flux, we can reach single-photon coupling rates of  $g_0 = 2\pi \cdot 120 \text{kHz}$  for a  $\beta_L \sim 1$ . This is 2.4 times higher than the rates obtained for a coupling configuration based on the mutual inductance between the RF circuit and a SQUID of similar screening parameter.

This was the coupling approach explored in the device of chapter 7, and there the single-photon coupling strength  $g_0$  achieved at half of flux quantum was close to  $2\pi \cdot 150 \text{kHz}$ . Note that there, the value for the inductance  $L_{\text{JL}}$  considerably differed from the value of  $L_{\text{JL}} = 0.4L_{j0}$  used in the calculations presented above.

### 3.4.2. NANOFABRICATION TECHNIQUES

For the realization of our photon-pressure systems (see section 2.5.3), the fabrication of linear LC oscillators resonating in the MHz range was necessary. The approach we followed for the engineering of these circuits was based on a Parallel Plate Capacitor (PPC) in a parallel combination with a short inductor wire.

The fabrication consisted of three steps. The first, where the bottom plate of the capacitor was patterned. For simplicity, the material of this plate was chosen to match the

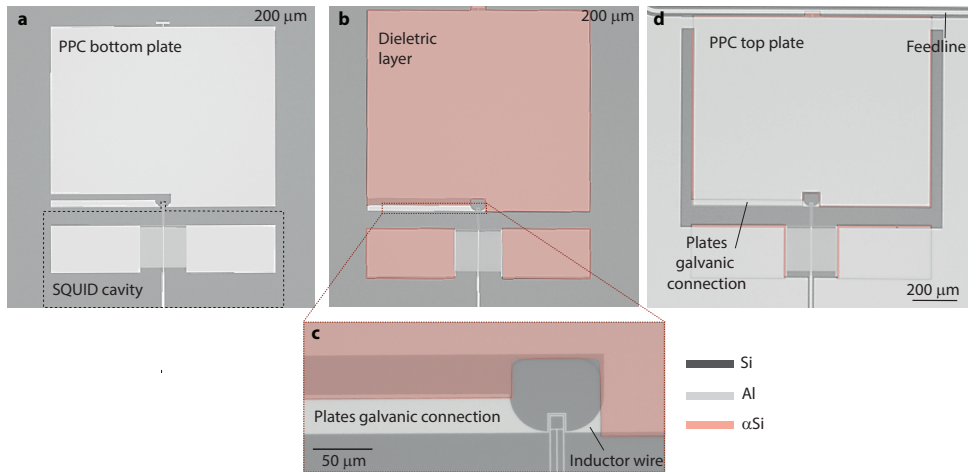


**Figure 3.16: Optical images posterior to each step of the RF microwave cavity fabrication workflow described in the text.** Figure **a** shows a device after the first fabrication step, which consists of an Aluminum layer forming the bottom plate of the Parallel Plate Capacitor (PPC) and inductor wire. In addition, the figure also shows a SQUID cavity, whose fabrication was discussed in section 3.2.3. In **b**, the device, now containing a  $\alpha$ Si dielectric layer patterned on top of the bottom plate except for the galvanic connection area, is shown. **c** displays a zoom-in of the plates galvanic connection and of the inductor wire, which is in close proximity with a SQUID loop (not part of the RF microwave cavity). At last, **d** shows the final device where a top layer of aluminum is patterned to act as the PPC top plate and which is also galvanically connected to the GND plane. The presented optical images were false colored for better visibility and do not correspond to the same device. Note that the device presented in this figure explored the photon-pressure coupling via mutual inductance as described in section 3.4.1.

one of the SQUID cavity, so their patterning could be done simultaneously. Note that, for the case of a 2D SQUID geometry this would correspond to a 20 nm thick sputtered aluminum layer and in a 3D geometry to a  $\sim$  80 nm sputtered aluminum film, followed by a lift-off process. An optical image at the end of this fabrication step is shown in Fig. 3.16a. In the second step, the dielectric material, consisting of a  $\approx$  130 nm thick  $\alpha$ Si layer, would be deposited via a low temperature ( $\approx$  90°) *Plasma Enhanced Chemical Vapour Deposition*<sup>13</sup>. After the dielectric deposition, an e-beam patterning followed by a RIE SF<sub>6</sub> etch would be performed to etch away the dielectric material from all areas, aside from the capacitor plate. A O<sub>2</sub> plasma ashing step would be subsequently performed to remove the remaining resist layer, resulting in a device like the one of Fig. 3.16b. Lastly, the final step involved the patterning of the top capacitor plate, which consisted of a thick  $\sim$  250 nm aluminum layer. For the patterning of this last layer, we used a combination of a sputtering deposition step and a lift-off technique, where the chip would be placed at the bottom of a beaker containing Anisole and undergo an ultrasonic bath for a few minutes. In addition, an important part of the fabrication was to include an argon milling step on the galvanic contact area prior to the last aluminum deposition, as this was cru-

<sup>13</sup>In a PECVD process, reactant gases are inserted between a grounded electrode and a RF driven electrode. The resulting plasma subsequently undergoes a chemical reaction and the final product is deposited on the substrate.

cial to guarantee a good electrical contact between the two plates. The final device can be seen in Fig. 3.16c.

One of the most critical parts of the fabrication would be the existence of shorts between the two capacitor plates, either as an outcome of dirt particles lying on the bottom plate, or due to the previously mentioned *dog-ears*. This could be countered by an extensive surface cleaning and a prolonged lift-off process of the first layer, in order to eliminate most of the thin aluminum covering the resist sidewalls.

## 3.5. THE MEASUREMENT CHALLENGE OF SQUID CAVITIES: FLUX NOISE

One of the biggest experimental challenges when working with SQUID cavities is the presence of flux noise. This type of noise can either arise from an external source, which generates fluctuations of the magnetic flux threading the SQUID loop or it can be intrinsically generated in the SQUID. Despite of its origin, the larger the cavity flux responsivity  $\partial\omega_0/\partial\Phi$ , the higher will be the fluctuations in the SQUID cavity resonance frequency. Therefore, to guarantee the experimental exploration of photon-pressure and flux-mediated optomechanical systems with large single-photon coupling rates, the flux noise in these systems has to be minimized.

For SQUIDs working at GHz frequencies, the dominant intrinsic source of flux noise is associated to the Johnson-Nyquist noise arising from the flow of dissipative quasi-particle currents in the Josephson junctions. The spectral density of this white noise contribution is given in units of  $\Phi_0^2/\text{Hz}$  by [106]

$$S_\Phi = 4(1 + \beta_L) \frac{k_b T L_{\text{loop}}}{\Phi_0 I_{c0} R_n}, \quad (3.26)$$

where  $k_b$  is the Boltzmann constant and  $R_n = \frac{\pi\Delta}{2eI_{c0}}$  is the SQUID normal state resistance, with  $\Delta = 0.2 \text{ meV}$  denoting the superconducting gap of Aluminum at 0 temperature. For a SQUID with a screening parameter of  $\beta_L = 1$  and a critical current per junction of  $10 \mu\text{A}$ , the rms (root mean square) flux noise is  $\sqrt{S_\Phi} \sim 26 \text{ n}\Phi_0/\sqrt{\text{Hz}}$ . For a SQUID cavity with a flux responsivity of  $500 \text{ MHz}/\Phi_0$  this would give rise to rms resonance frequency fluctuations of  $\sim 13\sqrt{\kappa/2\pi}$ . Since this value will always be considerably below the cavity linewidth  $\kappa$ , it will be considered a negligible source of flux noise in our systems.

When considering external sources of low frequency flux noise (below the cavity linewidth) we can differ between noise sources with frequencies above the measurement bandwidth, which are responsible for a broadening effect appearing as a reduction of the cavity quality factor (also known as a source of dephasing by the superconducting qubit community [128, 130, 130]), or noise sources with wave period below the measurement time, resulting in resonance frequency shifts. This section focuses on presenting several examples of measurements affected by the presence of external flux noise of the latter type, which might arise from different mechanisms, and on providing a solution for reducing their contribution.

In Fig. 3.17b the response spectrum of a SQUID cavity coupled to a RF circuit via a photon-pressure interaction in the presence of a strong pump tone which sweeps through

3

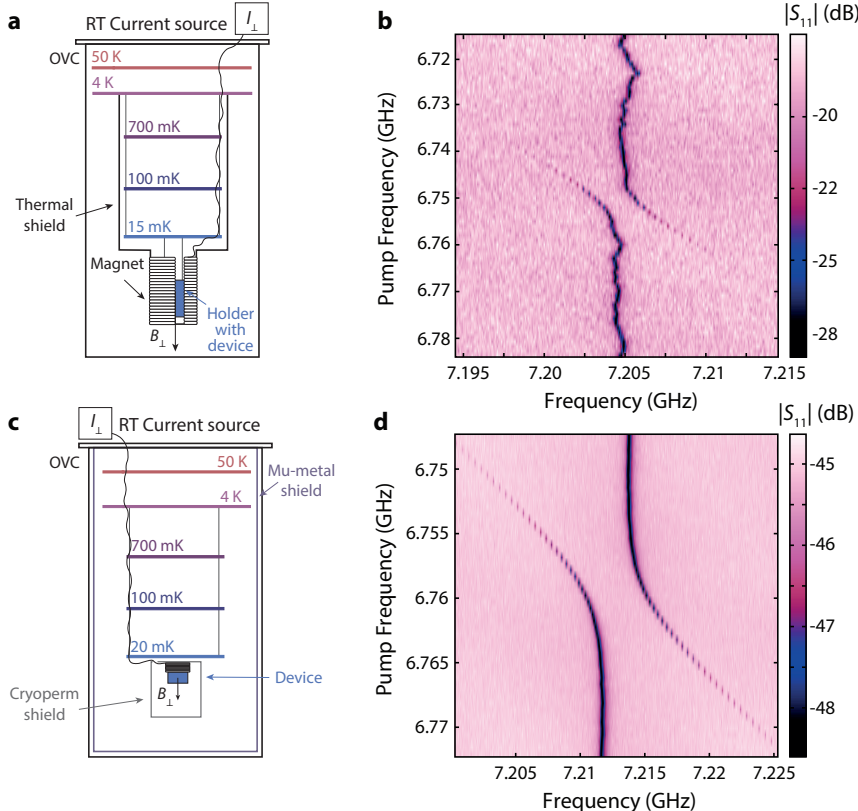
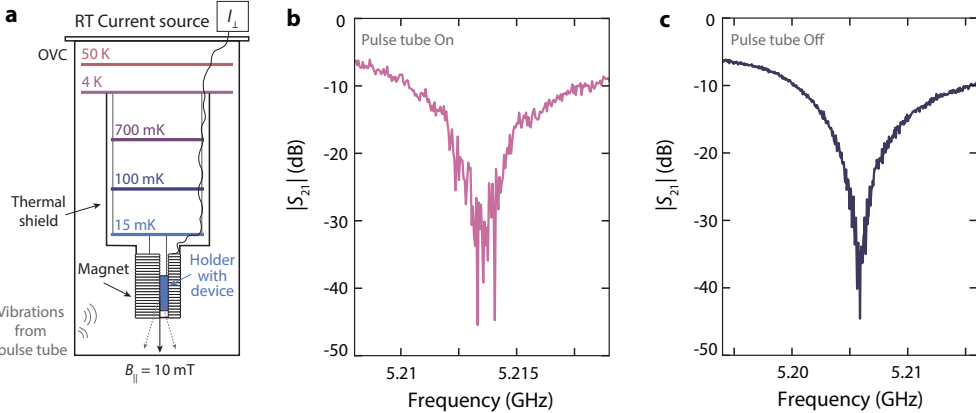


Figure 3.17: **Effects of external flux noise on the response spectrum of a photon-pressure system in the strong-coupling regime.** **a** shows the measurement setup of the experimental dataset plotted in **b**. Here the device was mounted in a holder, which was loaded through the bottom of the dilution fridge and attached to the mK plate. The out-of-plane magnetic field  $B_{\perp}$  was applied by means of a coil wound around the thermal shield (which is mounted on the 4K plate) and an external current source operating at room temperature (RT). In **b**, the response spectrum of a photon-pressure system in the strong coupling regime  $|S_{11}|$ (dB) while a pump tone  $\omega_p = \omega_0 - \Omega_0 \pm \delta$  is swept through the red sideband is shown. **c** displays a schematic representation of the measurement configuration for which the dataset in **d** was taken. Here the sample and a magnet were placed inside a cryoperm shield and mounted at the mK plate of the dilution fridge. A second magnetic shield was assembled below the OVC radiation shield. The measured cavity response spectrum vs red sideband pump detuning in the setup displayed in **c** is shown in **d**.

the cavity red sideband  $\omega_p = \omega_0 - \Omega_0 \pm \delta$  is shown. Here  $\omega_0$  is the cavity resonance frequency and  $\Omega_0$  the natural frequency of the RF mode. The presence of the red sideband pump induces a strong beam-splitter interaction, resulting in the observation of a normal mode splitting, where the two modes are hybridized. Despite of the presence of this photon-pressure feature, there is a clear observation of several drifts in the SQUID cavity resonance frequency during the time of the measurement. The measurement setup used for the acquisition of this dataset can be seen in Fig. 3.17**a**. Here the out-of-plane mag-

netic field  $B_{\perp}$  used for flux-biasing the SQUID cavity was applied via a magnet wound around the inner shield of the dilution fridge, which was connected to an external current source. Furthermore, the sample was mounted inside a holder and subsequently connected to the mK plate, by means of a loading procedure from the bottom of the fridge. Due to the absence of a magnetic shield in the setup, fluctuations in the external magnetic field would strongly couple to the SQUID, inducing the frequency drifts observed in Fig. 3.17b.

This problem could be reduced by mounting the device in the setup of Fig. 3.17c. In this configuration both the sample and a magnet were placed inside a small cryoperm shield and a second mu-metal shield was fixed below the Outer Vacuum Chamber (OVC) radiation shield. In this way we could greatly reduce the amount of flux noise coupling from the exterior into the SQUID loop and therefore avoid the frequency drifts previously observed. A similar dataset to the one of Fig. 3.17b but in the modified setup can be seen in Fig. 3.17d. Note that other ways to reduce the flux noise in the system would be, for example, by decreasing the area of the SQUID, as the flux generated from any external magnetic field  $B_{\perp}$  perpendicular to a SQUID loop of area  $A$  is given by  $\Phi = B_{\perp}A$  or by adopting other SQUID geometries, as a SQUID gradiometer [131]. Since the latter option would add several difficulties when designing optomechanical or photon pressure systems, in our devices we mostly focused on the inclusion of magnetic shields and on reducing the SQUID loop size<sup>14</sup>.



**Figure 3.18: Effects of pulse tube vibrations on the response spectrum of a flux-mediated optomechanical system.** a shows the experimental setup of the measurement. The device was mounted in a sample holder which was thermally anchored to the mK plate of the dilution fridge. An in-plane magnetic field  $B_{\parallel}$  was applied to the device by means of a magnet wound around an inner thermal shield and an external current source operating at room temperature (RT). b and c show a linescan of the cavity response spectrum  $|S_{21}|$  (dB) while the pulse tube cooler was switched on and off, respectively. The device shown here is the system under study in chapter 4.

Fig. 3.18 shows another example of a system affected by external flux noise. In this

<sup>14</sup>This was in fact a win-win solution, since a smaller loop is not only beneficial to reduce flux noise, but also to decrease the loop inductance and the screening parameter  $\beta_L$ .

case, a flux-mediated optomechanical system was measured in the setup of Fig. 3.18a, where the sample was placed in a holder which was thermally anchored to the mK plate of the dilution fridge. Here the in-plane magnetic field, used for enhancing the single-photon coupling strength  $g_0$  was applied by means of a coil wound around the inner radiation shield of the fridge. In this configuration, the mechanical vibrations arising from the pulse tube cooling of the dilution fridge were a big source of external flux noise. As the pulse tube was shaking the measurement apparatus, the shield containing the magnet could be displaced with respect to the sample holder, causing the in-plane magnetic field to generate a fluctuating out-of-plane component. Fig. 3.18b and c show the response spectrum  $|S_{21}|$  of the SQUID cavity acquired while the pulse tube was turned on and off, respectively. Both datasets were taken while the in-plane field  $B_{\parallel}$  was set to 10 mT.

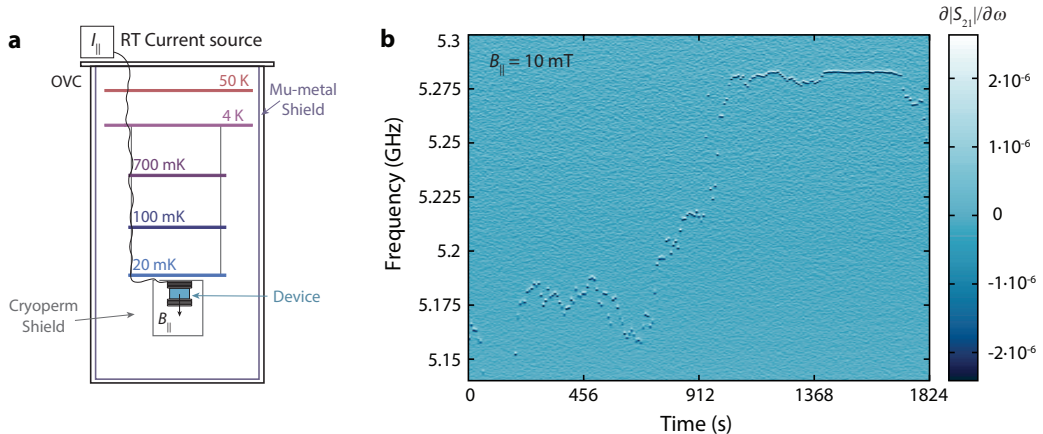
By comparing the two datasets we observe a pronounced modification of the cavity lineshape when the pulse tube is switched on, suggesting that the mechanical vibrations arising from the operation of pulse tube are inducing oscillations in the flux seen by the SQUID. These modifications in the magnetic flux threading the SQUID loop will induce small resonance frequency shifts. Therefore, when a probe tone is scanning the cavity it will detect strong oscillations in its response spectrum.

A quick but not ideal solution for this problem was to switch the pulse tube off during the data acquisition time. Nonetheless, since the fridge cooling power was reduced during the time of the measurement, a recovery time of  $\sim 10 - 15$  min, where the pulse tube was turned on, posterior to the measurement was crucial to maintain the fridge operating at base temperature.

Another solution for this problem was to switch to the setup presented in Fig. 3.19a, where the sample and the magnet were simultaneously placed inside a cryoperm magnetic shield and mounted at the mK plate of the dilution fridge. In this configuration a second magnetic mu-metal shield was also assembled below the OVC radiation shield.

This new setup was extremely advantageous for two reasons. First, it helped reducing the amount of external flux noise arising from the exterior, as the system was now protected by the two shielding layers, and second because the pulse tube vibrations would no longer be translated into a displacement of the sample relatively to the magnet, reducing the oscillations of the out-of-plane magnetic field component. In fact, for this purpose we designed a vector magnet containing a slot for the mounting of the sample, allowing us to fully eliminate the pulse tube induced noise and at the same time counter for any misalignment of the device. The latter was relevant to counter for the out-of-plane component arising from the in-plane magnetic field due to the sample tilt. For simplicity, the out-of-plane coil was not presented in the schematic representation of Fig. 3.19a as it was not in use during the time of the measurement presented in Fig. 3.19b.

Nevertheless, as shown in Fig. 3.19b, the device still suffered from other sources of external flux noise. Here, the measurement routine consisted on iteratively measuring the cavity response spectrum after setting the in-plane magnetic field  $B_{\parallel}$  to 10 mT. Right after the application of the in-plane field, which had been done by means of an external current source at room temperature, the cavity resonance underwent several shifts and eventually drifted towards higher frequency values. When operating at higher frequencies, i.e. closer to its sweet-spot, the cavity flux responsivity is decreased and therefore



3

**Figure 3.19: Resonance frequency drifts arising from external flux noise.** a shows the measurement setup of the experimental dataset plotted in b. In this measurement configuration, the device was mounted simultaneously with a vector magnet inside a cryoperm shield at the mK plate of a dilution fridge, and a second magnetic mu-metal shield was placed below the thermal OVC radiation shield. The in-plane magnetic field was applied by means of a room temperature (RT) external current source. Both the out-of-plane coil and respective current source were omitted for clarity, as they were switched off during the measurement shown in b. In b the derivative of the cavity response spectrum  $S_{21}$  with respect to the frequency was plotted versus frequency and time, after setting the in-plane magnetic field to  $B_{\parallel} = 10 \text{ mT}$ . The cavity can be identified by the dark regions in the colormap. Furthermore, the device shown here is the system under study in chapter 5.

its sensitivity to external flux fluctuations is also reduced, resulting in a period where the cavity seemed to have stabilized. There are several possibilities for the flux noise mechanisms behind these drifts.

One option is current noise generated by the external source. Since the application of high in-plane magnetic fields ( $\sim 10 - 100 \text{ mT}$ ) in this setup required currents in the order of  $\sim 0.1 - 1 \text{ A}$ , the current noise associated with the source was no longer negligible, as the typical peak-to-peak noise value of standard DC current sources operating in that range is within hundreds of  $\mu\text{A}$ <sup>15</sup>. When operating our device with a flux responsivity of  $500 \text{ MHz}/\Phi_0$  this current noise would be translated into frequency oscillations on the order of a few MHz. A solution which minimized this problem was to acquire a low noise current source from *High Finesse* [132]. Here, the current noise density was around  $1 \mu\text{A}/\sqrt{\text{Hz}}$  and it could suppress the current noise by  $10^{-5}$  of the maximum output current. Even though we did not perform a systematic study of this problem, we experimentally observed that the use of the low noise current source decreased the flux noise in the setup and prevented the cavity from *flux jumping* at higher in-plane fields.

A second mechanism which could explain the frequency drifts observed in Fig. 3.19b is moving *Abrikosov* vortices [133]. When the applied magnetic field on a thin aluminum film is sufficiently strong, the superconductor will allow for magnetic flux to enter in

<sup>15</sup>Some examples of such a source is the unit B2901A from Keysight operating in the range  $\pm 1.5 \text{ A}$ , or one of the models from the Keithley series 2400.

quantized packages of a single flux quantum. These vortices, also known as *fluxons* will be pinned by the superconducting film and distribute over its area to form a lattice whose density increases with the magnitude of the field. With each of these localized vortices, there is supercurrent which flows around the non-superconducting core and decays with the distance of the London penetration depth. This has been reported as a source of flux noise and decoherence in superconducting circuits [130, 134, 135]. Experimentally, if a sample is misaligned with the direction of the in-plane field and its magnitude is sufficiently increased, the generated out-of-plane component will induce the appearance of these Abrikosov vortices.

### 3

Once in the superconductor, the vortices can hop between pinning sites and be transported by the currents flowing in the film [136, 137]. Therefore, if any of them would occasionally pass nearby a SQUID, the supercurrent generated by the fluxon would modify the flux threading the SQUID loop and induce a frequency shift of the cavity [138]. Note that this probability is higher as we apply higher fields and raise the vortex population. A way around this issue passes by compensating for the misalignment and apply a counteracting out-of-plane magnetic field, reducing the amount of vortices in the superconductor. Another option could be to include the patterning of defects in the film [139, 140], allowing for a stronger pinning and reducing the amount of flying vortices. In our current setup, if the introduction of these vortices had occurred, a quick solution for their removal was to shortly heat the device above its critical temperature.

# 4

## COUPLING MICROWAVE PHOTONS TO A MECHANICAL RESONATOR USING QUANTUM INTERFERENCE

The field of optomechanics has emerged as leading platform for achieving quantum control of macroscopic mechanical objects. Implementations of microwave optomechanics to date have coupled microwave photons to mechanical resonators using a moving capacitance. While simple and effective, the capacitive scheme suffers from limitations on the maximum achievable coupling strength. Here, we experimentally implement a fundamentally different approach: flux-mediated optomechanical coupling. In this scheme, mechanical displacements modulate the flux in a superconducting quantum interference device (SQUID) that forms the inductor of a microwave resonant circuit. We demonstrate that this flux-mediated coupling can be tuned *in situ* by the magnetic flux in the SQUID, enabling nanosecond flux tuning of the optomechanical coupling. Furthermore, we observe linear scaling of the single-photon coupling rate with the in-plane magnetic transduction field, a trend with the potential to overcome the limits of capacitive optomechanics, opening the door for a new generation of groundbreaking optomechanical experiments.

---

This chapter has been published as *Coupling microwave photons to a mechanical resonator using quantum interference*. I. C. Rodrigues\*, D. Bothner\*, & G. A. Steele, Nature Communications **10**, 5359 (2019)

\*these authors contributed equally

## 4.1. INTRODUCTION

Parametrically coupling mechanical motion to light fields confined inside a cavity has allowed for major scientific and technological breakthroughs within the recent decade [56]. Such optomechanical systems have been used for sideband-cooling of mechanical motion into the quantum ground state [31, 32], for the detection of mechanical displacement with an imprecision below the standard quantum limit [41, 42], for the generation of non-classical mechanical states of motion [36–38] and for the entanglement of mechanical oscillators [39, 40]. As the mechanical elements can be coupled to both, light fields in the optical and in the microwave domain, current efforts using optomechanical systems target towards the implementation of a quantum link between superconducting microwave quantum processors and optical frequency quantum communication [51, 52]. Another exciting perspective of optomechanical systems is testing quantum collapse and quantum gravity models by preparing Fock and Schroedinger cat states of massive mechanical oscillators [141, 142].

The state transfer fidelity between photons and phonons in optomechanical systems is determined by the coupling rate between the subsystems, and most optomechanical systems so far have single-photon coupling rates much smaller than the decay rates of the cavity. The strong-coupling regime, necessary for efficient coherent state transfer, is achieved by enhancing the total coupling rate  $g = \sqrt{n_c}g_0$  through large intracavity photon numbers  $n_c$  [25, 33, 59]. In the optical domain, large photon numbers result in absorption that heats the mechanical mode far above the mode temperature [61]. In the microwave domain, large photon numbers result in non-equilibrium cavity noise [31, 62] that is not completely understood. Both of these sources of noise limit ground state cooling and the fidelity of mechanical quantum ground state preparation. An approach to reduce these parasitic side-effects is to increase the single-photon coupling rate  $g_0$  significantly. Doing so, optomechanics could even reach the single-photon strong-coupling regime, where the optomechanical system acquires sufficient non-linearity from the parametric coupling such that non-Gaussian mechanical states can be directly prepared by coherently driving the system [63, 67].

In the microwave domain, the most common approach to build an optomechanical system is to combine a superconducting microwave LC circuit with a metallized suspended membrane or nanobeam as mechanical oscillator. The devices are constructed in a way that the displacement of the mechanical oscillator changes the capacitance of the circuit  $C(x)$  and hence its resonance frequency  $\omega_0(x) = 1/\sqrt{LC(x)}$ . In this configuration, however, the single-photon coupling rate is limited to  $g_0 \leq \frac{\omega_0}{2} \frac{x_{\text{zpf}}}{d}$  with the zero-point fluctuation amplitude  $x_{\text{zpf}}$  and the capacitor gap  $d$ . Current devices are highly optimized, but still achieve typically only  $x_{\text{zpf}}/d \approx 10^{-7}$  for a parallel plate capacitor gap of  $d = 50\text{ nm}$  and it is extremely challenging to increase  $g_0$  beyond 300 Hz with this approach. Here, we realize a fundamentally different approach for a microwave optomechanical device by incorporating a suspended mechanical beam into the loop of a superconducting quantum interference device (SQUID). The SQUID itself is part of a superconducting LC circuit and essentially acts as an inductor, whose inductance depends on the magnetic flux threading through the loop. In contrast to the capacitive approach, this magnetic flux-mediated inductive coupling scheme provides quickly tunable single-photon coupling rates [68, 69], which in addition scale linearly with a magnetic field

applied in the plane of the SQUID loop [70]. In contrast to capacitive microwave optomechanics, the coupling rates are not limited by geometric and technological restrictions and there is a realistic prospective for achieving the optomechanical single-photon strong coupling regime.

## 4.2. CONCEPT AND DEVICE

The concept of coupling mechanical resonators to SQUIDs has been developed in many works [143–146], including earlier experimental work with DC SQUIDs [147, 148]. Recently, this concept was extended theoretically to optomechanics [70], describing a way using SQUIDs to achieve strong and tunable optomechanical coupling between a vibrating beam and a superconducting cavity. The circuit used here for its realisation is schematically shown in Fig. 4.1a. The idea is based on transducing mechanical displace-

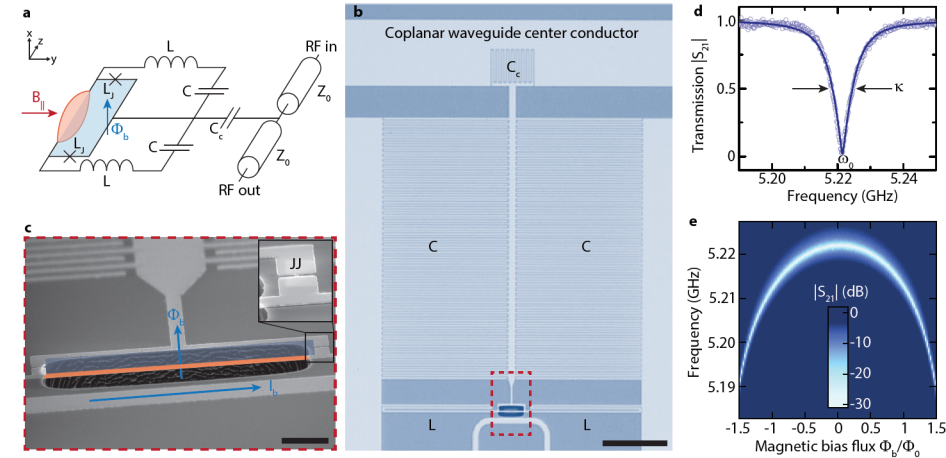


**Figure 4.1: A superconducting microwave circuit with magnetic-flux mediated optomechanical coupling to a mechanical oscillator.** a Circuit schematic of the device. The LC circuit is capacitively coupled to a microwave transmission line with characteristic impedance  $Z_0$  by means of a coupling capacitor  $C_c$ . In addition to the linear capacitors  $C$  and inductors  $L$ , a superconducting quantum interference device (SQUID) is built into the circuit, consisting of two Josephson junctions with inductance  $L_J$  in a closed superconducting loop, of which a part is suspended and free to move perpendicular to the circuit plane. To bias the SQUID with magnetic flux  $\Phi_b$ , a magnetic field can be applied perpendicular to the circuit plane. Motion of the mechanical element is transduced into modulations of the bias flux by a magnetic in-plane field  $B_{||}$ . An optical micrograph of the circuit is shown in b, light gray parts correspond to a 20 nm thick layer of aluminum, dark parts to silicon substrate. The black scale bar corresponds to 50  $\mu\text{m}$ . The red dashed box shows the region, which is depicted in a tilted scanning electron micrograph in c, showing the SQUID loop with the released aluminum beam. The bias flux through the SQUID loop  $\Phi_b$  can be changed by a bias current  $I_b$  sent through the on-chip flux bias line. The black scale bar corresponds to 3  $\mu\text{m}$ . The inset shows a zoom into one of the constriction type Josephson junctions (JJs). In d the cavity resonance is shown, measured by sending a microwave tone to the microwave feedline and detecting the transmitted signal  $S_{21}$ . A fit to the data points (circles), shown as line, reveals a resonance frequency of  $\omega_0 = 2\pi \cdot 5.221 \text{ GHz}$  and a linewidth  $\kappa = 2\pi \cdot 9 \text{ MHz}$ . Panel e shows color-coded the tuning of the cavity resonance absorption dip with magnetic bias flux in units of flux quanta  $\Phi_b/\Phi_0$ , measured at  $B_{||} = 1 \text{ mT}$ . Due to a large loop inductance of the SQUID, the arch exceeds a single flux quantum, for details see section 4.5.3.

ment to magnetic flux, which in turn modulates the effective inductance of a SQUID and therefore the resonance frequency of the LC circuit hosting it. To achieve this transduction from displacement to flux, a part of the SQUID loop is suspended and the device is exposed to an external magnetic field  $B_{||}$  applied parallel to the device plane. The suspended loop part acts as a mechanical beam resonator and its vibrational motion, perpendicular to the device plane, will create an effective SQUID area perpendicular to the applied field  $B_{||}$ , i.e., couple a net magnetic flux into the loop.

The inductance  $L(\Phi_b)$  of an LC circuit containing a SQUID depends on the magnetic flux threading the SQUID loop, and translates to a flux-dependent resonance frequency

$$\omega_0(\Phi_b) = \frac{1}{\sqrt{L(\Phi_b)C}}. \quad (4.1)$$

## 4

When the displacement of a mechanical oscillator is transduced to additional flux, an optomechanical interaction between mechanical mode and cavity resonance frequency emerges and the single-photon coupling rate is given by [70]

$$g_0 = \frac{\partial \omega_0}{\partial \Phi} \Phi_{zpf} = \frac{\partial \omega_0}{\partial \Phi} \gamma B_{||} l x_{zpf}. \quad (4.2)$$

The first term  $\partial \omega_0 / \partial \Phi$  corresponds to the responsivity of the SQUID cavity resonance frequency to small changes of flux through the loop and allows for very fast tuning of  $g_0$ . The second term  $\Phi_{zpf} = \gamma B_{||} l x_{zpf}$  is the magnetic flux fluctuation induced in the SQUID by the mechanical zero-point fluctuations  $x_{zpf}$  of the beam with length  $l$  and scales linearly with an in-plane magnetic field  $B_{||}$ , cf. Fig. 4.1. The scaling factor  $\gamma$  accounts for the mode shape of the mechanical oscillations and is on the order of 1.

The microwave SQUID cavity in our experiment is made of a single 20 nm thick layer of sputtered aluminum on a silicon substrate and it contains a SQUID consisting of two constriction-type Josephson junctions placed in parallel in a  $21 \times 5 \mu\text{m}^2$  closed loop. An optical image of the device is shown in Fig. 4.1b and an electron microscope image of the SQUID loop in c, the fabrication is detailed in section 4.5.1. The capacitance of the LC circuit is formed by two interdigitated capacitors  $C$  to ground and a coupling capacitor  $C_c$  to the center conductor of a coplanar waveguide feedline. Additionally to the SQUID inductance  $L_S = L_J/2$ , there are two linear inductances  $L$  built into the circuit in order to dilute the non-linearity of the cavity, arising from the non-linear Josephson inductance. By this measure we achieve an anharmonicity of approximately 15 Hz per photon and enable the multi-photon coupling rate enhancement  $g = \sqrt{n_c} g_0$  of linearized optomechanics.

The cavity is side-coupled to a coplanar waveguide microwave feedline, which is used to drive and read-out the cavity response by means of the transmission parameter  $S_{21}$ . The device is mounted into a radiation tight metal housing and attached to the mK plate of a dilution refrigerator with a base temperature of approximately  $T_b = 15 \text{ mK}$ , cf. section 4.5.2. Without any flux biasing, the cavity has a resonance frequency  $\omega_0 = 2\pi \cdot 5.221 \text{ GHz}$  and a linewidth  $\kappa = 2\pi \cdot 9 \text{ MHz}$ , which at the same time corresponds to the external linewidth  $\kappa \approx \kappa_e$  due to being deep in the over-coupled regime, cf. the cavity resonance curve shown in Fig. 4.1d. When magnetic flux is applied to the SQUID loop by sending a current to the chip via the on-chip flux bias line, the cavity resonance

frequency is shifted towards lower values due to an increase of the Josephson inductances inside the SQUID. The flux-dependent transmission  $|S_{21}|(\Phi)$  is shown in Fig. 4.1e and a total tuning of about 30MHz can be achieved, mainly limited by a non-negligible SQUID loop-inductance of the SQUID and the dilution of the Josephson inductance by  $L_J/(L + L_J) \approx 0.01$ , see also section 4.5.3. The largest flux responsivities we could achieve here were approximately  $\partial\omega_0/\partial\Phi = 70\text{ MHz}/\Phi_0$ .

We note, that the cavity linewidth  $\kappa$  depends on the flux bias and both, the linewidth and the shape of the resonance frequency flux tuning depend slightly on the magnetic in-plane field. Also, the observation that the SQUID cavity tuning curve shown in Fig. 4.1e extends beyond  $\pm\Phi_0/2$  might be surprising at first, but is explained by a non-negligible SQUID loop inductance relative to the Josephson inductance. A detailed discussion with additional data on both these effects is given in the section 4.5.3.

The mechanical oscillator is a  $20 \times 1\mu\text{m}^2$  large aluminum beam and is suspended as result of releasing part of the superconducting loop forming the SQUID by removing the underlying silicon substrate in an isotropic reactive ion etching process [126]. The beam has a total mass  $m = 1\text{ pg}$  and its fundamental out-of-plane mode oscillates at a frequency  $\Omega_m = 2\pi \cdot 7.129\text{ MHz}$  with an intrinsic mechanical damping rate of  $\Gamma_m \approx 2\pi \cdot 8\text{ Hz}$  or quality factor  $Q_m = \Omega_m/\Gamma_m \approx 9 \cdot 10^5$ , which is exceptionally high for a mechanical oscillator made from a sputter-deposited metal film. From the mass and resonance frequency, the zero-point motion of the oscillator is estimated to be  $x_{\text{zpf}} = \sqrt{\frac{\hbar}{2m\Omega_m}} = 33\text{ fm}$ .

### 4.3. INTERFEROMETRIC CHARACTERIZATION OF THE MECHANICAL OSCILLATOR

The mechanical beam can be coherently driven by Lorentz-force actuation using the on-chip flux bias line. When a current is sent through the bias line, magnetic flux is coupled into the SQUID loop and a circulating loop current is flowing through the mechanical oscillator. We apply a current  $I_\Omega(t) = I_{\text{dc}} + I_0 \cos \Omega t$  with  $\Omega \approx \Omega_m$ , where the DC component  $I_{\text{dc}}$  is simultaneously biasing the SQUID and – in presence of an in-plane magnetic field  $B_{||}$  – exerting a constant Lorentz force to the beam. The oscillating part  $I_0 \cos \Omega t$  modulates the total Lorentz-force  $F_L(t) = F_{\text{dc}} + F_0 \cos \Omega t$  around the equilibrium value  $F_{\text{dc}}$  and effectively drives the mechanical oscillator. The concept is illustrated in Fig. 4.2a, for more details cf. section 4.5.4.

The resulting mechanical motion modulates the cavity resonance frequency and generates sidebands at  $\omega_d \pm \Omega$  to a microwave signal sent into the cavity at  $\omega_d = \omega_0$ , cf. the schematic in Fig. 4.2b. By sweeping  $\Omega$  through  $\Omega_m$  and down-converting the sidebands generated at  $\omega = \omega_0 - \Omega$  and  $\omega = \omega_0 + \Omega$ , we measure the mechanical resonance as shown in Fig. 4.2c. This interferometric detection scheme of displacement can also be used to detect the thermal motion of the mechanical oscillator. At the dilution refrigerator base temperature  $T_b = 15\text{ mK}$ , we expect a thermal mode occupation of the beam of approximately  $n_{\text{th}} = k_B T_b / \hbar \Omega_m \approx 46$  phonons with  $k_B$  being the Boltzmann constant. In the inset of Fig. 4.2c we show the down-converted sideband power spectral density  $S$  of the cavity output field, normalized to the background noise, without any external drive applied to the mechanical oscillator. On top of the imprecision noise background  $S_{\text{imp}}$  of

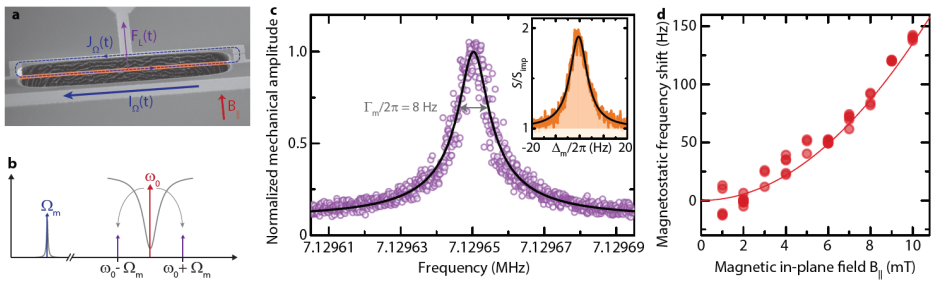


**Figure 4.2: Detection of mechanical motion using a superconducting SQUID cavity interferometer and observation of magnetostatic spring stiffening.** a Schematic of coherently driving the mechanical oscillator by means of the Lorentz force. The current sent through the bias line has a DC component to bias the SQUID with a flux  $\Phi_b$ . This generates a circulating current  $J$  in the SQUID loop. In addition, an oscillating current is sent through the line with a frequency close to the mechanical oscillator resonance frequency  $\Omega \approx \Omega_m$ . Thus, the loop current through the mechanical beam oscillates correspondingly, leading to an oscillating Lorentz force  $F_L(t)$  due to the presence of the magnetic in-plane field  $B_{||}$ . The mechanical motion modulates the total magnetic flux through the SQUID loop and hence the cavity resonance frequency. When a resonant coherent microwave tone is sent into the cavity, the mechanical oscillations generate sidebands at  $\omega = \omega_0 \pm \Omega$ , cf. panel b, which are observed to detect the mechanical motion. In c the down-converted sideband signal is shown during a sweep of the excitation frequency  $\Omega$ . Circles are data, the line is a Lorentzian fit and both are normalized to the maximum of the fit curve. The inset depicts the down-converted sideband thermal noise spectral density in absence of a coherent driving force, normalized to the background noise floor. Orange line are data, black line is a Lorentzian fit. The contribution from the background noise is shaded in white and the contribution from the mechanical displacement noise is orange. The experimental settings for these measurements were  $B_{||} = 9\text{ mT}$  and  $\partial\omega_0/\partial\Phi \sim 20\text{ MHz}/\Phi_0$ . When increasing the magnetic in-plane field, we observe a shift of the mechanical oscillator resonance frequency, shown in panel d. This frequency shift is induced by a position-dependent contribution to the Lorentz-force and corresponds to a magnetostatic stiffening of the mechanical spring constant. The circles are data and the line corresponds to a theoretical curve with  $\delta\Omega_m \propto B_{||}^2$ .

the measurement chain, a Lorentzian peak with a linewidth of  $\sim 8\text{ Hz}$  is visible, generated by the residual thermal motion of the beam.

When we sweep the magnetic in-plane field  $B_{||}$ , we observe an increase of the mechanical resonance frequency as shown in Fig. 4.2d induced by Lorentz-force backaction [148]. Complementary to the electrostatic spring softening in mechanical capacitors with a bias voltage, this effect can be understood as a magnetostatic spring stiffening. When the mechanical oscillator is displaced from its equilibrium position, an additional magnetic flux is coupled into the SQUID loop, which leads to an adjustment of the circulating current  $J$  to fulfill fluxoid quantization inside the loop. Hence, the Lorentz-force  $F_L \propto B_{||}J$  will change accordingly and therefore has a contribution dependent on the mechanical position. For small mechanical amplitudes and circulating currents not too close to the critical current of the Josephson junctions, this position dependence will be linear, causing a frequency shift  $\delta\Omega_m \propto B_{||}^2$ , cf. the discussion in section 4.5.4.

## 4.4. TUNING THE OPTOMECHANICAL SINGLE-PHOTON COUPLING RATE

When a magnetic bias flux is applied to the SQUID, not only the cavity resonance frequency changes, but also the flux responsivity  $\partial\omega_0/\partial\Phi$ . As the optomechanical single-photon coupling rate is directly proportional to the responsivity, it can in principle be switched on and off on extremely short timescales or can be dynamically controlled by flux modulating the SQUID. We demonstrate this tuning of the single-photon coupling rate with bias flux by determining  $g_0$  for different values of  $\Phi_b/\Phi_0$ .

One possibility to determine the multi-photon coupling rate  $g$  in an optomechanical system is to perform the experimental scheme of optomechanically induced transparency [149, 150]. For this scheme, a strong coherent microwave tone is driving the cavity on the red sideband  $\omega_d = \omega_0 - \Omega_m$  and a weak probe tone is sent to the cavity around  $\omega_p \approx \omega_0$ . The two tones interfere inside the cavity, resulting in an amplitude beating with the frequency difference  $\Omega = \omega_p - \omega_d$ . If the beating frequency is resonant with the mechanical mode, the radiation pressure force resonantly drives mechanical motion which, in turn, modulates the cavity resonance and the red sideband drive tone. The modulation generates a sideband to the drive at  $\omega = \omega_d + \Omega$ , which interferes with the original probe field in the cavity. This interference effect opens up a narrow transparency window within the cavity response, which has the shape of the mechanical resonance, modified by the dynamical backaction of the red sideband tone. For  $\omega_d = \omega_0 - \Omega_m$  the magnitude of the transparency window  $|S_m|$  with respect to the depth of the cavity resonance dip  $|S_c|$  is directly related to the coupling rate via

$$\frac{|S_m|}{|S_c|} = \frac{4g^2}{\kappa\Gamma_{\text{eff}}} \quad (4.3)$$

where  $\Gamma_{\text{eff}} = \Gamma_m + \Gamma_o$  is the width of the transparency window, given by the intrinsic mechanical damping  $\Gamma_m$  and the optomechanically induced damping  $\Gamma_o$ . In combination with a careful calibration of the intracavity photon numbers  $n_c$ , we use this approach to get an estimate for the single-photon coupling rate  $g_0 = g/\sqrt{n_c}$ . More details on the photon number calibration and the extraction of  $g$  from the OMIT data are given in section 4.5.5.

When performing this experiment for several different flux bias points, we find a clear increase of  $g_0$  with the cavity flux responsivity. The experimental scheme and the obtained single-photon coupling rates for a constant in-plane field of  $B_{||} = 10\text{mT}$  are shown in Fig. 4.3. In Fig. 4.3e we also plot as line the theoretical curve, where the only free parameter is the scaling factor  $\gamma = 0.86$ , taking into account the mode shape of the mechanical oscillations. All other contributions to the calculations were obtained from independent measurements, such as the bias flux dependence of the cavity frequency, the mechanical resonance frequency and estimations for the beam length and its mass. The largest single-photon coupling rate we achieve here  $g_0 \approx 2\pi \cdot 230\text{Hz}$  is comparable with the best values obtained for highly optimized capacitively coupled devices. As it is possible to achieve responsivities of several  $\text{GHz}/\Phi_0$  with SQUID cavities [120, 152], we

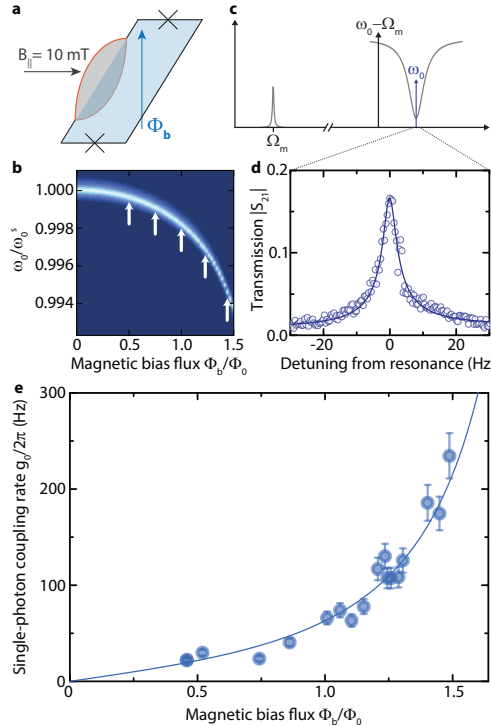
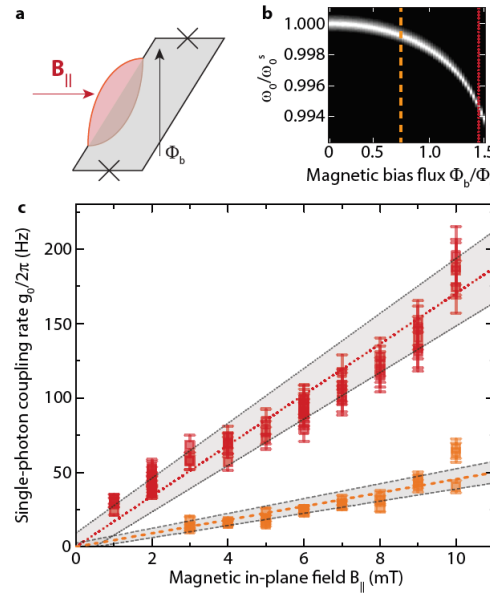


Figure 4.3: **Tuning the optomechanical single-photon coupling rate by changing the flux operating point of the SQUID** **a** Schematic of the applied magnetic field components to the SQUID loop. The in-plane magnetic field  $B_{||}$  is set by means of a cylindrical coil wrapped around the whole sample mounting. During this experiment, it was kept constant at  $B_{||} = 10 \text{ mT}$ . Additionally, an out-of-plane magnetic field was varied by changing the current sent through the on-chip flux bias line, generating a magnetic bias flux  $\Phi_b$ . **b** As consequence of changing the amount of flux threading the SQUID loop, both the resonance frequency as well as the flux responsivity  $\partial\omega_0/\partial\Phi$  of the cavity are changed. The plot shows  $|S_{21}|$  ( $B_{||} = 1 \text{ mT}$ ), the color code is given in Fig. 4.1e. The white arrows represent the points, for which we performed the measurement scheme of optomechanically induced transparency ( OMIT ) as shown schematically in c. A coherent drive tone is set to the red sideband of the SQUID cavity ( $\omega_d = \omega_0 - \Omega_m$ ), while a small probe tone is scanning the cavity resonance  $\omega_p \approx \omega_0$ . As result of an interference effect, a transparency window in the transmitted signal  $S_{21}$  is visible around  $\omega_d + \Omega_m$ , as shown in d, where the circles represent the data and the line the corresponding fit curve. By setting the cavity to different flux bias points (white arrows in b), we change the cavity flux responsivity and therefore the single-photon optomechanical coupling rate  $g_0 \propto \partial\omega_0/\partial\Phi$ . From the magnitude of the transparency window,  $g_0$  can be extracted for each flux bias point. The result is plotted in e as circles. The line is the theoretical curve as described in the main text.

expect that with an optimized cavity it is possible to boost the single-photon coupling rates to several kHz per mT of in-plane field. This optimization with respect to  $\partial\omega_0/\partial\Phi$  can be achieved by reducing either the SQUID loop inductance or the Josephson junction critical current or by a combination of both. From the Kerr-nonlinearity of our device  $\chi/2\pi \sim 120 \text{ Hz}$  for the largest measured responsivity, we estimate intracavity photon numbers up to  $\sim 10^5$  to be compatible with the cavity, which corresponds to maximally achievable multi-photon coupling rates of  $g = 2\pi \cdot 70 \text{ kHz}$  and cooperativities of  $C \sim 300$ .

Due to the large loop-inductance of the used SQUID, however, the cavity is operated in a metastable flux branch (see section 4.5.3) and we were limited to work with  $n_c \sim 150$  intracavity photons at the largest flux responsivities before switching to the stable flux branch, which limited  $g$  and  $C$  to  $g \sim 2\pi \cdot 3\text{kHz}$  and  $C = 0.5$  in current experiments.

As an ultimate experimental signature that our device transduces mechanical displacement to magnetic flux, we investigate the scaling of the optomechanical coupling rate with magnetic in-plane field  $B_{||}$ . Therefore, we performed the scheme of optomechanically induced transparency for constant values of flux responsivity  $\partial\omega_0/\partial\Phi$  but for varying in-plane magnetic field. First, we chose a fixed responsivity of about  $\partial\omega_0/\partial\Phi \approx$



**Figure 4.4: Scaling up the optomechanical single-photon coupling rate with the applied in-plane magnetic field.** a Representation of the applied magnetic field components to the SQUID loop. During the experiment, the cavity flux responsivity was fixed at two different values by adjusting the flux bias point  $\Phi_b$ . In addition to this constant parameter, the in-plane magnetic field  $B_{||}$  was swept from 1 to 10 mT in steps of 1 mT. The transmission  $|S_{21}|$  depending on the normalized bias flux is shown in b for  $B_{||} = 1\text{ mT}$  (black: 0dB, white: -30dB). The two different set-points represented as orange dashed and red dotted lines, respectively, correspond to a flux responsivity of  $\sim 17\text{MHz}/\Phi_0$  and  $\sim 60\text{MHz}/\Phi_0$ . Posterior to tuning the cavity to the desired working point, an OMIT experiment was performed and the single-photon coupling rate of the system was extracted. The experimental procedure was repeated in increasing steps of 1 mT of in-plane field. The resulting single-photon coupling rates  $g_0$  are shown in c as squares. The dashed and dotted lines show theoretical lines and the gray areas consider uncertainties in the flux responsivity of 10% and a possible in-plane field offset of  $\pm 0.5\text{ mT}$ .

17 MHz/ $\Phi_0$  and then adjusted  $B_{||}$  in steps of 1 mT. For each  $B_{||}$  we perform several OMIT experiments and extract the single-photon coupling rates as described above. This whole scheme was repeated for  $\partial\omega_0/\partial\Phi \approx 60\text{MHz}/\Phi_0$ .

The resulting single-photon coupling rates are shown in Fig. 4.4 and follow approximately a linear increase with in-plane magnetic field. The theoretical lines correspond

to independent calculations based on the flux-dependence of the cavity, and the parameters of the mechanical oscillator. The data clearly demonstrate that we observe a flux-mediated optomechanical coupling, a system in which the coupling rates can be further increased with higher magnetic in-plane fields. In the current setup, we were limited to the field range up to 10 mT. Due to an imperfect alignment between the chip and the in-plane field, a considerable out-of-plane component was present and, most probably by introducing vortices, strongly influenced the properties of the cavities above  $B_{||} = 10$  mT. Using a vector magnet to compensate for possible misalignments will allow to go up to about 100 mT with thin film Aluminum devices [105, 151] resulting in coupling rates of several hundreds of kHz. When extending the used material to other superconductors such as Niobium or Niobium alloys such as NbTiN, where similar constriction type SQUIDs have recently been used for tunable resonators [122], the possible field range for the in-plane field increases up to the Tesla regime [153]. We believe that the maximum applicable in-plane field is the most relevant practical limitation for the scaling of the optomechanical coupling rate but it is unknown at this point how large it can be made while preserving high quality factor SQUID cavities and mechanical beams using other superconductors.

With the realisation of flux-mediated optomechanical coupling reported in this article, the door is opened for a new generation of microwave optomechanical systems. The single-photon coupling rates achieved with this first device are already competing with the best electromechanical systems and can be boosted towards the MHz regime by optimizing flux responsivity and applying higher magnetic in-plane fields. In addition, reducing the cavity linewidth to values of  $\leq 100$  kHz will lead us into the single-photon strong-coupling regime, where a new type of devices and experiments can be realized, amongst others the realization of a new class of microwave qubits, where the nonlinearity arises from the coupling to a mechanical element, the generation of mechanical quantum states or optomechanically induced photon blockade [67]. The coupling mechanism between a mechanical oscillator and a microwave circuit, which we realised here, has also been intensely discussed in the context of superconducting flux and transmon qubits instead of linear cavities [143, 146, 154] and could now be implemented using circuits with a large Josephson non-linearity leading to a new regime of quantum control of macroscopic mechanical objects. Utilizing quantum states of mechanical resonators as resource for quantum information and quantum sensing technologies is a promising approach due to the typically very long lifetimes of mechanical excitations and the possibility to couple mechanical systems simultaneously to microwave cavities and optical fields [52, 155, 156] and at the same time can be used to test quantum collapse models and decoherence mechanisms in the presence of large masses, i.e., test quantum mechanics itself with massive quantum states [141, 142, 157].

## 4.5. SUPPLEMENTARY INFORMATION

### 4.5.1. DEVICE FABRICATION

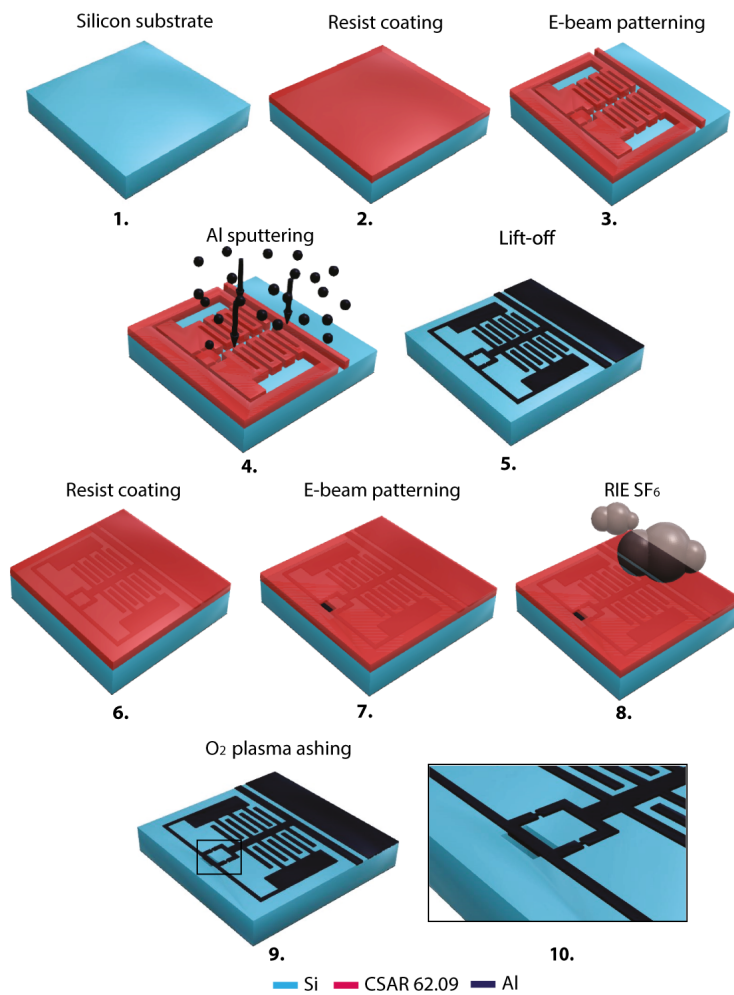


Figure 4.5: **Schematic device fabrication.** a 1.-5. show the deposition and patterning of the superconducting microwave structures and 6.-9. show the etching window patterning and nanobeam release. 10. Zoom-in of a SQUID loop with a released beam. Dimensions are not to scale. A description of the individual steps is given in the text.

The fabrication of the device starts by patterning alignment markers (made of a 100 nm layer of sputter-deposited Molybdenum-Rhenium alloy) on top of a 2 inch silicon wafer. CSAR62.13 was used as patterning mask for the subsequent EBL (Electron Beam Lithography) step and warm Anisole at  $\sim 80^\circ\text{C}$  as solution for the lift-off process. Afterwards the wafer was diced in  $14 \times 14\text{ mm}^2$  chips which were then individually used for the following fabrication steps.

The superconducting structures were patterned in a single EBL step where CSAR62.09 was used as resist. Posterior to the exposure, the sample was developed in Pentyacetate for 60 seconds followed by a solution of MIBK:IPA (1:1) for another 60 seconds and finally rinsed in IPA.

Once the mask was developed, the chip was loaded into a sputtering machine where a thin 20 nm layer of Aluminum (1% Silicon) was deposited after a short in-situ cleaning step by means of Argon ion milling. After the deposition, the sample was placed in the bottom of a beaker containing a small amount of room-temperature Anisole and left in a ultrasonic bath for a few minutes. During this time, the patterning resist is dissolved and the Aluminum layer sitting on top is lifted off.

At this point in the fabrication all the superconducting structures were patterned, leaving the most sensitive step, the mechanical release, for the end. Before the final release, however, the sample is once again diced to a smaller  $10 \times 10\text{ mm}^2$  size in order to fit into the sample mountings and PCBs (Printed Circuit Boards).

For the final EBL step, a CSAR62.09 resist was once again used as mask and the development of the pattern was done in a similar way as for the first layer. Once the etch mask (consisting of two small windows enclosing one arm of the SQUID loop) was patterned, the sample underwent an isotropic SF<sub>6</sub> etch (at approx.  $(\sim -10^\circ\text{C})$ ) for two minutes. During this time the substrate under the beam is etched without attacking the thin aluminum layer forming the cavity and the mechanical beam. Once the beams are released, we proceeded with a O<sub>2</sub> plasma ashing step in order to remove the remaining resist from the sample.

In the end of the fabrication, the sample is glued to a PCB and wire-bonded both to ground and to the  $50\Omega$  connector lines. A schematic representation of this fabrication process can be seen in Supplementary Fig. 4.5, omitting the patterning of the electron beam markers.

#### 4.5.2. MEASUREMENT SETUP

All the experiments reported in this paper were performed in a dilution refrigerator operating at a base temperature  $T_b \approx 15\text{ mK}$ . A schematic of the experimental setup and of the external configurations used in the different experiments can be seen in Supplementary Fig. 4.6.

The PCB (Printed Circuit Board) onto which the fabricated sample was mounted, was placed in a radiation tight copper housing and connected to three high frequency coaxial lines. For a rudimentary shielding of magnetic out-of-plane noise without impacting significantly the in-plane magnetic field, a thin superconducting Aluminum cover was placed in parallel  $\sim 1\text{ mm}$  above the chip (not shown in the schematic).

Two of the coaxial lines were used as standard input and output microwave lines,

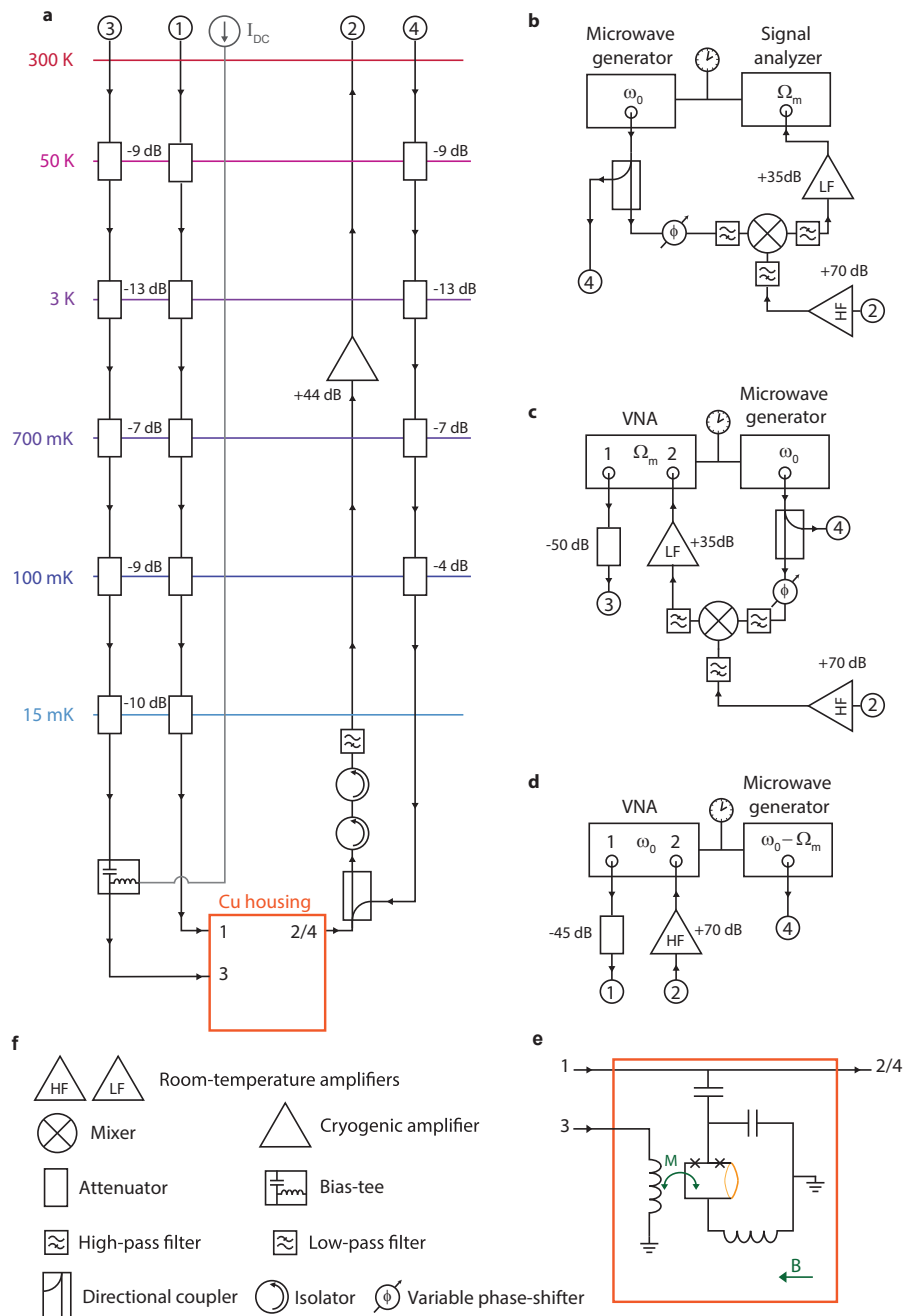


Figure 4.6: Schematic of the measurement setup. Detailed information is provided in text.

used to measure the SQUID cavities in a side-coupled transmission configuration. Furthermore, in order to generate an out-of-plane magnetic field component, required for the tuning of the SQUID, and for the Lorentz-force actuation of the mechanical resonator, DC currents and low-frequency (LF) signals were sent via a third input line. To combine the DC and the LF signals, the center conductor of the coaxial cable was connected to a DC wire by means of a bias-tee.

All coaxial input lines were heavily attenuated in order to balance the thermal radiation from the line to the base temperature of the refrigerator. Outside of the refrigerator, we used different configurations of microwave signal sources and high-frequency electronics for the three experiments. A representation of the setups can be seen in Supplementary Figs. 4.6**b**, **c** and **d**, where the setup for the thermomechanical noise detection is shown in **b**, the setup for the up-conversion of mechanical motion in **c**, and the setup for optomechanically induced transparency is shown in **d**. A detailed schematic of the connections inside the cooper housing box is shown in **e**, and the symbol legend is given in **e**.

For all experiments, the microwave sources and vector network analyzers (VNA) as well as the spectrum analyzer used a single reference clock of one of the devices.

## ESTIMATION OF THE ATTENUATION CHAIN

To estimate the microwave power on the on-chip microwave feedline, we follow two distinct approaches. First, we add all specified loss elements like attenuators or directional couplers. Then, we estimate the total additional losses induced by non-specified components like cables and connectors based on a transmission measurement and attribute those additional losses to input and to output cabling, giving significantly more weight to the input lines due to the longer input cables with more potentially lossy connectors. For the probe signal line 1, we measure an average transmission of  $-5\text{ dB}$ , when having  $45\text{ dB}$  room-temperature attenuation,  $48\text{ dB}$  cryogenic attenuation,  $44\text{ dB}$  cryogenic gain at the HEMT amplifier and  $70\text{ dB}$  gain by room-temperature amplifiers. This leaves about  $26\text{ dB}$  of unaccounted losses, of which we attribute about  $17\text{ dB}$  to the input and  $9\text{ dB}$  to the output line, respectively. In total, this corresponds to an input attenuation of  $-110\text{ dB}$ .

Assuming a similar procedure for the pump input line (line number 2), we get a total attenuation of  $\sim -68\text{ dB}$  there.

As second approach, we consider the thermal noise of the HEMT amplifier as calibration standard. The HEMT noise power can be determined by

$$P_{\text{HEMT}} = 10 \log \left( \frac{k_B T_{\text{HEMT}} \Delta f}{1 \text{ mW}} \right) \quad (4.4)$$

where  $k_B$  is the Boltzmann constant,  $T_{\text{HEMT}}$  is the HEMT noise temperature and according to the data sheet is  $T_{\text{HEMT}} \approx 2\text{ K}$ . The measurement IF bandwidth of our calibration measurement is  $\Delta f = 1\text{ kHz}$ . In total, we get with these numbers  $P_{\text{HEMT}} = -165.6\text{ dBm}$  or the corresponding noise RMS voltage  $\Delta V = 1.66\text{ nV}$ . From the signal-to-noise ratio of  $\text{SNR} = 34.2\text{ dB}$  for a VNA output power of  $-20\text{ dBm}$ , we then get the signal power arriving at the HEMT input as  $-131.4\text{ dBm}$ . Assuming an attenuation between the sample

and the HEMT of 2 dB leaves us with a total input attenuation between VNA output and sample of  $-109.4$  dB.

When performing this procedure with the pump line, we get about  $-66$  dB of attenuation.

For the calibration of the photon numbers in this paper we therefore work with the attenuations  $G_{\text{signal}} = -110$  dB and  $G_{\text{pump}} = -67$  dBm in good agreement with both methods and estimate the accuracy of the achieved calibration on the order of 3 dB. Note that in addition to the uncertainty mentioned here, the power arriving on the chip is also frequency dependent, as we usually observe background transmission oscillations of about 2 dB peak-to-peak amplitude due to cable resonances. Therefore, the experimental single-photon coupling-rate  $g_0$ , calculated by using an estimate of the on-chip power based on the attenuation chain, has an estimated uncertainty  $\approx \pm 0.2 g_0$ .

### 4.5.3. CAVITY CHARACTERIZATION

#### CAVITY MODELING

##### 1. INTERDIGITATED CAPACITORS

The two interdigitated capacitors  $C$  of our device consist of  $N = 120$  fingers each, with finger and gap widths of  $1\mu\text{m}$  and a finger length  $l_f = 100\mu\text{m}$ . With the relative permittivity  $\epsilon_r = 11.8$  of the Silicon substrate and using the equations given in Ref. [158] we calculate the capacitance of one of the main interdigitated capacitors to be  $C = 680\text{ fF}$  and the interdigitated part of the coupling capacitor as  $C'_c = 27\text{ fF}$ .

For the total coupling capacitance, we also have to take into account the capacitance between the center conductor of the feedline and the fingers of both cavity capacitors  $C$ . We do this by calculating the feedline capacitance per unit length  $C' = 144\text{ pF/m}$  and with a total length of  $204\mu\text{m}$  we get  $29\text{ fF}$ . The capacitance between the center conductor and the cavity center electrode, however, is only approximately a factor of 0.25 of that, such that  $C_c = 34\text{ fF}$ .

The resonance frequency of the circuit is  $\omega_0 = 2\pi \cdot 5.221\text{ GHz}$  and related to the circuit parameters by

$$\omega_0 = \frac{1}{\sqrt{L_{\text{tot}}(2C + C_c)}} \quad (4.5)$$

where the total inductance  $L_{\text{tot}} = (L + L_J)/2$ . The linear inductance  $L$  is a combination of the SQUID loop inductance  $L_l$  and other linear inductance contributions in the circuit. All those have a geometric and a kinetic contribution and from the SONNET simulations discussed below, we estimate the kinetic contribution of the linear inductance to be  $L_k = 0.73L$ . The total inductance is approximately  $L_{\text{tot}} = 666\text{ pH}$ . This value is in good agreement with numbers we got using numerical inductance calculation of the whole device and assuming a London penetration depth  $\lambda_L = 160\text{ nm}$ , which corresponds to  $L_k \approx 2.75L_g$ .

##### 2. SONNET SIMULATIONS AND THE KINETIC INDUCTANCE

We simulated the cavity with the software package SONNET to determine the kinetic inductance per square  $L_{\square}$ . For a vanishing surface impedance we find a resonance fre-

quency  $\omega_{00} = 2\pi \cdot 10.05 \text{ GHz}$  and achieve high agreement with the experimental value of  $\omega_0 = 2\pi \cdot 5.221 \text{ GHz}$  when  $L_{\square} = 2.3 \text{ pH/sq}$ .

### 3. ANALYTICAL CAVITY MODEL

The cavity used in this experiment is a lumped element SQUID cavity capacitively coupled to a transmission line through a coupling capacitor  $C_c$ . Supplementary Fig. 4.7 shows a circuit equivalent of the cavity including the coupling capacitor and the feedline with characteristic impedance  $Z_0$ . In **a**, a circuit equivalent is shown, which resembles the geometric cavity elements. To get a simplified circuit, we first transform the inductances  $L_m, L_0$  forming an inductance-bridge via the  $\Delta$ -Y-approach to the new equivalent inductors

$$L_b = \frac{L_0 L_m}{2L_0 + L_m} \quad (4.6)$$

$$L_2 = \frac{L_0^2}{2L_0 + L_m} \quad (4.7)$$

and then combine series and parallel elements to arrive with the simple circuit equivalent shown in Supplementary Fig. 4.7 **e**. The additional relations between the inductors given in **a** and **e** are given by

$$L = L_A + 2L_3 \quad (4.8)$$

$$L_A = L_a + L_b \quad (4.9)$$

$$L_3 = L_1 + L_2. \quad (4.10)$$

As values for our device we estimate  $L_0 = 1 \text{ nH}$ ,  $L_1 = 140 \text{ pH}$ ,  $L_m = 60 \text{ pH}$  and  $L_a = 45 \text{ pH}$ . We estimate the critical currents of our Josephson junctions  $I_c = 25 \mu\text{A}$ , which corresponds to a Josephson inductance of  $L_J = 13 \text{ pH}$ .

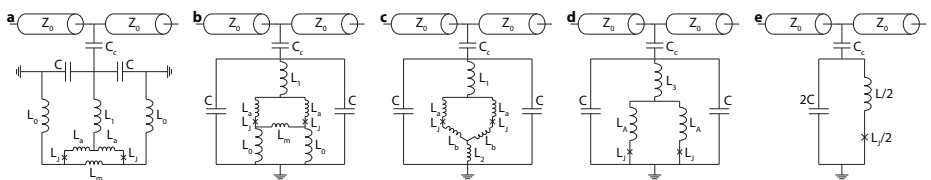


Figure 4.7: **Schematic of the device circuit and its simplification.** **a** The device equivalent circuit with individual circuit elements for each geometric element. **b** Re-arrangement of the circuit elements with a single ground connection. **c** Transformation of the inductors  $L_0, L_m$  to  $L_2, L_b$  using the  $\Delta$ -Y-approach for impedance-bridges. **d** Combining series inductors into single inductors  $L_3$  and  $L_A$ . **e** Combining parallel elements to get the reduced circuit equivalent.

Thus, the total inductance of the circuit is given by  $L_{\text{tot}} = (L + L_J)/2$  and the total capacitance by  $C_{\text{tot}} = 2C + C_c$ .

#### 4. CHARACTERISTIC FEEDLINE IMPEDANCE AND EXTERNAL LINewidth

The external linewidth  $\kappa_e$  of the circuit shown in Supplementary Fig. 4.7e is given by

$$\kappa_e = \frac{\omega_0^2 C_c^2 Z_0}{2C_{\text{tot}}} \quad (4.11)$$

which for our device and a feedline impedance of  $Z_0 = 50\Omega$  predicts  $\kappa_e = 2\pi \cdot 3.5\text{MHz}$ . This is in slight disagreement with the experimentally determined linewidth of about 9 MHz around the flux sweetspot, which can be explained by a combination of two effects. First, the on-chip feedline was designed to have a geometric characteristic impedance  $Z_{0g} = 50\Omega$ , which is considerably increased due to the high kinetic inductance of the thin Aluminum film. And secondly, we have strong cable resonances in the setup on the order of 2 dB peak-to-peak amplitude. Both effects considerably modify the effective impedance attached to the circuit.

When the cavity resonance frequency is tuned and moves through the cable resonances, we also find that the (external) linewidth considerably reduces to about  $\kappa = 2\pi \cdot 5\text{MHz}$ , cf. Supplementary Fig. 4.11.

#### 5. INTRACAVITY PHOTON NUMBER

The photon number in the cavity is estimated using

$$n_c = \frac{2P_{\text{in}}}{\hbar\omega_d} \frac{\kappa_e}{\kappa^2 + 4\Delta^2}, \quad (4.12)$$

where  $P_{\text{in}}$  is the input power (in Watt) on the feedline,  $\omega_d$  is the frequency of the drive tone and  $\Delta = \omega_d - \omega_0$  the detuning from the cavity resonance. Note, that we use  $\kappa_e = \kappa$  for this estimation as the device is highly overcoupled.

### RESPONSE FUNCTION AND FITTING ROUTINE

#### 1. THE IDEAL CAVITY RESPONSE FUNCTION

The  $S_{21}^{\text{ideal}}$  response function of a parallel LC circuit capacitively side-coupled to a transmission line is given by

$$S_{21}^{\text{ideal}} = 1 - \frac{\kappa_e}{\kappa_i + \kappa_e + 2i\Delta} \quad (4.13)$$

with internal and external decay rates

$$\kappa_i = \frac{1}{RC_{\text{tot}}}, \quad \kappa_e = \frac{\omega_0^2 C_c^2 Z_0}{2C_{\text{tot}}} \quad (4.14)$$

and detuning from the resonance frequency

$$\Delta = \omega - \omega_0, \quad \omega_0 = \frac{1}{\sqrt{L_{\text{tot}} C_{\text{tot}}}} \quad (4.15)$$

## 2. THE REAL CAVITY RESPONSE FUNCTION

The presence of attenuation, cable resonances and parasitic transmission channels is usually captured by additional terms added and multiplied to the ideal cavity response function

$$S_{21} = A \left( S_{21}^{\text{ideal}} + B e^{i\beta} \right) e^{i\alpha} \quad (4.16)$$

where  $A, B, \alpha, \beta$  are possibly frequency-dependent factors changing the overall transmission function. This can also be written as

$$S_{21} = P \left( 1 - \frac{K e^{i\theta}}{\kappa + 2i\Delta} \right) e^{i\phi} \quad (4.17)$$

where  $K$  and  $\theta$  are functions of  $\kappa_e$ ,  $B$  and  $\beta$  and  $P$  and  $\phi$  are functions of  $A, B, \alpha$  and  $\beta$ . Equation (4.17) is used throughout this work for fitting the cavity response function and to extract the total linewidth and resonance frequency. Note that a reliable extraction of external and internal linewidths is not possible anymore in the presence of cable resonances and parasitic transmission channels.

4

## 3. FULL CAVITY FITTING ROUTINE

During the experiments, the transmitted signals suffer from interferences and losses due to the presence of microwave elements such as attenuators, circulators and amplifiers in the lines, cf. Supplementary Fig. 4.6 as well as additional losses from microwave cables. For fitting and calibrating the transmitted fields, we follow a step-by-step fitting routine, which is described as follows. First, we consider the presence of a frequency dependent background signal expressed as

$$S_{\text{back}} = P(\omega) e^{i\phi(\omega)}. \quad (4.18)$$

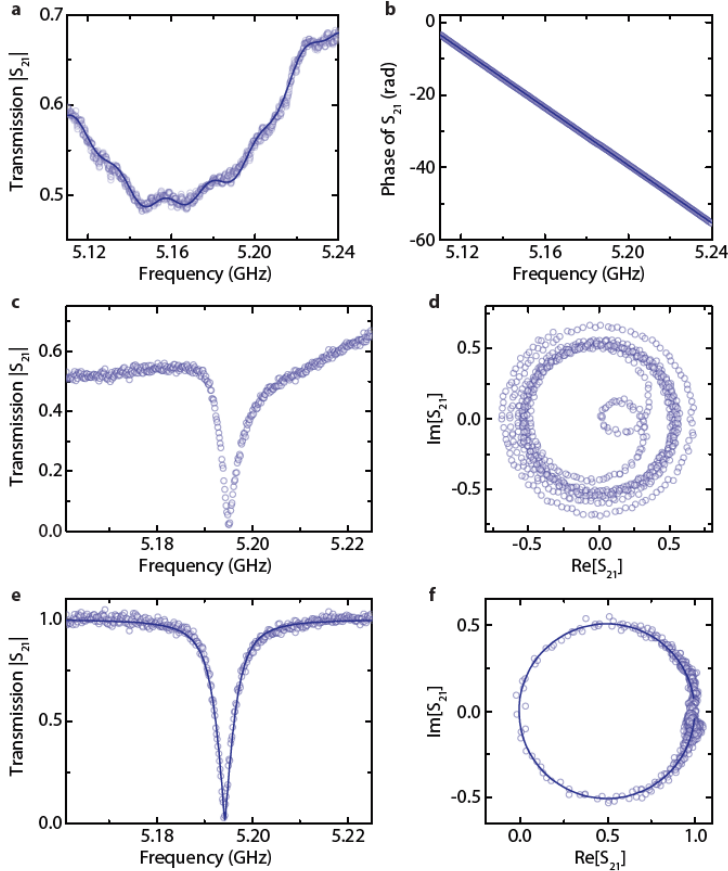
For the experimental extraction of the background curve, the cavity is initially set to two distant flux bias points with frequencies  $\omega_1 = 2\pi \cdot 5.15$  GHz and  $\omega_2 = 2\pi \cdot 5.22$  GHz and afterwards the spectrum is reconstructed by combining the individual parts where the cavity is non-resonant. The amplitude and phase data obtained by this procedure are shown in Supplementary Fig. 4.8a and b as circles. Then, we fit the whole background with a complex function whose magnitude and phase are written as a function of frequency as

$$P(\omega) = a_p \omega^5 + b_p \omega^4 + c_p \omega^3 + d_p \omega^2 + e_p \omega + f_p + a_{1c} \cos(b_{1c}\omega + c_{1c}) + a_{2c} \cos(b_{2c}\omega + c_{2c}) \quad (4.19)$$

$$\phi(\omega) = a_\phi \omega + b_\phi, \quad (4.20)$$

i.e., we perform a linear fit to the phase and both a polynomial and cosine fit to the magnitude of the stitched background data. The corresponding fits are shown as lines in Supplementary Fig. 4.8a and b.

A measured transmission spectrum with the cavity resonance included is shown in Supplementary Fig. 4.8c and d. Prior to all cavity fits and fits of optomechanically induced transparency, we remove the reconstructed background signal from the measured signal by complex division.



4

**Figure 4.8: The background transmission and how we correct for it.** **a** Background transmission signal amplitude in the relevant frequency range obtained by tuning the cavity to the maximum and minimum frequency and stitching together the unperturbed parts of the background signal. The corresponding phase is shown in **b**. Circles show measurement data, lines are fits as described in the text. **c** and **d** show the response signal of the cavity in raw data. The amplitude is shown in **c** and the complex response in **d**. By means of complex division, we divide off the background fit curves obtained from **a** and **b**. The resulting curve is fitted by Eq. (4.21). After this fit, we rotate and rescale the cavity resonance and obtain the signal shown in **e** and **f** as circles. The lines show the accordingly rescaled and rotated fits.

Considering the possibility that the measured signal might still be influenced by a small frequency-dependent background modulation, we fit the resulting cavity line with

$$S_{21} = (a_{p2} + b_{p2}\omega) \left( 1 - \frac{Ke^{i\theta}}{\kappa + 2i\Delta} \right) e^{i(a_{\phi 2}\omega + b_{\phi 2})} \quad (4.21)$$

where we consider once more a background using the complex scaling factor

$$S_{\text{back2}} = (a_{p2} + b_{p2}\omega) e^{i(a_{\phi 2}\omega + b_{\phi 2})}. \quad (4.22)$$

Supplementary Figs. 4.8e and f show a resonance curve of the SQUID cavity after background division and rotation by the obtained value of  $\theta$  including the cavity response fit using Eq. (4.21).

## THE JOSEPHSON JUNCTIONS AND THE SQUID

### 1. THE JUNCTIONS

The constriction type Josephson junctions in our SQUID are designed to be 50 nm wide and 200 nm long nanobridges in between two superconducting pads, similar to what has been investigated previously by other authors [120]. The pads and the junctions have a constant film thickness of about 20 nm and thus we have what is referred to as 2D SQUID geometry in literature [114]. We estimate the critical current to be approximately  $I_{c0} \approx 25 \mu\text{A}$ . Although our junctions might show deviations from an ideal sinusoidal current-phase relation [114], we can estimate the zero-bias junction inductance from the critical current to be

$$L_J = \frac{\Phi_0}{2\pi I_c} \approx 13 \text{ pH}. \quad (4.23)$$

### 2. THE SQUID LOOP INDUCTANCE

Due to the 2D SQUID geometry as well as the large kinetic inductance of our films, we have to consider a significant loop inductance when treating the SQUID. From our estimations above, the loop inductance is approximately given by  $L_l = 2L_a + L_m \approx 150 \text{ pH}$ , which gives for the so-called screening parameter

$$\beta_L = \frac{2I_{c0}L_l}{\Phi_0} \approx 3.7. \quad (4.24)$$

Such a large screening parameter is related to a hysteretic flux state of the SQUID and allows the SQUID to screen more than half a flux quantum before the critical current of the junctions is exceeded by the screening current [122].

### 3. BIAS FLUX DEPENDENCE OF THE RESONANCE FREQUENCY

Both, non-sinusoidal current-phase relationship in the form of skewed sine functions as well as large screening parameters lead to widening of the magnetic flux arch and to hysteretic switching of the SQUID flux state. Both descriptions have been used to model the hysteretic resonance frequency flux archs of superconducting resonators including SQUIDS with constriction type Josephson junctions [120, 122].

We phenomenologically include both effects in the description of the single-arch flux-dependence of our SQUID cavities by including a factor  $\gamma_L$  into the effective single junction inductance

$$L_J(\Phi) = \frac{L_{J0}}{\cos\left(\pi\gamma_L \frac{\Phi}{\Phi_0}\right)}. \quad (4.25)$$

The factor  $\gamma_L$  takes a widening of the flux arch and a tuning of the resonance frequency far beyond  $\pm\Phi_0/2$  into account, cf. Supplementary Fig. 4.9, where an ideal SQUID with a

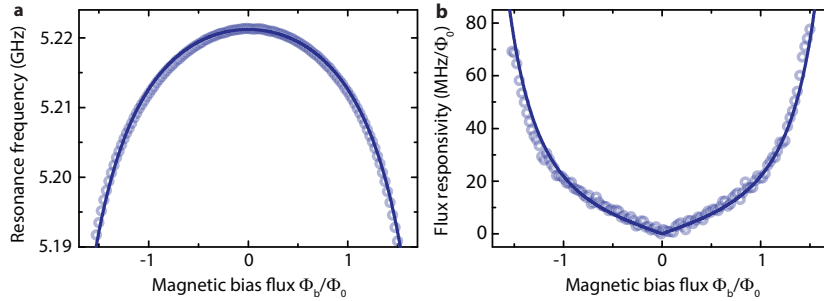


**Figure 4.9: Cavity frequency tuning and flux responsivity with magnetic bias flux.** **a** A Cavity resonance frequency vs magnetic bias flux for  $B_{||} = 3\text{ mT}$ . Circles are data points extracted from fits and the line is a fit using Eq. (4.28) with fixed  $\Lambda = 0.99$  and  $\gamma_L$  being the only free parameter. In **b** the flux responsivity  $|\partial\omega_0/\partial\Phi|$  is plotted. Both, the experimental and the theoretical curves are obtained by calculating the derivative of the data in **a**.

4

sinusoidal current-phase relationship and negligible loop inductance would have  $\gamma_L = 1$ . The resonance frequency of the SQUID cavity can therefore be expressed as

$$\omega_0(\Phi) = \frac{1}{\sqrt{C_{\text{tot}}(L + L_J(\Phi))/2}}. \quad (4.26)$$

Defining the sweet spot resonance frequency by

$$\omega_0^s = \frac{1}{\sqrt{C_{\text{tot}}(L + L_{J0})/2}} \quad (4.27)$$

we can write the flux-dependent frequency as

$$\omega_0(\Phi) = \frac{\omega_0^s}{\sqrt{\Lambda + \frac{1-\Lambda}{\cos(\pi\gamma_L \frac{\Phi}{\Phi_0})}}}. \quad (4.28)$$

with  $\Lambda = L/(L + L_{J0})$ . For our device parameters, we get  $\Lambda \approx 0.99$ .

Supplementary Fig. 4.9a shows the resonance frequency of the SQUID cavity when biased with the on-chip bias line and the resulting flux arch was fitted with Eq. (4.28). The only free parameter for the fit was  $\gamma_L = 0.23$ , indicating a large screening parameter and/or a non-sinusoidal current-phase relation. We note here, however, that the theoretical  $\beta_L = 3.7$  derived above is too small to explain the widening of the arch as we observe it. One possible explanation is a non-sinusoidal current-phase relation. A second possibility, which is at the same time in agreement with the deviation between theory and experiment of the mechanical resonance frequency shift with in-plane field, is that we underestimate the loop inductance significantly. A discussion of this possibility with a possible explanation is given in section 4.5.4.

In Supplementary Fig. 4.9b, we plot the derivative of both, the data points and the fit curve, to obtain the flux responsivity  $\partial\omega_0/\partial\Phi$ , which is directly proportional to the optomechanical single-photon coupling rate  $g_0$ .

Both parameters,  $\Lambda$  and  $\gamma_L$  seem to depend slightly on the magnetic in-plane field, which is taken into account in our analysis. The values given here are extracted for  $B_{||} = 1\text{ mT}$ . The origin of this dependence, however, is not fully clear. It might be due to a change of the bias current flow for large in-plane fields or to a change of kinetic loop inductance, while the rest of the kinetic cavity inductance stays nearly unchanged.

#### 4. CALIBRATION OF THE FLUX AXIS

We use the measured  $\Phi_0$ -periodicity of jumps in the hysteretic resonance frequency to calibrate the flux axis for the bias flux dependence.

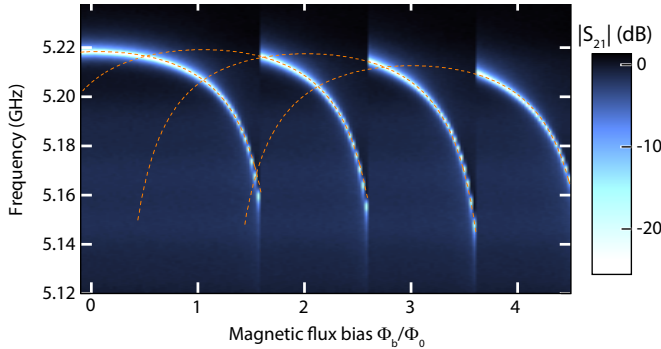


Figure 4.10: **Cavity frequency tuning with magnetic bias flux beyond a single flux arch.** When we sweep the bias flux to larger values than about  $1.6\Phi_0$ , we find periodic jumps in the resonance frequency and partial arches. This is an indication for a non-negligible screening parameter and/or a non-sinusoidal current-phase relation. The periodicity can be used to calibrate the flux axis to the flux quantum  $\Phi_0$ . The dashed lines correspond to copies of the flux arch dependence used in Supplementary Fig. 4.9a each shifted in flux and sweetspot frequency only to match the observed resonance frequencies. The data shown here are for  $B_{||} = 1\text{ mT}$

Supplementary Fig. 4.10 shows an example for the hysteretic jumps of the cavity frequency with flux, indicating a significant loop inductance and/or a non-sinusoidal current-phase relation [120, 122]. We herewith calibrate the flux axis for all in-plane fields. Note, that in contrast to the description given in Ref.[122], the periodicity of the jumps corresponds to  $1\Phi_0$  instead of  $2\Phi_0$ .

Also, we note here that according to this flux calibration based on the periodicity of the resonance frequency, the experimentally obtained current-to-flux conversion  $40\mu\text{A}\hat{=}1\Phi_0$  is not in agreement with what we would expect from calculating the flux in the SQUID loop generated by a flux bias line current  $I_b = 40\mu\text{A}$ . We suspect that the bias current is flowing to ground through the SQUID and the mechanical oscillator itself, which is possible as all corresponding wires, the linear inductors of the cavity as well as the bias current, are galvanically connected through the superconducting ground planes to each other.

#### 5. IN-PLANE FIELD DEPENDENCE OF THE CAVITY PARAMETERS

The cavity parameters of the SQUID cavity such as the linewidth  $\kappa$  and the shape of the flux dependence depend on the magnetic in-plane field. In Supplementary Fig. 4.11 we

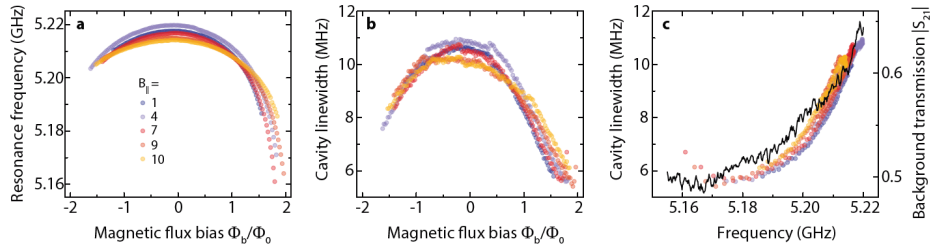


**Figure 4.11: Bias flux dependence of the cavity parameters and their development with in-plane field.** **a** SQUID cavity resonance frequency vs magnetic bias flux for 5 different magnetic in-plane fields. **b** Cavity linewidth vs magnetic bias flux for 5 different magnetic in-plane fields. **c** Cavity linewidth plotted vs the simultaneously fitted resonance frequency for 5 different magnetic in-plane fields. The black line shows the background transmission amplitude in the corresponding frequency range, showing a very similar trend as the cavity linewidth. The color legend for the data points in all three plots is given in **a**. Data in **a** and **b** have been shifted in flux such that the sweetspot is positioned at  $\Phi_b = 0$ .

4

show exemplary results for the cavity resonance frequency in **a** and the cavity linewidth in **b** vs the bias flux and for several magnetic in-plane fields. Due to the fact, that the parameters depend only slightly on the magnetic in-plane field for  $B_{||} \leq 7$  mT, we only plot a subset of curves from this regime here and add the two curves for  $B_{||} = 9$  mT and 10 mT, where we observe systematic deviations.

Besides different frequencies at the flux sweet spot, the bias flux dependences for  $B_{||} = 1, 4, 7$  mT are very similar. For 9 and 10 mT, however, a slight widening of the arch is visible. For now, it is unclear to us what exactly causes this widening. Some effects such as a global increase of kinetic inductance or a global Abrikosov vortex pollution can probably be disregarded, as we expect that they would significantly impact the total cavity resonance frequency and/or linewidth.

In **b** we plot the extracted total cavity linewidth, which is dominated by the external linewidth for all shown values. We observe a strong linewidth decrease by about a factor of 2 with bias flux and only small variations due to the in-plane field. We attribute this linewidth decrease with bias flux not to the bias flux directly, but think it is related to the frequency position of the cavity within a standing wave pattern of cable and feed-line resonances in the setup. In panel **c** we plot the same linewidth data for all in-plane fields vs the cavity resonance frequency and find that besides a very slight dependence on in-plane field all points fall onto the same curve. We plot in panel **c** as black curve the background transmission signal discussed in Supplementary Fig. 4.8, indicating that linewidth and background transmission are correlated. We notice in particular that the linewidth increases again for the smallest frequency points around the value where the background transmission increases again as well.

Simulations with the package QUCS confirm the possibility of a significant linewidth dependence on the resonance frequency in presence of feedline resonances. An intuitive picture would be that by shifting the cavity resonance frequency with bias flux, it is moved from an antinode to a node of a standing wave formed on the feedline.

As concluding remarks for this part we would like to state, that we compensate for a flux arch widening at the highest fields by adjusting the flux bias point to the desired

$\partial\omega_0/\partial\Phi$ . Also, the sweetspot resonance frequency and linewidth tend to be influenced by the magnetic history and by microwave triggered flux avalanches. They can vary by several MHz for a given in-plane field, indicating that we trap flux in form of Abrikosov vortices inside the sample originating from the out-of-plane component of the transduction field. Thermal cycling before each measurement could partially overcome this issue, but is too time consuming to be a practical solution.

## 6. CAVITY ANHARMONICITY

Assuming a sinusoidal current-phase relation, we calculate the shift per photon to first order by

$$\chi = -\frac{e^2}{2\hbar C_{\text{tot}}} (1 - \Lambda)^3 \approx 2\pi \cdot 14 \text{ Hz}. \quad (4.29)$$

Therefore, the cavity can be considered in good approximation as linear, as long as the photon number does not exceed a few 10000.

### 4.5.4. MECHANICAL CHARACTERIZATION THEORY OF LORENTZ-FORCE ACTUATION

The equation of motion of the mechanical resonator is given by

$$\ddot{x} + \frac{\Omega_0}{Q_m} \dot{x} + \Omega_0^2 x = \frac{F(t)}{m} \quad (4.30)$$

where  $m$  is the effective mass,  $Q_m$  is the mechanical quality factor and  $\Omega_0$  is the resonance frequency. External forces onto the mechanical oscillator are contained in  $F(t)$ .

The current through the mechanical beam in presence of flux biasing and a magnetic in-plane field is given by the flux quantization and conservation in the SQUID loop. In the absence of a bias current and for identical junctions, the general relation between the phase difference across one junction  $\delta$  and the total flux through the loop  $\Phi$  is given by

$$\frac{\delta}{\pi} = \frac{\Phi}{\Phi_0}. \quad (4.31)$$

The circulating current at the same time is related to the phase difference by

$$J = I_{c0} \sin \delta \quad (4.32)$$

The total flux through the loop  $\Phi$  is a sum of the bias flux  $\Phi_b$ , the flux generated by a loop current via the loop inductance  $\Phi_J = L_I J$ , and a contribution from the in-plane field when the mechanical oscillator is displaced from its equilibrium position  $\Phi_x = \gamma B_{||} l x$ , thus

$$\Phi = \Phi_b + \Phi_J + \Phi_x \quad (4.33)$$

$$= \Phi_b + L_I J + \gamma B_{||} l x. \quad (4.34)$$

For a constant flux bias  $\Phi_{b0}$  there is a circulating current  $J_0$  and the mechanical beam is in the equilibrium position  $x_0$ . We assume now that all quantities only slightly differ

from their equilibrium values  $\Phi_b(t) = \Phi_{b0} - \Delta\Phi_b$ ,  $x(t) = x_0 + \Delta x$  and  $J(t) = J_0 + \Delta J$ . Re-defining  $x = \Delta x$  and  $L_J = L_J(\Phi_{b0})$ , we can approximate to first order

$$\Delta J = \frac{\Delta\Phi_b}{L_l + 2L_J} - \frac{\gamma B_{||} l x}{L_l + 2L_J}. \quad (4.35)$$

The dynamical part of the Lorentz-force is given by  $F_L(t) = \gamma B_{||} l \Delta J$  and thus the equation of motion becomes

$$\ddot{x} + \frac{\Omega_0}{Q_m} \dot{x} + \left( \Omega_0^2 + \frac{\gamma^2 B_{||}^2 l^2}{m(L_l + 2L_J)} \right) x = \frac{\gamma B_{||} l}{m(L_l + 2L_J)} \Delta\Phi_b(t). \quad (4.36)$$

Thus, a time-varying magnetic flux is translated into a time-varying Lorentz-force and can be used to directly drive the mechanical motion. In addition, a position-dependent force emerges from the mechanical oscillator placed in a SQUID loop, which shifts the mechanical resonance frequency.

4

## IN-PLANE MAGNETIC FIELD DEPENDENCE

The position dependent part of the Lorentz-force is equivalent to a mechanical spring stiffening, in analogy to the electrostatic softening in electromechanical capacitors. The shifted resonance frequency is given by

$$\Omega_m^2 = \Omega_0^2 + \frac{\gamma^2 B_{||}^2 l^2}{m(L_l + 2L_J)} \quad (4.37)$$

what can be approximated as

$$\Omega_m \approx \Omega_0 + \frac{\gamma^2 B_{||}^2 l^2}{2m\Omega_0(L_l + 2L_J)}. \quad (4.38)$$

We indeed observe a shift of the mechanical resonance frequency with in-plane field as shown in Supplementary Fig. 4.12 for two different flux responsivities, i.e., for two different Josephson inductances. The absolute numbers, however, are smaller by about a factor of  $\sim 2$  than the result of independent calculations based on the device parameters and the in-plane field. Possible reasons for this mismatch is the overestimation of the mode scaling factor  $\gamma = 0.86$ , which we determined through matching the experimental  $g_0$  with the theoretical calculations, an underestimated loop inductance or a field-dependent loop or Josephson inductance.

In combination with the observation of flux arch widening, we consider the most probable explanation that the loop inductance is significantly higher than expected. For the mechanical resonance frequency shift, we find a good agreement between theory and experiment for a loop inductance of  $\sim 350\text{pH}$ . This would correspond to  $\beta_L = 8.6$ . A possible origin for this deviation is possibly related to the suspension of the mechanical part of the loop and the release process, which ends with oxygen plasma ashing of the resist and might induce an enhanced oxidation of the bottom side of the beam. The mechanical beam oxidizes from the top and the bottom, while the rest of the circuit only

oxidizes from the top. For very thin films as used here, the oxide layer of a few nm thickness might change the thickness of the superconducting layer significantly, which will increase the kinetic inductance of that region. As the inductance of our circuit is dominated by kinetic inductance anyways, such a two-sided oxidization might indeed be responsible for a significantly increased inductance of the suspended parts. This would explain, why the results related to the loop inductance are deviating from theoretical calculations, while all results where the loop inductance is not relevant, are in excellent agreement.

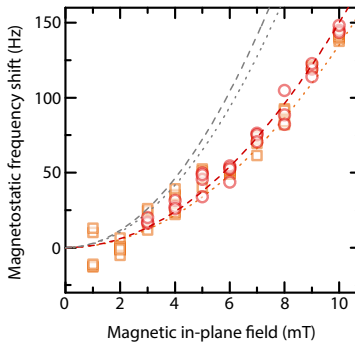


Figure 4.12: **Magnetostatic spring stiffening by Lorentz-force backaction.** The measured frequency shift is plotted as points for two different values of bias flux. Circles correspond to  $\Phi_b/\Phi_0 = 0.75$  and squares to  $\Phi_b/\Phi_0 = 1.45$ . The gray dashed and dotted lines are the theoretical calculations without free parameters and overestimate the measured effect by a factor of  $\sim 2$ . The red dashed and orange dotted lines correspond to the theoretical lines with a scaling factor of  $\sim 0.52$  and agree well with the observed frequency shift.

## UPCONVERSION OF COHERENTLY DRIVEN MECHANICAL MOTION

We excite the mechanical resonator by Lorentz-force actuation and measure the cavity sidebands generated by the corresponding cavity field phase modulation when sending a tone resonant with the cavity  $\omega_d = \omega_0$ . The excitation current is generated by the output port of a vector network analyzer and sent through the on-chip bias line, cf. Supplementary Fig. 4.6c. At the same time, we drive the cavity with a resonant microwave tone generated by a signal generator. The cavity output field, including the motional sidebands, is amplified and sent through a high-pass filter into a mixer, where it is down-converted by being mixed with the original carrier tone. The mixer output is low-pass filtered and sent into the input port of the network analyzer. As we are driving the cavity on resonance, we must adjust the phase of the carrier signal in order to get constructive interference of the sidebands at  $+\Omega$  and  $-\Omega$ . We adjust the phase-shifter manually until the detected sideband signal is maximized.

In this setup, however, we do not only detect the additional flux induced into the SQUID by the mechanical motion, but also the phase modulations directly generated by the bias flux modulation itself. Other possible parasitic tones come from mixing due to the cavity nonlinearity or in the nonlinear elements of the detection chain. The detected

sideband amplitude  $|S_{21}|$  is thus proportional to

$$|S_{21}(\Omega)| \propto \left| \frac{\gamma B_{||} l}{2m\Omega_m} \frac{F_L(\Omega)}{\Omega_m - \Omega - i\frac{\Gamma_m}{2}} + Se^{i\sigma} \right| \quad (4.39)$$

with an additional signal  $Se^{i\sigma}$  interfering with the motional sideband. Therefore, the measured, upconverted mechanical resonance will have a slight Fano lineshape as shown in Supplementary Fig. 4.13a. We correct for this slight asymmetry by subtracting a constant complex number from the detected signal. The result is shown in Supplementary Fig. 4.13b and in Fig. 4.2.

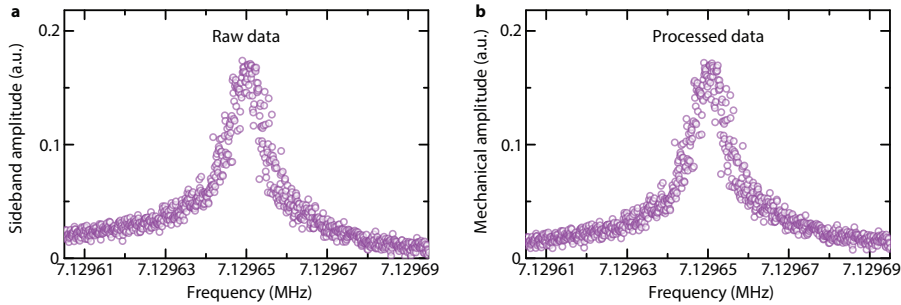


**Figure 4.13: Processing the motional sideband generated by mechanical displacement.** **a** Raw data for the sideband amplitude detected by means of sending a resonant tone into the cavity while exciting the mechanical mode by Lorentz-force. The Lorentz-force drive current frequency is swept through the mechanical resonance. Due to additional contributions to the SQUID cavity sideband such as direct flux modulation of the SQUID by the Lorentz-force current, the sideband does not only contain information about the mechanical displacement. **b** shows the amplitude data of **a**, where a constant complex number has been subtracted from the complex  $S_{21}$  data.

## INTERFEROMETRIC DETECTION OF THERMAL MECHANICAL MOTION

The measurement routine is very similar to the one for the detection of coherently driven motion. Instead of using a network analyzer, however, we do not apply any driving current, but just detect the down-converted sideband-voltage quadratures  $I$  and  $Q$  with a vector signal analyzer. From the Fourier-transform of the quadratures, we calculate the corresponding power spectral density.

## ESTIMATE OF THE THERMAL PHONON OCCUPATION

We assume the SQUID cavity to have negligible thermal occupation at the fridge base temperature  $T_b = 15\text{ mK}$  and the thermal occupation of the mechanical mode to be  $n_{\text{th}} \gg 1$ . Then, for a resonant cavity drive, the power spectral density of the system output is approximately given by

$$\frac{S(\omega)}{\hbar\omega} = \frac{1}{2} + n'_{\text{add}} + 2C\kappa_e \frac{\kappa}{\kappa^2 + 4\Omega_m^2} \frac{\Gamma_m^2}{\Gamma_m^2 + 4\Delta_m^2} n_{\text{th}} \quad (4.40)$$

where  $n'_{\text{add}}$  is the effective number of added noise photons and in our case is mainly determined by the HEMT noise temperature  $T_{\text{HEMT}} \approx 2\text{ K}$  and the attenuation of 2dB between the sample output and the HEMT amplifier. From these numbers, we estimate  $n'_{\text{add}} \sim 14$ .

With the cooperativity  $\mathcal{C} \approx 0.2$  and  $\kappa_e \approx \kappa \approx \Omega_m$ , we calculate from this  $n_{\text{th}} \approx 160$  for the measurement shown in Fig. 4.2. This occupation corresponds to a mode temperature of  $n_{\text{th}} \approx 50\text{ mK}$  and suggests that the mechanical oscillator is not fully thermalized to the fridge base temperature. We also note, however, that the estimation of this number has several significant uncertainties related to the phase of the local oscillator in our homodyne detection scheme (manually adjusted), to the possibility that the cavity field emission is not symmetric into both sides of the transmission line and to small uncertainties related to the parameters  $\mathcal{C}$  and  $\kappa$ .

## 4

### 4.5.5. OPTOMECHANICAL DEVICE CHARACTERIZATION OPTOMECHANICAL EQUATIONS OF MOTION

The system is modelled with the classical equations of motion for the mechanical displacement  $x$  and normalized intracavity field amplitude  $\alpha$

$$\ddot{x} = -\Gamma_m \dot{x} - \Omega_m^2 x + \frac{1}{m} (F_r + F_e) \quad (4.41)$$

$$\dot{\alpha} = \left[ i(\Delta + Gx) - \frac{\kappa}{2} \right] \alpha + \sqrt{\frac{\kappa_e}{2}} S_{\text{in}}, \quad (4.42)$$

where  $\Delta = \omega_d - \omega_0$  is the detuning from the cavity resonance frequency,  $\kappa = \kappa_i + \kappa_e$  is the total cavity linewidth and  $S_{\text{in}}$  is the normalized input field. The external forces onto the mechanical oscillator are expressed by  $F_e$  and the radiation pressure force contribution is taken into account in  $F_r$  and expressed as a function of the intracavity field by

$$F_r = \hbar G |\alpha|^2, \quad (4.43)$$

with pull parameter  $G$

$$G = -\frac{\partial \omega_0}{\partial x}. \quad (4.44)$$

Assuming that the intracavity field is high enough to only consider small deviations from the steady state solutions with  $x = \bar{x} + \delta x$  and  $\alpha = \bar{\alpha} + \delta \alpha$  and no external driving force  $F_e$ , the equations of motion can be linearized as

$$\delta \ddot{x} = -\Gamma_m \delta \dot{x} - \Omega_m^2 \delta x + \frac{\hbar G \bar{\alpha}}{m} (\delta \alpha + \delta \alpha^*) \quad (4.45)$$

$$\delta \dot{\alpha} = \left[ i\bar{\Delta} - \frac{\kappa}{2} \right] \delta \alpha + i G \bar{\alpha} \delta x + \sqrt{\frac{\kappa_e}{2}} S_p \quad (4.46)$$

In the above expressions, the detuning  $\bar{\Delta} = \omega_d - \omega_c + G\bar{x}$  takes into account the shift from the equilibrium position  $\bar{x}$  due to the radiation pressure force and  $\sqrt{\frac{\kappa_e}{2}}S_p$  with  $S_p = S_0 e^{-i\Omega t}$ ,  $\Omega = \omega - \omega_d$  accounts for field fluctuations. As in our experiments  $\bar{\Delta} \approx \Delta$ , we will just use  $\Delta$  instead of  $\bar{\Delta}$  throughout this paper.

The response of the optomechanical cavity is then given by

$$S_{21} = 1 - \sqrt{\frac{\kappa_e}{2}} \frac{a_-}{S_0} \quad (4.47)$$

with

$$a_- = \chi_c \left[ 1 + i2m\Omega_m g^2 \chi_c \chi_m^{\text{eff}} \right] \sqrt{\frac{\kappa_e}{2}} S_0. \quad (4.48)$$

Here

$$\chi_c = \frac{1}{\frac{\kappa}{2} - i(\Delta + \Omega)} \quad (4.49)$$

is the cavity susceptibility and

$$\chi_m^{\text{eff}} = \frac{1}{2m\Omega_m} \frac{1}{\Omega_m - \Omega - i\frac{\Gamma_m}{2} + \Sigma(\Omega_m)} \quad (4.50)$$

with

$$\Sigma(\Omega_m) = -ig^2 [\chi_c(\Omega_m) - \chi_c^*(-\Omega_m)] \quad (4.51)$$

is the effective mechanical susceptibility in the high- $Q_m$  approximation.

## OPTICAL SPRING AND OPTICAL DAMPING

By re-writing Eq. (4.51) as  $\Sigma = \delta\Omega_m - i\Gamma_0/2$  and analyzing the real and imaginary part we can write the change in mechanical frequency  $\delta\Omega_m$  (optical spring) and the additional mechanical damping term  $\Gamma_o$  (optical damping) as

$$\delta\Omega_m = g^2 \left[ \frac{\Delta + \Omega_m}{\frac{\kappa^2}{4} + (\Delta + \Omega_m)^2} + \frac{\Delta - \Omega_m}{\frac{\kappa^2}{4} + (\Delta - \Omega_m)^2} \right] \quad (4.52)$$

$$\Gamma_o = g^2 \kappa \left[ \frac{1}{\frac{\kappa^2}{4} + (\Delta + \Omega_m)^2} - \frac{1}{\frac{\kappa^2}{4} + (\Delta - \Omega_m)^2} \right] \quad (4.53)$$

For all our experimental parameters, the optical frequency shift is negligibly small  $\delta\Omega_m < 1\text{ Hz}$ , i.e.,  $\delta\Omega_m \ll \Gamma_m$ , and therefore is not accounted for in any of the measurements or analyses.

## OPTOMECHANICALLY INDUCED TRANSPARENCY IN THE UNRESOLVED SIDE-BAND REGIME

For our device, we have  $\kappa \sim \Omega_m$  and thus we cannot use the approximate equations and results for the resolved sideband regime. We used two related methods to analyze our

experiments on optomechanically induced transparency and to determine the single-photon coupling rate  $g_0$  from these measurements. For a drive on the red sideband and  $\Gamma_m \ll \kappa$ , both resonances, the cavity response as well as the response window of the mechanical oscillator inside the cavity describe a circle in the complex response. The ratio of the diameters of these circles can be used to determine the optomechanical multi-photon coupling rate  $g$  as described below. In the second way, we fit both resonances with a complex resonance function as Eq. (4.21) and determine the cooperativity from the ratio of the amplitudes on resonance.

### 1. CAVITY CIRCLE DIAMETER $d_c$

To demonstrate that the circle diameter ratio is not influenced by the presence of parasitic resonances and transmission channels of the setup, we start with the modified optomechanical response function similar to what we described above for the bare cavity

$$S_{21} = A \left( 1 - \frac{\kappa_e}{\kappa + 2i(\Delta + \Omega)} \left[ 1 + i2m\Omega_m g^2 \chi_c \chi_m^{\text{eff}} \right] + Be^{i\beta} \right) e^{i\alpha} \quad (4.54)$$

which can be rewritten as

$$S_{21} = P \left( 1 - \frac{Ke^{i\theta}}{\kappa + 2i(\Delta + \Omega)} \left[ 1 + i2m\Omega_m g^2 \chi_c \chi_m^{\text{eff}} \right] \right) e^{i\phi}. \quad (4.55)$$

From the bare cavity fit, we determined the background  $S_{\text{back}} = Pe^{i\phi}$  and we divide this background off to get

$$S_{21} = 1 - \frac{Ke^{i\theta}}{\kappa + 2i(\Delta + \Omega)} \left[ 1 + i2m\Omega_m g^2 \chi_c \chi_m^{\text{eff}} \right] \quad (4.56)$$

For  $|\Omega_m - \Omega| \gg \Gamma_m$ , the mechanical susceptibility essentially vanishes in the weak coupling limit and we get back the bare cavity response function

$$S_{21} = 1 - \frac{Ke^{i\theta}}{\kappa + 2i(\Delta + \Omega)}. \quad (4.57)$$

By calculating the cavity response at the points  $\Omega = -\Delta - \kappa/2$  and  $\Omega = -\Delta + \kappa/2$  we get

$$S_{21-} = 1 - \frac{Ke^{i\theta}}{\kappa + i\kappa}, \quad S_{21+} = 1 - \frac{Ke^{i\theta}}{\kappa - i\kappa} \quad (4.58)$$

The distance between these two points gives us the bare cavity circle diameter

$$d_c = |S_{21-} - S_{21+}| = \frac{K}{\kappa}. \quad (4.59)$$

## 2. OMIT CIRCLE DIAMETER $d_m$

For the estimation of the diameter of the circle related to the mechanical signal as optomechanically induced transparency (OMIT), we first consider that the anchor point of the mechanical circle does not necessarily correspond exactly to the cavity resonance frequency in order to account for cases where there is still a small detuning present in the experiment. This offset  $\delta_m = \omega_0 - \omega_d - \Omega_m$  will modify the diameter of the circle with respect to the resonant case. Considering  $\Gamma_{\text{eff}} = \Gamma_m + \Gamma_o \ll \kappa$  we can expect that, for a fixed pump frequency close to the the cavity red sideband  $\Delta \approx -\Omega_m - \delta_m$ , the cavity has a constant reponse during the OMIT circle, given by

$$\chi_c = \frac{2}{\kappa - 2i\delta_m} \quad (4.60)$$

By evaluating the total response function at the points  $\Omega = \Omega_m - \Gamma_{\text{eff}}/2$  and  $\Omega = \Omega_m + \Gamma_{\text{eff}}/2$  we calculate the OMIT circle diameter

$$d_m = |S_{21-} - S_{21+}| = \left| -4iKm\Omega_m g^2 \frac{1}{(\kappa - 2i\delta)^2} [\chi_m^{\text{eff}-} - \chi_m^{\text{eff}+}] e^{i\theta} \right| \quad (4.61)$$

$$= 4K \frac{g^2}{\Gamma_{\text{eff}}} \frac{1}{\kappa^2 + 4\delta_m^2}. \quad (4.62)$$

## 3. EFFECTIVE COOPERATIVITY $\mathcal{C}_{\text{eff}}$ AND THE EXTRACTION OF $g_0$

We define the effective cooperativity as

$$\mathcal{C}_{\text{eff}} = \frac{4g^2}{\kappa\Gamma_{\text{eff}}} \quad (4.63)$$

and with this the ratio of the cavity and mechanical resonance circle diameters is given by

$$\frac{d_m}{d_c} = \mathcal{C}_{\text{eff}} \frac{\kappa^2}{\kappa^2 + 4\delta_m^2} \quad (4.64)$$

Thus, as a measurement of the cavity and the transparency window of OMIT provide us with the circle diameters, the cavity linewidth  $\kappa$  and the detuning  $\delta_m$ , we can extract the effective cooperativity, which in combination with the width of the transparency window  $\Gamma_{\text{eff}}$  allows for the extraction of the multi-photon coupling rate  $g$ . Using the estimated intracavity photon number  $n_c$  finally leads to the single-photon coupling rate

$$g_0 = \frac{g}{\sqrt{n_c}}. \quad (4.65)$$

## FULL EXPERIMENTAL AND FITTING PROCEDURE FOR OPTOMECHANICALLY INDUCED TRANSPARENCY

### 1. ADJUSTING THE CAVITY PARAMETERS AND MEASUREMENT ROUTINE

**I.** As first step in all measurements, we fix the in-plane field to a desired value  $B_{||}$ .

**II.** As second step, we sweep the bias flux in small steps and for each value take a transmission spectrum of the cavity with a network analyzer. The cavity resonance is fitted within the measurement script using Eq. (4.21) and quality factor and resonance frequency are extracted. To approximately bias the cavity with a desired value for  $\partial\omega_0/\partial\Phi$ , we run this biasing and fitting procedure until the resonance frequency shift between two subsequent bias points matches the set value.

**III.** Then, we switch on the drive tone at a frequency  $\omega_d$  slightly below the red sideband frequency  $\omega_0 - \Omega_m$  with  $\omega_0$  being the last resonance frequency measured in the bias flux sweep, and move the drive tone frequency in small steps towards the cavity resonance frequency. For each pump frequency, we take a resonance curve and extract  $\omega_0$  by a fit again, until  $\omega_0 - \omega_d - \Omega_m < \kappa/100$ , i.e., until the drive tone is approximately on the red sideband.

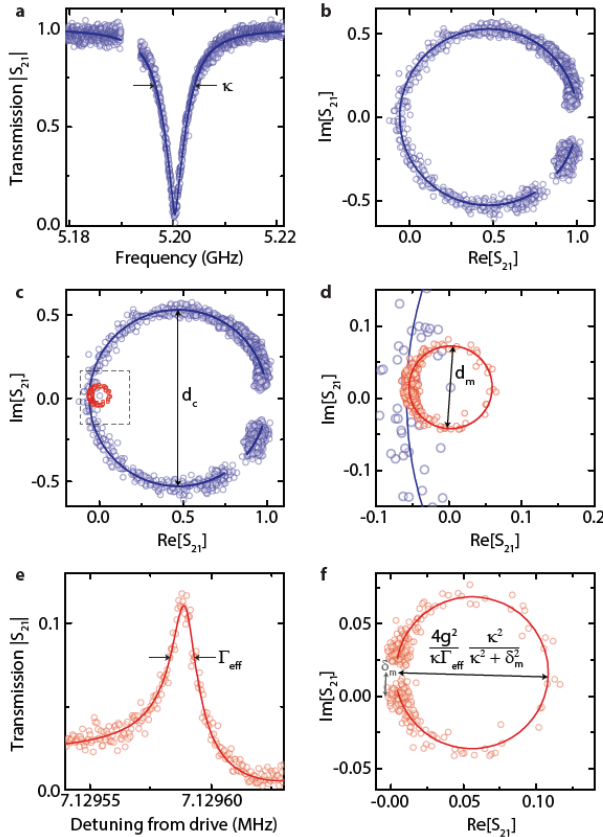
**IV.** When this criterion is fulfilled, the iteration stops, we switch off the pulse-tube cooler of the dilution refrigerator and measure one full cavity transmission spectrum as well as a narrow-band zoom-in transmission to the frequency range where the transparency occurs  $\Omega \approx \Omega_m$ . If we do not switch off the pulse tube cooler, we observe strong frequency fluctuations of the SQUID cavity and often cavity switching out of the metastable into the stable flux branch, which both can be significantly suppressed when the pulse tube cooler is switched off.

This relatively complicated iterative procedure is needed for several reasons. First, due to the non-negligible loop inductance and the possibly non-sinusoidal current-phase relation, we operate the cavity for most measurements in a metastable and hysteretic biasing regime. Second, the cavity resonance frequency depends slightly on the intracavity photon number despite the small anharmonicity. Many parameters such as the flux sweetspot biasing value or the sweetspot frequency depend furthermore slightly on the in-plane field value, what we attribute mainly to an imperfect alignment between sample and magnetic in-plane field, leading to a non-negligible out-of-plane component. Taking all these factors together, a simple fixed biasing procedure to achieve similar parameters for each measurement would not be sufficient.

### 2. FITTING ROUTINE

**I.** For the extraction of the single-photon coupling rate  $g_0$  we initially perform a wide range scan as described in section 4.5.3 and get the background fit function  $S_{\text{back}} = P(\omega)e^{i\phi(\omega)}$ . For all other measurements, we then calculate the complex background signal for the corresponding frequency range and divide it off the data.

**II.** To fit the resonance curve for each measurement, the pump tone signal, which lies within the cavity line due to  $\kappa \sim \Omega_m$ , is cut away and the result is fitted as described in section 4.5.3 in order to obtain resonance frequency  $\omega_0$  and linewidth  $\kappa$ . One example is shown in Supplementary Fig. 4.14a and b.



4

**Figure 4.14: Fitting the optomechanical response and extracting the multi-photon coupling rate  $g = \sqrt{n_c} g_0$ .** **a** Fit of the cavity response amplitude in presence of a red-sideband drive tone. The frequency window of the drive tone is removed for a reliable fitting procedure. **b** Data and fit as in a, shown in the complex plane. **c** The large circle corresponds to the cavity response, the small circle to the signal of the optomechanically induced transparency, which is measured separately due to the narrow mechanical linewidth. The diameter of the cavity circle is  $d_c$ . The dashed box shows the zoom window plotted in d, where the diameter of the OMIT circle is denoted as  $d_m$ . In addition to a simple circle fit as represented by the line in d, we perform a fit of the complex resonance function to extract the effective mechanical linewidth. The result for the amplitude is shown in e and in the complex plane in f. Note that the data in e and f have been shifted and rescaled in the complex plane with respect to c and d. The scaling has been performed to anchor the cavity circle at  $S_{21} = 1$  with  $d_c = 1$ . With this scaling the amplitude of the OMIT response is given by  $\frac{4g^2}{\kappa \Gamma_{\text{eff}}} \frac{\kappa^2}{\kappa^2 + 4g_m^2}$  as indicated in f. The experimental parameters for this dataset was  $B_{||} = 6 \text{ mT}$ ,  $\partial \omega_0 / \partial \Phi \sim 2\pi \cdot 17 \text{ MHz}/\Phi_0$  and  $n_c \sim 800$  intracavity photons.

**III.** For the analysis of the transparency window, once again the backgrounds are divided off in a similar way as previously done for the cavity. During the cavity fit, the parameters  $K$  and  $\theta$  are determined and the cavity resonance was corrected for them, anchoring the resonance circle at  $S_{21} = 1$ . In addition, we apply all corrections to the mechanical response as well. An example for the real and imaginary part of both modi-

fied cavity and OMIT response functions are shown in Supplementary Fig. 4.14c and d. Performing a circle fit as shown in Supplementary Fig. 4.14d, we get the circle diameter  $d_m$ .

**IV.** From a response fit to the mechanical resonance, we finally extract the last missing parameters  $\Gamma_{\text{eff}}$  and  $\Omega_m$ . At this stage, we can also determine the detuning between the cavity resonance frequency and the OMIT resonance  $\delta_m$ , which can be seen in Supplementary Fig. 4.14 as slight rotation of the OMIT response along the cavity circle and a Fano-like resonance in Supplementary Fig. 4.14e. For the resonance shown in Fig. 4.3, we manually corrected for this rotation.

**V.** Now we calculate the effective cooperativity and the multi-photon coupling rate  $g$ . The single-photon coupling rate  $g_0$  is determined in the last step from  $g$  using the independently calculated intracavity photon number  $n_c$ .

# 5

## FOUR-WAVE-COOLING TO THE SINGLE PHONON LEVEL IN KERR OPTOMECHANICS

The field of cavity optomechanics has achieved groundbreaking photonic control and detection of mechanical oscillators, based on their coupling to linear electromagnetic modes. Lately, however, there is an uprising interest in exploring cavity nonlinearities as a powerful new resource in radiation-pressure interacting systems. Here, we present a flux-mediated optomechanical device combining a nonlinear Josephson-based superconducting quantum interference cavity with a mechanical nanobeam. We demonstrate how the intrinsic Kerr nonlinearity of the microwave circuit can be used for a counter-intuitive blue-detuned sideband-cooling scheme based on multi-tone cavity driving and intracavity four-wave-mixing. Based on the large single-photon coupling rate of the system of up to  $g_0 = 2\pi \cdot 3.6 \text{ kHz}$  and a high mechanical quality factor  $Q_m \approx 4 \cdot 10^5$ , we achieve an effective four-wave cooperativity of  $C_{fw} > 100$  and demonstrate four-wave cooling of the mechanical oscillator close to its quantum groundstate, achieving a final occupancy of  $n_m \sim 1.6$ . Our results significantly advance the recently developed platform of flux-mediated optomechanics and demonstrate how cavity Kerr nonlinearities can be utilized for novel control schemes in cavity optomechanics.

---

This chapter is available as an arXiv preprint (2104.02511) *Four-wave-cooling to the single phonon level in Kerr optomechanics*. D. Bothner\*, I. C. Rodrigues\* & G. A. Steele.

\*these authors contributed equally

## 5.1. INTRODUCTION

Cavity optomechanical systems are the leading platform for the detection and manipulation of mechanical oscillators with electromagnetic fields from the nano- to the macro-scale [56]. Displacement detection with an imprecision below the standard quantum limit [41, 43], sideband-cooling to the motional quantum groundstate [25, 32], the preparation of nonclassical states of motion [36, 38, 189, 190], quantum entanglement of distinct mechanical oscillators [39, 40], topological energy transfer using exceptional points [159] and microwave-to-optical frequency transducers [52, 54] are just some of the highlights that have been reported during the last decade. Essentially all of these impressive results have been achieved with linear cavities and linear mechanical oscillators, but the exploration of intrinsic cavity nonlinearities, often considered undesired and parasitic in optomechanics as they impose limitations on the maximally achievable multi-photon coupling rate [60], has attracted increasing interest lately [145, 191–196].

An exciting new scheme to couple a mechanical oscillator to microwave photons in a superconducting LC circuit has very recently been realized: Flux-mediated optomechanical coupling [71–73, 162]. In this approach, the displacement of a mechanical oscillator is transduced to magnetic flux threading a superconducting quantum interference device (SQUID) embedded in a microwave LC circuit as flux-dependent inductance [70, 143, 145]. Due to the scaling of the optomechanical single-photon coupling rate  $g_0$  with the external magnetic transduction field in flux-mediated optomechanics [70, 162], record single-photon coupling rates for the microwave domain have been reported [71–73]. In future devices, the optomechanical single-photon regime [63, 67] or even the ultrastrong coupling to superconducting qubits [66] seem feasible. In addition to being a flux-tunable inductor, a SQUID simultaneously constitutes a flexible and highly controllable Kerr nonlinearity, which is widely utilized in superconducting qubits [197], Josephson parametric amplifiers [198] and four-wave-mixing based bosonic code quantum information processing [199]. Therefore, flux-mediated optomechanics is also an ideal platform for realizing and studying Kerr optomechanics and for the development of new detection and control schemes of mechanical motion. Here, we implement a flux-mediated optomechanical device with a large single-photon coupling rate of up to  $g_0 \approx 2\pi \cdot 3.6\text{ kHz}$  and demonstrate sideband cooling of the mechanical oscillator close to its quantum groundstate by intracavity four-wave mixing (FWM). By using a strong parametric cavity drive, we activate the emergence of two Kerr quasi-modes in the SQUID circuit and realize an optomechanical coupling of these quasi-modes to the mechanical oscillator by an additional optomechanical sideband pump field. The drive-activated Kerr-modes show enhanced properties such as a reduced effective linewidth compared to the undriven circuit and we achieve effective single-photon cooperativities  $\mathcal{C}_0 \gtrsim 10$ . Strikingly, we find that blue-detuned optomechanical sideband-pumping on one of the Kerr-modes leads to dynamical backaction with the characteristics of red-sideband pumping in a standard optomechanical system, in particular to positive optical damping. We use this FWM based blue-detuned optical damping to cool the mechanical oscillator extremely close to its quantum groundstate with a residual occupation of  $n_m \sim 1.6$ . Our results demonstrate how cavity Kerr nonlinearities can be used in optomechanics to achieve both, enhanced device performance and new control schemes for mechanical oscillators. At the same time they reveal the potential of flux-mediated optomechan-

ics regarding low-power groundstate-cooling of mechanical oscillators and the future preparation of quantum states of motion.

## 5.2. THE DEVICE

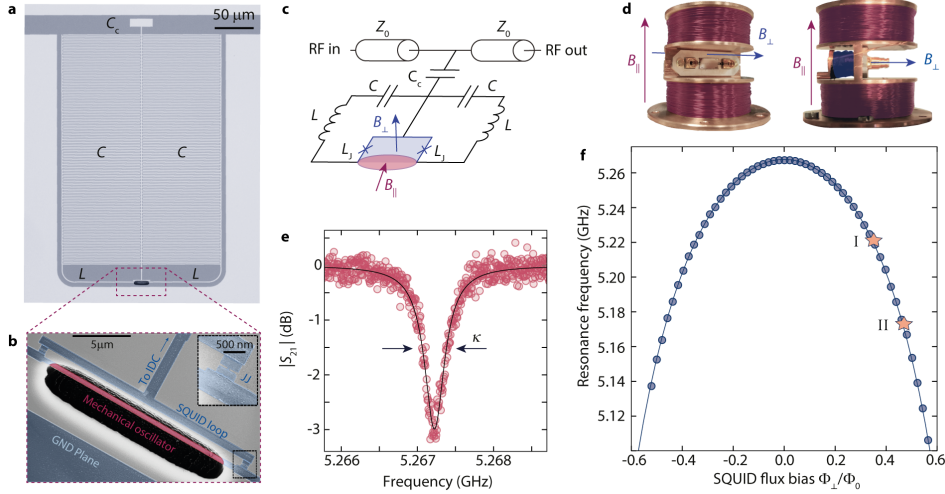


**Figure 5.1: A superconducting quantum interference cavity parametrically coupled to a mechanical nanobeam.** **a** Optical micrograph of the circuit. Bright parts are Aluminum, dark parts are Silicon substrate. The LC circuit combines two interdigitated capacitors  $C$  with two linear inductors  $L$ , connected through a superconducting quantum interference device (SQUID) with total Josephson inductance  $L_S = L_J/2$ . The circuit is capacitively coupled to a  $Z_0 = 50\Omega$  coplanar waveguide feedline (top of image) with a coupling capacitor  $C_c$  and surrounded by ground-plane. Scale bar corresponds to  $50\mu\text{m}$ . **b** Scanning electron micrograph of the constriction-type SQUID, showing the two Josephson junctions and the mechanical oscillator as part of the loop released from the substrate. Inset shows a zoom-in to one of the nano-bridge Josephson junctions. **c** Circuit equivalent of the device. For the experiments, two magnetic fields can be applied. The field  $B_\perp$  is oriented perpendicular to the chip plane and is used to set the flux bias working point of the SQUID  $\Phi_\perp$ . The parallel field  $B_\parallel$  transduces mechanical displacement of the out-of-plane mode to additional flux  $\Delta\Phi_\parallel = B_\parallel/l\Delta x$  threading the SQUID loop. **d** shows the sample integrated into a printed circuit board with two microwave connectors and mounted into a 2D vector magnet. The large split coil is used to generate  $B_\parallel$ , a small single coil behind the chip generates  $B_\perp$ . **e** Transmission response  $|S_{21}|$  of the cavity at  $B_\parallel = 25\text{ mT}$  and  $B_\perp = 0$ . From a fit to the data, we extract the resonance frequency  $\omega_0 = 2\pi \cdot 5.267\text{ GHz}$ , the total linewidth  $\kappa = 2\pi \cdot 380\text{ kHz}$ , and the external linewidth  $\kappa_e = 2\pi \cdot 110\text{ kHz}$ . Data are shown as circles, fit as black line. **f** Resonance frequency  $\omega_0$  vs magnetic flux  $\Phi_\perp$ , normalized to one flux quantum  $\Phi_0$  at  $B_\parallel = 25\text{ mT}$ . Circles are data, line is a fit. The two operation points for this paper are marked with stars and denoted "I" for  $\omega_0 \approx 2\pi \cdot 5.22\text{ GHz}$  and "II" for  $\omega_0 \approx 2\pi \cdot 5.17\text{ GHz}$ . Details on measurements and fits can be found in section 5.7.4.

Our device combines a superconducting quantum interference LC circuit with a mechanical nanobeam oscillator embedded into the loop of the SQUID, cf. Fig. 5.1. Details on device fabrication are given in section 5.7.1. At the core of the circuit, the SQUID acts as a magnetic-flux-dependent inductance  $L_S(\Phi)$ , where  $\Phi$  is the total magnetic flux threading the  $21 \times 3\mu\text{m}^2$  large loop. For the tunable optomechanical coupling between the displacement of the mechanical nanobeam and the microwave circuit, two distinct

external magnetic fields are required. First, a magnetic field perpendicular to the chip surface  $B_{\perp}$  is used to change the magnetic flux bias  $\Phi_{\perp}$  through the SQUID loop, allowing to tune the circuit resonance frequency  $\omega_0$  and flux responsivity  $\mathcal{F} = \partial\omega_0/\partial\Phi$ . Secondly, a magnetic in-plane field  $B_{\parallel}$  is used to transduce the out-of-plane displacement  $\Delta x$  of the mechanical oscillator to additional flux  $\Delta\Phi_{\parallel} = B_{\parallel}l_m\Delta x$ , where  $l_m = 18\text{ }\mu\text{m}$  is the length of the mechanical beam. To apply these two fields, the chip is mounted into a home-made 2D vector magnet, consisting of a large split coil for  $B_{\parallel}$  and an additional small coil mounted below the chip for the generation of  $B_{\perp}$ , cf. Fig. 5.1d. The whole configuration is placed in a cryoperm magnetic shielding and attached to the mK plate of a dilution refrigerator with a base temperature  $T_b \approx 15\text{ mK}$ . More details on the measurement setup are given in section 5.7.2.

We perform the experiments presented here at in-plane fields of  $B_{\parallel} = 21\text{ mT}$  and  $B_{\parallel} = 25\text{ mT}$ . Figure 5.1e shows the transmission response of the cavity for  $B_{\parallel} = 25\text{ mT}$  and at the bias-flux sweetspot. It has a resonance frequency  $\omega_0 = 2\pi \cdot 5.2673\text{ GHz}$ , a total linewidth  $\kappa = 2\pi \cdot 380\text{ kHz}$  and an external linewidth  $\kappa_e = 2\pi \cdot 110\text{ kHz}$ . Figure 5.1f shows how the cavity resonance frequency can be tuned by  $\sim 150\text{ MHz}$  by changing the applied flux bias  $\Phi_{\perp}$  threading the SQUID loop. The curves and cavity parameters at  $B_{\parallel} = 21\text{ mT}$  only deviate slightly from the ones given here, the corresponding additional data can be found in section 5.7.4. Due to an improved SQUID design and fabrication, the cavity flux responsivity  $\mathcal{F}$  is increased by one order of magnitude compared to our previous results [162], which leads to a significantly enhanced single-photon coupling rate

$$g_0 = \mathcal{F}B_{\parallel}l_m x_{\text{zpf}} \quad (5.1)$$

where  $x_{\text{zpf}}$  is the mechanical zero-point fluctuation amplitude.

The mechanical nanobeam, visible in Fig. 5.1b and released from the substrate in an isotropic reactive ion etching process using SF<sub>6</sub> plasma [126], is 500 nm wide and 70 nm thick. From its total mass of  $m \approx 1.9\text{ pg}$  and the resonance frequency of the out-of-plane mode  $\Omega_m \approx 2\pi \cdot 5.32\text{ MHz}$ , we get  $x_{\text{zpf}} = \sqrt{\frac{\hbar}{2m\Omega_m}} \approx 30\text{ fm}$ . For an in-plane field of  $B_{\parallel} = 25\text{ mT}$ , and the two flux-bias points I and II, cf. Fig. 5.1f, we obtain single-photon coupling rates  $g_{0,\text{I}} = 2\pi \cdot 2.2\text{ kHz}$  and  $g_{0,\text{II}} = 2\pi \cdot 3.6\text{ kHz}$  with  $\mathcal{F}_{\text{I}} = 2\pi \cdot 300\text{ MHz}/\Phi_0$  and  $\mathcal{F}_{\text{II}} = 2\pi \cdot 520\text{ MHz}/\Phi_0$ . For the smaller in-plane field of  $B_{\parallel} = 21\text{ mT}$ , the  $g_0$ -values are scaled accordingly, cf. section 5.7.5.

The final important parameter of the device is its Kerr nonlinearity, which at the flux sweetspot is  $\mathcal{K}/2\pi = -30\text{ kHz}$ . For the two flux bias operation points I and II we obtain  $\mathcal{K}_{\text{I}}/2\pi = -40\text{ kHz}$  and  $\mathcal{K}_{\text{II}}/2\pi = -55\text{ kHz}$ , respectively. More details on the determination of the circuit parameters and their flux dependence can be found in section 5.7.4.

### 5.3. DRIVEN KERR-MODES AND DYNAMICAL KERR BACKACTION

Owing to the Kerr anharmonicity  $\mathcal{K}$ , the application of a strong microwave drive tone close to the cavity resonance frequency  $\omega_0$  significantly modifies the cavity response to an additional probe field. In Fig. 5.2, we discuss this modified response in the presence of a parametric drive tone with a fixed frequency  $\omega_d$ , when the cavity is tuned to cross this drive tone by means of the bias field  $B_{\perp}$ . For large detunings between cavity and drive, the circuit response  $S_{21}$  exhibits a standard single-mode resonance lineshape. However,

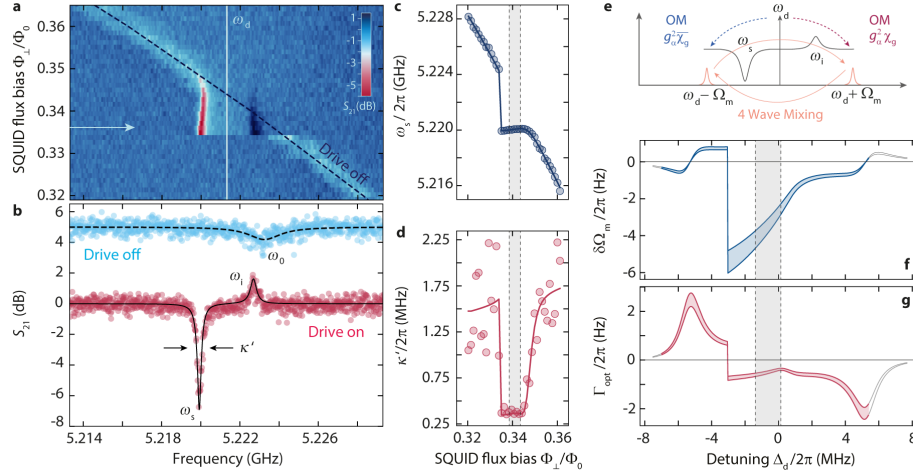


**Figure 5.2: Activating the driven Kerr quasi-mode state and single-tone dynamical Kerr backaction.** **a** displays color-coded the magnitude of the SQUID cavity response  $S_{21}$  for varying SQUID flux bias  $\Phi_{\perp}/\Phi_0$  in the presence of a strong drive placed at  $\omega_d$ . The flux bias range corresponds to a small variation of  $\Phi_{\perp}$  around operation point I and the in-plane field is  $B_{\parallel} = 21\text{ mT}$ . When the flux-tunable resonance frequency  $\omega_0$ , indicated as dashed line and labelled "Drive off", is far detuned from the drive tone, the cavity response exhibits a single broad absorption resonance. As the detuning between cavity and drive  $\Delta_d = \omega_d - \omega_0$  is reduced, the cavity response is significantly modified and the original resonance is developing into a double-mode structure. The appearance of these driven Kerr quasi-modes indicates the onset of parametric amplification and degenerate FWM in the SQUID circuit. We denote the two modes as signal and idler resonance with the resonance frequencies  $\omega_s$  and  $\omega_i$ , respectively. Arrow on the left indicates the position of the linescan shown in panel **b**. In addition to the linescan from **a** (red circles) and the result of the analytical response calculation (solid black line), we show the equivalent linescan without parametric drive (blue circles) and its corresponding theoretical response (dashed black line). The curves without parametric drive are offset by +5dB for clarity. Panels **c** and **d** show the extracted resonance frequency  $\omega_s$  and effective linewidth  $\kappa'$  of the signal resonance vs flux bias. Lines show the result of modelling the effective quantities with the driven Kerr cavity equations and taking into account flux-noise broadening and two-level systems. The regime of operation for the experiments reported below is indicated by dashed lines and shaded areas. In this regime, the linewidth is nearly constant with  $\kappa'/2\pi \approx 340\text{ kHz}$ . The width of the operation range corresponds to the flux noise standard deviation, which we estimate to be  $\sigma_{\Phi} \sim 5\text{ m}\Phi_0$ . Panel **e** illustrates the contributions to the dynamical Kerr backaction of the intracavity drive fields to the nanobeam. Optomechanical (OM) up- and downscattering induces cooling and heating/amplification to the mechanical mode, respectively, where  $g_a$  is the multiphoton coupling rate and  $\chi_g$  is the probe susceptibility of the driven Kerr oscillator. In addition, interference between up- and downscattered fields due to degenerate FWM has to be taken into account. **f** and **g** show the calculated optical spring and optical damping due to dynamical Kerr backaction. The two blue/red lines and shaded area correspond to  $g_0/2\pi = (1.78 \pm 0.1)\text{ kHz}$ . The detuning range  $\Delta_d$  is slightly increased compared to **a-d**. In the additional range, the backaction is plotted in gray. The device operation range is indicated by the shaded area in between the vertical dashed lines.

as the detuning  $\Delta_d = \omega_d - \omega_0$  is reduced, the driven cavity susceptibility

$$\chi_g(\Omega) = \frac{\tilde{\chi}_p(\Omega)}{1 - \mathcal{K}^2 n_d^2 \tilde{\chi}_p(\Omega) \tilde{\chi}_p^*(-\Omega)} \quad (5.2)$$

deviates considerably from a single linear cavity, leading to the regime of parametric amplification and degenerate four-wave mixing, which is experimentally identified by the appearance of a second mode. Here,  $\Omega = \omega - \omega_d$  denotes the detuning between the probe field at  $\omega$  and the parametric drive and

$$\tilde{\chi}_p(\Omega) = \frac{1}{\frac{\kappa}{2} + i(\Delta_d - 2\mathcal{K}n_d + \Omega)}. \quad (5.3)$$

The two Kerr quasi-modes, which we denote as signal and idler resonance, appear symmetrically around the drive with complex resonance frequencies

$$\omega_{i/s} = \omega_d + i\frac{\kappa}{2} \pm \sqrt{(\Delta_d - \mathcal{K}n_d)(\Delta_d - 3\mathcal{K}n_d)} \quad (5.4)$$

where  $n_d$  is the parametric drive intracavity photon number. These Kerr-modes have been observed and discussed also in the context of optical cavities and mechanical oscillators [200–202]. The signal mode can be identified by the shifted and significantly deepened cavity absorption dip and the idler mode by the resonance peak, indicating net transmission gain by Josephson parametric amplification.

5

With the activation of the quasi-mode state, we also obtain a highly stabilized effective resonance frequency and linewidth, while the bare cavity suffers from considerable frequency fluctuations due to flux noise. Due to the reduction of frequency fluctuations in combination with a saturation of two-level system losses by the parametric drive (cf. section 5.7.6), the effective cavity linewidth is reduced from the flux-noise broadened  $\kappa'_{\text{off}} \sim 2\pi \cdot 1.5 \text{ MHz}$  to the driven  $\kappa'_{\text{on}} \approx 2\pi \cdot 340 \text{ kHz}$ . An analysis of the signal mode resonance frequency and linewidth in the presence of the parametric drive is provided in Figs. 5.2c and d. Within a small region of flux bias values, the drive-tone induced Kerr shift compensates for the flux-noise induced frequency shifts by means of an internal feedback loop. Strikingly, this mechanism yields a stabilization of the driven resonance, which thereby becomes the natural choice of operation regime during the following experiments.

In an optomechanical system, any intracavity field also acts back on the mechanical oscillator by altering its resonance frequency and decay rate, an effect known as dynamical backaction [11, 41]. Therefore, the effect of the parametric drive to the mechanical oscillator also requires some careful consideration. From the linearized equations of motion for the mechanical amplitude field  $\hat{b}$  and the intracavity fluctuation field  $\hat{a}$  in a single-tone driven Kerr cavity

$$\dot{\hat{b}} = \left( i\Omega_m - \frac{\Gamma_m}{2} \right) \hat{b} - ig_\alpha (\hat{a} + \hat{a}^\dagger) + \sqrt{\Gamma_m} \hat{\zeta} \quad (5.5)$$

$$\dot{\hat{a}} = \left[ -i(\Delta_d - 2\mathcal{K}n_d) - \frac{\kappa}{2} \right] \hat{a} + i\mathcal{K}n_d \hat{a}^\dagger - ig_\alpha (\hat{b} + \hat{b}^\dagger) + \sqrt{\kappa_i} \hat{\xi}_i + \sqrt{\kappa_e} \hat{\xi}_e \quad (5.6)$$

with multi-photon coupling rate  $g_\alpha = \sqrt{n_d} g_0$  and input fields  $\hat{\zeta}$ ,  $\hat{\xi}_i$  and  $\hat{\xi}_e$ , the effective mechanical susceptibility can be derived as

$$\chi_0^{\text{eff}}(\Omega) = \frac{1}{\frac{\Gamma_m}{2} + i(\Omega - \Omega_m) + \Sigma_k(\Omega_m)} \quad (5.7)$$

for the weak-coupling and high- $Q_m$  limit, which is safely fulfilled for our mechanical oscillator with a linewidth of  $\Gamma_m \approx 2\pi \cdot 13$  Hz. The single-tone dynamical Kerr backaction

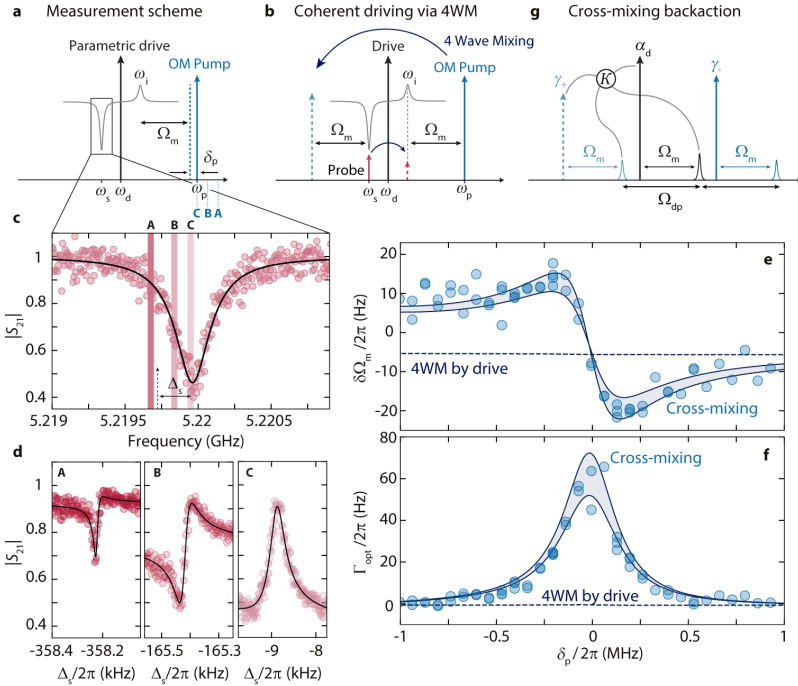
$$\Sigma_k(\Omega_m) = g_a^2 [\chi_g(1 - \bar{\mathcal{A}}) - \bar{\chi}_g(1 - \mathcal{A})] \quad (5.8)$$

with  $\chi_g = \chi_g(\Omega_m)$  and  $\bar{\chi}_g = \chi_g^*(-\Omega_m)$  has almost the same form as in linear optomechanics, but with a modified cavity susceptibility  $\chi_g$ . A striking difference, however, is found in the terms  $\mathcal{A} = -i\mathcal{K}n_d\tilde{\chi}_p(\Omega_m)$  and  $\bar{\mathcal{A}} = i\mathcal{K}n_d\tilde{\chi}_p^*(-\Omega_m)$ . These terms correspond to an interference of the red and blue mechanical sideband fields, which occurs due to intracavity four-wave mixing in a driven Kerr cavity. By this FWM, the two standard mechanical sidebands become idler fields of each other. A schematic of the dynamical backaction and the sideband interference is shown in Fig. 5.2e.

The optical spring  $\delta\Omega_m = -\text{Im}[\Sigma_k(\Omega_m)]$  and optical damping  $\Gamma_{\text{opt}} = 2\text{Re}[\Sigma_k(\Omega_m)]$  caused by the dynamical Kerr backaction are displayed in Figs 5.2f and g. When the drive is located around one mechanical frequency detuned from the cavity  $|\Delta_d| \approx \Omega_m = 2\pi \cdot 5.32$  MHz, the backaction looks very similar to that of a linear cavity. However, when the drive and the cavity are near-resonant, the backaction is strongly dominated by the intracavity photon number and a Duffing-like behaviour can be observed with a sudden transition from high- to low-amplitude state at  $\Delta_d \approx -2\pi \cdot 3$  MHz. In the operation regime for the experiments described here, the drive-induced backaction for operation point I is small with  $\Gamma_{\text{opt}}/2\pi \sim -1$  Hz and  $\delta\Omega_m/2\pi \sim -5$  Hz. Using the bare mechanical linewidth  $\Gamma_m \sim 2\pi \cdot 13$  Hz, the corresponding phonon occupation is therefore increased by about 10%, a detailed calculation and discussion of the resulting mechanical mode occupation is given in section 5.7.7.

Due to the considerable cavity flux noise outside of the driven quasi-mode regime, we unfortunately cannot experimentally access the dynamical Kerr backaction for the detuning range shown in Fig. 5.2. Nevertheless, with a larger single-photon coupling rate  $g_0$  at operation point II and a stronger drive tone, we observe regimes of mechanical instability induced by the dynamical Kerr backaction, which are in excellent agreement with the prediction from the theory. The corresponding data and analysis are explained in detail in section 5.7.7. The presented formalism for the dynamical Kerr backaction can also directly be applied to the sideband-unresolved regime and explain the experimental findings of a recent experiment with a similar SQUID cavity optomechanical device [71], cf. also section 5.7.7.

## 5.4. MULTI-TONE DYNAMICAL FOUR-WAVE BACKACTION



5

**Figure 5.3: Four-wave-OMIT and four-wave-backaction for optomechanical blue-sideband pumping of the idler quasi-mode.** a shows the experimental protocol. The SQUID cavity is prepared in the quasi-mode state by a strong parametric drive (PD). In addition, we apply an optomechanical (OM) pump tone on the blue sideband of the idler resonance (IR)  $\omega_p = \omega_i + \Omega_m + \delta_p$ . Finally, we use a weak probe tone around the signal resonance (SR) to detect optomechanically induced transparency. We repeat this scheme for varying detunings  $\delta_p$ . b explains how this protocol to first order leads to coherent driving of the mechanical oscillator. By PD-induced intracavity 4WM, the OM pump (probe tone) gets an idler field on the opposite side of the drive, which has the right detuning to the probe tone (pump)  $\sim \Omega_m$  to coherently drive the mechanical oscillator. c shows the signal resonance transmission  $S_{21}$  measured with the weak probe field (OM pump off). Circles are data, line is a fit. Vertical bars labelled with A, B, and C indicate zoom regions for the corresponding panels shown in c and  $\Delta_s = \omega - \omega_s$  denotes the detuning between probe field and SR. d probe tone response (OM pump on) in three narrow frequency windows around  $\omega \approx 2\omega_d - \omega_p + \Omega_m$  for three different pump detunings  $\delta_p$ , cf. panel a. Note that the frequency difference between OM pump and probe field is  $\Omega \approx \Omega_m - 2\Omega_{dp}$ , which implies that when the pump field frequency is reduced, the probe field frequency is increasing. Each probe tone response displays a narrow-band resonance, indicating optomechanically induced transparency (OMIT) via excitation of the mechanical oscillator. For each  $\delta_p$ , we fit the OMIT response (lines in c) and extract the effective mechanical resonance frequency  $\Omega_{\text{eff}} = \Omega_m + \delta\Omega_m$  and the effective mechanical linewidth  $\Gamma_{\text{eff}} = \Gamma_m + \Gamma_{\text{opt}}$ . The contributions  $\delta\Omega_m$  and  $\Gamma_{\text{opt}}$ , induced by dynamical backaction of all intracavity fields, are plotted in panels e and f as circles vs  $\delta_p$ . The result of analytical calculations is shown as two solid lines with shaded area, where the range described by the lines captures uncertainties in the device parameters, cf. section 5.7.11. The dashed line shows the result of equivalent calculations without cross-mixing (non-degenerate 4WM) terms. f illustrates schematically one four-wave cross-mixing term that leads to the observed dynamical backaction. Hereby, two mechanical sidebands with frequency difference  $\Omega_{dp} = \omega_d - \omega_p$  and both, the PD and the OM pump, contribute to the interaction.

An interesting question arising now is how the Kerr quasi-modes couple to the mechanical nanobeam, when an additional optomechanical pump tone is applied to one of the Kerr-mode sidebands. One might expect that the coupling to the mechanical oscillator is suppressed in this state, similar to the reduced impact of flux noise, as the Kerr-mode frequencies  $\omega_s$  and  $\omega_i$  display only a very weak dependence on flux through the SQUID. Fluctuations of the bare resonance frequency, however, lead to modulations of  $\alpha_d$  and parametric gain, and therefore will impact the mechanical oscillator by inducing changes in the radiation-pressure force. A straightforward way to investigate this setting experimentally is to apply an additional optomechanical pump tone on the red sideband of the signal resonance, i.e., with a pump frequency  $\omega_p \approx \omega_s - \Omega_m$ . Once in this configuration, a weak probe signal around  $\omega \approx \omega_p + \Omega_m$  can be used to detect optomechanically induced transparency (OMIT) [150] and thereby characterize the optomechanical interaction. A detailed theoretical description as well as a discussion of the experimental findings for this red-sideband pumping setup is given in sections 5.7.12 to 5.7.15.

A conceptually less straightforward and more exciting possibility is to pump the idler resonance on its blue sideband  $\omega_p \approx \omega_i + \Omega_m$ , cf. Fig. 5.3a. A blue-detuned pump is commonly associated with amplification/heating due to the favoured Stokes-scattering to lower energy photons. The Kerr-mode susceptibility  $\chi_g$  close to the idler resonance, however, resembles that of an "inverted" mode. Any small intracavity field in the driven Kerr cavity experiences in addition a mirroring effect due to degenerate four-wave mixing with the parametric drive tone. The presence of the blue-sideband pump field enriches this situation even further. Then the Kerr cavity is effectively oscillating with  $\Omega_{dp} = \omega_d - \omega_p$  due to the presence of two strong fields, and effects arising from non-degenerate four-wave mixing can impact probe fields and mechanical sideband fields and finally also the OMIT response and the backaction to the mechanical oscillator.

A clear signature of the parametric state and four-wave mixing is the appearance of optomechanically induced transparency in the probe response of the signal resonance, when the idler Kerr-mode is pumped on its blue sideband. Corresponding data are shown in Fig. 5.3b and c. Here and in stark contrast to the usual OMIT protocol, the frequency detuning between the idler blue-sideband pump and the probe tone is not even close to the mechanical resonance frequency but given by  $\Omega = \omega - \omega_p \approx 2\Omega_{dp} - \Omega_m$ . To first order, the observation of this transparency can be understood by considering the intracavity generated tones in addition to the ones that are sent externally. The parametric drive generates an intracavity field with amplitude  $\alpha_d$  at  $\omega_d$ , and the optomechanical pump at  $\omega_p$  generates an intracavity field with amplitude  $\gamma_-$ . Just by this doubly-driven configuration, a third intracavity "pump" field is generated by degenerate FWM at  $\omega_+ = \omega_p + 2\Omega_{dp}$  and we denote its amplitude as  $\gamma_+$ . Therefore, when  $\omega_p = \omega_i + \Omega_m$ , the  $\gamma_+$ -field is located at the red sideband of the signal resonance  $\omega_+ = \omega_s - \Omega_m$ . The beating between a probe field at  $\omega \approx \omega_s$  and the  $\gamma_+$ -field is then near-resonant with the mechanical oscillator and will drive it into coherent motion. A second beating component, which is driving the mechanical oscillator, originates from the beating of the  $\gamma_-$ -field and the idler field of the weak probe itself, cf. Fig. 5.3a. These two are also near-resonant with the mechanical oscillator. Once in coherent motion, the mechanical oscillator generates sidebands to all intracavity field Fourier components, some of which interfere with the original probe tone causing the observed appearance of four-wave OMIT.

To characterize the dynamical backaction imprinted by the intracavity fields on the mechanical oscillator in the presence of the  $\alpha_d$ ,  $\gamma_-$  and  $\gamma_+$  fields, we measure the optomechanical transparency response for varying detuning  $\delta_p$  between the  $\gamma_-$ -field and the idler-mode blue sideband, cf. Fig. 5.3. For each detuning, we determine the effective mechanical resonance frequency  $\Omega_{\text{eff}}$  and effective mechanical linewidth  $\Gamma_{\text{eff}}$  from a fit to the transparency signal and subtract the intrinsic values  $\Omega_m$  and  $\Gamma_m$ . The remaining contributions to the resonance frequency and linewidth  $\delta\Omega_m$  and  $\Gamma_{\text{opt}}$ , respectively, correspond to the optical spring and optical damping by the microwave fields.

The result, shown in Fig. 5.3d and e, is quite surprising. Even though the optomechanical pump field is blue-detuned to all cavity resonances  $\omega_0, \omega_s$  and  $\omega_i$ , we observe dynamical backaction with characteristics resembling red-sideband pumping in linear optomechanical systems. Most strikingly, we find a positive optical damping, which is usually a clear signature for red-sideband physics and the basis for sideband-cooling of the mechanical mode[25]. We use a linearized, optomechanical multi-tone Kerr cavity model, and implement the hierarchy from the experiment  $\alpha_d \gg \gamma_{\mp} \gg \langle \hat{a} \rangle$  to reveal which interactions are responsible for the observed behaviour, cf. sections 5.7.8 to 5.7.10. The resulting effective mechanical susceptibility

$$\chi_0^{\text{eff}}(\Omega) = \frac{1}{\frac{\Gamma_m}{2} + i(\Omega - \Omega_m) + \Sigma_{\text{fw}}(\Omega_m)} \quad (5.9)$$

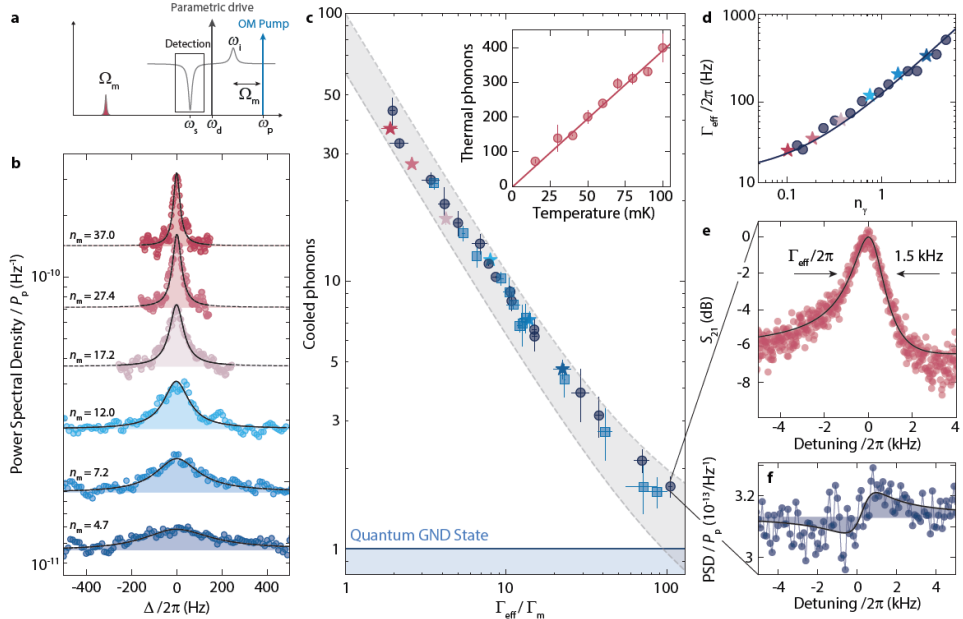
has still the same form as for a standard optomechanical system, and all the FWM contributions can be captured in  $\mathcal{J}$ -factors in the dynamical four-wave backaction

$$\Sigma_{\text{fw}}(\Omega_m) = \sum_{j=-,\alpha,+} |g_j|^2 \left[ \chi_{g,j} \mathcal{J}_j - \bar{\chi}_{g,j} \bar{\mathcal{J}}_j \right] \quad (5.10)$$

with  $g_- = \gamma_- g_0$ ,  $g_+ = \gamma_+ g_0$ ,  $\chi_{g,-} = \chi_g(\Omega_m)$ ,  $\chi_{g,\alpha} = \chi_g(\Omega_m + \Omega_{dp})$  and  $\chi_{g,+} = \chi_g(\Omega_m + 2\Omega_{dp})$ . Closed-form expressions for the  $\mathcal{J}$  are given in section 5.7.9. We identify non-degenerate four-wave mixing terms in the  $\mathcal{J}$ -factors as the dominant origin of the observed backaction. These terms have contributions from the drive field  $\alpha_d$ , from one of the  $\gamma_{\pm}$  fields and couple any two distinct mechanical sidebands which have the frequency difference  $\pm\Omega_{dp}$ , cf. Fig. 5.3f for a schematic of one of these terms. Hence, these terms correspond to intracavity cross-mixing based on  $\alpha_d$  and  $\gamma_{\pm}$  fields. Using independently determined system parameters, we find excellent agreement between the experimental data and the analytical model when we take these cross-mixing terms into account, cf. solid lines in Fig. 5.3d and e. If we take only the degenerate FWM terms into account, which are induced by the presence of  $\alpha_d$ , we find a small and nearly constant backaction for all  $\delta_p$ , cf. dashed lines.

## 5.5. BLUE-DETUNED FOUR-WAVE COOLING CLOSE TO THE QUANTUM GROUND-STATE

Positive optical damping is commonly related to cooling of the mechanical mode. Therefore, the blue-detuned pumping scheme described in Fig. 5.3 seems feasible to be utilized as a counter-intuitive, yet innovative, method to eliminate the residual thermal excitations in the mechanical resonator.



5

**Figure 5.4: Blue-detuned four-wave-cooling of a mechanical oscillator close to its quantum ground-state.** **a** Schematic representation of the experiment. A parametric drive is used to activate the quasi-mode state and an OM pump is sent to the blue sideband of the idler resonance  $\omega_p \approx \omega_i + \Omega_m$ . The signal resonance output power spectral density is measured using a spectrum analyzer around  $\omega = \omega_p + 2\Omega_{dp} + \Omega_m \approx \omega_s$ . **b** Power spectral densities normalized to the optomechanical pump input power  $P_p$  for various pump powers. Frequency axis is given with respect to  $\omega = \omega_p + 2\Omega_{dp} + \Omega_m$ . With increasing pump power, the linewidth of the upconverted mechanical noise spectrum is increasing, indicating four-wave dynamical backaction damping. Simultaneously, the area of the normalized signal decreases, indicating cooling of the mode. From fits (lines and shaded areas) to the data (points), we determine the resulting phonon occupation  $n_m$ . In **c** we show the cooled phonon number vs  $\Gamma_{\text{eff}}/\Gamma_m$  in a collection of several different datasets. Intracavity drive photon numbers vary between different points in the range  $40 < n_d < 100$ . Circles correspond to data from measurements at operation point I and squares to data from operation point II. Stars show the points that correspond to the data shown in **b**, taken at operation point I. All measurements have been taken at  $B_{\parallel} = 25$  mT. Inset shows the result of a thermal calibration measurement, indicating that the mechanical oscillator mode equilibrates with the fridge base temperature and the residual thermal occupation at  $T_b = 15$  mK is  $n_m^{\text{th}} \approx 70 - 90$ . Dashed lines and shaded area display the theoretically calculated range of four-wave-cooled phonon occupation, taking into account a possible range of  $60 \leq n_m^{\text{th}} \leq 100$  and  $45 \leq n_d \leq 90$ . Parametric amplification of cavity quantum noise limits the minimally achievable phonon occupation in our parameter regime to  $n_m^{\text{lim}} \sim 0.6$ . For the highest powers, we exceed this theoretical limit by only a factor  $\sim 3$ . **d** shows the effective effective mechanical linewidth vs intracavity sideband photon number  $n_\gamma = |\gamma_-|^2 + |\gamma_+|^2$  for points from **c**, which have nearly constant  $n_d \approx 60 \pm 10$ , demonstrating that we achieve significant cooling with a small number of photons. Line corresponds to theory with  $\Gamma_m = 2\pi \cdot 15$  Hz. **e** shows an OMIT scan at the point of largest cooling with an effective linewidth  $\Gamma_{\text{eff}} \approx 2\pi \cdot 1.5$  kHz, which corresponds to an effective four-wave cooperativity of  $\mathcal{C}_{\text{fw}} \gtrsim 100$ . **f** shows the corresponding power spectral density in units of quanta with noise squashing due to a small, but finite effective temperature of the cavity by amplified quantum noise. Error bars in **c** consider uncertainties in the fitting procedure and in the bare mechanical linewidth, for details see section 5.7.14.

To characterize the mechanical mode temperature, we detect the upconverted thermal displacement fluctuations in the signal resonance output field with a spectrum analyzer. For this measurement, the SQUID cavity in the quasi-mode state is pumped with an optomechanical tone on the blue sideband of the idler mode. Using a probe tone, we then measure the signal mode response  $S_{21}$  in a wide frequency range and the OMIT response in a narrow range. Finally, we detect the output spectrum in the same frequency window where the OMIT is observed. A collection of spectra for varying optomechanical pump power  $P_p$  is presented in Fig. 5.4b. From a careful analysis of the combined data sets, cf. sections 5.7.8 to 5.7.13, the equilibrium phonon occupation of the mechanical oscillator as well as the phonon occupation resulting from four-wave-cooling can be inferred.

The mechanical oscillator is well thermalized to the mixing chamber base temperature and its residual phonon occupation at the lowest operation temperature  $T_b = 15\text{ mK}$  is about  $n_m^{\text{th}} \approx 70 - 90$  phonons. With increasing optical damping caused by the blue-detuned pump tone, we observe a corresponding reduction of the initial thermal occupation and the cooling factor is determined by  $\Gamma_{\text{opt}}$ , very similar to usual optomechanical sideband-cooling. The observed four-wave cooling is also very robust with respect to pump and drive strengths and we achieve at both flux bias operation points a final four-wave-cooled occupation extremely close to the quantum groundstate  $n_m \sim 1.6$ . Due to the high single-photon coupling rates, it requires only a small amount of effective sideband photons  $n_\gamma = |\gamma_-|^2 + |\gamma_+|^2 \lesssim 10$  to achieve these low occupations.

## 5

The fact that we use strongly driven Kerr quasi-modes as cold bath, however, modifies the minimally achievable occupation. Due to Josephson parametric amplification of quantum noise in the quasi-mode state, the cavity will acquire an effective temperature, even if the bare cavity is in the quantum groundstate. This drive-induced cavity heating defines the cooling limit for the mechanical resonator. In the state we are operating here, the Josephson gain is small and the effective thermal occupation of the cavity is still considerably below 1. We estimate the current cooling limit due to amplified quantum noise to be  $\sim 0.6$ , where the exact value depends on the drive strength  $n_d$  and on the bias-flux operation point. With higher bias flux stability the cavity could be stabilized at a point where the Josephson gain is small enough to enable  $n_m^{\text{lim}} < 0.3$ .

Achieving the lowest occupation in the current device requires a careful balancing of drive and pump strength and for the highest pump powers, we observe the onset of additional cavity shifts and line broadening, possibly related to drive depletion or higher-order nonlinear effects. With slightly optimized device parameters regarding  $\mathcal{K}$  and  $g_0$ , we should therefore be able to cool to  $n_m < 1$ . We emphasize though, that the blue-detuned cooling scheme allowed to achieve a significantly lower phonon occupation than signal-mode red-sideband pumping. With a pump on the red signal-mode sideband, a second cavity bifurcation instability occurs at moderately high pump powers, as the red sideband pump is attracting the cavity, while the blue-detuned pump is repelling it. The related jump to a high-amplitude state with a different signal resonance frequency, prevents us from cooling below  $n_m^{\text{red}} \sim 4$ . The corresponding red-sideband cooling data and analysis can be found in section 5.7.16.

## 5.6. DISCUSSION

The results we presented here demonstrate clearly that the young field of flux-mediated optomechanics is quickly advancing towards an exciting and competitive optomechanical platform, which intrinsically allows for novel ways of manipulating mechanical motion. Our device provides a large single-photon coupling rate of up to  $g_0 = 2\pi \cdot 3.6\text{kHz}$  and achieves large cooperativities of up to  $\mathcal{C}_{\text{fw}} > 100$  for small numbers of intracavity photons. By using strong parametric driving, we show how the intrinsic Josephson-based Kerr nonlinearity can be utilized as a resource for improved sideband-resolution and frequency-stability and for the implementation of a novel four-wave-mixing-based phonon control scheme. In combination, these properties enabled us to use four-wave-cooling in a Kerr cavity to prepare a MHz mechanical nanobeam resonator close to its quantum groundstate.

Future device improvements can be achieved by reducing the SQUID loop inductance further in order to increase the flux responsivity and the single-photon coupling rate. One order of magnitude is a feasible goal in this direction, as related platforms have already demonstrated such high responsivities [71, 72]. This improvement alone would bring the device to a cooperativity of  $10^4$  and to the onset of the strong-coupling regime with  $g \sim 2\pi \cdot 150\text{kHz} \sim \kappa/2$ . With increased in-plane fields, up to  $\sim 1\text{T}$  with e.g. Niobium or granular Aluminum, those numbers could be improved by another order of magnitude.

In the current device, however, the main limiting factor to achieve higher coupling rates and cooling the mechanical oscillator into the groundstate was external flux noise coupling into the SQUID in large in-plane fields. We suspect that the origin of this flux noise is in the vector magnet leads and the used current sources, respectively, or in parasitic out-of-plane components that lead to flux instabilities, vortex avalanches and microwave-triggered vortex motion in proximity to the SQUID. Flux noise in the leads and current sources could potentially be reduced by using a superconducting magnet in persistent current mode. And although our current setup can locally cancel parasitic out-of-plane fields, it cannot do so over the complete chip simultaneously due to the geometry of the small coil. A global compensation might be necessary, however, to completely avoid any flux instabilities arising from the out-of-plane fields, which can cause flux fluctuations also in large distances from their occurrence.

Using intrinsic Kerr nonlinearities as a resource in optomechanical systems has just begun. Further interesting directions in Kerr optomechanics might involve intracavity squeezing, intracavity Josephson parametric amplification, intracavity cat-state generation, groundstate cooling in the sideband unresolved regime or enhanced quantum transduction. Significantly larger Kerr nonlinearites than the ones presented here, implemented in superconducting transmon qubits, have also been discussed recently for mechanical quantum state preparation [66, 203, 204]. Similar schemes investigating and exploiting the Kerr nonlinearity of SQUID circuits could furthermore be implemented naturally in the platform of photon-pressure coupled circuits [81, 85, 127].

## 5.7. SUPPLEMENTARY INFORMATION

### 5.7.1. DEVICE FABRICATION

Here we present a step-by-step description of the device fabrication. The individual steps are schematically shown in Supplementary Fig. 7.5, where we omitted step 0, the patterning of the electron beam lithography (EBL) alignment markers, as well as the wafer dicing steps and the final device mounting.

5

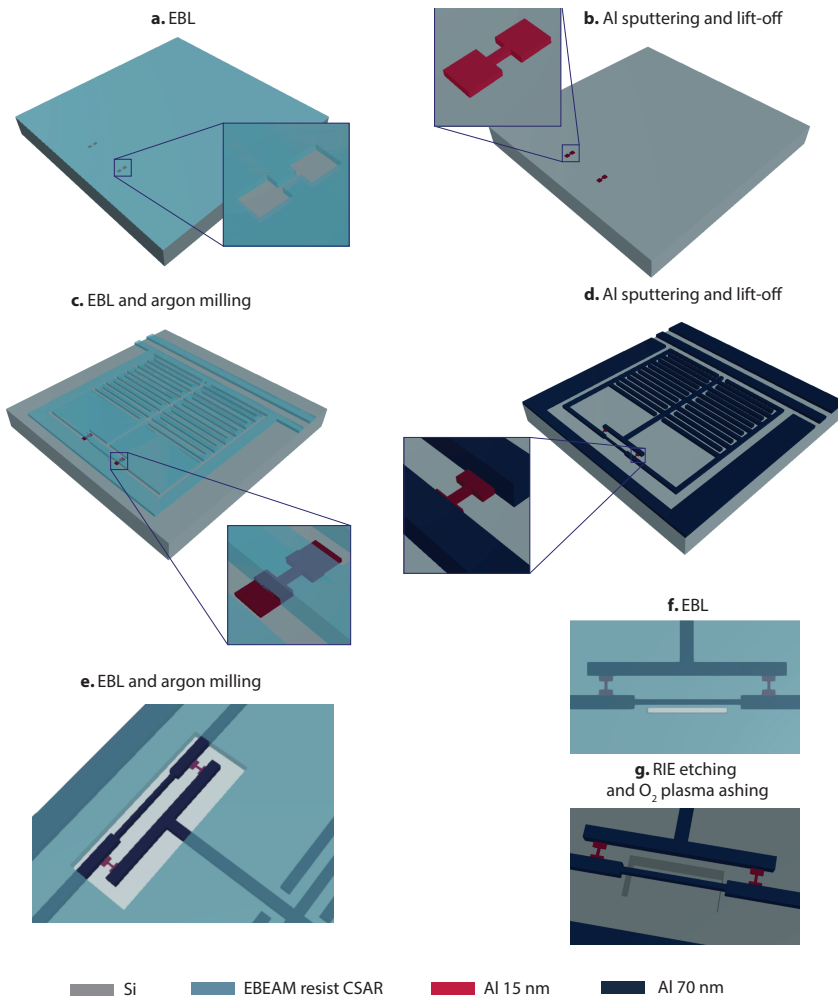


Figure 5.5: **Schematic device fabrication.** **a, b** show the deposition and patterning of the nanobridge junctions and contact pads (Step 1). **c, d** show the patterning and deposition of the remaining superconducting structures (Step 2). **e** shows the nanobridge thinning by Argon ion milling on the SQUID (Step 3). **f, g** show the window patterning and nanobeam release (Step 5). Dimensions are not to scale. A detailed description of the individual steps is given in the text.

**Step 0: Marker patterning.** The fabrication of the device starts by the patterning of alignment markers on top of a 2 inch silicon wafer using electron beam lithography (EBL). The marker structures are patterned using a CSAR62.13 resist mask and a sputter deposition of 50 nm Molybdenum-Rhenium alloy. After undergoing a lift-off process, the only remaining structures on the wafer are the markers. The complete 2 inch wafer is then diced into individual  $14 \times 14 \text{ mm}^2$  chips, which are used individually for the subsequent fabrication steps. On each of these fabrication chips, we structure 2 device chips with dimensions of  $5 \times 10 \text{ mm}^2$ , each of which contain one coplanar waveguide microwave feedline and seven quantum interference LC circuits.

**Step 1: Junctions patterning.** As first real step of the device fabrication we pattern two nanobridges (the later Josephson junctions) for each LC circuit using CSAR62.09, cf. Supplementary Fig. 5.5a. The two bridges of each pair of nanobridges forming one superconducting quantum interference device (SQUID) are hereby always identical. All bridges have a length of  $\sim 100 \text{ nm}$  but vary in width between 30 and 60 nm for different SQUIDs in order to compensate for small variations and uncertainties in final structure size and select the most suitable device during the experiment. The nanobridges also have two  $700 \times 1150 \text{ nm}^2$  large pads for achieving good galvanic contact to the rest of the circuit, which is patterned in fabrication step 2. After the EBL exposure, the sample is developed in Pentyacetate for 60 seconds followed by a 1:1 solution of MIBK:IPA (Methyl IsoButyl Ketone:IsoPropyl Alcohol) for another 60 seconds and finally rinsed in IPA. Once the resist is developed, the chip is loaded into a sputtering machine where a 15 nm thick layer of Aluminum (1% Silicon) is deposited. After the deposition, the sample is placed horizontally at the bottom of a glass beaker containing a small amount of room-temperature Anisole and left in an ultrasonic bath for a few minutes. During this time, the remaining resist is dissolved and the Aluminum layer sitting on top is lifted off, the result is schematically shown in Supplementary Fig. 5.5b.

**Step 2: Microwave cavity patterning.** After the junctions are patterned, we once again spin-coat the sample with CSAR62.13 and pattern the SQUID arms together with all the remaining superconducting structures. After the EBL exposure, the sample is developed as for the previous fabrication step and afterwards loaded into a sputtering machine. Hereby, the nanobridges themselves are covered and protected by resist, cf. Supplementary Fig. 5.5c. At this point and prior to the deposition of the second Aluminum layer, an Argon milling process is performed in-situ in order eliminate any oxide present on top of the contact pads. This measure is necessary to generate good electrical contact between the two layers. After the sputtering process of the second, 70 nm thick Aluminum (1% Silicon) layer, the sample undergoes an ultrasonic lift-off process similar to the one in Step 1, the result is shown schematically in Supplementary Fig. 5.5d.

**Step 3: Nanobridge thinning by Ar ion milling.** In order to reduce the cross-section and the critical current of the nanobridges even further, we apply a short ion milling step to the SQUID at this point. To do so, we pattern and develop another layer of CSAR62.13 on top of the device as described in Steps 1 and 2, which protects the whole chip except for rectangular windows around the SQUIDs themselves, cf. Supplementary Fig. 5.5e.

From test measurements, we observe that if we do not protect the rest of the circuit from the milling in this step, we obtain a significant reduction of the circuit quality factor, which we think might be due to ion implantation into the substrate. Note that with the milling parameters we use for this step, we do not get a directional milling, but mainly a narrowing of the nanobridges from the sides. This is also the reason why we need the contact pads in the first place. If we work with bare nanobridges in Step 1, they are milled away completely during the essential in-situ native oxide removal in Step 2.

**Step 4: Dicing.** Right before the final release of the mechanical oscillator, the sample is once again diced to two smaller  $5 \times 10 \text{ mm}^2$  sized chips in order to fit into the sample mountings and the microwave PCB (Printed Circuit Board). The remaining 2 mm at each edge of the original  $14 \times 14 \text{ mm}^2$  large chip is only a margin for the fabrication and is disposed of.

**Step 5: Mechanical beam release.** For the final EBL step, a CSAR62.13 resist was once again used as mask and the development of the pattern was done in a similar way as for the first two layers. Once the etch mask, consisting of a small window close to the outer side of the SQUID loop (cf. Supplementary Fig. 5.5f), is patterned, the sample undergoes an isotropic, reactive ion etching process in  $\text{SF}_6$  at a sample temperature of  $\sim -10^\circ\text{C}$  for two minutes [126]. During this time the Silicon substrate under the SQUID arm/the mechanical beam is etched without attacking the aluminum layer forming the cavity and the mechanical beam. Once the beam is released, we proceeded with an  $\text{O}_2$  plasma ashing step in order to remove the remaining resist from the sample. At this point the fabrication is completed, the result is shown schematically in Supplementary Fig. 5.5g.

**Step 6: Device mounting.** After the fabrication, the sample is glued into a microwave printed circuit board (PCB) using GE varnish and wirebonded both to ground and to  $50\Omega$  connector lines. An optical image of the chip and the PCB, both mounted into a magnet, is shown in Fig. 5.1.

### 5.7.2. MEASUREMENT SETUP

#### SETUP CONFIGURATION

The experiments reported in this paper were performed in a dilution refrigerator with a base temperature  $T_b \approx 15 \text{ mK}$ . Within the outer vacuum can of the system, a mu-metal shield is installed to provide basic magnetic shielding for the whole sample space from the 3 K plate to the mK plate. A schematic diagram of the experimental setup and of the external measurement configuration used in the reported experiments can be seen in Supplementary Fig. 5.6.

The PCB, onto which the fabricated sample was glued and wirebonded, is mounted into a 2D vector magnet casing and connected to two coaxial lines. The complete configuration including the vector magnet is placed in a magnetic cryoperm shield. The vector magnet combines two distinct superconducting magnets, a small one for the generation of an out-of-plane field and a larger split coil for the in-plane field. The coils are used

to independently generate a magnetic field in the two different directions by providing a DC current to the corresponding coil. A more detailed information about the design and setup of the vector magnet is provided in the following subsection.

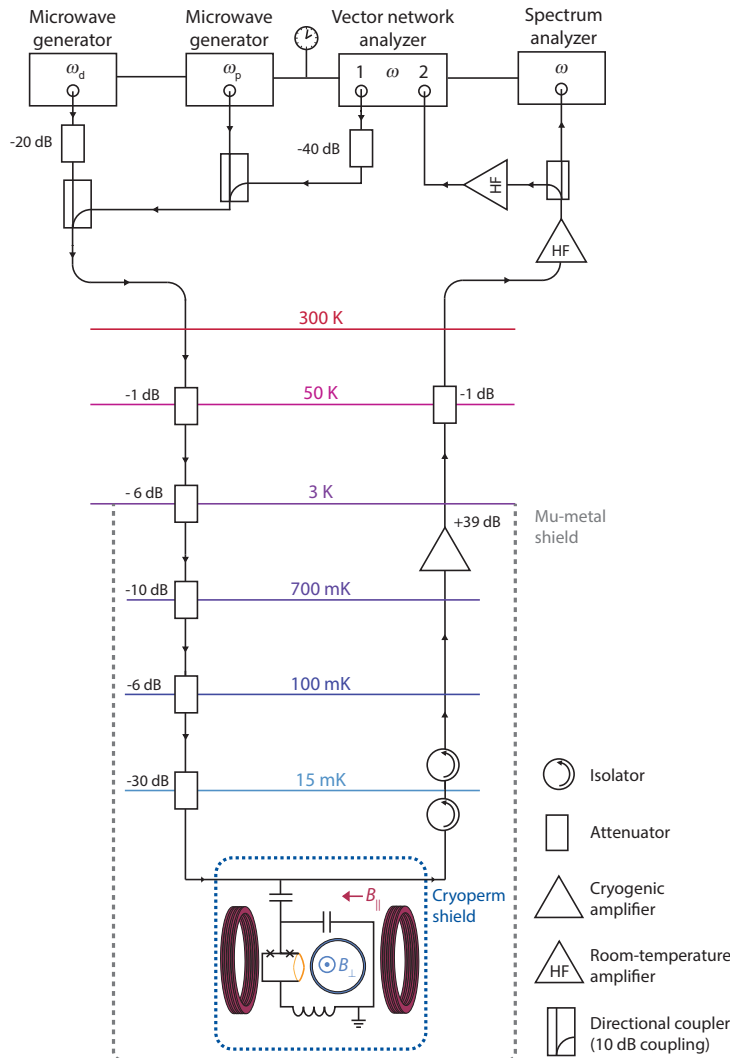


Figure 5.6: Schematic of the measurement setup. Detailed information is provided in text.

Since the optomechanical circuit that we present in this paper was designed in a side-coupled geometry, the input and output signals were sent/received through separate coaxial lines in order to measure the transmission spectrum of the feedline to which the system is coupled. The input line is heavily attenuated in order to balance the thermal radiation from the line to the base temperature of the fridge and the output line

contains a cryogenic HEMT (High-Electron-Mobility Transistor) amplifier working in a range from 4 to 8 GHz and two isolators to block the thermal radiation from the HEMT to reach the sample.

Outside of the refrigerator, we used a single measurement scheme for all the different experiments. The VNA was used to measure the response spectrum  $S_{21}$  of the electromechanical system, one microwave generator sends a coherent signal at  $\omega_d$  as parametric drive for the SQUID cavity and the second microwave generator sends a tone at  $\omega_p$  as optomechanical pump for the parametrically driven cavity. Finally, a spectrum analyzer was used to record the output power spectrum around the cavity resonance.

For all experiments, the microwave sources and vector network analyzers (VNA) as well as the spectrum analyzer used a single reference clock of one of the devices.

## VECTOR MAGNET DESIGN

Figure 5.1 shows photographs of the sample mounted on the PCB and fixed in the vector magnet bobbin. The two large parallel coils on each side of the sample are wound from a single wire (niobium-titanium in copper-nickel matrix) and in the same orientation and therefore form a Helmholtz-like split coil (the distance between the coils is slightly larger than their effective radius), which creates a nearly homogeneous in-plane magnetic field at the location of the device. At room temperature the coil has a resistance of  $R_{\parallel} \approx 6\text{k}\Omega$ , which approximately corresponds to 2000 windings of superconducting wire on each side. From the coil geometry and the number of windings, we estimate the current-to-field conversion factor to be  $70\text{mT/A}$ .

On the backside of the sample/PCB platform within the magnet bobbin is a second small coil mounted for providing the out-of-plane magnetic field used to tune the SQUID flux bias point, cf. Fig. 5.1. This out-of-plane coil can also be used to compensate for a parasitic out-of-plane component of the in-plane field due to misalignments of the sample/PCB with respect to the in-plane field axis (estimated to be around  $2^\circ - 3^\circ$  from the SQUID flux response). For in-plane fields  $B_{\parallel} \lesssim 25\text{mT}$ , however, the compensation is not yet critical. For larger in-plane fields, vortices start to penetrate the film and there is a dramatic reduction in the cavity quality factor observable. The room-temperature resistance of the out-of-plane coil is  $R_{\perp} \approx 120\Omega$  which corresponds to approximately 400 turns of superconducting wire and to a conversion factor of  $1\text{mT/A}$ .

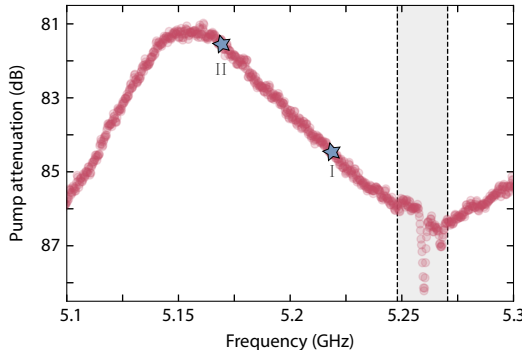
The superconducting wires leading to each of the coils from the 3 K plate are twisted in pairs, in order to reduced the amount of captured flux noise. Furthermore, since the critical temperature of the wire is about  $\sim 12\text{K}$ , the wires can go unbroken until the 3 K stage. Above this plate, the wires are no longer superconducting and therefore a transition to normal conducting wires is required. For this, we connected each of the superconducting in-plane coil wires to 9 wires of a 24-line copper loom provided by Bluefors and each of the out-of-plane coil wires to 3 wires of the loom. From the 3 K stage until room temperature the current flows in parallel through the respective loom wires, decreasing the additional heat load on the plate. With this approach we are able to send  $I_{\parallel} \sim 0.5\text{A}$  through the in-plane coil without any considerable heat added to any of the plates and maintaining the fridge base temperature. At room temperature we are left with 4 cables, two for each coil, which are used with individual directed current (DC) sources to independently generate the magnetic fields.

### 5.7.3. POWER CALIBRATION

In order to estimate the input power on the on-chip feedline of the device, we use the thermal noise of the HEMT (High-Electron-Mobility Transistor) amplifier as calibration method. The cryogenic HEMT amplifier thermal noise power is given by

$$P_{\text{HEMT}} = 10 \log \left( \frac{k_B T_{\text{HEMT}} \Delta f}{1 \text{ mW}} \right) \quad (5.11)$$

where  $k_B$  is the Boltzmann constant,  $T_{\text{HEMT}}$  is the noise temperature of the amplifier, which, according to the specification datasheet, is approximately 2 K, and  $\Delta f = 2000 \text{ Hz}$  is the measurement IF bandwidth. The calculated noise power is  $P_{\text{HEMT}} = -162.6 \text{ dBm}$ , or as noise RMS voltage  $\Delta V = 1.66 \text{ nV}$ .



5

**Figure 5.7: Estimation of the frequency-dependent input line attenuation for the pump tone.** The shown data are obtained by measuring 501 traces in the shown frequency range using the vector network analyzer shown in Supplementary Fig. 5.6. For each frequency point, we determine from the 501 traces the signal-to-noise ratio and with the assumption of a frequency-independent HEMT noise temperature and 2 dB losses between the sample and the HEMT, we get the input line attenuation as plotted. The gray area shows where the cavity was during the calibration. Due to its presence, the attenuation in this range can not be considered a reliable value. Our experiments, however, mainly take place around 5.22 GHz and 5.17 GHz (labeled with I and II, respectively) and therefore the presence of the cavity at around 5.26 GHz does not lead to any calibration problems. We also note, that we observe almost identical amplitude oscillations in the transmitted signal, indicating that we are indeed dealing with strong cable resonances.

Taking into account the room temperature attenuators of 60 dB as well as additional 3 dB of room-temperature cable losses between the VNA output and the directional couplers for the pump tones and assuming an attenuation between the sample and the HEMT of 2 dB we extract a frequency-dependent input attenuation for the pump tones as shown in Supplementary Fig. 5.7. In addition and for confirmation, we perform a fixed-frequency measurement of the signal-to-noise ratio using the pump signal generator itself and a spectrum analyzer for selected frequency points around 5.22 and 5.17 GHz. We observe agreement between the two methods better than 0.5 dB.

### 5.7.4. THE SQUID CAVITY

#### CIRCUIT MODEL

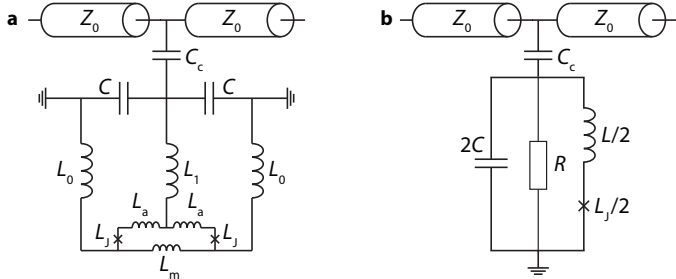


Figure 5.8: **The circuit model.** **a** Circuit equivalent of the SQUID cavity shown in Fig. 5.1. Each  $C$  corresponds to one interdigitated capacitor (IDC) and  $C_c$  to the coupling capacitance to the feedline with characteristic impedance  $Z_0$ . The SQUID loop inductance  $L_{\text{loop}} = 2L_a + L_m$  has contributions from the non-released arms  $L_a$  and from the loop part that acts as mechanical oscillator  $L_m$ . The remaining linear inductances  $L_1$  and  $L_0$  correspond to the inductances of the circuit wires and IDCs and each nanobridge Josephson junction is described by a Josephson inductance  $L_J$ . **b** shows a simplified circuit model, where all linear contributions to the inductance are expressed through  $L/2$ , the nonlinear Josephson inductance is in good approximation given by  $L_J/2$  and the two IDCs are contained in the single capacitance  $2C$ . All internal losses of the circuit are captured by the resistor  $R$ . Another possible version for the circuit equivalent is shown in Fig. 5.1 where all linear contributions to the inductance are split symmetrically between the two inductors  $L$ .

5

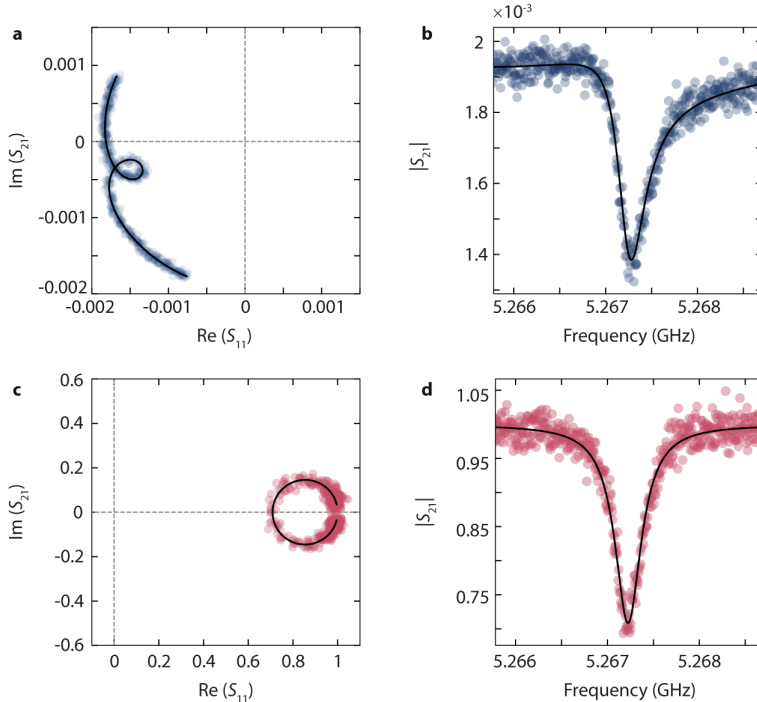
A simplified circuit equivalent of the SQUID cavity used in this experiment is shown in Supplementary Fig. 5.8a. We model it as a simple parallel  $RLC$  circuit capacitively coupled by a coupling capacitance  $C_c$  to a microwave feedline with characteristic impedance  $Z_0$  as shown in b, cf. also Ref. [162]. The resistance in this model captures all intracavity losses. The resonance frequency, external and internal linewidth of the circuit shown in b are given by

$$\omega_0 = \frac{1}{\sqrt{(2C + C_c)\left(\frac{L}{2} + \frac{L_J}{2}\right)}}, \quad \kappa_i = \frac{1}{R(2C + C_c)}, \quad \kappa_e = \frac{\omega_0^2 C_c^2 Z_0}{2(2C + C_c)} \quad (5.12)$$

respectively.

Each of the two physical capacitors in the main circuit, cf. Fig. 5.1, is an interdigitated capacitor (IDC) with  $N = 148$  fingers, each  $100\mu\text{m}$  long and  $1\mu\text{m}$  wide. With the gap between two fingers of also  $1\mu\text{m}$  and the relative permittivity of the Silicon substrate  $\epsilon_r = 11.7$ , we obtain for each of the IDCs  $C \approx 824\text{fF}$  using the analytical expressions provided in Ref. [158]. The total capacitance is then approximately given by  $C_{\text{tot}} = 2C + C_c \approx 1.65\text{pF}$ , where we included also the (mostly negligible) coupling capacitance  $C_c \approx 6.5\text{fF}$ . The value for  $C_c$  was obtained via the external cavity linewidth of  $\kappa_e \approx 2\pi \cdot 110\text{kHz}$ , the feedline characteristic impedance  $Z_0 = 50\Omega$  and the resonance frequency  $\omega_0 = 2\pi \cdot 5.267\text{GHz}$ . Using the resonance frequency, we can also estimate the total inductance as  $L_{\text{tot}} = \frac{1}{\omega_0^2 C_{\text{tot}}} \approx 552\text{pH}$ .

## RESPONSE FUNCTION AND FITTING ROUTINE



5

**Figure 5.9: Cavity response fitting and background-correction.** Raw data for the cavity response  $S_{21}$  in the complex plane and in linear magnitude are shown in **a** and **b** as circles. Black line is a full fit including a phase rotation factor and a complex, frequency-dependent background. In **c** and **d** the corresponding data after a background correction and a corresponding phase factor rotation are shown as circles, the corresponding background-corrected fit curves are shown as lines. Data correspond to an in-plane field  $B_{\parallel} = 25 \text{ mT}$  and SQUID bias flux  $\Phi_b = 0$ . Dashed lines in **a** and **c** show the real and imaginary axes, respectively.

In the linear regime, a capacitively side-coupled LC circuit is described by the  $S_{21}$  response function

$$S_{21}^{\text{ideal}} = 1 - \frac{\kappa_e}{\kappa_i + \kappa_e + 2i\Delta} \quad (5.13)$$

with detuning of the probe tone from the resonance frequency

$$\Delta = \omega - \omega_0 \quad (5.14)$$

and the internal and external linewidths  $\kappa_i$  and  $\kappa_e$ , respectively. Implicitly, we assume symmetric coupling to the left and right feedline part in this relation. Due to considerable cable resonances in our setup, however, this assumption might be not strictly valid. We also observe, that for a consistent modelling of all our datasets, small adjustments to  $\kappa_e$  in different experimental situations are leading to higher agreement between data and theory.

The different microwave components in the setup (cables, attenuators, directional couplers, isolators etc) affect the ideal cavity transmission spectrum by amplitude and phase modulations, and we consider a modification in the response function by introducing a frequency-dependent complex-valued microwave background. The modified cavity response is written as

$$S_{21} = (\alpha_0 + \alpha_1 \omega) \left( 1 - \frac{\kappa_e e^{i\theta}}{\kappa_i + \kappa_e + 2i\Delta} \right) e^{i(\beta_1 \omega + \beta_0)} \quad (5.15)$$

where we consider a frequency-dependent complex background

$$S_{21}^{\text{bg}} = (\alpha_0 + \alpha_1 \omega) e^{i(\beta_1 \omega + \beta_0)} \quad (5.16)$$

and an additional, possible interference rotation of the resonance circle around its anchor point with the phase factor  $e^{i\theta}$ .

In our fitting routine the background is extracted by first excluding the cavity resonance from the response and fitting the remaining data with Eq. (5.16). After complex division of the data with the background model, the remaining cavity response is fitted independently. As final step the original data are fitted with the full function for  $S_{21}$  including the background again using the obtained fit values from the first two independent fits as starting values for the full fit. From the final fit, we remove the background of the full dataset by complex division for the resonance data shown this paper. Also, we correct for the additional rotation factor  $e^{i\theta}$ .

In Supplementary Fig. 5.9, we show an exemplary fit of the cavity response around resonance as raw data and as background-corrected data in both, the complex plane and in the magnitude of  $S_{21}$ . From the fit to the data, taken at  $B_{\parallel} = 25 \text{ mT}$  and  $B_{\perp} = 0$  (the sweetspot), we obtain  $\omega_0 = 2\pi \cdot 5.2672 \text{ GHz}$ ,  $\kappa_i = 2\pi \cdot 269 \text{ kHz}$  and  $\kappa_e \approx 2\pi \cdot 111 \text{ kHz}$ .

## THE SQUID JOSEPHSON INDUCTANCE

The total flux  $\Phi$  in a superconducting quantum interference device (SQUID) with non-negligible loop inductance  $L_{\text{loop}}$  is given by

$$\frac{\Phi}{\Phi_0} = \frac{\Phi_b}{\Phi_0} + L_{\text{loop}} J \quad (5.17)$$

where  $\Phi_b$  is the bias flux by external magnetic fields,  $J$  is the screening current circulating in the SQUID loop and  $\Phi_0 = \frac{h}{2e} = 2.07 \cdot 10^{-15} \text{ Tm}^2$  is the flux quantum. Note that  $L_{\text{loop}}$  contains both, the geometric and the kinetic inductance contribution to the inductance of the SQUID loop.

In the absence of a bias current and for identical Josephson junctions with a sinusoidal current-phase relation, the circulating current is given by

$$J = -I_c \sin\left(\pi \frac{\Phi}{\Phi_0}\right) \quad (5.18)$$

with the zero-flux-bias of a single junction  $I_c$ . Using the screening parameter  $\beta_L = \frac{2L_{\text{loop}} I_c}{\Phi_0}$ , the relation for the total flux can be written as

$$\frac{\Phi}{\Phi_0} = \frac{\Phi_b}{\Phi_0} - \frac{\beta_L}{2} \sin\left(\pi \frac{\Phi}{\Phi_0}\right). \quad (5.19)$$

We use this equation to numerically calculate the total flux in the SQUID for a given external flux.

With the total flux in the SQUID known, the Josephson inductance of a single junction

$$L_J(\Phi) = \frac{\Phi_0}{2\pi I_c \cos\left(\pi \frac{\Phi}{\Phi_0}\right)} \quad (5.20)$$

and the total Josephson inductance of the SQUID

$$L_S(\Phi) = \frac{L_J(\Phi)}{2} \quad (5.21)$$

can be determined.

## CAVITY FIELD DEPENDENCE

Using the flux-dependence of the SQUID Josephson inductance and our simplified circuit model, the resonance frequency of the cavity as function of the perpendicular bias flux  $\Phi_{\perp}$  can be written as

$$\omega_0(\Phi_{\perp}) = \frac{\omega_0(0)}{\sqrt{\Lambda + \frac{1-\Lambda}{\cos\left(\pi \frac{\Phi}{\Phi_0}\right)}}} \quad (5.22)$$

with the linear inductance participation ratio

$$\Lambda = \frac{L}{L + L_{J0}} \quad (5.23)$$

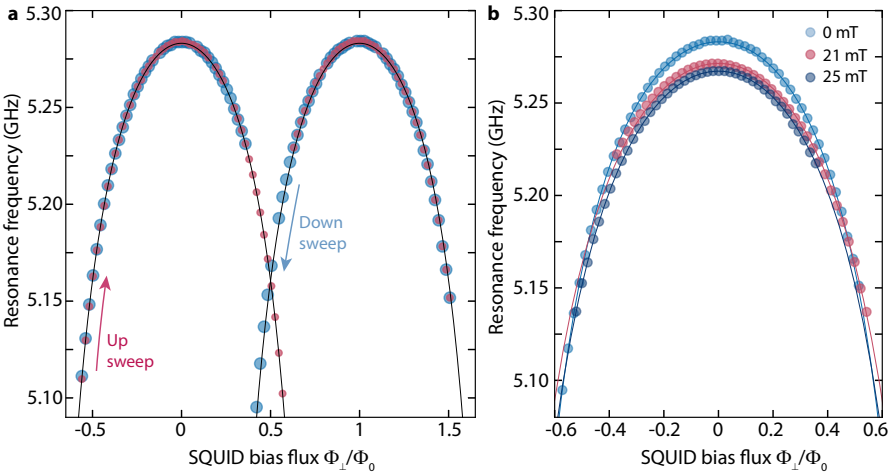
and the total flux in the SQUID

$$\tilde{\Phi} = \Phi \Big|_{\Phi_b = \Phi_{\perp}}. \quad (5.24)$$

The zero-bias junction inductance is hereby given as  $L_{J0} = L_J(\Phi = 0)$ .

The first experimental step to fit the flux-dependence of the cavity resonance frequency and to determine Josephson inductance  $L_J$  and screening parameter  $\beta_L$  is a calibration of the bias flux axis and to find the current-to-flux conversion for the small coil generating  $\Phi_{\perp}$ , respectively. Supplementary Fig. 5.10a shows as circles the experimentally obtained resonance frequencies at  $B_{\parallel} = 0$  for a sweep of the bias flux  $\Phi_{\perp}$ . The dataset combines the data points obtained during a bias flux upsweep and a downsweep. This is necessary as the SQUID has a non-negligible loop inductance, which leads to a hysteretic flux response [120, 121, 162]. The distance between two neighboring flux arches corresponds to one flux quantum  $\Phi_0$  and via this procedure the current-to-flux conversion is obtained. Subsequently, the flux-dependence of  $\omega_0$  can be fitted using Eqs. (5.22) and (5.19). From the fits, we obtain the zero-bias junction critical current  $I_c$  and the screening parameter  $\beta_L$ , the corresponding fit curves are shown as lines in Supplementary Fig. 5.10a.

From the fit at zero in-plane field we get  $I_c \approx 2.6 \mu\text{A}$  and a screening parameter  $\beta_L \approx 0.7$ . Using  $L_{J0} = \frac{\Phi_0}{2\pi I_c}$ , we get for the inductance of a single Josephson junction  $L_{J0} \approx 127 \text{ pH}$ , which corresponds to a linear inductance participation ratio  $\Lambda \approx 0.89$  and a total SQUID loop inductance  $L_{\text{loop}} \approx 278 \text{ pH}$ .



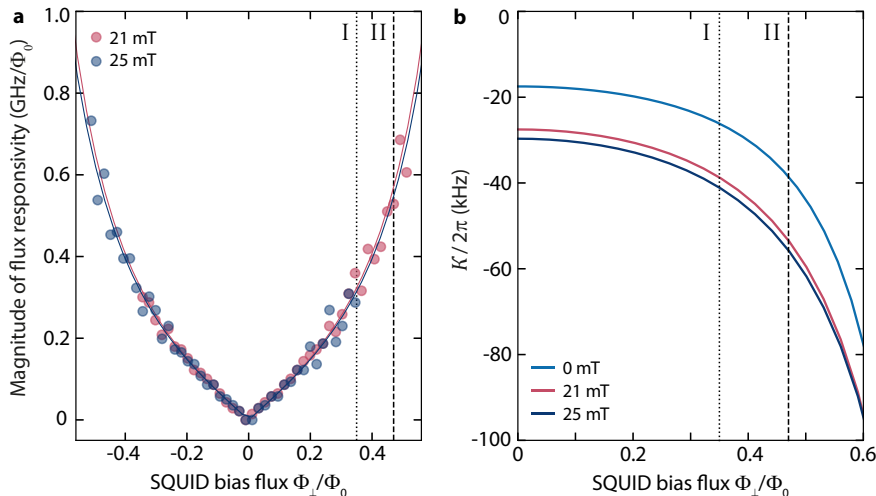
5

Figure 5.10: **Bias flux axis calibration and bias flux arch fitting.** In **a**, the SQUID cavity resonance frequency vs flux bias  $\Phi_{\perp}$  is shown for  $B_{\parallel} = 0$ . Red circles correspond to the resonance frequencies obtained during a flux upsweep, blue larger circles are data obtained during a flux downsweep. The hysteretic flux jumps around  $\Phi_{\perp}/\Phi_0 \sim 0.5$  indicate a non-negligible loop inductance of the SQUID [120, 121]. The distance between the two shown arches corresponds to one flux quantum  $\Phi_0$  and allows for a calibration of the flux axis. Lines correspond to fits using Eq. (5.22) in combination with Eq. (5.19). **b**, a single arch for three different in-plane magnetic fields as labelled in the legend. With increasing  $B_{\parallel}$ , the sweetspot resonance frequency  $\omega_0(\Phi_{\perp} = 0)$  slightly decreases and the width of the arch increases, indicating an increase in SQUID screening parameter  $\beta_L$ . Circles are data, lines are fits. Fit parameters are given and discussed in the text.

Enabling the optomechanical coupling between the nanobeam and the SQUID cavity requires an additional in-plane magnetic transduction field, and therefore we also record the resonance frequency flux-dependence at the in-plane fields of  $B_{\parallel} = 21$  mT and  $B_{\parallel} = 25$  mT, where we operate the device for the optomechanical experiments. The result is shown in Supplementary Fig. 5.10**b** as circles. From the data, we observe a small decrease of the sweetspot resonance frequency with increasing  $B_{\parallel}$ . In addition, we observe a slight widening of the flux arch with increasing  $B_{\parallel}$ , indicating a nonlinear increase of the kinetic contribution to the SQUID loop inductance and a consequently increased  $\beta_L$ . From the fits, we get for both in-plane fields a slightly reduced critical junction current  $I_{c\parallel} \approx 2.2 \mu\text{A}$  and slightly increased screening parameters  $\beta_{L,21} \approx 0.79$  and  $\beta_{L,25} \approx 0.82$ . These values correspond to  $\Lambda_{\parallel} \approx 0.865$ ,  $L_{\text{loop},21} \approx 371 \text{ pH}$  and  $L_{\text{loop},25} \approx 385 \text{ pH}$ . We observe that the loop inductance seems to increase by more than both, the Josephson inductance and the linear circuit inductance due to the in-plane field. Our suspicion is that this effect is caused by a modification of the nanobridge current-phase relation in the in-plane field, but for a final conclusion more experiments would have to be conducted.

For the optomechanical multi-photon interaction two more quantities of the SQUID cavity and their flux dependence are highly important. The first is the flux responsivity  $\mathcal{F} = \partial\omega_0/\partial\Phi_b$ , i.e., the change of resonance frequency with change of bias flux through

the SQUID loop. It is directly proportional to the optomechanical single-photon coupling rate  $g_0$ , cf. section 5.7.5. The responsivity is identical to the slope of the flux tuning curve shown in Supplementary Fig. 5.10b and the numerically obtained results for both, experimental data and the fit curve, are shown in Supplementary Fig. 5.11a. The bias-flux operation points relevant for this paper are marked with a dotted and dashed line, respectively, and labeled as "I" and "II". The corresponding flux responsivities are  $\mathcal{F}_I \approx 2\pi \cdot 300 \text{ MHz}/\Phi_0$  and  $\mathcal{F}_{II} \approx 2\pi \cdot 520 \text{ MHz}/\Phi_0$ , respectively, and nearly identical to each other for the two chosen in-plane fields. The second important quantity is the Kerr



**Figure 5.11: Flux responsivity and Kerr anharmonicity at the device operation points.** In a, we plot the numerically obtained magnitude of the flux responsivity  $\mathcal{F} = \partial\omega_0/\partial\Phi_{\perp}$  vs bias flux  $\Phi_{\perp}$  for non-vanishing magnetic in-plane fields. b shows the Kerr anharmonicity vs bias flux for  $B_{\parallel} = 0$ ,  $B_{\parallel} = 21 \text{ mT}$  and  $B_{\parallel} = 25 \text{ mT}$ . The two operation points relevant for this paper are marked by vertical dotted and dashed lines and labeled with I and II, respectively.

anharmonicity related to the nonlinear Josephson inductance of the SQUID. It is given by

$$\mathcal{K}(\Phi_{\perp}) = -\frac{e^2}{2\hbar C_{\text{tot}}} \left( \frac{L_S(\Phi_{\perp})}{L_{\text{tot}}(\Phi_{\perp})} \right)^3 \quad (5.25)$$

and depends in addition on the in-plane field via the in-plane dependence of the nanobridge critical current or Josephson inductance, respectively. The result of this calculation, based on the flux arch fits of Supplementary Fig. 5.10b is shown in Supplementary Fig. 5.11b. The dependence of the anharmonicity on flux bias  $\Phi_{\perp}$  shows a very similar trend for all in-plane fields with different starting values at the sweetspot  $\Phi_{\perp} = 0$ . The completely unbiased cavity has  $\mathcal{K} \approx -2\pi \cdot 17.5 \text{ kHz}$ . For an in-plane field of  $B_{\parallel} = 21 \text{ mT}$ , we obtain  $\mathcal{K}_{I,21} \approx -2\pi \cdot 39 \text{ kHz}$  and  $\mathcal{K}_{II,21} \approx -2\pi \cdot 54 \text{ kHz}$  at the operation points "I" and "II", respectively, and for  $B_{\parallel} = 25 \text{ mT}$ , we find  $\mathcal{K}_{I,25} \approx -2\pi \cdot 41 \text{ kHz}$  and  $\mathcal{K}_{II,25} \approx -2\pi \cdot 56 \text{ kHz}$ . As the difference between the two in-plane field is small and subject to uncertainties due to

uncertainties in the circuit parameters, we will work with the same approximate anharmonicities for both in-plane fields of  $\mathcal{K}_I \approx -2\pi \cdot 40 \text{ kHz}$  and  $\mathcal{K}_{II} \approx -2\pi \cdot 55 \text{ kHz}$ .

### 5.7.5. THE OPTOMECHANICAL SINGLE-PHOTON COUPLING RATE

The optomechanical single-photon coupling rate in flux-mediated optomechanics is given by [70, 162]

$$g_0 = \gamma \mathcal{F} B_{\parallel} l_m x_{\text{zpf}} \quad (5.26)$$

where  $\mathcal{F}$  is the cavity frequency flux responsivity,  $B_{\parallel}$  is the in-plane magnetic field,  $l_m$  is the length of the mechanical nanobeam and  $\gamma$  is a scaling factor on the order of unity taking into account the mode shape of the beam. The zero-point fluctuation amplitude of the mechanical displacement is given by

$$x_{\text{zpf}} = \sqrt{\frac{\hbar}{2m\Omega_m}} \quad (5.27)$$

where  $m$  is the effective mass of the beam and  $\Omega_m$  its resonance frequency.

For our nanobeam, cf. Fig. 5.1b, we get from a scanning electron micrograph the length as approximately  $l_m = 18 \mu\text{m}$ . Using the beam film thickness of  $\sim 70 \text{ nm}$ , its width of  $\sim 500 \text{ nm}$  and the density of Aluminum  $\rho_{\text{Al}} = 2700 \text{ kg m}^{-3}$ , we get a total mass of  $m = 1.7 \cdot 10^{-15} \text{ kg}$ . In the experiment, we observe a mechanical resonance frequency  $\Omega_m \approx 2\pi \cdot 5.32 \text{ MHz}$  and therefore, we find a zero-point fluctuation amplitude of  $x_{\text{zpf}} \approx 30 \cdot 10^{-15} \text{ m} = 30 \text{ fm}$ .

With the flux responsivities shown in Supplementary Fig. 5.11a and assuming  $\gamma \approx 1$ , we calculate the corresponding single-photon coupling rates  $g_0$ , the result is shown in Supplementary Fig. 5.12. For the different operation points, we obtain single-photon coupling rates  $g_0$  between  $g_0^{\min} \approx 2\pi \cdot 1.78 \text{ kHz}$  (point I) and  $g_0^{\max} \approx 2\pi \cdot 3.57 \text{ kHz}$  (point II). For all presented results, we will add the corresponding coupling rates either in the figure legend or in the caption.

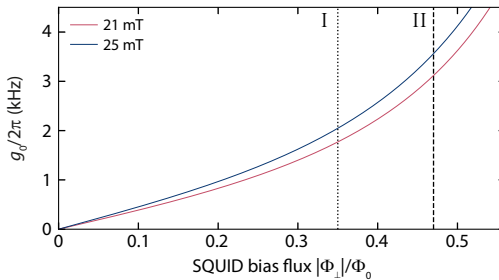


Figure 5.12: **The optomechanical single-photon coupling rate.** Using the flux responsivity  $\mathcal{F}$  from the flux arch fits and the estimated mechanical zero-point-amplitude  $x_{\text{zpf}}$ , we calculate the single-photon coupling rate  $g_0$  for both in-plane fields as labelled in the legend. The two operation points "I" and "II" are marked with dotted and dashed lines, respectively.

### 5.7.6. THE DRIVEN KERR CAVITY

#### EQUATION OF MOTION

We model the side-coupled SQUID cavity including the Kerr nonlinearity with the equation of motion

$$\dot{\alpha} = \left[ i(\omega_0 + \mathcal{K}|\alpha|^2) - \frac{\kappa}{2} \right] \alpha + i\sqrt{\frac{\kappa_e}{2}} S_{\text{in}} \quad (5.28)$$

where the intracavity field  $\alpha$  is normalized such that  $|\alpha|^2 = n_c$  is the intracavity photon number and  $|S_{\text{in}}|^2$  corresponds to the input field photon flux.

#### SINGLE-TONE SOLUTION

If the cavity is driven with a single tone at frequency  $\omega_d$ , the input field is given by

$$S_{\text{in}} = S_d e^{i(\omega_d t + \phi_d)} \quad (5.29)$$

and for the intracavity field we make the Ansatz

$$\alpha = \alpha_d e^{i\omega_d t} \quad (5.30)$$

5

with real-valued  $S_{\text{in}}$  and  $\alpha_d$ . Any phase difference between the drive and the intracavity field is captured in the drive phase  $\phi_d$ . Inserting drive and intracavity field Ansatz into the equation of motion gives

$$\alpha_d \left[ \frac{\kappa}{2} + i(\Delta_d - \mathcal{K}\alpha_d^2) \right] = i\sqrt{\frac{\kappa_e}{2}} S_d e^{i\phi_d} \quad (5.31)$$

where  $\Delta_d = \omega_d - \omega_0$  is the detuning between drive and undriven cavity resonance frequency. Multiplication of this equation with its complex conjugate leads to the determination polynomial for the drive intracavity photon number  $n_d = \alpha_d^2$

$$\mathcal{K}^2 n_d^3 - 2\mathcal{K}\Delta_d n_d^2 + \left( \Delta_d^2 + \frac{\kappa^2}{4} \right) n_d - \frac{\kappa_e}{2} S_d^2 = 0. \quad (5.32)$$

In general, this polynomial has three roots for  $n_d$ . The real-valued solutions correspond to physical states and for certain parameters all three solutions are real-valued. This regime corresponds to the bifurcation regime, where two of the three oscillator states are stable, one low- and one high-amplitude solution. The middle solution is unstable and irrelevant for the experiments described here. The phase difference between drive and intracavity oscillations can be found via

$$\phi_d = \text{atan}2\left(-\frac{\kappa}{2}, \Delta_d - \mathcal{K}n_d\right). \quad (5.33)$$

#### NONLINEAR CAVITY RESPONSE MODELING

We measure the power dependence of the SQUID cavity response  $S_{21}$  by means of a vector network analyzer at the bias flux sweetspot and at  $B_{\parallel} = 25$  mT. The result is shown and

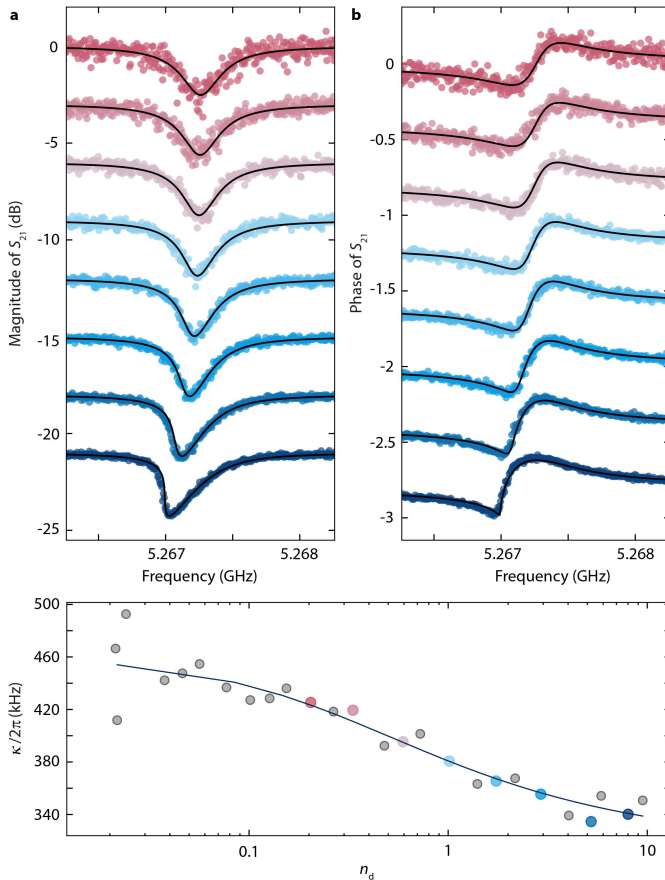


Figure 5.13: **Nonlinear cavity single-tone response.** **a** shows the magnitude and **b** the phase of the SQUID cavity response  $S_{21}$  at the flux sweetspot  $B_{\perp} = 0$  and at  $B_{\parallel} = 25$  mT for increasing probe power. Lowest probe power is shown in red at the top, highest power at the bottom in blue. Subsequent curves are offset by  $-3$  dB in **a** and  $-0.4$  in **b** with the unshifted curves at the top. Circles are data, lines correspond to the model, for details see text. To model the experimentally obtained data accurately, we have to consider a power-dependent linewidth. The linewidths we obtain by fitting the nonlinear response curves with  $\kappa$  as fit parameter are shown in **c** as circles vs intracavity photons on resonance. The line in **c** shows a fit based on the two-level-system model for nonlinear dissipation in superconducting circuits. Colored circles in **c** correspond to the equally colored data in **a,b**.

discussed in Supplementary Fig. 5.13, where in **a** the magnitude and in **b** the phase of the complex  $S_{21}$  is plotted. The data shown have been background-corrected as described above using the background fit of the first line. To model the response, we employ the

single-tone model described in the previous section and calculate the response via

$$\begin{aligned} S_{21} &= 1 + i \sqrt{\frac{\kappa_e}{2}} \frac{\alpha_d}{S_d} \\ &= 1 + i \sqrt{\frac{\kappa_e}{2}} \sqrt{\frac{\hbar \omega_d n_d}{P_d}} e^{-i\phi_d} \end{aligned} \quad (5.34)$$

where  $P_d$  is the drive power on the on-chip microwave feedline. For the model, we use the Kerr anharmonicity obtained from the independent cavity modeling  $\mathcal{K} = -2\pi \cdot 30\text{kHz}$ , the resonance frequency  $\omega_0 = 2\pi \cdot 5.2672\text{GHz}$  and the corresponding external linewidth  $\kappa_e = 2\pi \cdot 106.5\text{kHz}$  as obtained from the lowest-power response of the current dataset.

As apparent from the increase in resonance absorption dip depth and the reduction of total linewidth with increasing drive power, we also have to consider nonlinear dissipation, that decreases with increasing power. As first step in the nonlinear resonance analysis, we fit each of the nonlinear response curves using the Kerr polynomial and using a single decay rate for each power as fit parameter. The result of this procedure for  $\kappa$  is shown in Supplementary Fig. 5.13c, where we plot the fit linewidth vs the photon number  $n_d$  on resonance. We model this decrease of linewidth with the functional dependence for two-level systems

$$\kappa_i(n_d) = \kappa_0 + \frac{\kappa_1}{\sqrt{1 + \frac{n_d}{n_{\text{crit}}}}} \quad (5.35)$$

where  $n_{\text{crit}}$  describes the characteristic photon number for two-level saturation. From a fit to the linewidth data we obtain  $\kappa_0 = 2\pi \cdot 209\text{kHz}$ ,  $\kappa_1 = 2\pi \cdot 145\text{kHz}$ , and  $n_{\text{crit}} \approx 0.26$ , cf. line in Supplementary Fig. 5.13c. As next and final step, we implement this analytical function into the Kerr polynomial and solve for the final photon number at each drive power and detuning. To find convergence in the solution for the photon number  $n_d$  due to the power dependent  $\kappa$  we have to iterate the polynomial solution multiple times in this approach for each frequency point, feeding back in each iteration the  $\kappa(n_d)$  from the previous iteration. The result is added as lines in Supplementary Fig. 5.13a and b and shows good agreement between experimental data and theoretical modeling.

The only free parameter used in the end is the in-fridge attenuation between the VNA output and the sample, and we find best agreement for choosing  $G_{\text{STK}} = -89.2\text{dB}$ . This value is very close to the independently estimated probe attenuation of  $G_{\text{SNR}} = -89.5\text{dB}$  at the corresponding frequency, cf. Supplementary Fig. 5.7 with consideration that the probe attenuation is 3 dB larger than the shown pump attenuation.

## LINEARIZED TWO-TONE SOLUTION

If the Kerr cavity is driven by a strong drive tone  $S_d$  and a weaker second tone  $S_p$  with frequency  $\omega_p$ , the total input field is given by

$$S_{\text{in}} = S_d e^{i(\omega_d t + \phi_d)} + S_p e^{i\omega_p t} \quad (5.36)$$

where we again choose  $S_d$  to be real-valued. As Ansatz for the intracavity field, we then use

$$\alpha = \alpha_d e^{i\omega_d t} + \gamma_- e^{i\omega_p t} + \gamma_+ e^{i(2\omega_d - \omega_p)t} \quad (5.37)$$

where  $\gamma_-$  and  $\gamma_+$  are complex-valued and  $\gamma_+$  corresponds to the idler field of  $\gamma_-$ , generated by degenerate four-wave-mixing due to the Kerr nonlinearity. Note that with this choice of Ansatz, we omit all higher order Fourier components to the total intracavity field, as in the operation regime of our device, they can be neglected to first order. Inserting drive and intracavity field Ansatz into the equation of motion yields

$$\begin{aligned} i\omega_d \alpha_d e^{i\Omega_{dp}t} + i\omega_p \gamma_- + i(2\omega_d - \omega_p) \gamma_+ e^{i2\Omega_{dp}t} &= \left[ i\omega_0 - \frac{\kappa}{2} \right] \alpha_d e^{i\Omega_{dp}t} + \left[ i\omega_0 - \frac{\kappa}{2} \right] \gamma_- \\ &+ \left[ i\omega_0 - \frac{\kappa}{2} \right] \gamma_+ e^{i2\Omega_{dp}t} + i\mathcal{K} [n_d + |\gamma_-|^2 + |\gamma_+|^2] (\alpha_d e^{i\Omega_{dp}t} + \gamma_- + \gamma_+ e^{i2\Omega_{dp}t}) \\ &+ i\mathcal{K} \alpha_d e^{i\Omega_{dp}t} [\gamma_-^* + \gamma_+^* e^{-i2\Omega_{dp}t}] (\alpha_d e^{i\Omega_{dp}t} + \gamma_- + \gamma_+ e^{i2\Omega_{dp}t}) \\ &+ i\mathcal{K} \alpha_d e^{-i\Omega_{dp}t} [\gamma_- + \gamma_+ e^{i2\Omega_{dp}t}] (\alpha_d e^{i\Omega_{dp}t} + \gamma_- + \gamma_+ e^{i2\Omega_{dp}t}) \\ &+ i\mathcal{K} [\gamma_- \gamma_+^* e^{-i2\Omega_{dp}t} + \gamma_-^* \gamma_+ e^{i2\Omega_{dp}t}] (\alpha_d e^{i\Omega_{dp}t} + \gamma_- + \gamma_+ e^{i2\Omega_{dp}t}) \\ &+ i\sqrt{\frac{\kappa_e}{2}} S_d e^{i\Omega_{dp}t} e^{i\phi_d} + i\sqrt{\frac{\kappa_e}{2}} S_p. \end{aligned} \quad (5.38)$$

5

With  $n_d + |\gamma_-|^2 + |\gamma_+|^2 \approx n_d$  and after omitting all terms not linear in the small quantities  $\gamma_-, \gamma_+$ , we obtain

$$\begin{aligned} \left[ \frac{\kappa}{2} + i(\Delta_d - \mathcal{K}n_d) \right] \alpha_d e^{i\Omega_{dp}t} + \left[ \frac{\kappa}{2} + i(\Delta_p - \mathcal{K}n_d) \right] \gamma_- + \left[ \frac{\kappa}{2} + i(\Delta_p - \mathcal{K}n_d + 2\Omega_{dp}) \right] \gamma_+ e^{i2\Omega_{dp}t} \\ = i\mathcal{K}n_d [\gamma_-^* e^{i2\Omega_{dp}t} + \gamma_+^*] + i\mathcal{K}n_d [\gamma_- + \gamma_+ e^{i2\Omega_{dp}t}] + i\sqrt{\frac{\kappa_e}{2}} S_d e^{i\Omega_{dp}t} e^{i\phi_d} + i\sqrt{\frac{\kappa_e}{2}} S_p, \end{aligned} \quad (5.39)$$

where  $\Delta_d = \omega_d - \omega_0$  and  $\Delta_p = \omega_p - \omega_0$  describe the detunings of the two input field frequencies from the undriven cavity resonance. Sorting for frequency contributions leaves us with three equations

$$\left[ \frac{\kappa}{2} + i(\Delta_d - \mathcal{K}n_d) \right] \alpha_d = i\sqrt{\frac{\kappa_e}{2}} S_d e^{i\phi_d} \quad (5.40)$$

$$\left[ \frac{\kappa}{2} + i(\Delta_p - 2\mathcal{K}n_d) \right] \gamma_- - i\mathcal{K}n_d \gamma_+^* = i\sqrt{\frac{\kappa_e}{2}} S_p \quad (5.41)$$

$$\left[ \frac{\kappa}{2} + i(\Delta_p - 2\mathcal{K}n_d + 2\Omega_{dp}) \right] \gamma_+ - i\mathcal{K}n_d \gamma_-^* = 0. \quad (5.42)$$

The first of these three equations is the steady-state equation for the single-tone case and can be solved for  $n_d$  using the approach presented above. To solve the other two coupled equations, we use  $\Delta_p = \Delta_d - \Omega_{dp}$  and define the susceptibilities

$$\chi_p = \frac{1}{\frac{\kappa}{2} + i(\Delta_d - 2\mathcal{K}n_d - \Omega_{dp})}, \quad \chi'_p = \frac{1}{\frac{\kappa}{2} + i(\Delta_d - 2\mathcal{K}n_d + \Omega_{dp})} \quad (5.43)$$

and

$$\chi_g = \frac{\chi_p}{1 - \mathcal{K}^2 n_d^2 \chi_p \chi_p'^*} \quad (5.44)$$

and get

$$\gamma_- = i \chi_g \sqrt{\frac{\kappa_e}{2}} S_p \quad (5.45)$$

$$\gamma_+ = \mathcal{K} n_d \chi_p' \chi_g^* \sqrt{\frac{\kappa_e}{2}} S_p \quad (5.46)$$

$$= i \mathcal{K} n_d \chi_p' \gamma_-^* \quad (5.47)$$

## THE DRIVEN KERR-MODES AND THEIR RESPONSE

To find the resonance frequency of the quasi-mode with susceptibility  $\chi_g$ , we solve for the complex frequency  $\tilde{\omega} = \omega_p$ , for which  $\chi_g^{-1} = 0$ . Therefore, the condition is

$$1 - \mathcal{K}^2 n_d^2 \chi_p \chi_p' = 0 \quad (5.48)$$

which is solved by

$$\tilde{\omega}_{1/2} = \omega_d + i \frac{\kappa}{2} \pm \sqrt{(\Delta_d - \mathcal{K} n_d)(\Delta_d - 3\mathcal{K} n_d)}. \quad (5.49)$$

where the real part corresponds to the resonance frequency and the imaginary part corresponds to half the mode linewidth. So, as a consequence of the presence of the strong drive, the system has two resonances, which are split symmetrically with respect to the drive frequency  $\omega_d$ . The two Kerr-modes correspond to the cases when the cavity field  $\gamma_-$  is resonant or when its idler field  $\gamma_+$  is resonant and they have been discussed also in the context of nonlinear optical cavities [200, 201] and mechanical oscillators [202]. For the experiments described here, the argument of the square root will always be positive and hence, we get as resonance frequency of signal and idler mode

$$\omega_{s/i} = \omega_d \pm \sqrt{(\Delta_d - \mathcal{K} n_d)(\Delta_d - 3\mathcal{K} n_d)} \quad (5.50)$$

and both modes are having a constant linewidth of  $\kappa$ . The most relevant regime for our experiment is given by  $\Delta_d < 0$  and  $\Delta_d < \mathcal{K} n_d$ . Then, the signal resonance is given by

$$\omega_s = \omega_d - \sqrt{(\Delta_d - \mathcal{K} n_d)(\Delta_d - 3\mathcal{K} n_d)} \quad (5.51)$$

and the idler resonance by

$$\omega_i = \omega_d + \sqrt{(\Delta_d - \mathcal{K} n_d)(\Delta_d - 3\mathcal{K} n_d)}. \quad (5.52)$$

Hence, if  $S_p$  is a probe tone scanning the driven SQUID cavity, we expect the response to be given by

$$S_{21} = 1 + i \sqrt{\frac{\kappa_e}{2}} \frac{\gamma_-}{S_p} \quad (5.53)$$

and to observe two resonances symmetrically positioned around the drive, that correspond to the two Kerr-modes of the driven Kerr cavity.

## KERR CAVITY TWO-TONE RESPONSE MODELING

To observe and model the two-tone response of the driven Kerr cavity, we set a drive tone with fixed power  $P_d$  and fixed frequency  $\omega_d$  to a point of non-zero flux bias and sweep the bare resonance frequency of the cavity  $\omega_0$  through the drive frequency by sweeping the bias flux  $\Phi_\perp$ . For each flux bias value during the sweep, we record a response trace  $S_{21}$  of the SQUID cavity using the VNA. In Supplementary Fig. 5.14 we show in comparison the result of such a measurement with and without parametric drive. When  $\omega_0 \sim \omega_d$ , the flux-dependence of the cavity is modified considerably with respect to the case without a drive. The resonance frequency of the observed mode becomes nearly constant with flux and on the opposite side of the drive, a second resonance line appears. This second mode on the right side of the drive tone with net transmission gain indicates that we are entering the quasi-mode regime and have Josephson parametric amplification in both Kerr-modes.

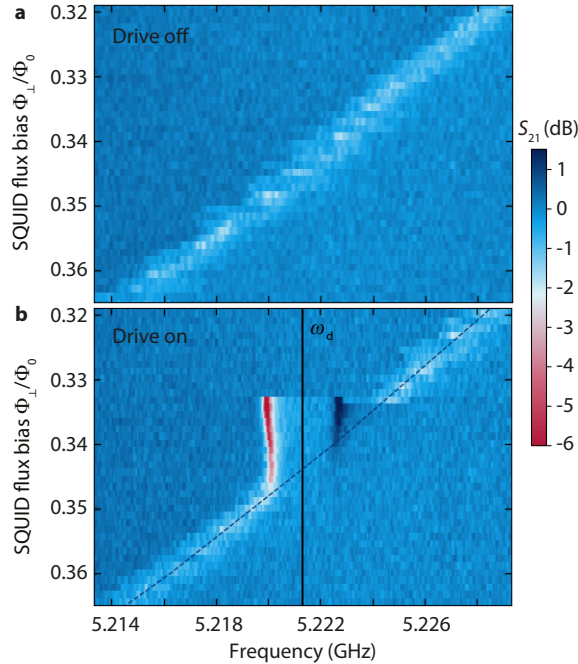
Fig. 5.2 shows and discusses a similar dataset in more detail including linescans and also analyzing the linewidths and the Kerr-mode resonance frequency and comparing the experimentally obtained values with theoretical calculations. The overall behaviour of cavity and Kerr-modes is in excellent agreement with the two-tone model of a Kerr oscillator as demonstrated by the high-level agreement between theory lines and experimental data for the resonance frequencies. The only subtlety we have to consider additionally is an effective linewidth broadening due to low-frequency flux noise out of the two-mode regime. From the data, it is obvious that the lineshape is not just broadened but distorted also on timescales comparable to the measurement time. Although due to this noise modulation the cavity response is not anymore described by its ideal response with an increased linewidth [205], we fit it using Eq. (5.15). The apparent  $\kappa'$  we obtain from this procedure is however still a good measure for the effective linewidth. These flux-noise broadened linewidths are considerably larger than the intrinsic energy decay rate of the cavity and to take the noise-broadening and the two-level systems simultaneously into account we model the noise-free linewidth using

$$\kappa_i = \kappa_0 + \kappa_1 \left[ 1 - \frac{n_d/n_{\text{crit}}}{\sqrt{1+n_d/n_{\text{crit}}}} \frac{1 + \sqrt{1+n_d/n_{\text{crit}}}}{(\Delta_d/\Gamma_2)^2 + (1 + \sqrt{1+n_d/n_{\text{crit}}})^2} \right] \quad (5.54)$$

where the first term  $\kappa_0$  is the bare power and flux-independent decay rate, and the second term describes the generalized two-level system impact for detuning between drive and cavity/probe with the two-level system dephasing rate  $\Gamma_2$  [206]. Finally, we phenomenologically take into account a broadening of the linewidth using

$$\kappa'_i = \kappa_i \sqrt{1 + |\mathcal{F}|^2 \sigma_\Phi^2} \quad (5.55)$$

where  $\mathcal{F}$  is the flux responsivity and  $\sigma_\Phi$  is the rms value of the flux fluctuations through the SQUID. This relation seems to resemble closely what has been found numerically for tunable and frequency-fluctuating cavities [205]. The line in Fig. 5.2 is a modeling of the experimentally obtained linewidths with Eqs. (5.54) and (5.55). The fit parameters are  $\kappa_0 = 2\pi \cdot 200 \text{ kHz}$ ,  $\kappa_1 = 2\pi \cdot 145 \text{ kHz}$ ,  $n_{\text{crit}} = 0.26$ ,  $\Gamma_2 = 2\pi \cdot 300 \text{ kHz}$  and  $\sigma_\Phi = 5.1 \cdot 10^{-3} \Phi_0$ .



5

**Figure 5.14: Probe tone response of the SQUID cavity with and without parametric drive.** **a** shows the color-coded cavity response to a weak probe tone  $S_{21}$  in a small flux and frequency window around operation point I. The cavity absorption is visible as bright and fluctuating feature. In **b** the same measurement in the same flux and frequency range is shown, but in presence of a fixed frequency drive tone at  $\omega_d = 2\pi \cdot 5.2213$  GHz. The dashed line shows the theoretical resonance frequency without drive. When  $\omega_d \approx \omega_0$ , the response of the cavity deviates significantly from the undriven response. Two modes are visible, one on the left side of the drive with increased absorption and reduced linewidth compared to the undriven case, and a second on the right side of the drive as a peak. The increased depth and reduced linewidth of the signal mode absorption dip reflects both, reduced impact of flux noise on the cavity line and Josephson parametric amplification. The Josephson amplification is also apparent in the idler mode on the right side of the drive, which shows net gain of the input signal. Due to the underlying four-wave mixing process, the resonance frequencies of the two Kerr-modes with respect to the parametric drive are equal in magnitude and opposite in sign.

Note that the values used and obtained here are also in good agreement with the numbers we extracted from the modeling of the nonlinear single-tone response.

For the flux operation point II, we can use almost exactly the same parameters, except for a slightly increased  $\kappa_0 = 2\pi \cdot 210$  kHz.

### 5.7.7. LINEARIZED KERR OPTOMECHANICS

#### CLASSICAL EQUATIONS OF MOTION

To model the optomechanical system with a Kerr nonlinearity, we use the classical equations of motion (EOM)

$$\ddot{x} = -\Omega_m^2 x - \Gamma_m \dot{x} + \frac{\hbar G}{m} |\alpha|^2 \quad (5.56)$$

$$\dot{\alpha} = \left[ i(\omega_0 - Gx + \mathcal{K}|\alpha|^2) - \frac{\kappa}{2} \right] \alpha + i\sqrt{\frac{\kappa_e}{2}} S_{\text{in}} \quad (5.57)$$

with the mechanical displacement  $x$ , the mechanical resonance frequency  $\Omega_m$ , the mechanical damping rate  $\Gamma_m$ , and the cavity pull parameter

$$G = -\frac{\partial \omega_0}{\partial x} = -\mathcal{F} B_{\parallel} l_m \quad (5.58)$$

These equations are identical to the EOMs of linear classical optomechanics [56], except for the additional Kerr term  $\mathcal{K}|\alpha|^2$  in the equation for the intracavity field.

#### SINGLE-DRIVE SOLUTION

For a single cavity drive field

$$S_{\text{in}} = S_d e^{i(\omega_d t + \phi_d)} \quad (5.59)$$

we make the Ansatz

$$x = x_0 \quad (5.60)$$

$$\alpha = \alpha_d e^{i\omega_d t} \quad (5.61)$$

and look for the steady-state solution  $\ddot{x} = \dot{x} = 0$ . For the equilibrium offset displacement  $x_0$ , we obtain

$$x_0 = \frac{\hbar G}{\Omega_m^2 m} n_d = n_d \frac{2g_0}{\Omega_m} x_{\text{zpf}} \quad (5.62)$$

where we used

$$g_0 = G x_{\text{zpf}}, \quad x_{\text{zpf}} = \sqrt{\frac{\hbar}{2m\Omega_m}}. \quad (5.63)$$

For the intracavity field amplitude  $\alpha_d$ , we find

$$\left[ \frac{\kappa}{2} + i \left( \Delta_d - \bar{\mathcal{K}} \alpha_d^2 \right) \right] \alpha_d = i \sqrt{\frac{\kappa_e}{2}} S_d e^{i\phi_d}. \quad (5.64)$$

with the modified Kerr anharmonicity

$$\bar{\mathcal{K}} = \mathcal{K} - \frac{2g_0^2}{\Omega_m}. \quad (5.65)$$

As for our device  $\mathcal{K} > 2\pi \cdot 10^4$  Hz and  $\frac{2g_0^2}{\Omega_m} < 2\pi \cdot 10$  Hz, we can assume in good approximation  $\bar{\mathcal{K}} \approx \mathcal{K}$ . From here it is straightforward to calculate the intracavity drive photon number  $n_d$  and the phase  $\phi_d$  using the third order polynomial as for the bare Kerr cavity.

## SINGLE-DRIVE KERR BACKACTION

If we allow also for fluctuations of the displacement and the intracavity field, we get the Ansatz

$$x = x_0 + \delta x(t) \quad (5.66)$$

$$\alpha = \alpha_d e^{i\omega_d t} + \delta\alpha(t) e^{i\omega_d t} \quad (5.67)$$

and the equation of motion for the mechanical oscillator becomes

$$\delta\ddot{x} = -\Omega_m^2 x_0 - \Omega_m^2 \delta x - \Gamma_m \delta\dot{x} + \frac{\hbar G}{m} (n_d + |\delta\alpha|^2) + \frac{\hbar G}{m} \alpha_d (\delta\alpha + \delta\alpha^*). \quad (5.68)$$

For the intracavity field, we find

$$\begin{aligned} i\omega_d \alpha_d + i\omega_d \delta\alpha + \delta\dot{\alpha} &= \left[ i\omega_0 - \frac{\kappa}{2} \right] \alpha_d + \left[ i\omega_0 - \frac{\kappa}{2} \right] \delta\alpha \\ &\quad - iG\alpha_d x_0 - iG\alpha_d \delta x - iGx_0 \delta\alpha - iG\delta\alpha \delta x \\ &\quad + i\mathcal{K}(n_d + |\delta\alpha|^2)(\alpha_d + \delta\alpha) \\ &\quad + i\mathcal{K}\alpha_d(\delta\alpha + \delta\alpha^*)(\alpha_d + \delta\alpha) \\ &\quad + i\sqrt{\frac{\kappa_e}{2}} S_d e^{i\phi_d}. \end{aligned} \quad (5.69)$$

5

For the linearization, we omit now all terms not linear in the small quantities  $\delta\alpha$  and  $\delta x$ , we apply  $\bar{\mathcal{K}} \approx \mathcal{K}$  and remove the steady state solution. The remaining equations are

$$\delta\ddot{x} = -\Omega_m^2 \delta x - \Gamma_m \delta\dot{x} + \frac{\hbar G \alpha_d}{m} (\delta\alpha + \delta\alpha^*) \quad (5.70)$$

$$\delta\dot{\alpha} = \left[ -i(\Delta_d - 2\mathcal{K}n_d) - \frac{\kappa}{2} \right] \delta\alpha + i\mathcal{K}n_d \delta\alpha^* - iG\alpha_d \delta x \quad (5.71)$$

which can be Fourier-transformed to

$$\delta x(\Omega) [\Omega_m^2 - \Omega^2 + i\Omega\Gamma_m] = \frac{\hbar G \alpha_d}{m} [\delta\alpha(\Omega) + \delta\alpha^*(-\Omega)] \quad (5.72)$$

$$\delta\alpha(\Omega) \left[ \frac{\kappa}{2} + i(\Delta_d - 2\mathcal{K}n_d + \Omega) \right] = i\mathcal{K}n_d \delta\alpha^*(-\Omega) - iG\alpha_d \delta x(\Omega). \quad (5.73)$$

Using the convention  $\overline{\delta\alpha} = \delta\alpha^*(-\Omega)$ , the observation that  $\delta x(\Omega) = \delta x^*(-\Omega)$  and the definitions

$$\chi_m = \frac{1}{\Omega_m^2 - \Omega^2 + i\Omega\Gamma_m}, \quad \chi_p = \frac{1}{\frac{\kappa}{2} + i(\Delta_d - 2\mathcal{K}n_d + \Omega)} \quad (5.74)$$

we write these equations as

$$\frac{\delta x}{\chi_m} = \frac{\hbar G \alpha_d}{m} (\delta\alpha + \overline{\delta\alpha}) \quad (5.75)$$

$$\delta\alpha = i\mathcal{K}n_d \chi_p \overline{\delta\alpha} - iG\chi_p \alpha_d \delta x \quad (5.76)$$

$$\overline{\delta\alpha} = -i\mathcal{K}n_d \overline{\chi_p} \delta\alpha + iG\overline{\chi_p} \alpha_d \delta x \quad (5.77)$$

$$(5.78)$$

and solve for

$$\delta\alpha = -i\chi_g\alpha_d G \left(1 - i\mathcal{K}n_d\bar{\chi}_p\right) \delta x \quad (5.79)$$

$$\overline{\delta\alpha} = i\bar{\chi}_g\alpha_d G \left(1 + i\mathcal{K}n_d\chi_p\right) \delta x. \quad (5.80)$$

Note that here we used the earlier definition of the two-tone Kerr susceptibility

$$\chi_g = \frac{\chi_p}{1 - \mathcal{K}^2 n_d^2 \chi_p \bar{\chi}_p}. \quad (5.81)$$

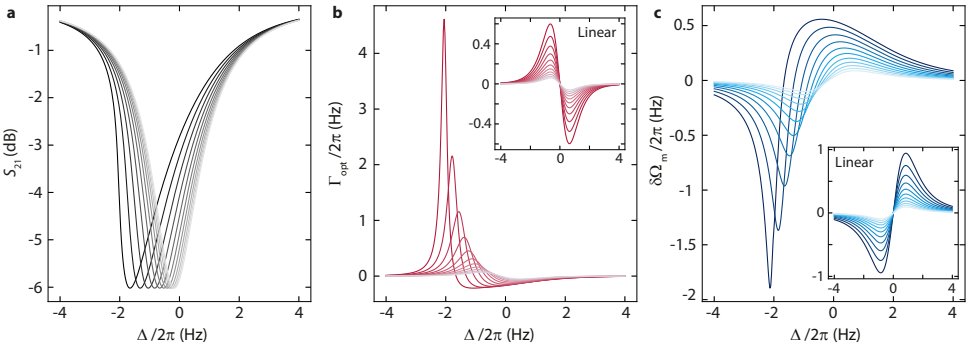


**Figure 5.15: Linearized dynamical Kerr backaction in the sideband-unresolved regime.** We calculate the cavity response and the dynamical Kerr backaction for a sideband-unresolved optomechanical system with parameters close to the device discussed in Ref. [71]. In **a**, we plot the magnitude of the transmission matrix element  $S_{21}$  at a side-coupled cavity with a resonance frequency  $\omega_0 = 2\pi \cdot 8.167$  GHz, a total linewidth  $\kappa = 2\pi \cdot 2.8$  MHz, an external linewidth  $\kappa_e = 2\pi \cdot 1.4$  MHz and an anharmonicity  $\mathcal{K} = -2\pi \cdot 2.5$  kHz for varying drive powers. We chose the drive powers such that the characteristic Duffing-like tilting of the resonance line to the left is clearly visible and keep the highest drive power below bifurcation. Using the obtained intracavity photon numbers  $n_d$ , a mechanical resonance frequency  $\Omega_m = 2\pi \cdot 274.4$  kHz, an optomechanical single-photon coupling rate  $g_0 = 2\pi \cdot 5.57$  Hz and our model presented in the text, we subsequently calculate the optical damping  $\Gamma_{\text{opt}}$  and the optical spring  $\delta\Omega_m$  induced by the drive in a Kerr cavity. The result is plotted in panels **b** and **c**, respectively, and seems to agree well with the experimental results reported in [71]. It is furthermore interesting to compare the obtained dynamical Kerr backaction with the dynamical backaction for a completely identical system but without anharmonicity. The corresponding calculations for the linear system  $\mathcal{K} = 0$  are shown as insets. The most striking and exciting difference is the eightfold enhancement of the optical damping on the "red" side of the Kerr cavity. This enhancement can also be understood by the increased slope of the intracavity field [145], cf. **a**, and the subsequently enhanced asymmetry for cavity photon up-scattering and down-scattering compared to the linear case. Different lines in each panel correspond to different drive powers and the detuning  $\Delta$  labelling the  $x$ -axes corresponds to the detuning from the zero-power resonance frequency  $\omega_0$ .

Inserting everything into the equation of motion for the mechanical oscillator, we obtain for a (real-valued) external driving force  $F_{\text{ex}}(\Omega)$

$$\delta x = \chi_m^{\text{eff}} \frac{F_{\text{ex}}}{m} \quad (5.82)$$

with the effective mechanical Kerr susceptibility

$$\frac{1}{\chi_m^{\text{eff}}} = \Omega_m^2 - \Omega^2 + i\Omega\Gamma_m + i2\Omega_m\Sigma_k \quad (5.83)$$

where

$$\Sigma_k = g_\alpha^2 \left[ \chi_g \left( 1 - i\mathcal{K}n_d \bar{\chi}_p \right) - \bar{\chi}_g \left( 1 + i\mathcal{K}n_d \chi_p \right) \right] \quad (5.84)$$

describes the dynamical backaction of a single-tone driven Kerr cavity to the mechanical oscillator with the multi-photon coupling rate  $g_\alpha = \alpha_d g_0 = \sqrt{n_d} g_0$ . We note, that the expression for  $\Sigma_k$  is formally equivalent to the dynamical backaction in a linear cavity. The first term in square brackets describes the quasi-mode susceptibility  $\chi_g$  for the blue motional sideband field (cooling), while the second term – its conjugate at the opposite side of the drive tone  $\bar{\chi}_g$  – is responsible for the red motional sideband field (amplification). The additional factors in parentheses  $(1 - i\mathcal{K}n_d \bar{\chi}_p)$  and  $(1 + i\mathcal{K}n_d \chi_p)$  take into account that the blue and red motional sidebands are interfering with each other due to the Kerr-drive induced four-wave mixing. The blue motional sideband coincides with the idler field of the red sideband and vice versa and their interference will contribute and modify the simple picture of dynamical backaction in a linear cavity.

For a high quality factor mechanical resonator and in the weak-coupling regime, we can approximate  $\Omega \approx \Omega_m$  and get

$$\frac{1}{\chi_0^{\text{eff}}} = \frac{\Gamma_m}{2} + i(\Omega - \Omega_m) + \Sigma_k(\Omega_m) \quad (5.85)$$

with

$$\Sigma_k(\Omega_m) = g_\alpha^2 \left[ \chi_g(\Omega_m) \left( 1 - i\mathcal{K}n_d \chi_p^*(-\Omega_m) \right) - \chi_g^*(-\Omega_m) \left( 1 + i\mathcal{K}n_d \chi_p(\Omega_m) \right) \right]. \quad (5.86)$$

Note that  $\chi_m^{\text{eff}}$  and  $\chi_0^{\text{eff}}$  do not have the same dimension and  $2i\Omega_m \chi_m^{\text{eff}} \approx \chi_0^{\text{eff}}$  for  $\Omega \approx \Omega_m$ . Nevertheless we will call both a susceptibility for simplicity.

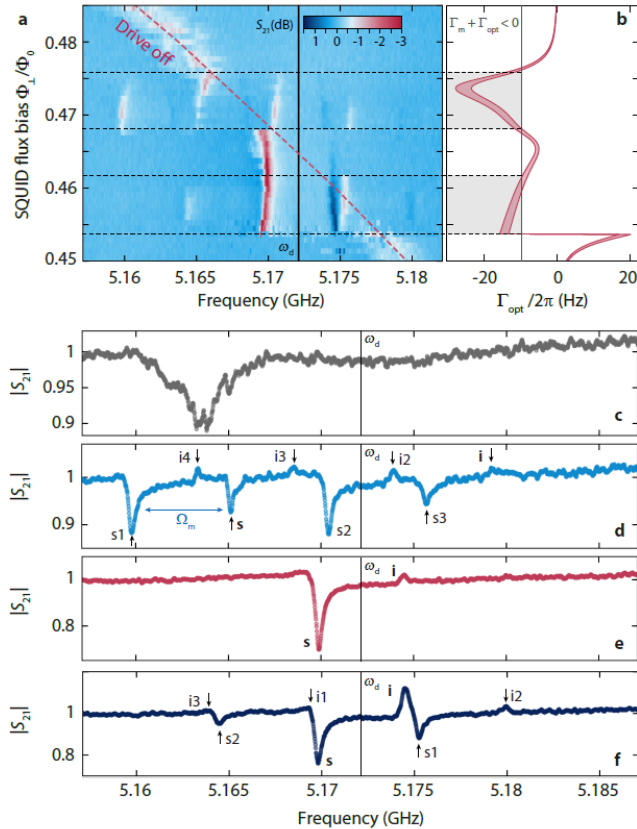
The optical spring  $\delta\Omega_m$  and optical damping  $\Gamma_{\text{opt}}$  are then given by

$$\delta\Omega_m = -\text{Im}[\Sigma_k(\Omega_m)] \quad (5.87)$$

$$\Gamma_{\text{opt}} = 2\text{Re}[\Sigma_k(\Omega_m)]. \quad (5.88)$$

Very recently, there has been an experimental report on dynamical backaction with a SQUID Kerr cavity in the sideband-unresolved regime [71] and we demonstrate in Supplementary Fig. 5.15 that our expressions lead to very similar results to the ones reported in Ref. [71] using parameters comparable with the reported ones.

Using our expressions for the Kerr backaction, we can also model with high accuracy the regimes for mechanical self-oscillation induced by the strong parametric cavity drive in the device presented here. To do this, we perform a similar experiment to the one discussed in Fig. 5.2, but at bias flux operation point II. At this operation point, we have a larger  $g_0 \sim 2\pi \cdot 3.56 \text{ kHz}$  as well as a larger Kerr nonlinearity  $\mathcal{K} \approx -2\pi \cdot 55 \text{ kHz}$ . In addition, we use a slightly higher drive power. The result of the probe tone transmission  $S_{21}$  for a bias flux sweep of the cavity resonance through the parametric drive tone is shown



5

Figure 5.16: **Observing and modeling Kerr-backaction induced mechanical self-oscillations.** **a** Magnitude of the cavity response  $S_{21}$  vs SQUID flux bias around operation point II in presence of a strong drive with  $\omega_d = 2\pi \cdot 5.1721$  GHz. The red dashed line shows the expected resonance frequency in absence of a drive. In the response, five regimes can be discriminated, which are described in detail in the text. Black horizontal dashed lines show the boundaries of the different regimes, which are closely related to the dynamical Kerr backaction onto the mechanical resonator. **b** shows the calculated optical damping for the flux range shown in **a**. The two solid red lines are the result for  $g_0 = 2\pi \cdot 3.4$  kHz and  $g_0 = 2\pi \cdot 3.7$  kHz, the red-shaded area captures the range in between these values. For two particular flux ranges (which correspond to two different ranges of detunings between the bare cavity and the parametric drive and therefore to different intracavity drive photon numbers) the total damping rate of the mechanical oscillator with a intrinsic damping rate of  $\Gamma_m \approx 2\pi \cdot 10$  Hz becomes negative. These ranges are indicated by gray areas and the threshold  $\Gamma_{tot} < 0$  is indicated by a vertical black line. Here, the mechanical oscillator will become unstable and undergoes self-oscillations. These self-oscillations induce oscillations of the SQUID cavity resonance frequency due to the optomechanical interaction, which will in turn lead to the observation of multiple replicas of the cavity and idler modes in regime 2 and regime 4, where regime 1 corresponds to the highest bias flux values. In the regimes 2 and 4, shown in panels **d** and **f**, respectively, these Kerr-mode replicas are visible and labeled with  $sX$  and  $iX$  with  $X = 1, 2, 3$ . The original signal and idler Kerr modes are labeled with  $s$  and  $i$ .

and discussed in Supplementary Fig. 5.16. The red dashed line shows how the bare cavity resonance frequency would be moving with bias flux  $\Phi_{\perp}$  in absence of a drive with frequency  $\omega_d$ . We can discriminate between five different regimes in the displayed data set.

- **Regime 1:** For the highest bias flux values, the cavity follows the undriven behaviour and its resonance frequency increases with reduced flux. The cavity linewidth and shape is significantly distorted by low-frequency flux noise. Panel **c** shows a linecut in this regime with a very broad and noisy single cavity absorption dip.
- **Regime 2:** At approximately  $\Phi_{\perp}/\Phi_0 \sim 0.476$ , the drive is positioned close to the blue sideband of the cavity  $\omega_d \approx \omega_0 + \Omega_m$  and multiple resonance lines appear in  $S_{21}$ , four absorption modes and four gain modes are visible. The frequency distance between two neighboring absorption modes or two neighboring gain modes is always the mechanical frequency  $\Delta\omega \approx \Omega_m$ . The appearance of a multiple-modes response is characteristic for a cavity with a strongly oscillating resonance frequency. In our device, the behaviour in this regime is generated and explained by the optomechanical instability and mechanical self-oscillations induced by the parametric drive being at the same time a very strong optomechanical blue-sideband pump tone. In panel **b**, we plot the calculated optical Kerr damping based on our equations for the dynamical backaction and on the independently determined device parameters. It is clearly visible that regime 2 corresponds to negative optomechanical damping, which exceeds the intrinsic mechanical linewidth  $\Gamma_m \approx 2\pi \cdot 10\text{ Hz}$  and therefore the mechanical oscillator is in the instability regime of self-oscillations. In panel **d**, a linecut of regime 2 is shown. The original cavity is labeled with "s" and its oscillation-induced replicas with "s1", "s2", and "s3". In addition, we observe 4 versions of the idler Kerr-mode as small peaks, where the original mode is labelled with "i" and its replicas with "i1", "i2", and "i3".
- **Regime 3:** For  $0.462 \lesssim \Phi_{\perp}/\Phi_0 \lesssim 0.468$  the observed resonances return to a single absorption dip on the left side of the drive and a single small gain mode on the right side of the pump, indicating that the cavity frequency is not strongly oscillating anymore. A linecut in this regime is shown in panel **e**.
- **Regime 4:** For  $0.453 \lesssim \Phi_{\perp}/\Phi_0 \lesssim 0.462$  the negative optical damping once again exceeds the intrinsic mechanical linewidth and a second regime of instability is entered. A linecut in this regime is shown in panel **f**, where three signal-modes and three idler-modes are visible and labeled as in regime 2. As the frequency difference between signal and idler Kerr-mode in this regime is close to the mechanical frequency, each mode almost overlaps with one replica of the corresponding mirror-mode and they form dip-peak pairs.
- **Regime 5:** For  $\Phi_{\perp}/\Phi_0 \lesssim 0.453$  the cavity jumps to the low-amplitude oscillation branch and the impact of both, the parametric drive and the dynamical backaction on the cavity lineshape become negligible. The cavity continues to shift with flux just as the undriven cavity would do. A linecut in this regime is not explicitly shown.

We note again that for the calculation of the Kerr backaction and the instability regimes as shown in panel **b**, the only free parameter was the line attenuation for the drive tone, which was adjusted to  $-81.5$  dB for a good agreement between theory and experiment, a value very close to what was obtained from the line calibration in section 5.7.3 for operation point II. The other parameters used here are  $\omega_0, \mathcal{K}, \mathcal{F}, \Omega_m, \Gamma_m, \kappa_e, \kappa_i, \kappa_0, n_{crit}, \Gamma_2, \sigma_\Phi$  and they were all obtained from independent measurements or taken from theoretical estimates in the case of  $g_0$ .

## PHONON POPULATION WITH KERR BACKACTION

To calculate the equilibrium phonon population in the mechanical oscillator with Kerr backaction, we will use the linearized equations of motion for the quantum fields  $\hat{a}, \hat{a}^\dagger$  and  $\hat{b}, \hat{b}^\dagger$  representing the classical intracavity fluctuations  $\delta\alpha, \delta\alpha^*$  and  $\beta, \beta^*$  with  $\delta x = x_{zpf}(\beta + \beta^*)$ , respectively. For the input noise, we use  $\hat{\zeta}_m$  for the mechanical oscillator and  $\hat{\xi}_i, \hat{\xi}_e$  for the internal and external cavity baths, respectively. We denote the input noise operators of the cavity at different frequencies with subscripts "+" and "-". The equations of motion become

5

$$\dot{\hat{b}} = i\Omega_m \hat{b} - \frac{\Gamma_m}{2} \hat{b} - ig_\alpha (\hat{a} + \hat{a}^\dagger) + \sqrt{\Gamma_m} \hat{\zeta} \quad (5.89)$$

$$\dot{\hat{a}} = \left[ -i(\Delta_d - 2\mathcal{K}n_d) - \frac{\kappa}{2} \right] \hat{a} + i\mathcal{K}n_d \hat{a}^\dagger - ig_\alpha (\hat{b} + \hat{b}^\dagger) + \sqrt{\kappa_e} \hat{\xi}_e + \sqrt{\kappa_i} \hat{\xi}_i \quad (5.90)$$

or in Fourier space and with the equations for the creation operators too

$$\frac{\dot{\hat{b}}}{\chi_0} = -ig_\alpha (\hat{a} + \hat{a}^\dagger) + \sqrt{\Gamma_m} \hat{\zeta} \quad (5.91)$$

$$\frac{\dot{\hat{b}}^\dagger}{\chi_0} = ig_\alpha (\hat{a} + \hat{a}^\dagger) + \sqrt{\Gamma_m} \hat{\zeta}^\dagger \quad (5.92)$$

$$\frac{\dot{\hat{a}}}{\chi_p} = i\mathcal{K}n_d \hat{a}^\dagger - ig_\alpha (\hat{b} + \hat{b}^\dagger) + \sqrt{\kappa_e} \hat{\xi}_{e+} + \sqrt{\kappa_i} \hat{\xi}_{i+} \quad (5.93)$$

$$\frac{\dot{\hat{a}}^\dagger}{\chi_p} = -i\mathcal{K}n_d \hat{a} + ig_\alpha (\hat{b} + \hat{b}^\dagger) + \sqrt{\kappa_e} \hat{\xi}_{e-}^\dagger + \sqrt{\kappa_i} \hat{\xi}_{i-}^\dagger. \quad (5.94)$$

Note that for the external bath of the cavity, we assumed a single port, although strictly speaking the temperature on the left side of the transmission line could be different from the right side.

As first step, we shorten the expressions by using

$$\hat{\mathcal{N}}_\pm = \sqrt{\kappa_e} \hat{\xi}_{e\pm} + \sqrt{\kappa_i} \hat{\xi}_{i\pm}, \quad \mathcal{A} = -i\mathcal{K}n_d \chi_p \quad (5.95)$$

and decouple the equations for  $\hat{a}$  and  $\hat{a}^\dagger$ . We get

$$\hat{a} = -ig_\alpha \chi_g (1 - \bar{\mathcal{A}}) (\hat{b} + \hat{b}^\dagger) + \chi_g (\hat{\mathcal{N}}_+ + \bar{\mathcal{A}} \hat{\mathcal{N}}_-^\dagger) \quad (5.96)$$

$$\hat{a}^\dagger = ig_\alpha \bar{\chi}_g (1 - \mathcal{A}) (\hat{b} + \hat{b}^\dagger) + \bar{\chi}_g (\hat{\mathcal{N}}_-^\dagger + \mathcal{A} \hat{\mathcal{N}}_+). \quad (5.97)$$

We can go even more compact

$$\hat{a} = -ig_\alpha \chi_k (\hat{b} + \hat{b}^\dagger) + \chi_g \hat{\mathcal{M}}_+ \quad (5.98)$$

$$\hat{a}^\dagger = ig_\alpha \bar{\chi}_k (\hat{b} + \hat{b}^\dagger) + \bar{\chi}_g \hat{\mathcal{M}}_-^\dagger. \quad (5.99)$$

with

$$\chi_k = \chi_g (1 - \bar{\mathcal{A}}), \quad \hat{\mathcal{M}}_+ = \hat{\mathcal{N}}_+ + \bar{\mathcal{A}} \hat{\mathcal{N}}_-^\dagger, \quad \hat{\mathcal{M}}_-^\dagger = \hat{\mathcal{N}}_-^\dagger + \mathcal{A} \hat{\mathcal{N}}_+. \quad (5.100)$$

As next step, we substitute

$$\hat{b} + \hat{b}^\dagger = -ig_\alpha (\chi_0 - \bar{\chi}_0) (\hat{a} + \hat{a}^\dagger) + \sqrt{\Gamma_m} (\chi_0 \hat{\zeta} + \bar{\chi}_0 \hat{\zeta}^\dagger) \quad (5.101)$$

$$= -ig_\alpha (\chi_0 - \bar{\chi}_0) (\hat{a} + \hat{a}^\dagger) + \hat{\mathcal{S}} \quad (5.102)$$

and obtain

$$\hat{a} = -g_\alpha^2 \chi_k (\chi_0 - \bar{\chi}_0) (\hat{a} + \hat{a}^\dagger) - ig_\alpha \chi_k \hat{\mathcal{S}} + \chi_g \hat{\mathcal{M}}_+ \quad (5.103)$$

$$\hat{a}^\dagger = g_\alpha^2 \bar{\chi}_k (\chi_0 - \bar{\chi}_0) (\hat{a} + \hat{a}^\dagger) + ig_\alpha \bar{\chi}_k \hat{\mathcal{S}}^\dagger + \bar{\chi}_g \hat{\mathcal{M}}_-^\dagger \quad (5.104)$$

or

$$\hat{a} + \hat{a}^\dagger = \frac{-ig_\alpha (\chi_k \hat{\mathcal{S}} - \bar{\chi}_k \hat{\mathcal{S}}^\dagger) + \chi_g \hat{\mathcal{M}}_+ + \bar{\chi}_g \hat{\mathcal{M}}_-^\dagger}{1 + g_\alpha^2 (\chi_0 - \bar{\chi}_0) (\chi_k - \bar{\chi}_k)} \quad (5.105)$$

with which we can finally express  $\hat{b}$  only as a function of the input noise operators

$$\hat{b} = -ig_\alpha \chi_0^{\text{eff}} \chi_g \hat{\mathcal{M}}_+ - ig_\alpha \chi_0^{\text{eff}} \bar{\chi}_g \hat{\mathcal{M}}_-^\dagger - g_\alpha^2 \chi_0^{\text{eff}} (\chi_k \hat{\mathcal{S}} - \bar{\chi}_k \hat{\mathcal{S}}^\dagger) + \chi_0 \sqrt{\Gamma_m} \hat{\zeta} \quad (5.106)$$

$$= -ig_\alpha \chi_0^{\text{eff}} \chi_k (\sqrt{\kappa_e} \hat{\xi}_{e+} + \sqrt{\kappa_i} \hat{\xi}_{i+}) - ig_\alpha \chi_0^{\text{eff}} \bar{\chi}_k (\sqrt{\kappa_e} \hat{\xi}_{e-}^\dagger + \sqrt{\kappa_i} \hat{\xi}_{i-}^\dagger) \\ + \sqrt{\Gamma_m} \chi_0 [1 - g_\alpha^2 \chi_0^{\text{eff}} (\chi_k - \bar{\chi}_k)] \hat{\zeta} - \sqrt{\Gamma_m} \chi_0^{\text{eff}} g_\alpha^2 \chi_0 (\chi_k - \bar{\chi}_k) \hat{\zeta}^\dagger \quad (5.107)$$

where the effective mechanical susceptibility is given by

$$\chi_0^{\text{eff}} = \frac{\chi_0}{1 + g_\alpha^2 (\chi_0 - \bar{\chi}_0) (\chi_k - \bar{\chi}_k)} \approx \frac{\chi_0}{1 + g_\alpha^2 \chi_0 (\chi_k - \bar{\chi}_k)}. \quad (5.108)$$

The last approximation is valid for a high- $Q_m$  mechanical oscillator.

Using the common relations for the expectation values of the noise correlators, we can calculate the phonon power spectral density in the mechanical resonator under dynamical Kerr backaction as

$$\langle \hat{b}^\dagger \hat{b} \rangle = g_\alpha^2 |\chi_0^{\text{eff}}|^2 |\chi_k|^2 \kappa n_c + g_\alpha^2 |\chi_0^{\text{eff}}|^2 |\bar{\chi}_k|^2 \kappa (n_c + 1) \quad (5.109)$$

$$+ |\chi_0^{\text{eff}}|^2 |1 - g_\alpha^2 \bar{\chi}_0 (\chi_k - \bar{\chi}_k)|^2 \Gamma_m n_m^{\text{th}} \quad (5.110)$$

$$+ g_\alpha^4 |\chi_0^{\text{eff}}|^2 |\bar{\chi}_0|^2 |\chi_k - \bar{\chi}_k|^2 \Gamma_m (n_m^{\text{th}} + 1)$$

and the total phonon number via

$$n_m^{\text{KDB}} = \int_{-\infty}^{\infty} \langle \hat{b}^\dagger \hat{b} \rangle \frac{d\Omega}{2\pi}. \quad (5.111)$$

This integration is performed numerically. We also note that we assumed a constant effective cavity bath occupation

$$n_c = \frac{\kappa_e n_e + \kappa_i n_i}{\kappa} \quad (5.112)$$

in the relevant frequency range. In Supplementary Fig. 5.17 we discuss the phonon occupation that results from a parametrically driven Kerr cavity for the relevant operation points I and II. Related discussions on optomechanical cooling using a Kerr cavity can be found in Refs. [145, 193, 194].

5

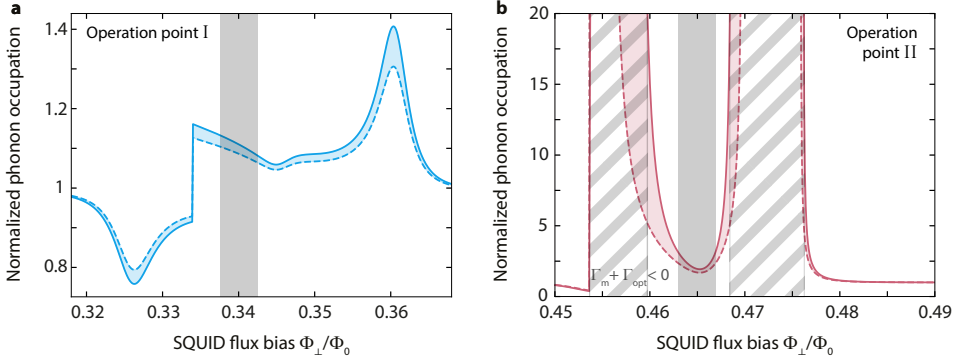


Figure 5.17: **Phonon occupation in the mechanical oscillator due to the parametric drive.** Due to the dynamical backaction induced by the parametric drive, the phonon occupation of the mechanical oscillator will deviate from the steady-state equilibrium value. In Fig. 5.2, we show the corresponding effect on the phonon occupation, normalized to the (maximum) case without parametric drive  $n_m^{\text{th}} = 80$ . For  $\Phi_\perp/\Phi_0 \sim 0.36$ , the drive is located on the blue sideband of the cavity and amplification/heating is observed. For  $\Phi_\perp/\Phi_0 \sim 0.327$ , the drive is located on the red sideband and cooling of the mechanical mode is visible. In the regime of interest, where our experiments take place (gray area), the effective occupation is increased by about 10%. The dashed and solid blue lines correspond to  $g_0 = 2\pi \cdot 1.8 \text{ kHz}$  and  $g_0 = 2\pi \cdot 2 \text{ kHz}$ , respectively. All other parameters are taken from independent measurements. In b, we show the equivalent occupation at operation point II with  $g_0 = 2\pi \cdot 3.4 \text{ kHz}$  and  $g_0 = 2\pi \cdot 3.7 \text{ kHz}$  for the dashed and solid red lines, respectively. The striped areas correspond to the instability regime  $\Gamma_m + \Gamma_{\text{opt}} < 0$  in the case  $g_0 = 2\pi \cdot 3.7 \text{ kHz}$ . All parameters are identical to the ones used for the backaction calculation shown in Fig. 5.16b, except for the drive power which is 1dB reduced as this is the regime for our cooling experiments. In the experimentally relevant flux regime, marked by solid gray shading, the phonon occupation is increased by about a factor of  $\sim 2.5$  due to dynamical backaction.

### 5.7.8. EQUATIONS OF MOTION FOR LINEARIZED MULTI-TONE KERR OPTOMECHANICS

## THREE-TONE LINEARIZATION

Finally, we discuss the linearized equations of motion with three input fields, i.e.,

$$S_{\text{in}} = S_d e^{i(\omega_d t + \phi_d)} + S_p e^{i\omega_p t} + S_0(t) e^{i\omega_p t} \quad (5.113)$$

where  $S_0(t)$  is a third, weak probe field. We choose as Ansatz

$$x = x_0 + \delta x \quad (5.114)$$

$$\alpha = \alpha_d e^{i\omega_d t} + \gamma_- e^{i\omega_p t} + \gamma_+ e^{i(2\omega_d - \omega_p)t} + \delta \alpha(t) e^{i\omega_p t} \quad (5.115)$$

with real-valued and time-independent  $\alpha_d$ , complex-valued and time-independent  $\gamma_-$ ,  $\gamma_+$  and complex-valued and time-dependent  $\delta \alpha$ .

For the mechanical oscillator, we get with this

$$\begin{aligned} \delta \ddot{x} = & -\Omega_m^2 x_0 - \Omega_m^2 \delta x - \Gamma_m \delta \dot{x} + \frac{\hbar G}{m} [\alpha_d^2 + |\gamma_-|^2 + |\gamma_+|^2 + |\delta \alpha|^2] \\ & + \frac{\hbar G \alpha_d}{m} [\gamma_-^* + \gamma_+^* e^{-i2\Omega_{dp}t} + \delta \alpha^*] e^{i\Omega_{dp}t} + \frac{\hbar G \alpha_d}{m} [\gamma_- + \gamma_+ e^{i2\Omega_{dp}t} + \delta \alpha] e^{-i\Omega_{dp}t} \\ & + \frac{\hbar G}{m} [\gamma_- \gamma_+^* e^{-i2\Omega_{dp}t} + \gamma_-^* \gamma_+ e^{i2\Omega_{dp}t}] + \frac{\hbar G}{m} [\gamma_- \delta \alpha^* + \gamma_-^* \delta \alpha] \\ & + \frac{\hbar G}{m} [\gamma_+ \delta \alpha^* e^{i2\Omega_{dp}t} + \gamma_+^* \delta \alpha e^{-i2\Omega_{dp}t}]. \end{aligned} \quad (5.116)$$

5

In our experiments presented in the section 5.3 we choose both  $\Omega_{dp}$  and  $2\Omega_{dp}$  to be very far-detuned from the mechanical resonance frequency  $\Omega_m$  and therefore we can neglect the pure driving force terms with  $\pm \Omega_{dp}$  and  $\pm 2\Omega_{dp}$ . After omitting the steady-state solution we get

$$\begin{aligned} \delta \ddot{x} = & -\Omega_m^2 \delta x - \Gamma_m \delta \dot{x} + \frac{\hbar G \alpha_d}{m} [\delta \alpha^* e^{i\Omega_{dp}t} + \delta \alpha e^{-i\Omega_{dp}t}] + \frac{\hbar G}{m} [\gamma_- \delta \alpha^* + \gamma_-^* \delta \alpha] \\ & + \frac{\hbar G}{m} [\gamma_+ \delta \alpha^* e^{i2\Omega_{dp}t} + \gamma_+^* \delta \alpha e^{-i2\Omega_{dp}t}]. \end{aligned} \quad (5.117)$$

For the intracavity field we get

$$\begin{aligned} & i\omega_d \alpha_d e^{i\Omega_{dp}t} + i\omega_p \gamma_- + i(2\omega_d - \omega_p) \gamma_+ e^{i2\Omega_{dp}t} + i\omega_p \delta \alpha + \delta \dot{\alpha} \\ = & \left[ i\omega_0 - \frac{\kappa}{2} \right] \alpha_d e^{i\Omega_{dp}t} + \left[ i\omega_0 - \frac{\kappa}{2} \right] \gamma_- + \left[ i\omega_0 - \frac{\kappa}{2} \right] \gamma_+ e^{i2\Omega_{dp}t} + \left[ i\omega_0 - \frac{\kappa}{2} \right] \delta \alpha \\ & - iG x_0 (\alpha_d e^{i\Omega_{dp}t} + \gamma_- + \gamma_+ e^{i2\Omega_{dp}t} + \delta \alpha) - iG \delta x (\alpha_d e^{i\Omega_{dp}t} + \gamma_- + \gamma_+ e^{i2\Omega_{dp}t} + \delta \alpha) \\ & + i\mathcal{K} [\alpha_d^2 + |\gamma_-|^2 + |\gamma_+|^2 + |\delta \alpha|^2] (\alpha_d e^{i\Omega_{dp}t} + \gamma_- + \gamma_+ e^{i2\Omega_{dp}t} + \delta \alpha) \\ & + i\mathcal{K} \alpha_d [\gamma_-^* + \gamma_+^* e^{-i2\Omega_{dp}t} + \delta \alpha^*] e^{i\Omega_{dp}t} (\alpha_d e^{i\Omega_{dp}t} + \gamma_- + \gamma_+ e^{i2\Omega_{dp}t} + \delta \alpha) \end{aligned}$$

$$\begin{aligned}
& + i\mathcal{K}\alpha_d \left[ \gamma_- + \gamma_+ e^{i2\Omega_{dp}t} + \delta\alpha \right] e^{-i\Omega_{dp}t} \left( \alpha_d e^{i\Omega_{dp}t} + \gamma_- + \gamma_+ e^{i2\Omega_{dp}t} + \delta\alpha \right) \\
& + i\mathcal{K} \left[ \gamma_- \gamma_+^* e^{-i2\Omega_{dp}t} + \gamma_-^* \gamma_+ e^{i2\Omega_{dp}t} \right] \left( \alpha_d e^{i\Omega_{dp}t} + \gamma_- + \gamma_+ e^{i2\Omega_{dp}t} + \delta\alpha \right) \\
& + i\mathcal{K} [\gamma_- \delta\alpha^* + \gamma_-^* \delta\alpha] \left( \alpha_d e^{i\Omega_{dp}t} + \gamma_- + \gamma_+ e^{i2\Omega_{dp}t} + \delta\alpha \right) \\
& + i\mathcal{K} [\gamma_+ \delta\alpha^* e^{i2\Omega_{dp}t} + \gamma_+^* \delta\alpha e^{-i2\Omega_{dp}t}] \left( \alpha_d e^{i\Omega_{dp}t} + \gamma_- + \gamma_+ e^{i2\Omega_{dp}t} + \delta\alpha \right) \\
& + i\sqrt{\frac{\kappa_e}{2}} \left( S_d e^{i(\Omega_{dp}t+\phi_d)} + S_p + S_0 \right). \tag{5.118}
\end{aligned}$$

Now we perform the linearization. First with respect to the Kerr drive, i.e., we omit all terms that describe amplification induced by  $\gamma_-$ ,  $\gamma_+$  and include all steady-state shifts as above in  $\mathcal{K}n_d$ . This corresponds to assuming  $\alpha_d \gg |\gamma_-|, |\gamma_+| \gg |\delta\alpha|, |Gx_0|$ . In addition, we omit terms proportional to  $\delta\alpha\delta x$ , i.e., do the optomechanical linearization. The result is

$$\begin{aligned}
& 5 \quad i\omega_d \alpha_d e^{i\Omega_{dp}t} + i\omega_p \gamma_- + i(2\omega_d - \omega_p) \gamma_+ e^{i2\Omega_{dp}t} + i\omega_p \delta\alpha + \delta\dot{\alpha} \\
= & \left[ i(\omega_0 + \mathcal{K}n_d) - \frac{\kappa}{2} \right] \alpha_d e^{i\Omega_{dp}t} + \left[ i(\omega_0 + 2\mathcal{K}n_d) - \frac{\kappa}{2} \right] \gamma_- + \left[ i(\omega_0 + 2\mathcal{K}n_d) - \frac{\kappa}{2} \right] \gamma_+ e^{i2\Omega_{dp}t} \\
& + \left[ i(\omega_0 + 2\mathcal{K}n_d) - \frac{\kappa}{2} \right] \delta\alpha - iG\delta x \left( \alpha_d e^{i\Omega_{dp}t} + \gamma_- + \gamma_+ e^{i2\Omega_{dp}t} \right) \\
& + i\mathcal{K}n_d \left( \gamma_-^* e^{i2\Omega_{dp}t} + \gamma_+^* + \delta\alpha^* e^{i2\Omega_{dp}t} \right) + i2\mathcal{K}\alpha_d [\gamma_-^* + \gamma_+] \delta\alpha e^{i\Omega_{dp}t} \\
& + i2\mathcal{K}\alpha_d [\gamma_+^* + \gamma_-] \delta\alpha e^{-i\Omega_{dp}t} + i2\mathcal{K}\alpha_d e^{i\Omega_{dp}t} \gamma_- \delta\alpha^* + i2\mathcal{K}\alpha_d e^{i3\Omega_{dp}t} \gamma_+ \delta\alpha^* \\
& + i\sqrt{\frac{\kappa_e}{2}} \left( S_d e^{i(\Omega_{dp}t+\phi_d)} + S_p + S_0 \right). \tag{5.119}
\end{aligned}$$

where the blue terms correspond to non-degenerate four-wave mixing contributions. We split this equation into four equations

$$\begin{aligned}
& \left[ \frac{\kappa}{2} + i(\Delta_d - \mathcal{K}n_d) \right] \alpha_d = i\sqrt{\frac{\kappa_e}{2}} S_d e^{i\phi_d} \\
& \left[ \frac{\kappa}{2} + i(\Delta_d - 2\mathcal{K}n_d - \Omega_{dp}) \right] \gamma_- - i\mathcal{K}n_d \gamma_+^* = i\sqrt{\frac{\kappa_e}{2}} S_p \\
& \left[ \frac{\kappa}{2} + i(\Delta_d - 2\mathcal{K}n_d + \Omega_{dp}) \right] \gamma_+ - i\mathcal{K}n_d \gamma_-^* = 0 \\
& \delta\dot{\alpha} + \left[ \frac{\kappa}{2} + i(\Delta_d - 2\mathcal{K}n_d - \Omega_{dp}) \right] \delta\alpha - i\mathcal{K}n_d \delta\alpha^* e^{i2\Omega_{dp}t} + iG\delta x \left( \alpha_d e^{i\Omega_{dp}t} + \gamma_- + \gamma_+ e^{i2\Omega_{dp}t} \right) \\
& - i2\mathcal{K}\alpha_d \left( [\gamma_-^* + \gamma_+] \delta\alpha e^{i\Omega_{dp}t} + [\gamma_- + \gamma_+] \delta\alpha e^{-i\Omega_{dp}t} + \gamma_- \delta\alpha^* e^{i\Omega_{dp}t} + \gamma_+ \delta\alpha^* e^{i3\Omega_{dp}t} \right) = i\sqrt{\frac{\kappa_e}{2}} S_0.
\end{aligned}$$

The first three of these equations are the Kerr equations for a linearized two-tone driving. Therefore, the first step of the solution is to find  $n_d$  using the third order polynomial as described above. Afterwards, we solve the equations for  $\gamma_-$  and  $\gamma_+$ . With all these numbers at hand, we proceed to solve for the optomechanical field components.

The Fourier transforms of the remaining two optomechanical equations of motion

are

$$\begin{aligned} \frac{\delta x(\Omega)}{\chi_m(\Omega)} &= \frac{\hbar G}{m} [\gamma_-^* \delta \alpha(\Omega) + \gamma_- \delta \alpha^*(-\Omega)] + \frac{\hbar G \alpha_d}{m} [\delta \alpha(\Omega + \Omega_{dp}) + \delta \alpha^*(-\Omega + \Omega_{dp})] \\ &\quad + \frac{\hbar G}{m} [\gamma_+^* \delta \alpha(\Omega + 2\Omega_{dp}) + \gamma_+ \delta \alpha^*(-\Omega + 2\Omega_{dp})] \end{aligned} \quad (5.120)$$

$$\begin{aligned} \frac{\delta \alpha(\Omega)}{\chi_p(\Omega)} &= i\mathcal{K}n_d \delta \alpha^*(-\Omega + 2\Omega_{dp}) - iG\gamma_- \delta x(\Omega) - iG\alpha_d \delta x(\Omega - \Omega_{dp}) - iG\gamma_+ \delta x(\Omega - 2\Omega_{dp}) \\ &\quad + i2\mathcal{K}\alpha_d [\gamma_-^* + \gamma_+] \delta \alpha(\Omega - \Omega_{dp}) + i2\mathcal{K}\alpha_d [\gamma_- + \gamma_+]^* \delta \alpha(\Omega + \Omega_{dp}) \\ &\quad + i2\mathcal{K}\alpha_d \gamma_- \delta \alpha^*(-\Omega + \Omega_{dp}) + i2\mathcal{K}\alpha_d \gamma_+ \delta \alpha^*(-\Omega + 3\Omega_{dp}) + i\sqrt{\frac{\kappa_e}{2}} S_0(\Omega). \end{aligned} \quad (5.121)$$

We introduce now the short-version

$$f(\Omega + j\Omega_{dp}) = f_j \quad (5.122)$$

$$f^*(-\Omega + j\Omega_{dp}) = \bar{f}_j \quad (5.123)$$

5

for any function  $f$  with  $j$  being an integer, with which the equations of motion become

$$\frac{\delta x_0}{\chi_{m,0}} = \frac{\hbar G}{m} [\gamma_-^* \delta \alpha_0 + \gamma_- \overline{\delta \alpha}_0] + \frac{\hbar G \alpha_d}{m} [\delta \alpha_1 + \overline{\delta \alpha}_1] + \frac{\hbar G}{m} [\gamma_+^* \delta \alpha_2 + \gamma_+ \overline{\delta \alpha}_2] \quad (5.124)$$

$$\begin{aligned} \frac{\delta \alpha_0}{\chi_{p,0}} &= i2\mathcal{K}\alpha_d \gamma_+ \overline{\delta \alpha}_3 + i\mathcal{K}n_d \overline{\delta \alpha}_2 + i2\mathcal{K}\alpha_d \gamma_- \overline{\delta \alpha}_1 + i2\mathcal{K}\alpha_d [\gamma_-^* + \gamma_+] \delta \alpha_{-1} \\ &\quad + i2\mathcal{K}\alpha_d [\gamma_- + \gamma_+]^* \delta \alpha_1 - iG\gamma_- \delta x_0 - iG\alpha_d \delta x_{-1} \\ &\quad - iG\gamma_+ \delta x_{-2} + i\sqrt{\frac{\kappa_e}{2}} S_{0,0}. \end{aligned} \quad (5.125)$$

Using now

$$\begin{aligned} \frac{\overline{\delta \alpha}_2}{\chi_{p,2}} &= -i2\mathcal{K}\alpha_d \gamma_+^* \delta \alpha_1 - i\mathcal{K}n_d \delta \alpha_0 - i2\mathcal{K}\alpha_d \gamma_-^* \delta \alpha_{-1} - i2\mathcal{K}\alpha_d [\gamma_- + \gamma_+]^* \overline{\delta \alpha}_1 \\ &\quad - i2\mathcal{K}\alpha_d [\gamma_-^* + \gamma_+] \overline{\delta \alpha}_3 + iG\gamma_-^* \delta x_{-2} + iG\alpha_d \delta x_{-1} + iG\gamma_+^* \delta x_0 - i\sqrt{\frac{\kappa_e}{2}} \bar{S}_{0,2} \end{aligned} \quad (5.126)$$

we can eliminate the parametric field-contribution and obtain

$$\begin{aligned} \frac{\delta \alpha_0}{\chi_{g,0}} &= i2\mathcal{K}\alpha_d [\gamma_+ - \overline{\mathcal{A}}_2 (\gamma_-^* + \gamma_+)] \overline{\delta \alpha}_3 + i2\mathcal{K}\alpha_d [\gamma_- - \overline{\mathcal{A}}_2 (\gamma_- + \gamma_+)] \overline{\delta \alpha}_1 \\ &\quad + i2\mathcal{K}\alpha_d [\gamma_-^* + \gamma_+ - \overline{\mathcal{A}}_2 \gamma_-^*] \delta \alpha_{-1} + i2\mathcal{K}\alpha_d [\gamma_- + \gamma_+^* - \overline{\mathcal{A}}_2 \gamma_+] \delta \alpha_1 \\ &\quad - iG [\gamma_- - \overline{\mathcal{A}}_2 \gamma_+] \delta x_0 - iG\alpha_d [1 - \overline{\mathcal{A}}_2] \delta x_{-1} - iG [\gamma_+ - \overline{\mathcal{A}}_2 \gamma_-^*] \delta x_{-2} \\ &\quad + i\sqrt{\frac{\kappa_e}{2}} S_{0,0} - i\overline{\mathcal{A}}_2 \sqrt{\frac{\kappa_e}{2}} \bar{S}_{0,2} \end{aligned} \quad (5.127)$$

where we used

$$\mathcal{A}_j = -i\mathcal{K}n_d \chi_{p,j}. \quad (5.128)$$

Instead of for  $j = 0$ , this equation and its parametric counterpart can easily be written down for general  $j$

$$\begin{aligned} \frac{\delta\alpha_j}{\chi_{g,j}} &= i2\mathcal{K}\alpha_d [\gamma_+ - \bar{\mathcal{A}}_{2-j}(\gamma_-^* + \gamma_+)] \bar{\delta\alpha}_{3-j} + i2\mathcal{K}\alpha_d [\gamma_- - \bar{\mathcal{A}}_{2-j}(\gamma_- + \gamma_+^*)] \bar{\delta\alpha}_{1-j} \\ &\quad + i2\mathcal{K}\alpha_d [\gamma_-^* + \gamma_+ - \bar{\mathcal{A}}_{2-j}\gamma_-^*] \delta\alpha_{j-1} + i2\mathcal{K}\alpha_d [\gamma_- + \gamma_+^* - \bar{\mathcal{A}}_{2-j}\gamma_+] \delta\alpha_{j+1} \\ &\quad - iG[\gamma_- - \bar{\mathcal{A}}_{2-j}\gamma_+] \delta x_j - iG\alpha_d [1 - \bar{\mathcal{A}}_{2-j}] \delta x_{j-1} - iG[\gamma_+ - \bar{\mathcal{A}}_{2-j}\gamma_-^*] \delta x_{j-2} \\ &\quad + i\sqrt{\frac{\kappa_e}{2}} S_{0,j} - i\bar{\mathcal{A}}_{2-j} \sqrt{\frac{\kappa_e}{2}} \bar{S}_{0,2-j} \end{aligned} \quad (5.129)$$

and

5

$$\begin{aligned} \frac{\overline{\delta\alpha}_j}{\chi_{g,j}} &= -i2\mathcal{K}\alpha_d [\gamma_+^* - \mathcal{A}_{2-j}(\gamma_- + \gamma_+^*)] \delta\alpha_{3-j} - i2\mathcal{K}\alpha_d [\gamma_-^* - \mathcal{A}_{2-j}(\gamma_-^* + \gamma_+)] \delta\alpha_{1-j} \\ &\quad - i2\mathcal{K}\alpha_d [\gamma_- + \gamma_+^* - \mathcal{A}_{2-j}\gamma_-] \bar{\delta\alpha}_{j-1} - i2\mathcal{K}\alpha_d [\gamma_-^* + \gamma_+ - \mathcal{A}_{2-j}\gamma_+] \bar{\delta\alpha}_{j+1} \\ &\quad + iG[\gamma_-^* - \mathcal{A}_{2-j}\gamma_+] \delta x_{-j} + iG\alpha_d [1 - \mathcal{A}_{2-j}] \delta x_{1-j} + iG[\gamma_+^* - \mathcal{A}_{2-j}\gamma_-] \delta x_{2-j} \\ &\quad - i\sqrt{\frac{\kappa_e}{2}} \bar{S}_{0,j} + i\mathcal{A}_{2-j} \sqrt{\frac{\kappa_e}{2}} S_{0,2-j} \end{aligned} \quad (5.130)$$

Note the particular indices in the mechanical contributions, which are due to  $\bar{\delta x}_{n-j} = \delta x_{j-n}$ .

### 5.7.9. THREE-TONE DYNAMICAL KERR BACKACTION

To calculate the dynamical backaction induced by the doubly-driven Kerr cavity, we omit any probe drives  $S_{0,j}$  for now. Also, we only keep terms linear in  $\gamma_-$ ,  $\gamma_+$ . Finally, we omit  $\delta x_j$  for  $j \neq 0, 1, 2$ , as these will not contribute to first order to the dynamical backaction. Under these conditions, we can write down the remaining terms in the four next-iteration field components contained in Eq. (5.129).

$$\frac{\delta\alpha_{-1}}{\chi_{g,-1}} = -iG[\gamma_- \mathcal{B}_{-1} - \gamma_+^* \mathcal{D}_{-1}] \delta x_{-1} - iG\alpha_d [1 - \bar{\mathcal{A}}_3] \delta x_{-2} \quad (5.131)$$

$$\frac{\delta\alpha_1}{\chi_{g,1}} = -iG\alpha_d [1 - \bar{\mathcal{A}}_1] \delta x_0 - iG[\gamma_+ \mathcal{B}_1 - \gamma_-^* \mathcal{D}_1] \delta x_{-1} \quad (5.132)$$

$$\frac{\overline{\delta\alpha}_3}{\bar{\chi}_{g,3}} = iG[\gamma_+^* \bar{\mathcal{B}}_3 - \gamma_- \bar{\mathcal{D}}_3] \delta x_{-1} + iG\alpha_d [1 - \mathcal{A}_{-1}] \delta x_{-2} \quad (5.133)$$

$$\frac{\overline{\delta\alpha}_1}{\bar{\chi}_{g,1}} = iG\alpha_d [1 - \mathcal{A}_1] \delta x_0 + iG[\gamma_-^* \bar{\mathcal{B}}_1 - \gamma_+ \bar{\mathcal{D}}_1] \delta x_{-1}. \quad (5.134)$$

With the unique replacements

$$\mathcal{B}_{-1} = 1 - i2\mathcal{K}n_d \left[ (1 - \bar{\mathcal{A}}_3)(1 - \mathcal{A}_0)\bar{\chi}_{g,2} - (1 - \bar{\mathcal{A}}_2)\chi_{g,0} \right] \quad (5.135)$$

$$\mathcal{D}_{-1} = \bar{\mathcal{A}}_3 - i2\mathcal{K}n_d \left[ (1 - \bar{\mathcal{A}}_3)(1 - \bar{\mathcal{A}}_2)\chi_{g,0} + \bar{\mathcal{A}}_3(1 - \mathcal{A}_0)\bar{\chi}_{g,2} \right] \quad (5.136)$$

$$\mathcal{B}_1 = 1 - i2\mathcal{K}n_d \left[ (1 - \bar{\mathcal{A}}_1)(1 - \mathcal{A}_0)\bar{\chi}_{g,2} - (1 - \bar{\mathcal{A}}_2)\chi_{g,0} \right] \quad (5.137)$$

$$\mathcal{D}_1 = \bar{\mathcal{A}}_1 - i2\mathcal{K}n_d \left[ (1 - \bar{\mathcal{A}}_1)(1 - \bar{\mathcal{A}}_2)\chi_{g,0} + \bar{\mathcal{A}}_1(1 - \mathcal{A}_0)\bar{\chi}_{g,2} \right] \quad (5.138)$$

$$\bar{\mathcal{B}}_3 = 1 + i2\mathcal{K}n_d \left[ (1 - \mathcal{A}_{-1})(1 - \bar{\mathcal{A}}_2)\chi_{g,0} - (1 - \mathcal{A}_0)\bar{\chi}_{g,2} \right] \quad (5.139)$$

$$\bar{\mathcal{D}}_3 = \mathcal{A}_{-1} + i2\mathcal{K}n_d \left[ (1 - \mathcal{A}_{-1})(1 - \mathcal{A}_0)\bar{\chi}_{g,2} + \mathcal{A}_{-1}(1 - \bar{\mathcal{A}}_2)\chi_{g,0} \right] \quad (5.140)$$

$$\bar{\mathcal{B}}_1 = 1 + i2\mathcal{K}n_d \left[ (1 - \mathcal{A}_1)(1 - \bar{\mathcal{A}}_2)\chi_{g,0} - (1 - \mathcal{A}_0)\bar{\chi}_{g,2} \right] \quad (5.141)$$

$$\bar{\mathcal{D}}_1 = \mathcal{A}_1 + i2\mathcal{K}n_d \left[ (1 - \mathcal{A}_1)(1 - \mathcal{A}_0)\bar{\chi}_{g,2} + \mathcal{A}_1(1 - \bar{\mathcal{A}}_2)\chi_{g,0} \right] \quad (5.142)$$

Note that the indices on the  $\mathcal{B}$  and  $\mathcal{D}$  terms are not describing a frequency shift like in the  $\delta\alpha_j \chi_{g,j}$  and  $\mathcal{A}_j$  terms, neither the labeling with the overline refers to negative frequencies or complex conjugation. Instead, these rather indicate the terms unique definition given in Eqs. (5.135) to (5.142).

Next, we inject the field relations back into the original equation for  $\delta\alpha_0$  (without the probe input) and obtain

$$\begin{aligned} \frac{\delta\alpha_0}{\chi_{g,0}} &= -2G\mathcal{K}\alpha_d\bar{\chi}_{g,3} \left[ \gamma_+ \left( 1 - \bar{\mathcal{A}}_2 \right) - \gamma_-^* \bar{\mathcal{A}}_2 \right] \left[ \gamma_+^* \bar{\mathcal{B}}_3 - \gamma_- \bar{\mathcal{D}}_3 \right] \delta x_{-1} \\ &\quad - 2G\mathcal{K}n_d\bar{\chi}_{g,3} \left[ \gamma_+ \left( 1 - \bar{\mathcal{A}}_2 \right) - \gamma_-^* \bar{\mathcal{A}}_2 \right] [1 - \mathcal{A}_{-1}] \delta x_{-2} \\ &\quad - 2G\mathcal{K}\alpha_d\bar{\chi}_{g,1} \left[ \gamma_- \left( 1 - \bar{\mathcal{A}}_2 \right) - \gamma_+^* \bar{\mathcal{A}}_2 \right] \left[ \gamma_-^* \bar{\mathcal{B}}_1 - \gamma_+ \bar{\mathcal{D}}_1 \right] \delta x_{-1} \\ &\quad - 2G\mathcal{K}n_d\bar{\chi}_{g,1} \left[ \gamma_- \left( 1 - \bar{\mathcal{A}}_2 \right) - \gamma_+^* \bar{\mathcal{A}}_2 \right] [1 - \mathcal{A}_1] \delta x_0 \\ &\quad + 2G\mathcal{K}\alpha_d\chi_{g,-1} \left[ \gamma_+ + \gamma_-^* \left( 1 - \bar{\mathcal{A}}_2 \right) \right] [\gamma_- \mathcal{B}_{-1} - \gamma_+^* \mathcal{D}_{-1}] \delta x_{-1} \\ &\quad + 2G\mathcal{K}n_d\chi_{g,-1} \left[ \gamma_+ + \gamma_-^* \left( 1 - \bar{\mathcal{A}}_2 \right) \right] [1 - \bar{\mathcal{A}}_3] \delta x_{-2} \\ &\quad + 2G\mathcal{K}\alpha_d\chi_{g,1} \left[ \gamma_- + \gamma_+^* \left( 1 - \bar{\mathcal{A}}_2 \right) \right] [\gamma_+ \mathcal{B}_1 - \gamma_-^* \mathcal{D}_1] \delta x_{-1} \\ &\quad + 2G\mathcal{K}n_d\chi_{g,1} \left[ \gamma_- + \gamma_+^* \left( 1 - \bar{\mathcal{A}}_2 \right) \right] [1 - \bar{\mathcal{A}}_1] \delta x_0 \\ &\quad - iG \left[ \gamma_- - \gamma_+^* \bar{\mathcal{A}}_2 \right] \delta x_0 - iG\alpha_d \left[ 1 - \bar{\mathcal{A}}_2 \right] \delta x_{-1} - iG \left[ \gamma_+ - \gamma_-^* \bar{\mathcal{A}}_2 \right] \delta x_{-2}. \end{aligned} \quad (5.143)$$

We perform a final variable substitution now

$$\mathcal{J}_-(\Omega) = 1 - \frac{\gamma_+^*}{\gamma_-} \bar{\mathcal{A}}_2 + i2\mathcal{K}n_d\chi_{g,1} \left[ 1 + \frac{\gamma_+^*}{\gamma_-} (1 - \bar{\mathcal{A}}_2) \right] [1 - \bar{\mathcal{A}}_1] - i2\mathcal{K}n_d\bar{\chi}_{g,1} \left[ 1 - \bar{\mathcal{A}}_2 - \frac{\gamma_+^*}{\gamma_-} \bar{\mathcal{A}}_2 \right] [1 - \mathcal{A}_1] \quad (5.144)$$

$$\mathcal{J}_+(\Omega) = 1 - \frac{\gamma_-^*}{\gamma_+} \bar{\mathcal{A}}_2 + i2\mathcal{K}n_d\chi_{g,-1} \left[ 1 + \frac{\gamma_-^*}{\gamma_+} (1 - \bar{\mathcal{A}}_2) \right] [1 - \bar{\mathcal{A}}_3] - i2\mathcal{K}n_d\bar{\chi}_{g,3} \left[ 1 - \bar{\mathcal{A}}_2 - \frac{\gamma_-^*}{\gamma_+} \bar{\mathcal{A}}_2 \right] [1 - \mathcal{A}_{-1}] \quad (5.145)$$

$$\begin{aligned} \mathcal{J}_\alpha(\Omega) = & 1 - \bar{\mathcal{A}}_2 + i2\mathcal{K}\chi_{g,1} \left[ \gamma_- + \gamma_+^* (1 - \bar{\mathcal{A}}_2) \right] [\gamma_+ \mathcal{B}_1 - \gamma_-^* \mathcal{D}_1] \\ & - i2\mathcal{K}\bar{\chi}_{g,1} \left[ \gamma_- (1 - \bar{\mathcal{A}}_2) - \gamma_+^* \bar{\mathcal{A}}_2 \right] [\gamma_-^* \bar{\mathcal{B}}_1 - \gamma_+ \bar{\mathcal{D}}_1] + i2\mathcal{K}\chi_{g,-1} \left[ \gamma_+ + \gamma_-^* (1 - \bar{\mathcal{A}}_2) \right] [\gamma_- \mathcal{B}_{-1} - \gamma_+^* \mathcal{D}_{-1}] \\ & - i2\mathcal{K}\bar{\chi}_{g,3} \left[ \gamma_+ (1 - \bar{\mathcal{A}}_2) - \gamma_-^* \bar{\mathcal{A}}_2 \right] [\gamma_+^* \bar{\mathcal{B}}_3 - \gamma_- \bar{\mathcal{D}}_3] \end{aligned} \quad (5.146)$$

where the nondegenerate four-wave mixing terms are still coded in blue and we obtain

$$\frac{\delta\alpha(\Omega)}{\chi_g(\Omega)} = -iG\gamma_- \mathcal{J}_-(\Omega) \delta x(\Omega) - iG\alpha_d \mathcal{J}_\alpha(\Omega) \delta x(\Omega - \Omega_{dp}) - iG\gamma_+ \mathcal{J}_+(\Omega) \delta x(\Omega - 2\Omega_{dp}). \quad (5.147)$$

Inserting this result into the equation of motion for the mechanical oscillator and omitting higher order displacement terms leads to the mechanical susceptibility in the weak-coupling and high- $Q_m$  regime

$$\chi_0^{\text{eff}}(\Omega) = \frac{1}{\frac{\Gamma_m}{2} + i(\Omega - \Omega_m) + \Sigma_{\text{fw}}(\Omega_m)} \quad (5.148)$$

with the four-wave backaction

$$\begin{aligned} \Sigma_{\text{fw}}(\Omega_m) = & |g_-|^2 \left[ \chi_g(\Omega_m) \mathcal{J}_-(\Omega_m) - \chi_g^*(-\Omega_m) \mathcal{J}_-^*(-\Omega_m) \right] \\ & + |g_+|^2 \left[ \chi_g(\Omega_m + 2\Omega_{dp}) \mathcal{J}_+(\Omega_m + 2\Omega_{dp}) - \chi_g^*(-\Omega_m + 2\Omega_{dp}) \mathcal{J}_+^*(-\Omega_m + 2\Omega_{dp}) \right] \\ & + g_\alpha^2 \left[ \chi_g(\Omega_m + \Omega_{dp}) \mathcal{J}_\alpha(\Omega_m + \Omega_{dp}) - \chi_g^*(-\Omega_m + \Omega_{dp}) \mathcal{J}_\alpha^*(-\Omega_m + \Omega_{dp}) \right] \end{aligned} \quad (5.149)$$

This multi-tone dynamical Kerr backaction has a very similar shape as a standard linear multi-tone backaction expression for several pump tones whose frequency difference is far detuned from the mechanical frequency. The main difference, besides the modified susceptibility  $\chi_g$ , is the  $\mathcal{J}$ -factors. These  $\mathcal{J}$ -factors take into account that the intra-cavity field one mechanical resonance frequency detuned from each of the pump tones  $\alpha_d, \gamma_-, \gamma_+$  also has contributions from the other fields due to four-wave-mixing. Without any Kerr nonlinearity, all  $\mathcal{A}$ s would be zero and all  $\mathcal{J}$ s would be 1. With exclusively degenerate FWM, only the black terms in Eqs. (5.144)-(5.146) would survive. These terms describe the interference between the red and blue sidebands of  $\alpha_d$ , which are the idler fields of each other, but they also describe the interference between the red (blue) sideband of the  $\gamma_-$  field with the blue (red) sideband of the  $\gamma_+$  field. Also these form two pairs of signal and idler fields.

In addition to these terms, there are the (in the equations blue-colored) non-degenerate FWM contributions. These modify the total backaction significantly, as can be seen in

the Fig. 5.3 or in Supplementary Fig. 5.18. Their origin and impact can be understood in two different ways. The first way is to consider that the cavity resonance frequency is permanently oscillating with the frequency  $\Omega_{dp}$  due to the beating of the  $\alpha_d$ -field with the  $\gamma_{\pm}$ -fields and by taking into account the dependence of the cavity susceptibility on the total intracavity field intensity via the Kerr nonlinearity. In this scenario, when a sideband of one of the tones is generated by mechanical motion at  $\pm\Omega_m$ , higher-order sidebands of the scattered field will be generated by the oscillating susceptibility of the modulated cavity. These higher-order sidebands are detuned by the cavity oscillation frequency  $\Omega_{dp}$  from the original field and they will fall on top of other first order mechanical sidebands at  $\pm\Omega_m \pm \Omega_{dp}$ . The second way to understand this effect is that there are four-photon processes occurring, which involve one photon at the  $\gamma_-$ -frequency  $\omega_p$  or at the  $\gamma_+$ -frequency  $2\omega_d - \omega_p$ , one photon at  $\omega_d$  and two sideband photons at different mechanical sideband frequencies.

The result is that by these processes the intracavity fluctuation field at  $\Omega$  also gets contributions from five other fluctuation frequencies, as can be clearly seen in the Eq. (114). Note that in the general picture, an infinite number of fields will contribute to the field at  $\Omega$ , but in our experimental situation, we can restrict the Fourier components to the most dominant ones.

### 5.7.10. FOUR-WAVE OMIT

If we take into account input probe fields at the frequencies of the relevant field components, the relations become

$$\frac{\delta\alpha_{-1}}{\chi_{g,-1}} = -iG[\gamma_-B_{-1} - \gamma_+^*D_{-1}] \delta x_{-1} - iG\alpha_d [1 - \bar{A}_3] \delta x_{-2} + i\sqrt{\frac{\kappa_e}{2}} S_{0,-1} - i\bar{A}_3 \sqrt{\frac{\kappa_e}{2}} \bar{S}_{0,3} \quad (5.150)$$

$$\frac{\delta\alpha_1}{\chi_{g,1}} = -iG\alpha_d [1 - \bar{A}_1] \delta x_0 - iG[\gamma_+B_1 - \gamma_-^*D_1] \delta x_{-1} + i\sqrt{\frac{\kappa_e}{2}} S_{0,1} - i\bar{A}_1 \sqrt{\frac{\kappa_e}{2}} \bar{S}_{0,1} \quad (5.151)$$

$$\frac{\delta\bar{a}_3}{\chi_{g,3}} = iG[\gamma_+^*B_3 - \gamma_-D_3] \delta x_{-1} + iG\alpha_d [1 - \bar{A}_{-1}] \delta x_{-2} - i\sqrt{\frac{\kappa_e}{2}} \bar{S}_{0,3} + i\bar{A}_{-1} \sqrt{\frac{\kappa_e}{2}} S_{0,-1} \quad (5.152)$$

$$\frac{\delta\bar{a}_1}{\chi_{g,1}} = iG\alpha_d [1 - \bar{A}_1] \delta x_0 + iG[\gamma_-^*B_1 - \gamma_+D_1] \delta x_{-1} - i\sqrt{\frac{\kappa_e}{2}} \bar{S}_{0,1} + i\bar{A}_1 \sqrt{\frac{\kappa_e}{2}} S_{0,1}. \quad (5.153)$$

Keeping all these terms, we get for the intracavity field

$$\begin{aligned} \frac{\delta\alpha(\Omega)}{\chi_g(\Omega)} &= -iG\gamma_-J_-(\Omega)\delta x(\Omega) - iG\alpha_d J_\alpha(\Omega)\delta x(\Omega - \Omega_{dp}) - iG\gamma_+J_+(\Omega)\delta x(\Omega - 2\Omega_{dp}) \\ &+ 2\mathcal{K}\alpha_d [\gamma_+ (1 - \bar{A}_2) - \gamma_-^* \bar{A}_2] \bar{\chi}_{g,3} \sqrt{\frac{\kappa_e}{2}} \bar{S}_{0,3} - 2\mathcal{K}\alpha_d \bar{A}_{-1} [\gamma_+ (1 - \bar{A}_2) - \gamma_-^* \bar{A}_2] \bar{\chi}_{g,3} \sqrt{\frac{\kappa_e}{2}} S_{0,-1} \end{aligned}$$

$$\begin{aligned}
& +2\mathcal{K}\alpha_d \left[ \gamma_- \left( 1 - \bar{\mathcal{A}}_2 \right) - \gamma_+^* \bar{\mathcal{A}}_2 \right] \bar{\chi}_{g,1} \sqrt{\frac{\kappa_e}{2}} \bar{S}_{0,1} - 2\mathcal{K}\alpha_d \mathcal{A}_1 \left[ \gamma_- \left( 1 - \bar{\mathcal{A}}_2 \right) - \gamma_+^* \bar{\mathcal{A}}_2 \right] \bar{\chi}_{g,1} \sqrt{\frac{\kappa_e}{2}} S_{0,1} \\
& - 2\mathcal{K}\alpha_d \left[ \gamma_+ + \gamma_-^* \left( 1 - \bar{\mathcal{A}}_2 \right) \right] \chi_{g,-1} \sqrt{\frac{\kappa_e}{2}} S_{0,-1} + 2\mathcal{K}\alpha_d \bar{\mathcal{A}}_3 \left[ \gamma_+ + \gamma_-^* \left( 1 - \bar{\mathcal{A}}_2 \right) \right] \chi_{g,-1} \sqrt{\frac{\kappa_e}{2}} \bar{S}_{0,3} \\
& - 2\mathcal{K}\alpha_d \left[ \gamma_- + \gamma_+^* \left( 1 - \bar{\mathcal{A}}_2 \right) \right] \chi_{g,1} \sqrt{\frac{\kappa_e}{2}} S_{0,1} + 2\mathcal{K}\alpha_d \bar{\mathcal{A}}_1 \left[ \gamma_- + \gamma_+^* \left( 1 - \bar{\mathcal{A}}_2 \right) \right] \chi_{g,1} \sqrt{\frac{\kappa_e}{2}} \bar{S}_{0,1} \\
& + i \sqrt{\frac{\kappa_e}{2}} \left[ S_{0,0} - \bar{\mathcal{A}}_2 \bar{S}_{0,2} \right]
\end{aligned} \tag{5.154}$$

To calculate the cavity response around the probe frequency, we will only have to keep a single term of these probe fields later, the one proportional to  $S_{0,0}$ . To express the total driving force to the mechanical oscillator though, we have to keep them all for now. The four-wave mixing will generate fields also at frequencies that beat with the  $\alpha_d$  and the  $\gamma_+$  field and therefore drive the mechanical oscillator. Nevertheless, the equations can be simplified according to the experimental situation

## 5

### SIGNAL RESONANCE RED-SIDEBAND PUMPING

If the optomechanical pump field  $\gamma_-$  is around the red sideband of the signal resonance and we probe around one mechanical frequency detuned from this pump, we have  $\Omega \approx \Omega_m$ . Due to the high quality factor of the mechanical oscillator, mechanical motion with  $\Omega - \Omega_{dp}$  or  $\Omega - 2\Omega_{dp}$  will be suppressed and we can neglect these terms in the equation for the field. As equation of motion for the mechanical oscillator under these conditions, we obtain

$$\begin{aligned}
\frac{\delta x_0}{\chi_{0,0}^{\text{eff}}} = & -i \frac{\hbar G}{2m\Omega_m} \left[ i\gamma_-^* \chi_{g,0} + i\gamma_+ \bar{\chi}_{g,2} \mathcal{A}_0 \right] \sqrt{\frac{\kappa_e}{2}} S_{0,0} \\
& -i \frac{\hbar G \alpha_d}{2m\Omega_m} \left[ -2\mathcal{K}\alpha_d \mathcal{A}_0 \left[ \gamma_+ \left( 1 - \bar{\mathcal{A}}_1 \right) - \gamma_-^* \bar{\mathcal{A}}_1 \right] \chi_{g,1} \bar{\chi}_{g,2} \right] \sqrt{\frac{\kappa_e}{2}} S_{0,0} \\
& -i \frac{\hbar G \alpha_d}{2m\Omega_m} \left[ -2\mathcal{K}\alpha_d \left[ \gamma_+ + \gamma_-^* \left( 1 - \bar{\mathcal{A}}_1 \right) \right] \chi_{g,1} \chi_{g,0} \right] \sqrt{\frac{\kappa_e}{2}} S_{0,0} \\
& -i \frac{\hbar G \alpha_d}{2m\Omega_m} \left[ 2\mathcal{K}\alpha_d \mathcal{A}_0 \left[ \gamma_-^* + \gamma_+ \left( 1 - \mathcal{A}_1 \right) \right] \bar{\chi}_{g,1} \bar{\chi}_{g,2} \right] \sqrt{\frac{\kappa_e}{2}} S_{0,0} \\
& -i \frac{\hbar G \alpha_d}{2m\Omega_m} \left[ 2\mathcal{K}\alpha_d \left[ \gamma_-^* \left( 1 - \mathcal{A}_1 \right) - \gamma_+ \mathcal{A}_1 \right] \bar{\chi}_{g,1} \chi_{g,0} \right] \sqrt{\frac{\kappa_e}{2}} S_{0,0}
\end{aligned} \tag{5.155}$$

which can also be written as

$$\begin{aligned}
\frac{\delta x_0}{\chi_{0,0}^{\text{eff}}} = & \frac{\hbar G}{2m\Omega_m} \gamma_-^* \chi_{g,0} \left[ 1 + i2\mathcal{K}n_d \chi_{g,1} \left( 1 - \bar{\mathcal{A}}_1 + \frac{\gamma_+}{\gamma_-^*} \right) - i2\mathcal{K}n_d \bar{\chi}_{g,1} \left( 1 - \mathcal{A}_1 - \frac{\gamma_+}{\gamma_-^*} \mathcal{A}_1 \right) \right] \sqrt{\frac{\kappa_e}{2}} S_{0,0} \\
& \frac{\hbar G}{2m\Omega_m} \gamma_+ \bar{\chi}_{g,2} \mathcal{A}_0 \left[ 1 - i2\mathcal{K}n_d \bar{\chi}_{g,1} \left( 1 - \mathcal{A}_1 + \frac{\gamma_-^*}{\gamma_+} \right) + i2\mathcal{K}n_d \chi_{g,1} \left( 1 - \bar{\mathcal{A}}_1 - \frac{\gamma_-^*}{\gamma_+} \bar{\mathcal{A}}_1 \right) \right] \sqrt{\frac{\kappa_e}{2}} S_{0,0} \\
= & \frac{\hbar G}{2m\Omega_m} \left[ \gamma_-^* \chi_{g,0} \mathcal{P}_- + \gamma_+ \bar{\chi}_{g,2} \mathcal{A}_0 \mathcal{P}_+ \right] \sqrt{\frac{\kappa_e}{2}} S_{0,0}
\end{aligned} \tag{5.156}$$

Injecting this back into the equation for the intracavity field, we get

$$\frac{\delta\alpha(\Omega)}{\chi_g(\Omega)} = i \left( 1 - g_- \left[ g_+^* \chi_g(\Omega) \mathcal{P}_-(\Omega) + g_+ \chi_g^*(-\Omega + 2\Omega_{dp}) \mathcal{A}(\Omega) \mathcal{P}_+(\Omega) \right] \mathcal{J}_-(\Omega) \chi_0^{\text{eff}}(\Omega) \right) \sqrt{\frac{\kappa_e}{2}} S_0(\Omega) \quad (5.157)$$

### IDLER RESONANCE BLUE-SIDEBAND PUMPING

If on the other hand the pump field  $\gamma_-$  is located on the blue sideband of the idler resonance and we probe around one mechanical frequency away from the corresponding  $\gamma_+$  field, we have  $\Omega - 2\Omega_{dp} \approx \Omega_m$ . In this case, mechanical motion with  $\Omega$  and  $\Omega - \Omega_{dp}$  will be irrelevant. Then,

$$\begin{aligned} \frac{\delta x_{-2}}{\chi_{0,-2}^{\text{eff}}} &= -i \frac{\hbar G}{2m\Omega_m} \left[ i\gamma_+^* \chi_{g,0} + i\gamma_- \bar{\chi}_{g,2} \mathcal{A}_0 \right] \sqrt{\frac{\kappa_e}{2}} S_{0,0} \\ &\quad -i \frac{\hbar G \alpha_d}{2m\Omega_m} \left[ -2\mathcal{K}\alpha_d \mathcal{A}_0 \left[ \gamma_- \left( 1 - \bar{\mathcal{A}}_3 \right) - \gamma_+^* \bar{\mathcal{A}}_3 \right] \chi_{g,-1} \bar{\chi}_{g,2} \right] \sqrt{\frac{\kappa_e}{2}} S_{0,0} \\ &\quad -i \frac{\hbar G \alpha_d}{2m\Omega_m} \left[ -2\mathcal{K}\alpha_d \left[ \gamma_- + \gamma_+^* \left( 1 - \bar{\mathcal{A}}_3 \right) \right] \chi_{g,-1} \chi_{g,0} \right] \sqrt{\frac{\kappa_e}{2}} S_{0,0} \\ &\quad -i \frac{\hbar G \alpha_d}{2m\Omega_m} \left[ 2\mathcal{K}\alpha_d \mathcal{A}_0 \left[ \gamma_+^* + \gamma_- \left( 1 - \mathcal{A}_{-1} \right) \right] \bar{\chi}_{g,3} \bar{\chi}_{g,2} \right] \sqrt{\frac{\kappa_e}{2}} S_{0,0} \\ &\quad -i \frac{\hbar G \alpha_d}{2m\Omega_m} \left[ 2\mathcal{K}\alpha_d \left[ \gamma_+^* \left( 1 - \mathcal{A}_{-1} \right) - \gamma_- \mathcal{A}_{-1} \right] \bar{\chi}_{g,3} \chi_{g,0} \right] \sqrt{\frac{\kappa_e}{2}} S_{0,0} \end{aligned} \quad (5.158)$$

5

$$\begin{aligned} \frac{\delta x_{-2}}{\chi_{0,-2}^{\text{eff}}} &= \frac{\hbar G}{2m\Omega_m} \gamma_+^* \chi_{g,0} \left[ 1 + i2\mathcal{K}n_d \chi_{g,-1} \left( 1 - \bar{\mathcal{A}}_3 + \frac{\gamma_-}{\gamma_+^*} \right) - i2\mathcal{K}n_d \bar{\chi}_{g,3} \left( 1 - \mathcal{A}_{-1} - \frac{\gamma_-}{\gamma_+^*} \mathcal{A}_{-1} \right) \right] \sqrt{\frac{\kappa_e}{2}} S_{0,0} \\ &\quad + \frac{\hbar G}{2m\Omega_m} \gamma_- \bar{\chi}_{g,2} \mathcal{A}_0 \left[ 1 - i2\mathcal{K}n_d \bar{\chi}_{g,3} \left( 1 - \mathcal{A}_{-1} + \frac{\gamma_+^*}{\gamma_-} \right) + i2\mathcal{K}n_d \chi_{g,-1} \left( 1 - \bar{\mathcal{A}}_3 - \frac{\gamma_+^*}{\gamma_-} \bar{\mathcal{A}}_3 \right) \right] \sqrt{\frac{\kappa_e}{2}} S_{0,0} \\ &= \frac{\hbar G}{2m\Omega_m} \left[ \gamma_+^* \chi_{g,0} \mathcal{Q}_+ + \gamma_- \bar{\chi}_{g,2} \mathcal{A}_0 \mathcal{Q}_- \right] \sqrt{\frac{\kappa_e}{2}} S_{0,0} \end{aligned} \quad (5.159)$$

Injecting this back into the equation for the intracavity field, we get

$$\frac{\delta\alpha(\Omega)}{\chi_g(\Omega)} = i \left( 1 - g_+ \left[ g_+^* \chi_g(\Omega) \mathcal{Q}_+(\Omega) + g_- \chi_g^*(-\Omega + 2\Omega_{dp}) \mathcal{A}(\Omega) \mathcal{Q}_-(\Omega) \right] \mathcal{J}_+(\Omega) \chi_0^{\text{eff}}(\Omega - 2\Omega_{dp}) \right) \sqrt{\frac{\kappa_e}{2}} S_0(\Omega) \quad (5.160)$$

### OPTOMECHANICAL CAVITY RESPONSE

The response in both cases is given by

$$S_{21}(\Omega) = 1 + i \sqrt{\frac{\kappa_e}{2}} \frac{\delta\alpha(\Omega)}{S_0(\Omega)} \quad (5.161)$$

### 5.7.11. MEASUREMENT AND DATA ANALYSIS PROTOCOL FOR FOUR-WAVE OMIT AND FOUR-WAVE DYNAMICAL BACKACTION

#### PREPARATION

- We start the experimental cycle with choosing the bias-flux operation point, either point I, and an in-plane magnetic field  $B_{\parallel}$ . We ramp the in-plane current to its corresponding value.
- A parametric drive tone is sent to the cavity with fixed frequency  $\omega_d$  and power  $P_d$  to match the chosen operation point.
- The cavity bias flux is adjusted manually to prepare the SQUID cavity in the driven Kerr-mode state.
- The frequency of the optomechanical pump is chosen to be either on the red sideband of the signal resonance or on the blue sideband of the idler resonance. The pump is activated with fixed frequency  $\omega_p$  and power  $P_p$ .

## 5

#### THE MEASUREMENT

- For the actual measurement, we start a python-based control and data acquisition script, which is programmed to wait for a terminal starting command before each data point.
- Prior to running the measurement, we input some fixed parameters to the script such as all values of the attenuators.
- We then manually adjust the probe VNA to a parameter set regarding frequency window, probe power and bandwidth in order to measure a clean OMIT response curve.
- Upon a terminal command, the script begins the acquisition and first catches all relevant information such as powers, frequencies, frequency spans, bandwidths as well as magnet DC currents from all relevant measurement equipment.
- The parameters obtained from the manually adjusted OMIT settings on the VNA are then re-used for all subsequent measurements. Based on the mechanical frequency and cavity frequency, an array of optomechanical pump frequencies is generated, which corresponds to an array of  $\delta_p$ . At the same time a corresponding set of VNA frequency ranges is generated to track the OMIT response for all the different pump frequencies.
- The script performs a narrow-band VNA scan to measure the OMIT response and stores the data in file 1, where all subsequent narrow-band scans for varying pump frequencies are attached as well.
- The script performs a wide-band VNA scan to measure the cavity response and stores the data in file 2, where all subsequent wide-band scans for varying pump frequencies are attached as well.

- At this point the script will expect an input via the terminal, which tells whether we want to take the exact same measurement again for identical parameters or if we are going to proceed to the next pump detuning.
- After receiving our choice, the script sets the VNA to the cavity center frequency with a fixed span of 1 kHz and waits upon a terminal command for measuring the two VNA scans of the next point. During this waiting window, we have the possibility to counter possible bias flux drifts by manually adjusting the out-of-plane current, while permanently monitoring the cavity response at the response minimum.
- Both measures described in the latter two bullet points are critical to obtain a consistent set of data, as sometimes the bias flux and cavity starts to drift considerably on a slow timescale (~seconds). This drift can significantly distort the captured OMIT response, which cannot be measured too fast due to the small mechanical linewidth. Another risk is that the cavity leaves the driven Kerr-state without the manual feedback control loop in between measurement points.
- After the cavity is stabilized and the measurement can proceed, the script repeats the cycle from gathering all relevant parameters from all machines to taking the two VNA traces and the waiting and stabilization time.

## DATA ANALYSIS

- Data analysis starts with a fit of the wide-band signal resonance response  $S_{21}$  using Eq. (5.15). From this fit, we obtain effective parameters for  $\kappa'$ ,  $\kappa_e$  and  $\omega_s$  and a fit of the complex background.
- Using the background fit parameters, we calculate the complex background in the narrow-band frequency window of the corresponding OMIT response scan and divide it off the measured signal.
- We convert the frequency axis of the OMIT response to frequencies relative to  $\gamma_-$  in the red-sideband case and relative to  $\gamma_+$  in the blue-sideband case and fit the background corrected and frequency-shifted OMIT response using Eq. (5.15) as well. As we are only interested in the resonance frequency and the effective linewidth of the OMIT resonance at this point, this procedure is as reliable but significantly simpler than using the full four-wave OMIT expression. As fit parameters we obtain  $\Omega_m^{\text{eff}}$  and  $\Gamma_{\text{eff}}$ .
- We subtract the corresponding bare values  $\Omega_m$  and  $\Gamma_m$  to obtain the dynamical backaction contributions  $\delta\Omega_m$  and  $\Gamma_{\text{opt}}$ . We note that to make them match with theory for the red-sideband case and the blue-sideband case simultaneously with a single set of otherwise identical parameters, the bare values slightly differ between the red and blue case. For the mechanical resonance frequency, this blue-red-difference is about 8 Hz and for the linewidth it is about 1 Hz. As the bare mechanical frequency and linewidth depend strongly on temperature (cf. section

5.7.14), a small temperature difference of the mechanical oscillator during the two measurements might be the origin of these differences.

- For the range of theoretical values (shaded area between the two solid lines in Fig. 5.3 and Supplementary Fig. 5.18), we consider uncertainties in the parameters going into the theoretical calculations. These include variations of the optomechanical single-photon coupling rate  $g_0 = 1.85 \pm 0.05$  kHz, of the driven cavity linewidth  $\kappa' = 349 \pm 20$  kHz and of the bare cavity resonance frequency  $\omega_0 = 5.2236 \pm 0.1$  MHz.

### 5.7.12. DATA FOR OMIT AND DYNAMICAL BACKACTION ON THE RED SIDE-BAND OF THE SIGNAL RESONANCE

In this section, we present data on four-wave-OMIT and dynamical four-wave backaction for an optomechanical pump field  $\gamma_-$  on the red sideband of the signal resonance with  $\omega_p = \omega_s - \Omega_m + \delta_p$ , where  $\delta_p$  is the detuning between the pump tone and the red sideband. The experimental setting is schematically shown in Supplementary Fig. 5.18a

In this configuration, we follow the usual OMIT protocol in the experiment, i.e., we pump at a frequency  $\omega_p$  around the signal resonance red sideband and probe the cavity response  $S_{21}$  in a narrow frequency window around  $\omega \approx \omega_p + \Omega_m$ . In addition, we measure the transmission in a wider range to capture the complete cavity absorption. We repeat this scheme for different detunings  $\delta_p$ , where the range of  $\delta_p$  is chosen to cover more than 2 signal resonance linewidths around the red sideband. One exemplary wide-band cavity transmission is displayed in Supplementary Fig. 5.18b, in c three corresponding narrow-band measurements are shown for three different  $\delta_p$ , clearly showing the characteristic OMIT window, representing the mechanical oscillator.

From a fit to the OMIT response, shown as lines, we extract the mechanical oscillator resonance frequency and the effective mechanical linewidth. After subtracting the bare values, we obtain the dynamical backaction contributions  $\delta\Omega_m$  and  $\Gamma_{\text{opt}}$ , which are plotted in d and e as circles.

### 5.7.13. MULTI-TONE KERR OPTOMECHANICS WITH NOISE INPUT

Working with quantum formalism for the equations of motion with noise input we obtain for the mechanical oscillator

$$\begin{aligned} \frac{\hat{b}_0}{\chi_{0,0}} &= -i \left( g_-^* \hat{a}_0 + g_- \hat{a}_0^\dagger \right) - i g_\alpha \left( \hat{a}_1 + \hat{a}_1^\dagger \right) - i \left( g_+^* \hat{a}_2 + g_+ \hat{a}_2^\dagger \right) + \sqrt{\Gamma_m} \hat{\zeta}_0 \\ \frac{\hat{b}_0^\dagger}{\chi_{0,0}} &= i \left( g_-^* \hat{a}_0 + g_- \hat{a}_0^\dagger \right) + i g_\alpha \left( \hat{a}_1 + \hat{a}_1^\dagger \right) + i \left( g_+^* \hat{a}_2 + g_+ \hat{a}_2^\dagger \right) + \sqrt{\Gamma_m} \hat{\zeta}_0^\dagger \end{aligned} \quad (5.162)$$

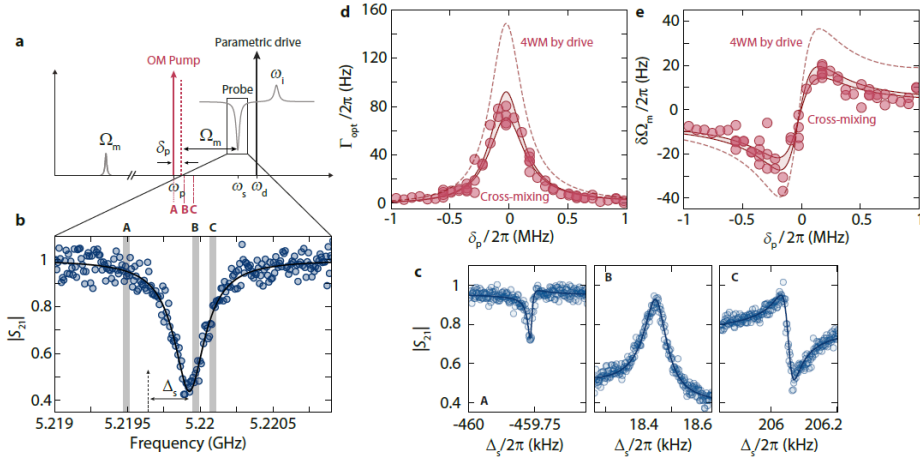


**Figure 5.18: Four-wave-OMIT and four-wave-backaction for optomechanical red-sideband pumping of the signal resonance.** Panel a shows schematically the experimental protocol. The SQUID cavity is prepared in the Kerr-mode state by a strong parametric drive. In addition, we apply an optomechanical pump tone one mechanical frequency red-detuned from the signal resonance  $\omega_p = \omega_s - \Omega_m + \delta_p$ . Finally, we use a weak probe tone around the signal resonance to detect optomechanically induced transparency. We repeat this scheme for varying detunings  $\delta_p$ . b shows the Kerr-mode signal resonance transmission  $S_{21}$  measured with the weak probe field in presence of the drive and pump tones. Circles are data, line is a fit. Gray vertical bars labeled with A, B, and C indicate zoom regions for the corresponding panels shown in c and  $\Delta_s = \omega - \omega_s$  denotes the detuning between probe field and signal resonance. In c, the probe tone response in three narrow frequency windows around  $\omega \approx \omega_p + \Omega_m$  is plotted for three different pump detunings  $\delta_p$ , cf. panel a and b. Each probe tone response displays a narrow-band resonance, indicating the phenomenon of optomechanically induced transparency ( OMIT) via excitation of the mechanical oscillator and corresponding interference between the probe field and mechanical sidebands of intracavity drive and pump fields. For each  $\delta_p$ , we fit the OMIT response, corresponding curves are shown as lines in c, and extract the effective mechanical resonance frequency  $\Omega_{\text{eff}} = \Omega_m + \delta\Omega_m$  and the effective mechanical linewidth  $\Gamma_{\text{eff}} = \Gamma_m + \Gamma_{\text{opt}}$ . The contributions  $\delta\Omega_m$  and  $\Gamma_{\text{opt}}$ , induced by dynamical backaction of the total intracavity fields, are plotted in panels d and e as circles vs detuning of the pump tone from the red sideband of the signal resonance. The result of analytical calculations is shown as two solid lines with shaded area, where the range described by the lines captures uncertainties in the device parameters, cf. text. The dashed line shows the result of equivalent calculations without taking into account cross-mixing terms.

and for the intracavity fluctuation fields

$$\begin{aligned} \frac{\hat{a}_0}{\chi_{p,0}} &= i\mathcal{K}n_d\hat{a}_2^\dagger - ig_- (\hat{b}_0 + \hat{b}_0^\dagger) - ig_\alpha (\hat{b}_{-1} + \hat{b}_1^\dagger) - ig_+ (\hat{b}_{-2} + \hat{b}_2^\dagger) \\ &\quad + i2\mathcal{K}\alpha_d [\gamma_-^* + \gamma_+] \hat{a}_{-1} + i2\mathcal{K}\alpha_d [\gamma_- + \gamma_+] \hat{a}_1 + i2\mathcal{K}\alpha_d \gamma_- \hat{a}_1^\dagger + i2\mathcal{K}\alpha_d \gamma_+ \hat{a}_3^\dagger \\ &\quad + \sqrt{\kappa_e} \hat{\xi}_{e0+} + \sqrt{\kappa_i} \hat{\xi}_{i0+} \end{aligned} \quad (5.163)$$

$$\begin{aligned} \frac{\hat{a}_2^\dagger}{\chi_{p,2}} &= -i\mathcal{K}n_d \hat{a}_0 + ig_-^* (\hat{b}_{-2} + \hat{b}_2^\dagger) + ig_\alpha (\hat{b}_{-1} + \hat{b}_{-1}^\dagger) + ig_+^* (\hat{b}_0 + \hat{b}_0^\dagger) \\ &\quad - i2\mathcal{K}\alpha_d [\gamma_- + \gamma_+] \hat{a}_1^\dagger - i2\mathcal{K}\alpha_d [\gamma_-^* + \gamma_+] \hat{a}_3^\dagger - i2\mathcal{K}\alpha_d \gamma_-^* \hat{a}_{-1} - i2\mathcal{K}\alpha_d \gamma_+^* \hat{a}_1 \\ &\quad + \sqrt{\kappa_e} \hat{\xi}_{e2-}^\dagger + \sqrt{\kappa_i} \hat{\xi}_{i2-}^\dagger \end{aligned} \quad (5.164)$$

The latter two equations can be combined into

$$\begin{aligned} \frac{\hat{a}_0}{\chi_{g,0}} &= i2\mathcal{K}\alpha_d \left[ \gamma_- \left( 1 - \bar{\mathcal{A}}_2 \right) - \gamma_+^* \bar{\mathcal{A}}_2 \right] \hat{a}_1^\dagger + i2\mathcal{K}\alpha_d \left[ \gamma_+ \left( 1 - \bar{\mathcal{A}}_2 \right) - \gamma_-^* \bar{\mathcal{A}}_2 \right] \hat{a}_3^\dagger \\ &\quad + i2\mathcal{K}\alpha_d \left[ \gamma_+ + \gamma_-^* \left( 1 - \bar{\mathcal{A}}_2 \right) \right] \hat{a}_{-1} + i2\mathcal{K}\alpha_d \left[ \gamma_- + \gamma_+^* \left( 1 - \bar{\mathcal{A}}_2 \right) \right] \hat{a}_1 \\ &\quad - i \left( g_- - g_+^* \bar{\mathcal{A}}_2 \right) \left( \hat{b}_0 + \hat{b}_0^\dagger \right) - ig_\alpha \left( 1 - \bar{\mathcal{A}}_2 \right) \left( \hat{b}_{-1} + \hat{b}_1^\dagger \right) \\ &\quad - i \left( g_+ - g_-^* \bar{\mathcal{A}}_2 \right) \left( \hat{b}_{-2} + \hat{b}_2^\dagger \right) + \hat{\mathcal{N}}_{0+} + \bar{\mathcal{A}}_2 \hat{\mathcal{N}}_{2-}^\dagger \end{aligned} \quad (5.165)$$

with

$$\hat{\mathcal{N}}_{0+} = \sqrt{\kappa_e} \hat{\xi}_{e0+} + \sqrt{\kappa_i} \hat{\xi}_{i0+} \quad \hat{\mathcal{N}}_{2-}^\dagger = \sqrt{\kappa_e} \hat{\xi}_{e2-}^\dagger + \sqrt{\kappa_i} \hat{\xi}_{i2-}^\dagger. \quad (5.166)$$

Just as for the classical equations, we need now the next iteration field components

$$\frac{\hat{a}_{-1}}{\chi_{g,-1}} = -i [g_- \mathcal{B}_{-1} - g_+^* \mathcal{D}_{-1}] \left( \hat{b}_{-1} + \hat{b}_1^\dagger \right) - ig_\alpha \left( 1 - \bar{\mathcal{A}}_3 \right) \left( \hat{b}_{-2} + \hat{b}_2^\dagger \right) + \hat{\mathcal{N}}_{-1+} + \bar{\mathcal{A}}_3 \hat{\mathcal{N}}_{3-}^\dagger \quad (5.167)$$

$$\frac{\hat{a}_1}{\chi_{g,1}} = -ig_\alpha \left( 1 - \bar{\mathcal{A}}_1 \right) \left( \hat{b}_0 + \hat{b}_0^\dagger \right) - i [g_+ \mathcal{B}_1 - g_-^* \mathcal{D}_1] \left( \hat{b}_{-1} + \hat{b}_1^\dagger \right) + \hat{\mathcal{N}}_{1+} + \bar{\mathcal{A}}_1 \hat{\mathcal{N}}_{1-}^\dagger \quad (5.168)$$

$$\frac{\hat{a}_1^\dagger}{\chi_{g,1}} = ig_\alpha \left( 1 - \mathcal{A}_1 \right) \left( \hat{b}_0 + \hat{b}_0^\dagger \right) + i [g_+^* \bar{\mathcal{B}}_1 - g_+ \bar{\mathcal{D}}_1] \left( \hat{b}_{-1} + \hat{b}_1^\dagger \right) + \hat{\mathcal{N}}_{1-}^\dagger + \mathcal{A}_1 \hat{\mathcal{N}}_{1+} \quad (5.169)$$

$$\frac{\hat{a}_3^\dagger}{\chi_{g,3}} = i [g_+^* \bar{\mathcal{B}}_3 - g_- \bar{\mathcal{D}}_3] \left( \hat{b}_{-1} + \hat{b}_1^\dagger \right) + ig_\alpha \left( 1 - \mathcal{A}_{-1} \right) \left( \hat{b}_{-2} + \hat{b}_2^\dagger \right) + \hat{\mathcal{N}}_{3-}^\dagger + \mathcal{A}_{-1} \hat{\mathcal{N}}_{-1+} \quad (5.170)$$

which lead to an expression for  $\hat{a}_0$  given by

$$\begin{aligned} \frac{\hat{a}_0}{\chi_{g,0}} &= -ig_- \mathcal{J}_- \left( \hat{b}_0 + \hat{b}_0^\dagger \right) - ig_\alpha \mathcal{J}_\alpha \left( \hat{b}_{-1} + \hat{b}_1^\dagger \right) - ig_+ \mathcal{J}_+ \left( \hat{b}_{-2} + \hat{b}_2^\dagger \right) \\ &\quad + i2\mathcal{K}\alpha_d \left[ \left[ \gamma_- \left( 1 - \bar{\mathcal{A}}_2 \right) - \gamma_+^* \bar{\mathcal{A}}_2 \right] \mathcal{A}_1 \bar{\chi}_{g,1} + \left[ \gamma_- + \gamma_+^* \left( 1 - \bar{\mathcal{A}}_2 \right) \right] \chi_{g,1} \right] \hat{\mathcal{N}}_{1+} \\ &\quad + i2\mathcal{K}\alpha_d \left[ \left[ \gamma_- \left( 1 - \bar{\mathcal{A}}_2 \right) - \gamma_+^* \bar{\mathcal{A}}_2 \right] \bar{\chi}_{g,1} + \left[ \gamma_- + \gamma_+^* \left( 1 - \bar{\mathcal{A}}_2 \right) \right] \bar{\mathcal{A}}_1 \chi_{g,1} \right] \hat{\mathcal{N}}_{1-}^\dagger \\ &\quad + i2\mathcal{K}\alpha_d \left[ \left[ \gamma_+ \left( 1 - \bar{\mathcal{A}}_2 \right) - \gamma_-^* \bar{\mathcal{A}}_2 \right] \bar{\chi}_{g,3} + \left[ \gamma_+ + \gamma_-^* \left( 1 - \bar{\mathcal{A}}_2 \right) \right] \bar{\mathcal{A}}_3 \chi_{g,-1} \right] \hat{\mathcal{N}}_{3-}^\dagger \\ &\quad + i2\mathcal{K}\alpha_d \left[ \left[ \gamma_+ \left( 1 - \bar{\mathcal{A}}_2 \right) - \gamma_-^* \bar{\mathcal{A}}_2 \right] \mathcal{A}_{-1} \bar{\chi}_{g,3} + \left[ \gamma_+ + \gamma_-^* \left( 1 - \bar{\mathcal{A}}_2 \right) \right] \chi_{g,-1} \right] \hat{\mathcal{N}}_{-1+} \\ &\quad + \hat{\mathcal{N}}_{0+} + \bar{\mathcal{A}}_2 \hat{\mathcal{N}}_{2-}^\dagger \\ &= -ig_- \mathcal{J}_- \left( \hat{b}_0 + \hat{b}_0^\dagger \right) - ig_\alpha \mathcal{J}_\alpha \left( \hat{b}_{-1} + \hat{b}_1^\dagger \right) - ig_+ \mathcal{J}_+ \left( \hat{b}_{-2} + \hat{b}_2^\dagger \right) \\ &\quad + \mathcal{Y}_{1+} \hat{\mathcal{N}}_{1+} + \bar{\mathcal{Y}}_{1-} \hat{\mathcal{N}}_{1-}^\dagger + \bar{\mathcal{Y}}_{3-} \hat{\mathcal{N}}_{3-}^\dagger + \mathcal{Y}_{-1+} \hat{\mathcal{N}}_{-1+} + \hat{\mathcal{N}}_{0+} + \bar{\mathcal{A}}_2 \hat{\mathcal{N}}_{2-}^\dagger \end{aligned} \quad (5.171)$$

or, in its shortest version

$$\frac{\hat{a}_0}{\chi_{g,0}} = -ig_- \mathcal{J}_- (\Omega) \left( \hat{b}_0 + \hat{b}_0^\dagger \right) - ig_\alpha \mathcal{J}_\alpha (\Omega) \left( \hat{b}_{-1} + \hat{b}_1^\dagger \right) - ig_+ \mathcal{J}_+ (\Omega) \left( \hat{b}_{-2} + \hat{b}_2^\dagger \right) + \hat{\mathcal{M}}_{0+} \quad (5.172)$$

and the corresponding equation for  $\hat{a}^\dagger$

$$\frac{\hat{a}_0^\dagger}{\bar{\chi}_{g,0}} = ig_-^* \mathcal{J}_-^*(-\Omega) \left( \hat{b}_0 + \hat{b}_0^\dagger \right) + ig_\alpha \mathcal{J}_\alpha^*(-\Omega) \left( \hat{b}_1 + \hat{b}_{-1}^\dagger \right) + ig_+ \mathcal{J}_+^*(-\Omega) \left( \hat{b}_2 + \hat{b}_{-2}^\dagger \right) + \hat{\mathcal{M}}_{0-}^\dagger. \quad (5.173)$$

## SIGNAL RESONANCE RED SIDEBAND PUMPING

Next we use

$$\hat{b}_0 + \hat{b}_0^\dagger = -i(\chi_{0,0} - \bar{\chi}_{0,0}) \left( g_-^* \hat{a}_0 + g_- \hat{a}_0^\dagger \right) - i g_\alpha (\chi_{0,0} - \bar{\chi}_{0,0}) \left( \hat{a}_1 + \hat{a}_1^\dagger \right) - i(\chi_{0,0} - \bar{\chi}_{0,0}) \left( g_+^* \hat{a}_2 + g_+ \hat{a}_2^\dagger \right) + \hat{S} \quad (5.174)$$

and keep only first order terms to obtain

$$\begin{aligned} \hat{b}_0 + \hat{b}_0^\dagger &= -|g_-|^2 (\chi_{0,0} - \bar{\chi}_{0,0}) \left[ \mathcal{J}_-(\Omega) \chi_{g,0} - \mathcal{J}_-^*(-\Omega) \bar{\chi}_{g,0} \right] \left( \hat{b}_0 + \hat{b}_0^\dagger \right) \\ &- g_\alpha^2 (\chi_{0,0} - \bar{\chi}_{0,0}) \left[ \mathcal{J}_\alpha(\Omega + \Omega_{dp}) \chi_{g,1} - \mathcal{J}_\alpha^*(-\Omega + \Omega_{dp}) \bar{\chi}_{g,1} \right] \left( \hat{b}_0 + \hat{b}_0^\dagger \right) \\ &- |g_+|^2 (\chi_{0,0} - \bar{\chi}_{0,0}) \left[ \mathcal{J}_+(\Omega + 2\Omega_{dp}) \chi_{g,2} - \mathcal{J}_+^*(-\Omega + 2\Omega_{dp}) \bar{\chi}_{g,2} \right] \left( \hat{b}_0 + \hat{b}_0^\dagger \right) \\ &- i(\chi_{0,0} - \bar{\chi}_{0,0}) \left[ g_-^* \chi_{g,0} \hat{\mathcal{M}}_{0+} + g_- \bar{\chi}_{g,0} \hat{\mathcal{M}}_{0-}^\dagger + g_\alpha \chi_{g,1} \hat{\mathcal{M}}_{1+} + g_\alpha \bar{\chi}_{g,1} \hat{\mathcal{M}}_{1-}^\dagger + g_+^* \chi_{g,2} \hat{\mathcal{M}}_{2+} + g_+ \bar{\chi}_{g,2} \hat{\mathcal{M}}_{2-}^\dagger \right] + \hat{S} \end{aligned} \quad (5.175)$$

We can find our earlier obtained four-wave dynamical backaction in this relation and write

$$\begin{aligned} \hat{b}_0 + \hat{b}_0^\dagger &= -i \frac{\chi_{0,0} - \bar{\chi}_{0,0}}{1 + (\chi_{0,0} - \bar{\chi}_{0,0}) \Sigma_{fw}(\Omega_m)} \left[ g_-^* \chi_{g,0} \hat{\mathcal{M}}_{0+} + g_- \bar{\chi}_{g,0} \hat{\mathcal{M}}_{0-}^\dagger + g_\alpha \chi_{g,1} \hat{\mathcal{M}}_{1+} \right. \\ &\quad \left. + g_\alpha \bar{\chi}_{g,1} \hat{\mathcal{M}}_{1-}^\dagger + g_+^* \chi_{g,2} \hat{\mathcal{M}}_{2+} + g_+ \bar{\chi}_{g,2} \hat{\mathcal{M}}_{2-}^\dagger \right] + \frac{\hat{S}}{1 + (\chi_{0,0} - \bar{\chi}_{0,0}) \Sigma_{fw}(\Omega_m)} \end{aligned} \quad (5.176)$$

For a pump on the red sideband of the signal resonance, a high mechanical quality factor and the detection frequency to be  $\Omega \approx \Omega_m$ , we can simplify the relations, i.e., keep only dominant terms and obtain

$$\hat{a}_0 = -ig_- \mathcal{J}_-(\Omega) \chi_{g,0} \hat{b}_0 + \chi_{g,0} \hat{\mathcal{M}}_{0+} \quad (5.177)$$

$$\hat{a}_0^\dagger = ig_-^* \mathcal{J}_-^*(-\Omega) \bar{\chi}_{g,0} \hat{b}_0 + \bar{\chi}_{g,0} \hat{\mathcal{M}}_{0-}^\dagger \quad (5.178)$$

$$\hat{a}_1 = -ig_\alpha \mathcal{J}_\alpha(\Omega + \Omega_{dp}) \chi_{g,1} \hat{b}_0 + \chi_{g,1} \hat{\mathcal{M}}_{1+} \quad (5.179)$$

$$\hat{a}_1^\dagger = ig_\alpha \mathcal{J}_\alpha^*(-\Omega + \Omega_{dp}) \bar{\chi}_{g,1} \hat{b}_0 + \bar{\chi}_{g,1} \hat{\mathcal{M}}_{1-}^\dagger \quad (5.180)$$

$$\hat{a}_2 = -ig_+ \mathcal{J}_+(\Omega + 2\Omega_{dp}) \chi_{g,2} \hat{b}_0 + \chi_{g,2} \hat{\mathcal{M}}_{2+} \quad (5.181)$$

$$\hat{a}_2^\dagger = ig_+^* \mathcal{J}_+^*(-\Omega + 2\Omega_{dp}) \bar{\chi}_{g,2} \hat{b}_0 + \bar{\chi}_{g,2} \hat{\mathcal{M}}_{2-}^\dagger \quad (5.182)$$

For the detection frequency range, we therefore get

$$\begin{aligned} \hat{a}_0 &= -g_- \mathcal{J}_-(\Omega) \chi_{g,0} \chi_{0,0}^{\text{eff}} \left[ g_-^* \chi_{g,0} \hat{\mathcal{M}}_{0+} + g_- \bar{\chi}_{g,0} \hat{\mathcal{M}}_{0-}^\dagger + g_\alpha \chi_{g,1} \hat{\mathcal{M}}_{1+} + g_\alpha \bar{\chi}_{g,1} \hat{\mathcal{M}}_{1-}^\dagger \right. \\ &\quad \left. + g_+^* \chi_{g,2} \hat{\mathcal{M}}_{2+} + g_+ \bar{\chi}_{g,2} \hat{\mathcal{M}}_{2-}^\dagger \right] - ig_- \mathcal{J}_-(\Omega) \chi_{g,0} \chi_{0,0}^{\text{eff}} \sqrt{\Gamma_m} \hat{\zeta} + \chi_{g,0} \hat{\mathcal{M}}_{0+} \end{aligned} \quad (5.183)$$

where we applied  $\bar{\chi}_{0,0} \approx 0$  for  $\Omega \approx \Omega_m$ . Note that the cavity noise is well described for all frequencies in this approximation, but the upconverted mechanical noise is limited

to one of the many sidebands. We can resolve and sort now for input noise frequency components, where we only keep cavity input noise terms around the signal and the idler resonances. The result is

$$\begin{aligned}\hat{a}_0 &= -g_- \mathcal{J}_-(\Omega) \chi_{g,0} \chi_{0,0}^{\text{eff}} \left[ g_-^* \chi_{g,0} \hat{\mathcal{M}}_{0+} + g_- \bar{\chi}_{g,0} \hat{\mathcal{M}}_{0-}^\dagger + g_\alpha \chi_{g,1} \hat{\mathcal{M}}_{1+} + g_\alpha \bar{\chi}_{g,1} \hat{\mathcal{M}}_{1-}^\dagger \right. \\ &\quad \left. + g_+ \chi_{g,2} \hat{\mathcal{M}}_{2+} + g_+^* \bar{\chi}_{g,2} \hat{\mathcal{M}}_{2-}^\dagger \right] - i g_- \mathcal{J}_-(\Omega) \chi_{g,0} \chi_{0,0}^{\text{eff}} \sqrt{\Gamma_m} \hat{\zeta} + \chi_{g,0} \hat{\mathcal{M}}_{0+} \\ &\approx -i g_- \mathcal{J}_-(\Omega) \chi_{g,0} \chi_{0,0}^{\text{eff}} \left[ \sqrt{\Gamma_m} \hat{\zeta} - i \left( g_-^* \chi_{g,0} \mathcal{P}_- + g_+ \mathcal{A}_0 \mathcal{P}_+ \bar{\chi}_{g,2} \right) \hat{\mathcal{N}}_{0+} \right. \\ &\quad \left. - i \left( g_-^* \bar{\mathcal{A}}_2 \mathcal{P}_- \chi_{g,0} + g_+ \mathcal{P}_+ \bar{\chi}_{g,2} \right) \hat{\mathcal{N}}_{2-}^\dagger \right] + \chi_{g,0} \hat{\mathcal{N}}_{0+} + \chi_{g,0} \bar{\mathcal{A}}_2 \hat{\mathcal{N}}_{2-}^\dagger \end{aligned} \quad (5.184)$$

with

$$\mathcal{P}_- = \left[ 1 + i 2 \mathcal{K} n_d \chi_{g,1} \left( 1 - \bar{\mathcal{A}}_1 + \frac{g_+}{g_-^*} \right) - i 2 \mathcal{K} n_d \bar{\chi}_{g,1} \left( 1 - \mathcal{A}_1 - \frac{g_+}{g_-^*} \mathcal{A}_1 \right) \right] \quad (5.185)$$

$$\mathcal{P}_+ = \left[ 1 - i 2 \mathcal{K} n_d \bar{\chi}_{g,1} \left( 1 - \mathcal{A}_1 + \frac{g_-^*}{g_+} \right) + i 2 \mathcal{K} n_d \chi_{g,1} \left( 1 - \bar{\mathcal{A}}_1 - \frac{g_-^*}{g_+} \bar{\mathcal{A}}_1 \right) \right] \quad (5.186)$$

For the cavity output field on one side of the feedline, we get

$$\begin{aligned}\hat{a}_{\text{out}} &= \hat{\xi}_{e0+}^{\text{left}} - \sqrt{\frac{\kappa_e}{2}} \hat{a}_0 \\ &= -i g_- \mathcal{J}_-(\Omega) \chi_{g,0} \chi_{0,0}^{\text{eff}} \sqrt{\frac{\kappa_e}{2}} \sqrt{\Gamma_m} \hat{\zeta} \\ &\quad + \chi_{g,0} \sqrt{\frac{\kappa_e}{2}} \left[ 1 - g_- \mathcal{J}_-(\Omega) \chi_{0,0}^{\text{eff}} \left( g_-^* \chi_{g,0} \mathcal{P}_- + g_+ \mathcal{A}_0 \mathcal{P}_+ \bar{\chi}_{g,2} \right) \right] \sqrt{\kappa_i} \hat{\xi}_{i0+} \\ &\quad + \chi_{g,0} \sqrt{\frac{\kappa_e}{2}} \left[ 1 - g_- \mathcal{J}_-(\Omega) \chi_{0,0}^{\text{eff}} \left( g_-^* \chi_{g,0} \mathcal{P}_- + g_+ \mathcal{A}_0 \mathcal{P}_+ \bar{\chi}_{g,2} \right) \right] \sqrt{\frac{\kappa_e}{2}} \hat{\xi}_{e0+}^{\text{right}} \\ &\quad + \chi_{g,0} \sqrt{\frac{\kappa_e}{2}} \left[ \bar{\mathcal{A}}_2 - g_- \mathcal{J}_-(\Omega) \chi_{0,0}^{\text{eff}} \left( g_-^* \chi_{g,0} \bar{\mathcal{A}}_2 \mathcal{P}_- + g_+ \mathcal{P}_+ \bar{\chi}_{g,2} \right) \right] \sqrt{\kappa_i} \hat{\xi}_{i2-}^\dagger \\ &\quad + \chi_{g,0} \sqrt{\frac{\kappa_e}{2}} \left[ \bar{\mathcal{A}}_2 - g_- \mathcal{J}_-(\Omega) \chi_{0,0}^{\text{eff}} \left( g_-^* \chi_{g,0} \bar{\mathcal{A}}_2 \mathcal{P}_- + g_+ \mathcal{P}_+ \bar{\chi}_{g,2} \right) \right] \sqrt{\kappa_e} \hat{\xi}_{e2-}^\dagger \\ &\quad + \left( 1 - \chi_{g,0} \sqrt{\frac{\kappa_e}{2}} \left[ 1 - g_- \mathcal{J}_-(\Omega) \chi_{0,0}^{\text{eff}} \left( g_-^* \chi_{g,0} \mathcal{P}_- + g_+ \mathcal{A}_0 \mathcal{P}_+ \bar{\chi}_{g,2} \right) \right] \sqrt{\frac{\kappa_e}{2}} \right) \hat{\xi}_{e0+}^{\text{left}} \end{aligned} \quad (5.187)$$

where we split the relevant external input noise into the contributions from the left and the right side of the feedline. This can be used directly to calculate the symmetrized output field power spectral density in units of phonons as

$$\frac{S(\omega)}{\hbar \omega} = n_{\text{add}} + \frac{1}{2} \langle \hat{a}_{\text{out}}^\dagger \hat{a}_{\text{out}} + \hat{a}_{\text{out}} \hat{a}_{\text{out}}^\dagger \rangle. \quad (5.188)$$

The total number of noise photons added by our detection chain is found to be  $n_{\text{add}} \approx 13$  from a thermal calibration of the residual occupation of the mechanical oscillator, cf. sections 5.7.14 and 5.7.15.

To calculate the corresponding phonon occupation, we use the relations (5.177) - (5.182) and keep only cavity noise input terms for  $\hat{\mathcal{N}}_{0+}$  and  $\hat{\mathcal{N}}_{2-}^\dagger$

$$\frac{\hat{b}_0}{\chi_{0,0}^{\text{eff}}} = -ig_-^* \mathcal{P}_- \chi_{g,0} [\hat{\mathcal{N}}_{0+} + \bar{\mathcal{A}}_2 \hat{\mathcal{N}}_{2-}^\dagger] - ig_+ \mathcal{P}_+ \bar{\chi}_{g,2} [\hat{\mathcal{N}}_{2-}^\dagger + \mathcal{A}_0 \hat{\mathcal{N}}_{0+}] + \sqrt{\Gamma_m} \hat{\zeta} \quad (5.189)$$

which gives the mechanical power spectral density

$$\langle \hat{b}_0^\dagger \hat{b}_0 \rangle = |\chi_{0,0}^{\text{eff}}|^2 |g_-^* \mathcal{P}_- \chi_{g,0} + g_+ \mathcal{P}_+ \mathcal{A}_0 \bar{\chi}_{g,2}|^2 \kappa n_c^{\text{th}} + |\chi_{0,0}^{\text{eff}}|^2 |g_-^* \mathcal{P}_- \bar{\mathcal{A}}_2 \chi_{g,0} + g_+ \mathcal{P}_+ \bar{\chi}_{g,2}|^2 \kappa (n_c^{\text{th}} + 1) + |\chi_{0,0}^{\text{eff}}|^2 \Gamma_m n_m^{\text{th}}. \quad (5.190)$$

The integration of this relation over all frequencies then results in the effective phonon occupation in presence of the optomechanical coupling.

## IDLER RESONANCE BLUE SIDEBAND PUMPING

In this case, we use

$$\begin{aligned} \hat{b}_{-2} + \hat{b}_2^\dagger &= -i(\chi_{0,-2} - \bar{\chi}_{0,2}) (g_-^* \hat{a}_{-2} + g_- \hat{a}_2^\dagger) - ig_\alpha (\chi_{0,-2} - \bar{\chi}_{0,-2}) (\hat{a}_{-1} + \hat{a}_3^\dagger) \\ &\quad - i(\chi_{0,-2} - \bar{\chi}_{0,2}) (g_+^* \hat{a}_0 + g_+ \hat{a}_4^\dagger) + \hat{S} \end{aligned} \quad (5.191)$$

and keep only first order terms to obtain

$$\begin{aligned} \hat{b}_{-2} + \hat{b}_2^\dagger &= -|g_-|^2 (\chi_{0,-2} - \bar{\chi}_{0,2}) [\mathcal{J}_-(\Omega - 2\Omega_{dp}) \chi_{g,-2} - \mathcal{J}_-^*(-\Omega + 2\Omega_{dp}) \bar{\chi}_{g,2}] (\hat{b}_{-2} + \hat{b}_2^\dagger) \\ &\quad - g_\alpha^2 (\chi_{0,-2} - \bar{\chi}_{0,2}) [\mathcal{J}_\alpha(\Omega - \Omega_{dp}) \chi_{g,-1} - \mathcal{J}_\alpha^*(-\Omega + 3\Omega_{dp}) \bar{\chi}_{g,3}] (\hat{b}_{-2} + \hat{b}_2^\dagger) \\ &\quad - |g_+|^2 (\chi_{0,-2} - \bar{\chi}_{0,2}) [\mathcal{J}_+(\Omega) \chi_{g,0} - \mathcal{J}_+^*(-\Omega + 4\Omega_{dp}) \bar{\chi}_{g,4}] (\hat{b}_{-2} + \hat{b}_2^\dagger) \\ &\quad - i(\chi_{0,-2} - \bar{\chi}_{0,2}) [g_-^* \chi_{g,-2} \hat{\mathcal{M}}_{-2+} + g_- \bar{\chi}_{g,2} \hat{\mathcal{M}}_{2-}^\dagger + g_\alpha \chi_{g,-1} \hat{\mathcal{M}}_{-1+} \\ &\quad + g_\alpha \bar{\chi}_{g,3} \hat{\mathcal{M}}_{3-}^\dagger + g_+^* \chi_{g,0} \hat{\mathcal{M}}_{0+} + g_+ \bar{\chi}_{g,4} \hat{\mathcal{M}}_{4-}^\dagger] + \hat{S} \end{aligned} \quad (5.192)$$

We can find our earlier obtained four-wave dynamical backaction in this relation and write

$$\begin{aligned} \hat{b}_{-2} + \hat{b}_2^\dagger &= -i \frac{\chi_{0,-2} - \bar{\chi}_{0,2}}{1 + (\chi_{0,-2} - \bar{\chi}_{0,2}) \Sigma_{\text{fw}}(\Omega_m)} [g_-^* \chi_{g,-2} \hat{\mathcal{M}}_{-2+} + g_- \bar{\chi}_{g,2} \hat{\mathcal{M}}_{2-}^\dagger + g_\alpha \chi_{g,-1} \hat{\mathcal{M}}_{-1+} \\ &\quad + g_\alpha \bar{\chi}_{g,3} \hat{\mathcal{M}}_{3-}^\dagger + g_+^* \chi_{g,0} \hat{\mathcal{M}}_{0+} + g_+ \bar{\chi}_{g,4} \hat{\mathcal{M}}_{4-}^\dagger] + \frac{\hat{S}}{1 + (\chi_{0,-2} - \bar{\chi}_{0,2}) \Sigma_{\text{fw}}(\Omega_m)} \end{aligned} \quad (5.193)$$

For a pump on the blue sideband of the idler resonance, a high mechanical quality factor and the detection frequency to be  $\Omega \approx \Omega_m - 2\Omega_{dp}$ , we can simplify the cavity field

operator relations, i.e., keep only dominant terms and obtain

$$\hat{a}_{-2} = -ig_{-}\mathcal{J}_{-}(\Omega - 2\Omega_{dp})\chi_{g,-2}\hat{b}_{-2} + \chi_{g,-2}\hat{\mathcal{M}}_{-2+} \quad (5.194)$$

$$\hat{a}_2^{\dagger} = ig_{-}^{*}\mathcal{J}_{-}^{*}(-\Omega + 2\Omega_{dp})\bar{\chi}_{g,2}\hat{b}_{-2} + \bar{\chi}_{g,2}\hat{\mathcal{M}}_{2-}^{\dagger} \quad (5.195)$$

$$\hat{a}_{-1} = -ig_{\alpha}\mathcal{J}_{\alpha}(\Omega - \Omega_{dp})\chi_{g,-1}\hat{b}_{-2} + \chi_{g,-1}\hat{\mathcal{M}}_{-1+} \quad (5.196)$$

$$\hat{a}_3^{\dagger} = ig_{\alpha}\mathcal{J}_{\alpha}^{*}(-\Omega + 3\Omega_{dp})\bar{\chi}_{g,3}\hat{b}_{-2} + \bar{\chi}_{g,3}\hat{\mathcal{M}}_{3-}^{\dagger} \quad (5.197)$$

$$\hat{a}_0 = -ig_{+}\mathcal{J}_{+}(\Omega)\chi_{g,0}\hat{b}_{-2} + \chi_{g,0}\hat{\mathcal{M}}_{0+} \quad (5.198)$$

$$\hat{a}_4^{\dagger} = ig_{+}^{*}\mathcal{J}_{+}^{*}(-\Omega + 4\Omega_{dp})\bar{\chi}_{g,4}\hat{b}_{-2} + \bar{\chi}_{g,4}\hat{\mathcal{M}}_{4-}^{\dagger}. \quad (5.199)$$

For the detection frequency range, we therefore get

$$\begin{aligned} \hat{a}_0 = & -g_{+}\mathcal{J}_{+}(\Omega)\chi_{g,0}\chi_{0,-2}^{\text{eff}} \left[ g_{-}^{*}\chi_{g,-2}\hat{\mathcal{M}}_{-2+} + g_{-}\bar{\chi}_{g,2}\hat{\mathcal{M}}_{2-}^{\dagger} + g_{\alpha}\chi_{g,-1}\hat{\mathcal{M}}_{-1+} + g_{\alpha}\bar{\chi}_{g,3}\hat{\mathcal{M}}_{3-}^{\dagger} \right. \\ & \left. + g_{+}^{*}\chi_{g,0}\hat{\mathcal{M}}_{0+} + g_{+}\bar{\chi}_{g,4}\hat{\mathcal{M}}_{4-}^{\dagger} \right] - ig_{+}\mathcal{J}_{+}(\Omega)\chi_{g,0}\chi_{0,-2}^{\text{eff}}\sqrt{\Gamma_m}\hat{\zeta} + \chi_{g,0}\hat{\mathcal{M}}_{0+} \end{aligned} \quad (5.200)$$

where we applied  $\bar{\chi}_{0,2} \approx 0$  for  $\Omega \approx \Omega_m - 2\Omega_{dp}$ . We can resolve and sort now for input noise frequency components again, where we only keep cavity input noise terms around the signal and the idler resonances. The result is

$$\begin{aligned} \hat{a}_0 \approx & -ig_{+}\mathcal{J}_{+}(\Omega)\chi_{g,0}\chi_{0,-2}^{\text{eff}} \left[ \sqrt{\Gamma_m}\hat{\zeta} - i \left( g_{+}^{*}\mathcal{Q}_{+}\chi_{g,0} + g_{-}\mathcal{A}_0\mathcal{Q}_{-}\bar{\chi}_{g,2} \right) \hat{\mathcal{N}}_{0+} \right. \\ & \left. - i \left( g_{+}^{*}\bar{\mathcal{A}}_2\mathcal{Q}_{+}\chi_{g,0} + g_{-}\mathcal{Q}_{-}\bar{\chi}_{g,2} \right) \hat{\mathcal{N}}_{2-}^{\dagger} \right] + \chi_{g,0}\hat{\mathcal{N}}_{0+} + \chi_{g,0}\bar{\mathcal{A}}_2\hat{\mathcal{N}}_{2-}^{\dagger} \end{aligned} \quad (5.201)$$

with

$$\mathcal{Q}_{-} = \left[ 1 + i2\mathcal{K}n_d\chi_{g,-1} \left( 1 - \bar{\mathcal{A}}_3 - \frac{g_{+}^{*}}{g_{-}}\bar{\mathcal{A}}_3 \right) - i2\mathcal{K}n_d\bar{\chi}_{g,3} \left( 1 - \mathcal{A}_{-1} - \frac{g_{+}^{*}}{g_{-}} \right) \right] \quad (5.202)$$

$$\mathcal{Q}_{+} = \left[ 1 - i2\mathcal{K}n_d\bar{\chi}_{g,3} \left( 1 - \mathcal{A}_{-1} - \frac{g_{-}}{g_{+}^{*}}\mathcal{A}_{-1} \right) + i2\mathcal{K}n_d\chi_{g,-1} \left( 1 - \bar{\mathcal{A}}_3 - \frac{g_{-}}{g_{+}^{*}}\bar{\mathcal{A}}_3 \right) \right] \quad (5.203)$$

For the cavity output field on one side of the feedline, we get

$$\begin{aligned} \hat{a}_{\text{out}} = & \hat{\xi}_{e0+}^{\text{left}} - \sqrt{\frac{\kappa_e}{2}}\hat{a}_0 \\ = & ig_{+}\mathcal{J}_{+}(\Omega)\chi_{g,0}\chi_{0,-2}^{\text{eff}}\sqrt{\frac{\kappa_e}{2}}\sqrt{\Gamma_m}\hat{\zeta} \\ & - \chi_{g,0}\sqrt{\frac{\kappa_e}{2}} \left[ 1 - g_{+}\mathcal{J}_{+}(\Omega)\chi_{0,-2}^{\text{eff}} \left( g_{+}^{*}\mathcal{Q}_{+}\chi_{g,0} + g_{-}\mathcal{A}_0\mathcal{Q}_{-}\bar{\chi}_{g,2} \right) \right] \sqrt{\kappa_i}\hat{\xi}_{i0+} \\ & - \chi_{g,0}\sqrt{\frac{\kappa_e}{2}} \left[ 1 - g_{+}\mathcal{J}_{+}(\Omega)\chi_{0,-2}^{\text{eff}} \left( g_{+}^{*}\mathcal{Q}_{+}\chi_{g,0} + g_{-}\mathcal{A}_0\mathcal{Q}_{-}\bar{\chi}_{g,2} \right) \right] \sqrt{\frac{\kappa_e}{2}}\hat{\xi}_{e0+}^{\text{right}} \\ & - \chi_{g,0}\sqrt{\frac{\kappa_e}{2}} \left[ \bar{\mathcal{A}}_2 - g_{+}\mathcal{J}_{+}(\Omega)\chi_{0,-2}^{\text{eff}} \left( g_{+}^{*}\bar{\mathcal{A}}_2\mathcal{Q}_{+}\chi_{g,0} + g_{-}\mathcal{Q}_{-}\bar{\chi}_{g,2} \right) \right] \sqrt{\kappa_i}\hat{\xi}_{i2-}^{\dagger} \\ & - \chi_{g,0}\sqrt{\frac{\kappa_e}{2}} \left[ \bar{\mathcal{A}}_2 - g_{+}\mathcal{J}_{+}(\Omega)\chi_{0,-2}^{\text{eff}} \left( g_{+}^{*}\bar{\mathcal{A}}_2\mathcal{Q}_{+}\chi_{g,0} + g_{-}\mathcal{Q}_{-}\bar{\chi}_{g,2} \right) \right] \sqrt{\kappa_e}\hat{\xi}_{e2-}^{\dagger} \\ & + \left( 1 - \chi_{g,0}\sqrt{\frac{\kappa_e}{2}} \left[ 1 - g_{+}\mathcal{J}_{+}(\Omega)\chi_{0,-2}^{\text{eff}} \left( g_{+}^{*}\mathcal{Q}_{+}\chi_{g,0} + g_{-}\mathcal{A}_0\mathcal{Q}_{-}\bar{\chi}_{g,2} \right) \right] \sqrt{\frac{\kappa_e}{2}} \right) \hat{\xi}_{e0+}^{\text{left}} \end{aligned} \quad (5.204)$$

This can be used just as in the red sideband case to calculate the output field power spectral density in units of phonons.

To calculate the corresponding phonon occupation, we use relations (5.194) - (5.199) and keep only cavity noise input terms for  $\hat{N}_{0+}$  and  $\hat{N}_{2-}^\dagger$

$$\frac{\hat{b}_{-2}}{\chi_{0,-2}^{\text{eff}}} = -ig_+^* \mathcal{Q}_+ \chi_{g,0} [\hat{N}_{0+} + \bar{\mathcal{A}}_2 \hat{N}_{2-}^\dagger] - ig_- \mathcal{Q}_- \bar{\chi}_{g,2} [\hat{N}_{2-}^\dagger + \mathcal{A}_0 \hat{N}_{0+}] + \sqrt{\Gamma_m} \hat{\zeta} \quad (5.205)$$

which gives the mechanical power spectral density

$$\begin{aligned} \langle \hat{b}_{-2}^\dagger \hat{b}_{-2} \rangle &= |\chi_{0,-2}^{\text{eff}}|^2 |g_+^* \mathcal{Q}_+ \chi_{g,0} + g_- \mathcal{Q}_- \bar{\chi}_{g,2}|^2 \kappa n_c^{\text{th}} + \\ &\quad |\chi_{0,-2}^{\text{eff}}|^2 |g_+^* \mathcal{Q}_+ \bar{\mathcal{A}}_2 \chi_{g,0} + g_- \mathcal{Q}_- \bar{\chi}_{g,2}|^2 \kappa (n_c^{\text{th}} + 1) + |\chi_{0,-2}^{\text{eff}}|^2 \Gamma_m n_m^{\text{th}}. \end{aligned} \quad (5.206)$$

The integration of this relation over all frequencies then results in the effective phonon occupation in presence of the optomechanical coupling.

### 5.7.14. MEASUREMENT AND ANALYSIS PROTOCOLS FOR THERMAL NOISE DETECTION AND FOUR-WAVE COOLING PREPARATION

- We start the experimental cycle with choosing a bias flux operation point, either point I or point II, and an in-plane magnetic field  $B_{\parallel}$ . We ramp the in-plane magnet current to its corresponding value.
- A parametric drive tone is sent to the cavity with fixed frequency  $\omega_d$  and power  $P_d$  to match the chosen operation point.
- The cavity flux bias is adjusted manually to prepare the SQUID cavity in the driven Kerr mode state.
- The frequency of the optomechanical pump is chosen to be either on the red sideband of the signal resonance or on the blue sideband of the idler resonance. The pump is activated with frequency  $\omega_p$  and power  $P_p$ .

#### THERMAL CALIBRATION MEASUREMENT

- The optomechanical pump is positioned on the red sideband of the signal resonance and the fridge is sitting at base temperature.
- For the actual measurement, we start a python-based control and data acquisition script.
- Prior to running the measurement, we input some fixed parameters to the script such as the values of all external attenuators in the input lines and the number of room-temperature amplifiers on the output line.
- We manually adjust the probe VNA to the parameter set regarding frequency window, probe power and bandwidth in order to measure a clean OMIT response. We

hereby choose a red-sideband pump power, that is large enough to yield a clear OMIT response, but low enough to keep the effective cooperativity in the regime  $\sim 1$ .

- Upon a terminal input command, the script begins data acquisition and first catches all relevant parameters such as powers, frequencies, frequency spans, bandwidths as well as magnet DC currents from all participating electronic devices.
- Afterwards, the script takes three datasets.
- First, it performs a scan of the narrow-band OMIT window using the VNA and the manually adjusted settings.
- Secondly, the center frequency and frequency span are sent to the spectrum analyzer to measure a power spectrum in the OMIT frequency range. During this spectrum analyzer measurement, the VNA frequency is set to a frequency 4kHz detuned from the detection window of the spectrum analyzer to avoid any interference and the cavity response at a single frequency point is monitored permanently during the spectrum acquisition. This measure enables to control the cavity response by out-of-plane current feedback for the case the cavity is drifting during the spectrum measurement.
- Lastly, a wide-band VNA scan of the complete cavity response is taken.
- Each of the three data traces is stored in a separate file.
- For most temperatures, we repeat the measurement once.
- We adjust the fridge temperature to its new set value and after a temperature settling time of  $\sim 10$  minutes, we begin the cycle from the beginning at the new base temperature.
- Parametric drive and optomechanical pump powers  $P_d$  and  $P_p$ , respectively, were adjusted during the temperature sweep to keep driven cavity state and effective cooperativity nearly constant.

## FOUR-WAVE-COOLING MEASUREMENT

- For the four-wave-cooling measurement we start a python-based control and data acquisition script, which is programmed to wait for an input terminal starting command before each data point.
- Prior to running the measurement, we input some fixed parameters to the script such as the values of all external attenuators in the input lines and the number of room-temperature amplifiers on the output lines.
- We set the parametric drive power and the optomechanical pump powers to the desired values  $P_d$  and  $P_p$ , respectively, and manually adjust the probe VNA to the parameter set regarding frequency window, probe power and bandwidth in order to measure a clean OMIT response.

- Upon a terminal input command, the script begins data acquisition and first catches all relevant parameters such as powers, frequencies, frequency spans, bandwidths as well as magnet DC currents from all participating electronic devices.
- At this point, the script waits for the final command to measure three traces. Once we observe a stable response in the OMIT window on the VNA screen, the script is continued.
- The first data trace acquired by the script is a narrow-band VNA scan of the OMIT response using the manually adjusted settings.
- Secondly, the center frequency and frequency span of the VNA trace are sent to the spectrum analyzer and an output power spectrum in the OMIT frequency range is acquired. During this spectrum measurement, the probe VNA frequency is set to a value several spectrum analyzer frequency spans detuned from the detection window of the spectrum analyzer window to avoid any interference between the VNA signal and the power spectrum. The VNA is continuously scanning a single frequency point of the cavity response to enable monitoring and feedback control of the bias flux for the case the cavity response is drifting due to flux drifts.
- Lastly, a wide-band VNA trace of the complete signal resonance  $S_{21}$  is acquired.
- The three data traces are stored in individual files, where also the subsequent equivalent traces for the next settings are appended.
- The VNA settings are reset to the OMIT window and manual VNA control is enabled by the measurement script.
- At this point, we can choose by a terminal input between a repetition of the same measurement or a continuation to the next settings.
- In case of continuation to the next settings, the optomechanical pump power  $P_p$  is manually set to its new value and the VNA probe settings are adjusted for the next measurement iteration. The most important parameter is the frequency range for the OMIT and the spectrum analyzer window, which has to be increased with increasing dynamical backaction due to the considerable increase of the mechanical linewidth from the bare value of  $\sim 10$  Hz to the largest effective linewidth of  $\sim 2$  kHz for the highest achieved effective cooperativity.
- Depending on the optomechanical pump power, we also adjust the parametric drive power  $P_d$  in some cases to keep the driven cavity response nearly constant. We suspect this measure is necessary as for large optomechanical pump powers, the experiment is at the edge of the linearized regime with respect to  $\gamma_-$ ,  $\gamma_+$  and parametric drive depletion is occurring.
- Once the new parameters are adjusted, the data acquisition cycle starts from the beginning.

## THERMAL CALIBRATION DATA ANALYSIS

- The data analysis of the thermal calibration begins with fitting the cavity response  $S_{21}$  for each temperature using Eq. (5.15). This fit provides us with a value for the linewidth  $\kappa'$  and a fit function for the complex background.
- We divide off the complex background from both, the cavity response and the OMIT response in their corresponding frequency ranges. In addition we correct for a small phase rotation which is intrinsic to the Kerr cavity susceptibility and therefore not captured by the complex background.
- Next, we use the full Kerr-mode model function Eq. (5.53) to fit the background-corrected cavity response once again. As fixed parameter for this second fit, we use  $\kappa'$  from the first fit, the parametric drive power  $P_d$  and the in-line attenuation. We also use the independently obtained  $\kappa_e = 2\pi \cdot 120 \pm 20$  kHz of the undriven cavity and allow for small variations, necessary to match the observed resonances. As fit parameters in this second fit, we get the detuning between drive and undriven cavity  $\Delta_d$  and by using the Kerr polynomial (5.32) we get the corresponding intracavity drive photon number  $n_d$ .
- Next, we fit the background-corrected and rotated OMIT VNA response with Eq. (5.15) and obtain  $\Gamma_{\text{eff}}$  and  $\Omega_m$  as fit parameter.
- We fit the OMIT VNA response with the full four-wave OMIT model Eqs. (5.157) and (5.161). We input as fixed parameters  $\mathcal{K}$  and  $g_0$  from the flux arch, the parametric drive power  $P_d$ , the optomechanical pump power  $P_p$  and the in-line attenuation. Also, we use the fitted  $\kappa_e$  from the previous full model cavity fit. As starting values for the remaining model parameters, we use  $\Delta_d$ ,  $n_d$  and  $\kappa'$  from the previous fits of the cavity. In the routine, we allow for a change of the bare cavity resonance frequency, i.e., of  $\Delta_d$  due to possible flux fluctuations. Based on the characteristic polynomial Eq. (5.32), we then dynamically adjust  $n_d$  to the modified  $\Delta_d$ . Additionally, we allow for changes in  $\kappa'$  of up to  $\pm 100$  kHz, with a lower limit of  $\kappa'_{\min} = 2\pi \cdot 320$  kHz. As in the experiment between the VNA cavity scan and the VNA OMIT scan several minutes pass, during which the thermal noise spectrum is recorded, these allowed changes in fit parameters reflect possible drifts of the bare cavity resonance due to flux fluctuations in this time span. We calculate the intracavity  $\gamma_-$  and  $\gamma_+$  fields based on Eqs. (5.45) and (5.47). Ultimately, we obtain from this OMIT fit with the full model a value for the bare mechanical linewidth  $\Gamma_m$  and the mechanical resonance frequency  $\Omega_m$ . As last fit parameter, we allow for a small correction of the OMIT resonance circle, which is necessary due to the uncertainty of the background extraction during the initial cavity fitting routine at the cavity resonance frequency. This is taken into account by allowing for a multiplication of the OMIT response by a small complex scaling factor  $(1 + x) e^{i\beta}$  with  $x, \beta \ll 1$ .
- Finally, we fit the measured thermal noise spectrum using the full model Eqs. (5.187) and (5.188). We input as fixed parameters here all relevant quantities as obtained from the previous full model OMIT fit. The only remaining fit parameters at this

point are the total detection output gain, converting the PSD in numbers of quanta to an absolute power and the uncalibrated equilibrium occupation of the mechanical oscillator  $n'_m$ . The last used parameter  $n_{\text{add}}$  is adjusted to match the temperature dependence of the uncalibrated  $n'_m$  in the linear regime to the Bose distribution, which corresponds to a calibration of  $n'_m$  to  $n_m^{\text{th}}$ . As a result we obtain a number for the added photons  $n_{\text{add}} \approx 14$  and the residual thermal phonon occupation shown in Fig. 5.4. In section 5.7.15, we present some additional data on the temperature dependence of  $\Omega_m$  and  $\Gamma_m$  as obtained from this procedure.

- Note: Due to slow SQUID cavity resonance frequency fluctuations and drifts, the measurement time of the spectrum acquisition was limited and we took these data with a reasonable compromise between number of data points, frequency span and bandwidth. For the lowest cooperativities however, when the mechanical linewidth is close to the intrinsic linewidth, the resolution bandwidth of the spectrum analyzer and the mechanical linewidth are comparable in size. In this case the effect of the resolution bandwidth is to smoothen and broaden the real mechanical power spectral density Lorentzian. To consider this effect in the fit curve for the power spectral density, we apply a moving-average-filter with the corresponding width in frequency space to the theory curve within the fitting routine itself. In the thermal calibration experiment, the resolution bandwidth of the spectrum analyzer was set to 5 Hz and therefore considerably smaller than the effective mechanical linewidths, cf. Supplementary Fig. 5.19.
- Error bars in thermal occupation: During the fitting procedure we simultaneously calculate the corresponding error bars for each point. These translate the impact of deviations of the cavity from its operation point. From this we estimate the difference in thermal occupation by fitting the thermal noise spectrum with the cavity parameters  $\kappa'$ ,  $\Delta_d$  and  $n_d$ . This difference is plotted as the error in y-axis of the inset of in Fig. 5.4c.

## FOUR-WAVE COOLING DATA ANALYSIS

- The data analysis of the four-wave cooling experiment begins with fitting the cavity response  $S_{21}$  for each power setting of  $P_d$  and  $P_p$  using Eq. (5.15). This fit provides us with a value for the linewidth  $\kappa'$  and a fit function for the complex background.
- We divide off the complex background from both, the cavity response and the OMIT response in their corresponding frequency ranges. In addition, we correct for a small phase rotation which is intrinsic to the driven Kerr cavity susceptibility, and therefore not captured by the complex background.
- Next, we use the full Kerr-mode model function Eq. (5.53) to fit the cavity response once again. As fixed parameter for this second fit, we use  $\kappa'$  from the first fit, the parametric drive power  $P_d$  and the in-line attenuation. We also allow for small variations of the bare external decay rate of each operation point  $\kappa_e^{\text{I,II}}$  and allow for  $\kappa_e = 2\pi \cdot (\kappa_e^{\text{I,II}} \pm 10)$  kHz, which is necessary to match the observed resonances for

all powers. As fit parameters in this second fit, we get the detuning between parametric drive and undriven cavity  $\Delta_d$ . Additionally, by using the Kerr polynomial Eq. (5.32) within the fit routine we get the corresponding intracavity drive photon number  $n_d$ .

- We fit the background-corrected and rotated OMIT VNA response with Eq. (5.15) and obtain  $\Gamma_{\text{eff}}$  and  $\Omega_m$  as fit parameters.
- We fit the OMIT VNA response with the full four-wave OMIT model Eqs. (5.157) and (5.161) for red-signal-sideband pumping or Eqs. (5.161) and (5.161) for the blue-idler-sideband case, respectively. We input as fixed parameters  $\mathcal{K}$  and  $g_0$  as determined from their flux dependence, the parametric drive power  $P_d$ , the optomechanical pump power  $P_p$  and the input line attenuation. Also, we use the  $\kappa_e$  as determined from the full model cavity fit. As starting values for the remaining model parameters, we use  $\Delta_d$ ,  $n_d$  and  $\kappa'$  from the previous fits of the cavity. In the routine, we allow for adjustments of the bare cavity resonance frequency, i.e., of  $\Delta_d$  up to  $\pm 2 \text{ MHz}$  due to possible flux fluctuations, cf. operation range in Fig. 5.2. Based on the characteristic polynomial Eq. (5.32), the intracavity drive photon number  $n_d$  is adjusted correspondingly within the fit routine. Additionally, we allow for adjustments of the total linewidth  $\kappa'$  of up to  $\pm 100 \text{ kHz}$ , but with a lower limit  $\kappa'_{\min,I} = 2\pi \cdot 320 \text{ kHz}$  at operation point I and  $\kappa'_{\min,II} = 2\pi \cdot 350 \text{ kHz}$  at point II. Several minutes pass in the experiment between the VNA scan of the OMIT response and the VNA scan of the signal resonance, during which the thermal noise spectrum is recorded. We allow for adjustments of some of fit parameters between the two scans, which reflects possible drifts of the bare cavity resonance due to flux drifts in this time span. We note that in principle also  $\mathcal{K}$  and  $g_0$  might experience small drifts due to the effective change in bias flux. As the flux-drift related variations of these two parameters are small within the operation range however, cf. Fig. 5.2 and section 5.7.4, we work with constant average values for the analysis here. Based on Eqs. (5.45) and (5.47), we calculate also the intra-cavity fields  $\gamma_-$  and  $\gamma_+$ . As last fit parameter, we allow for a small correction of the OMIT resonance circle, which is necessary due to the uncertainty of the background extraction during the initial cavity fitting routine at the cavity resonance frequency. This is taken into account by allowing for a multiplication of the OMIT response by a small complex scaling factor  $(1 + x) e^{i\beta}$  with  $x, \beta \ll 1$ .
- Finally, we fit the measured thermal noise spectrum using the full model Eqs. (5.187) and (5.188) for the red-signal-sideband case and Eqs. (5.204) and (5.188) for the blue-idler-sideband case, respectively. Once again, in this fitting procedure we allow for fluctuations of the cavity decay rate  $\delta\kappa' = \pm 2\pi \cdot 60 \text{ kHz}$  and  $\delta\Delta_d = \pm 2\pi \cdot 0.8 \text{ MHz}$  which are limited to small deviations around the average values obtained from the cavity and OMIT fitting routines. Note that the OMIT measurement and the cavity scan were taken prior and posterior (respectively) to the thermal noise detection and therefore we account for possible deviations of the cavity state due to the fluctuations in the system. Finally, the only remaining fit parameters are the total detection output gain and the equilibrium occupation of the mechanical oscillator  $n_m^{\text{th}}$ . Note that this last fit parameter was allowed to vary between 70-90

phonons for blue sideband driving and 60-90 phonons for red-sideband driving. Without these restriction, the fit often fails and the corresponding thermal phonon numbers are oscillating unsystematically between 50 and 130 phonons. The corresponding values without restrictions are considered in the error bars though, see below. The number of added photons  $n_{\text{add}} \approx 14$  was determined via the thermal calibration procedure.

- Note: Due to slow SQUID cavity resonance frequency fluctuations and drifts, the measurement time of the spectrum acquisition was limited and we took these data with a reasonable compromise between number of data points, frequency span and bandwidth. For the lowest cooperativities however, when the mechanical linewidth is close to the intrinsic linewidth, the resolution bandwidth of the spectrum analyzer and the mechanical linewidth are comparable in size. In this case the effect of the resolution bandwidth is to smoothen and broaden the mechanical power spectral density Lorentzian. To consider this effect in the fit curve for the power spectral density, we apply a moving-average-filter with the corresponding width in frequency space to the theory curve within the fitting routine itself. An additional broadening effect of the spectrum might arise due to slow mechanical frequency fluctuations induced by a variation of the optical spring during bias flux drifts, cf. Fig. 5.2.
- Based on the full ensemble of system parameters obtained by this multi-step analysis and fit procedure, we finally infer the resulting cooled phonon number  $n_m$  of the mechanical oscillator by integrating Eq. (5.190) for the red-signal-sideband case and Eq. (5.206) for the blue-idler-sideband case, respectively. The results are plotted in Fig. 5.4 and in Supplementary Fig. 5.20.
- Error bars for cooled number of phonons: During the fitting procedure we simultaneously calculate the corresponding error bars of each point. These translate the impact of deviations of the cavity from its operation point and of a different thermal occupation in the extraction of cooled photon number. For this we estimate the difference in the cooled phonons by fitting the thermal noise spectrum with the cavity parameters, which were extracted from the OMIT fit, in this case without any restriction to the thermal phonon number. This difference is plotted as the error in the y-axis of Fig. 4 and in Supplementary Fig. 5.20. Furthermore, we calculate the error in the extraction of the effective mechanical linewidth by computing the difference of  $\Gamma_{\text{eff}}$  obtained from the full model noise fit and the one obtained from the fit of the OMIT VNA response with Eq. (5.15). In addition, we consider an uncertainty in  $\Gamma_m$  of  $\pm 1\text{Hz}$ . The sum of these errors is plotted as the error bar in the  $\Gamma_{\text{eff}}/\Gamma_m$  direction.

### 5.7.15. THERMAL CALIBRATION OF THE RESIDUAL MECHANICAL PHONON OCCUPATION

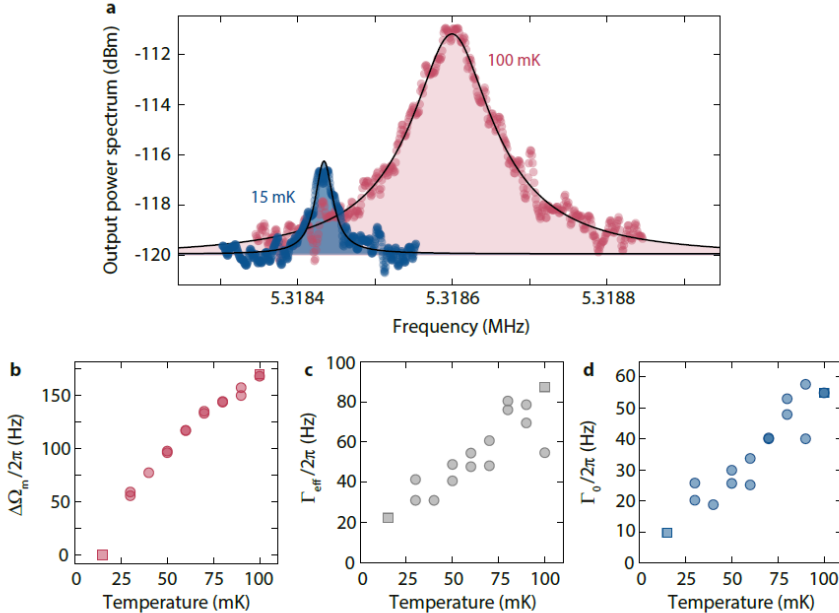


Figure 5.19: **Temperature dependence of the mechanical oscillator.** a shows the power spectra of the signal resonance output field during optomechanical red-sideband pumping at two different refrigerator base temperatures  $T_b^{\min} = 15 \text{ mK}$  and  $T_b^{\max} = 100 \text{ mK}$ . The measurement scheme is detailed in section 5.7.14. Points show data, lines and shaded areas show fits to the full four-wave model, where all system parameters have been obtained from a VNA measurement of the cavity and the OMIT response, except for the thermal phonon occupation  $n_m^{\text{th}}(T_b)$  and the total output gain conversion, defining the absolute power scale of the spectra. Frequency-axis is given with respect to the red sideband optomechanical pump frequency  $\omega_p$ . b shows the resonance frequency shift  $\Delta\Omega_m = \Omega_m(T) - \Omega_m(15 \text{ mK})$  of the mechanical oscillator with dilution refrigerator base temperature. Panels c and d show the effective and intrinsic mechanical linewidth  $\Gamma_{\text{eff}}(T)$  and  $\Gamma_m(T)$  vs base temperature  $T_b$ . The effective linewidth is broadened by dynamical backaction and obtained from a fit to the OMIT response, the intrinsic linewidth is obtained from a fit to the OMIT response using the full four-wave model. The parameters obtained from this temperature dependence are used to calculate the residual thermal phonon occupation vs fridge temperature, the result is shown in Fig. 5.4, where the values for each temperature have been averaged. Thermal calibration measurements were done at operation point I with an in-plane field of  $B_{||} = 21 \text{ mT}$ . Square points in b-d indicate the results for the two datasets shown in a.

We perform the thermal calibration measurement and data analysis as described in section 5.7.14. In Supplementary Fig. 5.19 we present some of the results obtained from this experiment. In particular, we show the detected thermal noise spectrum in units of quanta for the lowest and highest temperatures  $T_b^{\min} = 15 \text{ mK}$  and  $T_b^{\max} = 100 \text{ mK}$ , including the fit from the full model, and we show the obtained temperature dependence of the mechanical parameters  $\Omega_m$ ,  $\Gamma_{\text{eff}}$  and  $\Gamma_m$ . From the data it is clear, that both, the

mechanical frequency and the intrinsic mechanical linewidth increase significantly with temperature and have a strong dependence on temperature at the lowest temperatures. Either intrinsic or pump-power-induced small variations of the chip temperature might therefore be a source for the observation that for good agreement of our datasets with the theory, we have to consider variations between the datasets of some 10 Hz in the mechanical resonance frequency and of a few Hz for the mechanical linewidth in the range  $10 \text{ Hz} < \frac{\Gamma_m}{2\pi} < 15 \text{ Hz}$ .

### 5.7.16. FOUR-WAVE-COOLING WITH A PUMP ON THE RED SIDEBAND OF THE SIGNAL RESONANCE

We perform a four-wave cooling experiment with an optomechanical pump positioned on the red sideband of the signal resonance, cf. Supplementary Fig. 5.20. Data acquisition and data analysis are described in section 5.7.14.

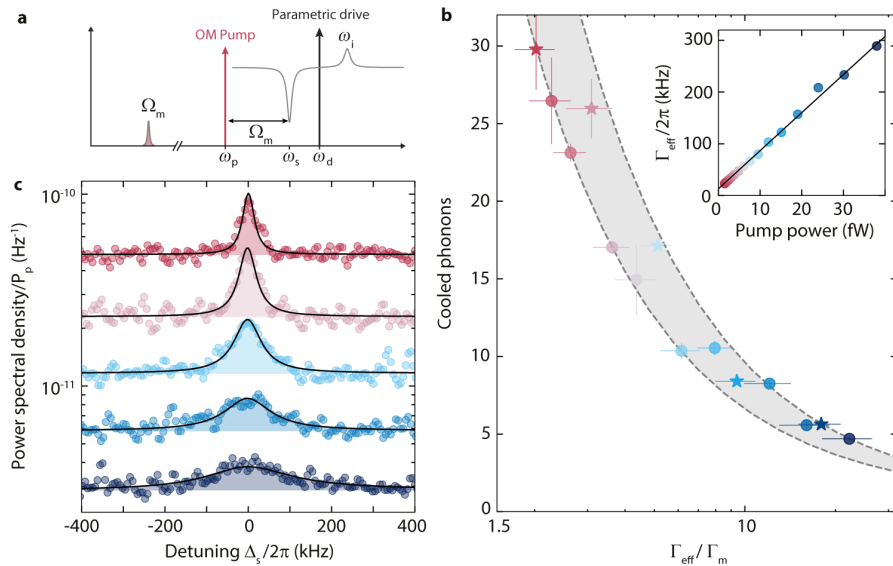


**Figure 5.20: Red-sideband four-wave cooling of the mechanical oscillator.** a Schematic representation of the experiment. A parametric drive is used to activate the Kerr quasi-mode state and an optomechanical pump is sent to the red sideband of the signal resonance  $\omega_p \approx \omega_s - \Omega_m$ . From  $S_{21}$  measurements of signal resonance and OMIT, as well as a signal mode output power spectrum, we determine the cooled mechanical phonon occupation. The result for increasing sideband pump power  $P_p$  and effective mechanical linewidth, respectively, is shown in panel b. Inset shows that  $\Gamma_{\text{eff}} \propto P_p$ . Circles and stars are data, the lowest achieved occupation is  $n_m \sim 4$ , limited by cavity bifurcation instability. Dashed lines and shaded areas display the theoretical value range of  $n_m$ , taking into account  $60 < n_m^{\text{th}} < 90$ . Data were taken at operation point I and at  $B_{\parallel} = 21 \text{ mT}$ . In addition, the error bars represent possible deviations in the extraction of the plotted values based on their difference from the ones calculated based on the parameters extracted from the corresponding OMIT fit. For more details, see section 5.7.14. Panel c shows selected power spectra data for the points in b, which are plotted as stars.



# 6

## PHOTON-PRESSURE STRONG COUPLING BETWEEN TWO SUPERCONDUCTING CIRCUITS

*The radiation-pressure coupling between two harmonic oscillators has been used in optomechanics for breakthrough experiments in the control and detection of mechanical displacements. Used primarily in optomechanics, there have been few reports of exploiting such a type of interaction in other platforms. Here, we engineer two superconducting LC circuits coupled by a strong photon-pressure interaction, a term we use in analogy to the radiation-pressure interaction between light and mechanical objects. The coupling arises from a change in the resonant frequency of one circuit in response to the current flowing in the second. We observe dynamical backaction between the two circuits, photon-pressure-induced transparency and absorption, and enter the strong-coupling regime. Furthermore, we observe parametrically amplified thermal current fluctuations in a radio-frequency circuit close to its quantum ground-state. Due to the high design-flexibility of superconducting circuits, our approach will enable new experiments with radio-frequency photons and parameter regimes of photon-pressure coupling not accessible in other platforms.*

---

This chapter has been published as an *Photon-pressure strong-coupling between two superconducting circuits*.  
D. Bothner\*, I. C. Rodrigues\*, & G. A. Steele, in *Nature Physics* **17**, 85-91 (2020)

\*these authors contributed equally

## 6.1. INTRODUCTION

The nonlinear, parametric coupling between two harmonic oscillators has been used in cavity optomechanical systems for groundbreaking developments regarding the detection and control of macroscopic mechanical systems [56]. The most impressive results include the demonstration of quantum ground-state cooling of mechanical oscillators with light fields [31, 32], displacement detection below the standard quantum limit [41, 42], the quantum-entanglement between distinct mechanical systems [39, 40] or the generation of non-classical states of motion [36–38]. Besides offering remarkable control over mechanical objects, optomechanical systems have also shown great potential for signal processing by means of slow light [183, 184], parametric microwave amplification [26, 82, 84–86] and light-field frequency conversion [51, 52, 54, 84]. Very recently, exciting new developments using optomechanical devices such as the realization of non-reciprocity [87–90], the implementation of synthetic magnetism and reservoir engineering [91, 92] as well as topological operations at exceptional points [159] have been reported.

The radiation-pressure type of nonlinear coupling between two harmonic oscillators, which forms the basis of all breakthrough experiments and developments in cavity optomechanics, however, is not limited to mechanical systems coupled to light fields. It can, in principle, be implemented for any system in which the amplitude of one oscillator couples linearly to the resonance frequency of a second. In nanomechanics, such coupling has been applied for dynamically controlling the coupling of different modes of a nanomechanical resonator [74–77]. Ideas for implementing this type of interaction with superconducting circuits have also been proposed [78–80, 93] and recently realized in a first experiment [81]. This coupling between two circuits, which has been referred to as photon-pressure coupling [93] in analogy with the optomechanical radiation-pressure coupling, offers a wide range of possible applications and experiments with superconducting circuits in both the classical and quantum regimes [26, 31, 32, 36, 37, 56, 82, 84–92, 159, 183, 184] and has been proposed for quantum computation with bosonic codes [93]. Due to the large design flexibility and precision in engineering resonance frequency and quality factor of superconducting circuits, experiments in unconventional photon-pressure parameter regimes such as the reversed dissipation [82] and the reversed resonance frequency regimes [83] or even the optomechanical single-photon strong-coupling regime [63, 67] could be possible. The circuit implementation of many breakthrough developments in radiaton-pressure coupled systems, however, require either large cooperativities  $\mathcal{C} \gg 1$  or the strong-coupling regime [25, 58, 59]. Neither regime has been achieved to date in photon-pressure coupled superconducting circuits.

Here, we present a device consisting of two superconducting microwave resonators, which are coupled to each other by a photon-pressure interaction with a considerable single-photon coupling strength on the order of 10 percent of the largest system decay rate. Our technology is based on a nanobridge junction platform that enables lower anhamonicity and higher drive powers than typical tunnel junction devices. One resonator is a radio-frequency circuit with a resonance frequency in the MHz regime and the second is a microwave quantum interference cavity in the GHz regime. We demon-

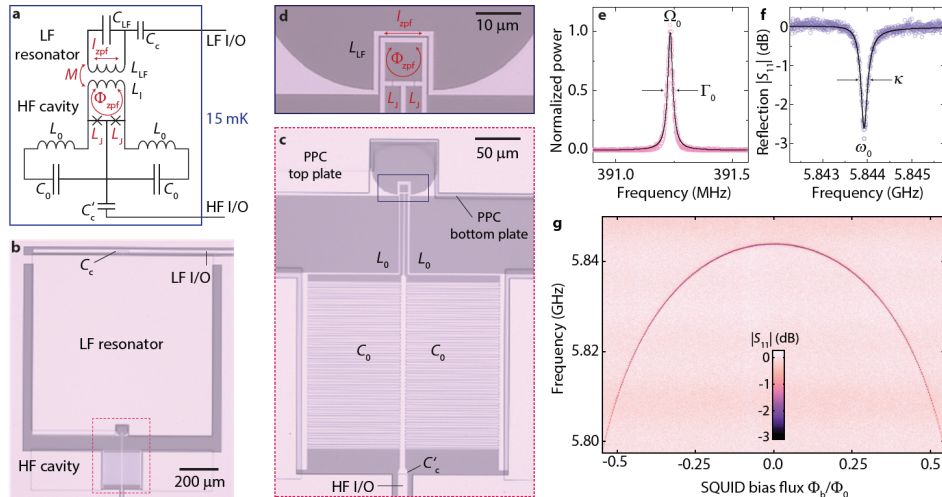


**Figure 6.1: Two superconducting LC circuits coupled by a photon-pressure interaction.** **a** Circuit equivalent of the device. The current of a radio-frequency LC circuit is coupled via mutual inductance to a superconducting quantum interference device (SQUID) embedded into a microwave cavity. Both circuits are capacitively coupled to individual feedlines for driving and readout. **b** Optical image of the device showing both circuits and their corresponding feedlines. The red dashed box indicates the zoom region for panel **c**. Panel **c** shows the high-frequency SQUID cavity with feedline and coupling capacitor  $C'_c$  at the bottom, interdigitated capacitors  $C_0$  to ground in the center, and linear inductance wires with  $L_0$  grounding the SQUID symmetrically on both sides. At the top, a small part of the LF parallel plate capacitor (PPC) with the LF inductor wire connecting the two plates is visible. The black box indicates the zoom region for panel **d**, which shows in detail the SQUID loop and the LF inductance  $L_{LF}$  surrounding the loop with a gap of 500 nm. In **b-d**, brighter parts correspond to Aluminum, darker and transparent parts to Silicon. **e** shows the resonance curve of the LF resonator vs excitation frequency, measured by coherently exciting the LF resonator and using the driven HF SQUID cavity as interferometer. **f** shows the amplitude of the reflection coefficient  $|S_{11}|$  at the SQUID cavity vs excitation frequency. In **e** and **f**, colored points are data, and the black lines correspond to fits. In **g** we show the reflection response of the SQUID cavity dependent on the external magnetic bias flux. For increasing flux, the resonance frequency of the cavity absorption (dark line) is shifted towards lower values. The magnetic field was applied by a small coil below the device, mounted inside the cryopump magnetic shields surrounding the sample.

strate dynamical backaction between the two LC circuits and observe the transition from the photon-pressure-induced transparency (PPIT) [149, 150] to the parametric strong-coupling regime [25, 58, 59], manifested by the observation of a pronounced normal-mode splitting. The largest cooperativities we achieve in this regime are  $\mathcal{C} \sim 100 \gg 1$ , an improvement of two orders of magnitude compared to existing realizations [81]. Finally, we interferometrically observe the photon-pressure-amplified thermal current fluctuations in a radio-frequency LC oscillator by a blue-detuned sideband pump tone.

## 6.2. CONCEPT AND DEVICE

Our device combines two superconducting LC circuits with about an order of magnitude difference in resonance frequencies. The full circuit schematic and optical images of the device are shown in Fig. 6.1a-d. The low-frequency (LF) resonator consists of a large parallel plate capacitor, whose plates are connected via a short inductor wire, and it is capacitively coupled to a coplanar waveguide feedline for driving and readout. It has a resonance frequency  $\Omega_0 = 2\pi \cdot 391\text{ MHz}$  and a linewidth  $\Gamma_0 = 2\pi \cdot 22\text{ kHz}$ , cf. Fig 6.1e. The inductor wire of the LF resonator surrounds a superconducting quantum interference device (SQUID) in close proximity, which is embedded into the inductance of a high-frequency (HF) cavity with resonance frequency  $\omega_0 = 2\pi \cdot 5.844\text{ GHz}$  and linewidth  $\kappa = 2\pi \cdot 250\text{ kHz}$ , see Fig. 6.1f. The HF SQUID cavity is formed by two interdigitated capacitors and two linear inductors, which are connected to the SQUID loop in the center of the cavity, and it is capacitively coupled to a coplanar waveguide feedline for driving and readout. Both, inductance and resonance frequency of the HF SQUID cavity depend on the magnetic flux threading the SQUID loop  $\omega_0(\Phi) = 1/\sqrt{L_{\text{HF}}(\Phi)C_{\text{HF}}}$  as shown in Fig. 6.1g and can be tuned by applying a magnetic field perpendicular to the chip surface, in our case generated by an external coil below the chip. The device is mounted to the mixing chamber of a dilution refrigerator with a base temperature  $T_b = 15\text{ mK}$ , details on the setup can be found in section 6.7.2. All details regarding the device fabrication, device parameters and modelling are described in sections 6.7.1 and 6.7.3-6.7.5.

A radio-frequency current flowing through the inductor wire of the LF resonator will couple oscillating magnetic flux into the SQUID of the HF cavity and thereby modulate its resonance frequency, giving rise to a parametric photon-pressure interaction between the two circuits. With the creation and annihilation operators  $\hat{a}^\dagger, \hat{a}$  and  $\hat{b}^\dagger, \hat{b}$  for the SQUID cavity and LF resonator, respectively, the Hamiltonian of the system is given by

$$\hat{H} = \hbar\omega_0 \hat{a}^\dagger \hat{a} + \hbar\Omega_0 \hat{b}^\dagger \hat{b} + \hbar g_0 \hat{a}^\dagger \hat{a} (\hat{b} + \hat{b}^\dagger). \quad (6.1)$$

The single-photon coupling rate in the interaction part of the Hamiltonian is given by

$$g_0 = \frac{\partial\omega_0}{\partial\Phi} \Phi_{\text{zpf}} \quad (6.2)$$

with the SQUID cavity flux responsivity  $\partial\omega_0/\partial\Phi$  and the zero-point flux fluctuations  $\Phi_{\text{zpf}} = MI_{\text{zpf}}$  of the LF resonator. The zero-point fluctuations of the current are given by  $I_{\text{zpf}} = \sqrt{\frac{\hbar\Omega_0}{2L_{\text{LF}}}} \approx 21\text{ nA}$ , which with the mutual inductance  $M = 14\text{ pH}$  translates to zero-point flux fluctuations threading the SQUID loop of  $\Phi_{\text{zpf}} = 145\mu\Phi_0$ . The flux responsivity  $\partial\omega_0/\partial\Phi$  is determined by the flux biasing point, cf. Fig. 6.1g, and can be tuned in-situ by changing the external SQUID flux bias.

We model the SQUID cavity here as a harmonic oscillator without Kerr-nonlinearity, which is justified by its small anharmonicity. Due to the small Josephson inductance of the used constriction type Josephson junctions  $L_J = \Phi_0/2\pi I_c \sim 30\text{ pH}$  and the inductance dilution of  $L_J/L_{\text{HF}} \sim 0.04$ , the measured frequency shift per photon at the sweetspot  $\chi \sim 2\pi \cdot 1\text{ kHz}$  (cf. section 6.7.4) is much smaller than the cavity linewidth and  $\chi/\kappa \sim 10^{-2}$ .

In the driven multi-photon regime, the system is well described by the linearized interaction Hamiltonian

$$\hat{H}_{\text{int}} = \hbar g(\delta \hat{a} + \delta \hat{a}^\dagger)(\hat{b} + \hat{b}^\dagger) \quad (6.3)$$

with the multi-photon coupling rate  $g = \sqrt{n_c} g_0$ , the field fluctuation creation and annihilation operators  $\delta \hat{a}$  and  $\delta \hat{a}^\dagger$  and the equilibrium intracavity photon number  $n_c$  of the SQUID cavity.

We note here that the SQUID cavity resonance frequency  $\omega_0$  and linewidth  $\kappa$  depend on both, the flux bias point as well as the intracavity photon number, while the flux bias point also impacts the anharmonicity  $\chi$ . Additional data and a detailed discussion can be found in section 6.7.4.

## 6.3. DYNAMICAL BACKACTION BETWEEN TWO CIRCUITS

A famous consequence of the parametric photon-pressure interaction is the possibility to manipulate the quality factor and the resonance frequency of the low-frequency resonator by applying a strong coherent pump tone to the high frequency cavity around one of its sidebands  $\omega = \omega_0 \pm \Omega_0$ . This effect, which corresponds to a modification of the LF resonator susceptibility, is known in optomechanical systems as dynamical backaction [11, 160]. It arises from a retarded adjustment of the HF intracavity fields and therefore of the photon-pressure coupling to changes of the SQUID cavity resonance frequency induced by the LF flux threading the SQUID loop.

For the observation of dynamical backaction between the two circuits, we iteratively sweep a pump tone with  $\omega_p = \omega_0 + \Delta$  through the red sideband of the high frequency cavity, i.e.,  $\Delta = -\Omega_0 + \delta_r$ , for details on the experimental setup, cf. section 6.7.2. The cavity is flux biased here at  $\Phi_b = 0.16\Phi_0$ . For each value of  $\delta_r$ , we measure the reflection response of the LF resonator  $S_{11}$  by probing it directly with a weak radio-frequency probe tone  $\Omega \sim \Omega_0$ , cf. the schematic in Fig. 6.2a and the response shown in b and c. In the regime  $|\delta_r| \lesssim \kappa/2$ , the low-frequency resonance absorption dip experiences a significant modification in shape, shifting both in resonance frequency and linewidth.

For each pump detuning, we extract resonance frequency  $\Omega'_0$  and linewidth  $\Gamma'_0$  of the LF resonator from a fit to its measured response (cf. section 6.7.3) and determine the photon-pressure induced contributions by subtracting the intrinsic values  $\Omega_0$  and  $\Gamma_0$ . The resulting frequency shift  $\delta\Omega_0 = \Omega'_0 - \Omega_0$  and photon-pressure damping  $\delta\Gamma_0 = \Gamma'_0 - \Gamma_0$ , known in optomechanical systems as optical spring and optical damping, respectively, are plotted in Figs. 6.2d and e. The increase of linewidth for  $\delta_r = 0$  is about  $\delta\Gamma_0 = 2\pi \cdot 22 \text{ kHz} \sim \Gamma_0$ , i.e., of the same magnitude as the intrinsic damping rate, indicating a cooperativity  $\mathcal{C} = \frac{4g^2}{\kappa\Gamma_0} \sim 1$  for the chosen parameters. The lines in Fig. 6.2d and e are simultaneously adjusted theoretical curves using the expressions for photon-pressure induced dynamical backaction in the resolved sideband regime,  $\Omega_0 \gg \kappa$ ,

$$\delta\Omega_0 = 4g^2 \frac{\delta_r}{\tilde{\kappa}^2 + 4\delta_r^2} \quad (6.4)$$

$$\delta\Gamma_0 = 4g^2 \frac{\tilde{\kappa}}{\tilde{\kappa}^2 + 4\delta_r^2} \quad (6.5)$$

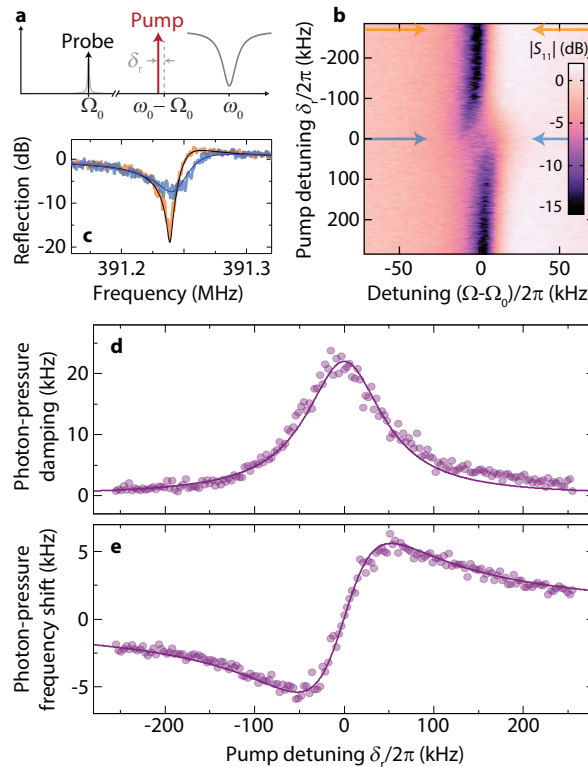


**Figure 6.2: Observation of photon-pressure dynamical backaction between two superconducting circuits.** **a** Schematic of the measurement scheme. After flux biasing the cavity to  $\Phi_b = 0.16\Phi_0$ , a pump tone with  $\omega_p = \omega_0 - \Omega_0 + \delta_r$  is swept stepwise through the red sideband of the high frequency SQUID cavity. For each pump detuning  $\delta_r$ , the reflection at the low-frequency resonator was scanned with a weak radio-frequency probe tone  $\Omega \sim \Omega_0$  and the corresponding reflection parameter  $S_{11}$  was measured. The result is shown color-coded in **b**, where a strong modification of the resonance is visible around  $|\delta_r| \lesssim \kappa/2$ . In **c**, a linescan for a far detuned pump  $\delta_r = 2\pi \cdot 260$  kHz and another for a pump tone exactly on the red sideband  $\delta_r = 0$  are shown as orange and light blue curves, respectively. Two pairs of arrows in **b** visualize the linescan positions. From the corresponding fit curves, shown as black lines in **c**, the pump-detuning dependent LF resonance frequency  $\Omega'_0$  and linewidth  $\Gamma'_0$  were extracted. This fitting procedure was repeated for each  $\delta_r$ . The extracted addition to the low-frequency linewidth, the photon-pressure damping  $\delta\Gamma_0 = \Gamma'_0 - \Gamma_0$ , and the photon-pressure induced shift of the LF resonance frequency  $\delta\Omega_0 = \Omega'_0 - \Omega_0$  are plotted in **d** and **e** as circles, respectively. The lines are theoretical curves, for details see main text.

and give an excellent agreement with the experimental data for  $\tilde{\kappa} = 2\pi \cdot 110$  kHz, indicating that we indeed observe dynamical backaction between two superconducting circuits. The reduced cavity linewidth  $\tilde{\kappa}$  compared to the directly probed resonance shown in Fig. 6.1 originates from two effects. First, the SQUID cavity linewidth is power dependent, cf. section 6.7.4. And secondly is the effective SQUID cavity linewidth reduced by the onset of mode hybridization close to the strong-coupling regime.

More data on dynamical backaction for different pump powers as well as for a blue-detuned pump frequency with  $\Delta \approx +\Omega_0$  can be found in the section 6.7.6.

## 6.4. FROM PHOTON-PRESSURE INDUCED TRANSPARENCY TO THE PARAMETRIC STRONG-COUPLING REGIME

When we choose a similar experimental setting as before, but probe the high-frequency SQUID cavity instead of the radio-frequency circuit with a second weak microwave tone, cf. Fig. 6.3a and section 6.7.2, a new effect occurs, which we call photon-pressure induced transparency (PPIT), similar to electromagnetically induced transparency in atoms [161] and optomechanically induced transparency in optomechanical systems [149, 150]. A pump tone on the red cavity sideband with  $\omega_p = \omega_0 - \Omega_0$  and a weak probe signal with  $\omega_{pr} \approx \omega_0$  will interfere inside the SQUID cavity and generate an amplitude beating with the difference frequency  $\Omega = \omega_p - \omega_{pr}$ . When  $\Omega \approx \pm\Omega_0$ , the LF resonator is driven to coherent oscillations by the parametric interaction between the oscillators. This, in turn, modulates the SQUID cavity resonance frequency and hereby generates a sideband to the pump tone at  $\omega = \omega_p + \Omega$ , which interferes with the original probe tone.

The interference effect of PPIT is experimentally identified by a narrow transparency window in the SQUID cavity response. In the bottom data of Fig. 6.3d, the transparency window is visible as a small peak in the center of the cavity absorption dip and its shape is given by the LF resonator response including dynamical backaction from the red-detuned pump field. When the multi-photon coupling strength  $g = \sqrt{n_c} g_0$  is increased, this transparency window grows in magnitude and width, and in typical optomechanical setups such an enhancement of the multi-photon coupling strength is achieved by increasing the number of intracavity photons by an increased strength of the sideband pump tone [25]. In our device, however, we can control the single-photon coupling rate  $g_0$  by changing the flux bias value of the SQUID, similar to flux-mediated microwave optomechanics [70, 162]. We are therefore able to enhance the multi-photon coupling rate while keeping the number of intracavity photons constant, cf. Fig. 6.3b and c.

With increasing flux bias and correspondingly increasing single-photon coupling rate  $g_0$ , the transparency window in the SQUID cavity response grows larger in amplitude and width as can be seen in Fig. 6.3d from bottom to top, until for the largest flux bias values two distinct, new eigenmodes define the response. These new modes of the pumped system correspond to hybridized modes between the LF resonance and intracavity field modulations and both modes are approaching a hybridized linewidth of  $(\kappa + \Gamma_0)/2$  and a frequency splitting of  $2g$ . This hybridization is apparent as an avoided crossing of the two modes, when the pump frequency is iteratively swept through the red sideband as shown for different flux bias points in e.

From theoretical modelling of the reflection response, shown as black lines in Fig. 6.3d, we extract the cooperativity  $C = \frac{4g^2}{\kappa\Gamma_0}$  and the multi-photon coupling rate  $g$ . The largest value we show here corresponds to a cooperativity  $C \approx 53$  and to a coupling rate  $g/\pi = 0.5\text{MHz}$ . Additional data on the intracavity photon number dependence for a fixed flux bias point with maximum cooperativity  $C \approx 130$  and  $g/\pi \approx 1\text{MHz}$  can be found in section 6.7.6. With a calibration of the setup attenuation, we can determine the intracavity photon number  $n_c \approx 70$  for the data presented in Fig. 6.3 and from there the single-photon

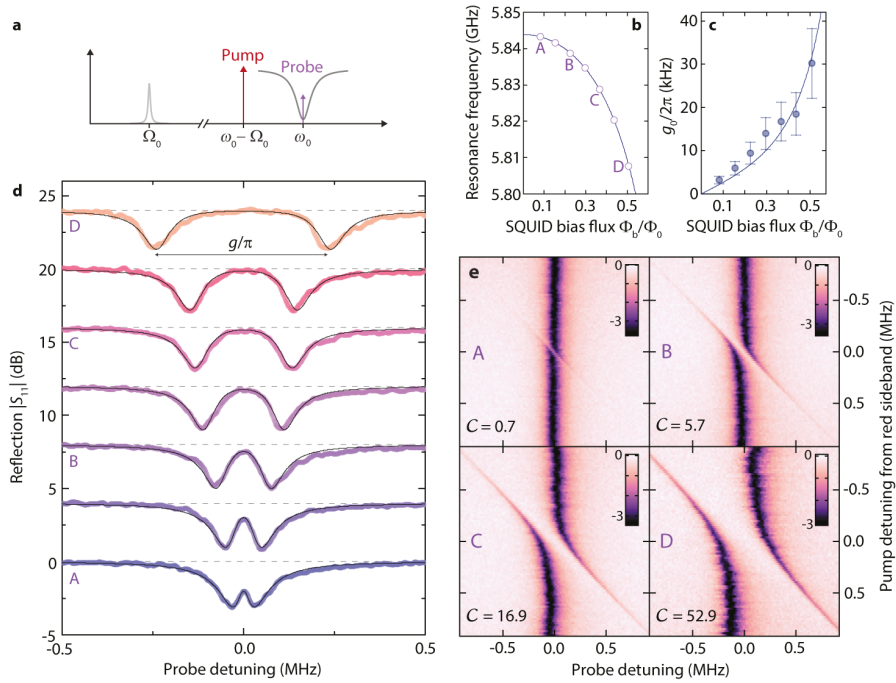


**Figure 6.3: From photon-pressure induced transparency to the parametric strong-coupling regime by tuning the SQUID flux bias.** **a**, Schematic of a photon-pressure-induced transparency (PPIT) experiment. A pump tone is set to the red sideband of the SQUID cavity  $\omega_p = \omega_0 - \Omega_0$ , while a weak probe tone is scanning the SQUID cavity response around resonance with  $\omega_{pr} \sim \omega_0$ . **b**, shows the SQUID cavity resonance frequency vs magnetic flux as a line, together with the seven flux bias points used for the PPIT experiment here, indicated as circles. By increasing the bias flux through the SQUID, the cavity flux responsivity  $\partial\omega_0/\partial\Phi$  and therefore the single-photon coupling strength  $g_0$  are increased accordingly. This can be seen in panel **c**, where the expected single-photon coupling rate  $g_0$  vs flux bias is shown as line. The measurement configuration described in **a** was performed for the seven different flux-bias points shown in **b**, and for each of these biasing points the SQUID cavity reflection  $|S_{11}|$  is shown in **d**. From bottom to top, the flux bias value is increased, and subsequent data are shifted by +4dB for better visibility. For the lowest flux bias value, we find a small peak in the center of the SQUID cavity absorption dip, indicating the PPIT regime. For larger flux bias values, the PPIT window grows in both, amplitude and width, ultimately leading to two distinct absorption resonances for the largest flux value (top curve). In this regime, where the frequency splitting between the two modes is given by  $g/\pi \approx 500$  kHz, the system has entered the parametric, photon-pressure induced strong-coupling regime. The values for  $g_0$  extracted from the theoretical black lines added to the data in **d**, are plotted as circles in **c**. In **e**, we show the SQUID cavity reflection  $|S_{11}|$  (color scale given in dB) for four distinct flux bias points, denoted in **b** with A, B, C, and D, and for non-zero pump detunings  $|\delta_r| \leq 2\pi \cdot 0.9$  MHz. For small flux bias (A), a small transparency signature is slicing through the cavity response. With increasing flux bias, this transparency window gets stronger and wider, developing into a pronounced normal-mode splitting for the largest flux bias value (D). The intracavity photon number for all data shown here was  $n_c \approx 70$  and the cooperativities  $\mathcal{C}$  for the biasing points A-D are given within the sub-panels of **e**.

coupling rate  $g_0$ . The results are plotted in panel **c** as circles and follow closely the theoretically expected line with maximum values corresponding to  $g_0/\kappa \sim 0.1$ . We attribute

deviations to a frequency dependent system attenuation and a frequency-dependent conversion from pump power to intracavity photon numbers due to cable resonances in our setup. As our system provides access to the LF resonator response, we can also detect the normal-mode-splitting directly in the LF reflection, cf. section 6.7.6.

## 6.5. OBSERVATION OF PHOTON-PRESSURE-AMPLIFIED THERMAL RADIO-FREQUENCY PHOTONS

Photon-pressure induced dynamical backaction in parametrically coupled systems does not only influence the resonance frequency and the linewidth of the LF resonator, but at the same time impacts its internal state by cooling or parametric amplification. This effect has been used to cool mechanical oscillators into the quantum ground-state [31, 32] with a red-detuned pump tone or to realise parametric, mechanical-oscillator-mediated microwave amplification using a blue-detuned pump [26]. At the base temperature of our dilution refrigerator  $T_b = 15\text{mK}$ , the LF resonator is expected to have a thermal photon occupation of  $n_{\text{LF}} = (e^{\hbar\Omega_0/k_B T_b} - 1)^{-1} \approx 0.44$ , hence to be close to the quantum ground-state.

A pump tone on the blue SQUID cavity sideband  $\omega_p = \omega_0 + \Omega_0$  will have two effects to the LF resonator. It will reduce its effective linewidth by negative photon-pressure damping and at the same time it will amplify the intrinsic state of the resonator. For the observation of the negative damping, we first perform a measurement scheme similar to PPIT in the previous section, but now with a blue-detuned pump tone at  $\omega_p = \omega_0 + \Omega_0$ . The reflection of the SQUID cavity probed with a weak second tone around  $\omega_{\text{pr}} \approx \omega_0$  in presence of a blue-detuned pump is shown in Fig. 6.4a. Instead of an interference peak as observed for the red-detuned pump field, we now observe a very narrow absorption dip with  $\Gamma'_0 \approx 2\pi \cdot 10\text{kHz}$ , indicating the regime of photon-pressure induced absorption (PPIA) and negative photon-pressure damping with  $\delta\Gamma_0 \approx -2\pi \cdot 12\text{kHz}$ . From this response curve, we can extract all system parameters such as the linewidths  $\kappa, \kappa_e, \Gamma'_0$  and cooperativity  $\mathcal{C}$ , as indicated in Fig. 6.4a.

To detect the state of the LF resonator, we switch off the probe tone and measure the SQUID cavity output field around its resonance with a signal analyzer in presence of a blue-detuned pump. The thermal and quantum fluctuations in the LF resonator generate a sideband to the pump, also described as Stokes process in the scattering picture of optomechanics [56], and this noise-induced sideband is detected using a signal analyzer. For a negligible SQUID cavity occupancy, the detected power spectral density  $S(\omega)$ , in units of photon numbers, is related to the current fluctuation spectral density in the LF resonator  $S_I(\Omega)$  by

$$\frac{S(\omega)}{\hbar\omega} = \frac{1}{2} + n'_{\text{add}} + \frac{\kappa_e}{\kappa} \frac{\mathcal{C}}{2} \frac{\Gamma_0}{I_{\text{zpf}}^2} S_I(-\Omega) \quad (6.6)$$

with

$$S_I(-\Omega) = \frac{8\Gamma_0}{\Gamma_0'^2 + 4\Delta_0^2} I_{\text{zpf}}^2 (n_{\text{LF}} + 1) \quad (6.7)$$

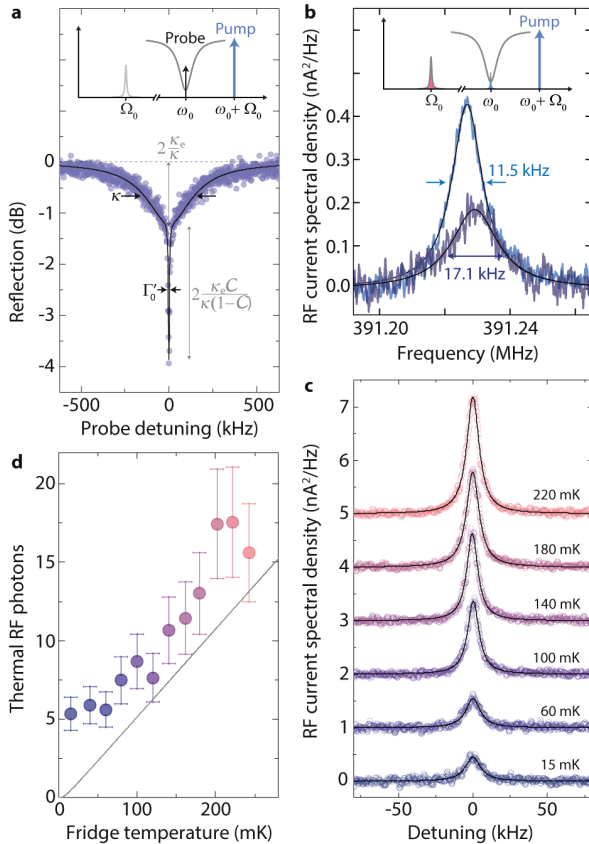


**Figure 6.4: Observation of photon-pressure-amplified thermal noise of a radio-frequency superconducting circuit.** **a** When a pump tone is set to the blue cavity sideband  $\omega_p = \omega_0 + \Omega_0$  and a weak probe tone is swept through the cavity resonance (schematic as inset), a narrow absorption window appears in the center of the cavity resonance. From the response, we extract  $\kappa, \kappa_e$ , the effective LF resonator linewidth  $\Gamma'_0$  and  $C$ . The flux bias value is  $\Phi_b/\Phi_0 \sim 0.5$  and the fridge temperature  $T_b = 15\text{mK}$ . **b** Without the probe signal, the residual thermal and quantum fluctuations in the LF resonator are amplified by the blue-detuned tone and generate a sideband to the pump tone at the SQUID cavity center frequency, cf. inset schematic. This noise sideband around the cavity center is detected with a signal analyzer and converted to RF current spectral density. Shown are two exemplary data sets (black lines are fits) for different photon-pressure amplification gain, the numbers indicate the respective  $\Gamma'_0$ s. The photon-pressure damping is modified here by slightly detuning the pump from the blue sideband, and a corresponding photon-pressure frequency shift is visible. The LF resonator current noise spectral density for varying fridge temperature is shown as colored lines from 15mK to 220mK together with Lorentzian fits as black lines in **c**. Subsequent data are manually shifted by  $1\text{nA}^2/\text{Hz}$  for better visibility. From the amplitude of the current noise, the equilibrium thermal photon number is calculated and plotted in panel **d** vs the fridge temperature. Error bars indicate a 20% uncertainty and the gray line follows the Bose-factor. For large fridge temperatures, the RF resonator is thermalised with the fridge, for low fridge temperatures a residual thermal occupation of  $\sim 5$  RF photons remains, indicating a mode temperature of  $\sim 100\text{mK}$ .

where  $n_{\text{LF}}$  is the thermal RF resonator population and  $n'_{\text{add}} \approx 15$  is the effective number of noise photons added by the detection chain.

With these equations, we transform the detected power spectral density into a current fluctuation spectral density, cf. also section 6.7.7, and the result is plotted for two different values of photon-pressure amplification in Fig. 6.4b. We can calibrate the residual thermal occupation of RF photons in the low-frequency resonator by varying the fridge temperature and detect the thermal current spectral density as shown in Fig. 6.4c for six different fridge temperatures. With increasing temperature, the noise amplitude grows, indicating the increased thermal population of the LF resonator. For each curve, we determine the thermal RF photon population  $n_{\text{LF}}$  from its amplitude on resonance. The result is plotted in Fig. 6.4c as circles and shows a trend for higher temperatures, that follows closely the nearly linear behaviour expected from the Bose-factor shown as gray line. For lower temperatures, the LF mode saturates around  $n_{\text{LF}} \approx 5$  thermal photons, which corresponds to a mode temperature of  $\sim 100 \text{ mK}$ . We attribute the difference between the base temperature and the mode temperature to imperfect thermalization of the LF input line, cf. the setup in section 6.7.2, and to imperfect thermalization of the chip itself.

In principle, our device also enables sideband-cooling by up to a factor of  $\sim 10$  [58], which corresponds to cooling the radio-frequency resonator into its quantum ground-state with  $n_{\text{LF}} < 1$ . Due to the intrinsic sideband asymmetry of the detection scheme [163], the highly undercoupled SQUID cavity  $\kappa_e/\kappa \sim 0.1$  and the large number of added photons  $n'_{\text{add}} \approx 15$ , however, we are not able to detect the signal within our current setup.

## 6.6. DISCUSSION

We presented a device consisting of two superconducting circuits, which are coupled via a parametric photon-pressure interaction. Performing a series of experiments, we demonstrated dynamical backaction between two superconducting circuits, observed photon-pressure-induced transparency and normal-mode splitting, indicating the parametric strong-coupling regime. Finally, we observed photon-pressure-amplified radio-frequency photons by blue-sideband SQUID cavity pumping. In summary our device constitutes a novel platform for the control and readout of superconducting quantum circuits of a broad range of frequencies and enables new ways to manipulate and detect radio-frequency photons. We also note that multimode Josephson parametric converter (JPC) devices [164–166] can exhibit similar physics to the linearized multi-photon coupling that can arise from the photon-pressure interaction, and in particular, a pump-tunable normal-mode splitting can be induced with the appropriate driving [165, 166]. Photon-pressure couplings (3-wave mixing between two modes) in JPCs, however, are undesired [164] and are typically eliminated by design. Another important distinction is that our photon-pressure device contains no Josephson junctions in the low-frequency circuit, resulting in a much higher degree of linearity than in a JPC. Furthermore, the coupling is asymmetric: current in the low-frequency mode modulates the HF mode resonance frequency, but not vice versa. In the single-photon strong-coupling regime, this allows for example for modular quadrature measurements [93] or the implementation of coupling-induced photon-blockade [67].

As the system dynamics of our platform is completely equivalent to cavity optomechanics, many technological developments of the last decade such as parametric amplifiers, non-reciprocal devices or bath engineered systems, which are based on photon-pressure coupling, can be realised now with a purely circuit-based approach. Our results also open the door for the investigation of parametrically coupled harmonic oscillators in novel parameter regimes, as superconducting circuits have an extremely high design flexibility and precision regarding resonance frequencies and linewidths compared to opto- or electromechanical systems. With further advances, this platform also provides the potential for the realization of recently discussed possibilities for quantum computation, using bosonic codes based on Gottesmann-Kitaev-Preskill states [93, 167], and for the quantum control of radio-frequency circuits and photons [98] relevant for fields ranging from radio-astronomy to nuclear magnetic resonance imaging.

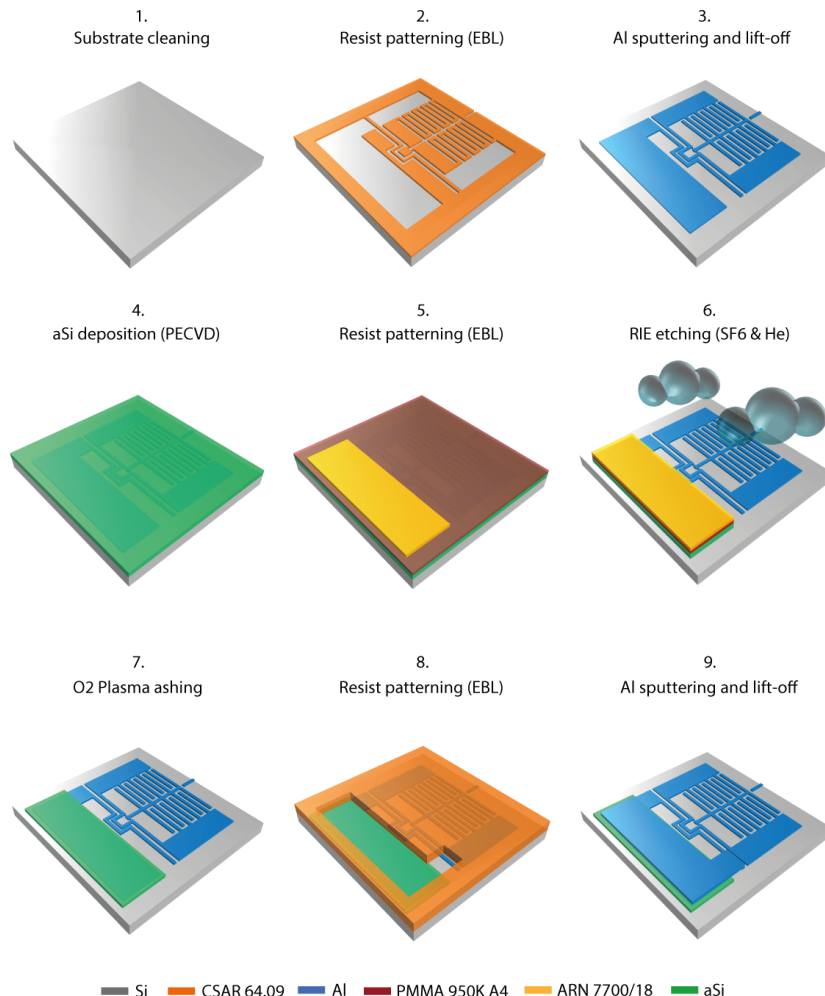
## 6.7. SUPPLEMENTARY INFORMATION

### 6.7.1. DEVICE FABRICATION

The device fabrication starts with the patterning of alignment markers on a full 4inch Silicon wafer, required for the EBL (Electron Beam Lithography) alignment of the following fabrication steps. The structures were patterned using a CSAR62.13 resist mask and a sputter deposition of 50nm Molybdenum-Rhenium alloy. After undergoing a lift-off process, the only remaining structures on the wafer were the  $20 \times 20 \mu\text{m}^2$  square markers. The complete wafer was diced into individual  $14 \times 14 \text{ mm}^2$  chips, which were used individually for the subsequent fabrication steps. As second step in the fabrication (Supplementary Fig. 6.5 steps 2. & 3.), we pattern the bottom plate of the parallel plate capacitor, the inductor wire of the low-frequency cavity, the SQUID cavity and the center conductor of the SQUID cavity feedline by means of EBL using CSAR62.09 as resist. After the exposure, the sample was developed in Pentyacetate for 60seconds, followed by a solution of MIBK:IPA (1:1) for 60seconds, and finally rinsed in IPA.

The sample was subsequently loaded into a sputtering machine where a 20nm layer of Aluminum was deposited. Finally, the chip was placed in the bottom of a beaker containing a small amount of anisole and inserted in a ultrasonic bath for a few minutes. This lift-off process turned out to be very efficient compared to warm anisole bath without ultrasound, where sometimes some of the unwritten structures would not lift-off.

The deposition of the dielectric layer of the parallel plate capacitors was done using a plasma-enhanced chemical vapor deposition (PECVD). To guarantee low dielectric losses in the material, the chamber underwent an RF cleaning process overnight and only afterwards the deposition of  $\sim 130 \text{ nm}$  of amorphous silicon was performed. At this point the whole sample is covered with dielectric, cf. Supplementary Fig. 6.5 step 4. Afterwards, a double layer of resist (PMMA 950K A4 and ARN-7700-18) was spin-coated and exposed with EBL. Prior to the development of the pattern, a post-bake of 2 minutes at  $\sim 115^\circ\text{C}$  was required. Directly after, the sample was dipped in MF321 for 2 minutes and 30 seconds, followed by  $\text{H}_2\text{O}$  for 30 seconds and lastly rinsed in IPA, cf. Supplementary Fig. 6.5 step 5. To finish the third step of the fabrication, the developed sample underwent a  $\text{SF}_6/\text{He}$  reactive ion etching (RIE) to remove the amorphous Silicon, followed by an in-situ  $\text{O}_2$  plasma ashing to remove resist residues, cf. Supplementary Fig. 6.5



6

**Figure 6.5: Schematic device fabrication.** Steps 1.-3. show the deposition and patterning of the SQUID cavity and both bottom plate and inductor wire of the low frequency cavity. Steps 4.-6. sketch the deposition and patterning of the amorphous Silicon (aSi) dielectric layer for the parallel plate capacitor. Steps 7. and 8. show the patterning and deposition of the top plate of the low-frequency circuit capacitor. Step 9. shows the final device. A detailed description of the individual steps is given in the text.

steps 6.& 7.

As final step, the sample was again coated in CSAR62.13 and the top plate of the capacitor as well as all ground plane and the low-frequency feedline was patterned with EBL. The development of the resist was done in a similar way to the one mentioned in the second step. Afterwards, the sample was loaded into a sputtering machine where an argon milling process was performed in-situ for 2 minutes. This etching step prior to

the deposition was done to remove the native aluminum oxide present on top of the first layer and allow for good electrical contact between the top and bottom plates of the low-frequency capacitor. Posterior to the milling, a 200 nm layer of Aluminum was deposited and finally a lift-off procedure, similar to the one of the second step, was performed, cf. Supplementary Fig. 6.5 step 9.

At the end of the fabrication, the sample was diced to a  $10 \times 10 \text{ mm}^2$  size and mounted into a PCB (Printed Circuit Board). A schematic representation of this fabrication process can be seen in Supplementary Fig. 6.5, omitting the initial patterning of the electron beam markers.

### 6.7.2. MEASUREMENT SETUP

#### SETUP CONFIGURATION

All the experiments reported in this paper were performed in a dilution refrigerator operating at a base temperature close to  $T_b = 15 \text{ mK}$ . A schematic of the experimental setup and of the external configurations used in the different performed experiments can be seen in Supplementary Fig. 6.6.

The PCB, onto which the fabricated sample was glued and wirebonded, was placed in a radiation tight copper housing and connected to two coaxial lines. One of the lines was used as input/output port for the high-frequency (HF) SQUID cavity and the second line was set in a similar way for the low-frequency (LF) cavity. Both of the cavities were measured in a reflection geometry, and therefore the input and output signals were split via a directional coupler on the 15 mK stage (HF) and 100 mK stage (LF), respectively. Both output signals went into a cryogenic HEMT (High Electron Mobility Transistor) amplifier for their particular frequency range.

Furthermore, in order to generate an out-of-plane magnetic field, required to flux bias the SQUID cavity, an external magnet (not shown in the figure) was put in very close proximity below the device and the two were placed inside a cryoperm magnetic shield. The magnet was connected with DC wires, allowing for the field to be tuned by means of a DC current (not shown).

Both high-frequency input lines were heavily attenuated in order to balance the thermal radiation from the line to the base temperature of the fridge. Due to a lack of low-frequency isolators/circulators, the LF input lines were attenuated less than usually necessary for fully equilibrating the input noise to the fridge base temperature. Outside of the refrigerator, we used different configurations of microwave signal sources and high-frequency electronics for the different experiments.

In Supplementary Fig. 6.6b we show the configuration for the measurement of dynamical backaction. A microwave generator sends a continuous wave signal to the SQUID cavity around one of its sidebands, while the LF resonator is probed in reflection with a vector network analyzer (VNA). We also used this setup to measure the normal-mode splitting on the LF side as shown in Supplementary Fig. 6.16.

Supplementary Fig. 6.6c shows the setup for photon-pressure induced transparency and the strong-coupling regime detected at the SQUID cavity. During the experiment a continuous wave tone from a microwave generator is combined with a weak probe signal via a directional coupler and sent to the SQUID cavity. The output signal of the SQUID

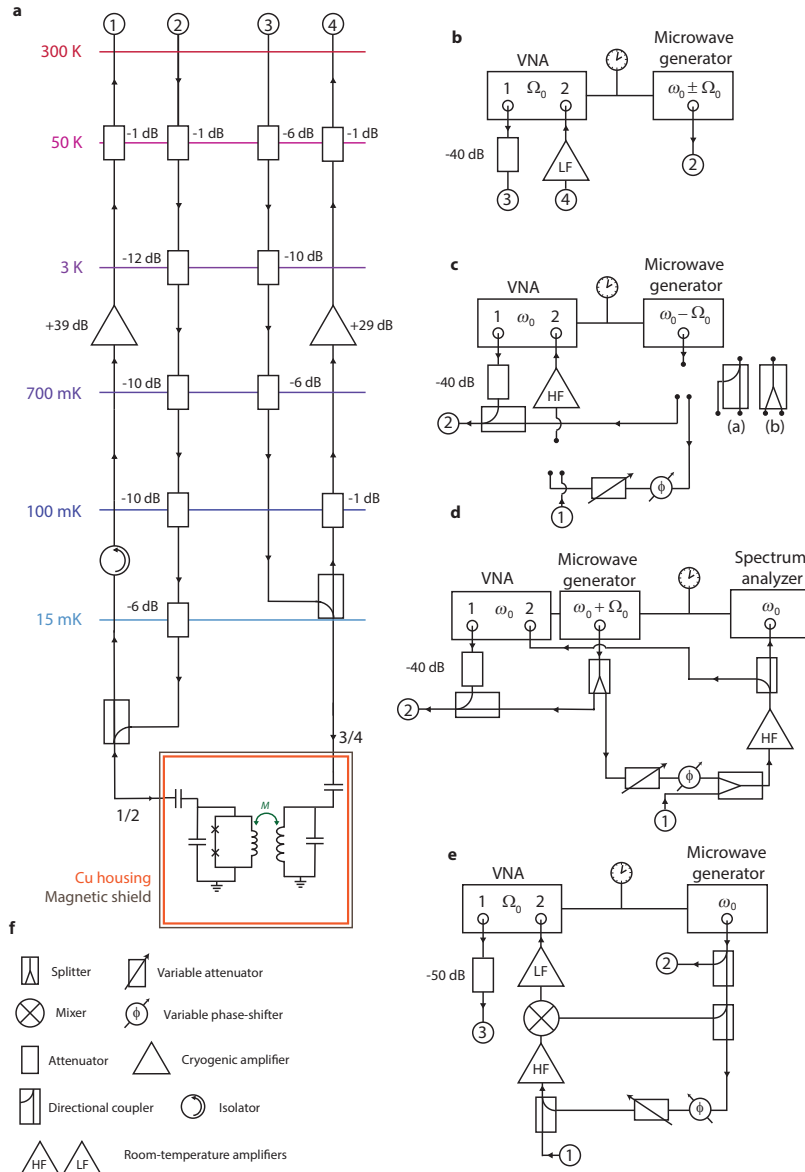


Figure 6.6: **Schematic of the measurement setup.** Detailed information is provided in text.

cavity, coming from the dilution refrigerator, is afterwards carrier-cancelled with part of the original pump tone in order to avoid reaching the saturation regime of our room temperature (RT) amplifiers, and analyzed by means of a VNA. For the data shown in sections 6.2-6.5, a directional coupler was used at the output of the microwave generator

and before the RT high-frequency amplifier. In order to drive the SQUID cavity with higher powers for the data shown in Supplementary Fig. 6.15, the directional couplers, which have an insertion loss of 10 dB, were replaced by splitters. The two configurations are denoted (a) for the directional coupler case and (b) for the splitter/combiner case.

In Supplementary Fig. 6.6d we show the setup for photon-pressure induced absorption and thermal noise amplification and detection (Figs. 6.4a, c and d), where a continuous tone is sent to the blue sideband of the SQUID cavity. In addition, in order to observe the cavity response and adjust the pump tone frequency with respect to the power-dependent cavity resonance, a weak VNA signal is combined with the pump tone via a directional coupler. The output signal is then carrier-cancelled with the original pump tone, amplified and split in two signals that are analyzed individually by a spectrum analyzer and a VNA. During the detection of thermal noise with the signal analyzer, the VNA scan was stopped and the VNA output power was completely switched off.

In Supplementary Fig. 6.6e the setup for LF resonance up-conversion is shown (Fig. 6.1e). During the experiment, a resonant pump tone is sent to the SQUID cavity using a signal generator. Simultaneously a weak scanning probe signal coming from the VNA is sent to the LF resonator. The SQUID cavity output field is carrier-cancelled with the original pump tone, amplified, down-converted and once again amplified with a LF amplifier before reaching the VNA input port.

For the data shown in Fig. 6.4b, we used a combination of setups d and e. Everything is identical to d, but instead of directly detecting the high-frequency sideband signal after the final directional coupler, we added a mixer with the pump tone as local oscillator for down-conversion. Also, we added another LF amplifier before the signal was entering the signal analyzer. This way, we detected the LF thermal noise directly at its original oscillation frequency.

For all experiments, the microwave sources and vector network analyzers (VNA) as well as the spectrum analyzer used a single reference clock of one of the devices.

## ESTIMATION OF THE ATTENUATION CHAIN AND ADDED NOISE

### 1. ADDED NOISE

We can estimate the added noise in our setup in two ways. First and simplest, we can calculate the added noise photons by the HEMT (High Electron Mobility Transistor) amplifier by using its noise temperature which, according to the specification datasheet, is approximately 5.5 K at an ambient temperature of 12 K. This noise temperature corresponds to approximately  $n_{\text{add}} \sim 19$  photons. Due to some finite attenuation between the sample and the amplifier however, the effective number of added noise photons is increased and with an estimated 1 dB loss between device and amplifier, we get  $n'_{\text{add}} \approx 24$  photons by this method.

The second method is to use the base temperature dependence of the thermal occupation of the LF resonator as presented in Fig. 6.4. From matching the slope of the temperature dependent RF photon number in the nearly linear regime with the Bose factor, we find approximately  $n'_{\text{add}} \sim 15$  photons, which would correspond to a noise temperature of  $\sim 3.4$  K.

Possible sources and reasons for this mismatch are frequency-dependence, voltage-biasing dependence and ambient-temperature dependence of the HEMT noise temper-

ature. At least for the ambient/operation temperature of the amplifier, we deviate by about a factor of 4 of the data sheet with  $T_{\text{op}} \sim 3\text{ K}$ . The precise value of the attenuation between sample and amplifier might additionally modify the extracted added noise photon number.

For the data presented in Fig. 6.4, we worked with  $n'_{\text{add}} \sim 15$ .

## 2. ESTIMATION OF THE ATTENUATION CHAIN

The determination of the single-photon coupling rate  $g_0$  and the cavity anharmonicity  $\chi$  from our data requires an estimate of the intracavity photon number. All other extracted quantities such as the cooperativity  $\mathcal{C}$ , the multi-photon coupling rate  $g$  or the photon-pressure induced dynamical backaction effects, however, do not require an estimate of the intracavity photon number.

One way to estimate the input power on the on-chip feedline of the device is to use the thermal noise of the HEMT amplifier as calibration method. For a VNA output power of  $-30\text{ dBm}$ , room-temperature attenuation of  $\sim 30\text{ dB}$ , and a measurement bandwidth of  $200\text{ Hz}$ , we extract a signal-to-noise ratio  $\text{SNR} \approx 46\text{ dB}$  from a VNA measurement in the red-sideband frequency range. From this and the HEMT noise temperature, we estimate a total power arriving at the HEMT of  $-123 \pm 1\text{ dBm}$  where the error takes into account the range of possible noise temperatures of the HEMT as discussed above. Furthermore, assuming an attenuation between the sample and the HEMT of  $1\text{ dB}$ , we estimate a total input attenuation in the line of  $-62\text{ dB}$ . This calibration method was repeated for different frequency ranges, showing a frequency-dependent variation of approximately  $\pm 2\text{ dB}$ .

The experiment of power-dependent coupling presented in Supplementary Fig. 6.15 was performed in the same cooldown as aforementioned power-calibration and using the theoretical value of  $g_0 \sim 2\pi \cdot 30\text{ kHz}$  in the corresponding data analysis yields a line attenuation of  $-61\text{ dB}$ , which is close to the estimated value. With this attenuation, we get a Kerr nonlinearity of  $\chi \approx 2\pi \cdot 11\text{ kHz}$  for the chosen flux bias point  $\Phi_b/\Phi_0 = 0.51$ . The data presented in Fig. 6.3 and Fig. 6.11 were taken during an earlier cooldown and to achieve consistency between the datasets from the two cooldowns regarding  $g_0$  and  $\chi$ , we have to assume an attenuation of  $\sim 59\text{ dB}$  for the earlier cooldown. Unfortunately, we have not taken systematic data for an estimate of the input attenuation during the earlier cooldown via a signal-to-noise ratio determination around the red sideband. As the flux-dependence of the HF cavity is unaltered between the cooldowns, however, we assume that the difference originates not from a change in the SQUID cavity itself, but from an unaccounted RT attenuation difference between the two experiments in different cooldowns.

If we were to strictly take the input attenuation of  $62\text{ dB}$  as estimated above for all data, we would get  $g_0$ -values about a factor of 1.5 larger and  $\chi$ -values about 2 larger than the ones given. The main results of our experiments, however, are not impacted by the precise value of attenuation,  $g_0$  or  $\chi$ .

### 6.7.3. THE LF RESONATOR

#### ANALYTICAL CIRCUIT MODEL

The LF resonator used in this experiment is a simple LC circuit coupled to a feedline with characteristic impedance  $Z_0$ . The resonator consists of a parallel plate capacitor with an area of  $A_{\text{LF}} = 7.68 \cdot 10^{-7} \text{ m}^2$ , filled with  $t \approx 130 \text{ nm}$  thick amorphous silicon as dielectric. With

$$C_{\text{LF}} = \epsilon_0 \epsilon_r \frac{A_{\text{LF}}}{t} \quad (6.8)$$

the capacitance is calculated to be  $C_{\text{LF}} \approx 620 \text{ pF}$ , where  $\epsilon_0 = 8.854 \cdot 10^{-12} \text{ F m}^{-1}$  is the vacuum permittivity and  $\epsilon_r = 11.8$  is the relative permittivity of silicon. In addition, the resonator is capacitively coupled to a coplanar waveguide feedline by means of a parallel plate coupling capacitor with  $C_c = 434 \text{ fF}$ .

From the resonance frequency of  $\Omega_0 = 2\pi \cdot 391 \text{ MHz}$  and using

$$\Omega_0 = \frac{1}{\sqrt{L_{\text{LF}}(C_{\text{LF}} + C_c)}} \quad (6.9)$$

we calculate the total inductance of the circuit as  $L_{\text{LF}} = 267 \text{ pH}$ . This effective inductance includes the contribution from the mutual inductive coupling of the two circuits.

A significant contribution to the total inductance is coming from kinetic inductance due to the thin film used for the bottom layer and the inductor wire. From corresponding simulation with the software package SONNET, we estimate the kinetic inductance  $L_k \sim 2.2 \text{ pH}$  per square to contribute about 0.59 to the total inductance or  $L_k = 1.44 L_g$  with the kinetic inductance  $L_k$  and the geometric inductance  $L_g$ .

For the capacitively coupled parallel LC circuit, the external linewidth is given by

$$\Gamma_e = \frac{Z_0 C_c^2}{L_{\text{LF}}(C_{\text{LF}} + C_c)^2} \quad (6.10)$$

which gives with  $Z_0 = 50 \Omega$  a value of  $\Gamma_e = 2\pi \cdot 14.5 \text{ kHz}$ .

#### CURRENT ZERO-POINT FLUCTUATIONS

The current zero-point fluctuations through the LF inductor are calculated via

$$I_{\text{zpf}} = \sqrt{\frac{\hbar \Omega_0}{2 L_{\text{LF}}}} \quad (6.11)$$

and with the parameters of the circuit we get  $I_{\text{zpf}} \approx 21 \text{ nA}$ .

#### CAVITY PARAMETER EXTRACTION FROM A REFLECTION MEASUREMENT

Supplementary Fig. 6.7 shows a background-corrected LF resonator reflection measurement in amplitude data  $|S_{11}|$  in **a** as well as in the complex plane in **b**, together with the corresponding fit curves. From fitting the data with the response function

$$S_{11} = 1 - \frac{2\Gamma_e}{\Gamma_i + \Gamma_e + 2i\Delta_0} \quad (6.12)$$

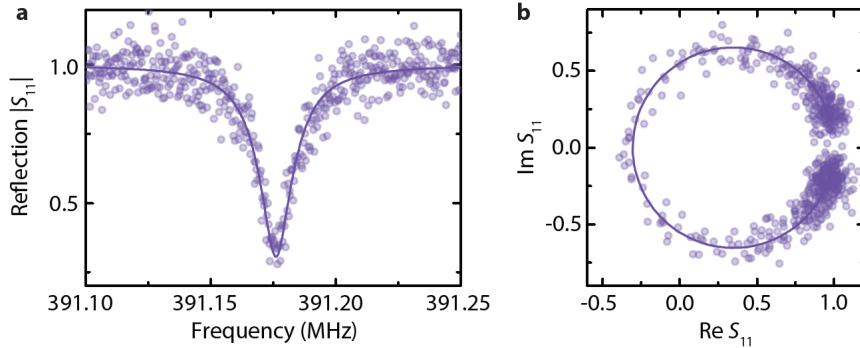


Figure 6.7: **The LF resonator response.** **a** The magnitude of the reflection response  $|S_{11}|$  of the low-frequency resonator. Circles are data, line is a fit. **b** The complex scattering data  $S_{11}$  around the LF resonance frequency. Circles are data, line is a fit. The data and fits shown here have been background-corrected before plotting as described in section 6.7.5. From the fit, we extract  $\Gamma_e, \Gamma_i$ , and  $\Omega_0$  as given in the text.

with  $\Delta_0 = \Omega - \Omega_0$  and the internal and external decay rates  $\Gamma_i$  and  $\Gamma_e$ , we extract the resonator parameters

$$\Omega_0 = 2\pi \cdot 391.18 \text{ MHz}, \quad \Gamma_i = 2\pi \cdot 7.4 \text{ kHz}, \quad \Gamma_e = 2\pi \cdot 13.8 \text{ kHz} \quad (6.13)$$

where the extracted  $\Gamma_e$  is very close to the theoretical value of 14.5 kHz.

#### 6.7.4. THE HF SQUID CAVITY

##### ANALYTICAL CIRCUIT MODEL

###### 1. CAPACITANCE, INDUCTANCE, AND FEEDLINE COUPLING

The capacitance of an interdigitated capacitor (IDC) can be approximately calculated as given in Ref. [158], where

$$C_{\text{IDC}} = (N - 3) \frac{C_1}{2} + 2 \frac{C_1 C_2}{C_1 + C_2} \quad (6.14)$$

with

$$C_i = 2\epsilon_0 \epsilon_{\text{eff}} l \frac{K(k_i)}{K(k'_i)}, \quad i = 1, 2. \quad (6.15)$$

Here,  $K(k_i)$  are elliptic integrals of the first kind,  $l$  is the finger length,  $\epsilon_{\text{eff}} = (\epsilon_r + 1)/2$  is the effective permittivity with the Silicon substrate permittivity  $\epsilon_r = 11.8$ ,  $N$  is the total number of fingers and

$$k_1 = \sin\left(\frac{\pi}{2} \frac{a}{a+b}\right) \quad (6.16)$$

$$k_2 = 2 \frac{\sqrt{a(a+b)}}{2a+b} \quad (6.17)$$

$$k'_i = \sqrt{1 - k_i^2} \quad (6.18)$$

with  $a$  the finger width and  $b$  the gap width in between two fingers.

For a single capacitor  $C_{\text{IDC}}$  of our circuit with  $N = 90$ ,  $l = 100 \mu\text{m}$ ,  $a = b = 1 \mu\text{m}$ , we get  $C_{\text{IDC}} = 507 \text{ fF}$ . Since we have two of these capacitors in parallel, the total circuit capacitance is  $C_{\text{HF}} = 2C_{\text{IDC}} = 1.01 \text{ pF}$ .

The ground side of each of the two IDCs is not galvanically connected to the ground plane but via a large parallel plate capacitor with  $C_{\text{pp}} \sim 70 \text{ pF}$  in order to avoid the generation of a closed superconducting loop around the SQUID, which would act as flux transformer and induce flux-induced frequency noise to the cavity.

Furthermore, the coupling capacitor to the feedline is provided by a  $1 \mu\text{m}$  gap between the feedline and the cavity and it is estimated to be  $C'_c \sim 2 \text{ fF}$ . The resonance frequency of the circuit is  $\omega_0 = 2\pi \cdot 5.844 \text{ GHz}$  and related to the circuit parameters by

$$\omega_0 = \frac{1}{\sqrt{L_{\text{HF}}(C_{\text{HF}} + C'_c)}} \quad (6.19)$$

which gives a total inductance of  $L_{\text{HF}} = 742 \text{ pH}$  at the cavity sweet spot. This effective inductance is composed of the linear inductors  $L_0$ , the loop inductance  $L_l$ , the junction inductances  $L_j$  (cf. Fig. 6.1a) and includes the contribution from the mutual inductive coupling of the two circuits.

The external linewidth is given by

$$\kappa_e = \frac{Z_0 C'_c^2}{L_{\text{HF}}(C_{\text{HF}} + C'_c)^2} \quad (6.20)$$

and with  $C'_c = 2 \text{ fF}$  results in  $\kappa_e = 2\pi \cdot 43 \text{ kHz}$ .

## 2. SONNET SIMULATIONS AND KINETIC INDUCTANCE

The total inductance of both cavities has a significant contribution from the kinetic inductance of the  $20 \text{ nm}$  thick Aluminum film. The kinetic inductance contribution is estimated from simulations using the software package SONNET, where we match the bare cavity resonance frequency with the experimental value by tuning the kinetic inductance per square  $L_\square$ . For a vanishing surface impedance we find a resonance frequency  $\omega_0 = 2\pi \cdot 10.3 \text{ GHz}$  in the simulations and achieve high agreement with the experimental value of  $\omega_0 = 2\pi \cdot 5.844 \text{ GHz}$  when  $L_\square = 2.2 \text{ pH}$  per square. Using this kinetic inductance for the bottom plate and the inductor wire of the LF resonator, the LF resonance frequency is simultaneously shifted from  $\Omega'_0 = 2\pi \cdot 610 \text{ MHz}$  for zero kinetic inductance to  $\Omega_0 \approx 2\pi \cdot 390 \text{ MHz}$ .

### CAVITY PARAMETER EXTRACTION FROM A REFLECTION MEASUREMENT

Supplementary Fig. 6.8 shows a SQUID cavity reflection measurement in amplitude data  $|S_{11}|$  in **a** as well as in the complex plane in **b** and the corresponding fit curves as lines. From fitting the data with the response function

$$S_{11} = 1 - \frac{2\kappa_e}{\kappa_i + \kappa_e + 2i\Delta} \quad (6.21)$$

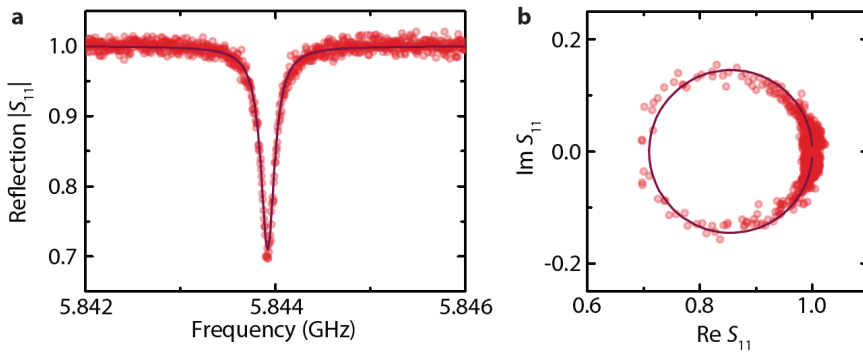


Figure 6.8: **The SQUID cavity response.** **a** The magnitude of the reflection response  $|S_{11}|$  of the high-frequency SQUID cavity. Circles are data, line is a fit. **b** The complex scattering data  $S_{11}$  around the HF resonance frequency. Circles are data, line is a fit. The data and fits shown here have been background-corrected before plotting as described in section 6.7.5. From the fit, we extract  $\kappa_e, \kappa_i$ , and  $\omega_0$  as given in the text.

where  $\Delta = \omega - \omega_0$  and the internal and external decay rates are  $\kappa_i$  and  $\kappa_e$ , we extract the parameters

$$\omega_0 = 2\pi \cdot 5.844 \text{ GHz}, \quad \kappa_i = 2\pi \cdot 163 \text{ kHz}, \quad \kappa_e = 2\pi \cdot 28 \text{ kHz} \quad (6.22)$$

The extracted  $\kappa_e$  slightly deviates from the theoretical value of 43 kHz, probably due to a coupling capacitance of  $C'_c \approx 1.5 \text{ fF}$ , which is lower than expected. The deviation of  $\kappa_i + \kappa_e$  from the value given in section 6.2 is explained by a different power used in both experiments. We observe that the internal linewidth is flux- and power-dependent as detailed in section 6.7.4.

### THE CONSTRICION TYPE JOSEPHSON JUNCTIONS, THE SQUID AND $\beta_L$

The constriction type Josephson junctions in our cavity are designed to be 150 nm long and 50 nm wide and we estimate their critical current to be  $I_c \sim 10 \mu\text{A}$ , which relates to a Josephson inductance of a single junction of  $L_J = \frac{\Phi_0}{2\pi I_c} = 32 \text{ pH}$ .

The SQUID loop is a  $10 \times 10 \mu\text{m}^2$  large loop made from a  $1 \mu\text{m}$  wide wire. From the total inductance per square  $L_\square \approx 3 \text{ pH}$  per square, we estimate the loop inductance to be  $L_L = 120 \text{ pH}$ .

From these numbers, we find the screening parameter of the SQUID as approximately  $\beta_L = 2L_L I_c / \Phi_0 = 1.2$ .

### SQUID CAVITY FLUX DEPENDENCE

#### 1. RESONANCE FREQUENCY

To take into account the non-negligible SQUID loop inductance and a possible non-sinusoidal current-phase relation, both leading to flux multistability and a widening of

the flux arch [114, 122], we phenomenologically describe the SQUID critical current dependence on magnetic flux as

$$I_c(\Phi_b) = 2I_c \cos\left(\pi\gamma_L \frac{\Phi_b}{\Phi_0}\right) \quad (6.23)$$

where  $\gamma_L$  is a parameter taking into account the widening of the flux arch.

This relates to the Josephson inductance of the SQUID as

$$L_{JJ} = \frac{L_J}{2\cos\left(\pi\gamma_L \frac{\Phi_b}{\Phi_0}\right)}. \quad (6.24)$$

The factor of 2 in the denominator originates from the two junctions in parallel in the SQUID.

With this, the resonance frequency of the SQUID cavity is approximately given by

$$\omega_0(\Phi_b) = \frac{\omega_0(0)}{\sqrt{\Lambda + \frac{1-\Lambda}{\cos\left(\pi\gamma_L \frac{\Phi_b}{\Phi_0}\right)}}} \quad (6.25)$$

where  $\Lambda = (L_{HF} - \frac{1}{2}L_J)/L_{HF}$ .

Supplementary Fig. 6.9a shows the experimentally determined flux dependence of the resonance frequency together with a fit line using Eq. (6.25). From this fit, we extract the parameters  $\Lambda = 0.982$  and  $\gamma_L = 0.59$ , which corresponds to a single junction Josephson inductance of approximately  $L_J = 27\text{ pH}$ , i.e., to a critical current of a single junction of  $I_c = 12\text{ }\mu\text{A}$ . The SQUID Josephson inductance dependent on magnetic flux as extracted from the cavity fit is plotted in panel b.

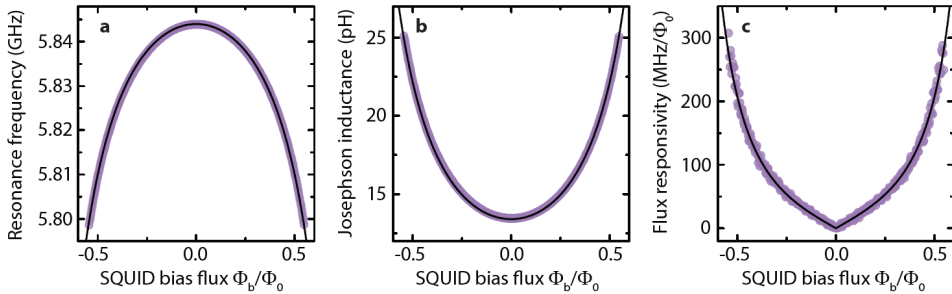
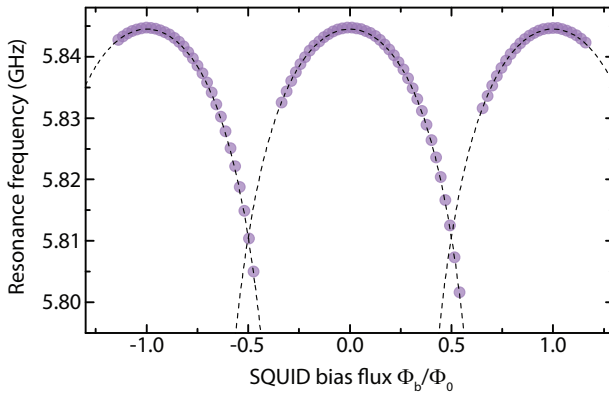


Figure 6.9: **Tuning the SQUID cavity with magnetic flux.** a SQUID cavity resonance frequency vs magnetic flux. Circles are data, the black line is a fit. b From the fit of the resonance frequency and with the total inductance  $L_{HF} = 742\text{ pH}$ , the Josephson inductance of the SQUID can be extracted. Circles are extracted from data, the line is a calculation based on the fit parameters from a. The change of resonance frequency with magnetic flux  $\partial\omega_0/\partial\Phi$  is shown in c. Both, data (circles) and fit (line) are obtained by differentiating the corresponding curves plotted in a.

In panel c, we plot the flux responsivity of the cavity  $|\partial\omega_0/\partial\Phi|$ , obtained as derivative from a, which is directly related to the coupling rate  $g_0$  between the circuits as discussed below. The maximum responsivity we obtain here, is  $|\partial\omega_0/\partial\Phi| \approx 2\pi \cdot 300\text{ MHz}/\Phi_0$ .

## 2. FLUX AXIS CALIBRATION

The flux axis is calibrated by measuring the SQUID cavity resonance frequency over a larger flux range and using a periodicity of one flux quantum. Supplementary Fig. 6.10 shows the SQUID cavity resonance frequency for a larger flux range with three different archs. The dashed line are copies of the fit function from Supplementary Fig. 6.9a, two of them have been shifted by  $-\Phi_0$  and  $+\Phi_0$ , respectively.



**Figure 6.10: Tuning the SQUID cavity with magnetic flux over multiple flux quanta.** Circles show the SQUID cavity resonance frequencies extracted from fits to the measurement data. Some points for very low frequencies  $\omega_0 < 2\pi \cdot 5.8 \text{ GHz}$  are not included, because the fit failed due to extremely shallow resonance dips at high bias flux values. The dashed lines are copies of the fit curve shown in Supplementary Fig. 6.9a, one is shifted by  $+\Phi_0$ , one by  $-\Phi_0$  on the flux axis.

6

## POWER DEPENDENCE AND ANHARMONICITY OF THE SQUID CAVITY

### 1. POWER DEPENDENCE OF CAVITY PARAMETERS

We observe that the cavity resonance frequency, due to the Kerr nonlinearity, as well as the internal cavity linewidth, due to nonlinear dissipation, depend on the intracavity photon number  $n_c$ . Both, as well as very slightly the external linewidth, depend, in addition, on the flux bias.

To measure the photon number dependence of  $\omega_0$  and  $\kappa$ , we bias the cavity at a desired flux value and send a microwave pump tone to the cavity around  $\omega_p(\Phi_b) = \omega_0(\Phi_b) - \Delta_p$  with  $\Delta_p \approx 2\pi \cdot 130 \text{ MHz}$ , chosen at a detuning which avoids interaction with the LF resonator. Then, we measure the cavity response with a weak probe tone and fit the curves to extract  $\omega_0$ ,  $\kappa_i$  and  $\kappa_e$ . Supplementary Fig. 6.11a shows the pump-induced frequency shift  $\delta\omega_0$  for different flux bias values vs the calculated intracavity photon number. The photon number is calculated using

$$n_c = \frac{4P_{\text{in}}}{\hbar\omega_p} \frac{\kappa_e}{\kappa^2 + 4\Delta_p^2} \quad (6.26)$$

where  $P_{\text{in}}$  is the on-chip pump tone power and  $\Delta_1 = (\omega_0 - \delta\omega_0/2) - \omega_p$  is the effective detuning between pump tone and power-shifted cavity. Lines in a show linear fits, from

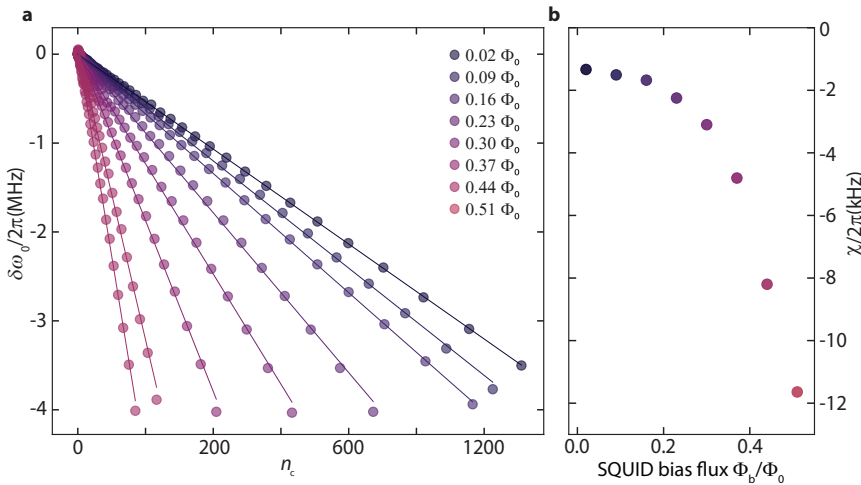


Figure 6.11: **Characterizing the SQUID cavity Kerr nonlinearity.** **a** A Resonance frequency shift  $\delta\omega_0 = \omega_0(n_c) - \omega_0(0)$  depending on intracavity photon number  $n_c$ , for different flux bias points. Circles are data, lines are linear fits. From the linear fits, we extract the frequency shift per photon for each bias flux value, as plotted as circles in **b**.

## 6

which we determine the shift per photon, i.e., the Kerr nonlinearity  $\chi$ . Note that surprisingly the Kerr nonlinearity is given by half the slope of the linear fit in these far-detuned two-tone experiments and not by the slope itself, i.e., the resonance frequency shift is given by  $\delta\omega_0 = 2\chi n_c$ .

In **b**, the nonlinearity is plotted vs flux bias value with a sweetspot nonlinearity of  $\chi \sim 2\pi \cdot 1.3$  kHz. We note, that depending on the pump frequency, we get quite significant variations in the extracted sweetspot nonlinearity with a range roughly between 0.7 kHz and 1.3 kHz, which we attribute to imprecise estimates of the intracavity photon number due to frequency dependent pump power arriving at the resonator input. This can be explained by cable resonances and a frequency dependent transmission in the setup. The values shown here are the largest we obtained.

The intrinsic linewidth itself is also photon-number dependent as discussed in the next paragraph. This, however, does not impact significantly the calculation of  $n_c$  by Eq. (6.26) in our two-tone configuration, as  $\Delta_1/\kappa \sim 10^2 - 10^3$ .

In Supplementary Fig. 6.12a, we show the total SQUID cavity linewidth vs intracavity photon number, once again for different values of SQUID flux bias. For better visibility, we restricted the shown data to three different flux bias values. The scattering of the data points is caused by the measurement details of this measurement series (low probe power, high bandwidth, large frequency span), which leads to large fit uncertainties in the linewidth. For all flux values, however, the linewidth follows a similar, decreasing trend with increasing photon number, which we interpret as indication for two-level system losses [169, 170]. The power dependence for two-level system (TLS) losses is given by  $\kappa_{\text{TLS}}(n_c) = \kappa_{\text{TLS}} / \sqrt{1 + \frac{n_c}{n_{\text{crit}}}}$  with the critical photon number  $n_{\text{crit}}$  being a measure for

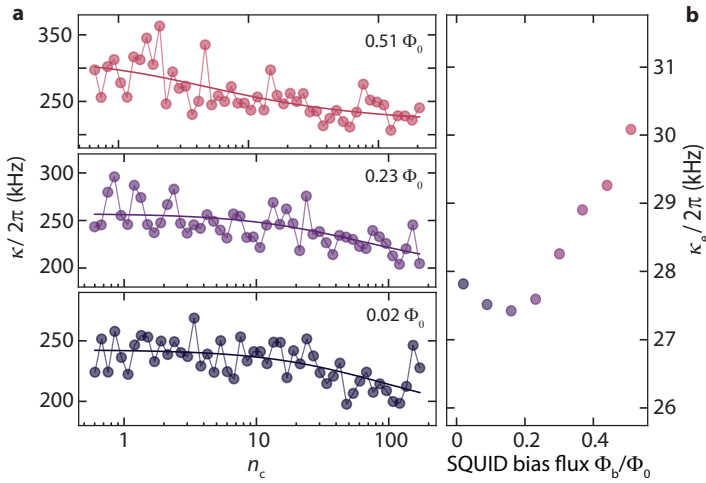


**Figure 6.12: Characterizing the SQUID cavity linewidth power dependence.** **a** Total SQUID cavity linewidth depending on intracavity photon number, shown for three different flux bias points. Circles are data, lines are fits using Eq. (6.27). In **b**, we show the values obtained for the external linewidth vs bias flux.

the TLS saturation photon number. The total linewidth therefore is given by

$$\kappa = \kappa_e + \kappa_1 + \frac{\kappa_{\text{TLS}}}{\sqrt{1 + \frac{n_c}{n_{\text{crit}}}}} \quad (6.27)$$

where  $\kappa_1$  represents the internal losses not related to the power-dependent TLS losses and  $\kappa_1 + \kappa_{\text{TLS}}(n_c) = \kappa_i(n_c)$ . We fit the data with this Eq. (6.27) shown in Supplementary Fig. 6.12a and find good agreement with the experimental observations. For a cleaner dataset with less linewidth scattering, cf. Supplementary Fig. 6.15b. The total linewidth slightly increases with flux, which could be either caused by an increased quasiparticle density or by a flux-noise induced linewidth broadening. In Supplementary Fig. 6.12b, we plot the external linewidth  $\kappa_e$  vs bias flux, and observe that is nearly independent of flux.

### 6.7.5. RESPONSE FUNCTIONS AND FITTING ROUTINE

#### IDEAL HF CAVITY AND LF RESONATOR RESPONSE FUNCTION

Both, our HF SQUID cavity and the LF resonator, can be modeled as a parallel LC circuit capacitively coupled to a transmission line in a reflection geometry. The  $S_{11}$  response function of such a circuit is given by

$$S_{11} = 1 - \frac{2\kappa_e}{\kappa_i + \kappa_e + 2i\Delta} \quad (6.28)$$

with detuning from the resonance frequency

$$\Delta = \omega - \omega_0. \quad (6.29)$$

For the LF resonator, we get fully equivalently

$$S_{11} = 1 - \frac{2\Gamma_e}{\Gamma_i + \Gamma_e + 2i\Delta_0} \quad (6.30)$$

with  $\Delta_0 = \Omega - \Omega_0$ .

#### REAL RESPONSE FUNCTION AND FITTING ROUTINE

When analyzing the measured cavity response, we consider a frequency dependent complex-valued microwave background with amplitude and phase modulations originating from a variety of microwave components in our input and output lines and possible interfering signal paths. Under this assumption, we model the modified cavity response with

$$S_{11} = (\alpha_0 + \alpha_1\omega) \left( 1 - \frac{2\kappa_e e^{i\theta}}{\kappa_i + \kappa_e + 2i\Delta} \right) e^{i(\beta_1\omega + \beta_0)} \quad (6.31)$$

where we consider a frequency dependent complex background

$$S_{11} = (\alpha_0 + \alpha_1\omega) e^{i(\beta_1\omega + \beta_0)} \quad (6.32)$$

and an additional rotation of the resonance circle due to the phase factor  $e^{i\theta}$ . The first step in the fitting routine removes the cavity resonance part from the data curve and fits the remaining background with Eq. (6.32). After removing the background contribution from the full dataset by complex division, the resonator response is fitted using the ideal response function. In the final step, the full function is re-fitted to the bare data using as starting parameters the individually obtained fit numbers from the first two steps. From this final fit, we extract the final background fit parameters and remove the background of the full dataset by complex division. Also, we correct for the additional rotation factor  $e^{i\theta}$ . As result we obtain clean resonance curves as shown in Supplementary Figs. 6.7 and 6.8.

6

#### 6.7.6. PARAMETRICALLY COUPLED LC OSCILLATORS

##### CLASSICAL EQUATIONS OF MOTION

We model the system for most experimental parts classically with the equations of motion for an oscillating magnetic flux  $\Phi_{LF}$  threading the SQUID loop, an analogue for the mechanical displacement in a typical optomechanical system, and for the SQUID cavity intracavity field amplitude  $\alpha$

$$\ddot{\Phi}_{LF} = -\Gamma_0 \dot{\Phi}_{LF} - \Omega_0^2 \Phi_{LF} + \frac{\hbar\gamma G |\alpha|^2}{C_{LF}} \quad (6.33)$$

$$\ddot{\alpha} = \left[ -i(\Delta - \gamma G \Phi_{LF}) - \frac{\kappa}{2} \right] \alpha + i\sqrt{\kappa_e} S_{in}. \quad (6.34)$$

Here  $C_{LF}$  is the capacitance of the low frequency resonator,  $\Delta = \omega_p - \omega_0$  is the detuning of a pump tone from the cavity resonance frequency,  $\kappa$  and  $\Gamma_0$  are the total resonator linewidths and  $\kappa_e$  and  $\Gamma_e$  are the external linewidth of high and low-frequency circuit,

respectively. The quantities  $S_{\text{in}}$  and  $S_{\text{LF}}$  are the normalized input fields on the high-frequency and low-frequency input line, respectively.

The photon-pressure (in optomechanical systems radiation-pressure force) from the high frequency cavity to the LF resonator is taken into account with the term  $\hbar\gamma G|\alpha|^2/C_{\text{LF}}$  with pull parameter

$$G = \frac{\partial\omega_0}{\partial\Phi}. \quad (6.35)$$

The dimensionless parameter  $\gamma = M/L_{\text{LF}}$  describes the amount of the LF resonator flux coupling into the SQUID loop with the mutual inductance  $M$  between the LF inductor  $L_{\text{LF}}$  and the SQUID loop inductance  $L_{\text{l}}$ .

Assuming that the intracavity field is high enough to only consider small deviations from the steady state solutions with  $\Phi_{\text{LF}} = \bar{\Phi}_{\text{LF}} + \delta\Phi_{\text{LF}}$  and  $\alpha = \bar{\alpha} + \delta\alpha$ , the equations of motion can be linearized as

$$\delta\ddot{\Phi}_{\text{LF}} = -\Gamma_0\delta\dot{\Phi}_{\text{LF}} - \Omega_0^2\delta\Phi_{\text{LF}} + \frac{\hbar\gamma G\bar{\alpha}}{C_{\text{LF}}}(\delta\alpha + \delta\alpha^*) \quad (6.36)$$

$$\delta\dot{\alpha} = \left[-i\bar{\Delta} - \frac{\kappa}{2}\right]\delta\alpha - i\gamma G\bar{\alpha}\delta\Phi_{\text{LF}} + i\sqrt{\kappa_e}S_p \quad (6.37)$$

In the above expressions, the detuning takes into account the shift from the equilibrium flux value  $\bar{\Phi}_{\text{LF}}$  due to the photon-pressure  $\bar{\Delta} = \omega_p - \omega_0 - G\bar{\Phi}_{\text{LF}}$  and  $\sqrt{\kappa_e}S_p$  with  $S_p = S_0 e^{i(\omega_{\text{pr}}-\omega_p)t}$  accounts for field fluctuations with the frequency  $\omega_{\text{pr}}$ . On a first look, it might seem surprising that the interaction is related to a DC equilibrium flux in the LF resonator. It corresponds to an additional, effective DC flux in the SQUID loop, generated by the HF currents in presence of an external SQUID flux bias. As by the mutual inductance, the flux in the SQUID loop is part of the LF flux, the origin and interpretation of this DC flux becomes clear.

By solving the equations of motion we get the modified low-frequency resonator susceptibility

$$\chi_0^{\text{eff}} = \frac{1}{\Omega_0^2 - \Omega^2 + i\Omega\Gamma_0 + 2i\Omega_0 g^2 [\chi_c(\Omega) - \chi_c^*(-\Omega)]} \quad (6.38)$$

with the multi-photon-coupling rate

$$g = \bar{\alpha}G\Phi_{\text{zpf}} = \sqrt{n_c}G\Phi_{\text{zpf}} \quad (6.39)$$

and the SQUID cavity susceptibility

$$\chi_c = \frac{1}{\frac{\kappa}{2} + i(\bar{\Delta} + \Omega)}. \quad (6.40)$$

From here on, we just use  $\Delta = \bar{\Delta}$  and always refer to the detuning as the detuning from the pump-shifted cavity resonance frequency.

For the SQUID cavity response, we get

$$S_{11} = 1 - \kappa_e \chi_c \left[ 1 - 2i\Omega_0 g^2 \chi_c \chi_0^{\text{eff}} \right]. \quad (6.41)$$

## ZERO-POINT FLUX FLUCTUATIONS AND SINGLE-PHOTON COUPLING RATE

The zero-point current of the low frequency resonator is given by  $I_{\text{zpf}} = 21 \text{ nA}$ . The zero-point flux fluctuations generated in the SQUID loop can therefore be calculated by estimating the flux  $\Phi_{\text{zpf}} = MI_{\text{zpf}}$  induced by  $I_{\text{zpf}}$  in the loop, where  $M$  denotes the mutual inductance between the LF wire and the SQUID loop. Supplementary Fig. 6.13 shows an optical image of the SQUID loop and the LF wire passing by three sides of the loop with a 500 nm wide gap between the 1  $\mu\text{m}$  wide wires. With the geometrical parameters of the configuration,  $D = 10 \mu\text{m}$  being the length of one loop side,  $d_1 = 1 \mu\text{m}$  being the distance between the LF wire and the nearest SQUID loop wire, and  $d_2 = 11 \mu\text{m}$  being the distance between the LF wire and the distant SQUID loop wire, the flux induced by  $I_{\text{zpf}}$  is calculated via

$$\Phi_{\text{zpf}} = 3 \frac{\mu_0}{2\pi} I_{\text{zpf}} D \ln\left(\frac{d_2}{d_1}\right) \approx 145 \mu\Phi_0. \quad (6.42)$$

For all geometrical distances  $D$ ,  $d_1$ , and  $d_2$ , we considered the center of the corresponding wires. This also gives directly an estimate for the mutual inductance  $M = 14 \text{ pH}$ .

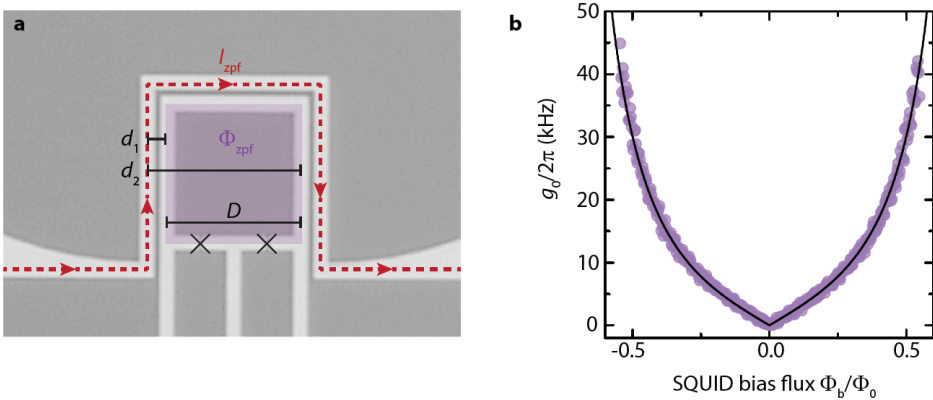


Figure 6.13: **Calculation of the single-photon coupling rate  $g_0$ .** **a** Optical image showing the SQUID loop and the low frequency inductor wire. Arrows represent the geometrical distances  $d_1$ ,  $d_2$  and  $D$ , used for the calculation of the LF resonator induced zero-point SQUID flux  $\Phi_{\text{zpf}}$ . The crosses indicate the positions of the Josephson junctions. **b** shows the calculated single-photon coupling rate vs SQUID bias flux. The points are calculated from the measured SQUID resonance frequency, the line from the fit to the flux arch.

The single-photon coupling rate is given by

$$g_0 = \frac{\partial \omega_0}{\partial \Phi} \Phi_{\text{zpf}} \quad (6.43)$$

where  $\Phi_{\text{zpf}} = 145 \mu\Phi_0$  is the zero-point flux and the flux responsivity is extracted from the SQUID cavity flux dependence, cf. Supplementary Fig. 6.9c.

Supplementary Fig. 6.13 shows the calculated single-photon coupling rates of the device depending on the flux-bias point. According to this calculation, the single-photon coupling rate can be tuned from  $g_0 = 0 \text{ Hz}$ , when the cavity is operated at the sweetspot, to  $g_0 \approx 2\pi \cdot 40 \text{ kHz}$  for the largest flux bias values.

### DYNAMICAL PHOTON-PRESSURE BACKACTION

The term  $\Sigma = 2i\Omega_0 g^2 [\chi_c(\Omega) - \chi_c^*(-\Omega)]$  in the modified LF resonator susceptibility  $\chi_0^{\text{eff}}$  can be understood as a SQUID cavity field induced term modifying the damping and the resonance frequency of the LF resonator. This becomes apparent, when we assume the high- $Q_0$  limit, where the susceptibility for a red-sideband pump tone with  $\Delta \approx -\Omega_0$  and  $\Omega \approx +\Omega_0$  can be approximated as

$$\chi_0^{\text{eff}} = \frac{1}{2\Omega_0} \frac{1}{(\Omega_0 - \Omega) + i\frac{\Gamma_0}{2} + ig^2[\chi_c(\Omega) - \chi_c^*(-\Omega)]} \quad (6.44)$$

By rewriting  $\Sigma' = ig^2[\chi_c(\Omega) - \chi_c^*(-\Omega)]$  as  $\Sigma' = \delta\Omega_0 + i\frac{\delta\Gamma_0}{2}$  and independently analyze the real and imaginary part, we can write the change in frequency  $\delta\Omega_0$  (photon-pressure frequency shift) and the additional damping term  $\delta\Gamma_0$  (photon-pressure damping), arising from the modified susceptibility as

$$\delta\Omega_0 = g^2 \left[ \frac{\Delta + \Omega_0}{\frac{\kappa^2}{4} + (\Delta + \Omega_0)^2} + \frac{\Delta - \Omega_0}{\frac{\kappa^2}{4} + (\Delta - \Omega_0)^2} \right] \quad (6.45)$$

$$\delta\Gamma_0 = g^2 \kappa \left[ \frac{1}{\frac{\kappa^2}{4} + (\Delta + \Omega_0)^2} - \frac{1}{\frac{\kappa^2}{4} + (\Delta - \Omega_0)^2} \right]. \quad (6.46)$$

For a blue-detuned pump field we find essentially the same expressions with a sign change for the photon-pressure damping  $\delta\Gamma_0^{\text{blue}} = -\delta\Gamma_0^{\text{red}}$ .

In order to observe the dynamical photon-pressure backaction between the two circuits, we flux-bias the SQUID cavity with  $\Phi_b \approx 0.16\Phi_0$  and stepwise sweep a pump tone through both, the red sideband  $\Delta = -\Omega_0 + \delta_r$ , and the blue sideband  $\Delta = +\Omega_0 + \delta_b$ , while the low-frequency resonator is scanned with a weak probe tone  $\Omega_{\text{pr}} = \Omega_0 + \Delta_0$ . The variables  $\delta_r$ ,  $\delta_b$  and  $\Delta_0$  denote small detunings from the red sideband, the blue sideband and the LF resonance frequency, respectively. As the device is deep in the resolved sideband regime with  $\Omega_0/\kappa \sim 1000$ , we can approximate the expressions for the optical damping and the optical spring as

$$\delta\Omega_0 = 4g^2 \frac{\delta_i}{\kappa^2 + 4\delta_i^2} \quad (6.47)$$

$$\delta\Gamma_0 = \pm 4g^2 \frac{\kappa}{\kappa^2 + 4\delta_i^2} \quad (6.48)$$

with  $i = b, r$  and  $+$  for the red sideband and  $-$  for the blue sideband. From fits to the LF resonator response, we extract  $\delta\Omega_0$  and  $\delta\Gamma_0$  as shown and dicussed in the Fig. 6.2. The two expressions Eqs. (6.47, 6.48) are only strictly valid for constant  $\kappa$  far away from the strong coupling regime  $g \ll (\kappa - \Gamma_0)/4 \sim 2\pi \cdot 50 \text{ kHz}$ . When the strong-coupling regime is approached, the LF resonator linewidth is not a linear function of power anymore and the SQUID cavity linewidth starts to decrease [60]. The weak-coupling condition is not strictly fulfilled anymore in our experiment for cooperativites  $\mathcal{C} \sim 1$  and hence we expect deviations. When we use a power-dependent effective cavity linewidth  $\tilde{\kappa}$  for these equations instead of the bare linewidth, however, we can describe the data with high accuracy using these expressions.

## 1. DYNAMICAL BACKACTION - ADDITIONAL DATA

In Supplementary Fig. 6.14, we show additional data for dynamical photon-pressure backaction, taken for two lower pump powers than the one used in section 6.4. The pump powers on the blue and on the red sideband were adjusted to give similar cooperativities.

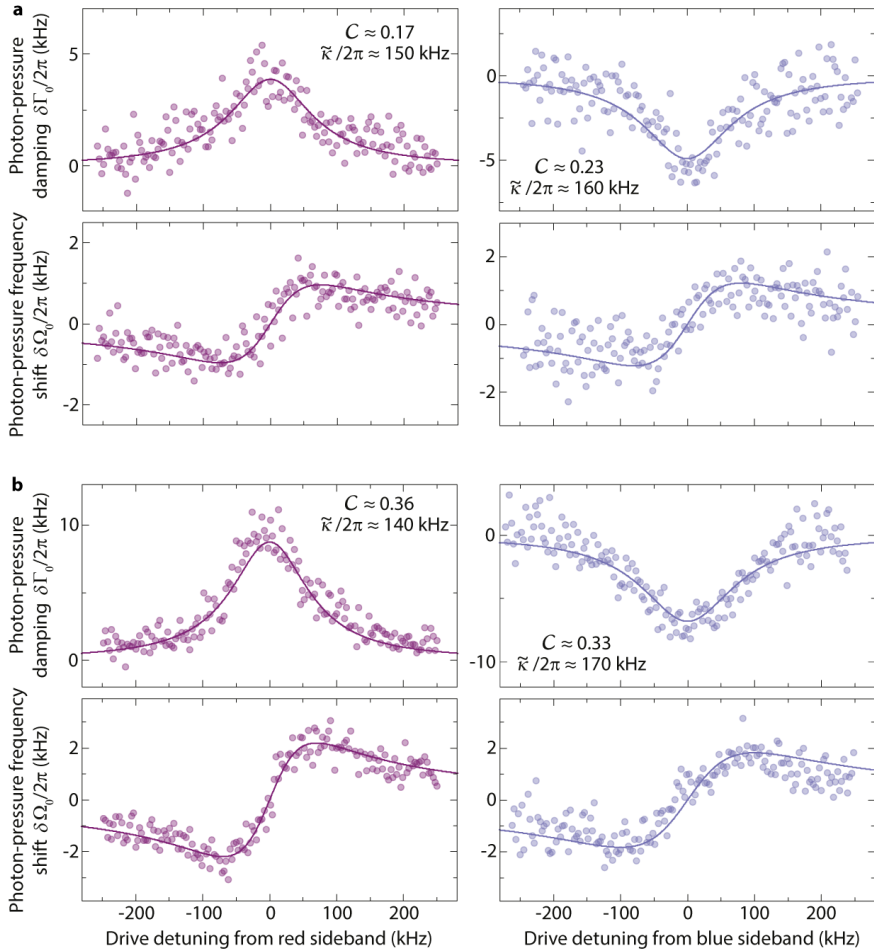


**Figure 6.14: Dynamical backaction for red- and blue-detuned pump tone, respectively, in the low cooperativity regime.** **a** and **b** show the extracted photon-pressure damping and photon-pressure frequency shift for a pump on the red sideband (left) and for a pump on the blue sideband (right). **a** is for approximately 10 intra-cavity photons and **b** for 20. The flux bias point was  $\Phi_b/\Phi_0 \approx 0.16$ . Circles are data, lines are theoretical curves with Eqs. (6.47, 6.48) and the parameters given in the panels. On the red sideband, the effective cavity linewidth  $\tilde{\kappa}$  needed to describe the data with the expressions (6.47, 6.48) decreases with pump strength/cooperativity, on the blue sideband it decreases. This indicates that it is not an effect of nonlinear cavity losses, but deviations from the used approximations due to the similarity of  $\kappa, g$  and  $\Gamma_0$  here, i.e., due to approaching the strong-coupling regime already for  $C \sim 1$  [60].

## THE SQUID CAVITY RESPONSE FUNCTION FOR A RED-SIDEBAND PUMP

With the modified low-frequency resonator susceptibility  $\chi_0^{\text{eff}}$  we can write the SQUID cavity response as

$$S_{11} = 1 - \kappa_e \chi_c \left[ 1 - 2i\Omega_0 g^2 \chi_c \chi_0^{\text{eff}} \right]. \quad (6.49)$$

### 1. EXTRACTING CAVITY AND COUPLING PARAMETERS FROM DATA

To model the data of the response in presence of a red-sideband pump, we use Eq. (6.49) and adjust the parameters  $\omega_0$ ,  $\kappa$ ,  $\Omega_0$  and  $g$  for fixed  $\Gamma_0 = 2\pi \cdot 22\text{kHz}$  and  $\kappa_e = 2\pi \cdot 28\text{kHz}$ . Corresponding lines are shown in the Fig. 6.3d and Supplementary Fig. 6.15c. With the extracted numbers, we calculate the cooperativity

$$\mathcal{C} = \frac{4g^2}{\kappa\Gamma_0} \quad (6.50)$$

and estimate the SQUID cavity photon number via

$$n_c = \frac{4P_{\text{in}}}{\hbar\omega_p} \frac{\kappa_e}{\kappa^2 + 4\Delta^2} \quad (6.51)$$

where  $P_{\text{in}}$  is the on-chip power calculated from the generator output power and the estimated input attenuation of 59 dB for the first cooldown (Fig. 6.3) and 61 dB for the second cooldown (Supplementary Fig. 6.15). From those numbers, we calculate the single-photon coupling rate  $g_0 = \frac{g}{\sqrt{n_c}}$ .

6

### THE STRONG-COUPLING REGIME

When increasing the multi-photon optomechanical coupling rate  $g = \sqrt{n_c} g_0$  to a point where  $g > (\kappa - \Gamma_0)/4$ , the system enters the strong-coupling regime [60], where the driven high-frequency mode and the low-frequency mode hybridize, forming two new modes split by  $2g$ , an effect also known as normal-mode splitting. When the high-frequency cavity is pumped exactly on the red-sideband  $\Delta = \omega_p - \omega_0 = -\Omega_0$ , the two new formed hybrid excitation modes of the system have (complex) eigenfrequencies given by [56]

$$\omega_{\pm} = \Omega_0 + i \frac{\kappa + \Gamma_0}{4} \pm \sqrt{g^2 - \left( \frac{\kappa - \Gamma_0}{4} \right)^2}, \quad (6.52)$$

with  $\omega_+ - \omega_- = 2g$  for  $g^2 \gg (\kappa - \Gamma_0)^2/16$ . The real part of  $\omega_{\pm}$  describes the resonance frequencies of the two hybridized modes and the imaginary part is half the linewidth. In the strong-coupling regime  $g^2 \gg (\kappa - \Gamma_0)^2/16$ , we get

$$\omega_{\pm} = \Omega_0 \pm g + i \frac{\kappa + \Gamma_0}{4} \quad (6.53)$$

showing that each of the new modes has a linewidth  $\Gamma_{\pm} = (\kappa + \Gamma_0)/2$ . We also note here, that the formal definition of the strong-coupling regime here with  $g > (\kappa - \Gamma_0)/4$ , corresponding to a sudden transition from split damping rates to split eigenfrequencies in Eq. (6.52), is different from the standard definition, where the mode splitting  $2g$  must exceed the hybridized mode linewidths  $(\kappa + \Gamma_0)/2$ . This would correspond to  $g > (\kappa + \Gamma_0)/4$ . Our device, however, reaches the strong-coupling regime unambiguously for either of the definitions.

### TRANSITION TO THE STRONG-COUPLING REGIME BY INCREASING $n_c$

In Fig. 6.3, we show the transition to the strong-coupling regime by increasing the single-photon coupling strength  $g_0$  through the flux responsivity  $\partial\omega_0/\partial\Phi$ , while keeping the red-sideband pump strength constant. A similar transition to the strong-coupling regime can also be accomplished by the common approach of enhancing the coupling strength of the system by increasing the number of photons in the cavity [31]. The experimental setup corresponds to what is described in Fig. 6.3a, where a pump tone was set to the red sideband of the high-frequency cavity  $\omega_p = \omega_0 - \Omega_0$ , and a probe tone was scanning through the cavity resonance  $\omega_{pr} \approx \omega_0$ . The presented measurements in this section were performed at  $\Phi_b \approx 0.5\Phi_0$  and the external measurement configuration is presented in detail in Supplementary Fig. 6.6c. The measurement was repeated for increasing values of drive power. Due to the residual SQUID cavity Kerr-nonlinearity, we have to adjust the pump frequency for each power to set the pump onto the actual red sideband. The cavity resonance frequency and linewidth vs photon number is shown in Supplementary Fig. 6.15b and c. Note, that this experiment was done during a later cooldown compared to most other experiments and the device parameters (linewidths and resonance frequencies) seem to have somewhat shifted in between the two cooldowns.

In Supplementary Fig. 6.15c, we plot the SQUID cavity response vs probe frequency for different pump powers, with increasing power from bottom to top. For the lowest power, the cavity resonance is almost unperturbed besides a very little interference peak in its center. With increasing pump power and therefore increasing intracavity photon number  $n_c$ , the PPIT interference effect of the low-frequency resonator in the high-frequency cavity response gets enhanced until for the highest powers a clear normal-mode splitting with up to  $g/\pi = 950$  kHz occurs. We model the data with Eq. (6.41). For each of the theoretical curves, the parameters  $\kappa_e$ ,  $\Gamma_0$  and  $g_0$  were fixed at  $2\pi \cdot 28$  kHz,  $2\pi \cdot 25$  kHz and  $2\pi \cdot 30$  kHz, respectively. To get agreement with the experimental data, we varied multi-photon coupling strength  $g$ , cavity frequency shift  $\delta\omega_0$ , LF resonator resonance frequency  $\Omega_0$  and internal linewidth  $\kappa_i$  of the SQUID cavity. The values for  $\delta\omega_0$ ,  $\kappa_i$  and  $g$  as extracted are plotted in Supplementary Fig. 6.15a, b and d, respectively. From the combination, we also determined the cooperativity  $\mathcal{C}$  as plotted in e.

The observed behaviour of the internal linewidth with intracavity photon number follows the prediction for two-level system (TLS) losses as given by Eq. (6.27). Furthermore, the extracted cooperativities in Supplementary Fig. 6.15e do not show a strictly linear behaviour, cf. the linear fit (black line). Including the decrease of the internal linewidth with photon number due to TLS losses, as shown as orange line, gives excellent agreement with the data points.

### DETECTING NORMAL-MODE SPLITTING IN THE LF RESONATOR RESPONSE

The normal-mode splitting in the strong-coupling regime can not only be detected in the SQUID cavity response, but also in the LF resonator response. When probing the LF resonator under the experimental conditions of Fig. 6.3e, case D, we observe the LF response as shown in Supplementary Fig. 6.16 with a pronounced normal-mode splitting. The dashed red line shows the SQUID cavity resonance frequency with respect to the moving red-sideband pump.

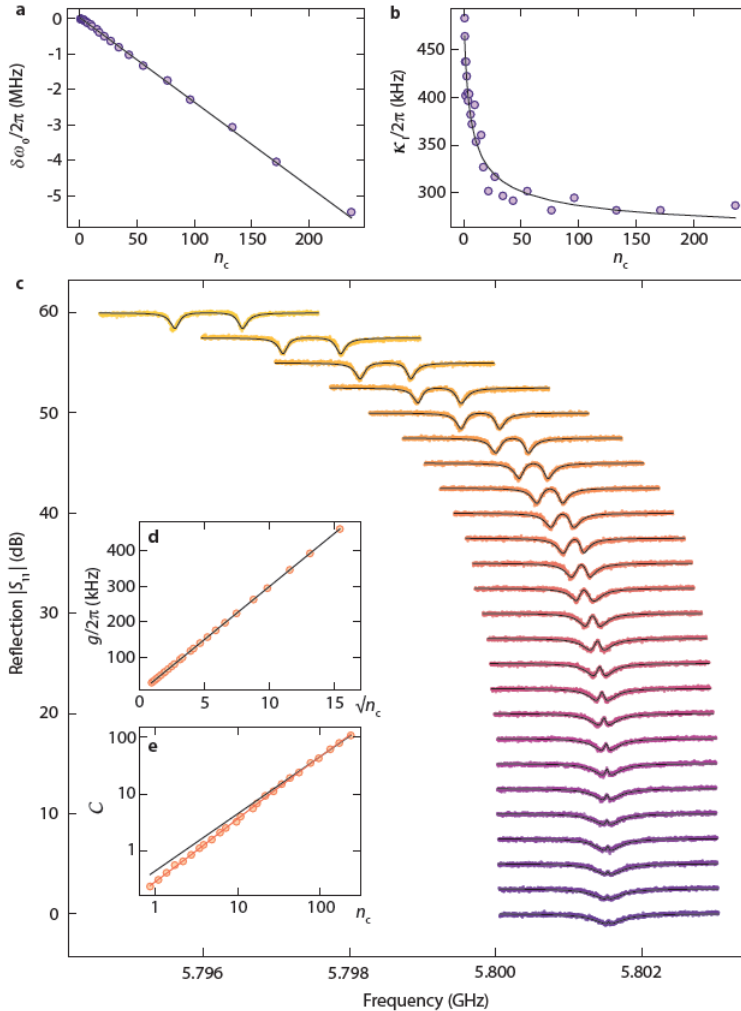


**Figure 6.15: Transition to the strong-coupling regime by increasing the intracavity photon number  $n_c$ .** **a** Resonance frequency shift from the bare cavity resonance  $\delta\omega_0 = \omega'_0 - \omega_0$  with  $n_c$ , where  $\omega_0$  is the resonance frequency at the lowest power. The points are data and the black line is a linear fit. **b** Internal linewidth  $\kappa_i$  of the HF cavity depending on  $n_c$ . The points are the extracted values from adjusting the theoretical curves to the data presented in **c**. The black line is a fit curve based on Eq. 6.27. **c** Observation of the transition from photon pressure-induced transparency to the strong-coupling regime by increasing the power of a pump tone on the red sideband of the SQUID cavity  $\omega_p = \omega_0 - \Omega_0$ . The colored points are the measured data and the black lines are theoretical curves. Each of the curves was upshifted by 2.5 dB for better visibility with the lowest curve being unshifted. **d** Linear increase of the coupling rate  $g$  with  $\sqrt{n_c}$ , where the points are the extracted values from the data and the line is a fit. **e** Cooperativity of the system vs intracavity photon number, plotted on a logarithmic scale. The black line is a linear fit (valid for constant  $\kappa$ ) and the orange line is the cooperativity calculated with the internal linewidth of the cavity based on the fit curve presented in **b**.

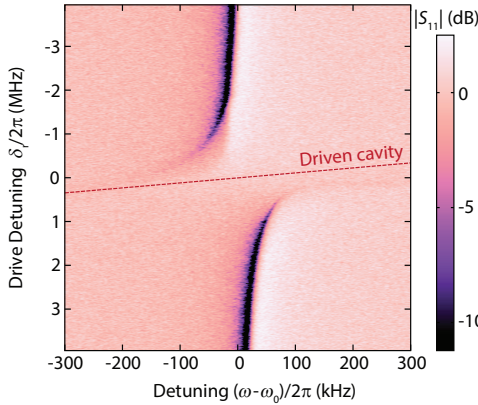


Figure 6.16: **Normal-mode splitting of the LF resonator response.** When measuring the response of the LF resonator with the parameters as in Fig. 6.3e, case D, i.e., with a red-detuned SQUID cavity drive,  $n_c \sim 70$  intracavity photons and  $\Phi_b/\Phi_0 \sim 0.5$ , we observe normal-mode splitting in the direct response of the LF resonator. The red dashed line indicates the resonance frequency of the SQUID cavity mode with respect to the pump tone.

## 6

### 6.7.7. DETECTION AND AMPLIFICATION OF THERMAL NOISE POWER SPECTRAL DENSITY FOR A BLUE-SIDEBAND DRIVE

Following the routine given in the Supplementary Material of Ref. [31], we derive the cavity field amplitude for a blue sideband drive to be given by

$$\delta \hat{a} = \frac{-ig\chi_c\bar{\chi}_0\sqrt{\Gamma_0}\hat{S}_{\text{LF}}^\dagger + \chi_c\sqrt{\kappa}\hat{S}_{\text{HF}}}{1-g^2\chi_c\bar{\chi}_0} \quad (6.54)$$

with the susceptibilities

$$\chi_c = \frac{1}{\frac{\kappa}{2} + i(\Delta + \Omega)} \quad (6.55)$$

$$\bar{\chi}_0 = \frac{1}{\frac{\Gamma_0}{2} + i(\Omega_0 + \Omega)}. \quad (6.56)$$

As usual,  $\Delta = \omega_p - \omega_0 \sim +\Omega_0$  describes the detuning between cavity resonance and the blue sideband pump here, and  $\Omega \sim -\Omega_0$  is the frequency where we measure and calculate the output field. The operators  $\hat{S}_{\text{LF}}$  and  $\hat{S}_{\text{HF}}$  denote the low-frequency resonator and high-frequency SQUID cavity noise input fields, respectively, and follow  $\langle \hat{S}_j \hat{S}_j^\dagger \rangle = n_j + 1$  and  $\langle \hat{S}_j^\dagger \hat{S}_j \rangle = n_j$ , where  $j = \text{LF}, \text{HF}$ .

#### 1. ADDED NOISE

According to Ref. [31], the effective number of added noise photons is given by

$$n'_{\text{add}} = \frac{n_{\text{add}}}{\eta} + \left( \frac{1-\eta}{\eta} \right) \frac{1}{2} \quad (6.57)$$

where  $n_{\text{add}}$  is the actual number of photons added by the HEMT amplifier in our case,  $n_{\text{add}} \sim 12$ , and  $\eta \sim 0.8$  accounts for losses of the cavity output field on its way to the HEMT. Thus, we estimate the effective total number of added photons to be  $n'_{\text{add}} \approx 15$ . This effective number was estimated from the thermal calibration of the LF resonator population with varying fridge base temperature. From matching the slope of the temperature dependence in the regime of nearly linear increase with  $T_b$  with the linear regime of the Bose factor.

## 2. THE TOTAL POWER SPECTRAL DENSITY

For the power spectral density at frequency  $\omega = \omega_p + \Omega$  of the SQUID cavity with a drive around the blue sideband, we get with this

$$\frac{S(\omega)}{\hbar\omega} = \frac{1}{2} + n'_{\text{add}} + \frac{\kappa_e g^2 |\tilde{\chi}_0|^2 |\chi_c|^2 \Gamma_0 (n_{\text{LF}} + 1) + \kappa_e |\chi_c|^2 \kappa n_{\text{HF}}}{|1 - g^2 \chi_c \tilde{\chi}_0|^2} \quad (6.58)$$

The thermal mode occupations follow a Bose distribution, i.e.,

$$n_{\text{HF}} = \frac{1}{e^{\frac{\hbar\omega_0}{k_B T_{\text{HF}}} - 1}} \quad (6.59)$$

$$n_{\text{LF}} = \frac{1}{e^{\frac{\hbar\Omega_0}{k_B T_{\text{LF}}} - 1}}. \quad (6.60)$$

6

We note that we decided to choose possibly different temperatures for the low-frequency and the high-frequency thermal distribution, as the two resonators are isolated differently from the noise of their environment, e.g. the input/output cabling.

Assuming a negligible SQUID cavity occupancy  $n_{\text{HF}} \sim 0$ , we can rewrite the power spectral density as

$$\frac{S(\omega)}{\hbar\omega} = \frac{1}{2} + n'_{\text{add}} + \frac{16\kappa_e g^2 \Gamma_0}{(\Gamma'_0)^2 + 4\Delta'^2} (\kappa^2 + 4\delta_b^2) (n_{\text{LF}} + 1) \quad (6.61)$$

where  $\Gamma'_0 = \Gamma_0 - \delta\Gamma_0$  includes the effect of photon-pressure damping, the detuning  $\Delta' = -\Omega - (\Omega_0 + \delta\Omega_0)$  includes the photon-pressure frequency shift, and  $\delta_b = \omega_p - (\omega_0 + \Omega_0)$  takes into account possible detunings of the pump tone from the blue cavity sideband.

## 3. PSD WITH PUMP EXACTLY ON THE BLUE SIDEBAND

When the blue sideband pump is exactly at  $\omega_p = \omega_0 + \Omega_0$ , i.e.,  $\delta_b = 0$ , the photon-pressure frequency shift vanishes  $\Delta' = \Delta$  and we get

$$\frac{S(\omega)}{\hbar\omega} = \frac{1}{2} + n'_{\text{add}} + 4 \frac{\kappa_e}{\kappa} \mathcal{C} \frac{\Gamma_0^2}{\Gamma'_0^2 + 4\Delta^2} (n_{\text{LF}} + 1) \quad (6.62)$$

which describes a Lorentzian sitting on top of a background with  $1/2 + n'_{\text{add}}$  photons.

With the power spectral density of the thermal current fluctuations in the LF resonator

$$S_I(-\Omega) = \frac{8\Gamma_0}{\Gamma'_0^2 + 4\Delta^2} I_{\text{zpf}}^2 (n_{\text{LF}} + 1) \quad (6.63)$$

we can write

$$\frac{S(\omega)}{\hbar\omega} = \frac{1}{2} + n'_{\text{add}} + \frac{\mathcal{C} \kappa_e}{2 \kappa} \frac{\Gamma_0}{I_{\text{zpf}}^2} S_I(-\Omega). \quad (6.64)$$

#### EXTRACTION OF THERMAL PHOTON NUMBERS FROM DATA

For the extraction of the thermal photon numbers, we first determine  $\mathcal{C}$ ,  $\Gamma'_0$ ,  $\kappa$  and  $\kappa_e$  from a measurement of photon-pressure induced absorption, cf. Fig. 6.4a. In addition, we use the calculated zero-point fluctuations  $I_{\text{zpf}} = 21 \text{nA}$  and the added noise photons  $n'_{\text{add}} = 15$ . With the background noise amplitude  $S_b = G_m \hbar \omega \left( \frac{1}{2} + n'_{\text{add}} \right)$  with  $G_m$  being the total gain of the amplifier detection line, determined from a Lorentzian fit of the PSD data  $S_V$ , we calculate

$$S_I(-\Omega) = \left[ \frac{S_V}{S_b} - 1 \right] \left[ \frac{1}{2} + n'_{\text{add}} \right] \frac{2\kappa}{\mathcal{C}\kappa_e\Gamma_0} I_{\text{zpf}}^2. \quad (6.65)$$

To extract the thermal number of photons in the LF resonator, we use the herewith calculated  $S_I(-\Omega)$  and consider the amplitude at resonance

$$S_{I0} = 8 \frac{\Gamma_0}{\Gamma_0'^2} I_{\text{zpf}}^2 (n_{\text{LF}} + 1) \quad (6.66)$$

6

which allows to calculate the thermal photon number according to

$$n_{\text{LF}} = S_{I0} \frac{\Gamma_0'^2}{8\Gamma_0 I_{\text{zpf}}^2} - 1. \quad (6.67)$$

# 7

## PHOTON-PRESSURE COUPLING WITH A HOT RADIO-FREQUENCY CIRCUIT IN THE QUANTUM REGIME

Quantum control over a physical system requires thermal fluctuations and thermal decoherence to be negligible, which becomes more challenging with decreasing natural frequencies of the target system. For microwave circuits, the quantum regime can be reached simply by cooling them to mK temperatures [171]. Radio-frequency (RF) systems in the MHz regime, however, require further cooling or have to be coupled to an auxiliary quantum system with a coupling rate exceeding their thermal decoherence rate [33]. A powerful tool to cool below the thermodynamic bath temperature is sideband-cooling, a technique that originated from the field of trapped ions and cold atoms [172–175] and that has been applied in cavity optomechanics for groundstate cooling of mechanical motion [31, 32]. Here, we engineer a system of two superconducting LC circuits coupled by a current-mediated photon-pressure interaction and demonstrate sideband-cooling of a hot RF circuit using a microwave cavity and the regime of quantum-coherent coupling between the circuits. Due to a dramatically increased coupling strength [81, 176], we obtain a large single-photon quantum cooperativity  $C_{q0} \sim 1$  and reduce the residual thermal RF occupancy by 75% through sideband-cooling with less than a single pump photon. For larger pump powers, the photon-pressure coupling rate exceeds the RF thermal decoherence rate by a factor of three and the RF circuit is cooled into the quantum groundstate. Our results demonstrate photon-pressure coupling with a hot radio-frequency circuit in the quantum regime and lay the foundation for radio-frequency quantum photonics.

This chapter is available as arXiv preprint (2010.07975) and entitled *Photon-pressure coupling with a hot radio-frequency circuit in the quantum regime* by I. C. Rodrigues\*, D. Bothner\* & G. A. Steele

\*these authors contributed equally

## 7.1. INTRODUCTION

In the recent decade, the parametric photon-pressure coupling between two harmonic oscillators has been demonstrated to allow for groundbreaking experiments in the control and detection of harmonic oscillators from the kHz to the GHz frequency regime [36, 38–41, 56, 90, 159]. The archetype of a photon-pressure coupled system is an optomechanical cavity [56], where the radiation-pressure interaction between a mechanical oscillator and the light fields trapped inside a cavity is used for displacement sensing and motion control of macroscopic objects with unprecedented precision. An outstanding feature of the optomechanical radiation-pressure interaction is the possibility to cool a low-frequency mechanical oscillator orders of magnitude below its thermodynamic bath temperature using cavity red-sideband driving [11–13, 177–180]. The application of this technique for trapped ions or mechanical oscillators to place them in the phononic groundstate [31, 32, 173, 181, 182] has been the prerequisite for the preparation and investigation of quantum states of motion [36, 38, 185].

The implementation of photon-pressure coupling between two superconducting LC circuits has recently gained significant attention [78, 80, 81, 93, 176], as these provide an extremely high degree of design flexibility and at the same time constitute a key technology for quantum information processing and quantum sensing. Photon-pressure coupled circuits as toolbox for the manipulation and detection of radio-frequency and microwave photons offer rich possibilities for quantum signal processing, such as quantum-limited parametric amplification [26, 82, 84–86], nonreciprocal photon transport [87–90], slow light [183, 184] and photonic reservoir engineering [91, 92]. Photon-pressure coupled circuits are also discussed as promising platform for the realization of fault-tolerant quantum computing using bosonic codes [93]. To date, however, photon-pressure coupled superconducting circuits have only been realized in the classical regime and in presence of significant residual thermal fluctuations [81, 176].

## 7.2. CONCEPT AND DEVICE

Here, we report photon-pressure coupling between a hot RF circuit and a high-frequency (HF) superconducting quantum interference cavity in the quantum regime. By engineering galvanically connected circuits, we increase the single-photon coupling strength and single-photon cooperativity by about one order of magnitude compared to the best results reported to date [81, 176]. This allows for sideband-cooling of the residual thermal occupation in the hot radio-frequency mode by a factor of  $\sim 4$  with less than one pump photon and a single-photon quantum cooperativity  $C_{q0} \sim 1$ . By the dramatically increased single-photon coupling rate in our device, we reach the strong-coupling regime with only 0.7 pump photons, where we observe the residual thermal fluctuations of the hybridized normal-modes and demonstrate groundstate cooling of the RF mode. Simultaneously, the multi-photon coupling rate significantly exceeds the thermal decoherence rate of the RF mode and the decay rate of the HF cavity, which corresponds to the quantum-coherent strong-coupling regime, the basis for coherent quantum-state transfer between the two circuits [33]. Our results pave the way towards quantum control of RF circuits and quantum-limited detection of photons in the radio-frequency regime.

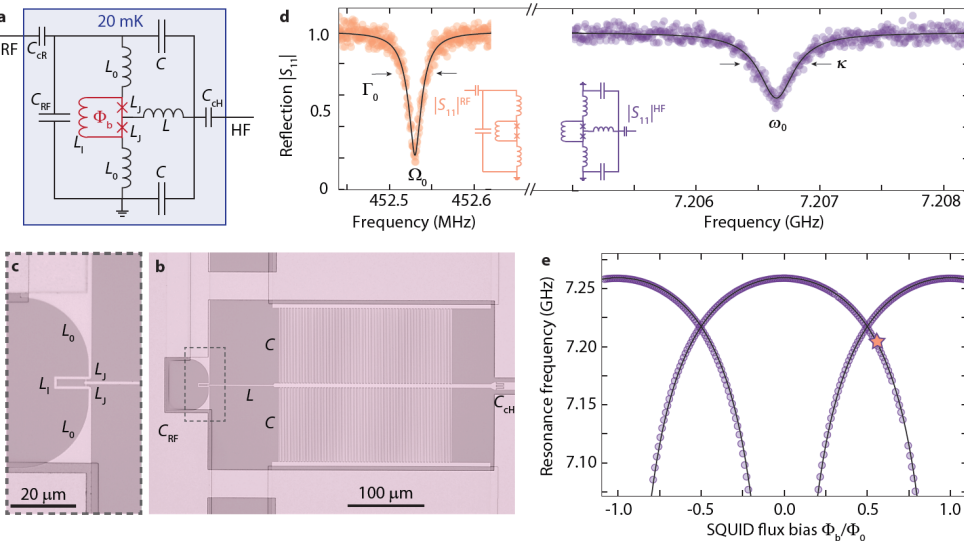


**Figure 7.1: A two-mode superconducting LC circuit with a tunable photon-pressure interaction.** **a** Circuit schematic. The full circuit has two modes, a low- and a high-frequency mode. The low, radio-frequency mode is formed by the capacitors and inductors  $C_{RF}$ ,  $L_0$  and the parallel combination of  $L_I$  and  $2L_J$ . The high-frequency microwave mode is formed by the combination of  $L$ ,  $C$  and  $L_0$  and  $L_I$ . The inductances  $L_I$  and  $L_J$  form a superconducting quantum interference device (SQUID). By changing the magnetic flux through the SQUID loop  $\Phi_b$ , the nonlinear inductances of the Josephson junctions  $L_J$  can be varied. The whole device is operated in a dilution refrigerator with a base temperature of  $T_b \sim 15\text{ mK}$ . Both modes are capacitively coupled to individual feedlines for driving and readout. **b** Optical image of the device showing the circuit (full image is shown in Supplementary Fig. 7.6). The dashed box shows the zoom region for panel c, which displays in detail the region with the SQUID loop and the different linear inductors. In b-c, brighter parts correspond to Aluminum, darker and transparent parts to Silicon. **d** shows the resonance curves of both modes vs excitation frequency in the reflection coefficient  $|S_{11}|$ , colored points are data and the black lines correspond to fits. The extracted mode parameters are given in the main text. The inset circuit schematics display the reduced circuit equivalents for the two modes. **e** shows the resonance frequency of the high frequency mode vs magnetic flux bias through the SQUID loop, generated by an external magnetic coil. The dataset was obtained by combining data from a flux up-sweep with the data from a flux down-sweep. Due to non-negligible loop inductance  $L_I$ , the flux-dependence is hysteretic and multi-valued for flux values around  $\pm 0.5\Phi_0 \pm 0.3\Phi_0$  [120, 122, 162]. The flux operation point  $\Phi_b/\Phi_0 \sim 0.54$  for the data shown in panel d and for the rest of this work is marked by a star.

Our device combines two integrated superconducting LC circuits, which are galvanically connected to each other at the heart of the circuit in a superconducting quantum interference device (SQUID). A circuit schematic of the device and optical micrographs are shown in Fig. 7.1a-c and the multi-layer device fabrication is presented in detail in section 7.7.1.

The radio-frequency (RF) mode circuit consists of a large parallel plate capacitor using amorphous silicon as dielectric, and of a short inductor wire, which at the same time forms the loop of the SQUID. The SQUID is completed by two constriction type Josephson junctions connecting the RF inductor wire to the high-frequency (HF) part of the circuit. The remaining part of the HF mode consists of an additional linear inductor

$L$  and two interdigitated capacitors  $C$ , cf. Fig. 7.1. Both circuit modes are capacitively coupled to individual coplanar waveguide feedlines for driving and readout. The chip is mounted into a printed circuit board, connected to microwave input/output cabling and packaged into a radiation tight copper (Cu) housing. A small superconducting magnet is attached to the Cu housing below the chip, allowing for the application of an external out-of-plane magnetic field. The experiments are carried out with the whole configuration placed inside a cryoperm magnetic shielding and attached to the mixing chamber of a dilution refrigerator with a base temperature of  $T_b \sim 15\text{ mK}$ . More details on the device and the setup are given in sections 7.7.2 and 7.7.3.

In Fig. 7.1d, the reflection response  $|S_{11}|$  of the two modes is shown, measured through their individual feedlines. The radio-frequency mode has a resonance frequency of  $\Omega_0 = 2\pi \cdot 452.5\text{ MHz}$  and a linewidth  $\Gamma_0 = 2\pi \cdot 26\text{ kHz}$ . For the high-frequency mode, the resonance frequency is  $\omega_0 = 2\pi \cdot 7.207\text{ GHz}$  and the total linewidth  $\kappa = 2\pi \cdot 380\text{ kHz}$ . The total linewidth of the HF mode is the sum of the internal loss rate  $\kappa_i = 2\pi \cdot 300\text{ kHz}$  and the external loss rate due to the coupling to the feedline of  $\kappa_e = 2\pi \cdot 80\text{ kHz}$ . For the low-frequency circuit, the internal losses contribute  $\Gamma_i = 2\pi \cdot 10\text{ kHz}$  and the external losses  $\Gamma_e = 2\pi \cdot 16\text{ kHz}$  to the total linewidth. Details on the fitting function and routine are given in section 7.7.4.

When a magnetic flux  $\Phi_b$  is applied through the SQUID by the external coil, the resulting circulating current changes the inductance of the Josephson junctions and the HF resonance frequency is shifted accordingly. In Fig. 1e, we show  $\omega_0(\Phi_b)$  depending on the external bias flux  $\Phi_b$  through the SQUID loop, a theoretical description and modeling of the circuit and the flux dependence is detailed in section 7.7.3. Any oscillating current flowing through the RF inductor induces additional flux through the SQUID loop and therefore modulates the resonance frequency of the HF mode. As a result, the two modes interact via an effective photon-pressure coupling and the Hamiltonian of the device is given by [78, 81, 176]

$$\hat{H}/\hbar = \omega_0 \hat{a}^\dagger \hat{a} + \Omega_0 \hat{b}^\dagger \hat{b} + g_0 \hat{a}^\dagger \hat{a} (\hat{b} + \hat{b}^\dagger), \quad (7.1)$$

where the creation (annihilation) operators for the HF and RF modes are given by  $\hat{a}^\dagger$  ( $\hat{a}$ ) and  $\hat{b}^\dagger$  ( $\hat{b}$ ), respectively. The coupling constant is given by

$$g_0 = \frac{\partial \omega_0}{\partial \Phi_b} \Phi_{\text{zpf}} \quad (7.2)$$

with the tunable flux responsivity of the HF cavity  $\partial \omega_0 / \partial \Phi_b$  and the effective root-mean-square value of the RF vacuum flux fluctuations  $\Phi_{\text{zpf}} \approx 635\text{ }\mu\Phi_0$ . Due to the low-power operation regime used for the experiments presented here, both circuits act in good approximation as harmonic oscillators and the Kerr nonlinearities arising from the Josephson junctions can be neglected. With the small Josephson inductance  $L_{J0} = 40\text{ pH}$  of the constriction type junctions and due to the significant dilution by linear inductors, both Kerr nonlinearities  $\chi_{\text{HF}} = 2\pi \cdot 2.4\text{ kHz} \ll \kappa$  and  $\chi_{\text{RF}} = 2\pi \cdot 1.3\text{ Hz} \ll \Gamma_0$  [98] are sufficiently low to justify this approximation.

From the resonance frequency fit curves shown in Fig. 7.1e, the flux responsivity at the operation point is found to be  $\partial \omega_0 / \partial \Phi \approx 2\pi \cdot 250\text{ MHz}/\Phi_0$ , and we get a coupling rate

of  $g_0 = 2\pi \cdot 160 \text{ kHz}$  at the operation point. At larger flux bias values  $\Phi_b/\Phi_0 \sim 0.75$  the single-photon coupling rate reaches values  $g_0 \sim 2\pi \cdot 1 \text{ MHz} \approx \kappa$ , cf. section 7.7.5, a regime typically very difficult to reach in other photon-pressure coupled systems. In the current setup, however, this operation point is related to considerable flux noise.

Considering the parameter regime of our device with  $g_0/\Omega_0 \sim 3 \cdot 10^{-4}$ , the photon-pressure nonlinearity [63, 67] induced in the HF cavity given by  $2g_0^2/\Omega_0 \sim 2\pi \cdot 110 \text{ Hz}$  is negligibly small. Therefore, the interaction between the two modes with a coherently driven HF cavity can be linearized [56] and the interaction part of the Hamiltonian with red-sideband driving is captured by a pump-tunable beam-splitter interaction

$$\hat{H}_{\text{int}}/\hbar = g(\delta \hat{a} \hat{b}^\dagger + \delta \hat{a}^\dagger \hat{b}). \quad (7.3)$$

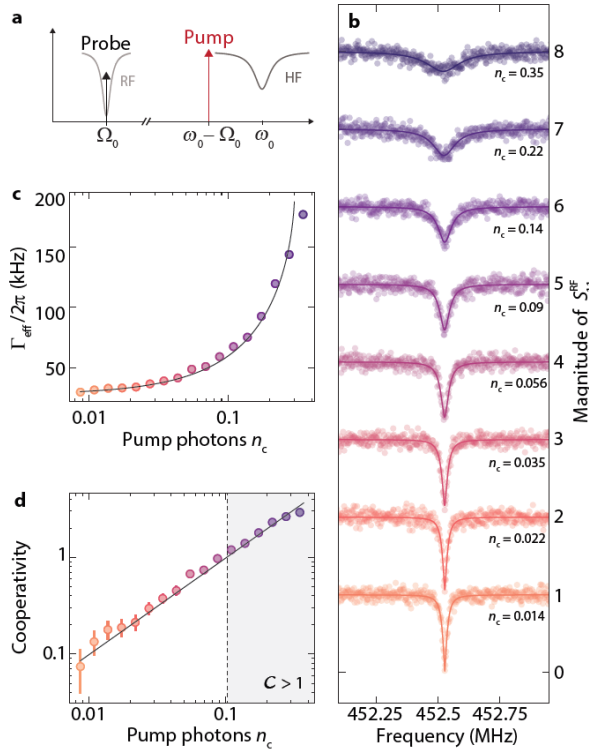
Here,  $g = \sqrt{n_c} g_0$  is the multi-photon coupling strength and  $\delta \hat{a}^\dagger, \delta \hat{a}$  describe the creation and annihilation of intracavity field fluctuations, respectively. In this situation, photons from the pump will scatter mainly to the HF resonance frequency  $\omega_0$ , each event removing one photon from the RF circuit. This process constitutes a cooling mechanism, which is exhibited by an additional damping term of the RF mode.

## 7.3. CHARACTERIZATION OF THE PHOTON-PRESSURE INTERACTION

We characterize the total damping rate of the RF resonator by probing its response  $S_{11}^{\text{RF}}$  in reflection with a small probe tone while pumping the HF mode with a variable power microwave tone exactly on the red sideband  $\omega_p = \omega_0 - \Omega_0$ . The experimental scheme is shown in Fig. 7.2a and the result of the response measurement is plotted in b for varying HF sideband pump powers. With increasing HF intracavity photon number  $n_c$ , the total linewidth  $\Gamma_{\text{eff}}$  of the RF mode increases from about  $2\pi \cdot 30 \text{ kHz}$  at low pump powers to  $\sim 2\pi \cdot 180 \text{ kHz}$  for pump powers that correspond to  $n_c \sim 0.4$  intracavity microwave photons. From fits to the response data, the effective damping rate for each pump power is extracted, the result is shown in Fig. 7.2c. The experimental data are fitted with the theoretical expression for the total damping

$$\Gamma_{\text{eff}} = \frac{\kappa + \Gamma_0}{2} - \sqrt{\frac{(\kappa - \Gamma_0)^2}{4} - 4g^2} \quad (7.4)$$

and as fit parameter we get the multi-photon coupling strength  $g$  and subsequently the multi-photon cooperativity  $\mathcal{C} = \frac{4g^2}{\kappa \Gamma_0}$ . The result is shown in Fig. 7.2d and demonstrates that we reach large values  $\mathcal{C} > 1$  for 0.1 pump photon and a single-photon cooperativity  $C_0 = \frac{4g_0^2}{\kappa \Gamma_0} \approx 10$ . With the knowledge of  $g, \Gamma_0$  and  $\kappa$  for a given pump strength, the photon-pressure interaction is fully characterized.



7

Figure 7.2: **Photon-pressure damping of the RF mode and large single-photon cooperativity.** a shows a schematic of the experiment. The high-frequency mode is driven by a pump tone on its red sideband  $\omega_p = \omega_0 - \Omega_0$  and the response of the radio-frequency mode is simultaneously measured with a weak probe tone around  $\Omega \sim \Omega_0$ . With increasing strength of the pump tone or intracavity pump photon number  $n_c$ , respectively, the linewidth of the RF resonance broadens significantly as shown in panel b, indicating the regime of photon-pressure damping induced by the red-sideband pump field. Circles are data, lines are fits. Subsequent curves are shifted vertically by 1 for clarity. From the fits, we extract the effective RF mode linewidth  $\Gamma_{\text{eff}}$  depending on the number of intracavity pump photons. The extracted values are plotted in panel c. By fitting the data (circles) with Eq. (7.4), fit curve is shown as line, we extract and quantify the multi-photon coupling strength  $g$  and the cooperativity  $C = \frac{4g^2}{\kappa\Gamma_0}$  depending on the number of pump photons. The cooperativity extracted from the experimental data is shown as circles in d, the theoretical curve based on the fit in c is shown as line. The gray shaded area for  $n_c > 0.1$  indicates the regime of cooperativity  $C > 1$ . Error bars in d correspond to a 1kHz uncertainty in the bare RF linewidth  $\Gamma_0$ . Here, the best agreement with the data was found with  $\Gamma_0 = 2\pi \cdot 27.5\text{kHz}$ .

## 7.4. PHOTON-PRESSURE SIDEBAND COOLING

Without the radio-frequency probe tone applied in the previous experiment, the currents in the RF mode are given by residual thermal and quantum fluctuations. These current fluctuations lead to resonance frequency fluctuations of the HF mode, mediated by the SQUID. Therefore, when the HF mode is driven with a continuous frequency pump tone on the red sideband, the resonance frequency fluctuations induced by the

LF mode lead to the generation of a sideband at  $\omega_p + \Omega_0$ . This sideband corresponds to upconverted thermal photons from the RF mode and its detection and analysis allows to determine the residual RF mode occupation. The power spectral density at the detector (HF HEMT amplifier) input in units of quanta for a pump around the red sideband is in good approximation given by

$$\frac{S(\omega)}{\hbar\omega} = \frac{1}{2} + n'_{\text{add}} + \frac{\kappa_e g^2 |\chi_0|^2 |\chi_c|^2 \Gamma_0}{|1 + g^2 \chi_c \chi_0|^2} n_{\text{th}}^{\text{RF}} \quad (7.5)$$

with the RF mode occupation as weighted sum of internal and external bath occupations  $n_{\text{th}}^{\text{RF}} = \frac{\Gamma_e}{\Gamma_0} n_e^{\text{RF}} + \frac{\Gamma_i}{\Gamma_0} n_i^{\text{RF}}$  and the HF and RF mode susceptibilities

$$\chi_c^{-1} = \frac{\kappa}{2} + i(\omega - \omega_0) \quad (7.6)$$

$$\chi_0^{-1} = \frac{\Gamma_0}{2} + i(\omega - \omega_p - \Omega_0), \quad (7.7)$$

respectively. For Eq. (7.5), we assumed that internal and external bath of the HF cavity are equilibrated to the fridge temperature  $n_i^{\text{HF}} = n_e^{\text{HF}} = n_{\text{th}}^{\text{HF}}$  and  $n_{\text{th}}^{\text{HF}} \ll n_{\text{th}}^{\text{RF}}, n'_{\text{add}}, 1/2$ . From a thermal calibration of the RF mode occupation with varying fridge temperature, shown in Fig. 7.8b, we determine the residual occupation at base temperature to be  $\sim 7 \pm 1$  RF photons and the effective number of noise photons added by the detection chain  $n'_{\text{add}} \approx 11 \pm 2$ , details are given in sections 7.7.7 and 7.7.8. We note that we observe a dependence of the bare linewidth  $\Gamma_0$  on temperature, but also on the residual RF occupation at  $T = T_b$ , which we attribute to two-level-system saturation in the amorphous silicon dielectric filling of the RF parallel plate capacitor. For the fridge base temperature data in Fig. 7.3b, we find  $\Gamma_0 \approx 2\pi \cdot 40\text{kHz}$ , an increased value compared to the values obtained from the reflection measurement. This  $\Gamma_0$  and  $n_{\text{th}}^{\text{RF}} \sim 7$  correspond to a single-photon quantum cooperativity  $C_{q0} = C_0 / n_{\text{th}}^{\text{RF}} \approx 1$ .

With the fridge temperature set back to its minimal value  $T_b = 15\text{mK}$ , we measure the HF mode output spectra for varying red-sideband pump power, cf. Fig. 7.3c. For the smallest pump power shown, the upcovered thermal noise spectrum displays a Lorentzian lineshape with an effective linewidth  $\Gamma_{\text{eff}} \approx 2\pi \cdot 65\text{kHz}$ , broadened by dynamical backaction. With increasing sideband pump power the thermal noise peak broadens further, until for the largest powers the lineshape deviates from a Lorentzian due to the onset of normal-mode splitting. Additional spectra for a larger residual RF occupation  $n_{\text{th}}^{\text{RF}} \sim 20$  are given in section 7.7.8.

By fitting the spectra with Eq. (7.5), shown as lines and shaded areas in Fig. 7.3c, the equilibrium RF photon numbers are determined and converted to the sideband-cooled photon occupation

$$n_{\text{cool}}^{\text{RF}} = n_{\text{th}}^{\text{RF}} \frac{\Gamma_0}{\kappa + \Gamma_0} \frac{4g^2 + \kappa(\kappa + \Gamma_0)}{4g^2 + \kappa\Gamma_0} + n_{\text{th}}^{\text{HF}} \frac{\kappa}{\kappa + \Gamma_0} \frac{4g^2}{4g^2 + \kappa\Gamma_0}. \quad (7.8)$$

Note that this relation differs from the result usually quoted in optomechanics [31, 56, 58], which is only valid for  $\kappa \gg \Gamma_0$  and significantly underestimates the cooling rate in the unusual regime  $\Gamma_0 \lesssim \kappa$ . The full equation taking into account also finite pump detunings  $\delta$  can be found at the end of section 7.7.6.

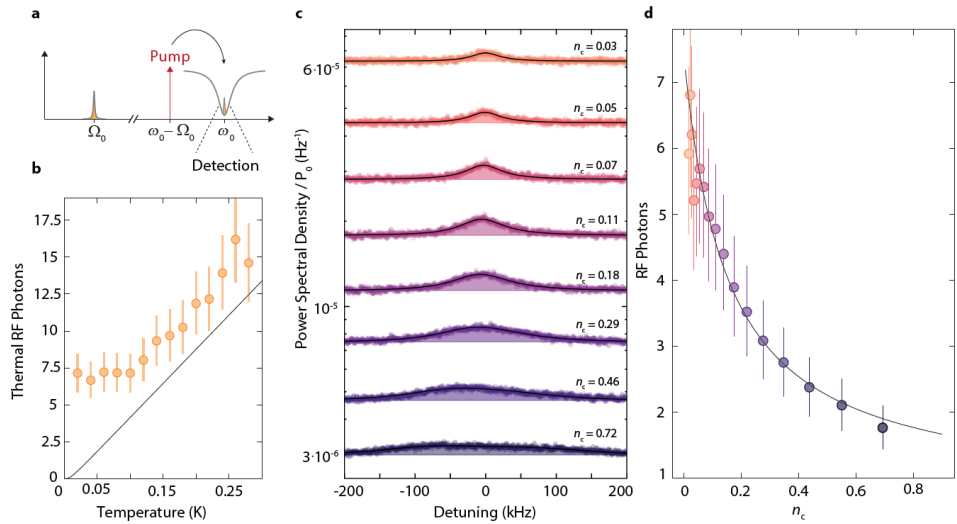


**Figure 7.3: Sideband-cooling of a hot radio-frequency resonator with less than a single pump photon.** **a** For the observation of upconverted thermal noise and cooling of the RF resonator, a pump tone is set to the red sideband of the high-frequency mode  $\omega_p = \omega_0 - \Omega_0$  and the cavity output field around  $\omega = \omega_0$  is detected with a signal analyzer. **b**, thermal RF photon number vs fridge temperature. Symbols are data, line is the Bose factor. From this thermal calibration, we determine the thermal occupation of the RF mode at fridge base temperature to be  $n_{\text{th}}^{\text{RF}} \sim 7 \pm 1$ . **c** shows the measured high-frequency output power spectral density for increasing red-sideband pump power, normalized to the on-chip pump power  $P_0$ . Frequency axis is given as detuning from the low-power noise center frequency. Circles are data, lines with shaded areas are fits. With increasing pump strength the RF resonance gets broadened by photon-pressure damping, and its total thermal noise power gets reduced, which corresponds to sideband-cooling of the RF mode. The slight asymmetry in the power spectral density for the largest pump powers originates from a small detuning  $\delta \approx 2\pi \cdot 30 \text{ kHz}$  of the pump from the red sideband, which is taken into account in our analysis. In **d**, the thermal mode occupation photon number is shown as symbols vs HF pump photon number. The initial thermal occupation is cooled by about a factor of  $\sim 4$ , theoretical expectation is shown as line. Error bars in **b** and **d** correspond to uncertainties of  $\pm 2$  HF photons of added noise in the detection chain and  $\pm 2 \text{ kHz}$  in bare RF linewidth  $\Gamma_0$ .

The resulting sideband-cooled RF mode occupation is shown in Fig. 7.3d. Therefore, with less than a single pump photon, the RF mode is cooled by about a factor of  $\sim 4$  to an occupation of only 1.7 RF quanta, demonstrating the applicability of sideband-cooling for photon-pressure coupled circuits and an extraordinarily large single-photon cooling rate. At higher pump powers than the ones discussed so far, the two circuits hybridize in the parametric normal-mode splitting regime [31, 58, 176].

## 7.5. NORMAL-MODE THERMOMETRY AND GROUND-STATE COOLING

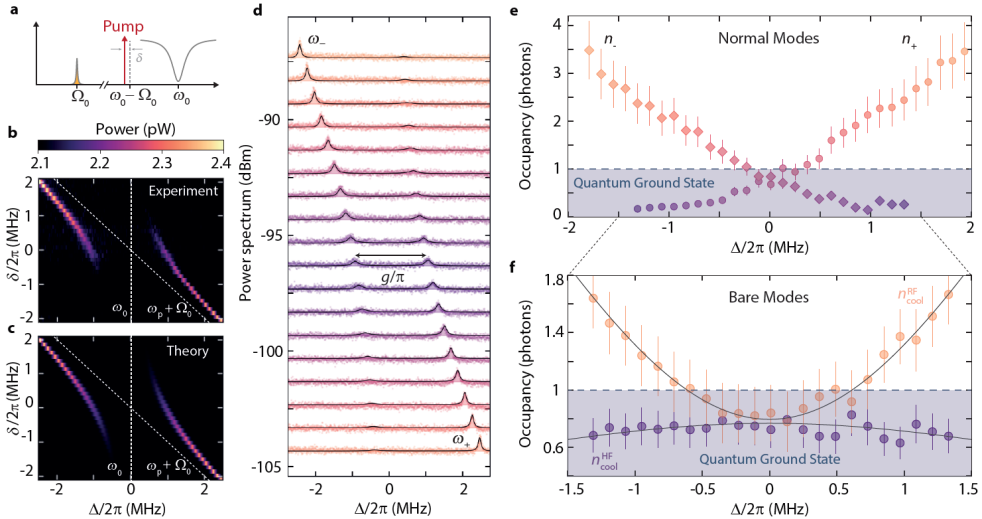


**Figure 7.4: Normal-mode thermometry and ground-state cooling in the quantum coherent strong-coupling regime.** **a** Experimental scheme. A strong pump tone is applied with detuning  $\delta$  from the red sideband of the HF mode. For each pump detuning  $\delta$ , the output spectrum around the bare HF mode resonance frequency  $\omega_0 + \Delta$  is measured. The resulting power spectra are plotted color-coded in **b**. We observe two noise peaks and an avoided crossing of the modes for  $\delta = 0$ . The bare mode at  $\Delta = 0$  corresponds to the HF cavity, while the bare mode at  $\omega_p + \Omega_0$  is moving with the pump and corresponds to the RF mode. Due to the large pump, the two modes fully hybridize around  $\delta = 0$  and the total thermal occupation of the system in terms of thermal photons gets minimized. **c** shows the result of calculations based on the theoretical model. In **d**, we plot the corresponding linecuts from **b** and **c** on top of each other, displaying a high level of agreement between experiment and theory. In the regime  $\delta = 0$ , the splitting between the modes is given by  $g/\pi$  with  $g = 2\pi \cdot 1 \text{ MHz}$ . We treat the two parametrically coupled normal-modes as individual HF modes with resonance frequencies  $\omega_-$  and  $\omega_+$  and extract the corresponding, effective thermal photon numbers  $n_-$  and  $n_+$  from the power spectral density shown in **d**. The values are plotted in **e**. The dashed, horizontal line shows a thermal occupancy of 1. At the point of symmetric normal-modes  $\delta = 0$ , both reach an occupancy of  $\sim 0.8 \pm 0.2$ . From the effective normal-mode occupations  $n_{\pm}$ , we determine the occupation of the bare HF and RF modes shown in **f**. Around zero detuning of the pump from the red sideband, both bare modes are in the quantum groundstate with residual occupations  $n_{\text{cool}}^{\text{HF}} \approx n_{\text{cool}}^{\text{RF}} \sim 0.8 \pm 0.2$ . For the theoretical calculations, shown as lines, we assume  $n_{\text{th}}^{\text{HF}} = 0.01$  and find as equilibrium thermal occupations  $n_{\text{th}}^{\text{RF}} = 8.0$ . Error bars in **e** and **f** correspond to uncertainties of  $\pm 2$  HF photons of added noise in the detection chain and estimated  $\pm 2 \text{ kHz}$  in bare RF linewidth  $\Gamma_0$ .

In the strong-coupling regime, i.e., when the frequency-splitting of the normal modes exceeds the hybridized linewidths, the residual thermal occupation of the RF mode is distributed between the hybridized normal-modes. Equation (7.8), however, remains valid and the onset of mode hybridization does not prevent the RF mode from being cooled further. The theoretical limit for cooling in the regime  $g \gg \kappa, \Gamma_0$  is given by  $n_{\text{lim}}^{\text{RF}} = n_{\text{th}}^{\text{RF}} \Gamma_0 / (\kappa + \Gamma_0) \approx 0.67$  photons, assuming a ground-state HF cavity. The remaining

thermal excitations of the system are then equally distributed between the RF and the HF modes, cf. also section 7.7.9.

To characterize the residual number of thermal RF photons in the strong-coupling regime, we detect the output noise of the normal-modes in the HF domain for varying detuning of the pump tone from the red sideband  $\delta$ . In Fig. 7.4, the measured output spectra around  $\Delta = \omega - \omega_0$  are shown color-coded in panel **b** and as individual linescans in panel **d**. We find an excellent agreement between the data and theoretical calculations, shown color-coded in **c** and as lines in **d**. For large detunings  $|\delta| > 2\pi \cdot 2 \text{ MHz}$ , a hot mode with a large noise amplitude is observed, whose frequency follows closely  $\omega_p + \Omega_0$  and corresponds to the normal-mode dominated by the RF circuit in this regime. At the same time, no output noise field is detected around the HF-cavity-like normal mode close to  $\Delta = 0$ , indicating that this mode is cold and in thermal equilibrium with its bath. For small detunings  $\delta \sim 0$ , we observe a pronounced avoided crossing of the RF mode with the driven HF cavity, centered at  $\Delta = 0$ . The splitting between the two hybridized modes is given by  $g/\pi \approx 2 \text{ MHz}$ , indicating that we reach the so-called quantum-coherent coupling regime where  $g > \kappa, \Gamma_0 n_{\text{th}}^{\text{RF}}$  [33] and a quantum cooperativity  $C_q = C/n_{\text{th}}^{\text{RF}} \approx 35$ .

For a quantification of the effective normal-mode thermal occupation, we treat the modes as two independent HF modes, a detailed description is given in sections 7.7.9 and 7.7.10. The lower frequency mode has the resonance frequency  $\omega_-$ , linewidth  $\kappa_-$  and external linewidth  $\kappa_{e-}$ , the higher frequency mode  $\omega_+$ ,  $\kappa_+$  and  $\kappa_{e+}$ , respectively. The complex resonances of the normal modes are given by [58]

$$\tilde{\omega}_{\pm} = \omega_0 + \frac{\delta}{2} + i \frac{\kappa + \Gamma_0}{4} \pm \sqrt{g^2 - \left( \frac{\kappa - \Gamma_0 + 2i\delta}{4} \right)^2} \quad (7.9)$$

7

and the resonance frequencies and linewidths are  $\omega_{\pm} = \text{Re}[\tilde{\omega}_{\pm}]$  and  $\kappa_{\pm} = 2\text{Im}[\tilde{\omega}_{\pm}]$ , respectively.

The power spectral density of the HF output field in terms of these normal-mode parameters can be written as

$$\frac{S_{\text{nms}}}{\hbar\omega} = \frac{1}{2} + n'_{\text{add}} + 4 \frac{\kappa_{e-}\kappa_-}{\kappa_-^2 + 4\Delta_-^2} n_- + 4 \frac{\kappa_{e+}\kappa_+}{\kappa_+^2 + 4\Delta_+^2} n_+ \quad (7.10)$$

where  $n_{\pm}$  are the effective photon occupations of the two normal modes,  $\Delta_{\pm} = \omega - \omega_{\pm}$  and the external linewidths  $\kappa_{e\pm} = \frac{\kappa_e}{2} \left( 1 \pm \frac{\delta}{\sqrt{\delta^2 + 4g^2}} \right)$ , cf. sections 7.7.9 and 7.7.10. The effective normal-mode occupation  $n_-$  and  $n_+$  depending on the pump detuning is shown in Fig. 7.4e. While for large detunings the RF-like normal mode is still hot and the HF-like mode is in the quantum ground-state, both normal modes appear to be in the quantum ground-state when they are close to the full mode hybridization at  $\delta \sim 0$ . The minimum occupation that we observe at the symmetry point is  $n_- = n_+ = 0.8$ .

From comparison between the two versions of the HF power spectral densities Eq. (7.10) and Eq. (7.5) and the condition  $S_{\text{nms}} = S$ , we obtain the HF mode occupation in the cooling regime  $n_{\text{cool}}^{\text{HF}}$  by

$$\kappa_e n_{\text{cool}}^{\text{HF}} = \kappa_{e-} n_- + \kappa_{e+} n_+, \quad (7.11)$$

For zero pump detuning, this simplifies to  $n_{\text{cool}}^{\text{HF}} = n_- = n_+ = 0.8$ . Using the equation for the total thermal occupation  $n_{\text{cool}}^{\text{tot}}$  of the system in the strong-coupling regime (cf.

section 7.7.9), we calculate the residual occupation of the RF mode  $n_{\text{cool}}^{\text{RF}} = n_{\text{cool}}^{\text{tot}} - n_{\text{cool}}^{\text{HF}}$ . The resulting occupation of both bare modes is shown in Fig. 7.4f, showing that  $n_{\text{cool}}^{\text{RF}} \approx n_{\text{cool}}^{\text{HF}} = 0.8 \pm 0.2$ , i.e., that both are in the quantum ground-state for  $\delta \sim 0$ .

## 7.6. DISCUSSION

With the results presented in this work, we demonstrated photon-pressure coupling of a hot radio-frequency circuit to a superconducting microwave cavity in the quantum regime. By a galvanically connected circuit design, we dramatically increased the single-photon coupling strength and achieved a single-photon quantum cooperativity of unity. Based on the large single-photon coupling rate, we were able to demonstrate both, sideband-cooling of the RF mode by a factor of 4 and the strong-coupling regime, with less than a single pump photon. For stronger pump powers, we enter the quantum-coherent coupling regime and demonstrate photon-pressure groundstate cooling of the originally hot RF mode. Compared to other recently developed radiative cooling techniques of circuits and other systems [186, 187], sideband-cooling can reduce the effective mode temperature far below the physical temperature of any bath [62]. Furthermore, in contrast to previous reports of sideband-cooling techniques with circuits using highly nonlinear systems such as superconducting qubits [168, 188], our approach allows for both participating circuits to have a very high degree of linearity which is highly desirable for many signal processing applications. This work lays the foundation for radio-frequency quantum photonics, for quantum-limited RF sensing and has potential applications in quantum-limited microwave signal and bosonic code quantum information processing based on photon-pressure coupled circuits.

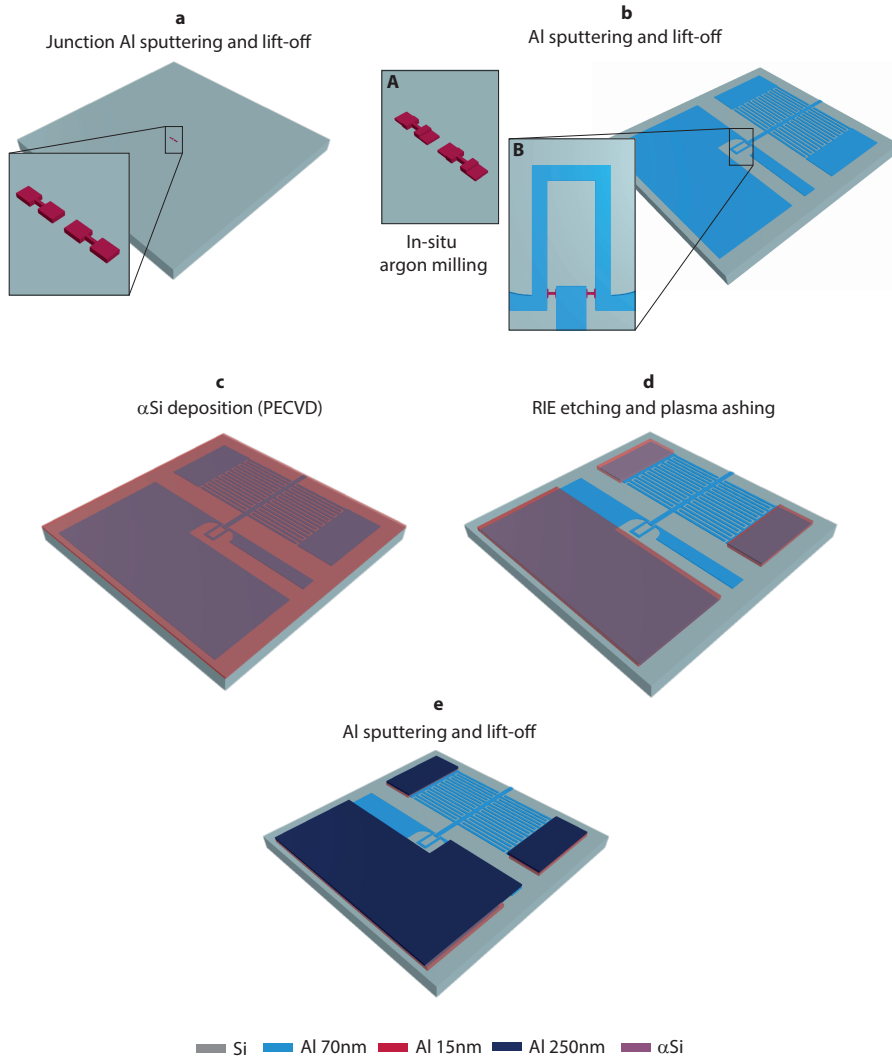
## 7.7. SUPPLEMENTARY INFORMATION

### 7.7.1. DEVICE FABRICATION

- **Step 0: Marker patterning.** Prior to the device fabrication, we perform the patterning of alignment markers on a full 4 inch Silicon wafer, required for the electron-beam lithography (EBL) alignment of the following fabrication steps. The structures were patterned using a CSAR62.13 resist mask and sputter deposition of 50 nm Molybdenum-Rhenium alloy. After undergoing a lift-off process, the only remaining structures on the wafer were the markers. The complete wafer was diced into  $14 \times 14 \text{ mm}^2$  chips, which were used individually for the subsequent fabrication steps. The step was finalized by a series of several acetone and IPA rinses.
- **Step 1: Junctions patterning.** As first step in the fabrication, we pattern weak links which afterwards result in constriction type Josephson junctions between the arms of the SQUID. The weak link nanowires were patterned together with larger pads, cf. Supplementary Fig. 7.5a, which were used to achieve good electrical contact with the rest of the circuit, cf. Step 3. The nanowires are designed to be  $\sim 50 \text{ nm}$  wide and  $\sim 100 \text{ nm}$  long at this point of the fabrication, and each pad is  $500 \times 500 \text{ nm}^2$  large. For this fabrication step, a CSAR62.09 was used as EBL resist and the development was done by dipping the exposed sample into Pentyacetate

for 60 seconds, followed by a solution of MIBK:IPA (1:1) for 60 seconds, and finally rinsed in IPA, where MIBK is short for methyl isobutyl ketone and IPA for isopropyl alcohol. The sample was subsequently loaded into a sputtering machine where a 15 nm layer of Aluminum was deposited. Finally, the chip was placed at the bottom of a beaker containing a small amount of Anisole and inserted into an ultrasonic bath for a few minutes where the sample underwent a lift-off process. The step was finalized by a series of several acetone and IPA rinses.

- **Step 2: Bottom RF capacitor plate and HF resonator patterning.** As second step in the fabrication, we pattern the bottom plate of the parallel plate capacitor, the inductor wire of the radio-frequency cavity, which also forms part of the SQUID loop, the remaining part of the SQUID cavity (cf. Supplementary Fig. 7.5b.) and the center conductor of the SQUID cavity feedline by means of EBL using CSAR62.13 as resist. After the exposure, the sample was developed in the same way as in the first fabrication step and loaded into a sputtering machine. In the sputter system, we performed an argon milling step for two minutes and afterwards deposited 70 nm of Aluminum. The milling step, performed in-situ and prior to the deposition, very efficiently removes the oxide layer which was formed on top of the previously sputtered weak link pads, and therefore allows for good electrical contact between the two layers. After the deposition, the unpatterned area was lifted-off by means of an ultrasonic bath in room-temperature Anisole for a few minutes. The step was finalized by a series of several acetone and IPA rinses.
- **Step 3: Amorphous silicon deposition.** The deposition of the dielectric layer of the parallel plate capacitor was done using a plasma-enhanced chemical vapor deposition (PECVD) process. To guarantee low dielectric losses in the material, the chamber underwent an RF cleaning process overnight and only afterwards the deposition of ~ 130 nm of amorphous silicon was performed. At this point of the fabrication, the whole sample is covered with dielectric, cf. Supplementary Fig. 7.5c.
- **Step 4: Reactive ion etch patterning of  $\alpha$ Si.** We spin-coat a double layer of resist (PMMA 950K A4 and ARN-7700-18) on top of the  $\alpha$ Si-covered sample, and expose the next pattern with EBL. Prior to the development of the pattern, a post-bake of 2 minutes at ~ 115 °C was required. Directly after, the sample was dipped into MF-321 developer for 2 minutes and 30 seconds, followed by H<sub>2</sub>O for 30 seconds and lastly rinsed in IPA. To finish the third step of the fabrication, the developed sample underwent a SF<sub>6</sub>/He reactive ion etching (RIE) to remove the amorphous Silicon. To conclude the etching step, we performed a O<sub>2</sub> plasma ashing in-situ with the RIE process to remove resist residues, the result is shown schematically in Supplementary Fig. 7.5d.
- **Step 5: Top capacitor plate and ground-plane patterning.** As final step, the sample was again coated in CSAR62.13 and the top plate of the RF capacitor as well as all ground plane and the low-frequency feedline was patterned with EBL. The resist development was done identical to the ones in the second and third steps. Afterwards, the sample was loaded into a sputtering machine where an argon milling



7

**Figure 7.5: Schematic device fabrication.** **a** shows the weak-link Josephson junctions with contact pads, patterned in the first fabrication step. **b** shows the patterned second Aluminum layer, forming the bottom of the RF parallel plate capacitor, the SQUID loop and the HF cavity. Inset **A** showing the in-situ argon milled Josephson junctions prior to the deposition (the existing resist is not shown for better visibility of the milled structures). Inset **B** shows a zoom-in of the 3D SQUID. **c** shows the sample after the deposition of  $\alpha$ Si. **d** shows the device after the subsequent  $SF_6/He$  reactive ion etching step, finished by an in-situ  $O_2$  plasma ashing. **e** shows the final device after the deposition of the last Aluminum layer.

process was performed in-situ for 2 minutes, in order to have good electrical contact between the top and bottom plates of the low-frequency capacitor, similar to what was done between the second and third fabrication steps. After the milling,

a 250 nm layer of Aluminum was deposited and finally an ultrasonic lift-off procedure was performed. The step was finalized by a series of several acetone and IPA rinses. With this, the sample fabrication process was essentially completed, cf. Supplementary Fig. 7.5e.

- **Step 6: Dicing and mounting.** At the end of the fabrication, the sample was diced to a  $10 \times 10\text{mm}^2$  size and mounted to a printed circuit board (PCB), wire-bonded to microwave feedlines and ground and packaged into a radiation tight copper housing.

A schematic representation of this fabrication process can be seen in Supplementary Fig. 7.5, omitting the initial patterning of the electron beam markers and the sample mounting. In addition, an optical image of the full device is shown in Supplementary Fig. 7.6.

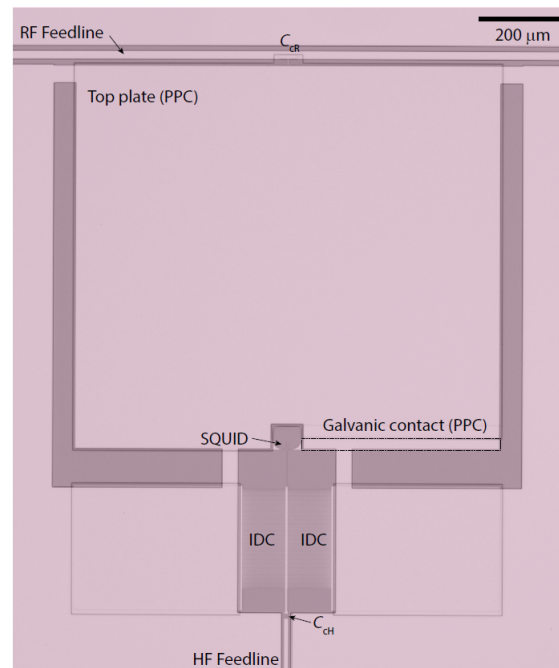


Figure 7.6: **Optical image of the full device.** Visible are both, the radio-frequency (top) and microwave (bottom) resonators including their corresponding RF and HF feedlines. The coupling capacitors are labelled with  $C_{cR}$  for the RF mode and  $C_{cH}$  for the HF mode, respectively. Also labelled are the RF parallel plate capacitor (PPC), the HF interdigitated capacitors (IDC), and the SQUID for orientation. Zoom-ins to the HF mode circuit including labels for the inductors are shown in Fig. 7.1. The galvanic contact area of the PPC top and bottom plates is marked with a dashed rectangle.

### 7.7.2. MEASUREMENT SETUP

All the experiments reported in this paper were performed in a dilution refrigerator operating at a base temperature close to  $T_b = 15\text{ mK}$ . A schematic of the experimental setup

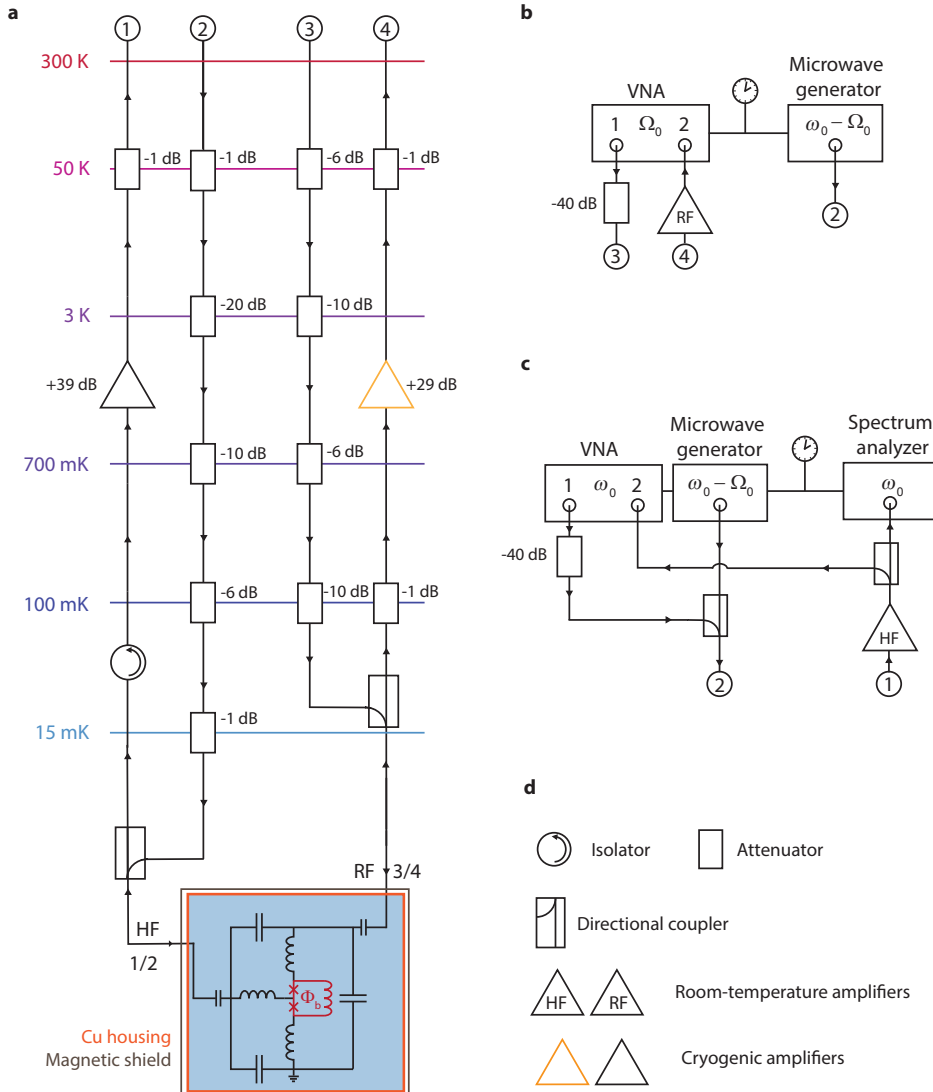


Figure 7.7: Schematic of the measurement setup. Detailed information is provided in text.

and of the external configurations used in the different performed experiments can be seen in Supplementary Fig. 7.7.

The printed circuit board (PCB), onto which the fabricated sample was glued and wire-bonded, was placed in a radiation tight copper housing and connected to two coaxial lines. One of the lines was used as input/output port for the high-frequency (HF) SQUID cavity and the second line was set in a similar way for the radio-frequency res-

onator. Both of the cavities were measured in a reflection geometry, and therefore the input and output signals were split via a directional coupler. For the HF line, the directional coupler was positioned on the 15 mK stage, while for the RF line it was mounted in between the 15 mK plate and the 100 mK plate. Both output signals went into a cryogenic amplifier for their particular frequency range.

Furthermore, in order to generate an out-of-plane magnetic field, required to flux bias the SQUID cavity, an external magnet (not shown in the figure) was put in very close proximity below the device and the two were placed inside a cryoperm magnetic shield. The magnet was connected with DC wires, allowing for the field to be tuned by means of a DC current (not shown).

Both input lines were heavily attenuated in order to balance the thermal radiation from the line to the base temperature of the fridge. The low-frequency line, however, is not fully equilibrated to the fridge base temperature due to the lack of cryogenic circulators/isolators for the particular frequency range. Outside of the refrigerator, we used different configurations of microwave signal sources and high-frequency electronics for the different experiments.

In **b** we show the configuration used to measure the photon-pressure damping of the radio-frequency mode (Fig. 7.2). A microwave generator sends a continuous wave signal to the SQUID cavity around its red sideband, while the RF resonator is probed in reflection with a vector network analyzer (VNA).

In **c** we show the setup for photon-pressure sideband-cooling experiment and the normal-mode thermometry (Figs. 7.3 and 7.4), where a continuous wave tone is send to the red sideband of the SQUID cavity. In addition, in order to observe the cavity response and adjust the pump tone frequency with respect to the power-dependent cavity resonance, a weak VNA signal is combined with the pump tone via a directional coupler. The output signal is analyzed individually by a spectrum analyzer and a VNA after being amplified. During the detection of thermal noise with the signal analyzer, the VNA scan was stopped and the VNA output power was completely switched off.

For the normal-mode thermometry experiment, we replaced the 20 dB attenuator on the 3 K plate of HF input line 2 by a 10 dB one. This allowed for stronger red-sideband pumping and therefore for reaching deeper into the strong-coupling regime.

For all experiments, the microwave sources and vector network analyzers (VNA) as well as the spectrum analyzer used a single reference clock of one of the devices.

### 7.7.3. THE CIRCUIT MODEL AND FLUX DEPENDENCE

#### THE CIRCUIT MODEL

The diagram shown in Supplementary Fig. 7.8 represents the full circuit model of the device. Similar to the simplified version shown in Fig. 7.1a, it contains the high-frequency (drawn in purple) and a radio-frequency (drawn in orange) mode, which share the center part of the circuit (drawn in gray). The shared part contains a non-linear, flux-tunable SQUID inductance. The Josephson junctions which form part of the tunable SQUID are constriction type Josephson junctions, which are known to have a current-phase relation (CPR) that can differ significantly from the typical sinusoidal CPR [114, 115]. To include this effect in the flux dependence of the modes, we model each weak-link inductance

to be a series combination of a non-linear element  $L_j$  with a sinusoidal current-phase relation and a linear inductor  $L_a$ .

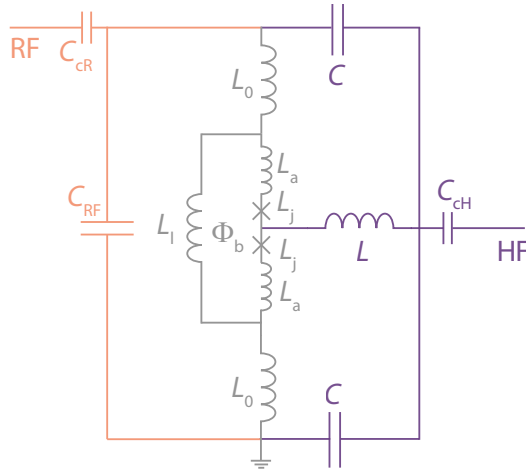


Figure 7.8: **Full circuit diagram of the device.** The orange part of the circuit represents the components belonging only to the radio-frequency mode. The circuit parts drawn in purple correspond to the high-frequency mode. Both modes share the part of the circuit drawn in gray.

7

## FLUX DEPENDENCE OF THE HF MODE

The resonance frequency of a SQUID cavity with a symmetric SQUID can be described by

$$\omega_0(\Phi_b) = \frac{\omega_0(0)}{\sqrt{\Lambda + \frac{1-\Lambda}{\cos(\pi \frac{\Phi}{\Phi_0})}}} \quad (7.12)$$

where  $\Phi$  corresponds to the total flux threading the SQUID loop and  $\omega_0(0)$  is the resonance frequency without external flux bias (sweetspot frequency). The parameter  $\Lambda = (L_{HF} - \frac{1}{2}L_{j0})/L_{HF}$  with the total high-frequency inductance  $L_{HF}$  and the single junction Josephson inductance  $L_{j0}$  is a measure for the contribution of the Josephson inductance to the total inductance. For zero bias current and the (magnetic plus kinetic) loop inductance  $L_{loop} = L_I + 2L_a$  the total flux threading the SQUID is given by

$$\frac{\Phi}{\Phi_0} = \frac{\Phi_b}{\Phi_0} + L_{loop}J \quad (7.13)$$

with the circulating current  $J$ . In the absence of a bias current and symmetric junctions, the circulating current is given by

$$J = -I_c \sin\left(\pi \frac{\Phi}{\Phi_0}\right) \quad (7.14)$$

with the zero bias critical current of a single junction  $I_c = \frac{\Phi_0}{2\pi L_{j0}}$ . Using the screening parameter  $\beta_L = \frac{2L_{\text{loop}}I_c}{\Phi_0} = \frac{L_{\text{loop}}}{\pi L_{j0}}$  the relation for the total flux can be written as

$$\frac{\Phi}{\Phi_0} = \frac{\Phi_b}{\Phi_0} - \frac{\beta_L}{2} \sin\left(\pi \frac{\Phi}{\Phi_0}\right). \quad (7.15)$$

Figure 7.1e shows the experimentally determined SQUID cavity resonance frequency modulating with external magnetic flux  $\Phi_b$  and a fit curve using Eq. 7.12, where the relation between the applied external flux  $\Phi_b$  and the total flux in the SQUID  $\Phi$  is given by Eq. (7.15). As fit parameters we obtain  $\beta_L = 1.07$  and  $\Lambda = 0.946$ , i.e., the SQUID Josephson inductance contributes about 5.4% to the total HF inductance. Furthermore, we estimate the capacitance of the SQUID cavity  $C_{\text{HF}} = 2C + C_{\text{cH}}$  with the expressions given in Ref. [158] to be  $\sim 1.3 \text{ pF}$ . Based on the sweetspot frequency of the SQUID cavity

$$\omega_0 = \frac{1}{\sqrt{L_{\text{HF}}(2C + C_{\text{cH}})}}, \quad (7.16)$$

we extract the total inductance of the high frequency mode to be  $L_{\text{HF}} = 370 \text{ pH}$  and with  $\Lambda$  we get the inductance of a single junction  $L_{j0} = 40 \text{ pH}$ . This inductance corresponds to a critical junction current  $I_c = \frac{\Phi_0}{2\pi L_{j0}} \approx 8.3 \mu\text{A}$ .

From the screening parameter  $\beta_L = 1.07$  and the single-junction inductance  $L_{j0} = 40 \text{ pH}$ , we get a loop inductance  $L_{\text{loop}} = 2L_a + L_l = \pi\beta_L L_{j0} \approx 134 \text{ pH}$ .

## FLUX DEPENDENCE OF THE RF MODE

Based on the circuit diagram shown in Supplementary Fig. 7.8, we find the total inductance of the radio-frequency mode  $L_{\text{RF}}$  as

$$L_{\text{RF}} = 2L_0 + \frac{2(L_j + L_a)L_l}{2(L_j + L_a) + L_l}, \quad (7.17)$$

with the Josephson inductance of a single junction  $L_j = \frac{L_{j0}}{\cos(\pi \frac{\Phi}{\Phi_0})}$  and the SQUID loop inductance  $L_{\text{loop}} = 2L_a + L_l \approx 134 \text{ pH}$  as boundary condition for  $L_l$  and  $L_a$ . In addition, we independently estimate the parallel plate capacitance  $C_{\text{RF}} = 659.7 \text{ pF}$  and the parallel plate coupling capacitance  $C_{\text{cR}} = 0.3 \text{ pF}$ . From the total capacitance  $C_{\text{tot}} = C_{\text{RF}} + C_{\text{cR}}$  and the resonance frequency  $\Omega_0$ , we determine the total inductance of the RF resonator as  $L_{\text{RF}} \sim 188 \text{ pH}$ .

As the total inductance of the radio-frequency mode is partly composed by the field-dependent Josephson inductance  $L_j$ , the resonator resonance frequency will as well modulate with applied magnetic flux  $\Phi_b$  as

$$\Omega_0 = \frac{1}{\sqrt{C_{\text{tot}} \left( 2L_0 + L_l \left( 1 + \frac{L_l}{2} \frac{\cos(\pi \frac{\Phi}{\Phi_0})}{L_{j0} + L_a \cos(\pi \frac{\Phi}{\Phi_0})} \right)^{-1} \right)}}. \quad (7.18)$$

where the relation between  $\Phi$  and  $\Phi_b$  is again given by Eq. (7.15). Supplementary Fig. 7.9 shows the RF resonance frequency depending on the applied magnetic flux together

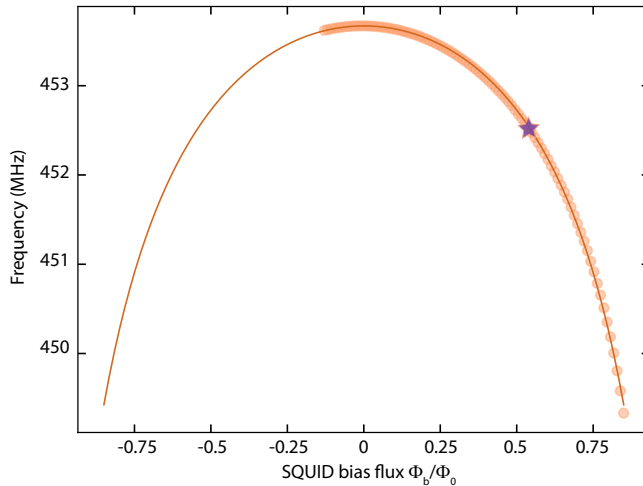


Figure 7.9: **RF mode resonance frequency depending on external magnetic flux.** Points are data and line is a fit curve using Eq. (7.18). The operation point in this work  $\Phi_b/\Phi_0 = 0.54$  is marked by a star.

with a fit curve using Eq. (7.18), where the parameter  $\beta_L = 1.07$  was kept constant as determined from the HF mode flux dependence. From the fit, we extract the parameters  $L_a = 43.5 \text{ pH}$  and  $L_i = 47 \text{ pH}$ . Based on the returned fit parameters and on Eq. (7.18), we obtain  $L_0 = 75 \text{ pH}$ .

We note here, that without the linear junction inductances  $L_a$ , it is not possible to fit both flux dependences with a single set of reasonable parameters.

7

## FLUX DEPENDENCE OF THE DECAY RATES $\kappa$ AND $\Gamma_0$

As the external magnetic field is kept at a non-zero value during the experiment, it is of interest to analyze how the applied magnetic flux  $\Phi_b$  affects the losses in the circuit. For that, we extract the decay rates of both modes  $\kappa$  and  $\Gamma_0$  while changing the flux bias point. The result is shown in Supplementary Fig. 7.10 for the positive tuning range. Both linewidths clearly show a strong dependence for values larger than  $\sim 0.7\Phi_0$  to  $\sim 0.8\Phi_0$ . For the operating point used here of  $\Phi_b/\Phi_0 = 0.54$ , however, they are nearly unmodified compared to the sweetspot values.

### 7.7.4. RESPONSE FUNCTIONS AND FITTING ROUTINE IDEAL HF AND RF RESONATORS RESPONSE FUNCTIONS

Both, our HF SQUID cavity and the RF resonator, can be modeled as a parallel LC circuit capacitively coupled to a transmission line in a reflection geometry. The  $S_{11}$  response function of such a circuit (here for the HF mode) is given by

$$S_{11}^{\text{HF}} = 1 - \frac{2\kappa_e}{\kappa_i + \kappa_e + 2i\Delta} \quad (7.19)$$

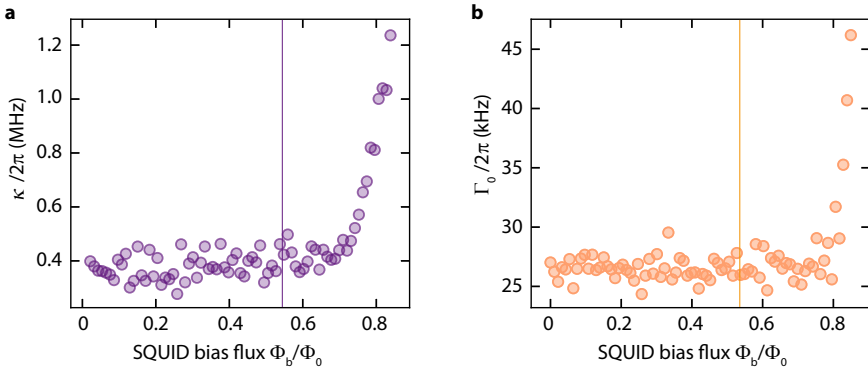


Figure 7.10: **Linewidths for varying SQUID bias flux.** Decay rate of the microwave mode  $\kappa$  (a) and of the radio-frequency mode  $\Gamma_0$  (b) depending on magnetic bias flux in units of flux quanta  $\Phi_0$ . The operation point  $\Phi_b/\Phi_0 \approx 0.54$  for the experiments reported here is marked by vertical lines.

with detuning from the resonance frequency

$$\Delta = \omega - \omega_0. \quad (7.20)$$

For the RF resonator, we get fully equivalently

$$S_{11}^{\text{RF}} = 1 - \frac{2\Gamma_e}{\Gamma_i + \Gamma_e + 2i\Delta_0} \quad (7.21)$$

7

with  $\Delta_0 = \Omega - \Omega_0$ .

### REAL RESPONSE FUNCTION AND FITTING ROUTINE

When analyzing the measured cavity response, we consider a frequency-dependent complex-valued reflection background with amplitude and phase modulations originating from a variety of microwave components in our input and output lines and possible interfering signal paths. Under this assumption, we model the modified cavity response with

$$S_{11} = (\alpha_0 + \alpha_1 \omega) \left( 1 - \frac{2\kappa_e e^{i\theta}}{\kappa_i + \kappa_e + 2i\Delta} \right) e^{i(\beta_1 \omega + \beta_0)} \quad (7.22)$$

where we consider a frequency dependent complex background

$$S_{11} = (\alpha_0 + \alpha_1 \omega) e^{i(\beta_1 \omega + \beta_0)} \quad (7.23)$$

and an additional rotation of the resonance circle with the phase factor  $e^{i\theta}$ .

The first step in the fitting routine removes the cavity resonance part from the data curve and fits the remaining background with Eq. (7.23). After removing the background contribution from the full dataset by complex division, the resonator response is fitted using the ideal response function. In the final step, the full function is re-fitted to the bare data using as starting parameters the individually obtained fit numbers from the

first two steps. From this final fit, we extract the final background fit parameters and remove the background of the full dataset by complex division. Also, we correct for the additional rotation factor  $e^{i\theta}$ . As result we obtain clean resonance curves as shown in Fig. 7.1d.

## COMPLEX FITS AND MODE PARAMETERS AT THE OPERATION POINT

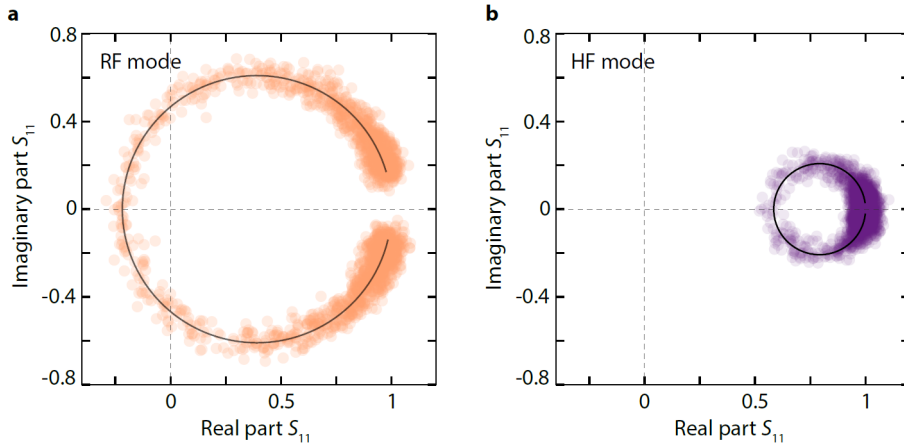


Figure 7.11: **RF and HF complex resonance fits.** In **a** the resonance of the radio-frequency mode is shown, in **b** the resonance of the high-frequency mode. Circles are data, line is a fit. Extracted fit parameters are given in the text.

7

In Supplementary Fig. 7.11 we show the complex reflection signal obtained from the measurements for the RF mode in **a** and the HF mode in **b**. The background has been removed by complex division and the corresponding fit curves are added as lines. From the fits, we extract for the radio-frequency mode data shown in **a** the resonance frequency  $\Omega_0 = 2\pi \cdot 452.5 \text{ MHz}$ , and the linewidths  $\Gamma_i = 2\pi \cdot 10 \text{ kHz}$  and  $\Gamma_e = 2\pi \cdot 16 \text{ kHz}$ . The fit parameters of the high-frequency mode data shown in **b** are  $\omega_0 = 2\pi \cdot 7.207 \text{ GHz}$ ,  $\kappa_i = 2\pi \cdot 310 \text{ kHz}$  and  $\kappa_e = 2\pi \cdot 80 \text{ kHz}$ . The absolute values of these two resonance are shown in Fig. 7.1d.

### 7.7.5. ZERO-POINT FLUCTUATIONS $\Phi_{\text{zpf}}$ AND COUPLING RATE $g_0$

The zero-point current fluctuations of the radio-frequency mode at the operation point are given by

$$I_{\text{zpf}} = \sqrt{\frac{\hbar\Omega_0}{2L_{\text{RF}}}} \approx 28 \text{ nA}, \quad (7.24)$$

where  $\Omega_0 = 2\pi \cdot 452.5 \text{ MHz}$  and  $L_{\text{RF}} = 188 \text{ pH}$ .

In presence of this zero-point current, which flows asymmetrically through the loop

wire arm and the junction arm of the SQUID, the total flux in the SQUID is given by

$$\Phi = \Phi_b + L_{\text{loop}} J - \alpha L_{\text{loop}} \frac{I_{\text{zpf}}}{2} \quad (7.25)$$

where  $\alpha = \frac{2L_a - L_l}{L_{\text{loop}}} \approx 0.3$  describes the inductance asymmetry of the SQUID from the perspective of the RF currents. With the current-phase relation of the JJ, this can also be written as

$$\Phi = \Phi_b + L_{\text{loop}} (1 - \alpha) \frac{I_{\text{zpf}}}{2} - L_{\text{loop}} I_c \sin\left(\pi \frac{\Phi}{\Phi_0}\right). \quad (7.26)$$

Therefore, the zero-point fluctuation current is formally equivalent to a fluctuating external flux with

$$\Phi_{\text{zpf}} = L_{\text{loop}} (1 - \alpha) \frac{I_{\text{zpf}}}{2} \quad (7.27)$$

$$= L_l I_{\text{zpf}} \quad (7.28)$$

$$\approx 635 \mu\Phi_0. \quad (7.29)$$

Using the derivative  $\frac{\partial \omega_0}{\partial \Phi_b}$  of the flux-dependence fit curve  $\omega_0(\Phi_b)$ , we can therefore calculate the single-photon coupling strength

$$g_0 = \frac{\partial \omega_0}{\partial \Phi_b} \Phi_{\text{zpf}}, \quad (7.30)$$

the result is shown in Supplementary Fig. 7.12

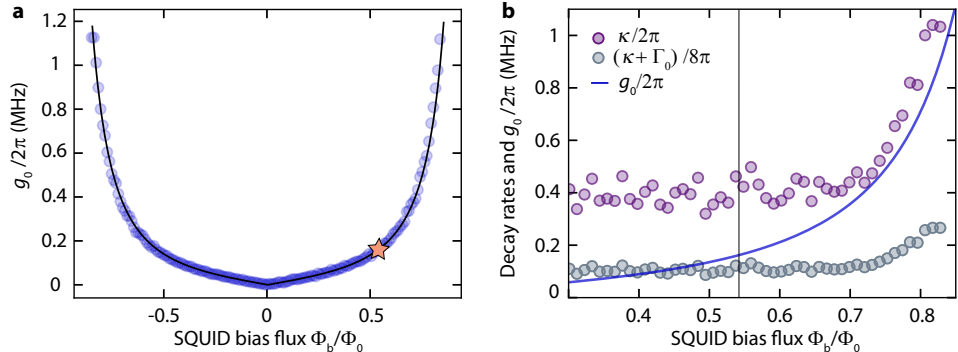


**Figure 7.12: Single photon-coupling rate  $g_0$  and decay rates vs SQUID bias flux.** **a** shows  $g_0$  vs SQUID bias flux. The points are calculated from the experimentally determined flux arch, the line is based on the arch fit, cf. Fig. 7.1. For both, we calculate the derivative and multiply with the theoretical value for  $\Phi_{\text{zpf}} = 635 \mu\Phi_0$ . **b** shows the theoretically estimated  $g_0$ , the extracted cavity decay rate  $\kappa$  and  $(\kappa + \Gamma_0)/4$  versus SQUID bias flux. The last quantity describes the  $g_0$  limit for where a single sideband photon will induce parametric normal mode splitting. The operation point for the experiments reported here  $\Phi_b/\Phi_0 = 0.54$  is marked by a star in **a** and as vertical gray line in **b**.

At the bias point used in the reported experiments, we get  $g_0 \approx 2\pi \cdot 160 \text{ kHz}$ . Around  $\Phi_b/\Phi_0 \sim 0.7$  though we get  $g_0 \sim \kappa$ , cf. also Supplementary Fig. 7.10. Also, for the regime  $\Phi_b/\Phi_0 > 0.5$ , we get  $g_0 \gtrsim \frac{\kappa + \Gamma_0}{4}$ , i.e. the regime where a single red-sideband photon will induce well-resolved, parametric normal-mode splitting [25, 176].

### 7.7.6. PHOTON-PRESSURE SIDEBAND COOLING EQUATIONS OF MOTION

We model the (approximately red-sideband) driven system with the linearized equations of motion for photon-pressure interacting harmonic oscillators [25, 56]

$$\delta\dot{a} = \left(-i\Delta - \frac{\kappa}{2}\right)\delta\hat{a} + ig(\hat{b} + \hat{b}^\dagger) + \sqrt{\kappa_i}\hat{S}_i^{\text{HF}} + i\sqrt{\kappa_e}\hat{S}_e^{\text{HF}} \quad (7.31)$$

$$\dot{\hat{b}} = \left(i\Omega_0 - \frac{\Gamma_0}{2}\right)\hat{b} + ig(\delta\hat{a} + \delta\hat{a}^\dagger) + \sqrt{\Gamma_i}\hat{S}_i^{\text{RF}} + i\sqrt{\Gamma_e}\hat{S}_e^{\text{RF}}. \quad (7.32)$$

Here,  $\delta\hat{a}$  and  $\delta\hat{a}^\dagger$  describe the annihilation and creation operator for HF cavity field fluctuations, respectively,  $\Delta = \omega_p - \omega_0$ ,  $g = \sqrt{n_c}g_0$ , and  $\hat{S}_i^{\text{HF}}$  and  $\hat{S}_e^{\text{HF}}$  corresponds to internal and external HF noise input fields. The RF mode annihilation and creation operators are given by  $\hat{b}$  and  $\hat{b}^\dagger$  and the internal and external RF noise input fields are taken into account by  $\hat{S}_i^{\text{RF}}$  and  $\hat{S}_e^{\text{RF}}$ . The input noise operators  $\hat{S}$  follow  $\langle \hat{S}^\dagger \hat{S} \rangle = n$  and  $\langle \hat{S} \hat{S}^\dagger \rangle = n + 1$ .

These equations can be solved by Fourier transform and the solutions read in frequency space

$$\delta\hat{a}(\Omega) = ig\chi_c \left[ \hat{b}(\Omega) + \hat{b}^\dagger(-\Omega) \right] + \chi_c \left[ \sqrt{\kappa_i}\hat{S}_i^{\text{HF}}(\Omega) + i\sqrt{\kappa_e}\hat{S}_i^{\text{HF}}(\Omega) \right] \quad (7.33)$$

$$\hat{b}(\Omega) = ig\chi_0 \left[ \delta\hat{a}(\Omega) + \delta\hat{a}^\dagger(-\Omega) \right] + \chi_0 \left[ \sqrt{\Gamma_i}\hat{S}_i^{\text{RF}}(\Omega) + i\sqrt{\Gamma_e}\hat{S}_e^{\text{RF}}(\Omega) \right] \quad (7.34)$$

with the susceptibilities

$$\chi_c = \frac{1}{\frac{\kappa}{2} + i(\Delta + \Omega)} \quad (7.35)$$

$$\chi_0 = \frac{1}{\frac{\Gamma_0}{2} + i\Delta_0}, \quad (7.36)$$

$\Omega$  being the frequency relative to the pump tone and  $\Delta_0 = \Omega - \Omega_0$ .

#### SIMPLIFIED EQUATIONS OF MOTION IN THE SIDEBAND-RESOLVED REGIME WITH RED-SIDEBAND PUMPING

Under red-sideband pumping  $\Delta \approx -\Omega_0$  and in the sideband-resolved regime  $\Omega_0 \gg \kappa$  the equations of motion can be simplified as

$$\delta\hat{a}(\Omega) = ig\chi_c \hat{b}(\Omega) + \chi_c \left[ \sqrt{\kappa_i}\hat{S}_i^{\text{HF}}(\Omega) + i\sqrt{\kappa_e}\hat{S}_i^{\text{HF}}(\Omega) \right] \quad (7.37)$$

$$\hat{b}(\Omega) = ig\chi_0 \delta\hat{a}(\Omega) + \chi_0 \left[ \sqrt{\Gamma_i}\hat{S}_i^{\text{RF}}(\Omega) + i\sqrt{\Gamma_e}\hat{S}_e^{\text{RF}}(\Omega) \right] \quad (7.38)$$

#### SOLUTION FOR THE RF MODE RESPONSE FUNCTION

To calculate the response to a radio-frequency probe tone, we replace the noise input by a probe tone input  $\hat{S}_0$  and get

$$\delta\hat{a}(\Omega) = ig\chi_c \hat{b}(\Omega) \quad (7.39)$$

$$\hat{b}(\Omega) = ig\chi_0 \delta\hat{a}(\Omega) + i\chi_0 \sqrt{\Gamma_e} \hat{S}_0(\Omega) \quad (7.40)$$

For the response function and the input-output relations [56] we find from this the result

$$S_{11}^{\text{RF}} = 1 - \Gamma_e \frac{\chi_0}{1 + g^2 \chi_c \chi_0}. \quad (7.41)$$

The resonance condition  $(\chi_0^{\text{eff}})^{-1} = 0$  for effective RF susceptibility

$$\chi_0^{\text{eff}} = \frac{\chi_0}{1 + g^2 \chi_c \chi_0} \quad (7.42)$$

delivers the complex solutions

$$\tilde{\Omega}_{\pm} = \Omega_0 - \frac{\delta}{2} + i \frac{\kappa + \Gamma_0}{4} \pm \sqrt{g^2 - \left( \frac{\kappa - \Gamma_0 + 2i\delta}{4} \right)^2} \quad (7.43)$$

where  $\delta$  is the pump detuning from the red sideband defined by  $\Delta = -\Omega_0 + \delta$ .

### SOLUTION FOR THE HF MODE RESPONSE FUNCTION

In full analogy to the RF mode, we get as probe tone response function for the HF mode

$$S_{11}^{\text{HF}} = 1 - \kappa_e \frac{\chi_c}{1 + g^2 \chi_c \chi_0}. \quad (7.44)$$

with the complex solutions

$$\tilde{\omega}_{\pm} = \omega_0 + \frac{\delta}{2} + i \frac{\kappa + \Gamma_0}{4} \pm \sqrt{g^2 - \left( \frac{\kappa - \Gamma_0 + 2i\delta}{4} \right)^2} \quad (7.45)$$

7

### SOLUTION FOR THE HF MODE THERMAL NOISE POWER SPECTRAL DENSITY

We solve Eqs. (7.37), (7.38) with noise input now and get

$$\delta \hat{a} = \frac{i g \chi_c \chi_0 [\sqrt{\Gamma_i} \hat{S}_i^{\text{RF}} + i \sqrt{\Gamma_e} \hat{S}_e^{\text{RF}}] + \chi_c [\sqrt{\kappa_i} \hat{S}_i^{\text{HF}} + i \sqrt{\kappa_e} \hat{S}_e^{\text{HF}}]}{1 + g^2 \chi_c \chi_0}. \quad (7.46)$$

which leads to the symmetrized output field power spectral density in units of photons [163]

$$\frac{S(\omega)}{\hbar \omega} = \frac{1}{2} + n_e^{\text{HF}} + \kappa_e \kappa_i \frac{|\chi_c(\omega)|^2}{|1 + g^2 \chi_0(\Omega) \chi_c(\omega)|^2} (n_i^{\text{HF}} - n_e^{\text{HF}}) + \kappa_e \Gamma_0 \frac{g^2 |\chi_c(\omega)|^2 |\chi_0(\Omega)|^2}{|1 + g^2 \chi_0(\Omega) \chi_c(\omega)|^2} (n_{\text{th}}^{\text{RF}} - n_e^{\text{HF}}) \quad (7.47)$$

where the effective thermal photon occupation of the RF mode is given by the weighted sum

$$n_{\text{th}}^{\text{RF}} = \frac{\Gamma_i}{\Gamma_0} n_i^{\text{RF}} + \frac{\Gamma_e}{\Gamma_0} n_e^{\text{RF}}. \quad (7.48)$$

For the high-frequency mode, we assume equilibration of the feedline and the circuit to the fridge temperature  $T_f$ , such that

$$n_{\text{th}}^{\text{HF}} = n_e^{\text{HF}} = n_i^{\text{HF}} = \frac{1}{e^{\frac{\hbar \omega_0}{k_B T_f}} - 1}. \quad (7.49)$$

which simplifies the PSD to

$$\frac{S(\omega)}{\hbar\omega} = \frac{1}{2} + n_{\text{th}}^{\text{HF}} + \kappa_e \Gamma_0 \frac{g^2 |\chi_c(\omega)|^2 |\chi_0(\Omega)|^2}{|1 + g^2 \chi_0(\Omega) \chi_c(\omega)|^2} (n_{\text{th}}^{\text{RF}} - n_{\text{th}}^{\text{HF}}) \quad (7.50)$$

For the RF mode, we will have to consider different effective temperatures of feedline bath and the internal bath.

### ADDED NOISE

The effective number of added noise photons by the amplifier chain is given by [25]

$$n'_{\text{add}} = \frac{n_{\text{add}}}{\eta} + \left( \frac{1-\eta}{\eta} \right) \frac{1}{2} \quad (7.51)$$

where  $n_{\text{add}}$  is the actual number of photons added by the HEMT amplifier noise in our case, and  $\eta \sim 0.5$  accounts for losses of the cavity output field on its way to the HEMT. We will estimate the number of added noise photons based on a temperature sweep calibration presented below. As a rough first estimate, we can use the datasheet noise temperature of the amplifier of  $\sim 2\text{ K}$  to find  $n_{\text{add}} \approx 5.3$  and  $n'_{\text{add}} \approx 11.1$ .

### THE TOTAL POWER SPECTRAL DENSITY

For the power spectral density in units of photons at frequency  $\omega = \omega_p + \Omega$  of the SQUID cavity with a drive around the red sideband, we get for  $n'_{\text{add}}, n_{\text{th}}^{\text{RF}} \gg n_{\text{th}}^{\text{HF}}$

$$\frac{S(\omega)}{\hbar\omega} = \frac{1}{2} + n'_{\text{add}} + \kappa_e \Gamma_0 \frac{g^2 |\chi_c(\omega)|^2 |\chi_0(\Omega)|^2}{|1 + g^2 \chi_0(\Omega) \chi_c(\omega)|^2} n_{\text{th}}^{\text{RF}} \quad (7.52)$$

This can be also written as

$$\frac{S(\omega)}{\hbar\omega} = \frac{1}{2} + n'_{\text{add}} + \frac{16 \kappa_e g^2 \Gamma_0 n_{\text{th}}^{\text{RF}}}{|4g^2 + [\kappa + 2i(\delta + \Delta_0)] [\Gamma_0 + 2i\Delta_0]|^2} \quad (7.53)$$

where  $\Delta_0 = \Omega - \Omega_0$  takes into account the detuning from the RF resonance frequency and  $\delta = \omega_0 - \Omega_0 - \omega_p$  takes into account the detuning of the pump from the red sideband of the cavity. By fitting the measured power spectral density with Eq. (7.53), as shown as fit curves in Fig. 7.3c, we obtain for each curve the thermal photon number occupancy of the RF mode as detailed below.

### COOLED RF PHOTONS

For the RF mode we get from the equations of motion

$$\hat{b} = \frac{i g \chi_c \chi_0 [\sqrt{\kappa_i} \hat{S}_i^{\text{HF}} + i \sqrt{\kappa_e} \hat{S}_e^{\text{HF}}] + \chi_0 [\sqrt{\Gamma_i} \hat{S}_i^{\text{RF}} + i \sqrt{\Gamma_e} \hat{S}_e^{\text{RF}}]}{1 + g^2 \chi_c \chi_0}. \quad (7.54)$$

We can use this to calculate the RF photon population with a sideband drive exactly on the red sideband and get

$$n_{\text{cool}}^{\text{RF}} = \frac{\Gamma_0}{\kappa + \Gamma_0} \frac{4g^2 + \kappa(\kappa + \Gamma_0)}{4g^2 + \kappa\Gamma_0} n_{\text{th}}^{\text{RF}} + \frac{\kappa}{\kappa + \Gamma_0} \frac{4g^2}{4g^2 + \kappa\Gamma_0} n_{\text{th}}^{\text{HF}}. \quad (7.55)$$

Compared to the usually quoted result [25, 56, 58], we find some corrections in the cooled RF occupation, in particular the appearance of the factor  $\kappa + \Gamma_0$  instead of  $\kappa$ . These corrections are negligible for  $\kappa \gg \Gamma_0$ , which in our case, however is not strictly true anymore.

For non-vanishing detuning we get

$$n_{\text{cool}}^{\text{RF}} = \frac{\Gamma_0}{\kappa + \Gamma_0} \frac{4g^2 + \kappa(\kappa + \Gamma_0) \left[ 1 + \frac{4\delta^2}{(\kappa + \Gamma_0)^2} \right]}{4g^2 + \kappa\Gamma_0 \left[ 1 + \frac{4\delta^2}{(\kappa + \Gamma_0)^2} \right]} n_{\text{th}}^{\text{RF}} + \frac{\kappa}{\kappa + \Gamma_0} \frac{4g^2}{4g^2 + \kappa\Gamma_0 \left[ 1 + \frac{4\delta^2}{(\kappa + \Gamma_0)^2} \right]} n_{\text{th}}^{\text{HF}}. \quad (7.56)$$

### 7.7.7. TEMPERATURE CALIBRATION

To perform a calibration of the RF resonator thermal occupation, we vary the fridge temperature  $T_f$  in steps of 20 mK and take a series of measurements for each  $T_f$ . During this procedure, we keep the flux bias constant at  $\Phi_b/\Phi_0 = 0.54$ . First, we take bare response measurements of the two modes  $S_{11}^{\text{RF}}$  and  $S_{11}^{\text{HF}}$ . From the response curves, we extract the resonance frequencies  $\omega_0$  and  $\Omega_0$  as well as the linewidths  $\kappa$ ,  $\kappa_e$  and  $\Gamma_i$ ,  $\Gamma_e$  by fitting the responses using Eq. (7.19). The linewidths are shown in Supplementary Fig. 7.13.

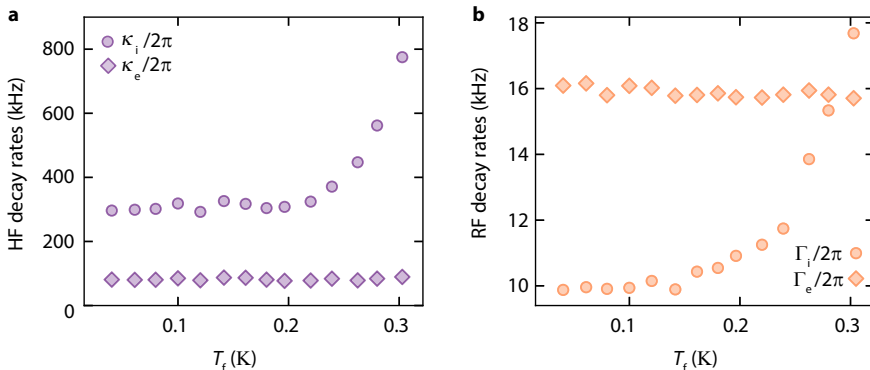


Figure 7.13: **Linewidths vs temperature.** Decay rates of the microwave mode  $\kappa$ ,  $\kappa_e$  in panel a and of the radio-frequency mode  $\Gamma_i$  and  $\Gamma_e$  in panel b depending on fridge temperature  $T_f$ .

Afterwards, we set a pump tone of constant power to the red sideband of the HF cavity and detect both, the photon-pressure induced transparency (PPIT) in a reflection measurement of the HF cavity and the upconverted RF thermal noise power spectrum. We adjust the pump power for each temperature to keep the cooperativity  $\mathcal{C} \leq 1$  in order to avoid being too close to the normal-mode splitting regime but still obtain a good signal. From the PPIT data, we determine the actual cooperativity. Using the resonance frequencies and the linewidths, we determine the thermal photon occupation number in the RF mode relative to the added noise photons from the detected thermal noise curve for each temperature as described in section 7.7.6.

We repeat the output noise detection for two distinct experimental conditions which

correspond to two different RF mode temperatures. The feedline of the RF circuit is connected to a cryogenic radio-frequency amplifier and as we do not have a radio-frequency isolator or circulator, the noise emitted by this amplifier will reach the RF input with only small attenuation. Hence, we can increase or decrease the RF input noise by switching this amplifier on or off, respectively, cf. Supplementary Fig 7.14b. From matching the slope of the "cold" RF mode temperature-dependent occupation in its linear regime to the Bose factor, we obtain an estimate for the number of added photons in the HF output line of  $n'_{\text{add}} \approx 11 \pm 2$ . This is in very good agreement with an estimate of the added photons assuming an HF HEMT noise temperature of  $\sim 2\text{ K}$  (datasheet) and 3 dB attenuation between sample and amplifier.

The result we obtain with this procedure for the RF mode occupation in both RF amplifier configurations is shown in Fig. 7.14c. For the RF amplifier switched off, we obtain a residual occupation of  $\sim 6.5 \pm 1.5$  photons at the fridge base temperature, which stays nearly constant until the fridge reaches about 150 mK. Then, the occupation starts to increase and approaches the Bose occupation shown as black line. For the configuration with the amplifier switched on the residual occupation is about a factor of three larger due to the noise coming along the input/output line from the amplifier and coupling into the circuit. Still, an increase of the total occupation with increasing fridge temperature is visible, which can be attributed to an increase of the internal RF mode bath temperature.

To model the thermal occupation, we use

$$n_{\text{th}}^{\text{RF}} = \frac{\Gamma_i}{\Gamma_0} n_i^{\text{RF}} + \frac{\Gamma_e}{\Gamma_0} n_e^{\text{RF}} \quad (7.57)$$

where the internal and external occupations are given by

$$n_{i/e}^{\text{RF}} = \left( e^{\frac{\hbar\omega_0}{k_B T_{i/e}}} - 1 \right)^{-1}. \quad (7.58)$$

For the effective internal and external temperatures  $T_i$  and  $T_e$ , respectively, we take into account possible deviations from the fridge temperature by a residual temperature  $T_{r,i/e}$ , which e.g. considers the RF amplifier noise arriving at the sample RF input. To phenomenologically model a gradual adjustment of the effective internal bath temperature to the fridge temperature, we use  $T_i = \sqrt{T_f^2 + T_{r,i}^2}$ . In addition, we fit the temperature dependence of  $\Gamma_i$  and take it into account in the calculation of  $n_{\text{th}}^{\text{RF}}$ . For the case of RF amplifier off, we observe an increased RF mode linewidth  $\Gamma_0 \approx 2\pi \cdot 40\text{ kHz}$ , which we attribute to two-level systems being saturated with the amplifier on. With all these factors considered, we obtain the lines shown in Fig. 7.14c from the modelling, giving good qualitative agreement with the data. The parameter set for both curves is identical, except for the residual temperature of the external bath  $T_{r,e}$ , which is modified by the amplifier power state, and for  $\Gamma_0$ , which differs between the amplifier ON and OFF states. The parameters are  $T_{r,i} = 80\text{ mK}$ ,  $\Gamma_e = 2\pi \cdot 16\text{ kHz}$ ,  $\Gamma_i^{\text{on}} = 2\pi \cdot 10\text{ kHz}$ ,  $\Gamma_i^{\text{off}} = 2\pi \cdot 24\text{ kHz}$  and the residual external temperatures  $T_{r,e}^{\text{on}} = 850\text{ mK}$  and  $T_{r,e}^{\text{off}} = 130\text{ mK}$ .

### 7.7.8. COOLING THE RF MODE WITH INCREASED THERMAL OCCUPANCY

We repeat the cooling experiment discussed in Fig. 7.3 also for the RF amplifier switched on, leaving the RF mode occupied with about 20.5 thermal photons at fridge base temperature. The resulting spectra of the sideband-cooling in this state are shown in Supplementary Fig. 7.14 and besides a larger amplitude due to the increased occupancy look nearly identical to the spectra shown in Fig. 7.3. The corresponding cooled RF photons are plotted in e together with the data for the amplifier switched off.

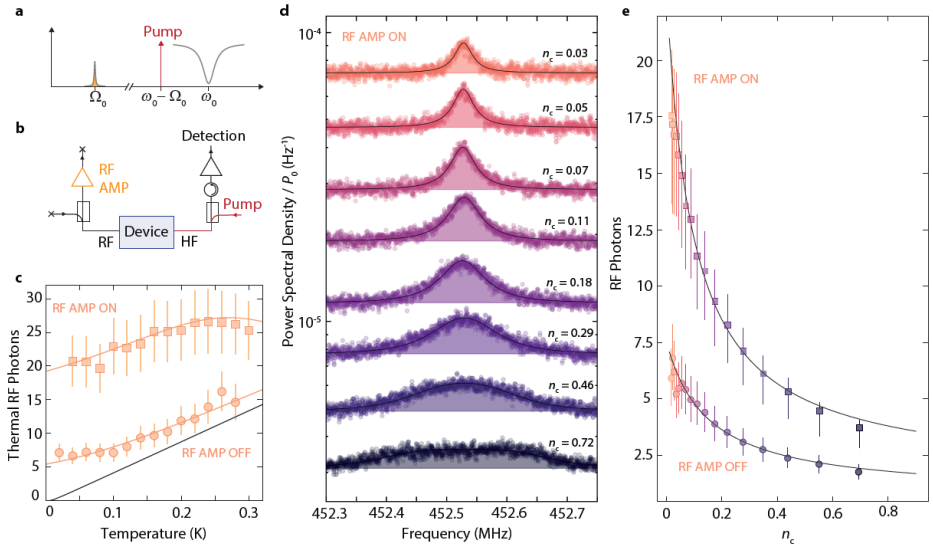


**Figure 7.14: Photon-pressure sideband-cooling of a hot and a hotter RF resonator.** **a** For the observation of upconverted thermal noise of the RF resonator, a pump tone is set to the red sideband of the high-frequency mode  $\omega_p = \omega_0 - \Omega_0$  and the cavity output field around  $\omega = \omega_0$  is detected with a signal analyzer. The RF input/output side of the device is connected to a cryogenic radio-frequency amplifier, which is used for the reflection characterization of the RF mode, cf. panel **b**. The state of this RF amplifier can be used to control the thermal occupation of the RF mode. When it is switched ON, its output noise increases the thermal occupation of the RF mode as shown in panel **c**, where the thermal photon number vs fridge temperature is plotted for both cases, RF amplifier switched ON and RF amplifier switched OFF. Symbols are data, black line is the Bose factor, orange lines are models for the thermal occupation and discussed in the text. From the thermal calibration, we determine the thermal occupation of the RF mode at fridge base temperature to be  $n_{\text{RF}}^{\text{ON}} \sim 20.5$  and  $n_{\text{RF}}^{\text{OFF}} \sim 7$ . **d** shows the measured high-frequency output power spectral density for increasing red-sideband pump power, normalized to the on-chip pump power  $P_0$  for RF amplifier ON. Frequency axis is given with respect to the constant pump frequency. Circles are data, lines and shaded areas are fits. With increasing pump strength, i.e., increasing intracavity photon number  $n_c$ , the RF resonance gets broadened by photon-pressure damping, and its total thermal noise power gets reduced, which corresponds to cooling of the mode. In **e**, the thermal RF mode occupation is shown as symbols vs pump photon number  $n_c$  for both cases, RF amplifier ON (squares) and RF amplifier OFF (circles). Error bars for the amplifier ON (OFF) data correspond to uncertainties of  $\pm 2$  HF photons of added noise in the detection chain and  $\pm 1$  kHz ( $\pm 2$  kHz) in bare RF linewidth  $\Gamma_0^{\text{ON}} = 26$  kHz ( $\Gamma_0^{\text{OFF}} = 40$  kHz).

### 7.7.9. THEORY OF NORMAL-MODE THERMOMETRY

#### THE HIGH-FREQUENCY RESPONSE FUNCTION WITH NORMAL MODE SUSCEPTIBILITIES

From the equations of motion, we obtained the response of the system around the HF mode as

$$S_{11}^{\text{HF}} = 1 - \kappa_e \frac{\chi_c}{1 + g^2 \chi_c \chi_0} \quad (7.59)$$

under the assumption of pumping around the red sideband and the sideband-resolved regime. The resonance condition  $(\chi_c^{\text{eff}})^{-1} = 0$  for the effective HF cavity susceptibility

$$\chi_c^{\text{eff}} = \frac{\chi_c}{1 + g^2 \chi_c \chi_0} \quad (7.60)$$

provided us with the complex solutions of the effective susceptibility

$$\tilde{\omega}_{\pm} = \omega_0 + \frac{\delta}{2} + i \frac{\kappa + \Gamma_0}{4} \pm \sqrt{g^2 - \left( \frac{\kappa - \Gamma_0 + 2i\delta}{4} \right)^2} \quad (7.61)$$

where  $\delta$  is the pump detuning from the red HF cavity sideband.

Now, we define the normal mode susceptibilities

$$\chi_+ = \frac{1}{\frac{\kappa_+}{2} + i\Delta_+}, \quad \chi_- = \frac{1}{\frac{\kappa_-}{2} + i\Delta_-} \quad (7.62)$$

where  $\Delta_{\pm} = \omega - \omega_{\pm}$  and

$$\omega_{\pm} = \text{Re}[\tilde{\omega}_{\pm}], \quad \kappa_{\pm} = \text{Im}[\tilde{\omega}_{\pm}] \quad (7.63)$$

are the real and imaginary parts, respectively, of the complex solutions.

With these, we can rewrite the HF response function as

$$S_{11}^{\text{HF}} = 1 - \kappa_{e,+} \chi_+ - \kappa_{e,-} \chi_- \quad (7.64)$$

which is exact with the (complex and frequency-dependent) external linewidths

$$\kappa_{e,\pm} = \mp \frac{i\kappa_e}{2\chi_0 \sqrt{g^2 - \left( \frac{\kappa - \Gamma_0 + 2i\delta}{4} \right)^2}}. \quad (7.65)$$

For the regime of considerable coupling  $g \gg \kappa/2, \Gamma_0/2$  and possibly large detunings  $\Delta \lesssim g$ , we approximate this by

$$\kappa_{e,\pm} \approx \frac{\kappa_e}{2} \left( 1 \pm \frac{\delta}{\sqrt{\delta^2 + 4g^2}} \right). \quad (7.66)$$

## NORMAL-MODE THERMOMETRY

Using the approximated normal-mode representation of the HF cavity in the strong-coupling regime, we get for the output field power spectral density in units of quanta

$$\frac{S_{\text{nms}}}{\hbar\omega} = \frac{1}{2} + n'_{\text{add}} + 4 \frac{\kappa_{e,+}\kappa_{i,+}}{\kappa_+^2 + 4\Delta_+^2} (n_{i,+} - n_{e,+}) + 4 \frac{\kappa_{e,-}\kappa_{i,-}}{\kappa_-^2 + 4\Delta_-^2} (n_{i,-} - n_{e,-}) \quad (7.67)$$

where  $\kappa_{i,\pm} = \kappa_\pm - \kappa_{e,\pm}$  and  $n_{e,+}, n_{e,-}$  and  $n_{i,+}, n_{i,-}$  are the effective external and internal bath occupations of the normal modes, respectively. If the external baths are given again by the fridge temperature, we get  $n_{e,\pm} \ll n_{i,\pm} \approx \frac{\kappa_\pm}{\kappa_{i,\pm}} n_\pm$ . From the condition  $S_{\text{nms}} = S$ , we can then follow

$$\kappa_{e,+} n_+ + \kappa_{e,-} n_- = \kappa_e n_{\text{cool}}^{\text{HF}} \quad (7.68)$$

where  $n_{\text{cool}}^{\text{HF}}$  is the thermal occupation (imbalance) of the HF mode while cooling the RF mode with a red sideband tone. As  $n_{\text{cool}}^{\text{HF}} \gg n_e^{\text{HF}}$ , the imbalance occupation corresponds in good approximation to the total occupation.

So this way we can calculate the effective HF cavity occupation which is given by

$$n_{\text{cool}}^{\text{HF}} = \frac{\kappa}{\kappa + \Gamma_0} \frac{4g^2 + \Gamma_0(\kappa + \Gamma_0) \left[ 1 + \frac{4\delta^2}{(\kappa + \Gamma_0)^2} \right]}{4g^2 + \kappa\Gamma_0 \left[ 1 + \frac{4\delta^2}{(\kappa + \Gamma_0)^2} \right]} n_{\text{th}}^{\text{HF}} + \frac{\Gamma_0}{\kappa + \Gamma_0} \frac{4g^2}{4g^2 + \kappa\Gamma_0 \left[ 1 + \frac{4\delta^2}{(\kappa + \Gamma_0)^2} \right]} n_{\text{th}}^{\text{RF}}. \quad (7.69)$$

when red-sideband driving.

The total number of noise photons in the hybridized mode regime is then given by

$$n_{\text{tot}} = n_{\text{cool}}^{\text{HF}} + n_{\text{cool}}^{\text{RF}}. \quad (7.70)$$

### 7.7.10. SYSTEM PARAMETERS FOR NORMAL-MODE THERMOMETRY

For the analysis of the normal-mode thermal spectra, it is essential to know the individual mode parameters, which we obtain from a characterization of the HF reflection response in the strong-coupling regime. Supplementary Fig. 7.15a shows  $S_{11}^{\text{HF}}$  for approximately  $n_c = 100$  pump intracavity photons. This data was measured simultaneously with the power spectral densities (PSD) shown in Fig. 7.4, but during the measurement of the PSDs the network analyzer was switched off. Both datasets were acquired while iteratively sweeping a pump tone through the red sideband with  $\omega_p = \omega_0 - \Omega_0 + \delta$ . As the pump tone approaches exactly the red sideband frequency, we observe photon-pressure induced hybridization between the modes with a resonant splitting of  $g/\pi \sim 2.1$  MHz, about one order of magnitude larger than the normal-mode linewidths  $(\kappa + \Gamma_0)/2 = 2\pi \cdot 200$  kHz and a factor of three larger than the RF thermal decoherence rate  $\Gamma_0 n_{\text{th}}^{\text{RF}} \approx 2\pi \cdot 300$  kHz.

For an analysis of the normal modes, we denote the lower-frequency mode with the superscript  $-$  and the higher-frequency mode with  $+$ , i.e., the resonance frequencies are identified as  $\omega_-$  and  $\omega_+$  and the total and external linewidths as  $\kappa_-$ ,  $\kappa_+$  and  $\kappa_{e,-}$ ,  $\kappa_{e,+}$ , respectively. The theoretical description of these parameters was given in section 7.7.9. To determine these parameters from the experimental data, each linescan of Supplementary Fig. 7.15a was split into two parts, each of them containing one of the two resonances. This splitting is shown in b by using two different colors, orange for the range

of  $\omega_-$  and purple for the range of  $\omega_+$ . Both sub-responses were fitted individually using Eq. (7.19).

The returned fit parameters  $\omega_{\pm}$ ,  $\kappa_{\pm}$  and  $\kappa_{e\pm}$  are plotted in Supplementary Figs. 7.15c, d, and e, respectively. The theoretical dependences as derived in section 7.7.9 are plotted as lines and show excellent agreement with the data. When the two modes are completely hybridized ( $\delta = 0$ ), we find for both a total decay rate  $\kappa_+ = \kappa_- = 2\pi \cdot 200$  kHz, which is what we expect from the theoretical expression for this case  $\kappa_{\pm} = (\kappa + \Gamma_0)/2$ . Also the external decay rates, usually defined by the coupling capacitance to the feedline, are half the value of the bare HF mode  $\kappa_{e,+} = \kappa_{e,-} = 2\pi \cdot 40$  kHz.

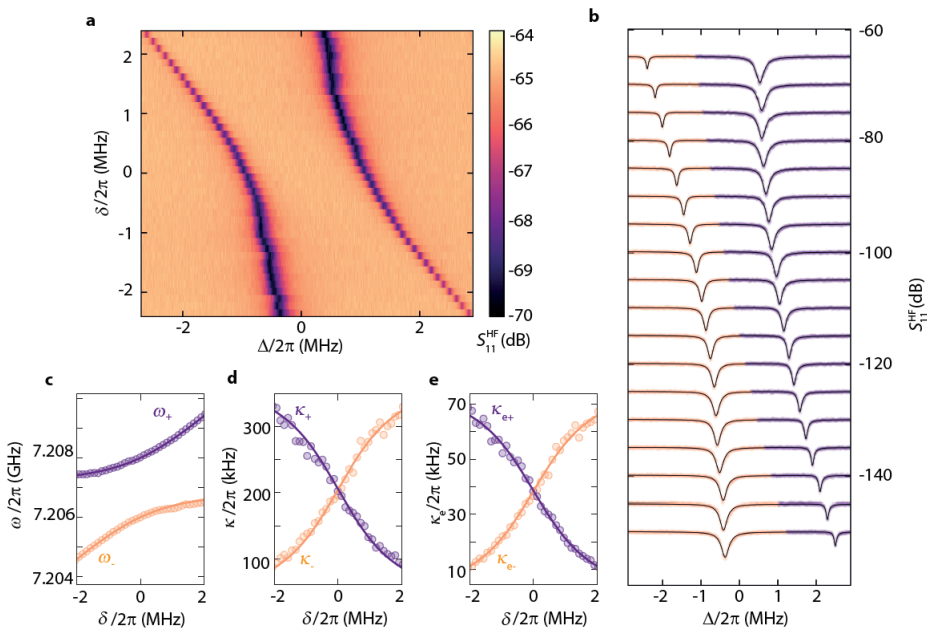


Figure 7.15: **HF response in the strong-coupling regime and normal-mode fit parameters.** **a** Color-coded HF reflection response in the strong-coupling regime. The pump tone is swept through the HF mode red sideband with  $\omega_p = \omega_0 - \Omega_0 + \delta$ . The response frequency is given relative to the bare HF cavity mode  $\Delta = \omega - \omega_0$ . **b** Linecuts of **a**, showing the individually fitted parts of the response as orange and purple. The top curve is plotted as measured (unshifted), subsequent curves are manually downshifted by  $-5$  dB each for clarity. Shown is every second linescan of **a**. Fit curves are plotted as black lines. From the fit curves shown in **b**, we get the three relevant normal-mode parameters resonance frequency  $\omega_{\pm}$ , total decay rate  $\kappa_{\pm}$  and external decay rate  $\kappa_{e,\pm}$ , plotted in **c**, **d**, and **e**, respectively.



# 8

## CONCLUSION

The work presented in this thesis consisted on developing and exploring two major platforms, *flux-mediated optomechanical systems* and *photon-pressure coupled systems*. In short, some of the main results of the work presented here are: the first experimental realization of flux-mediated microwave optomechanics (**chapter 4**), the implementation of a blue-detuned four-wave cooling technique in flux-mediated optomechanical systems (**chapter 5**), bringing a photon-pressure system into the strong-coupling regime (**chapter 6**) and ground-state cooling of a hot RF circuit via a photon-pressure interaction (**chapter 7**).

The accomplishment of these results required numerous iterations of design, fabrication and testing of different devices. The fact that both of these systems relied on a Superconducting Quantum Interference Cavity to act as a confinement of microwave light fields made the task of simultaneously developing these two distinct platforms considerably simpler. Nevertheless, the base of all the work presented in this thesis, which relied on the successful development of nano-bridge SQUID cavities, was also the most risky and the one which took the longest to complete.

As described in Chapter 3, the process of successfully fabricating nano-bridge Josephson junctions was extensive and required many iterations until a working nanofabrication process was found. Nonetheless, the high reproducibility and robustness of these junctions allowed us to easily include them in the subsequent device recipes and incorporate them in both platforms. Furthermore, once the fabrication steps were determined we could fabricate 2D SQUID cavities within a few hours and 3D SQUID cavities in one working day. This gave us the possibility to do fast iterations and optimization of optomechanical and photon-pressure systems until the desired system parameters were reached, leading to the results presented in chapters 4, 5, 6 and 7.

Even though *flux-mediated optomechanical systems* and *photon-pressure coupled systems* have numerous resemblances when it comes to their operation principle, they possess incredibly distinct applications and both have great potential for advancing different branches of the fields of microwave optomechanics and superconducting quantum

technologies. Therefore, let us now focus on each platform individually and discuss their applicability in more detail.

- ***Flux-mediated Optomechanical Systems:*** As theoretically discussed by the first proposals for this coupling approach, the current state of art has proven that these systems can indeed achieve single-photon coupling strengths orders of magnitude higher than capacitive optomechanical systems [71, 72, 162]. This platform is therefore extremely promising for reaching the so pursued single-photon strong coupling regime [63]. Achieving this milestone would unlock the door for the generation of non-classical states in mechanical oscillators [63–66] and possibly for the realization of a new type of superconducting qubits [67], where the non-linearity would arise from the coupling to the mechanical element. Since mechanical oscillators have considerably longer lifetimes compared to any superconducting qubit, the use of mechanical quantum states would be of extreme interest for the scientific community and would represent major advances in quantum information and sensing technologies. Furthermore, the generation of non-classical states would ultimately allow for testing quantum collapse and quantum gravity models by preparing Fock and Schröedinger cat states of massive mechanical oscillators [141, 142].

In addition to the utilization of SQUID cavities as linear systems, the results presented in chapter 5 show the exciting possibilities of incorporating non-linear SQUID cavities in microwave optomechanical systems. Chapter 5 has shown that the regime where a parametrically driven weakly-anharmonic cavity is coupled to mechanical resonator allows for new cooling schemes and new ways of controlling mechanical motion.

From a technological point-of-view, the fact that the rate at which a single-photon converts to a single-phonon can be tuned in-situ by increasing the in-plane magnetic field<sup>1</sup> opens up an opportunity to maximize the optomechanical coupling while minimizing the flux-noise coupled to the system. However, while Aluminum SQUID cavities have been a very fruitful resource for exploring these systems, the maximum coupling strengths one can achieve by increasing the in-plane field will always be limited by the critical field of the material. Since for aluminum films this is typically around 100 mT [105], switching to Niobium films would push these limits as their critical field is in the Tesla regime [153]. Furthermore, if one is purely interested on building a system which maximizes the single-photon coupling rate, reducing the screening parameter  $\beta_L$  and therefore boosting the flux responsivity of the cavity would be a crucial optimization point.

- ***Photon-pressure Systems:*** Adding an analogous of the radiation-pressure interaction to the field of superconducting circuits opens up endless possibilities for both the field of optomechanics and for the field of circuit quantum electrodynamics (cQED). On one hand, since photon-pressure coupled systems exhibit a large flexibility in engineering resonance frequencies and quality factors, they have the

---

<sup>1</sup>The field applied parallel to the SQUID loop, in a configuration where the cavity is coupled to the out-of-plane motion of the beam.

potential for the exploration of many unusual parameter regimes and quantum operations which are usually not accessible in optomechanical systems. On the other hand, having this coupling at reach when engineering superconducting devices would offer rich possibilities for quantum-limited sensing and quantum signal processing, such as quantum-limited parametric amplification [26, 82, 84–86], nonreciprocal photon transport [87–90], slow light [183, 184] and photonic reservoir engineering [91, 92]. As shown in Chapter 7, by using a sideband cooling technique, this photon-pressure coupling was brought to the quantum regime for the first time, making a first step towards radio-frequency quantum photonics. In addition, photon-pressure coupled circuits are also discussed as a promising platform for the realization of fault-tolerant quantum computing using bosonic codes [93].

Photon-pressure systems are an incredibly flexible platform which still remains highly unexplored. This definitely stimulates one's creativity for planning new experiments without imposing additional technological barriers. For this reason, the field of quantum technologies and microwave optomechanics will surely benefit from such platform.



## ACKNOWLEDGEMENTS

*Who would I be today if the people around me had been different?* That was the question that crossed my head once I started writing this chapter and to be honest, I let the question depart without an answer... It was absolutely impossible for me to imagine the last four years without the people with whom I shared this journey. Even though I also realized that it would be a very challenging task to narrow my acknowledgments down to a couple of pages, there were a few people that I could never forget to thank. They continuously shaped me as scientist and as person, and they often taught me lessons which I'm certain I will never forget.

**Gary**, being part of your group has been an amazing experience. The reason why I decided to do research was because I wanted to dive into challenging projects and be surrounded by inspiring people, and that was exactly what happened during my time here. The way you manage your group is truly fantastic. There were times when Steele Lab got really large, but even then you took the time to meet with everyone individually every week and keep on being up to date with their projects. I believe that your focus on the well-being of the people in your group is one of main reasons for the success of the lab. People often feel motivated and inspired, and you have a big part in that. Anyone that has attended your lectures or talks knows that your excitement about physics can be highly contagious. Seeing you so enthusiastically present the things we do, was for me always a very rewarding feeling and a total motivation booster. In short, thank you for introducing me to the world of research and give me the chance to experience what doing exciting science feels like.

**Daniel...** Ow boy! Where should I start? You have been there since day one. You felt every joy and every disappointment along with me... We have reached all these amazing results together and I could never imagine having done any of it without you by my side. There were times when I felt that we had entered a roller coaster and there was no way out, but soon we learned how to deal with the bounces and eventually we mastered it all. Because as we always say: *There are no peaks without dips!* The endless days, evenings and weekends sitting on the floor of the lab looking at the spectrum analyzer, the "parties" in the clearroom, our synchronized "development" techniques, the moment when we opened a bottle of champomy after measuring our first OMIT, or the moment when we published our first paper together are just a few of the times which will always be engraved on my memory. You are the person who most shaped me into the researcher that

I am today. I have learned so much with you. Your creativity, thoroughness and curiosity often led us on the right path, and your open mindset truly helped overcome many of my fears, personally and professionally. The dedication you put in everything you do is admirable and sometimes it feels that you have a good explanation for all things. You are a great scientist, and science is incredibly lucky to have you. I deeply hope that our journey as "optomechanical power couple" does not end here, and I look forward to continue rocking science with you in the future.

**Mark**, until today that every time I enter the lab, I keep thinking that I should organize the screwdrivers, even though you are not there to panic about them being out of place. You had a huge impact on how well Steele Lab functioned, and I am certain that many people in the group felt as lucky as me for having you around. I will always remember the afternoons at the Beestenmarkt, the fun times with tweezers technology and the awesome Beat Saber VR sessions. I wish you all the best for the future and I hope to see you again soon.

**Martijn** for some reason you have always surprised me... Either with your perspective on topics that I had never even thought about, with your most various interests, with your advices on difficult matters, with the amount of amazing places you had already seen in your life, or even for also sticking to canned tuna in times of laziness. Thank you for your friendship and for all the good moments we had together. I will never forget our times in Delft, or our adventures in LA. And I am sure that the Moeke is still waiting for us to return.

**Mario**, sharing the office with you during the last four years has been an absolute pleasure. I am pretty sure that in a few years I will still recognize the sound of your shoes coming down the hall. They will always make me laugh. Thank you for all the good moments we spent together and most of all, thank you for your friendship. I hope England treats you well and even though I know you won't need it, I wish you good luck for the future. I am certain that you have great things awaiting.

**Marios**, you joined Steele Lab a bit later than me. However, back then you already had a much more realistic idea of what research was than I did. What you told me a few years ago at the office became an inspiration for one of my propositions: "Understanding should be the primary goal of a PhD student." I am not sure if you were ever aware of this, but your words helped me countless times. They helped me realize that everyone has to start somewhere and that learning is the most important part of the way. Thanks for that! I hope Luxembourg is welcoming you and your family with open arms.

**Felix**, even though we did not spend much time together during my first years, I am grateful that I had the chance to collaborate with you before you left the group. Working with you was a very pleasant experience and your ability to step in once Mark left the group was very much appreciated by all of us. You cannot imagine how many times I wished that everybody was as organized and structured as you. You have a great talent there! You are now on a different path and I wish that this one brings many moments of

joy into your life. And I still hope to see you, Katherine and Felicitas sometime in Swabia.

**Jasper**, I first met you as a master student and I have seen you grow into the world of HBARs. Thank you for all the nice talks about the struggles of being a PhD student and for making sure that chaos doesn't take over our labs. I wish you all the best for the future, scientifically and personally. You have big adventures ahead.

Thank you **Yildiz** for bringing so much positivity into the lab. Being a bridge between two research groups is definitely not an easy task, but I think that during your PhD you have learned how to master the art. It was a pleasure to be your "labmate" during those few months right before covid hit the world. Your attentiveness and good advices during that time were really important for me. I hope that life brings you everything you are looking for.

**Jacob**, you joined the lab not a long time ago but it's amazing to see how good you have adjusted to the group and how many good things you already have under your wing! Working with you in the squeezing project has been a delightful experience. Your ability to catch up with the most various topics is impressive, and even though you came from a highly anharmonic field, photon-pressure systems could not be more grateful to have you on board. I am certain that you will have a very successful PhD! By the way, I hope that by the time you read this, we have already found the mystery behind our Bluefors investigation.

**Hans**, it's so weird that we have been working together for 9 months and 8 of them have been through the virtual world. I cannot find a better adjective for you than hard-working. You never stop trying to do better and you never think twice before embracing constructive criticism. It has been a pleasure for me to be your supervisor and to see you fight through this project. Also, it's a very gratifying feeling for me to be able to help you understand things that I've also once stumbled upon. Even though research is not in your plans, I wish you the best for whatever you end up doing and I hope that you take many valuable lessons from academia with you.

**Sarwan**, I think that there wasn't a single day that I went to the office on a weekend and didn't find you there. I have always been very impressed by your perseverance! Even though your project was extremely challenging, you never stopped moving forward and in the end, there's no one that can fab those membranes better than you. I wish you all the best for the future. And if you do it, I would really like to know how the Trans-Siberian train experience is like.

**Fatemeh**, you joined the team shortly after we measured our first devices and your dedication to continue exploring the QOMSim was exciting for all of us. Even though things did not always turn out so well, it was great to study the device further with you. I think all of us learned a lot from it. Steele Lab was lucky to have your good energy around. I hope that Canada has many good things waiting for you and your family.

**Adrian**, a simple answer is never enough for you and from what I have seen during your time in the lab, your curiosity never lets you stop halfway. I hope that you and team membrane will find lots of successes! **Byoung-moo, Hadi, Nikos, Edouard** and **Chris** thank you for the nice conversations and for your interest on my research during our common time at Steele Lab. **Jean-Paul** even though we don't know each other for that long, it was great to have you join the group. I still hope that one day you will teach me how to eat popcorn with chopsticks.

As my project would have got nowhere near to what it is today without the contribution of the people that worked on it before me, I would also like to thank **Shun** for all his efforts on trying to develop flux-mediated optomechanical systems and photon-pressure systems before I arrived. The knowledge you gained during your PhD was an important part of the development of those platforms and therefore, somehow their success is also thanks to you.

**Irene**, having you around during those few months of your internship was so great! You are such a positive person and I was always so happy to see you on conferences. Somehow I wished that you could have stayed longer at Steele Lab, but I know that Konstanz needed you too. I look forward to see you graduate soon as well and I hope that we can see each other in the near future.

I would like to thank **Alexander** and **Matthijs**, who I co-supervised at an earlier stage of my PhD. Looking back, I was definitely not yet prepared for the role. Nevertheless, trying to guide you in your projects helped me understand many concepts deeper, and sometimes even made me realize that I had not understood them at all. It was not only you who grew during that period, and supervising you taught me many things about physics and myself. Things that I would probably not have learned otherwise. I hope you are both doing good and wish you all the best.

## 8

Now it is time to thank a few people who made conferences worth going to. **Fernando** it was so great to meet you in California and to have you around in Holland from time to time. Your company was always a pleasure. Ow, and thanks for showing me what Karaoke really is! **Bo** it has been a long time since Trieste, but a person's first conference is always unforgettable. Thanks for making that week so great and for later on showing us Basel around. **Edouard** seeing you at the HOT meetings was always so nice. Thanks for the great chats and now that you are a doctor, I hope you find another exciting challenge.

**Simon** thank you for being my co-promotor and for keeping your door always open during my PhD. I would also like to thank the rest of the Gröblacher lab. More specifically **Igor** and **Andreas** for the fun evenings of darts and pool. **Moritz, Claus, Rodrigo, João** and **Rob** for all the nice chats in the corridor or at the lunch table. Thanks **Richard** for all the nice chats too, but also for sharing your fantastic silicon etch recipe with us. Your advice was a valuable contribution to the development of our devices.

**Robbie**, thanks for being such a nice officemate. Even though both of us spent a lot

of time in the lab, I always enjoyed our casual encounters at the office. I wish you the best for your PhD too.

I would like to thank **Tino** for keeping our labs on track, and I want to give a very special thank you to **Ronald** for his help building the vector magnet that we used for our latest flux-mediated device. I can imagine that it's not easy to deal with students under pressure, so I am very grateful for your efforts regarding that project.

Since this department would never be able to stand on its feet without its support team, I would like to acknowledge **Marijke, Maria, Heleen, Erika** and **Etty** for their efforts regarding the part of the job that most of us (including me) have no idea about.

Finally I would like to give a big thank you to all KN staff. Without them, none of us would be able to do the research we do. **Frank, Charles, Anja, Eugene, Arnold, Marco, Pauline, Marc, Ewan, Hozanna** and **Roel** thank you for your amazing work, which allows us to continue pushing the limits of physics and nanotechnology.

As life does not end outside the lab, I would also like to thank a few very special people without whom I would never be the person I am today.

**Pais, Rui e avós** vocês sabem melhor do que ninguém o esforço que eu investi ao longo destes últimos anos. Eu sei que muitas vezes foi difícil para vocês verem-me estressada ou ansiosa, mas quero que saibam que o vosso apoio durante dessas fases foi essencial para mim! Obrigada por me fazerem sentir perto de casa, mesmo estando tão longe. Obrigada pela vossa curiosidade relativamente ao meu trabalho e por me ouvirem falar de circuitos e "frigoríficos" durante séculos, mesmo sem perceberem nada do que eu estava para ali a dizer. Obrigada por sempre acreditarem em mim e por me apoiarem em todos caminhos que eu já quis seguir. Eu sou o que sou hoje graças a vocês, e é em grande parte graças a vocês que o mundo tem mais uma doutorada. O preço de estar fora é caro, mas mesmo longe, o meu coração está sempre em casa.

8

**Mariana, Joana Melo, Joana Faria, Catarina, Filipe, André e Rui** vocês estiveram lá desde o meu primeiro dia como estudante de engenharia física. O tempo passa mesmo a correr... Nem acredito que já nos conhecemos há mais de 10 anos! E é ainda mais incrível pensar que, apesar de eu ter passado a maior parte desses anos a viver no estrangeiro, não houve nenhum sítio que me trouxesse uma amizade como a vossa. Obrigada por me receberem sempre de braços abertos e me fazerem sentir como se o tempo não tivesse passado. Saber que vocês estarão lá independentemente do caminho que eu decida seguir significa o mundo para mim!

**Kati** sometimes I think I would've gone nuts if you hadn't been around to bring me back to earth. Delft is definitely not the same without you. I will miss our coffees, our body pump classes together, and your marvelous guacamole. Sofia is the luckiest girl in the world for having such a caring mom like you. I can't wait to meet her and to see you again. Maybe after my defence I will head off to Mexico!

I have accepted the fact that I will most probably fail to acknowledge all the people

that played a role in my journey during the last four years. Sometimes a smile on the QN corridor gave me the energy to tackle the problems I was facing. Other times, a random comment over lunch would make me think about something which I had never considered before. I am aware it will be impossible to summarize all the situations that somehow impacted me. However, I want to thank the QN department for making this community so inspiring and to all the people that, one way or the other, were a part of my path.

For those who are still on the way, in times of stress remember that  
*slow progress is still moving forward, and forward is always good!*

*Delft*  
15.04.2021

# CURRICULUM VITÆ

Inês C. Rodrigues

16-12-1992 Born in Coimbra, Portugal.

## EDUCATION

- 2007–2010 High School  
Escola Secundária Afonso Albuquerque, Guarda, Portugal
- 2010–2015 Integrated Masters in Physics Engineering  
FCTUC - University of Coimbra, Portugal
- 2014–2015 Erasmus+ Exchange Program  
Faculty of Mathematics and Natural Sciences  
University of Groningen, The Netherlands
- 2015 Internship at SRON (Netherlands Institute for Space Research)  
*Thesis:* Feasibility of a frequency division multiplexing TES  
read-out system with superconducting tunnel junctions as rectifiers and frequency mixers.  
*Supervisor:* Dr. Gert de Lange
- 2017–2021 PhD Physics  
Delft University of Technology, The Netherlands  
*Thesis:* Coupling Harmonic Oscillators to Superconducting  
Quantum Interference Cavities  
*Promotor:* Dr. G. A. Steele

## PROFESSIONAL EXPERIENCE

- 2016–2017 Consultant  
*Employer:* Knightec  
*Base:* Stockholm, Sweden



# LIST OF PUBLICATIONS

\*These authors contributed equally

5. **D. Bothner\*, I. C. Rodrigues\* & G. A. Steele**, *Four-wave-cooling to the single phonon level in Kerr optomechanics*, arXiv:[2104.02511](https://arxiv.org/abs/2104.02511) (2021).
4. **I. C. Rodrigues\*, D. Bothner\* & G. A. Steele**, *Photon-pressure coupling with a hot radio-frequency circuit in the quantum regime*, arXiv:[2010.07975](https://arxiv.org/abs/2010.07975) (2021).
3. **D. Bothner\*, I. C. Rodrigues\* & G. A. Steele**, *Photon-pressure strong coupling between two superconducting circuits*, *Nature Physics* **17**, 85-91 (2020).
2. **F. E. Schmidt, D. Bothner, I. C. Rodrigues, M. F. Gely, M. D. Jenkins & G. A. Steele**, *Current Detection Using a Josephson Parametric Upconverter*, *Phys. Rev. Applied* **14**, 024069 (2020).
1. **I. C. Rodrigues\*, D. Bothner\* & G. A. Steele**, *Coupling microwave photons to a mechanical resonator using quantum interference*, *Nature Communications* **10** (2019).



## REFERENCES

- [1] J. Kepler, *De cometis libelli tres.* (1619).
- [2] A. Dorsel, J. D. McCullen, P. Meystre, E. Vignes, and H. Walther, Optical Bistability and Mirror Confinement Induced by Radiation Pressure. *Phys. Rev. Lett.* **51**, 1550 (1983).
- [3] V. B. Braginsky and A. B. Manukin, Ponderomotive Effects of Electromagnetic Radiation. *Sov. Phys. JETP* **25**, 653 (1967).
- [4] V. B. Braginsky, A. B. Manukin and M. Yu. Tikhonov, Investigation of Dissipative Ponderomotive Effects of Electromagnetic Radiation. *Sov. Phys. JETP* **31**, 829 (1970).
- [5] V. B. Braginsky and A. B. Manukin, Measurement of weak forces in Physics experiments. University of Chicago Press (1977).
- [6] V. B. Braginsky and F. Y. A. Khalili, Quantum Measurements. Cambridge University Press (1995).
- [7] C. M. Caves Quantum-Mechanical Radiation-Pressure Fluctuations in an Interferometer. *Phys. Rev. Lett.* **45**, 75 (1980).
- [8] T. Carmon, H. Rokhsari, L. Yang, T. J. Kippenberg and K. J. Vahala, Temporal Behavior of Radiation-Pressure-Induced Vibrations of an Optical Microcavity Phonon Mode. *Phys. Rev. Lett.* **94**, 223902 (2005).
- [9] T. J. Kippenberg, H. Rokhsari, T. Carmon, A. Scherer and K. J. Vahala, Analysis of Radiation-Pressure Induced Mechanical Oscillation of an Optical Microcavity. *Phys. Rev. Lett.* **95**, 033901 (2005).
- [10] H. Rokhsari, T. J. Kippenberg, T. Carmon and K. J. Vahala, Radiation-pressure-driven micro-mechanical oscillator. *Opt. Express* **13**, 5293 (2005).
- [11] A. Schliesser, P. Del'Haye, N. Nooshi K. J. Vahala and T. J. Kippenberg, Radiation Pressure Cooling of a Micromechanical Oscillator Using Dynamical Backaction. *Phys. Rev. Lett.* **97**, 243905 (2006).
- [12] O. Arcizet, P. F. Cohadon, T. Briant, M. Pinard and A. Heidmann, Radiation-pressure Cooling and Optomechanical Instability of a Micromirror. *Nature* **444**, 71 (2006).

- [13] S. Gigan, H. R. Böhm, M. Paternostro, F. Blaser, G. Langer, J. B. Hertzberg, K. C. Bäuerle, M. Aspelmeyer and A. Zeilinger, Self-cooling of a micro-mirror by radiation pressure. *Nature* **444**, 67 (2006).
- [14] J. D. Thompson, B. M. Zwickl, A. M. Jayich, F. Marquardt, S. M. Girvin and J. Harris, Strong dispersive coupling of a high-finesse cavity to a micromechanical membrane. *Nature* **452**, 72 (2008).
- [15] I. Favero, S. Stapfner, D. Hunger, P. Paulitschke, J. Reichel H. Lorenz, E. M. Weig and K. Karrai, Fluctuating nanomechanical system in a high finesse optical microcavity. *Opt. Express* **17** (12), 813 (2009).
- [16] X. Jiang, Q. Lin, J. Rosenberg, K. Vahala and O. Painter, High-Q double-disk microcavities for cavity optomechanics. *Opt. Express* **17** (20), 911 (2009).
- [17] G. S. Wiederhecker, A. Brenn, H. L. Fragnito and P. S. Russell, Coherent Control of Ultrahigh-Frequency Acoustic Resonances in Photonic Crystal Fibers. *Phys. Rev. Lett.* **100**, 203903 (2008).
- [18] R. Ma, A. Schliesser, P. Del'Haye, A. Dabirian, G. Anetsberger and T. Kippenberg, Radiation-pressure-driven vibrational modes in ultrahigh-Q silica microspheres. *Opt. Lett.* **32**, 2200 (2007).
- [19] Y. S. Park and H. Wang, Resolved-sideband and cryogenic cooling of an optomechanical resonator. *Nat. Phys.* **5**, 489 (2009).
- [20] M. Tomes and T. Carmon, Photonic Micro-Electromechanical Systems Vibrating at X-band (11-GHz) Rates. *Phys. Rev. Lett.* **5102**, 113601 (2009).
- [21] M. Eichenfield, M. R. Camacho, J. Chan, K. J. Vahala, and O. Painter, A picogram- and nanometre-scale photonic-crystal optomechanical cavity. *Nature* **459**, 550 (2009).
- [22] M. Eichenfield, J. Chan, M. R. Camacho, K. J. Vahala, and O. Painter, Optomechanical crystals. *Nature* **462**, 78 (2009).
- [23] G. Anetsberger, O. Arcizet, Q. P. Unterreithmeier, R. Rivière, A. Schliesser, E. M. Weig, J. P. Kotthaus and T. J. Kippenberg, Near-field cavity optomechanics with nanomechanical oscillators. *Nat. Phys.* **5**, 909 (2009).
- [24] C. A. Regal, J. D. Teufel and K. Lehnert, Measuring nanomechanical motion with a microwave cavity interferometer. *Nat. Phys.* **4**, 555 (2008).
- [25] J. D. Teufel, D. Li, S. Allman, K. Cicak, A. J. Sirois, J. D. Whittaker, and R. W. Simmonds, Circuit Cavity Electromechanics in the Strong-Coupling Regime. *Nature* **471**, 204 (2011).
- [26] F. Massel, T. T. Heikkilä, J. M. Pirkkalainen, S. U. Cho, H. Saloniemi, P.J. Hakonen and M. A. Sillanpää, Microwave amplification with nanomechanical resonators. *Nature* **480**, 351 (2011).

- [27] F. Marquardt, J. G. E. Harris, and S. M. Girvin, Dynamical Multistability Induced by Radiation Pressure in High-Finesse Micromechanical Optical Cavities. *Phys. Rev. Lett.* **96**, 103901 (2006).
- [28] C. Metzger, M. Ludwig, C. Neuenhahn, A. Ortlieb, I. Favero, K. Karrai, and F. Marquardt, Self-Induced Oscillations in an Optomechanical System Driven by Bolometric Backaction. *Phys. Rev. Lett.* **101**, 133903 (2008).
- [29] A. G. Krause, J. T. Hill, M. Ludwig, A. H. Safavi-Naeini, J. Chan, F. Marquardt and O. Painter, Nonlinear Radiation Pressure Dynamics in an Optomechanical Crystal. *Phys. Rev. Lett.* **115**, 233601 (2015).
- [30] D. Navarro-Urrios, N. E. Capuj, M. F. Colombano, P. D. García, M. Sledzinska, F. Alzina, A. Griol, M. Martínez and C. M. Sotomayor-Torres, Nonlinear dynamics and chaos in an optomechanical beam. *Nature Communications* **8**, 14965 (2017).
- [31] J. D. Teufel, T. Donner, D. Li, J. W. Harlow, M. S. Allman, K. Cicak, A. J. Sirois, J. D. Whittaker, K. W. Lehnert and R. W. Simmonds, Sideband cooling of micromechanical motion to the quantum ground state. *Nature* **475**, 359 (2011).
- [32] J. Chan, T. P. M. Alegre, A. H. Safavi-Naeini, J. T. Hill, A. Krause, S. Gröblacher, M. Aspelmeyer and O. Painter, Laser cooling of a nanomechanical oscillator into its quantum ground state. *Nature* **478**, 89 (2011).
- [33] E. Verhagen, S. Deléglise, S. Weis, A. Schliesser, and T. J. Kippenberg. Quantum-coherent coupling of a mechanical oscillator to an optical cavity mode. *Nature* **482**, 63 (2012).
- [34] T. A. Palomaki, J. W. Harlow, J. D. Teufel, R. W. Simmonds and K. W. Lehnert. Coherent state transfer between itinerant microwave fields and a mechanical oscillator. *Nature* **495**, 210–214 (2013).
- [35] U. Delić, M. Reisenbauer, K. Dare, D. Grass, V. Vučetić, N. Kiesel and M. Aspelmeyer, Cooling of a levitated nanoparticle to the motional quantum ground state. *Science* **367**, 892 (2020).
- [36] E. E. Wollman, C. U. Lei, A. J. Weinstein, J. Suh, A. Kronwald, F. Marquardt, A. A. Clerk, and K. C. Schwab. Quantum squeezing of motion in a mechanical resonator. *Science* **349**, 952 (2015).
- [37] J.-M. Pirkkalainen, E. Damskägg, M. Brandt, F. Massel, and M. A. Sillanpää. Squeezing of Quantum Noise of Motion in a Micromechanical Resonator. *Physical Review Letters* **115**, 243601 (2015).
- [38] A. P. Reed, K. H. Mayer, J. D. Teufel, L. D. Burkhardt, W. Pfaff, M. Reagor, L. Sletten, X. Ma, R. J. Schoelkopf, E. Knill, and K. W. Lehnert. Faithful conversion of propagating quantum information to mechanical motion. *Nature Physics* **13**, 1163 (2017).

- [39] R. Riedinger, A. Wallucks, I. Marinković, C. Löschnauer, M. Aspelmeyer, S. Hong, and S. Gröblacher. Remote quantum entanglement between two micromechanical oscillators. *Nature* **556**, 473 (2018).
- [40] C. F. Ockeloen-Korppi, E. Damskägg, J.-M. Pirkkalainen, M. Asjad, A. A. Clerk, F. Massel, M. J. Woolley, and M. A. Sillanpää. Stabilized entanglement of massive mechanical oscillators. *Nature* **556**, 478 (2018).
- [41] J. D. Teufel, T. Donner, M. A. Castellanos-Beltran, J. W. Harlow, and K. W. Lehnert. Nanomechanical motion measured with an imprecision below that at the standard quantum limit. *Nature Nanotechnology* **4**, 820 (2009).
- [42] G. Anetsberger, E. Gavartin, O. Arcizet, O. P. Unterreithmeier, E. M. Weig, M. L. Gorodetsky, J. P. Kotthaus and T. J. Kippenberg. Measuring nanomechanical motion with an imprecision below the standard quantum limit. *Physical Review A* **82**, 061804(R) (2010).
- [43] D. Mason, J. Chen, M. Rossi, Y. Tsaturyan and A. Schliesser. Continuous force and displacement measurement below the standard quantum limit. *Nature Physics* **15**, 745–749 (2019).
- [44] T. P. Purdy, R. W. Peterson and C. A. Regal. Observation of Radiation Pressure Shot Noise on a Macroscopic Object. *Science* **339**, 801 (2013).
- [45] J. Chen, M. Rossi, D. Mason and A. Schliesser. Entanglement of propagating optical modes via a mechanical interface. *Nature Communications* **11**, 943 (2020).
- [46] S. Barzanjeh, E. S. Redchenko, M. Peruzzo, M. Wulf, D. P. Lewis, G. Arnold and J. M. Fink. Stationary entangled radiation from micromechanical motion. *Nature* **570**, 480–483 (2019).
- [47] C. F. Ockeloen-Korppi, E. Damskägg, J. M. Pirkkalainen, T. T. Heikkilä, F. Massel and M. A. Sillanpää, Noiseless Quantum Measurement and Squeezing of Microwave Fields Utilizing Mechanical Vibrations. *Phys. Rev. Lett.* **118**, 103601 (2017).
- [48] A. H. Safavi-Naeini, S. Gröblacher, J. T. Hill, J. Chan, M. Aspelmeyer and O. Painter. Squeezed light from a silicon micromechanical resonator. *Nature* **500**, 185–189 (2013).
- [49] T. P. Purdy, P. L. Yu, R. W. Peterson, N. S. Kampel and C. A. Regal. Strong Optomechanical Squeezing of Light. *Phys. Rev. X* **3**, 031012 (2013).
- [50] N. Aggarwal, T. J. Cullen, J. Cripe, G. Cole R. Lanza A. Libson D. Follman P. Heu T. Corbitt and N. Mavalvala. Room-temperature optomechanical squeezing. *Nature Physics* **16**, 784–788 (2020).
- [51] J. Bochmann, A. Vainsencher, D. D. Awschalom, and A. N. Cleland. Nanomechanical coupling between microwave and optical photons. *Nature Physics* **9**, 712 (2013).

- [52] R. W. Andrews, R. W. Peterson, T. P. Purdy, K. Cicak, R. W. Simmonds, C. A. Regal, and K. W. Lehnert. Bidirectional and efficient conversion between microwave and optical light. *Nature Physics* **10**, 321 (2014).
- [53] A. Vainsencher, K. J. Satzinger, G. A. Peairs and A. N. Cleland. Bi-directional conversion between microwave and optical frequencies in a piezoelectric optomechanical device. *Appl. Phys. Lett.* **109**, 033107 (2016).
- [54] M. Forsch, R. Stockill, A. Wallucks, I. Marinković, C. Gärtner, R. A. Norte, F. v. Otten, A. Fiore, K. Srinivasan and S. Gröblacher. Microwave-to-optics conversion using a mechanical oscillator in its quantum ground state. *Nature Physics* **16**, 69 (2020).
- [55] T. J. Kippenberg and K. J. Vahala. Cavity optomechanics. *Optics Express* **15**, 25 (17172) (2007).
- [56] M. Aspelmeyer, T. J. Kippenberg and F. Marquardt. Cavity optomechanics. *Rev. Mod. Phys* **86**, 1391 (2014).
- [57] P. Meystre. A short walk through quantum optomechanics. arXiv:1210.3619 (2012).
- [58] Dobrindt, J. M., Wilson-Rae, I., and Kippenberg, T. J., Parametric Normal-Mode Splitting in Cavity Optomechanics, *Physical Review Letters* **101**, 263602 (2008).
- [59] S. Gröblacher, K. Hammerer, M. R. Vanner, and M. Aspelmeyer. Observation of strong coupling between a micromechanical resonator and an optical cavity field. *Nature* **460**, 724 (2009).
- [60] G. A. Peterson, S. Kotler, F. Lecocq, K. Cicak, X. Y. Jin, R. W. Simmonds, J. Aumentado and J. D. Teufel. Ultrastrong Parametric Coupling between a Superconducting Cavity and a Mechanical Resonator. *Phys. Rev. Lett.* **123**, 247701 (2019).
- [61] S. M. Meenehan, J. D. Cohen, S. Gröblacher, J. T. Hill, A. H. Safavi-Naeini, M. Aspelmeyer, and O. Painter. Silicon optomechanical crystal resonator at millikelvin temperatures. *Physical Review A* **90**, 011803(R) (2014).
- [62] M. Yuan, V. Singh, Ya. M. Blanter, and G. A. Steele. Large cooperativity and microkelvin cooling with a three-dimensional optomechanical cavity. *Nature Communications* **6**, 8491 (2015).
- [63] A. Nunnenkamp, K. Børkje and S. M. Girvin. Single-Photon Optomechanics. *Phys. Rev. Lett.* **107**, 063602 (2011).
- [64] M. Ludwig, B. Kubala and F. Marquardt. The optomechanical instability in the quantum regime. *New J. Phys.* **10**, 095013 (2008).
- [65] U. Akram, W. P. Bowen and G. J. Milburn. Entangled mechanical cat states via conditional single photon optomechanics. *New J. Phys.* **15**, 093007 (2013).
- [66] M. Kounalakis, Ya. M. Blanter and G. A. Steele. Flux-mediated optomechanics with a transmon qubit in the single-photon ultrastrong-coupling regime. *Phys. Rev. Research* **2**, 023335 (2020).

- [67] P. Rabl. Photon Blockade Effect in Optomechanical Systems. *Phys. Rev. Lett.* **107**, 063601 (2011).
- [68] M. Via, G. Kirchmair and O. Romero-Isart. Strong Single-Photon Coupling in Superconducting Quantum Magnetomechanics. *Phys. Rev. Lett.* **114**, 143602 (2015).
- [69] P. D. Nation, J. Suh and M. P. Blencowe. Ultrastrong optomechanics incorporating the dynamical Casimir effect. *Phys. Rev. A* **93**, 022510 (2016).
- [70] O. Shevchuk, G. Steele and Ya. M. Blanter. Strong and tunable couplings in flux-mediated optomechanics. *Phys. Rev. B* **96**, 014508 (2017).
- [71] D. Zoepfl, M. L. Juan, C. M. F. Schneider and G. Kirchmair. Single-photon cooling in microwave magnetomechanics. *Phys. Rev. Lett.* **125**, 023601 (2020).
- [72] Schmidt, P., Amawi, M. T., Pogorzalek, S., Deppe, E., Marx, A., Gross, R., and Huebl, H., Sideband-resolved resonator electromechanics based on a nonlinear Josephson inductance probed on the single-photon level. *Communications Physics* **3**, 233 (2020).
- [73] T. Bera, S. Majumder, S. K. Sahu and V. Singh. Large flux-mediated coupling in hybrid electromechanical system with a transmon qubit. *Communications Physics* **4**, 12 (2021).
- [74] I. Mahboob, K. Nishiguchi, H. Okamoto, and H. Yamaguchi. Phonon-cavity electromechanics. *Nature Physics* **8**, 387 (2012).
- [75] R. De Alba, F. Massel, I. R. Storch, T. S. Abhilash, A. Hui, P. L. McEuen, H. G. Craighead, and J. M. Parpia. Tunable phonon-cavity coupling in graphene membranes. *Nature Nanotechnol.* **11**, 741-746 (2016).
- [76] J. P. Mathew, R. N. Patel, A. Borah, R. Vijay, and M. M. Deshmukh. Dynamical strong coupling and parametric amplification of mechanical modes of graphene drums. *Nature Nanotechnol.* **11**, 747-751 (2016).
- [77] S. Cho, S. U. Cho, M. Jo, J. Suh, H. C. Park, S. G. Kim, S.-B. Shim, and Y. D. Park. Strong Two-Mode Parametric Interaction and Amplification in a Nanomechanical Resonator. *Physical Review Applied* **9**, 064023 (2018).
- [78] J. R. Johansson, G. Johansson, and F. Nori. Optomechanical-like coupling between superconducting resonators. *Physical Review A* **90**, 053833 (2014).
- [79] E.-j. Kim, J. R. Johansson, and F. Nori. Circuit analog of quadratic optomechanics. *Physical Review A* **91**, 033835 (2015).
- [80] A. Ü. C. Hardal, N. Aslan, C. M. Wilson, and Ö. E. Müstecaplıoğlu. Quantum heat engine with coupled superconducting resonators. *Physical Review E* **96**, 062120 (2017).
- [81] C. Eichler, and J. R. Petta. Realizing a Circuit Analog of an Optomechanical System with Longitudinally Coupled Superconducting Resonators. *Physical Review Letters* **120**, 227702 (2018).

- [82] Nunnenkamp, A., Sudhir, V., Feofanov, A. K., Roulet, A., and Kippenberg, T. J., Quantum-Limited Amplification and Parametric Instability in the Reversed Dissipation Regime of Cavity Optomechanics, *Physical Review Letters* **113**, 023604 (2014).
- [83] E. Jansen, J. D. P. Machado, and Ya. M. Blanter, Realization of a degenerate parametric oscillator in electromechanical systems, *Physical Review B* **99**, 045401 (2019).
- [84] Ockeloen-Korppi, C. F., Damskägg, E., Pirkkalainen, J.-M., Heikkilä, T. T., Massel, F., and Sillanpää, M. A., Low-Noise Amplification and Frequency Conversion with a Multiport Microwave Optomechanical Device, *Physical Review X* **6**, 041024 (2016).
- [85] D. Bothner, S. Yanai, A. Iniguez-Rabag, M. Yuan, Ya. M. Blanter and G. A. Steele, Cavity electromechanics with parametric mechanical driving, *Nature Communications* **11**, 1589 (2020).
- [86] Metelmann, A., and Clerk, A. A., Quantum-Limited Amplification via Reservoir Engineering, *Physical Review Letters* **112**, 133904 (2014).
- [87] D. Malz, L. D. Tóth, N. R. Bernier, A. F. Feofanov, T. J. Kippenberg, and A. Nunnenkamp. Quantum-Limited Directional Amplifiers with Optomechanics. *Phys. Rev. Lett.* **120**, 023601 (2018).
- [88] Bernier, N. R., Toth, L. D., Koottandavida, A., Ioannou, M. A., Malz, D., Nunnenkamp, A., Feofanov, A. K., and Kippenberg, T. J., Nonreciprocal reconfigurable microwave optomechanical circuit, *Nature Communications* **8**, 604 (2017).
- [89] Barzanjeh, S., Wulf, M., Peruzzo, M., Kalaei, M., Dieterle, P. B., Painter, O., and Fink, J. M., Mechanical on-chip microwave circulator, *Nature Communications* **8**, 953 (2017).
- [90] Xu, H., Jiang, Luyao, Clerk, A. A., and Harris, J. G. E., Nonreciprocal control and cooling of phonon modes in an optomechanical system, *Nature* **568**, 65-69 (2019).
- [91] Fang, K., Luo, J., Metelmann, A., Matheny, M. H., Marquardt, F., Clerk, A. A., and Painter, O., Generalized non-reciprocity in an optomechanical circuit via synthetic magnetism and reservoir engineering, *Nature Physics* **13**, 465-471 (2017).
- [92] Tóth, L. D., Bernier, N. R., Nunnenkamp, A., Feofanov, A. K., and Kippenberg, T. J., A dissipative quantum reservoir for microwave light using a mechanical oscillator, *Nature Physics* **13**, 787-792 (2017).
- [93] Weigand, D. J., and Terhal, B. M., Realizing modular quadrature measurements via a tunable photon-pressure coupling in circuit QED, *Physical Review A* **101**, 053840 (2020).
- [94] P. M. A. Dirac, *The principles of quantum mechanics*. Oxford Univ. Press (1958).
- [95] U. Vool and M. Devoret, Introduction to Quantum Electromagnetic Circuits. *International journal of Circuit Theory and Applications* **45**, 897 (2017).

- [96] R. Gross and A. Marx, Applied Superconductivity: Josephson Effect and Superconducting Electronics. Lecture notes: Walther-Meissner-Institut and Technical University of Munich (2005).
- [97] S. Nigg, H. Paik, B. Vlastakis, G. Kirchmair, S. Shankar, L. Frunzio, M. H. Devoret, R. J. Schoelkopf and S. M. Girvin, Black-Box Superconducting Circuit Quantization. *Phys. Rev. Lett.* **108** (24), 240502 (2012).
- [98] M. Gely and G. A. Steele, QuCAT: Quantum Circuit Analyzer Tool in Python. *New Journal of Physics* **22**, (2020).
- [99] J. Koch, T. M. Yu, J. Gambetta, A. A. Houck, D. I. Schuster, J. Majer, A. Blais, M. H. Devoret, S. M. Girvin and R. J. Schoelkopf, Charge-insensitive qubit design derived from the Cooper pair box. *Phys. Rev. A* **76**, 042319 (2007).
- [100] J. A. Schreier, A. A. Houck, J. Koch, D. I. Schuster, B. R. Johnson, J. M. Chow, J. Gambetta, J. Majer, L. Frunzio, M. H. Devoret, S. M. Girvin and R. J. Schoelkopf, Suppressing charge noise decoherence in superconducting charge qubits. *Phys. Rev. A* **77**, 180502(R) (2008).
- [101] H. A. Haus, Waves and Fields in Optoelectronics. Prentice-Hall, New Jersey (1984).
- [102] S. Bradley, Sign Conventions in Electromagnetic (EM) Waves. Course Notes of Applied Electromagnetics, Massachusetts Institute of Technology (2007).
- [103] M. C. Beltran, Development of a Josephson Parametric Amplifier for the Preparation and Detection of Nonclassical States of Microwave Fields. Ph.D. Thesis University of Colorado (2010).
- [104] A. Clerk, Optomechanics and quantum measurement. Lectures notes, Les Houches (2015).
- [105] N. Antler, E. M. Levenson-Falk, R. Naik, Y.-D. Sun, A. Narla, R. Vijay, and I. Siddiqi. In-plane magnetic field tolerance of a dispersive aluminum nanobridge SQUID magnetometer. *Applied Physics Letters* **102**, 232602 (2013).
- [106] M. J. Martínez-Pérez and D. Koelle. NanoSQUIDs: Basics & recent advances. *Physical Sciences Reviews* **2(8)**, (2017).
- [107] M. Peruzzo, A. Trioni, F. Hassani, M. Zemlicka and J. M. Fink, Surpassing the Resistance Quantum with a Geometric Superinductor. *Phys. Rev. Applied* **14**, 044055 (2020).
- [108] A. A. Golubov, M. Yu. Kupriyanov and E. Il'ichev, The current-phase relation in Josephson junctions. *Rev. Mod. Phys.* **76**, 411 (2004).
- [109] R. P. Feynman, R. B. Leighton, and M. Sands The Feynman Lectures on Physics. Boston: Addison Wesley **vol. 3**, (1971).
- [110] B. D. Josephson, Possible new effects in superconductive tunnelling. *Physics Letters* **1**, 7 (1962).

- [111] M. Sugahara, Origin of the Nonsinusoidal current-phase relation of a superconducting bridge. *Journal of Applied Physics* **48**, 234 (1977).
- [112] K. Likharev, Superconducting weak links. *Rev. Mod. Phys.* **51**, 101 (1979).
- [113] I. O. Kulik, and A. N. Omel'yanchuk Current flow in long superconducting junctions. *Zh. Eksp. Teor. Fiz.* **68**, 2139-2148 (1975).
- [114] R. Vijay, E. M. Levenson-Falk, D. H. Slichter and I. Siddiqi, Approaching ideal weak link behavior with three dimensional aluminum nanobridges. *Appl. Phys. Lett.* **96**, 223112 (2010).
- [115] R. Vijay, J. D. Sau, M. L. Cohen and I. Siddiqi, Optimizing Anharmonicity in Nanoscale Weak Link Josephson Junction Oscillators. *Phys. Rev. Lett.* **103**, 087003 (2009).
- [116] E. M. Levenson-Falk, Static and Microwave Transport Properties of Aluminum Nanobridge Josephson Junctions. PhD thesis, UC Berkeley (2013).
- [117] J. Clarke and A. I. Braginski, *The SQUID Handbook: Fundamentals and Technology of SQUIDs and SQUID Systems* (2004).
- [118] A. J. Annunziata, D. F. Santavicca, L. Frunzio, G. Catelani, M. Rooks, A. Frydman and D. Prober. Tunable superconducting nanoinductors. *IOP Publishing* **21(44)**, 445202 (2010)
- [119] D. Slichter, Quantum Jumps and Measurement Backaction in a Superconducting Qubit. PhD thesis, UC Berkeley (2011).
- [120] E. M. Levenson-Falk, R. Vijay, and I. Siddiqi. Nonlinear microwave response of aluminum weak-link Josephson oscillators. *Applied Physics Letters* **98**, 123115 (2011)
- [121] S. Pogorzalek, K. G. Fedorov, L. Zhong, J. Goetz, F. Wulschner, M. Fischer, P. Eder, E. Xie, K. Inomata, T. Yamamoto, Y. Nakamura, A. Marx, F. Deppe and R. Gross. Hysteretic Flux Response and Nondegenerate Gain of Flux-Driven Josephson Parametric Amplifiers. *Phys. Rev. Applied* **8**, 024012 (2017)
- [122] O. W. Kennedy, J. Burnett, J. C. Fenton, N. G. N. Constantino, P. A. Warburton, J. J. L. Morton, and E. Dupont-Ferrier. Tunable Nb Superconducting Resonator Based on a Constriction Nano-SQUID Fabricated with a Ne Focused Ion Beam. *Physical Review Applied* **11**, 014006 (2019).
- [123] J. Birenbaum, The C-shunt Flux Qubit: A New Generation of Superconducting Flux Qubit. PhD thesis, UC Berkeley (2014).
- [124] S. Hosaka, Updates in Advanced Lithography (2013). .
- [125] S. S. Verbridge, J. M. Parpia, R. B. Reichenbach, L. M. Bellan and H. G. Craighead, High quality factor resonance at room temperature with nanostrings under high tensile stress. *Journal of Applied Physics* **99(12)**, 124304 (2018).

- [126] R. A. Norte, M. Forsch, A. Wallucks, I. Marinković and S. Gröblacher, Platform for Measurements of the Casimir Force between Two Superconductors. *Phys. Rev. Lett.* **121**, 030405 (2018).
- [127] Rodrigues, I. C., Bothner, D., and Steele, G. A.. Photon-pressure coupling with a hot radio-frequency circuit in the quantum regime. arXiv:2010.07975 (2020).
- [128] K. Kakuyanagi, T. Meno, H. Nakano, K. Semba, H. Takayanagi, F. Deppe and A. Shnirman, Dephasing of a Superconducting Flux Qubit. *Phys. Rev. Lett.* **98**, 047004 (2007).
- [130] S. Sendelbach, D. Hover, A. Kittel, M. Mück, J. M. Martinis and R. McDermott, Magnetism in SQUIDs at Millikelvin Temperatures. *Phys. Rev. Lett.* **100**, 227006 (2008).
- [130] S. M. Anton, C. Müller, J. S. Birenbaum, S. R. O'Kelley, A. D. Fefferman, D. S. Golubev, G. C. Hilton, H.-M. Cho, K.D. Irwin, F. C. Wellstood, G. Schön, A. Shnirman and J. Clarke, Pure dephasing in flux qubits due to flux noise with spectral density scaling as  $1/f^\alpha$ . *Phys. Rev. B* **85**, 224505 (2012).
- [131] R. Kleiner, D. Koelle, F. Ludwig and J. Clarke, Superconducting quantum interference devices: State of the art and applications. *IEEE* **92** (10), 1534 (2004).
- [132] High Finesse homepage: <https://www.highfinesse.com/en/>
- [133] A. A. Abrikosov. The magnetic properties of superconducting alloys. *Journal of Physics and Chemistry of Solids* **2**(3), 199-208 (1957).
- [134] A. Schneider, T. Wolz, M. Pfirrmann, M. Spiecker, H. Rotzinger, A. Ustinov and M. Weides. Transmon qubit in a magnetic field: Evolution of coherence and transition frequency. *Phys. Rev. Research* **1**, 023003 (2019).
- [135] D. Bothner, T. Gaber, M. Kemmler, D. Koelle, R. Kleiner, S. Wünsch and M. Siegel. Magnetic hysteresis effects in superconducting coplanar microwave resonators. *Phys. Rev. B* **86**, 014517 (2012).
- [136] L. Enbom, Y. Anahory, A. Suhov, D. Halbertal, J. Cuppens, A. Yakovenko, A. Uri, Y. Myasoedov, M. L. Rappaport, M. E. Huber, A. Gurevich and E. Zeldov. Probing dynamics and pinning of single vortices in superconductors at nanometer scales. *Scientific Reports* **5**, 7598 (2015).
- [137] G. Ghigoa, F. Laviano, L. Gozzelino, R. Gerbaldo and E. Mezzetti. Evidence of rf-driven dendritic vortex avalanches in MgB<sub>2</sub> microwave resonators. *Journal of Applied Physics* **102**, 113901 (2007).
- [138] K. G. Fedorov, A. V. Shcherbakova, M. J. Wolf, D. Beckmann and A. V. Ustinov. Fluxon Readout of a Superconducting Qubit. *Physical Review Letters* **112**, 160502 (2014).

- [139] D. Bothner, C. Clauss, E. Koroknay, M. Kemmler, T. Gaber, M. Jetter, M. Scheffler, P. Michler, M. Dressel, D. Koelle and R. Kleiner. Reducing vortex losses in superconducting microwave resonators with microsphere patterned antidot arrays. *Appl. Phys. Lett.* **100**, 012601 (2012).
- [140] C. Song, M. P. DeFeo, K. Yu and B. L. T. Plourde. Reducing microwave loss in superconducting resonators due to trapped vortices. *Appl. Phys. Lett.* **95**, 232501 (2009).
- [141] W. Marshall, C. Simon, R. Penrose, and D. Bouwmeester. Towards Quantum Superpositions of a Mirror. *Physical Review Letters* **91**, 130401 (2003).
- [142] M. Bahrami, M. Paternostro, A. Bassi, and H. Ulbricht. Proposal for a Noninterferometric Test of Collapse Models in Optomechanical Systems. *Physical Review Letters* **112**, 210404 (2014).
- [143] F. Xue, Y. D. Wang, C. P. Sun, H. Okamoto, H. Yamaguchi, and K. Semba. Controllable coupling between flux qubit and nanomechanical resonator by magnetic field. *New Journal of Physics* **9**, 35 (2007).
- [144] M. P. Blencowe and E. Buks. Quantum analysis of a linear dc SQUID mechanical displacement detector. *Physical Review B* **76**, 014511 (2007).
- [145] P. D. Nation, M. P. Blencowe, and E. Buks. Quantum analysis of a nonlinear microwave cavity-embedded dc SQUID displacement detector. *Physical Review B* **78**, 104516 (2008).
- [146] Y. D. Wang, K. Semba, and H. Yamaguchi. Cooling of a micro-mechanical resonator by the back-action of Lorentz force. *New Journal of Physics* **10**, 043015 (2008).
- [147] S. Etaki, M. Poot, I. Mahboob, K. Onomitsu, H. Yamaguchi, and H. S. J. van der Zant. Motion detection of a micromechanical resonator embedded in a d.c. SQUID. *Nature Physics* **4**, 785 (2008).
- [148] M. Poot, S. Etaki, I. Mahboob, K. Onomitsu, H. Yamaguchi, Ya. M. Blanter, and H. S. J. van der Zant. Tunable Backaction of a DC SQUID on an Integrated Micromechanical Resonator. *Physical Review Letters* **105**, 207203 (2010).
- [149] G. S. Agarwal, and S. Huang. Electromagnetically induced transparency in mechanical effects of light. *Physical Review A* **81**, 041803(R) (2010).
- [150] S. Weis, R. Rivière, S. Deléglise, E. Gavartin, O. Arcizet, A. Schliesser, and T. J. Kippenberg. Optomechanically Induced Transparency. *Science* **330**, 1520 (2010).
- [151] R. Meservey, and P. M. Tedrow. Properties of Very Thin Aluminum Films. *Journal of Applied Physics* **42**, 51 (1971).
- [152] T. Yamamoto, K. Inomata, M. Watanabe, K. Matsuba, T. Miyazaki, W. D. Oliver, Y. Nakamura, and J. S. Tsai. Flux-driven Josephson parametric amplifier. *Applied Physics Letters* **93**, 042510 (2008)

- [153] N Samkharadze, A. Bruno, P. Scarlino, G. Zheng, D. P. DiVincenzo, L. DiCarlo, and L. M. K. Vandersypen. High-Kinetic-Inductance Superconducting Nanowire Resonators for Circuit QED in a Magnetic Field. *Physical Review Applied* **5**, 044004 (2016).
- [154] X. Wang, A. Miranowicz, H.-R. Li, F.-L. Li, and F. Nori. Two-color electromagnetically induced transparency via modulated coupling between a mechanical resonator and a qubit. *Physical Review A* **98**, 023821 (2018).
- [155] K. Stannigel, P. Komar, S. J. M. Habraken, S. D. Bennett, M. D. Lukin, P. Zoller, and P. Rabl. Optomechanical Quantum Information Processing with Photons and Phonons. *Physical Review Letters* **109**, 013603 (2012).
- [156] S. A. McGee, D. Meiser, C. A. Regal, K. W. Lehnert, and M. J. Holland. Mechanical Resonators for storage and transfer of electrical and optical quantum states. *Physical Review A* **87**, 053818 (2013).
- [157] O. Romero-Isart. Quantum superposition of massive objects and collapse models. *Physical Review A* **84**, 052121 (2011).
- [158] Igreja, R., and Dias, C. J., Analytical evaluation of the interdigital electrodes capacitance for a multi-layered structures, *Sensors and Actuators A* **112**, 291-301 (2004).
- [159] Xu, H., Mason, D., Jiang, Luyao, and Harris, J. G. E., Topological energy transfer in an optomechanical system with exceptional points, *Nature* **537**, 80-83 (2016).
- [160] Teufel, J. D., Harlow, J. W., Regal, C. A., and Lehnert, K. W., Dynamical Backaction of Microwave Fields on a Nanomechanical Oscillator, *Physical Review Letters* **101**, 197203 (2008).
- [161] Fleischhauer, M., Imamoglu, A., and Marangos, J. P., Electromagnetically induced transparency: Optics in coherent media, *Reviews of Modern Physics* **77**, 633 (2005).
- [162] Rodrigues, I. C., Bothner, D., and Steele, G. A., Coupling microwave photons to a mechanical resonator using quantum interference, *Nature Communications* **10**, 5359 (2019).
- [163] Weinstein, A. J., Lei, C. U., Wollman, E. E., Suh, J., Metelmann, A., Clerk, A. A., and Schwab, K. C., Observation and Interpretation of Motional Sideband Asymmetry in a Quantum Electromechanical Device, *Physical Review X* **4**, 041003 (2014).
- [164] Bergeal, N., Vijay, R., Manucharyan, V. E., Siddiqi, I., Schoelkopf, R. J., Girvin, S. M., and Devoret, M. H., Analog information processing at the quantum limit with a Josephson ring modulator, *Nature Physics* **6**, 296-302 (2010).
- [165] Fedortchenko, S., Felicetti, S., Marković, D., Jezouin, S., Keller, A., Coudreau, T., Huard, B., and Milman, P., Quantum simulation of ultrastrongly coupled bosonic modes using superconducting circuits, *Physical Review A* **95**, 042313 (2017).
- [166] Marković, D., Jezouin, S., Ficheux, Q., Fedortchenko, S., Felicetti, S., Coudreau, T., Milman, P., Leghtas, Z., and Huard, B., Demonstration of an Effective Ultrastrong Coupling between Two Oscillators, *Physical Review A* **95**, 042313 (2017).

- [167] Gottesman, D., Kitaev, A., and Preskill, J., Encoding a qubit in an oscillator, *Physical Review A* **64**, 012310 (2001).
- [168] Gely, M. F., Kounalakis, M., Dickel, C., Dalle, J., Vatré, R., Baker, B., Jenkins, M. D., and Steele, G. A., Observation and stabilization of photonic Fock states in a hot radio-frequency resonator, *Science* **363**, 1072-1075 (2019).
- [169] Hunklinger, S., and Arnold, W., *Physical Acoustics*, New York: Academic, (1972).
- [170] Pappas, D. P., Vissers, M. R., Wisbey, D. S., Kline, J. S., and Gao, J., Two Level System Loss in Superconducting Microwave Resonators, *IEEE Transactions on Applied Superconductivity* **21**, 871-874 (2011).
- [171] Arute, F., Arya, K., Babbush, R., Bacon, D., Bardin, J. C., Barends, R., Biswas, R., Boixo, S., Brando, F. G. S. L., Buell, D. A., Burkett, B., Chen, Y., Chen, Z., Chiaro, B., Collins, R., Courtney, W., Dunsworth, A., Farhi, E., Foxen, B., Fowler, A., Gidney, C., Giustina, M., Graff, R., Guerin, K., Habegger, S., Harrigan, M. P., Hartmann, M. J., Ho, A., Hoffmann, M., Huang, T., Humble, T. S., Isakov, S. V., Jeffrey, I., Jiang, Z., Kafri, D., Kechedzhi, K., Kelly, J., Klimov, P. V., Knysh, S., Korotkov, A., Kostritsa, F., Landhuis, D., Lindmark, M., Lucero, E., Lyakh, D., Mandrà, S., McClean, J. R., McEwen, M., Megrant, A., Mi, X., Michelsen, K., Mohseni, M., Mutus, J., Naaman, O., Neeley, M., Neill, C., Niu, M. Y., Ostby, E., Petukhov, A., Platt, J. C., Quintana, C., Rieffel, E. J., Roushan, P., Rubin, N. C., Sank, D., Satzinger, K. J., Smelyanskiy, V., Sung, K. J., Trevithick, M. D., Vainsencher, A., Villalonga, B., White, T., Yao, Z. J., Yeh, P., Zalcman, A., Neven, H., and Martinis, J. M., Quantum supremacy using a programmable superconducting processor, *Nature* **574**, 505-510 (2019).
- [172] Wineland, D. J., Drullinger, R. E., and Walls, F. L., Radiation-Pressure Cooling of Bound Resonant Absorbers, *Physical Review Letters* **40**, 1639-1642 (1978).
- [173] Diedrich, F., Bergquist, J. C., Itano, W. M., and Wineland, D. J., Laser Cooling to the Zero-Point Energy of Motion, *Physical Review Letters* **62**, 403-406 (1989).
- [174] Neuhauser, W., Hohenstatt, M., Toschek, P., and Dehmelt, H., Optical-sideband-cooling of Visible Atom Cloud Confined in Parabolic Well, *Physical Review Letters* **41**, 233-236 (1978).
- [175] Hamann, S. E., Haycock, D. L., Klose, G., Pax, P. H., Deutsch, I. H., and Jessen, P. S., Resolved-Sideband Raman Cooling to the Ground State of an Optical Lattice, *Physical Review Letters* **80**, 4149-4152 (1998).
- [176] Bothner, D., Rodrigues, I. C., and Steele, G. A., Photon-pressure strong coupling between two superconducting circuits, *Nature Physics* (2020).
- [177] Cohadon, P.-F., Heidmann, A., and Pinard, M., Cooling of a Mirror by Radiation Pressure, *Physical Review Letters* **83**, 3174-3177 (1999).
- [178] Braginsky, V. B., and Vyatchanin, S. P., Low quantum noise tranquilizer for Fabry-Perot interferometer, *Physics Letters A* **293**, 228-234 (2002).

- [179] Höhberger Metzger, C., and Karrai, K., Cavity cooling of a microlever, *Nature* **432**, 1002-1005 (2004).
- [180] Kleckner, D., and Bouwmeester, D., Sub-kelvin optical cooling of a micromechanical resonator, *Nature* **444**, 75-78 (2006).
- [181] Wilson-Rae, I., Nooshi, N., Zwerger, W., and Kippenberg, T. J., Theory of Ground State Cooling of a Mechanical Oscillator Using Dynamical Backaction, *Physical Review Letters* **99**, 093901 (2007).
- [182] Marquardt, F., Chen, J. P., Clerk, A. A., and Girvin, S. M., Quantum Theory of Cavity-Assisted sideband-cooling of Mechanical Motion, *Physical Review Letters* **99**, 093902 (2007).
- [183] Safavi-Naeini, A. H., Mayer Alegre, T. P., Chan, J., Eichenfield, M., Winger, M., Lin, Q., Hill, J. T., Chang, D. E., and Painter, O., Electromagnetically induced transparency and slow light with optomechanics, *Nature* **472**, 69-73 (2011).
- [184] Zhou, X., Hocke, F., Schliesser, A., Marx, A., Huebl, H., Gross, R., and Kippenberg, T. J., Slowing, advancing and switching of microwave signals using circuit nanoelectromechanics, *Nature Physics* **9**, 179-184 (2013).
- [185] Meekhof, D. M., Monroe, C., King, B. E., Itano, W. M., and Wineland, D. J., Generation of Nonclassical Motional States of a Trapped Atom, *Physical Review Letters* **76**, 1796-1799 (1996).
- [186] Xu, M., Han, X., Zou, C.-L., Fu, W., Xu, Y., Zhong, C., Jiang, L., and Tang, H. X., Radiative cooling of a superconducting resonator, *Physical Review Letters* **124**, 033602 (2020).
- [187] Albanese, B., Probst, S., Ranjan, V., Zollitsch, C., Pechal, M., Wallraff, A., Morton, J. J. L., Vion, D., Esteve, D., Flurin, E., and Bertet, P., Radiative cooling of a spin ensemble, *Nature Physics* **16**, 751-755 (2020).
- [188] Valenzuela, S. O., Oliver, W. D., Berns, D. M., Berggren, K. K., Levitov, L. S., and Orlando, T. P., Microwave-Induced Cooling of a Superconducting Qubit, *Science* **314**, 1589-1592 (2006).
- [189] Riedinger, R., Hong, S., Norte, R. A., Slater, J. A., Shang, J., Krause, A. G., Anant, V., Aspelmeyer, M., and Gröblacher, S., Non-classical correlations between single photons and phonons from a mechanical oscillator, *Nature* **530**, 313-316 (2016).
- [190] Ma, X., Viennot, J. J., Kotler, S., Teufel, J. D., and Lehnert, K. W., Nonclassical energy squeezing of a macroscopic mechanical oscillator, arXiv:2005.04260 (2020).
- [191] Kumar, T., Bhattacharjee, A. B., and ManMohan, Dynamics of a movable micromirror in a nonlinear optical cavity, *Physical Review A* **81**, 013835 (2010).
- [192] Mikkelsen, M., Fogarty, T., Twamley, J., and Busch, Th., Optomechanics with a position-modulated Kerr-type nonlinear coupling, *Physical Review A* **96**, 043832 (2017).

- [193] Asjad, M., Abari, N. E., Zippilli, S., and Vitali, D., Optomechanical cooling with intracavity squeezed light, *Optics Express* **27**, 32427-32444 (2019).
- [194] Gan, J.-H., Liu, Y.-C., Lu, C., Wang, X., Tey, M.-K., and You, L., Intracavity-Squeezed Optomechanical Cooling, *Laser Photonics Reviews* **13**, 1900120 (2019).
- [195] Qiu, L., Shomroni, I., Ioannou, M. A., Piro, N., Malz, D., Nunnenkamp, A., and Kippenberg, T. J., Floquet dynamics in the quantum measurement of mechanical motion, *Physical Review A* **100**, 053852 (2019).
- [196] Lau, H.-K., and Clerk, A. A., Ground-State Cooling and High-Fidelity Quantum Transduction via Parametrically Driven Bad-Cavity Optomechanics, *Physical Review Letters* **124**, 103602 (2020).
- [197] Krantz, P., Kjaergaard, M., Yan, F., Orlando, T. P., Gustavsson, S., and Oliver, W. D., A quantum engineer's guide to superconducting qubits. *Applied Physics Reviews* **6**, 021318 (2019)
- [198] Castellanos-Beltran, M. A., Irwin, K. D., Hilton, G. C., Vale, L. R., and Lehnert, K. W., Amplification and squeezing of quantum noise with a tunable Josephson metamaterial. *Nature Physics* **4**, 929-931 (2008)
- [199] Leghtas, Z., Touzard, S., Pop, I. M., Kou, A., Vlastakis, B., Petrenko, A., Sliwa, K. M., Narla, A., Shankar, S., Hatridge, M. J., Reagor, M., Frunzio, L., Schoelkopf, R. J., Mirrahimi, M., and Devoret, M. H., Confining the state of light to a quantum manifold by engineered two-photon loss. *Science* **347**, 853-857 (2015)
- [200] Drummond, P. D. and Walls, D. F., Quantum theory of optical bistability. I. Non-linear polarisability model. *Journal of Physics A: Mathematical and General* **13**, 725 (1980)
- [201] Khandekar, C., Lin, Z., and Rodriguez, A. W., Thermal radiation from optically driven Kerr ( $\chi^{(3)}$ ) photonic cavities. *Applied Physics Letters* **106**, 151109 (2015)
- [202] Huber, J. S., Rastelli, G., Seitner, M. J., Kölbl, J., Belzig, W., Dykman, M. I., and Weig, E. M., Spectral Evidence of Squeezing of a Weakly Damped Driven Nanomechanical Mode. *Physical Review X* **10**, 021066 (2020)
- [203] Khosla, K. E., Vanner, M. R., Ares, N., and Laird, E. A., Displacemon Electromechanics: How to Detect Quantum Interference in a Nanomechanical Resonator. *Physical Review X* **8**, 021052 (2018)
- [204] Kounalakis, M., Blanter, Ya. M., and Steele, G. A., Synthesizing multi-phonon quantum superposition states using flux-mediated three-body interactions with superconducting qubits. *npj Quantum Information* **5**, 100 (2019)
- [205] Brock, B. L., Blencowe, M. P., and Rimberg, A. J., Frequency Fluctuations in Tunable and Nonlinear Microwave Cavities. *Physical Review Applied* **14**, 054026 (2020)

- [206] Capelle, T., Flurin, E., Ivanov, E., Palomo, J., Rosticher, M., Chua, S., Briant, T., Co-hadon, P.-F., Heidmann, A., Jacqmin, T., and Deléglise, S., Probing a Two-Level System Bath via the Frequency Shift of an Off-Resonantly Driven Cavity. *Physical Review Applied* **13**, 034022 (2020)